Porous drug-loaded nanoparticles with engineered coatings

Jingwen Qiu

Thèse de doctorat

NNT : 2021UPASF029

université PARIS-SACLAY

Porous drug-loaded nanoparticles with engineered coatings

Ingénierie de la surface de nanoparticules poreuses chargées en molécules actives

Thèse de doctorat de l'université Paris-Saclay

École doctorale n° 571 sciences chimiques : molécules, matériaux, instrumentations et biosystèmes (2MIB)
Spécialité de doctorat: Chimie
Unité de recherche : Université Paris-Saclay, CNRS, Institut des Sciences Moléculaires d'Orsay, 91405, Orsay, France
Référent : Faculté des Sciences d'Orsay

Thèse présentée et soutenue à Orsay, le 07 Septembre 2021, par

Jingwen QIU

Composition du Jury

Laure CATALA Professeure, Université Paris-Saclay	Présidente
Patrick SAULNIER Professeur, Université Angers	Rapporteur & examinateur
Jean-Luc SIX Professeur, Université de Lorraine	Rapporteur & examinateur
Giorgia URBINATI Chargée de recherche, Institut de Cancérologie Gustave Roussy	Examinatrice
Marion ESTELLE Professeure, Institut de Recherche et d'Ingénierie de la Santé	Examinatrice

Direction de la thèse

Ruxandra GREF Directrice de Recherche CNRS, Université Paris-Saclay	Directrice de thèse

Résumé : L'utilisation de nanomatériaux hybrides organiques-inorganiques (nanoMOFs) pour le diagnostic et le traitement de maladies graves, telles que le cancer et les infections, suscite un intérêt croissant. Cependant, immédiatement après leur administration, les nanoMOFs interagissent fortement avec leur environnement physiologique, notamment avec les protéines plasmatiques. Par conséquent, ils sont rapidement éliminés de la circulation sanguine et ne peuvent pas atteindre leur cible, par exemple, la tumeur à traiter. Cette élimination prématurée limite considérablement l'utilisation des nanoMOFs pour des applications pratiques.

Pour relever les défis liés à la séquestration des nanoMOFs par le système immunitaire, nous avons développé plusieures stratégies pour recouvrir les nanoMOFs de revêtements "furtifs". Pour ce faire, des chaînes de poly(éthylène glycol) (PEG) ont été greffées de manière covalente à des copolymères qui ont été adsorbés sur les nanoMOFs.

Cependant, par rapport aux nanoparticules denses non-poreuses, la modification de surface des nanoMOFs hautement poreux pose des verrous technologiques et est beaucoup plus délicate. En effet, il a été démontré que les chaînes de PEG peuvent pénétrer dans les pores des nanoMOFs, enduisant une libération prématurée des molécules actives encapsulées. Par conséquent, dans cette étude, nous avons développé différentes stratégies pour modifier la surface des particules de nanoMOFs avec des revêtements multifonctionnels sans perturber leur capacité d'encapsulation de médicaments. En même temps, nous nous sommes attachés à mettre au point des méthodes de recouvrement et d'encapsulation par chimie verte, sans emploi de solvants organiques.

La première stratégie a consisté à synthétiser des copolymères de type « peigne » constitués de dextrane (DEX), de PEG et d'alendronate (ALN). Le DEX joue le rôle de macromolécule volumineuse, empêchant les chaînes de PEG de pénétrer à l'intérieur des nanoMOFs, tandis que les chainons d'ALN sont des groupements complexant le fer en surface des nanoMOFs, pour ancrer fermement les copolymères de type « peigne » de manière rapide et stable aux nanoMOFs. Les copolymères DEX-ALN-PEG ont été obtenus par chimie click en faisant varier les nombre d'unités PEG et ALN qui ont été greffées. Ils ont été caractérisés par un ensemble de techniques physicochimiques, puis adsorbés spontanément sur les nanoMOFs par simple incubation dans l'eau, sans solvant ni agent de couplage.

Comme alternative, d'autres matériaux de recouvrement cette fois biodégradables ont été obtenus en réticulant la γ-cyclodextrine (CD) greffée avec des chaines de PEG avec l'acide citrique. En effet, l'acide citrique peut également se coordonner efficacement aux sites de fer disponibles situés au niveau de la surface des nanoMOFs. En outre, les cavités des CDs offrent des avantages supplémentaires, tels que l'incorporation de molécules actives à caractère hydrophobe qui forment des complexes d'inclusion.

De manière avantageuse, les copolymères CD-citrate peuvent également être fonctionnalisés avec des fluorophores tels que la cyanine-5, permettant ainsi de d'appréhender le mécanisme d'enrobage des nanoMOFs ainsi que leur stabilité dans de milieux variés. Une molécule anticancéreuse d'intérêt, la doxorubicine (DOX), a été incorporée avec succès dans les nanoMOFs, atteignant des charges allant jusqu'à 64±2 wt%. D'après les études de résonance magnétique nucléaire à l'état solide (ssNMR), la DOX se trouvait à la fois dans les cœurs et dans les coquilles des nanoMOFs. Fait remarquable, la DOX incorporée n'a pas été libérée à un pH physiologique de 7,4, alors qu'elle l'a été immédiatement dans un milieu mimant le milieu intracellulaire lysosomial.

Les études par microscopie confocale ont apporté des résultats intéressants et prometteurs, montrant l'influence de la charge en DOX sur son mécanisme de libération. A forte charge en DOX, lorsque les nanoMOFs ont été mis en contact avec des cellules cancéreuses (lignée cellulaire Hela), la DOX n'a pas été libérée dans le milieu extracellulaire. A des charges optimales en DOX, une libération a été possible avec une diffusion de la DOX au niveau du noyau cellulaire. En parallèle les nanoMOFs cœur-couronne ont été dégradés au sein des cellules et un signal fluorescent correspondant au recouvrement a été détecté dans le cytosol. Il est intéressant de noter que les nanoMOFs pénètrent à l'intérieur des cellules avec leur revêtement, puis se dégradent dans le milieu intracellulaire, libérant à la fois leur revêtement et la substance active, ce qui a permis d'éradiquer les cellules cancéreuses.

Les matériaux mis au point dans ce travail sont très versatiles, leur composition peut être modulée de part les paramètres mis en jeu lors de leur synthèse. Ils peuvent être greffés de manière simple et rapide sur les nanoMOFs dans l'eau, par incubation. Notre stratégie repose sur l'établissement de multiples interactions coopératives entre les copolymères et la surface des nanoMOFs, assurant une bonne stabilité même dans de milieux biologiques complexes ? Cette étude ouvre la voie à l'ingénierie de surface de particules hautement poreuses pour des applications biomédicales.

Title : Porous drug-loaded nanoparticles with engineered coatings

Keywords : core-shell nanoparticles; polymer/oligomer synthesis; "stealth" drug carrier; anticancer

Abstract: The use of nanoscale metal organic frameworks (nanoMOFs) in diagnosis and treatment of severe diseases such as cancer and infections is of increasing interest. Nonetheless, immediately after their administration, nanoMOFs strongly interact with their physiological environment, including plasma proteins and cells. As a result, they are rapidly cleared from the blood circulation and cannot reach their targets. This premature elimination significantly limits the nanoMOF use in clinical practice.

To address the challenges related to the nanoMOF sequestration by the immune system, we developed two strategies to cover the nanoMOFs with "stealth" coatings. To do so, poly(ethylene glycol) (PEG) chains were covalently grafted to polymers which were adsorbed onto the nanoMOFs.

Compared to dense non porous nanoparticles, the surface modification of porous nanoMOFs is much more challenging. Indeed, it was disclosed that PEG chains can penetrate into the pores, displacing the loaded drug. Therefore, in this study, we developed different strategies to modify the surface of nanoMOF particles with multi-functional coatings without disturbing their drug loading capacity.

The first strategy was to synthesize comb-like co-polymers made of of dextran (DEX), PEG and alendronate (ALN). DEX acts as bulky macromolecule preventing the PEG chains to penetrate inside the nanoMOFs, whereas ALN moieties are the iron complexing groups to firmly anchor the coatings to the nanoMOFs. The DEX-ALN-PEG copolymers were obtained by click chemistry. They were spontaneously coated onto the nanoMOFs by incubation in water.

The resulting stable shells successfully decreased the nanoMOFs' uptake by macrophages *in vitro*.

In an alternative approach, biodegradable PEG-based coatings were engineered by cross-linking PEG-grafted γ-cyclodextrin (CD) with citric acid, which could also efficiently coordinate with nanoMOF surface iron sites. In addition, the CD cavities offer additional benefits such as drug incorporation inside the shell. The copolymers could be functionalized also with fluorophores such as Cyanines-5, allowing deciphering the coating mechanism. Doxorubicin (DOX) was successfully incorporated into the core-shell nanoMOFs reaching loadings up to 64±2 wt%. According to solid state nuclear magnetic resonance (ssNMR) investigations, DOX located both in the cores and in the shells.

Remarkably, the incorporated DOX didn't release out at physiological pH 7.4, whereas it released out immediately in artificial lysosome fluid (ALF). Confocal microscopy investigations were in good agreement with these findings: when nanoMOFs were put in contact with cancer cells (Hela cell line), DOX was not released in the extracellular medium, but only inside the cells. Noteworthy, the engineered nanoMOFs penetrate inside the cells together with their coatings, and then degrade intracellularly, releasing both their coatings and the active dug cargo, which in turn eradicated the cancer cells.

This study pave the way towards engineered the surface of highly porous particles for biomedical applications.

Title : Ingénierie de la surface de nanoparticules poreuses chargées en molécules actives

Mots-clés : nanoparticules cœur-couronne ; synthèse de polymère/oligomère ; vecteur de médicament "furtif" ; principe actif anticancéreux.

L'utilisation de nanomatériaux hybrides organiques-inorganiques (nanoMOFs) pour le diagnostic et le traitement de maladies graves, telles que le cancer et les infections, suscite un intérêt croissant. Cependant, immédiatement après leur administration, les nanoMOFs interagissent fortement avec leur environnement physiologique, notamment avec les protéines plasmatiques. Par conséquent, ils sont rapidement éliminés de la circulation sanguine et ne peuvent atteindre leurs cibles. Cette élimination prématurée limite considérablement l'utilisation des nanoMOFs en pratique clinique.

Pour relever les défis liés à la séquestration des nanoMOFs par le système immunitaire, nous avons développé deux stratégies pour recouvrir les nanoMOFs de revêtements "furtifs". Pour ce faire, des chaînes de poly(éthylène glycol) (PEG) ont été greffées de manière covalente à des polymères qui ont été adsorbés sur les nanoMOFs.

Par rapport aux nanoparticules denses non-poreuses, la modification de surface des nanoMOFs poreux est beaucoup plus difficile. En effet, il a été révélé que les chaînes de PEG peuvent pénétrer dans les pores, chassant le médicament encapsulé. Par conséquent, dans cette étude, nous avons développé différentes stratégies pour modifier la surface des particules de nanoMOFs avec des revêtements multifonctionnels sans perturber leur capacité d'encapsulation de médicaments.

La première stratégie a consisté à synthétiser des copolymères de type « peigne » constitués de dextran (DEX), de PEG et d'alendronate (ALN). Le DEX agit comme une macromolécule volumineuse empêchant les chaînes de PEG de pénétrer à l'intérieur des nanoMOFs, tandis que les fragments d'ALN sont des groupes complexant le fer pour ancrer fermement les revêtements aux nanoMOFs.

Les copolymères DEX-ALN-PEG ont été obtenus par chimie click. Ils ont été spontanément adsorbés sur les nanoMOFs par incubation dans l'eau.

Comme alternative, d'autres matériaux de recouvrement cette fois biodégradables ont été obtenus en réticulant la γ-cyclodextrine (CD) greffée au PEG avec de l'acide citrique, qui peut également se coordonner efficacement avec les sites de fer disponibles de la surface des nanoMOFs. En outre, les cavités CD offrent des avantages supplémentaires tels que l'incorporation de médicaments à l'intérieur de la couronne. Les copolymères pourraient également être fonctionnalisés avec des fluorophores tels que les cyanines-5, permettant ainsi de comprendre le mécanisme d'enrobage.

La doxorubicine (DOX) a été incorporée avec succès dans les nanoMOFs, atteignant des charges allant jusqu'à 64.3±2.3 wt%. D'après les études de résonance magnétique nucléaire à l'état solide (ssNMR), la DOX se trouvait à la fois dans les cœurs et dans les coquilles.

Fait remarquable, la DOX incorporée n'a pas été libérée à un pH physiologique de 7,4, alors qu'elle l'a été immédiatement dans un milieu mimant le lysosome artificiel (ALF). Les études par microscopie confocale ont confirmé ces résultats : lorsque les nanoMOFs ont été mis en contact avec des cellules cancéreuses (lignée cellulaire Hela), la DOX n'a pas été libérée dans le milieu extracellulaire, mais uniquement à l'intérieur des cellules. Il est intéressant de noter que les nanoMOFs pénètrent à l'intérieur des cellules avec leur revêtement, puis se dégradent dans le milieu intracellulaire, libérant à la fois leur revêtement et la substance active, ce qui a permis d'éradiquer les cellules cancéreuses.

Cette étude ouvre la voie à l'ingénierie de surface de particules hautement poreuses pour des applications biomédicales.

Acknowledgement

First of all, I am very grateful for the support of my thesis supervisor Dr. Ruxandra Gref for creating the great research environment where I have performed my six months' internship and four years' PhD studies. I am super proud to be one of her PhD student. The joy and enthusiasm she possessed for her great work inspire me during all these years. Moreover, I am quite impressed by her intelligence, immense knowledge, patience, and kindness to me and my family. Not only do I appreciate the time she has taken to guide me in all of my research and the writing of this thesis, I am really thankful to all her contributions of ideas, and connections with the collaborators to make my PhD study productive. Furthermore, I will never forget that five years ago, it is all her great help both mentally and financially that makes the turning point in my life. I left the company in China where I have worked for five years and came back to university (in France) to expand my knowledge. This is a "key" for me to enter into a promising future with more opportunities to pursue my interest, fulfill my dream in science and realize the value of life. I am very happy to have my life established in France with my wife (Xue Li) who is also working with Dr. Ruxandra Gref and my son who is more than 3 years old. This is the life I could not image 5 years ago. Words cannot express all my gratitude, but she is the real angel that God sent to me in my life. I will never forget in all my life.

I would like to thank Prof. Jiwen Zhang in Shanghai Institute of Materia Medica, Chinese Academy of Sciences. He is my wife's master supervisor, who not only kindly recommended my wife as a Ph.D candidate, but also supported me to apply for my founding from China Scholarship Council (CSC). Without his valuable support it would be more difficult to start this research.

I appreciate Prof. Jingui Qin in Wuhan University, Prof. Jie Zeng in University of Science and Technology of China, Prof. Xuesi Chen and Jianxun Ding in Key Laboratory of Polymer Ecomaterials, Chinese Academy of Sciences for supporting me with the recommendation letter for my PhD application.

I would also like to thank my thesis committee: Prof. Patrick Saulnier in Université Angers, Prof. Jean-luc.Six in Université de Lorraine, Prof. Estelle MARION in Institut de Recherche et d'Ingénierie de la Santé, Prof. Giorgia.Urbinati in Institut de Cancérologie Gustave Roussy and

Prof. Catala Laure in Université Paris Saclay, for their insightful comments and encouragement, and also for their questions which urged me to widen my research from various perspectives.

My sincere thanks also goes to my colleagues in my team. Firstly, Dr. Xue Li is with me all my way during my PhD. She helped me especially in the biological experiments including the cell culture, confocal experiments, and cytotoxicity assay. She is very helpful, not only design the experiment, but also revise papers. I appreciate that she is super patient to explain me the experiments in detail. Dr. Mario Menendez-Miranda, Vikramjeet Singh, Ms. Ioanna Christodoulou and Seray Ural were very helpful. It will be a nice memory to work with them.

Many thanks to all my collaborators in completing my thesis. I appreciate Prof. Philippe Roger, Prof. Nadine Aubry-Barroca, and Prof. Caroline Aymes-Chodur in Institut de chimie moléculaire et des matériaux d'Orsay for providing me the working place for the synthesis and characterization of CD-citrate oligomers; Dr. Antonio Vargas-Berenguel, Dr. Juan M. Casas-Solvas in University of Almería (Spain) for the synthesis of CD-PEG and CD-cy5 etc; Dr. Luc Picton and Dr. Christophe Rihouey for the performance of Size-exclusion chromatography.

Last but not the least, I would like to express my profound gratitude to my parents and parents-in-law for their unfailing support throughout the process of researching and all my life. Although my mother-in-law was discovered to have small cell lung cancer in May, 2016, thanks be to God, she is still very strong and her continuous encouragement gave me great strength to face all of the difficulties. I am very thankful for my brother and my sister-in-law for the financial support. Most of all, I wish to thank my wife, Xue Li. She chose to accompany with me to help me complete my PhD study in Orsay after her PhD. “Words cannot express my thankfulness toward my wife.

Regrettably, but inevitably, the list of my gratitude will be incomplete, and I hope that those who are missing will forgive me, and will still accept my sincere appreciation of their influence on my work.

Table of Contents

Abbreviations

Ad	Adamantyl
ALF	artificial lysosomal fluid
ALN	alendronate
AMOX	Amoxicillin
AZT-MP	Azidothimidine monophosphate
AZT-TP	Azidothimidine triphosphate
BCA	bicinchoninic acid
BET	Brunauer, Emmett and Teller
BTC	1,3,5 benzene tricarboxylate
$CaCl_2$	calcium chloride
CD	Cyclodextrin
CD-CO	γ-cyclodextrin-citrate oligomers
CD-MOFs	Cyclodextrin-based metal organic frameworks
CD-P	phosphorylated CD
CD-PEG-CO	γ-cyclodextrin-PEG-citrate oligomers
ConA	concanavalin A
CP-MAS	cross-polarization under MAS
CTAB	Cetyl trimethylammonium bromide
Cy5	cyanine 5
DCM	Dichloromethane
DCTB	trans-2-[3-(4-tert-butylphenyl)-2-methyl-2-propenylidene]malononitrile
DDS	drug delivery systems
Dex	Dextran

DFOM	Deferoxamine mesylate salt
DHB	2,5-dihydroxybenzoic acid
DL	Drug loading
DLS	Dynamic light scattering
DMAP	4-dimethylaminopyridine
DMEM	Dulbecco's modified Eagle's medium
DMF	N,N-Dimethylformamide
DMSO	Dimethylsulfoxide
DOPC	1,2-dioleoyl-sn-glycero-3-phosphocholine
DOX	doxorubicin
DSBs	double strand breaks
DSPE-PEG 2000	1,2-distearoyl-sn-glycero-3-phosphoethanolamine-N-[amino (polyethylene glycol)-2000] sodium salt
EDC	N-(3-dimethylaminopropyl)-N′-ethylcarbodiimide hydrochloride
EDX	Energy-dispersive X-ray spectroscopy
EDTA	ethylenediaminetetraacetic acid disodium salt dihydrate
EtOAc	ethyl acetate
EtOH	Ethanol
EXSY	exchange spectroscopy
FBS	Fetal bovine serum
FDA	Food and Drug Administration
5-FU	fluorouracil
FTIR	Fouriertransform infrared
Gem-MP	Gemcitabine-monophosphate
HA	hyaluronic acid

HAADF-STEM	High-angle annular dark-field-STEM
HAS	Human serum albumin
hep	heparin
HOBt	hydroxybenzotriazole
HPLC	High Performance Liquid Chromatograph
HRTEM	High resolution TEM
ICP-MS	Inductively coupled plasma mass spectrometry
ITC	Isothermal titration calorimetry
LPZ	Lansoprazole
MALDI-TOF-MS	matrix-assisted laser desorption/ionization time-of-flight mass spectrometry
MAS NMR	magic-angle spinning NMR
MBLs	mannose-binding lectins
MIL	Materials of Institut Lavoisier
Mn	The number average molecular weight
MOFs	Metal-organic frameworks
MOGs	metal organic gels
MRI	Magnetic Resonance Imaging
MsCl	Methanesulfonyl chloride
MTT	3-[4,5-dimethylthiazol-2-yl]-3,5-diphenyl tetrazolium bromide
Mw	The weight average molecular weight
MWCO	molecular weight cut-off
NaCl	sodium chloride
nanoMOFs	nano-scaled MOFs
NaAsc	(+)-sodium l-ascorbate

NaOH	Sodium hydroxide
NanoMOFs	Nanoscale metal–organic frameworks
NHS	N-hydroxysuccinimide
NMR	nuclear magnetic resonance
NPs	Nanoparticles
NTA	Nanoparticle tracking analysis
PAA	Polyacrylic acid
PBS	Phosphate buffer saline
PEG	polyethylene glycol
PLGA	poly(lactic-co-glycolic) acid
RF	Radio Frequency
Rhod	Rhodamine
RPMI	Roswell Park Memorial Institute
SEC	Size-exclusion chromatography
SEM	Scanning electron microscopy
SiNPs	PEGylated silicon nanoparticles
SSB	single strand breaks
S-RESPDOR	Symmetry-based Resonance-Echo Saturation-Pulse Double-Resonance
ssNMR	solid state nuclear magnetic resonance
TDL	Theoretical drug loading
TEG	tetraethylene glycol
TEM	Transmission electron microscopy
TGA	Thermogravimetric analysis
THF	tetrahydrofuran
TLC	Thin layer chromatography
TMS	tetramethylsilane

2D	two-dimensional
XPS	X-ray photon spectroscopy
XRDP	X-ray powder diffraction patterns
ZP	Zeta potential

General Introduction

Among the increasing number of nano-drug delivery systems developed so far (e.g. liposomes, lipids, polymers, metallic nanoparticles, dendrimers, silicon, carbon nanotubes, etc), nanoscale hybrid Metal-Organic Frameworks (nanoMOFs) are presently drawing a growing attention due to their unprecedented porosity, versatile composition and topology, enabling high loadings of a large number of drugs together with their controlled release [1–5]. However, the biological applications of nanoMOFs are still in their infancy: no systems reached the clinic stage and the *in vivo* investigations of their pharmacological efficacy are still rare. The main reasons are the stability issues and the *in vivo* fate of nanoMOFs. Indeed, as-synthesized nanoMOFs without surface modification easily aggregate during storage. Moreover, once administered in vivo by the iv route, they can aggregate and are readily recognized and uptook by the immune system. Uncoated nanoMOFs are prone to be removed from the blood circulation quickly before reaching their targets. Therefore, it is crucial to functionalize the nanoMOFs surface in order to achieve stealth (long-circulating) and targeting properties for biomedical applications.

Since more than 30 years, among all the coating materials, such as silica, lipid, and polymers, it was revealed that surface modification with hydrophilic polymers such as poly (ethylene glycol) (PEG) in a "brush" configuration could remarkably prolong the blood circulation times of NPs by reducing their recognition by the reticuloendothelial system [6,7]. However, so far, only a few cases aiming to functionalize the surface of nanoMOFs with PEG shells have been reported[8–12]

Indeed, it is a big challenge to functionalize the surface of nanoMOFs with PEG chains, because they are: 1) biodegradable, requiring green coating methods which will not degrade them or fill their pores with side-products or reactants; and 2) highly porous, so the coating materials should not penetrate into the pores, leading to undesirable drug release. Consequently, the real challenge for the application of nanoMOFs in the field of biomedicine remains not only on achieving high payloads and controlled releases, proper particle size and stability but also on functionalizing the surface of the nanoMOFs, which plays an important role on the *in vivo* fate of the nanocarriers.

The ''ideal'' nanoMOFs coating should reach the following goals: 1) only anchor onto the surface of nanoMOFs, but not enter into the porous structure; 2) not disturb the loaded drugs; 3) improve the colloidal stability of nanoMOFs during storage and in biological media; 4) have stealth effect, i.e. avoid opsonization to enable a longer circulation time and 5) target to the

disease lesions. These topics are presented in Chapter 1, together with a detailed review of the literature[13].

To achieve these challenging objectives, two main strategies (Schema 1) have been developed to functionalize the surface of nanoMOFs.

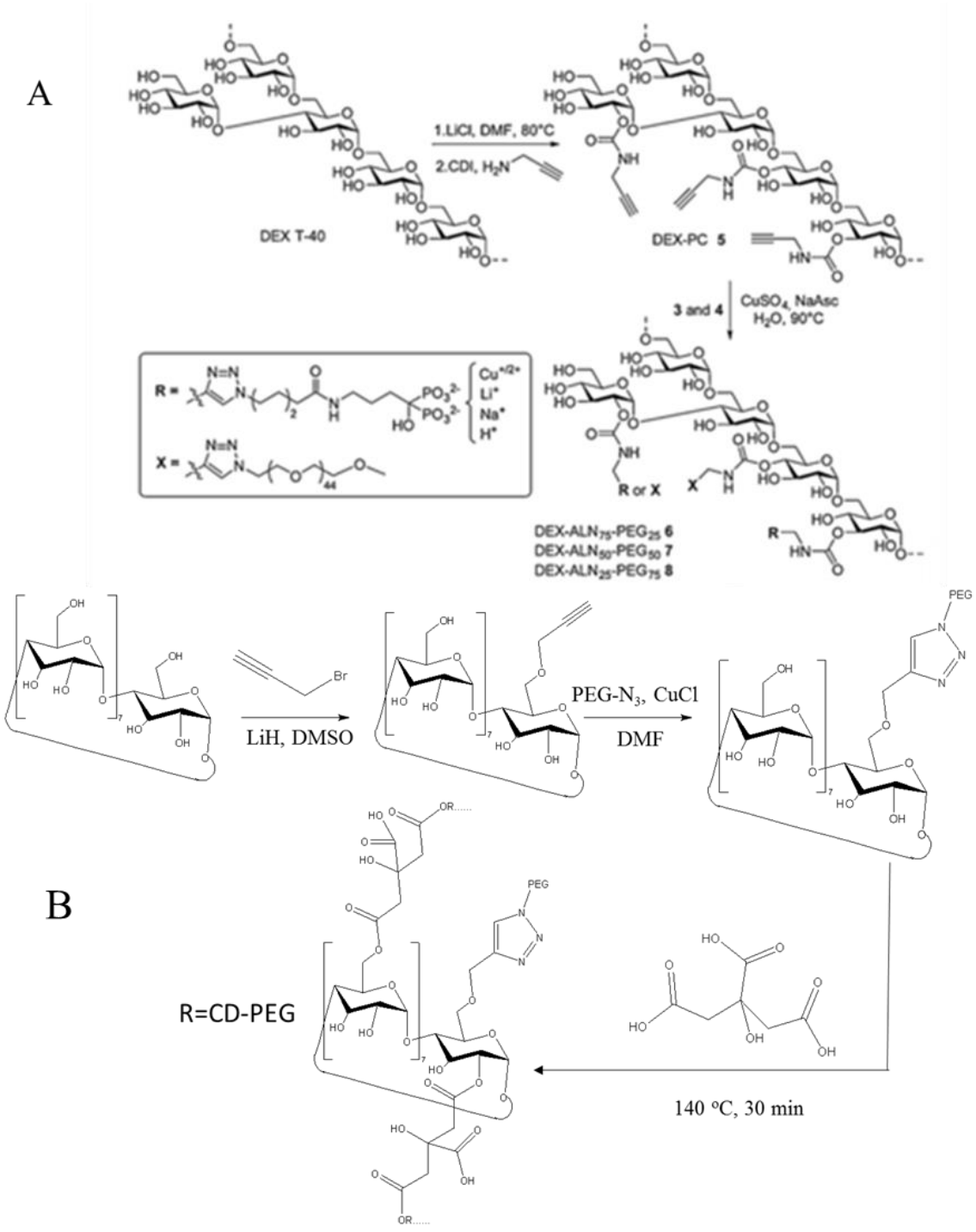

Schema 1: The synthesis of DEX-ALN-PEG (A) and CD-citrate-PEG oligomers (B)

The first strategy was synthesis of co-polymers by linking multifunctional chains in the backbone. In this study, biocompatible dextran was chosen as the backbone, and was grafted with alendronate (ALN) which can spontaneously coordinate to the nanoMOFs surface and PEG chains that can reduce macrophage uptake.

Dextran-alendronate-PEG copolymers (DEX-ALN-PEG) were successfully synthesized by click chemistry. The amounts of PEG and ALN moieties in this copolymers were controllable by tuning the molar ratio between them. DEX-ALN-PEG copolymers could spontaneously anchor onto the outer surface of MIL-100(Fe) by green method, without any surfactant or organic solvent, just socking nanoMOFs with DEX-ALN-PEG in pure water. The optimized coatings were able to greatly reduce the nanoMOFs adsorption by HSA, which is the most abundant protein in human blood plasma. What is more, the coating could improve the nanoMOFs's colloidal stability and decrease three times the *in vitro* macrophages uptake (Chapter 2). However, the synthesis of DEX-ALN-PEG was very complicated, involved multi-step reactions with low total yield; DEX-ALN-PEG is not biodegradable.

The second strategy was to synthesize biodegradable γ-CD oligomers using citric acid as cross linker, which also plays a key role in anchoring the oligomers onto the external surface of the nanoMOFs due to the coordination between citrate and available surface-located iron sites from the nanoMOFs. More interestingly, γ-CD-citrate-PEG oligomers were successfully synthesized with the same method.

In order to obtain a biodegradable coating materials, a water soluble biocompatible cyclodextrin (CD)-based materials (γ-CD-citrate oligomers) were successfully synthesized by a facile and environmental friendly method. Stable core–shell NPs relied on iron trimesate nanoMOFs cores with γ-CD-citrate oligomers coatings, successfully prepared through a fast and "green" method. Furthermore, fluorescence lifetime microscopy was used to decode the coating mechanism due to the presence of the fluorophore which was also linked with the shell. Remarkably, doxorubicin (DOX) encapsulations reached 48 ± 10 wt% or 65 ± 8 wt% respectively, after 1 day or 2 days incubation with the drug solution (Chapter 3). Interestingly, CD coating could promote the loading process and accelerate DOX release. In order to investigate the nanoMOFs component localization at a molecular scale and study their physicochemical properties, ^{13}C-labeled CD-CO oligomers were synthesized using the reported method, and further coated on the external surface of MIL-100 (Al). A set of high-resolution solid state nuclear magnetic resonance (ssNMR) experiments were employed to achieve a deep understanding of the

interactions involved in the MIL-100(Al) core-shell structure. CD-citrate-PEG oligomers were successfully synthesized and further engineered on the outer surface of MIL-100 (Fe), enabled to reduce 2 times the in vitro uptake by macrophages. Remarkably, the DOX release from the DOX loaded nanoMOFs was pH responsive.

Finally, Chapter 4 is a comparative discussion of the coatings considering their synthesis routes, biodegradability, stabilities, interactions with cells, influences on drug loading and release. Then, a general conclusion and the perspectives of the work are presented.

Reference:

1. Rojas, S., Arenas-Vivo, A. & Horcajada, P. Metal-organic frameworks: A novel platform for combined advanced therapies. *Coord. Chem. Rev.* **388**, 202–226 (2019).
2. Simon-Yarza, T., Mielcarek, A., Couvreur, P. & Serre, C. Nanoparticles of Metal-Organic Frameworks: On the Road to In Vivo Efficacy in Biomedicine. *Adv. Mater.* **30**, 1–15 (2018).
3. He, C., Liu, D. & Lin, W. Nanomedicine Applications of Hybrid Nanomaterials Built from Metal-Ligand Coordination Bonds: Nanoscale Metal-Organic Frameworks and Nanoscale Coordination Polymers. *Chem. Rev.* **115**, 11079–11108 (2015).
4. Yang, J. & Yang, Y. Metal – Organic Frameworks for Biomedical Applications. *Small* **1906846**, 1–24 (2020).
5. Quijia, C. R., Lima, C., Silva, C. & Alves, R. C. Application of MIL-100(Fe) in drug delivery and biomedicine. *J. Drug Deliv. Sci. Technol.* **100**, 102217 (2021).
6. Gref, R. *et al.* The controlled intravenous delivery of drugs using PEG-coated sterically stabilized nanospheres. *Adv. Drug Deliv. Rev.* **16**, 215–233 (1995).
7. Gref, R. *et al.* Biodegradable long-circulating polymeric nanospheres. *Science (80-.).* **263**, 1600–1603 (1994).
8. Agostoni, V. *et al.* A "green" strategy to construct non-covalent, stable and bioactive coatings on porous MOF nanoparticles. *Sci. Rep.* **5**, 7925 (2015).
9. Zhang, H. H. *et al.* Effects of PEGylated paclitaxel nanocrystals on breast cancer and its lung metastasis. *Nanoscale* **7**, 10790–10800 (2015).
10. Edward Semple, J., Sullivan, B., Vojkovsky, T. & Sill, K. N. Synthesis and facile end-group quantification of functionalized PEG azides. *J. Polym. Sci. Part A Polym. Chem.* **54**, 2888–2895 (2016).
11. Simon-Yarza, T. *et al.* A smart metal-organic framework nanomaterial for lung targeting. *Angew. Chemie Int. Ed.* **56**, 15565–15569 (2017).
12. Giménez-marqués, M. *et al.* GraftFast surface engineering to improve MOF nanoparticles furtiveness. *Small* **14**, 1801900 (2018).

13. Qiu, J., Li, X., Gref, R. & Vargas-berenguel, A. *Carbohydrates in metal organic frameworks : Supramolecular assembly and surface modification for biomedical applications*. *Metal-Organic Frameworks for Biomedical Applications* (Elsevier Inc., 2020). doi:10.1016/B978-0-12-816984-1.00022-6

Chapter 1.1: Introduction

Over the years, nanotechnology is introducing more and more in our daily routine.[1,2]. This revolutionary technology has been applied in multiple fields through an integrated approach. An increasing number of applications and products containing nanomaterials or at least with nano-based claims have become available. This also happens in pharmaceutical research. The use of nanotechnology in the development of new medicines is now part of our research and in the European Union (EU) it has been recognized as a Key Enabling Technology, capable of providing new and innovative medical solution to address unmet medical needs [3–6].

The application of nanotechnology for medical purposes has been termed nanomedicine and is defined as the use of nanomaterials for diagnosis, monitoring, control, prevention and treatment of diseases. Core shell nanoparticles (NPs) with engineered surface are designed to target specifically to diseased cells, which allows for the direct treatment of those unhealthy cells. Therefore, they are expected to improve efficacy, decrease side effects, and overall improve human health by acting as drug carrier[3,7,8]. Various nanostructures, including liposomes, SLN (solid lipid nanoparticles), polymers, dendrimers, silicon, carbon materials, metallic nanoparticles, and more recently metal organic frameworks (MOFs) have been used as carriers in drug delivery systems[9–13].

The first case of reported NP as drug carrier was liposome. Liposomes are mainly composed of phospholipids that form bilayers with an aqueous phase inside. They were considered as typical nanomedicine, frequently evaluated in basic research and clinical medicine. In the recent literature, liposomes have been revealed to enhance the solubility of drugs and ameliorate their pharmacokinetics. For example, they allowed circumventing drawbacks of chemotherapeutic reagents, such as rapid metabolism, they decreased side effects and increase of anticancer activity. There are plenty of drug examples based on liposomal formulations, for instance, anticancer drugs, neurotransmitters (serotonin), antibiotics, anti-inflammatory, and anti-rheumatic drugs[7,14]. But the main disadvantages of liposome lies in sometimes low drug loading capacity and lack of stability.

The Polymeric NPs (PNPs) are achieved from synthetic polymers[15], such as polyacrylamide and polyacrylate, or natural polymers, for instance, albumin, DNA, chitosan. PNPs are recognized as biodegradable materials according to the in vivo behavior. Recently, polylactide (PLA) and poly (lactide-co-glycolide) (PLGA) approved by FDA, are most common utilized

for the preparation of polymeric biodegradable nano-DDS.

Solid lipid NPs (SLN) are particles stemmed from solid lipids, for example, complex glyceride mixtures, highly purified triglycerides, or waxes stabilized by different kinds of surfactants[7,16]. Good colloidal stability, protection of incorporated drugs from degradation, controlled drug release, and good tolerability are the major advantaged properties, which makes that SLN can be widely used for the application in the biomedical field. However, in the recent literature, some disadvantages have been found, such as low loading capacity due to the low solubility of drug in the lipid and the structure and polymorphic state of the lipid matrix, drug bursting out after crystallization.

Dendrimers are unique polymers with well-defined size and structure. They are highly branched macromolecules with controlled near monodisperse three-dimensional architecture emanating from a central core. Dendritic architecture is one of the most common structures detected among all biological systems. Several examples of nanometric molecules with dendritic structure include: glycogen, amylopectin, and proteoglycans. Poly (amido amide) (PAMAM) is an example of synthetic dendrimer material which is widely utilized in biomedical applications[17]. Not only the synthesis and structure of PAMAM dendrimers, but also the distribution of drugs or genes inside these compounds have been intensively studied.

Carbon nanomaterials employed in DDS can be divided into nanotubes (CNTs) and nanohorns (CNH). CNTs possess particular structure composed of rolling of single or multilayers of graphite with a huge surface area and an outstanding thermal and electronic conductivity[18,19]. Biocompatibility of CNTs may be ameliorated by chemical modification of their surface with macromolecules, such as employing covalent anchoring of PAMAM dendrimers, or amphiphilic diblock copolymers. Nanohorns which is a single-wall nanotubes– demonstrate similar characters to nanotubes. They can be easily prepared with very cheap materials and can be produced in good quality[19].

Silica materials involved in controlled drug delivery systems are composed of xerogels and mesoporous silica NPs (MSNs). They revealed several advantages as drug carrier systems, containing biocompatibility, an ease in terms of functionalization, and highly porous framework[10]. Silica materials are extensively employed as drug carriers for biological purposes, and are considered of main interest among inorganic NPs.

Metallic nanocarriers are a material of choice, because of their special characteristics, such as controllable size, large surface area, facile synthesis, interesting optical properties, etc[3,8].

Moreover, metallic NPs have intrinsic properties useful in nanomedicine. For example, iron oxides NPs are usually synthesized as alkaline co-precipitations of Fe^{2+} and Fe^{3+} salts in H_2O in the presence of a hydrophilic polymer such as dextran (DEX) or poly(ethylene glycol) (PEG). This yields an iron core of 4–5 nm in diameter, which can be used as contrast agents for magnetic resonance imaging. Gold NPs (GNPs) have an unique photodynamic property through absorption of near-infrared lights and emission of light and heat, which has been employed for cancer photothermal therapy. What's more, GNPs are conjugated with plenty of therapeutic agents and targeting moieties, and act as efficient drug carriers.

NanoMOFs

Though there are already so many NPs which can be used as nano DDS with their own advantages, they are also confronted with some limitations, such as, depending on the system, instability, rapid biodegradation, side effects incapacity to load drug combinations, and toxicities. To overcome these limitations, the development of new engineered carriers is essential. It is indeed important to ensure a prolonged and controlled drug release, reducing the administered doses and frequencies to decrease the side effects and improve patient compliance to the treatment.

In this context, a new class of porous hybrid materials, named as Metal-Organic Frameworks (MOFs), has been recently discovered and since has intensively used as a drug carrier to overcome the above mentioned challenges. MOFs are organic-inorganic hybrid porous networks based on organic polydentate ligands and inorganic units. Since their discovery in 1989[20], there has been increasingly more attention paid on MOFs because of their fruitful applications in gas storage, separation, catalysis, sensing, energy, optics, and recently, in drug delivery system[9–13,21–23]. One of the crucial advantages of the MOFs is their easily tunable composition. The composition and structure of these porous hybrid materials can easily be adjusted through the almost unlimited possible combination of metal inorganic subunits and/or constitutive organic ligands, contributing to thousands of MOFs with special functions[24]. The first case of reported use of MOFs as DDS[25] and as contrast agents[26] was in 2006. The MOFs used for this study was iron polycarboxylate MOFs, which have emerged as a novel type of biodegradable, biocompatible, and non-toxic drug carriers. MOFs were demonstrated to entrap large amounts (within the 20–70 wt% range) of various drugs able to be effectively penetrate within the porous 3D structures. Successful drug incorporation relies on the high pore volumes and surface areas of the MOFs. Since 2006, MOFs were extensively investigated in the

biomedical applications.

Nanosized MOFs (nanoMOFs), due to their small particle size, can indeed ameliorate the drug delivery properties to treat many diseases[9,23]. Furthermore, MOFs possess lots of key characteristics that indeed confer them outstanding attributes as drug carriers for the controlled release of drugs[27]. Indeed, engineered nanoMOFs possess the following features: 1) high drug adsorption capacities (payload and efficiency), 2) controlled drug release getting rid of "burst" effect (rapid release of the selected drug in very short time), 3) ability to target abnormal cells and organs in a selective way, 4) low toxicity by gradually degrading and elimination of byproducts without accumulation in the body, 5) a facile modification of the outer surface of the NPs for an enhanced in vivo stability and/or targeting, and 6) possibility of incorporating biofriendly contrast agents[28,29].

In the past few years, various research works have revealed the great potential of MOFs in the biomedical field as DDS, biosensors, biocatalysts, contrast agents, decontamination agents and photothermal therapy (PTT), and so on[9,12,13]. Several of them were published until recently based primarily on their bioactive composition, treatment of severe diseases[11]. Noticeable, nanoMOFs approaching a preclinical in vivo investigation are those relying on Fe carboxylates[13,30].

Surface Modification of nanoMOFs

Up to now, there is a huge gap between the large number of studies reporting the potential of MOFs to be used for biomedical applications and contrasts with the few number of in vivo pharmacological efficacy investigations studied to date[11]. There are several reasons which can explain this situation.

Firstly, colloidal stability issues and/or lack of organ or tissue targeting properties. It is well known that intravenous (i.v.) injection of NPs needs dispersion in an isotonic solution (for instance 0.9% saline or 5% glucose) for isotonicity. Various nanoMOFs, especially once dried, cannot be re-dispensed yet in these media and have the tendency to aggregate rapidly, making administration impossible due to risk of embolization. Colloidal stability of nanoMOFs is still a main problem that becomes a big challenge for in vivo administration[10]. Selective modification of the outer surface of nanoMOFs is thus crucial in order to overcome such challenges.

Secondly, short blood circulation times (opsonization after injection of uncoated nanoMOFs). Very interestingly, surface modification of NPs with hydrophilic polymers can greatly decrease

the opsonization. Surface functionalization strategies of NPs and liposomes have been investigated during recent decades. The first case of PEGylated liposome was reported by Woodle and colleagues in 1992[31]. PEGylation of polymeric NPs was first reported in 1994 by Dr. Gref and co-workers[32,33], since then, an increasing number of studies focusing on PEGylation of other types of NPs have been reported[34–36]. NPs modified with PEG extends the circulation time *in vivo*, enabling their distribution in other organs. However, up to now, Doxil represents the only FDA-approved PEGylated liposomes for the treatment of cancer using doxorubicin (DOX)[37].

Generally, surface functionalization of NPs should meet some standard to be fit for drug delivery, such as a) bio-friendly synthesis method, without using any toxic additive, b) maintain drug release ability, c) not interfere with the loaded drugs, d) not penetrate into the porous architecture, e) improve nanoMOFs physical stability, and f) excellent stability under physiological conditions.

NanoMOFs can be functionalized with silica, lipid layer, carbohydrate, polymer, etc. In the following section, three types of coating materials containing silica coating, lipid layer encapsulation, and carbohydrate coating are considered.

Surface modification of nanoMOFs with thin silica shells can improve the stability of particles, elevate biocompatibility and water dispersibility, and enable functionalization with numerous silyl-derived compounds. In general, the outer surface of NanoMOFs are first modified with a polymer, such as polyvinylpyrrolidone (PVP) which can boost the silica coating process. Furthermore, tetraethylorthosilicate (TEOS) was used to treat the PVP-coated particles in basic ethanol to provide silica coatings. The silica shell thickness can be manipulated by tuning the reagent concentrations or/and reaction time. Release profile experiments revealed that a silica shell can remarkably slow down the rate of particle decomposition. Moreover, the outer surface of these core−shell architecture can be further functionalized through anchoring a silyl-derived molecule to the silica shell with surface silanol groups to provide important performance, such as optical contrast agents, sensory agents, and targeting ligands[10]. However, surface coatings were sometimes uneven and/or they were unstable. Moreover, no study so far dealt with PEG surface coatings.

Lipid have recently been used as coating materials of choice to modify the surfaces of nanoMOFs. Lipid bilayers not only slow the pharmacokinetic but also improve

biocompatibility[38]. The flexible nature of lipid bilayer is an advantage over the rigid silica coating. Wuttke and his colleagues reported the lipid DOPC (1,2-dioleoyl-snglycero-3-phosphocholine) coated nanoMOFs as a potential and new type of nanocarriers[38]. They revealed that this novel drug delivery system can efficiently load dye molecules inside the porous structure of the MOF while the lipid bilayer avoids their burst release. Effective uptake of the lipid coated nanoMOFs by cancer cells enables these nanocarriers promising for drug delivery and diagnostic. Based on this study, we further functionalized here nanoMOFs with PEGylated lipid, namely DSPE-PEG2000[27]. We found that the outer surface of nanoMOFs functionalization with lipids provides a better control over their degradation in biological media and drug release. Moreover, we found that the coatings were able not only to decrease macrophage uptake *in vitro* but also to eradicate cancer cells by carrying the drug inside.

Carbohydrates, one of the four major classes of biomolecules have been well-recognized as edible materials. The excellent properties of hydrophilicity and versatility play an important role for the carbohydrates to be used as surface modification materials for preformed drug nanocarriers. They present the advantages of: (i) low toxicity; (ii) could mediate the cell internalization; and (iii) can be easily further engineered with other functional moieties. Recently, carbohydrate-based materials, for instance, CDs[39], heparin[40], hyaluronic acid[34], and chitosan[41], which possess bigger molecular size than the pore size of nanoMOFs, have been frequently investigated as coating materials.

The first investigation of nanoMOF surface modification with carbohydrate coating material was reported by the group of Dr. Gref[39], where phosphorylated CD (CD-P) derivatives were employed to functionalize iron trimesate nanoMOFs MIL-100(Fe) in aqueous media, adopting a facile, one-step, and completely "green" (without any organic solvent or surfactant) method. Besides, CD-P were too bulky to penetrate into the porous of the nanoMOFs, leaving CD-P anchored only on the outer surface of nanoMOFs. In addition, the CD-P functionalization enables the possibility of PEGylation by formation of guest-host inclusion with adamantane-PEG chains[39]. Giménez-Marqués and her co-workers employed GraftFast surface engineering procedure to modify nanoMOF, using PEG and hyaluronic acid (HA) acrylates[34]. HA-PEG was covalently grafted by a single step GraftFast reaction on the surface of nanoMOFs. The resulting PEGylated nanoMOFs demonstrated improved colloidal stabilities in different kinds of biological media as compared with uncoated nanoMOFs, while preserving their porosity which enabled the adsorption of bioactive molecules. The PEG coating could decrease macrophage uptake *in vitro*. However, the *in*

situ synthesized HA-PEG is not biodegradable and the amount of PEG chains could not be well controlled by GraftFast reaction.

More recently, the water-soluble copolymer poly(3-hydroxyalkanoate) grafted with PEG chains were synthesized[42] to functionalize nanoMOFs. The resulting PEGylated nanoMOFs displayed improved colloidal stabilities in aqueous and physiological fluids and no cytotoxicity (up to 100 µg/mL) on murine macrophages J774.A1 cells. However, the stealth property still needs to be further investigated.

In this context, we focused in this thesis on the design and synthesis of novel biocompatible carbohydrate polymers with: 1) controlled PEG contents and 2) biodegradability. To reach the first goal, we grafted PEG chains to dextran backbones at different ratios[43]. As the second strategy, we applied polymerized PEGylated CDs, creating biodegradable ester bonds[44]. After the design and successful synthesis, we prepared core-shell NPs as drug delivery system using the synthesized coating materials as shell and the porous nanoMOFs as the core[43–46]. A set of complementary characterizing experiments were performed to characterize the coated nanoMOFs. Drug of interest was loaded into the coated nanoMOFs, in order to study the drug loading and release. The optimized formulations were finally evaluated *in vitro*.

References:

1. Chang, E. H. *et al.* Nanomedicine: past, present and future – a global perspective. *Biochem. Biophys. Res. Commun.* **468**, 511–517 (2015).
2. Kargozar, S. & Mozafari, M. Nanotechnology and Nanomedicine : Start small , think big. *Mater. Today Proc.* **5**, 15492–15500 (2018).
3. Matoba, T., Koga, J. & Nakano, K. Nanoparticle-mediated drug delivery system for atherosclerotic cardiovascular disease. *J. Cardiol.* **70**, 206–211 (2017).
4. Greish, K., Mathur, A., Bakhiet, M. & Taurin, S. Nanomedicine : is it lost in translation ? *Ther. Deliv* **9**, 269–285 (2018).
5. Webster, T. J. & Rafiee-, R. A review of drug delivery systems based on nanotechnology and green chemistry : green nanomedicine. *Int. J. Nanomedicine* **12**, 2957–2978 (2017).
6. Bayda, S., Adeel, M., Tuccinardi, T., Cordani, M. & Rizzolio, F. The History of Nanoscience and Nanotechnology : From Chemical – Physical Applications to Nanomedicine. *molecules* **25**, 1–15 (2020).

7. Wilczewska, A. Z., Niemirowicz, K., Markiewicz, K. H. & Car, H. Nanoparticles as drug delivery systems. *Pharmacol. Reports* **64**, 1020–1037 (2012).
8. Hossen, S. *et al.* Smart nanocarrier-based drug delivery systems for cancer therapy and toxicity studies : A review. *J. Adv. Res.* **15**, 1–18 (2019).
9. Horcajada, P. *et al.* Metal-Organic Frameworks in biomedicine. *Chem. Rev.* **112**, 1232–1268 (2012).
10. He, C., Liu, D. & Lin, W. Nanomedicine Applications of Hybrid Nanomaterials Built from Metal-Ligand Coordination Bonds: Nanoscale Metal-Organic Frameworks and Nanoscale Coordination Polymers. *Chem. Rev.* **115**, 11079–11108 (2015).
11. Simon-Yarza, T., Mielcarek, A., Couvreur, P. & Serre, C. Nanoparticles of Metal-Organic Frameworks: On the Road to In Vivo Efficacy in Biomedicine. *Adv. Mater.* **30**, 1–15 (2018).
12. Rojas, S., Arenas-Vivo, A. & Horcajada, P. Metal-organic frameworks: A novel platform for combined advanced therapies. *Coord. Chem. Rev.* **388**, 202–226 (2019).
13. Yang, J. & Yang, Y. Metal – Organic Frameworks for Biomedical Applications. *Small* **1906846**, 1–24 (2020).
14. Bulbake, U., Doppalapudi, S., Kommineni, N. & Khan, W. Liposomal Formulations in Clinical Use : An Updated Review development. *Pharmaceutics* **9**, 1–33 (2017).
15. Begines, B. *et al.* Polymeric Nanoparticles for Drug Delivery : Recent Developments and Future Prospects. *Nanomaterials* 1–38 (2020).
16. Montoto, S. S., Muraca, G. & Ruiz, M. E. Solid Lipid Nanoparticles for Drug Delivery : Pharmacological and Biopharmaceutical Aspects. *Front. Mol. Biosci.* **7**, 1–24 (2020).
17. Buwalda, S. J. *et al.* Ultrafast in situ forming poly(ethylene glycol)-poly(amido amine) hydrogels with tunable drug release properties via controllable degradation rates. *Eur. J. Pharm. Biopharm.* **139**, 232–239 (2019).
18. Mohajeri, M. Biomedical applications of carbon nanomaterials : Drug and gene delivery potentials. *J. cell physiol* **234**, 298–319 (2018).
19. Zhao, Q. *et al.* Mesoporous carbon nanomaterials in drug delivery and biomedical application. *Drug Deliv.* **24**, 94–107 (2017).
20. Robson, B. F. H. and R. Infinite Polymeric Frameworks Consisting of Three Dimensionally Linked Rod-like Segments. *J. Am. Chem. Soc* **15**, 5962–5964 (1989).
21. Dhakshinamoorthy, A. Catalysis and photocatalysis by metal organic frameworks. *Chem Soc Rev* **47**, 8134–8172 (2018).

22. Yang, J. *et al.* Recent advances in nanosized metal organic frameworks for drug delivery and tumor therapy. *RSC Adv.* **11**, 3241–3263 (2021).
23. Ahmed, S. A. *et al.* Nano-MOFs as targeted drug delivery agents to combat antibiotic-resistant bacterial infections. *R. Soc. Open Sci* **7**, (2020).
24. Horcajada, P. *et al.* Porous metal–organic-framework nanoscale carriers as a potential platform for drug delivery and imaging. *Nat. Mater.* **9**, 172–178 (2009).
25. Horcajada, P. *et al.* Metal-organic frameworks as efficient materials for drug delivery. *Angew. Chemie - Int. Ed.* **45**, 5974–5978 (2006).
26. Rieter, W. J., Taylor, K. M. L., An, H., Lin, W. & Lin, W. Nanoscale metal-organic frameworks as potential multimodal contrast enhancing agents. *J. Am. Chem. Soc.* **128**, 9024–9025 (2006).
27. Li, X. *et al.* Drug-Loaded Lipid-Coated Hybrid Organic-Inorganic " Stealth " Nanoparticles for Cancer Therapy. *Front. Bioeng. Biotechnol.* **8**, 1–12 (2020).
28. He, S. *et al.* Metal-organic frameworks for advanced drug delivery. *Acta Pharm. Sin. B* 1–89 (2021). doi:10.1016/j.apsb.2021.03.019
29. Qiu, J., Li, X., Gref, R. & Vargas-berenguel, A. *Carbohydrates in metal organic frameworks : Supramolecular assembly and surface modification for biomedical applications*. *Metal-Organic Frameworks for Biomedical Applications* (Elsevier Inc., 2020). doi:10.1016/B978-0-12-816984-1.00022-6
30. Tarek Baati, Leila Njim, Fadoua Neffati, Abdelhamid Kerkeni, Muriel Bouttemi, Ruxandra Gref, Mohamed Fadhel Najjar, Abdelfateh Zakhama, Patrick Couvreur, C. S. and P. H. In depth analysis of the in vivo toxicity of nanoparticles of porous iron(III) metal–organic frameworks. *Chem. Sci.* **4**, 1597–1607 (2013).
31. Woodle, M. C. *et al.* Versatility in lipid compositions showing prolonged circulation with sterically stabilized liposomes. *Biochim. ez Bh)physit'a Acta,* **5**, 193–200 (1992).
32. Gref, R. *et al.* Biodegradable long-circulating polymeric nanospheres. *Science (80-.).* **263**, 1600–1603 (1994).
33. Gref, R. *et al.* The controlled intravenous delivery of drugs using PEG-coated sterically stabilized nanospheres. *Adv. Drug Deliv. Rev.* **16**, 215–233 (1995).
34. Giménez-marqués, M. *et al.* GraftFast surface engineering to improve MOF nanoparticles furtiveness. *Small* **14**, 1801900 (2018).
35. Edward Semple, J., Sullivan, B., Vojkovsky, T. & Sill, K. N. Synthesis and facile end-group quantification of functionalized PEG azides. *J. Polym. Sci. Part A Polym. Chem.*

54, 2888–2895 (2016).

36. Zhang, H. H. *et al.* Effects of PEGylated paclitaxel nanocrystals on breast cancer and its lung metastasis. *Nanoscale* **7**, 10790–10800 (2015).
37. Barenholz, Y. Doxil® - The first FDA-approved nano-drug: lessons learned. *J. Control. Release* **160**, 117–134 (2012).
38. Sicklinger, J., Bellomo, C., Ra, J. O. & Vollmar, A. M. their uptake by cancer cells †MOF nanoparticles coated by lipid bilayers and their uptake by cancer cells. *Chem commun* **100**, 2–5 (2015).
39. Noiray, M., Malanga, M. & Aykac, A. A "green" strategy to construct non-covalent, stable and bioactive coatings on porous MOF nanoparticles. *Sci. Rep.* **5**, 1–7 (2015).
40. Bellido, E. *et al.* Heparin-Engineered Mesoporous Iron Metal-Organic Framework Nanoparticles: Toward Stealth Drug Nanocarriers. *Adv. Healthc. Mater.* **4**, 1246–1257 (2015).
41. Hidalgo, T. *et al.* Chitosan-coated mesoporous MIL-100(Fe) nanoparticles as improved bio-compatible oral nanocarriers. *Sci. Rep.* **7**, 1–14 (2017).
42. Jain-beuguel, C. *et al.* Water-Soluble Poly (3-hydroxyalkanoate) Sulfonate : Versatile Biomaterials Used as Coatings for Highly Porous Nano-Metal Organic Framework. *Biomacromolecules* **20**, 3324–3332 (2019).
43. Cutrone, G. *et al.* Comb-like dextran copolymers: A versatile strategy to coat highly porous MOF nanoparticles with a PEG shell. *Carbohydr. Polym.* **223**, 115085 (2019).
44. Cutrone, G. *et al.* Design of engineered cyclodextrin derivatives for spontaneous coating of highly porous metal-organic framework nanoparticles in aqueous media. *Nanomaterials* **9**, 1–26 (2019).
45. Qiu, J. *et al.* Self-assembled multifunctional core – shell highly porous metal – organic framework nanoparticles. *Int. J. Pharm.* **581**, 119281 (2020).
46. Li, X. *et al.* Doxorubicin-Loaded Metal-Organic Frameworks Nanoparticles with Engineered Cyclodextrin Coatings : Insights on Drug Location by Solid State NMR Spectroscopy. *Nanomaterials* **11**, 1–15 (2021).

Chapter 1.2: Carbohydrates in metal organic frameworks: Supramolecular assembly and surface modification for biomedical applications

CHAPTER 20

Carbohydrates in metal organic frameworks: Supramolecular assembly and surface modification for biomedical applications

Jingwen Qiu[a], Xue Li[a], Ruxandra Gref[a], Antonio Vargas-Berenguel[b]

[a]National Center for Scientific Research (CNRS), Institute of Molecular Sciences, Paris-Sud University, Paris-Saclay University, Orsay, France [b]Department of Chemistry and Physics, University of Almeria, Almería, Spain

20.1 Introduction

Nanotechnology revolutionizes drug delivery by achieving drug transcytosis, drug targeting, and theranostics. Biocompatible and biodegradable metal organic frameworks (MOFs) [1, 2] have been designed and synthesized for biomedical application. Recently, nanoscale MOFs (nanoMOFs) emerge as an attracting class of hybrid nanomaterials for biomedical application. MOFs are formed by the self-assembly of metal centers and bridging organic ligands, leading to the formation of crystalline architectures with regular and high porosities. They have been increasingly used for biomedical applications in the last decade, taking advantage of their high drug loading capability, biodegradability, and high versatility in terms of architecture and physico-chemical properties [1, 3–6]. However, the vast majority of MOFs described were composed of metallic ions or clusters and synthetic organic ligands. Recently, more and more attention was dedicated to the use of natural materials for the fabrication of MOFs, which are inherently compatible with the metabolic system [7, 8].

Carbohydrates (oligosaccharides and/or polysaccharides) have been well-recognized as edible materials. Together with lipids, proteins, and nucleic acids, they are one of the four major classes of biomolecules. Carbohydrates are unique candidates for drug-carrier preparation since they possess several advantages, such as biocompatibility and biodegradability. A variety of nanocarriers composed of carbohydrates have been reported [9, 10], including covalently/ionically cross-linked polysaccharide-based nanosponges [11], self-assemblies [12], dendrimers [10], nanocapsules [13], hydrogels [14], micelles [15], and multilayered polysaccharide vesicles [10]. However, the challenge in synthesizing MOFs from

Metal-Organic Frameworks for Biomedical Applications. https://doi.org/10.1016/B978-0-12-816984-1.00022-6

carbohydrates lies in the inherent asymmetry of the building units, which are not easily amenable to the formation of highly porous crystallized frameworks. A strategy was reported to overcome this problem by the adoption of the cyclic oligosaccharide cyclodextrin (CD), which is comprised of six to eight asymmetric α-1,4-linked D-glucopyranosyl residues. CDs are naturally available oligosaccharides enzymatically produced from starch. In contrast to other linear carbohydrates, CDs are typical "cage" molecules of a truncated cone shape with a hydrophobic cavity and a hydrophilic surface [16]. The most common natural CDs are α, β, and γ-CDs, containing 6, 7, and 8 glucopyranose units, respectively. Their ability to coordinate with metal ions makes possible the formation of CD-based MOFs. The CD building units could be linked by metal ions, such as K^+, Na^+, Rb^+, Cs^+, Sr^+, Pb^{2+}, Fe^{3+}, to form a body-centered porous crystalized MOF structure [17,18]. CDs remain the only type of carbohydrate being able to form MOF crystals.

In addition to their ability to form supramolecular constructs, the hydrophilicity and versatility of carbohydrate materials make them attractive materials for surface modification of preformed drug nanocarriers. For instance, several polysaccharides [19] are currently investigated as potential alternatives for poly(ethylene glycol) (PEG) coatings, which is one of the most popular strategies to decorate NPs' surface to increase the blood circulation time [20–22]. It has been reported that some modified dextrans, heparin (hep), low molecular weight chitosan, and starch derivatives have similar "stealth effects" by forming a hydrated layer, which allows the NPs to evade opsonization and subsequently phagocytosis, therefore prolonging NPs' circulation time in the blood stream [23]. Moreover, carbohydrates are of high interest for targeting. The surface of the cell is rich in carbohydrate moieties which constitute potential recognition sites for carbohydrate-mediated interactions between cells and drug carriers coated with suitable site-directing molecules. This ability to be specifically recognized by receptors on the cell-surface indicates their potential utility as targeting ligands for therapeutic applications. For example, mannose [24, 25], chitosan, hyaluronic acid, and chondroitin sulfate [26] have been used as targeting ligands to macrophages for intracellular infection treatment. In addition, surface modification with carbohydrates may offer NPs with higher stability and controlled release.

A variety of carbohydrates are used for surface functionalization of nanocarriers, including CDs, dextrin, chitosan, starch, galactose, fucose, sialic acid, glucose, rhamnose, mannose, etc. [23]. Various nanomaterials have been modified with different carbohydrates, including poly(lactic-*co*-glycolic) acid (PLGA), NPs, liposomes, metallic NPs, magnetic NPs, quantum dots, micelles, etc. [23, 25, 27, 28]. However, surface modification of the porous MOFs is challenging since it requires specific coating materials and methods to avoid penetration of the coating materials inside the porous structure of MOFs, thus altering their drug loading capability. Carbohydrates are among the most versatile materials to functionalize MOFs since they present the advantages of: (i) lack of toxicity; (ii) they could mediate the cell

internalization; and (iii) they are easily further modified with other functional moieties. Recently, carbohydrate-based materials such as CDs [29], hep [30], hyaluronic acid (HA) [31], and chitosan [32, 33], which have larger molecular size than the diameter of the MOF pores, have been studied as coating materials. Interestingly, carbohydrate materials (such as CDs) can be easily functionalized with ligands (targeting, fluorescent imaging, etc.), which paves the way for a versatile surface modification of MOFs for multifunctional targeted drug delivery. The MOFs currently used for these investigations are iron polycarboxylate MOFs, which have emerged as a new class of versatile, biodegradable, and nontoxic drug carriers. Because of their high pore volumes and surface areas, MOFs were shown to load unprecedented amounts (within the 20–70 wt% range) of a series of drugs able to efficiently penetrate within the porous 3D structures [1, 2].

Both carbohydrate-based MOFs (CD-MOFs) and the surface modification of preformed MOFs (iron polycarboxylate MOFs) with carbohydrate materials will be described in this chapter. Control of particle size is a key parameter for drug delivery because this dictates the physicochemical properties of particles to obtain well-defined, reproducible, and stable formulations. Different strategies to synthesize CD-MOFs with controlled dimensions as well as their capability to incorporate drugs will be summarized. Recently, significant progress has been made in engineering CD-MOFs for drug delivery. Indeed, these particles were initially used for other potential applications in separation, sensing, gas storage, catalysis, and template synthesis [18]. CD-MOFs with controlled sizes have shown excellent capacity to incorporate a series of drugs [17, 18]. The use of CD-MOFs as drug carriers will be discussed, including the different strategies employed for drug incorporation, particle characterization, and the efforts to stabilize the drug-loaded particles. The second part of the chapter will address the use of carbohydrates for the surface-functionalization of iron polycarboxylate MOFs. A series of issues involved in this procedure will be discussed, including: (i) different methods to coat the MOF; (ii) various techniques to characterize the MOFs before and after surface modification; and (iii) biological evaluation of the coated MOFs.

20.2 MOFs synthesized from edible building blocks of CDs

The first reported CD-MOF [34] is composed of γ-CD and K^+, which has regular cubic morphology and controllable size distribution. The spontaneous coordination of metal ions and γ-CDs generates cubic $(\gamma\text{-CD})_6$ units which further assemble, by regular repetition, into a body-centered packed architecture with interconnected pores (Fig. 20.1A, *yellow*) with a diameter of 17 Å delimited by a window of 7.8 Å (diameter of γ-CDs). In addition to γ-CD, α-CD and β-CD were shown to be able to form CD-MOFs with diverse structures as shown in Fig. 20.1 [35, 41–43].

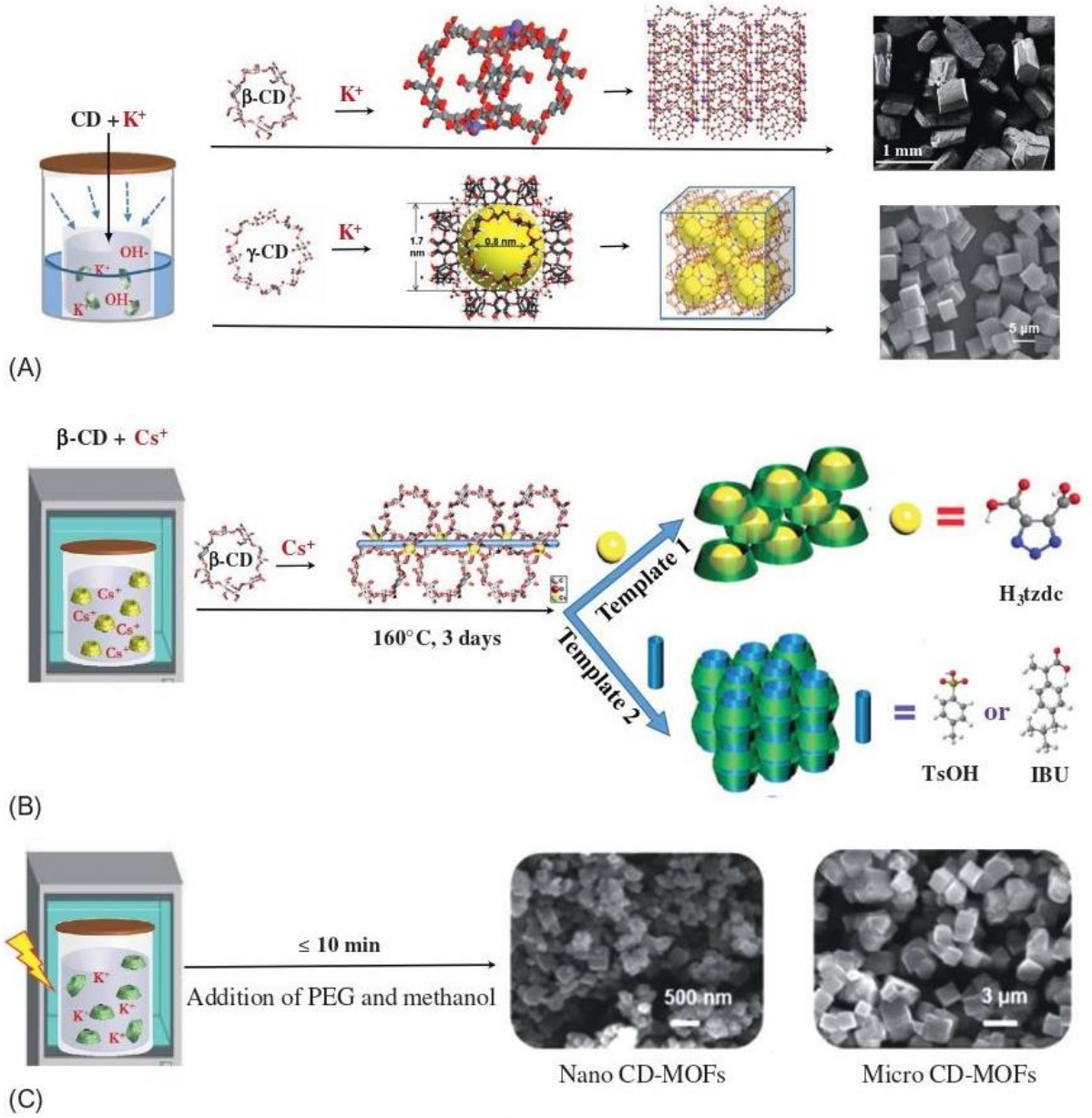

Fig. 20.1

Overview of CD-MOF synthesis methods. (A) Vapor diffusion methods were widely used for synthesis of different CD-MOFs. Examples were given for αCD-MOF (K) [35] and γCD-MOF(K) [36, 37]. (B) Hydrosolvothermal method [38] employed for βCD-MOF(Cs) synthesis using H_3tzdc, TsOH, or IBU as templates. *H_3tzdc*, 1,2,3-triazole-4,5-dicarboxylic acid; *TsOH*, methyl benzene sulfonic acid; *IBU*, ibuprofen. (C) Microwave-assisted method [39, 40] applied to optimize the synthesis of γCD-MOF(K) within 10 min. *Modified with permission from X. Li, et al., Cyclodextrin-based metal-organic frameworks particles as efficient carriers for lansoprazole: study of morphology and chemical composition of individual particles, Int. J. Pharm. 531(2) (2017) 424–432; A. Yang, et al., Green synthesis of β-cyclodextrin metal-organic frameworks and the adsorption of quercetin and emodin, Polyhedron 159 (2018) 116–126, copyright 2017 and 2018, Elsevier; J. Liu, et al., Controllable porosity conversion of metal-organic drug delivery, Chem. Commun. 53 (2017) 7804–7807, copyright 2017, Royal society of Chemistry; B. Liu, et al., Microwave-assisted rapid synthesis of gamma-cyclodextrin metal-organic frameworks for size control and efficient drug loading, Cryst. Growth Des. 17 (4) (2017) 1654–1660, copyright 2017, American Chemical Society.*

20.2.1 Synthesis methods for CD-MOFs

Abundant efforts have been made to synthesize CD-MOFs with homogeneous size distribution during the last few years. The main synthetic strategies used to develop CD-MOFs are summarized in Fig. 20.1.

Vapor diffusion method. The vapor diffusion method is the earliest synthetic pathway to produce CD-MOFs [34]. Essentially, γCD-MOF were prepared by reacting γ-CD with potassium hydroxide (KOH) in aqueous solution, followed by vapor diffusion of methanol into the solution during 2–7 days (Fig. 20.1A). A variety of CD-MOFs were first prepared combining γ-CD and K^+, Rb^+, Cs^+, Na^+, Sr^+ by Stoddart's group [34, 44]. This methodology requires only ambient temperature and pressure; however, the obtained crystals had diameter in the range of 200–400 μm. Furukawa et al. [45] modified this method by adding cetyltrimethyl ammonium bromide (CTAB) to control the growth of γCD-MOF crystals. When CTAB was added to the crystallization medium, it covered the surface of γCD-MOF crystals, and thus, slowed down the growth rate and reduced the final crystal size [45]. Homogeneous and monodisperse γCD-MOFs were generated in the diameter range of 1–10 μm. More interestingly, Furukawa et al. successfully achieved the nanoscaled γCD-MOFs (200–300 nm) by the addition of both methanol and CTAB in the crystallization medium. However, it still took several days for the synthesis. Liu et al. [46] developed an effective solvent evaporation approach to synthesize this type of γCD-MOFs by setting reaction temperature at 50°C. Remarkably, the reaction time was significantly reduced to 6 h. The size of the resulting CD-MOFs was well-controlled by addition of CTAB or/and methanol (in the range of 1–10 μm with CTAB and around 600 nm with CTAB and methanol) [36, 37]. Recently, a "green" seed-mediated method was designed to rapidly produce γCD-MOFs [47]. Instead of the surfactant CTAB which is potentially toxic and difficult to remove, short-chain starch NPs were employed as the seed to control the nucleation and growth of γCD-MOFs. The results demonstrated that the crystal structure and cubic morphology were preserved, while the size of the particles was monodisperse with mean diameter around 2 μm when the seed was added. However, this method could not be scaled-down CD-MOFs to the nano-regime.

In addition to γ-CD, α-CD and β-CD were shown to be able to form CD-MOFs [35, 41–43]. As shown in Fig. 20.1A, Sha et al. obtained the αCD-MOF by vapor diffusion method in one month using α-CD and KOH, where tetramethylammonium hydroxide solution was employed as a new additive [35]. The resulting αCD-MOF consists of the secondary units of $[K_6(CD)_2]$ dimer torus, which are further linked with adjacent six $[K_6(CD)_2]$ dimer forming 2D layer with both large pores with a diameter of 11.5 Å and small pores with a diameter of 7.3 Å. Similarly, αCD-MOF could be synthesized with NaOH as metal source. Modified vapor diffusion methods were adopted to synthesize βCD-MOF by dissolving β-CD and NaOH in ethanol/water in a sealed vessel. After two weeks reaction, βCD-MOFs were formed, with each K^+ ion coordinating with six oxygen atoms from the surrounding four β-CDs. Two adjacent β-CDs were connected by a K^+ to form the pores. Due to the structural

features of αCD-MOF and βCD-MOF which don't have regular cubic 3D structures as γCD-MOFs, observed morphologies of αCD-MOF and βCD-MOF exhibited relatively nonregular shapes compared to the cubic γCD-MOFs (Fig. 20.1A). It was found that the size of the particles was difficult to be controlled and inhomogeneous morphologies contrary to the regular cubic γCD-MOFs were observed.

Hydrosolvothermal method. Hydrosolvothermal method has been widely employed in MOFs synthesis [48]. Typically, the reaction took place under high-pressure and high-temperature conditions. Synthetic process was influenced by several parameters, such as the reaction time, temperature, stoichiometry, dilution pH, and additives. A βCD-MOF was successfully prepared from β-CD and sodium oxalate ($Na_2C_2O_4$) using a mixture of methanol and water and heating it at 160°C for 3 days [38]. Liu et al. designed a novel template-induced strategy to produce different βCD-MOFs (Cs) using 1,2,3-triazole-4,5-dicarboxylic acid (H_3tzdc), methyl benzene sulfonic acid (TsOH), or ibuprofen (IBU) molecules as templating agents [40]. As shown in Fig. 20.1B, different structures of βCD-MOFs were obtained when employing different templates. Sha et al. obtained a novel type of αCD-MOF by a solvothermal method at 160°C with a reaction time of 4 days starting with a mixture of α-CD and KOH. Moreover, metal-organic nanotubes built from β or γCD and Pb^{2+} were also synthesized through a solvothermal reaction [49].

Microwave-assisted hydro/solvothermal methods. As a classical synthetic protocol, the microwave-assisted method has also been employed in the synthesis of MOFs. This synthetic method offers the advantages of simple, rapid, inexpensive, environment-friendly, and efficient nonconventional heating with high yields. Liu et al. obtained γCD-MOFs using the microwave-assisted method within 10 min as shown in Fig. 20.1C [39]. Both size and morphology of γCD-MOF were systematically investigated by altering the reaction time, temperature, and solvent ratio, in order to obtain micro- and nanometer-sized crystals. Polyethylene glycol with a molecular weight of 20,000 g/mole (PEG 20,000) was used for the first time to control the size and morphology of γCD-MOFs. Monodispersed γCD-MOF were obtained with different sizes (200 nm to 300 μm) and were further used for drug encapsulation.

The three general methods described above have been the most employed strategies for CD-MOF synthesis. The best method to both obtain a rapid reaction and control the particle size was the microwave-assisted hydro/solvothermal synthesis. The mean diameter of synthesized CD-MOF was in the range of 200 nm to centimeter scale. There are still some other synthetic routes (e.g., ultrasonic, mechano-chemical, electrochemical) employed for MOF synthesis possibly worthy to try for CD-MOF aiming to further reduce the particle size. Regardless of the method used to synthesize CD-MOFs, the choice of the additives (CTAB, menthol, PEG, etc.) is obviously crucial for both size control and their biomedical applications. Up to date, PEG could be considered among the best additive, considering its low toxicity and great capabilities to control the mean diameter of the synthesized CD-MOF.

20.2.2 Drug entrapment

A variety of active molecules, including anticancer drugs (doxorubicin (DOX), fluorouracil (5-FU), methotrexate, quercetin), antiinflammatory drugs (IBU, furbiprofen, fenbufen, ketoprofen, and piroxicam), antihypertensive drug (azilsartan), angiotensin-converting enzyme inhibitors (captopril), various pharmaceutical ingredients (salicylic acid, ferulic acid, folic acid, and pseudolaric acid B), and food additives (curcumin and sucralose) have been successfully incorporated in CD-MOFs using three main strategies, which are the impregnation method, the co-crystallization method, and the grinding method.

Impregnation method. This is a conventional method which generally involves three steps: (1) synthesis of CD-MOFs, (2) activating MOFs by removing solvents/ligands from the pores, and (3) incorporation of drugs within CD-MOFs in suitable solvents. It is noteworthy that the nature of solvents, pH of CD-MOF (alkaline or neutral), and the encapsulation materials play an important role on the drug loading properties. For example, when relatively nonpolar solvents were used, the uptake of IBU into CD-MOFs was low (<5 wt%). In contrast, the encapsulation of IBU in ethanol increased dramatically to 26 wt%, which was close to the theoretical value calculated by Monte Carlo simulations [50]. The hypothesis is that the IBU encapsulation is related to an anion exchange process, which means that the hydroxyl group present in CD-MOFs was able to take away the protons from IBU. This process could take place easily in ethanol rather than in nonpolar solvents. Considering the pH of CD-MOFs, it was reported that the neutralized CD-MOFs were more effective than alkaline CD-MOFs to protect sucralose, possibly due to the fast hydrolysis of sucralose in alkaline condition [51]. As shown in Table 20.1, a large variety of active molecules have been successfully loaded into CD-MOFs by this method.

Co-crystallization method. In addition to impregnation, co-crystallization emerged as a promising strategy for drug encapsulation. To do so, the drugs were added in the crystallization medium before the formation of CD-MOFs. In the case of lansoprazole (LPZ), co-crystallization significantly improved the drug loading capacity in γCD-MOF (K), as compared to impregnation (9.4 wt% for impregnation and 23 wt% for co-crystallization) [37]. Indeed, in the impregnation process, drug molecules have to cross their way through the preformed tight CD-MOF channels. In contrast, in the co-crystallization process, γ-CD:drug complexes are directly formed and assembled into drug-loaded CD-MOF particles, still preserving their crystallinity. In a nutshell, co-crystallization was shown to offer more probability for the drugs to interact with the CDs in the crystalline matrix.

The LPZ-loaded γCD-MOF particles were characterized in terms of morphology, sizes, and crystallinity, showing almost perfect cubic structures with monodispersed size distributions (Fig. 20.2). Moreover, Raman spectra of randomly chosen particles were recorded, indicating that each individual cube had practically the same chemical composition, i.e., drug content [37]. Thus, it was shown that the LPZ-loaded particles

Table 20.1 Overview of drug encapsulation in CD-MOFs.

Loading methods	CD-MOFs		Drug	Drug payload (%, w/w)	Refs.
	CDs	Metal			
Impregnation	γ-CD	K^+	Azilsartan	23	[52]
		K^+	Budesonide	25	[53]
		K^+	Captopril	19	[46]
		K^+	Coenzyme Q10	31	[54]
		K^+	Curcumin	n.i.[a]	[55]
		K^+	Doxorubicin	6∼8	[56]
		K^+	Doxorubicin	6∼8	[57]
		K^+	Doxorubicin	7	[58]
		K^+	Epigallocatechin gallate	21	[59]
		K^+	Fenbufen	20	[46]
		K^+	Fenbufen	20	[39]
		K^+	Fenbufen	6	[60]
		K^+	Flurbiprofen	12	[46]
		K^+	Folic acid	60	[61]
		K^+	Ibuprofen	26	[50]
		K^+	Ibuprofen	13	[36, 37]
		K^+	Ketoprofen	4	[60]
		K^+	Lansoprazole	9/2	[36, 37]
		K^+	Leflunomide	14	[62]
		K^+	Sodium diclofenac	50	[63]
		Na^+	Sodium diclofenac	49	[63]
		Fe^{3+}	Sodium diclofenac	55	[63]
		K^+	Sucralose	28	[51]
		K^+	Vitamin A palmitate	10	[64]
	α-CD	Na^+	Ferulic acid	11	[35, 42]
		Na^+	5-FU	9	[35, 42]
		K^+	5-FU	26	[35, 42]
		Na^+	Methotrexate	38	[35, 42]
		Na^+	Quercetin	32	[35, 42]
		Na^+	Silybummarianum	13	[35, 42]
	β-CD	Cs^+ (H_3tzdc)	5-FU/methotrexate	138/69	[39, 40]
		Cs^+ (TsOH)	FU/methotrexate	151/122	[39, 40]
		K^+	Quercetin/emodin	15/20	[43]
Grinding	β-CD	K^+	Azithromycin	34	[65]
		Na^+	5-FU	23	[38]
		Na^+	5-FU/quercetin	n.i.[a]	[41]
		K^+	5-FU/quercetin	n.i.[a]	[41]
Co-crystallization	γ-CD	K^+	Ferulic acid	13	[66]
			Ibuprofen	23	[50]
			Ibuprofen	13	[36, 37]
			Lansoprazole	23	[36, 37]

[a]n.i., not indicated.

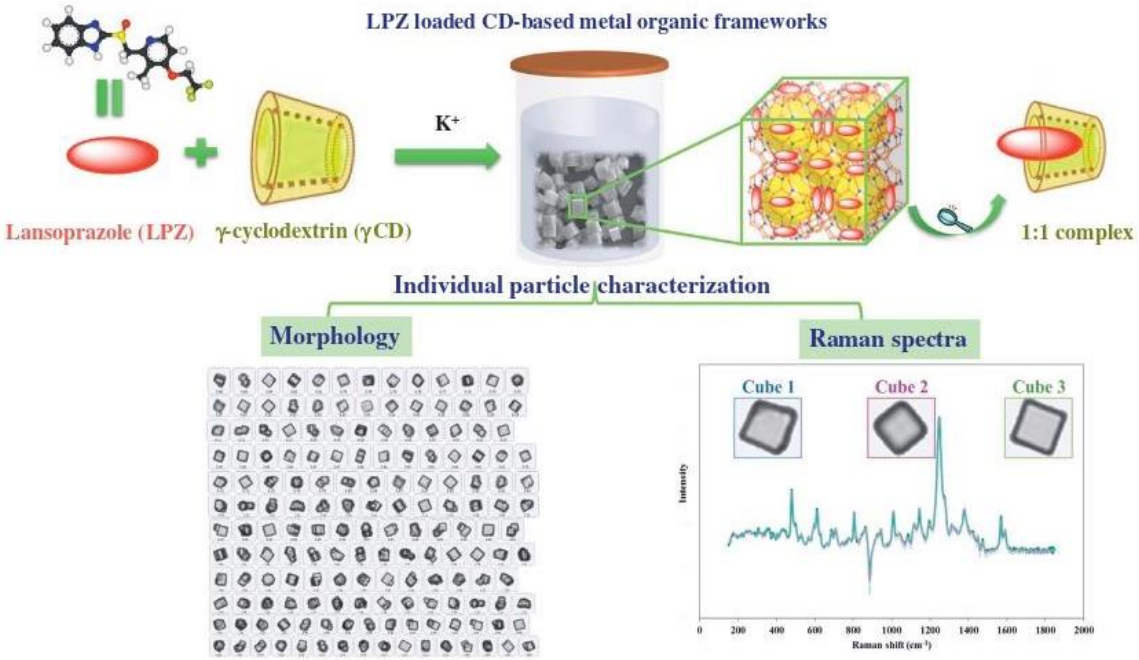

Fig. 20.2

Drug loading and characterization. LPZ was successfully loaded in CD-MOF by co-crystalization method, achieving high drug loadings up to 23 wt%, corresponding to LPZ:CD molar ratio of 1:1. The obtained LP-loaded particles were monodisperse with cubic morphologies and homogenous chemical compositions, as indicated by Raman spectra of randomly chosen individual particles. *Reproduced with permission from H. Li, et al., Composite CD-MOF nanocrystals-containing microspheres for sustained drug delivery, Nanoscale, 9 (2017a) 7454–7463; X. Li, et al., Cyclodextrin-based metal-organic frameworks particles as efficient carriers for lansoprazole: Study of morphology and chemical composition of individual particles, Int. J. Pharm., 531(2) (2017b) 424–432. Copyright 2017, Elsevier.*

had a remarkable homogeneity in terms of both drug loading and size. Advantageously, the one-pot co-crystallization synthesis simplifies the drug loading process together with avoiding the use of potentially toxic organic solvents sometimes needed for impregnation.

However, the co-crystallization method is highly dependent on the structure of the drug molecules and sensitive to the pH value of the crystallization medium. For instance, the inclusion of ferulic acid (FA) in γCD-MOF (K) was found to be strongly pH-dependent in a range of 6.8 to 13.1 [66]. The reaction yield dramatically decreased from 59.3% to 19.0% at low pH. Interestingly, the molar ratio of FA to γ-CD in FA/CD-MOF increased from 0.15 (pH 13.1) to 1.06 (pH 6.8), indicating that the drug loading capacity was improved at low pH. It is worth noting that when FA:γ-CD inclusions were prepared in a first step, followed by addition of KOH, FA was not encapsulated in CD-MOF, suggesting that FA:γ-CD complex was destabilized by KOH and that the free FA could not be adsorbed on the resulting CD-MOF in aqueous solution.

Another study reported the successful IBU loading in nanoscale γCD-MOF (K) by co-crystallization, showing similar drug payloads with impregnation methods (13.0 wt% for

impregnation and 12.7 wt% for co-crystallization) [36]. The drug payload achieved by this method is dependent on the drug molecules. Further investigation is still needed to comprehensively understand the mechanism of this drug-dependent phenomena. Possibly, the affinity between the drug and the cavity of γ-CD and/or CD-MOF, the drug: γ-CD ratio, and pH play important roles on the drug payloads.

The reported studies show that drug loadings obtained by co-crystallization and impregnation are highly dependent on drug structure and experimental conditions. Few data are available in the literature so far making it difficult to draw a general trend.

Grinding method. Mechanical grinding is one of the methods typically applied to prepare guest molecules/CD inclusion complexes. Recently, it has also been used to encapsulate the guest molecules into CD-MOFs [38,65]. Drug-loaded CD-MOFs could be prepared by simply grinding the guests with preformed CD-MOFs. Several parameters were shown to impact drug inclusion during grinding, such as the molar ratio between the guest drug and CD in CD-MOF, the grinding time, and the temperature [41]. For the first time, the 5-FU and quercetin drug combination could be successfully co-encapsulated in CD-MOFs using the grinding method. In brief, 5-FU, quercetin, and βCD-MOFs were milled at a molar ratio of 1:1:1 using ethanol as wetter at room temperature. The drug-loaded CD-MOF were obtained after grinding for 1 h. This study demonstrated that two drugs with different molecular structures and dimensions could be simultaneously incorporated into CD-MOFs; however, the drug payloads were not indicated. As reported by Lu et al. [38], when 5-FU was loaded individually, the obtained payload reached 23 wt%. The highest drug payload achieved by grinding method is 34 wt% in the case of azithromycin [65].

Benefits of drug incorporation in CD-MOFs. Once incorporated in CD-MOF via different strategies, the active molecules were shown to gain beneficial properties, including improved stability, enhanced water solubility, and bioavailability. For example, in reason of the protective effect of the CD-MOF matrix, the stability of incorporated vitamin A palmitate (VAP) was significantly improved [64]. It was hypothesized that the VAP molecules were curled inside the chambers formed by dual γ-CDs pairs in γCD-MOF(K). This in turn led to an enhanced stability upon storage, comparable or even better than other products in the market, with around 1.6-fold elongated half-life. Similarly, the stability of encapsulated curcumin was enhanced by at least 3 orders of magnitude as compared to free curcumin or to curcumin:γ-CD complexes [55]. In this latter case, the enhanced drug stability was attributed to the strong interaction between curcumin and CD-MOFs through hydrogen bond interaction between the OH group of CDs and the phenolic hydroxyl group of the curcumin.

Taking advantage of the unique structure of CDs, “cage” molecules with proven abilities to increase the apparent water solubility of many drugs, CD-MOFs were engineered to release supersaturated drug solutions upon their disassembly [52]. It was shown recently that the solubility of azilsartan could be improved by 340-fold as compared to free drug. This dramatic increase was attributed to drug nanoclusters formation in the confined nano-cages of CD-MOFs

followed by their release upon matrix dissolution in water [52]. Moreover, this strategy allowed to improve the bioavailability of azilsartan in Sprague-Dawley rats by 9.7-fold after loading into CD-MOF, as compared to free drug. These investigations indicate that CD-MOFs are efficient drug delivery carriers enabling to enhance drug bioavailability.

Surface coating. CD-MOFs demonstrated high drug loading capabilities together with several other advantages for drug delivery as compared with more traditional drug carriers based on other materials. However, due to their physical frailness and degradability in aqueous media, which may lead to their disassembly before reaching the target tissues or organs, CD-MOFs were considered inappropriate for some routes of administration, such as the intravenous one. In this context, considerable efforts have been made to improve the stability of CD-MOFs in aqueous media. Firstly, ethylene glycol diglycidyl ether was employed to cross-link the hydroxyl groups in adjacent CDs in the CD-MOF supramolecular assemblies, thus generating cubic gel particles stable towards dissolution in aqueous media [45]. However, the resulting particles were not biodegradable in biological media, which is another important requirement for biomedical applications. To address the challenges related to CD-MOF instability in aqueous solutions, another approach was carried on by Li et al. [36]. CD-MOF nanocrystals were incorporated into a biocompatible polymer (polyacrylic acid, PAA) matrix by a solid in oil-in-oil (s/o/o) emulsification-solvent evaporation method. The resulting composite microspheres showed enhanced stabilities in water and sustained drug release. However, this approach led to large particles, beyond the micrometer size.

In order to maintain the size of the CD-MOFs in the nanometric range, efforts have been made to coat directly CD-MOF nanoparticles. For example, γCD-MOFs with improved water stability were successfully achieved by incorporating hydrophobic C_{60} in their matrices through host-guest interactions between γCD and C_{60} [58]. Interestingly, neither the structural integrity nor the BET (Brunauer-Emmett-Teller) surface area was affected after surface modification. DOX was successfully incorporated reaching a payload of 6.5 wt%. Moreover, DOX was released in a sustained manner after CD-MOF incubation in phosphate buffer saline. When tetrakis(4-hydroxyphenyl) porphyrin (TCPP)-conjugated C_{60} was used instead of C_{60}, the resulting CD-MOFs were shown to have fluorescent properties, enabling their detection in vitro and in vivo [67]. More recently, CD-MOFs were surface-modified with cholesterol [56], thus exhibiting good stabilities in aqueous media. It was thus possible to administer the resulting cholesterol-shielded and DOX-loaded nanoparticles by intravenous route, and results showed a significantly increased blood half-life of DOX up to 0.5 h, which was four times higher than the one of free DOX. Moreover, the nanoparticles were well-tolerated also in vivo. However, this strategy involved the covalent grafting of cholesterol to the CDs at the CD-MOF surface. This might potentially lead to the release of modified CDs and the degradation process of the coated CD-MOFs still needs to be unraveled.

Further prospective of CD-MOFs. In a nutshell, CD-MOFs advantageously combined CD's proven biocompatibility for medical applications and CD's capacity to assemble in regular

porous structures which were further shown to be beneficial for drug incorporation. Among the three strategies for drug incorporation, co-crystallization method seems to be the most promising one, due to its simplicity and ability to enhance drug loadings. However, the most common method to load drugs remains the impregnation technique. All drug loading methods were shown to be strongly dependent upon drug physicochemical characteristics and abilities to form inclusion complexes with CDs.

When incorporated inside CD-MOF, the drugs were efficiently stabilized against degradations. Moreover, in the case of poorly soluble drugs, drug solubility in water was significantly increased due to the formation of drug:CD complexes, once the drug-loaded CD-MOFs disassemble in water. The poor stability in aqueous media remains the main drawback of CD-MOFs, which hampers their biomedical applications, especially for intravenous administration. Although versatile strategies have been deployed to improve their stability, they are limited by complex procedures and/or necessity to covalently graft the coating material.

In terms of stability, other MOFs made using different metal and linkers were shown to be more stable in aqueous environment. For instance, iron polycarboxylate MOFs are intrinsically stable, which widens their biomedical application as compared to CD-MOFs. The following section will be focused on the surface modification of iron polycarboxylates MOFs with carbohydrate-based materials.

20.3 Carbohydrates as functional surface coatings for MOFs

MOFs made of iron carboxylates, and especially iron (III) trimesate MIL-100(Fe), have emerged as an important class of porous, biodegradable, and multifunctional nanomaterials of main interest for biomedical applications (MIL, stands for Materials from Institut Lavoisier). Indeed, their high surface area allowed loading high amounts of a large variety of drugs able to penetrate within the porous MOF structures [2]. The porous MIL-100(Fe) solids are built up from Fe(III) octahedra trimers and trimesate linkers (1,3,5-benzene tricarboxylate) which self-assemble forming a porous architecture delimiting large (29 Å) and small (24 Å) mesoporous cages. In MIL-100(Fe) nanoMOFs, two types of cages are accessible for drug adsorption inside the open 3D-porosity. To access these cages, drugs penetrate through pentagonal (5.6 Å) and/or hexagonal windows (8.6 Å). Advantageously, due to the presence of Fe and free water molecules in their structure, the nanoMOFs acted as efficient T_2-weighted contrast agents for Magnetic Resonance Imaging (MRI), of interest for theranostics applications [68]. These nanoMOFs, loaded or not with drugs, were well-tolerated in vivo [69–71].

Like other types of nanoparticles, nanoMOFs need to be further functionalized with engineered coatings to control their in vivo fate. Surface modification is commonly used to

control drug release, reduce plasma protein binding, prolong blood circulation, and attach functional moieties for imaging and targeting. However, the surface modification of nanoMOFs is challenging because many coating materials such as PEG chains could penetrate inside the pores, which disturb drug loading. As stated in the introduction, carbohydrate-based materials are among the most versatile ones for surface modification. The first noncovalent nanoMOF coating study was reported by the group of Dr. Gref [29], where phosphorylated CD (CD-P) derivatives were used to modify iron trimesate nanoMOFs MIL-100(Fe) in aqueous media, employing a fast, one-step, and completely "green" (organic solvent-free) procedure (Fig. 20.3A). Briefly, the nanoMOFs were surface-modified by impregnation with CD-P aqueous solution at room temperature. The success of this strategy lies on the fact that the phosphate groups conjugated on the CD-P could efficiently coordinate with the available iron trimer sites on the surface of nanoMOFs. They played a cooperative role to ensure the stability of the coatings. Besides, CD-P were too bulky to cross the microporous windows of the nanoMOFs, leaving CD-P located only on the external MOF surface. The resulting coated nanoMOFs have been comprehensively characterized by a set of complementary techniques, including transmission electron microscopy (TEM), X-ray powder diffraction (XPRD), dynamic light scattering (DLS), solid state NMR, and X-ray photoelectron spectroscopy (XPS), among others.

As shown in Fig. 20.3A, the presence of CD-P within the nanoMOF top layers was visualized by confocal microscopy in the particular case of larger MOF particles (>10 μm) which were modified with Rhodamine (Rh)-labeled CD-P. XPS confirmed that CD-P was located on the nanoMOF top layers (5–10 nm depth) by showing both carbon C1s "fingerprints" of the carbon skeleton of MIL-100(Fe) (284.8 and 289 eV, C-C or C-OOH, respectively) and CD-P "fingerprint" (main contribution at 286.3 eV) in the CD-P-coated nanoMOFs. The phosphate-iron coordination was evidenced as the principal binding mechanism by Isothermal titration calorimetry (ITC), showing the absence of interaction between nonphosphated CD and nanoMOFs. On the contrary, the binding isotherm for the CD-P/nanoMOFs interaction displayed a strong interplay. Elemental analysis and spectrofluorimetry were used to quantify the amount of CD-P attached on the surface of nanoMOFs, exhibiting maximal adsorbed values around 20 wt%. The stability of the coating under physiological simulated conditions was also investigated, showing that less than 10% of the total CD-P coating was detached after 24 h incubation, whatever the incubation media (phosphate buffer saline or cell culture media). Moreover, it was illustrated that the CD coating did not impact the supramolecular architecture nor the porosity of the nanoMOFs, as confirmed by constant BET surface area before and after coating. The nanoMOF morphology, crystallinity, drug loading, and release properties were not affected after the coating procedure. Remarkably, CD-P-coated nanoMOFs were devoid of toxicity in vitro in different cell lines, as the uncoated ones. Finally, confocal microscopy investigations (Fig. 20.4A) showed that nanoMOFs readily internalized in J774 macrophages, maintaining their CD-based coating.

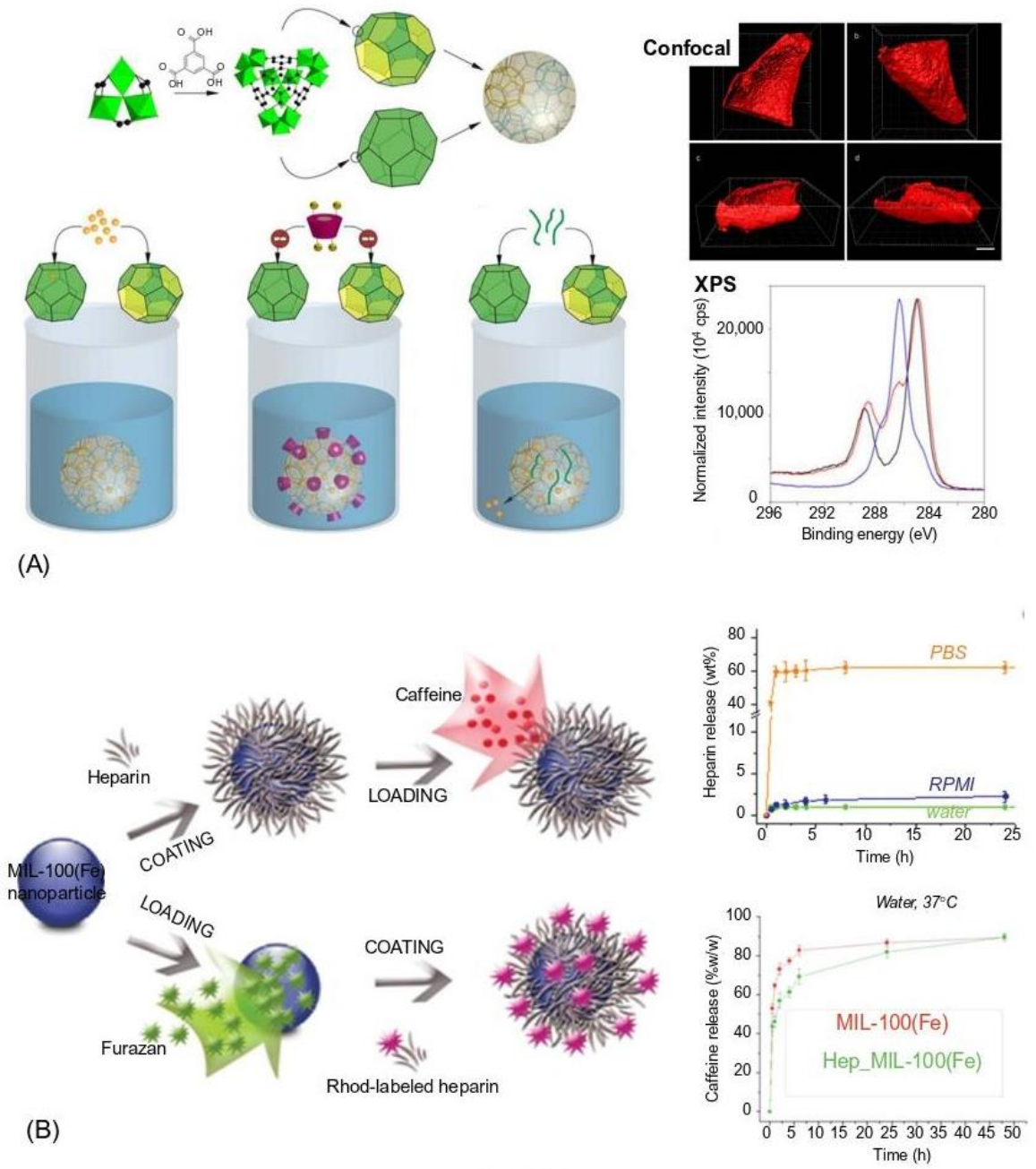

Fig. 20.3

Overview of surface modification strategies and characterization of nanoMOFs coated with carbohydrates. (A) CD-P was used to functionalize iron trimesate nanoMOF [29]. The methodology of characterization was set up using a series of complementary techniques including: (i) confocal images of the Rh-labeled CD-P located only on the surface of nanoMOFs; (ii) XPS showing C1s binding energy spectra for nanoMOFs *(black)*, CD-P *(blue)* and CD-P-modified nanoMOFs *(red)*. (B) When nanoMOFs were modified with hep [30], the hep release was investigated in different media and it allowed to sustain the release of the incorporated caffeine. *Reproduced with permission from V. Agostoni, et al., A "green" strategy to construct non-covalent, stable and bioactive coatings on porous MOF nanoparticles, Sci. Rep. 5 (2015) 7925–7931; E. Bellido, et al., Heparin-engineered mesoporous iron metal-organic framework nanoparticles: toward stealth drug nanocarriers, Adv. Healthc. Mater. 4(8) (2015) 1246–1257. Copyright 2015, Nature; 2015, Wiley Online Library.*

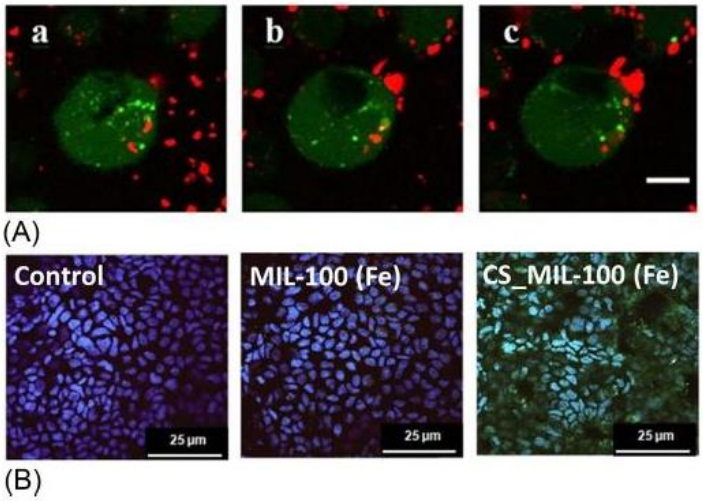

Fig. 20.4

Surface modification plays an important role on cell internalization. (A) Interaction between J774 macrophages and CD-P-coated MOFs studied by confocal microscopy. Cells were stained in *green* with calcein, whereas the *red* signal comes from Rh-labelled CD-P-coated nanoMOFs. Images represent three distinct optical sections inside cells at different heights above the glass slide: (a) 2.3 µm; (b) 4.9 µm, and (c) 7.6 µm. Cell nucleus appears in *black*. Bar represents 5 µm. (B) Coating with chitosan leads to an increased intestinal permeability with respect to the noncoated material [32]. Confocal microscopy images of Caco-2 cells containing uncoated and chitosan-coated MIL-100(Fe) NPs observed by iron self-reflection signal *(green channel)* and the nucleus stained by DAPI *(blue channel)*. The images were taken after 2.5 h incubation. *(A) Reproduced with permission from V. Agostoni, et al., A "green" strategy to construct non-covalent, stable and bioactive coatings on porous MOF nanoparticles, Sci. Rep. 5 (2015) 7925–7931. Copyright 2015, Nature; (B) T. Hidalgo, et al., Chitosan-coated mesoporous MIL-100 (Fe) nanoparticles as improved bio-compatible oral nanocarriers, Sci. Rep. 100 (2017) 1–14. Copyright 2017, Nature.*

Further studies were performed taking advantage of the versatility of CD coatings in terms of chemical modification. First, mannose was grafted onto CD-P previously to coat the nanoMOFs [29]. The CD-P-mannose derivative could be adsorbed readily onto the nanoMOF surfaces, allowing a better recognition by human retinoblastoma Y79 cells hyperexpressing the mannose receptor. The amounts of CD-P-mannose-modified nanoMOFs able to penetrate inside the cells were twice higher than using the uncoated nanoMOFs.

Another study was based on the strong host-guest interaction between adamantyl (Ad) and β-CD. Ad-conjugated PEG chains (Ad-PEG) were used to further functionalize the surface of the CD-P-coated nanoMOFs. By this way, CD-P: Ad-PEG inclusion complexes were bound strongly to the nanoMOFs and were firmly anchored [29]. PEGylation has been since many years an effective strategy to reduce premature clearance of NPs from the circulation by hindering adhesion of proteins on nanoMOFs' surface, avoiding their recognition and removal by macrophages. Another strategy for nanoMOF PEGylation was to employ GraftFast surface engineering using PEG or hyaluronic acid (HA) acrylates, which were polymerized [31]. In this study, HA-PEG was covalently linked by a single step GraftFast

reaction on the surface of nanoMOFs. A maximal polymer amount of 32.9 ± 0.3 wt% was reached in the case of PEG_{5kDa}-Rh. The resulting PEGyated nanoMOFs exhibited improved colloidal and chemical stabilities in different biological media as compared to uncoated nanoMOFs, while conserving their porosity which allowed the adsorption of bioactive molecules. Moreover, it was shown that the PEG coating could reduce macrophage uptake in vitro.

The study of CD-P surface modification was further extended by synthesizing a series of randomly phosphorylated β-CD monomers and polymers appended with mannose or Rh [72]. In all cases, the amount of CD-based materials attached to the nanoMOFs reached 20–26 wt%, which is similar to the CD-P one [29]. It was further demonstrated that the coating stability was directly related to the density of the grafted phosphate groups, further confirming that the interaction between the phosphate groups and the iron sites at the nanoMOFs' surface was crucial for the coating process. Recently, native β-CD was also used to functionalize the iron terephthalate nanoMOF (MOF-235) [73], taking advantage of the coordination interaction between the hydroxyl groups of β-CD and the unsaturated Fe(III) metal ions of MOF-235. The supramolecular assemblies further displayed properties as effective catalysts in H_2O_2-luminol chemiluminescence reaction due to the synergistic effect between β-CD and MOF-235. However, the stability of the CD coating was not evaluated.

In addition to CDs, hep was employed as an efficient coating material to decorate the surface of MIL-100(Fe) nanoMOFs by a similar impregnation method [30], whereas nanoMOFs were dispersed in ethanol instead of aqueous solution (Fig. 20.3B). The amount of hep attached to the nanoMOFs was 12.5 ±1.8 wt%. The stability of hep coating was also investigated in three different biological media (water, cell culture medium, and PBS). In water or cell culture medium, the release of a small quantity of hep (2 wt%) was observed after 24 h incubation. However, up to 50 wt% of hep was released in PBS within 1 h, which was much higher than the CD-P release from CD-P-coated MOFs in the same conditions [29], suggesting a lower stability of the hep coatings. Caffeine was selected as molecule of interest to investigate drug loading and release capacity. The payloads for the uncoated and hep-coated nanoMOFs were similar: 43 ± 2 and 42 ± 6 wt%, respectively. Interestingly, hep-coated nanoMOFs exhibited an ability to better control the drug release, as compared with uncoated nanoMOFs, especially during the first hours. As shown in Fig. 20.3B, 46 ± 3 and 56 ± 4 wt% were released from the uncoated nanoMOFs after 1 h in water and PBS, while only 20 wt% of caffeine was released during the same period for the coated nanoMOFs. The hypothesis was that the dispersive interaction of caffeine molecules with hep slowed down their diffusion outwards the nanoMOFs. Furthermore, in vitro investigations were performed with the murine macrophage cell line J774 in order to assess the potential stealth properties of fluorescent hep-coated nanoMOFs. It was reported that the hep coating significantly slowed down the internalization process, but this was the case only at early stages of incubation. It was hypothesized that this might be related to the removal of hep from the nanoMOFs' surfaces in the biological media.

Recently, chitosan was also employed to modify the same iron trimesate MIL-100(Fe) nanoMOFs [32] by similar methods. The amount of chitosan attached to the nanoMOFs reached 49.1 ± 0.3 wt % and was estimated by fluorescence spectrometry after impregnation of the nanoMOFs with Rh-labeled chitosan. In addition to the conventional techniques, a combination of high-resolution X-ray Absorption Near-Edge Structure (XANES) and computing simulation techniques was employed to investigate the specific interactions between the chitosan coating and the nanoMOFs. It was thus demonstrated that both Fe^{II} and Fe^{III} sites were able to interact with the chitosan macromolecules. No significant toxic effects on human colorectal carcinoma cells (Caco-2) were detected before or after chitosan coating. Interestingly, chitosan-coated nanoMOFs exhibited a significantly higher cell uptake as compared with the uncoated NPs after only 2.5 h incubation (Fig. 20.4B). Moreover, chitosan-coated nanoMOFs reduced the immune response, which might be related to a lower recognition by the immune system. The chitosan-coated nanoMOFs appeared promising for oral administration to improve intestinal barrier bypass of entrapped drugs.

To summarize, a variety of carbohydrate-based biocompatible materials were used for nanoMOF surface modification, improving colloidal stability, controlling drug release, and mediating cell penetration. It paves the way for a versatile surface modification of nanoMOFs for targeted multifunctional drug delivery and other applications.

20.4 Conclusions and future outlook

The development of carbohydrate-based MOFs or carbohydrate-coated MOFs for drug delivery is still in its infancy when compared to other nanocarriers. Nonetheless, these supramolecular porous architectures emerged as a promising platform owing to the combined advantages of both carbohydrates (biodegradability, biocompatibility, hydrophilicity, and the ability to mediate cell penetration of the nanocarriers) and MOFs (structural and chemical diversity, biodegradability, and the capacity to adsorb a series of drugs which could penetrate inside their pores reaching high loadings). Beside CD, hep, chitosan, and HA described here, we foresee that many other carbohydrate-based materials will be employed for MOF synthesis and/or surface modification in the future. There is a plethora of drugs which could benefit from incorporation in (CD) MOFs. The presence in some cases of different types of pores in (CD) MOFs could be used to load different drugs in each type of pore. Moreover, it was possible to form drug clusters in the pores, dramatically increasing the loadings. Moreover, pores could be used as microreactors to synthesize metal nanoparticles, which is another important recent trend. It was also demonstrated that MOFs could release supersaturated drug solutions.

Moreover, together with the drugs, the incorporation of contrast agents for MRI has not been investigated so far in the case of CD-MOFs. Together with drug insertion in the matrices, this approach could be of interest for the development of theranostic platforms.

Although several in vitro efficacy studies have been carried on with both carbohydrates-based MOFs and carbohydrates-coated MOFs, up to date, there still are only very few in vivo investigations with these new systems. To deeper assess the clinical relevance of these formulations, systematic in vivo toxicological studies are required to bring the concept from labscale to patient bedside. With more efforts for their design and optimization, these versatile supramolecular assemblies are expected to have a bright future in drug delivery.

Acknowledgments

Financial support for this work was provided by the French National Research Agency (ANR-14-CE08-0017, ANR-16-CE18-0018 and PCInano) and the Spanish Ministry of Economy and Competitiveness (Grants CTQ2017-90050-R).

References

[1] G. Férey, et al., A chromium terephthalate-based solid with unusually large pore volumes and surface area, Science 309 (5743) (2005) 2040–2042.
[2] P. Horcajada, et al., Metal-organic frameworks as efficient materials for drug delivery, Angew. Chem. Int. Ed. 45 (36) (2006) 5974–5978.
[3] M. Eddaoudi, et al., Modular chemistry: secondary building units as a basis for the design of highly porous and robust metal-organic carboxylate frameworks, Acc. Chem. Res. 34 (4) (2001) 319–330.
[4] G. Férey, Hybrid porous solids: past, present, future, Chem. Soc. Rev. 37 (1) (2008) 191–214.
[5] S. Kitagawa, R. Kitaura, S. Noro, Functional porous coordination polymers, Angew. Chem. Int. Ed. 43 (2004) 2334–2375.
[6] O.M. Yaghi, et al., Reticular synthesis and the design of new materials, Nature 423 (6941) (2003) 705–714.
[7] H. An, et al., Incorporation of biomolecules in metal-organic frameworks for advanced applications, Coord. Chem. Rev. 384 (2019) 90–106.
[8] J. Zhuang, A.P. Young, C.K. Tsung, Integration of biomolecules with metal–organic frameworks, Small 13 (32) (2017) 1–14.
[9] H.P.S. Abdul Khalil, et al., Biodegradable polymer films from seaweed polysaccharides: a review on cellulose as a reinforcement material, Express Polym. Lett. 11 (4) (2017) 244–265.
[10] B. Kang, et al., Carbohydrate nanocarriers in biomedical applications: functionalization and construction, Chem. Soc. Rev. 44 (22) (2015) 8301–8325.
[11] G. Tejashri, B. Amrita, J. Darshana, Cyclodextrin based nanosponges for pharmaceutical use: a review, Acta Pharma. 63 (3) (2013) 335–358.
[12] Y. Yang, et al., Advances in self-assembled chitosan nanomaterials for drug delivery, Biotechnol. Adv. 32 (7) (2014) 1301–1316.
[13] M. Swierczewska, et al., Polysaccharide-based nanoparticles for theranostic nanomedicine, Adv. Drug Deliv. Rev. 99 (2016) 70–84.
[14] S. Uthaman, et al., Carbohydrate-based nanogels as drug and gene delivery systems, J. Nanosci. Nanotechnol. 14 (1) (2014) 694–704.
[15] N. Zhang, P.R. Wardwell, R.A. Bader, Polysaccharide-based micelles for drug delivery, Pharmaceutics 5 (2) (2013) 329–352.
[16] D. Duchêne, et al., Cyclodextrin-based polymeric nanoparticles as efficient carriers for anticancer drugs, Curr. Pharm. Biotechnol. 17 (3) (2016) 248–255.
[17] Y. Han, et al., Cyclodextrin-based metal-organic frameworks (CD-MOFs) in pharmaceutics and biomedicine, Pharmaceutics 10 (2018) 1–21.

[18] T. Rajkumar, et al., Cyclodextrin-metal-organic framework (CD-MOF): from synthesis to applications, J. Ind. Eng. Chem. 72 (2019) 50–66.
[19] J. Simon, et al., Protein corona mediated stealth properties of biocompatible carbohydrate-based nanocarriers, Isr. J. Chem. 58 (2018) 1363–1372.
[20] A.L. Klibanov, et al., Amphipathic polyethyleneglycols effectively prolong the circulation time of liposomes, FEBS Lett. 268 (1) (1990) 235–237.
[21] R. Gref, et al., Biodegradable long-circulating polymeric nanospheres, Science 263 (5153) (1994) 1600–1603.
[22] R. Gref, et al., The controlled intravenous delivery of drugs using PEG-coated sterically stabilized nanospheres, Adv. Drug Deliv. Rev. 16 (2–3) (1995) 215–233.
[23] C. Lemarchand, R. Gref, P. Couvreur, Polysaccharide-decorated nanoparticles, Eur. J. Pharm. Biopharm. 58 (2) (2004) 327–341.
[24] L.Y. Filatova, N.L. Klyachko, E.V. Kudryashova, Targeted delivery of anti-tuberculosis drugs to macrophages: targeting mannose receptors, Russ. Chem. Rev. 87 (4) (2018) 374–391.
[25] B. Kang, et al., Carbohydrate-based nanocarriers exhibiting specific cell targeting with minimum influence from the protein corona, Angew. Chem. Int. Ed. Engl. 54 (2015) 7436–7440.
[26] V. Sihorkar, S.P. Vyas, Potential of polysaccharide anchored liposomes in drug delivery, targeting and immunization, J. Pharm. Pharm. Sci. 4 (2) (2001) 138–158.
[27] G. Cutrone, J.M. Casas-Solvas, A. Vargas-Berenguel, Cyclodextrin-modified inorganic materials for the construction of nanocarriers, Int. J. Pharm. 531 (2017) 621–639.
[28] K. Jain, et al., A review of glycosylated carriers for drug delivery, Biomaterials 33 (16) (2012) 4166–4186.
[29] V. Agostoni, et al., A "green" strategy to construct non-covalent, stable and bioactive coatings on porous MOF nanoparticles, Sci. Rep. 5 (2015) 7925–7931.
[30] E. Bellido, et al., Heparin-engineered mesoporous iron metal-organic framework nanoparticles: toward stealth drug nanocarriers, Adv. Healthc. Mater. 4 (8) (2015) 1246–1257.
[31] M. Giménez-Marqués, et al., GraftFast surface engineering to improve MOF nanoparticles furtiveness, Small 14 (40) (2018) 1–11.
[32] T. Hidalgo, et al., Chitosan-coated mesoporous MIL-100 (Fe) nanoparticles as improved bio-compatible oral nanocarriers, Sci. Rep. 100 (2017) 1–14.
[33] X. Liang, et al., Facile preparation of metal-organic framework (MIL-125)/chitosan beads for adsorption of Pb(II) from aqueous solutions, Molecules 23 (7) (2018) 1–14.
[34] R.A. Smaldone, et al., Metal-organic frameworks from edible natural products, Angew. Chem. 49 (46) (2010) 8630–8634.
[35] J. Sha, et al., Nontoxic and renewable metal-organic framework based on alpha-cyclodextrin with efficient drug delivery, RSC Adv. 6 (2) (2016) 82977–82983.
[36] H. Li, et al., Composite CD-MOF nanocrystals-containing microspheres for sustained drug delivery, Nanoscale 9 (2017) 7454–7463.
[37] X. Li, et al., Cyclodextrin-based metal-organic frameworks particles as efficient carriers for lansoprazole: study of morphology and chemical composition of individual particles, Int. J. Pharm. 531 (2) (2017) 424–432.
[38] H. Lu, et al., Study on a new cyclodextrin based metal-organic framework with chiral helices, Inorg. Chem. Commun. 61 (2015) 48–52.
[39] B. Liu, et al., Microwave-assisted rapid synthesis of gamma-cyclodextrin metal-organic frameworks for size control and efficient drug loading, Cryst. Growth Des. 17 (4) (2017) 1654–1660.
[40] J. Liu, et al., Controllable porosity conversion of metal-organic drug delivery, Chem. Commun. 53 (2017) 7804–7807.
[41] J. Sha, et al., Synthesis and structure of new carbohydrate metal-organic frameworks and inclusion complexes, J. Mol. Struct. 1101 (2015) 14–20.
[42] J. Sha, et al., Unprecedented α-cyclodextrin metal-organic frameworks with chirality: structure and drug adsorptions, Polyhedron 127 (2016) 396–402.
[43] A. Yang, et al., Green synthesis of β-cyclodextrin metal-organic frameworks and the adsorption of quercetin and emodin, Polyhedron 159 (2018) 116–126.

[44] R.S. Forgan, et al., Nanoporous carbohydrate metal-organic frameworks, J. Am. Chem. Soc. 134 (1) (2012) 406–417.
[45] Y. Furukawa, et al., Nano- and microsized cubic gel particles from cyclodextrin metal-organic frameworks, Angew. Chem. Int. Ed. 51 (42) (2012) 10566–10569.
[46] B. Liu, et al., Optimized synthesis and crystalline stability of γ-cyclodextrin metal-organic frameworks for drug adsorption, Int. J. Pharm. 514 (1) (2016) 212–219.
[47] C. Qiu, et al., Green synthesis of cyclodextrin-based metal-organic frameworks through the seed-mediated method for the encapsulation of hydrophobic molecules, J. Agric. Food Chem. 66 (2018) 4244–4250.
[48] C. He, et al., Nanomedicine applications of hybrid nanomaterials built from metal-ligand coordination bonds: nanoscale metal-organic frameworks and nanoscale coordination polymers, Chem. Rev. 115 (19) (2015) 11079–11108.
[49] Y. Wei, et al., Pb(ii) metal-organic nanotubes based on cyclodextrins: biphasic synthesis, structures and properties, Chem. Sci. 3 (7) (2012) 2282–2287.
[50] K.J. Hartlieb, et al., Encapsulation of ibuprofen in CD-MOF and related bioavailability studies, Mol. Pharm. 14 (1) (2017) 1831–1839.
[51] N. Lv, et al., Improvement in thermal stability of sucralose by γ-cyclodextrin metal-organic frameworks, Pharm. Res. 34 (2) (2016) 269–278.
[52] Y. He, et al., Drug nanoclusters formed in confined nano-cages of CD-MOF: dramatic enhancement of solubility, Acta Pharm. Sin. B 9 (1) (2018) 97–106.
[53] X. Hu, et al., Nanoporous CD-MOF particles with uniform and inhalable size for pulmonary delivery of budesonide, Int. J. Pharm. 564 (2019) 153–161.
[54] Y. Inoue, et al., Characterization of inclusion complex of coenzyme Q10 with the new carrier CD-MOF-1 prepared by solvent evaporation, AAPS PharmSciTech 19 (7) (2018) 3048–3056.
[55] Z. Moussa, et al., Encapsulation of curcumin in cyclodextrin-metal-organic frameworks: dissociation of loaded CD-MOFs enhances stability of curcumin, Food Chem. 212 (2016) 485–494.
[56] V. Singh, et al., Moisture resistant and biofriendly CD-MOF nanoparticles obtained via cholesterol shielding, Chem. Commun. 53 (2017) 9246–9249.
[57] V. Singh, et al., Template-directed synthesis of a cubic cyclodextrin polymer with aligned channels and enhanced drug payload, RSC Adv. 7 (2017) 20789–20794.
[58] H. Li, et al., Facile stabilization of cyclodextrin metal-organic frameworks under aqueous conditions via the incorporation of C_{60} in their matrices, Chem. Commun. 52 (35) (2016) 5973–5976.
[59] F. Ke, et al., Synergistic antioxidant activity and anticancer effect of green tea catechin stabilized on nanoscale cyclodextrin-based metal–organic frameworks, J. Mater. Sci. (2019). Available at: http://link.springer.com/10.1007/s10853-019-03604-7.
[60] X. Xu, et al., Evaluation of drug loading capabilities of γ-cyclodextrin-metal-organic frameworks by high performance liquid chromatography, J. Chromatogr. A 1488 (2017) 37–44.
[61] J. Xu, et al., A "Ship-in-a-Bottle" strategy to create folic acid nanoclusters inside the nanocages of γ-cyclodextrin metal-organic frameworks, Int. J. Pharm. 556 (2019) 89–96.
[62] I. Kritskiy, et al., γ-Cyclodextrin-metal organic frameworks as efficient microcontainers for encapsulation of leflunomide and acceleration of its transformation into teriflunomide, Carbohydr. Polym. 216 (2019) 224–230.
[63] M.P. Abuçafy, et al., Supramolecular cyclodextrin-based metal-organic frameworks as efficient carrier for anti-inflammatory drugs, Eur. J. Pharm. Biopharm. 127 (2018) 112–119.
[64] G. Zhang, Enhanced stability of vitamin A palmitate microencapsulated by γ-cyclodextrin metal-organic frameworks, J. Microencapsul. 35 (3) (2018) 249–258.
[65] H. Arima, et al., Recent advances in cyclodextrin delivery techniques, Expert Opin. Drug Deliv. 12 (9) (2015) 1425–1441.
[66] W. Michida, et al., Crystal growth of cyclodextrin-based metal-organic framework with inclusion of ferulic acid, Cryst. Res. Technol. 50 (7) (2015) 556–559.
[67] A. Nagai, et al., Encapsulation of isolated C_{60} molecules in a cyclodextrin-based metal-organic framework, J. Chem. Eng. Jpn 51 (7) (2018) 615–619.

[68] P. Horcajada, et al., Metal-organic frameworks in biomedicine, Chem. Rev. 112 (2012) 1232–1268.
[69] T. Baati, et al., In depth analysis of the in vivo toxicity of nanoparticles of porous iron(iii) metal-organic frameworks, Chem. Sci. 4 (2013) 1597–1607.
[70] T. Simon-Yarza, et al., Smart metal-organic-framework nanoparticles for lung targeting, Angew. Chem. Int. Ed. 56 (49) (2017) 15565–15569.
[71] T. Simon-Yarza, et al., Nanoparticles of metal-organic frameworks: on the road to in vivo efficacy in biomedicine, Adv. Mater. 30 (37) (2018) 1–15.
[72] A. Aykaç, et al., A non-covalent "click chemistry" strategy to efficiently coat highly porous MOF nanoparticles with a stable polymeric shell, Biochim. Biophys. Acta Gen. Subj. 1861 (4) (2017) 1606–1616.
[73] X. Mao, et al., Talanta β—cyclodextrin functionalization of metal-organic framework MOF-235 with excellent chemiluminescence activity for sensitive glucose biosensing, Talanta 188 (2018) 161–167.

Further reading

Z. Amoozgar, Y. Yeo, Recent advances in stealth coating of nanoparticle drug delivery systems, Wiley Interdiscip. Rev. Nanomed. Nanobiotechnol. 4 (2) (2012) 219–233.
L. Han, et al., Molecular mechanism of loading sulfur hexafluoride in γ-cyclodextrin metal-organic framework, J. Phys. Chem. B 122 (2018) 5225–5233.
D. Ko, Y. Yeo, Application of polysaccharides for surface modification of nanomedicines, Ther. Deliv. 3 (12) (2012) 1447–1456.
X. Li, et al., Compartmentalized encapsulation of two antibiotics in porous nanoparticles: an efficient strategy to treat intracellular infections, Part. Part. Syst. Char. 36 (3) (2019) 1800360.
J. Liu, S. Willför, C. Xu, A review of bioactive plant polysaccharides: biological activities, functionalization, and biomedical applications, Bioact. Carbohydr. Diet. Fibre 5 (1) (2015) 31–61.
L. Lumholdt, T.T. Nielsen, K.L. Larsen, Surface modification using self-assembled layers of amphiphilic cyclodextrins, J. Appl. Polym. Sci. 41047 (2014) 1–8.
G. Wenz, Cyclodextrins as building blocks for supramolecular structures and functional units, Angew. Chem. 33 (1994) 803–822.

Chapter 2

Comb-like dextran copolymers: A versatile strategy to coat highly porous MOF nanoparticles with a PEG shell

General Objectives and Author Contributions

The first case of nanoMOFs was reported by the scientists in 1989. Since their discovery, nanoMOFs have attracted a large number of interest because of their excellent properties. However, it is absolutely necessary to functionalize the outer surface of nanoMOFs with coating materials such as PEG chain to prevent them from the recognition and removal by the innate immune system, an indispensable condition for biomedical applications. Until recently, this was still a big challenge because of the highly porous composition and degradability of nanoMOFs. In this context, we achieved the surface modification of the external surface of MIL-100(Fe) nanoMOFs by a green and environmental friendly method, utilizing a new family of comb-like copolymers made of dextran (DEX) grafted with both PEG and alendronate (ALN) moieties. DEX-ALN-PEG copolymers were synthesized with click chemistry, controlling both the amount of PEG and ALN moieties by adjusting the molar ratio between them. A stable coating was formed while DEX-ALN-PEG copolymers spontaneously anchored onto the outer surface of MIL-100(Fe).

Complementary methods were used to prove the efficacy of DEX-ALN-PEG copolymers on the performance of stealth effect.

1) The interaction of coated or uncoated nanoMOFs with HSA, the most abundant protein in human blood plasma, was investigated in order to gain further understanding on protein adsorption. There results clearly revealed that the optimized coatings are able to decrease five times the adsorption of this modal protein.
2) Optical microscopy was used to observe the cells after incubation with the nanoMOFs. After 2 h incubation, lots of nanoMOFs were took up by macrophage. On the contrary, with the same incubation time, the uptake of coated nanoMOFs was dramatically reduced.
3) Inductively coupled plasma mass spectrometry (ICPMS) further quantified the amount of internalized uncoated and coated nanoMOFs. The optimized coating reduced three times the in vitro macrophages uptake, affording new perspectives for the applications in biomedical field.

All the authors have contributed in this work. I performed the experiments on the nanoMOFs synthesis, characterization, surface modification, colloidal stability and cell interaction, and also contributed to the analysis of the data and writing of the main manuscript.

Carbohydrate Polymers 223 (2019) 115085

Contents lists available at ScienceDirect

Carbohydrate Polymers

journal homepage: www.elsevier.com/locate/carbpol

Comb-like dextran copolymers: A versatile strategy to coat highly porous MOF nanoparticles with a PEG shell

Giovanna Cutrone[a,1], Jingwen Qiu[b,1], Mario Menendez-Miranda[b], Juan M. Casas-Solvas[a], Ahmet Aykaç[a,2], Xue Li[b], Daniel Foulkes[b], Borja Moreira-Alvarez[c], Jorge R. Encinar[c], Catherine Ladavière[d], Didier Desmaële[e], Antonio Vargas-Berenguel[a,*], Ruxandra Gref[b,*]

[a] Department of Chemistry and Physics, University of Almería, Ctra. de Sacramento s/n, 04120 Almería, Spain
[b] Institut des Sciences Moléculaires d'Orsay, UMR CNRS 8214, Université Paris-Sud, Université Paris Saclay, 91400 Orsay, France
[c] Department of Physical and Analytical Chemistry, University of Oviedo, Julián Clavería 8, 33006 Oviedo, Spain
[d] University of Lyon, CNRS, UMR 5223, IMP, 15 bd André Latarjet, F-69622 Villeurbanne, France
[e] Institut Galien Paris-Sud, UMR 8612, CNRS, Université Paris-Sud, Faculté de Pharmacie, 5 rue JB Clément, 92296 Châtenay-Malabry, France

ARTICLE INFO

Keywords:
Metal organic frameworks nanoparticles
Surface modification
Dextran
Poly(ethylene glycol)
Macrophage uptake
Click chemistry

ABSTRACT

Nanoparticles made of metal-organic frameworks (nanoMOFs) are becoming of increasing interest as drug carriers. However, engineered coatings such as poly(ethylene glycol) (PEG) based ones are required to prevent nanoMOFs recognition and clearance by the innate immune system, a prerequisite for biomedical applications. This still presents an important challenge due to the highly porous structure and degradability of nanoMOFs. We provide here a proof of concept that the surface of iron-based nanoMOFs can be functionalized in a rapid, organic solvent-free and non-covalent manner using a novel family of comb-like copolymers made of dextran (DEX) grafted with both PEG and alendronate (ALN) moieties, which are iron complexing groups to anchor to the nanoMOFs surface. We describe the synthesis of DEX-ALN-PEG copolymers by click chemistry, with control of both the amount of PEG and ALN moieties. Stable DEX-ALN-PEG coatings substantially decreased their internalization by macrophages *in vitro*, providing new perspectives for biomedical applications.

1. Introduction

Metal-organic frameworks (MOFs) are one of the latest classes of ordered porous solids which have attracted growing interest since their discovery in 1989 (Hoskins & Robson, 1989), in reason of their remarkable versatility. Indeed, almost any metal could be associated to polycomplexing linkers such as carboxylates, phosphonates, sulfonates or imidazolates leading to the discovery of thousands of MOFs with a variety of pore sizes and shapes (Horcajada et al., 2012; Liu et al., 2017; Yuan et al., 2018). Among the MOFs family, nanosized MOFs (nanoMOFs) based on porous iron(III) polycarboxylates have emerged as an important class of biodegradable and non-toxic (Horcajada et al., 2010; Baati et al., 2013) materials that can be loaded with exceptional quantities (within the 20–70 wt% range) of a large variety of therapeutic agents (Agostoni, Anand et al., 2013; Agostoni, Chalati et al., 2013; Horcajada et al., 2010). This paved the way to novel perspectives in terms of targeted delivery of drugs (Simon-Yarza et al., 2017; Simon-Yarza, Baati, Paci et al., 2016; Simon-Yarza, Baati, Neffati et al., 2016) and theranostics (Horcajada et al., 2010). For biomedical applications, it is of utmost importance to engineer the surface of the nanoMOFs, since the *in vivo* fate of any nanoparticles (NPs) in the living body (biodistribution, pharmacokinetics and targeting abilities) depends upon its surface physicochemical properties. For instance, it was shown that surface functionalization with hydrophilic polymers such as poly (ethylene glycol) (PEG) in a "brush" configuration could dramatically extend the blood circulation times of NPs by mitigating their recognition by the reticuloendothelial system (Gref et al., 1994, 1995). However, to date, Doxil® represents the only FDA-approved PEGylated liposome-based nanocarrier of anticancer drug (Doxorubicin) (Barenholz, 2012).

Functionalization of nanoMOFs surfaces will be critical to their success as potential nanocarriers in therapeutic contexts (Abdelhameed, Rehan, & Emam, 2018). However, thus far, only a limited number of cases have been reported that have aimed to modify the surface of

* Corresponding authors.
E-mail addresses: avargas@ual.es (A. Vargas-Berenguel), ruxandra.gref@u-psud.fr (R. Gref).
[1] These authors contributed equally.
[2] Current address: Faculty of Engineering and Architecture Izmir Kâtip Çelebi University Çiğli 35620 Izmir Turkey.

https://doi.org/10.1016/j.carbpol.2019.115085
Received 28 May 2019; Received in revised form 12 July 2019; Accepted 12 July 2019
Available online 15 July 2019
0144-8617/

nanoMOFs with PEG shells (Agostoni et al., 2015; Chen et al., 2017; Giménez-Marqués et al., 2018; Zhang et al., 2015; Zimpel et al., 2016). As compared to dense NPs made of biodegradable polymers or liposomes, the porous surface of MOFs is a challenging surface to functionalize. Indeed, it was reported that PEG chains are able to penetrate within the pores, blocking them and/or decreasing the drug loading capacity (Agostoni et al., 2015). To avoid PEG penetration into the highly porous MOFs, PEG-based shells were formed by GraftFast, a method involving polymerization of acryl PEGs (Giménez-Marqués et al., 2018). By this way, PEG derivatives with initial molecular weights of 480, 2000 and 5000 Da were polymerized leading to stable coatings. However, the molecular weight of the resulting PEG-based copolymer could not be efficiently controlled. Another recent strategy employed cyclodextrin (CD) derivatives, which were first adsorbed onto the MOFs surfaces prior to complex formation with PEG grafted with adamantane moieties (Agostoni et al., 2015). However, the two-step procedure required by this method resulted in a difficulty to control the quantity of grafted PEG.

Moreover, no study has yet demonstrated that a PEG coating on nanoMOFs could effectively reduce their reticuloendothelial sequestration. In this context, there is still a clear demand to engineer versatile PEG-based coatings onto the nanoMOFs surface, with proof of concept, by reducing uptake by macrophages. Here we address this challenge by using a novel family of copolymers, synthesized by grafting onto a dextran (DEX) backbone two types of moieties: i) PEG chains to avoid macrophage uptake and ii) alendronate (ALN) to spontaneously coordinate to the nanoMOFs surface. Iron trimesate MIL-100(Fe) (MIL stands for Material of the Institute Lavoisier) nanoMOFs were selected as core materials, in reason of their biodegradability, capacity to incorporate a series of drugs such as antibiotics (Li et al., 2019), anticancer drugs (Di Nunzio, Agostoni, Cohen, Gref, & Douhal, 2014; Rodriguez-Ruiz et al., 2015), and anti-infective agents (Agostoni, Anand et al., 2013; Agostoni, Chalati et al., 2013), reaching unprecedented payloads together with controlled releases, versatility in terms of drug loadings and lack of *in vivo* toxicity (Baati et al., 2013; Simon-Yarza, Baati, Paci et al., 2016; Simon-Yarza, Baati, Neffati et al., 2016).

Here we show the possibility to achieve stable coatings by a straightforward method, based on cooperative interactions between the ALN moieties and the external surface of MIL-100(Fe) nanoMOFs. Thus, we describe the synthetic strategies to control both PEG and ALN densities on the DEX backbone, as well as the convenient one-step method to coat the nanoMOFs. The PEG "brush" efficiently reduced macrophage uptake as demonstrated by both microscopic investigations and quantitative determination of the amount of internalized nanoMOFs using inductively coupled plasma mass spectrometry (ICP-MS).

2. Materials and methods

2.1. Chemicals and general methods

Thin layer chromatography (TLC) was performed on Merck silica gel 60 F_{254} aluminum sheets and developed by UV–vis light, iodine, 5% v/v sulfuric acid in ethanol, 5% w/v phosphomolybdic acid in ethanol, and 1% w/v potassium permanganate in aqueous 0.1% w/v NaOH containing 7% w/v potassium carbonate, depending on the case. Flash column chromatography was performed on Merck silica gel (230–400 mesh, ASTM). Infrared spectra were recorded on a Bruker Alpha FTIR equipped with a Bruker universal ATR sampling accessory. ^{1}H, ^{13}C, ^{31}P and 2D NMR spectra were recorded on a Bruker Avance III HD 600 MHz spectrometer equipped with a QCI $^{1}H/^{13}C/^{15}N/^{31}P$ proton-optimized quadrupole inverse cryoprobe with ^{1}H and ^{13}C cryochannels, or a Bruker Nanobay Avance III HD 300 MHz spectrometer equipped with a QNP $^{1}H/^{13}C/^{19}F/^{31}P$ probe, depending on the sample. Standard Bruker software was used for acquisition and processing routines. Chemical shifts (δ) are given in parts per million (ppm) and referenced to internal tetramethylsilane (TMS) signal (δ_H, δ_C 0.00). *J* values are given in hertz (Hz). ESI-TOF mass spectra were recorded on an Agilent LC/MSD-TOF spectrometer in both positive and negative modes. Syringe filtering was conducted using nylon 0.45 µm Milipore Millex® syringe-driven filter units. Dialysis was performed using Medicell Membranes Ltd 12000–14000 Da molecular weight cutoff (MWCO) Visking dialysis tubing. Elemental analyses were recorded on an Elementar Vario Micro CHNS analyzer. HR-ICP-MS results were obtained by using a Termo Finningan magnetic sector field ELEMENT 2 inductively coupled plasma mass spectrometer. A Hanna HI 98,192 EC/TDS/NaCl/Resistivity meter was employed to monitor dialysate solutions conductivity during dialysis.

6-Bromohexanoic acid (Aldrich, 97%), sodium azide (Panreac, 99%), *N*-hydroxysuccinimide (NHS, Aldrich, 98%), *N*-(3-dimethylaminopropyl)-*N'*-ethylcarbodiimide hydrochloride (EDC, Fluka, ≥98%), alendronic acid monosodium salt trihydrate (CarboSynth, purum), poly (ethylene glycol) methyl ether ($MeOPEG_{45}OH$, Aldrich, Mn ~2000), 4-dimethylaminopyridine (DMAP, Fluka, ≥98%), methanesulfonyl chloride (MsCl, Fluka, ≥99%), 1,1'-carbonyldiimidazole (CDI, Acros, 97%), propargylamine (Aldrich, 98%), anhydrous copper(II) sulfate (Fluka, 98%), (+)-sodium L-ascorbate (Sigma, BioXtra, ≥99%), and ethylenediaminetetraacetic acid disodium salt dihydrate (EDTA, Fluka, purum) were purchased from commercial sources and used without further purification otherwise indicated. Anhydrous LiCl (Sigma-Aldrich, 99%) and dextran T-40 (Pharmacosmos, purum, Nominative Mw 40,000 Da) were purchased from commercial sources and dried at 80 °C under high vacuum for 48 h in the presence of P_2O_5 prior to use. Triethylamine (Sigma-Aldrich, > 99%) and organic solvents were dried according to literature procedures (Perrin & Armarego, 1989). Dry DMF (AcroSeal, 99.8%, over molecular sieves) was purchased from Acros. Iron (III) chloride hexahydrate (Alfa Aesar, Schiltigheim, France, 98%), 1,3,5-benzenetricarboxylic acid (BTC, Sigma-Aldrich, Saint-Quentin-Fallavier, France, 95%) and absolute ethanol (Carlo Erba, Val-de-Reuil, France, 99%) were used for the synthesis of nanoMOFs. Potassium chloride (Sigma-Aldrich) was used for nanoMOFs Zeta potential (ZP) measurements. Doxorubicin (DOX, Sigma-Aldrich, 98%) was used for drug encapsulation. Human serum albumin (HSA, Sigma-Aldrich) and bicinchoninic acid (BCA) protein assay kit (Pierce™ Thermo Fisher) was used for HSA adsorption test. Deionized Milli-Q water was obtained from a Millipore apparatus with a 0.22 µm filter.

The number average molecular weight (*Mn*) and the molar-mass dispersity values of dextran derivatives **5** and **7** were measured by using a SEC column (TSKgel G2500PW and G6000PW columns) coupled with a differential refractometer (RI, Optilab T-rEX, Wyatt Technology) with a laser at λ = 658 nm, thermostated at 25 °C, and a multi-angle laser light scattering instrument (MALLS, HELEOS II, Wyatt Technology) equipped with a laser operating at λ = 664 nm. Degassed and filtered (0.1 µm membrane) 0.15 M ammonium acetate/0.20 M acetic acid buffer (pH = 4.5) was used as eluent at a flow rate of 0.5 mL/min (with a refractive index increment value, *dn/dc* of 0.147 ml/g for DEX). These eluents were also used as solvent of samples, and the resulting solutions were filtered on a 0.45 µm membrane before injection. Finally, 200 µL of each sample at 1 mg/mL were injected. The data have been exploited thanks to the ASTRA 6.1.7.17 software (Wyatt Technology).

Murine macrophage cell line J774A.1 (ATCC) were grown in Dulbecco's Modified Eagle's Medium (Thermo Fischer) supplemented with 10% v/v decomplemented fetal bovine serum (FBS) at 37 °C in humidified conditions with 5% CO_2. Prussian blue iron staining kit (Sigma-Aldrich) containing potassium ferrocyanide, pararosaniline and hydrochloric acid was used for cell staining.

2.2. Synthesis and characterization of dextran-PEG

2.2.1. Synthesis of 6-azidohexanoic acid (1)

Compound **1** was prepared as described in literature (Alemán,

Pedini, & Rueda, 2009; Kuil, Branderhorst, Pieters, De Mol, & Liskamp, 2009) with small modifications. Specifically, NaN_3 (1 g, 15.4 mmol) was added to a solution of 6-bromohexanoic acid (1.5 g, 7.7 mmol) in dry DMF (10 mL) under N_2 atmosphere and stirred at 85 °C overnight until TLC (2:1 hexane:EtOAc) showed complete disappearance of the starting material and the appearance of a spot at $R_f = 0.59$. The solvent was rotary evaporated under high vacuum and the residue was dissolved in H_2O (20 mL) and extracted with EtOAc (3 x 30 mL). The organic layers were combined, dried ($MgSO_4$), and rotary evaporated to give 6-azidohexanoic acid **1** (0.866 g, 5.5 mmol, 70%) as slightly yellow oil. NMR data agreed with those previously reported (Kuil et al., 2009): ^{1}H NMR (300 MHz, $CDCl_3$) δ (ppm): 11.04 (s, 1H, COOH), 3.24 (t, 2H, ^3J = 6.9 Hz, CH_2N_3), 2.32 (t, 2H, ^3J = 7.3 Hz, CH_2COOH), 1.70-1.50 (m, 4H, CH_2CH_2COOH, $CH_2CH_2N_3$), 1.40 (m, 2H, $CH_2CH_2CH_2N_3$); ^{13}C NMR (75 MHz, $CDCl_3$) δ (ppm): 179.1 (COOH), 51.2 (CH_2N_3), 34.0 (CH_2COOH), 28.6 ($CH_2CH_2N_3$), 26.2 ($CH_2CH_2CH_2N_3$), 24.3 (CH_2CH_2COOH).

2.2.2. Synthesis of 2,5-dioxopyrrolidin-1-yl 6-azidohexanoate (2)

Compound **2** was prepared as described in literature (Grandjean, Boutonnier, Guerreiro, Fournier, & Mulard, 2005) with small modifications. Specifically, *N*-hydroxysuccinimide (520 mg, 4.5 mmol) was added to a solution of 6-azidohexanoic acid **1** (650 mg, 4.1 mmol) in dry CH_2Cl_2 (10 mL) under N_2 atmosphere at room temperature and the mixture was stirred until complete solubilisation. Then, EDC (860 mg, 4.5 mmol) was added and the solution was stirred at room temperature until TLC (2:1 hexane:EtOAc) showed complete disappearance of the starting material and the appearance of a spot at $R_f = 0.41$. After 16 h, the mixture was washed with 1 N HCl (2 × 15 mL) and saturated aq. $NaHCO_3$ (2 × 15 mL). The aqueous layer was extracted with CH_2Cl_2 (2 x 10 mL). All organic phases were combined, dried ($MgSO_4$), and rotary evaporated. The residue was purified by column chromatography using 2:1 hexane:EtOAc as eluent to yield compound **2** (790 mg, 3.1 mmol, 76%) as a colourless liquid. NMR data agreed with those previously reported (Grandjean et al., 2005): ^{1}H NMR (300 MHz, $CDCl_3$) δ (ppm): 3.23 (t, 2H, ^3J = 6.7 Hz, CH_2N_3), 2.75 (s, 4H, COCH_2CH_2CO), 2.56 (t, 2H, ^3J = 7.3 Hz, CH_2COO), 1.90-1.30 (m, 6H, $CH_2CH_2CH_2CH_2N_3$); ^{13}C NMR (75 MHz, $CDCl_3$) δ (ppm): 169.1 (NCOCH_2), 168.4 (COO), 51.1 (CH_2N_3), 30.8 (CH_2COO), 28.4 (CH_2), 25.9 (CH_2), 25.6 (COCH_2CH_2CO), 24.1 (CH_2).

2.2.3. Synthesis of the sodium salt of [4-(6-azidohexanamido)-1-hydroxy-1-(hydroxy-oxido-phosphoryl)-butyl]phosphonic acid (3)

Aqueous 0.1 M NaOH (~32 mL) was added dropwise to a suspension of alendronic acid monosodium salt trihydrate (0.83 g, 2.56 mmol) in MilliQ water (18 mL) until pH ~8.5, forming a clear solution. A solution of 2,5-dioxopyrrolidin-1-yl 6-azidohexanoate **2** (0.78 g, 3.1 mmol) in acetonitrile (18 mL) was added in four portions each 15 min. Before each portion, pH was measured and readjusted to ~8.5 with aqueous 0.1 M NaOH if needed. The reaction mixture was stirred overnight at room temperature and then the solvent was rotary evaporated. The residue was purified by a short column chromatography using 5:1→2:1 CH_3CN:H_2O as eluent to yield compound **3** (0.84 g, 2.05 mmol, 80%) as a white solid after lyophilising: FT-IR (KBr) ν/cm^{-1}: 3445, 2938, 2867, 2100, 1632, 1558, 1105, 913, 620, 551; ^{1}H NMR (600 MHz, D_2O) δ (ppm): 3.34 (t, 2H, ^3J = 6.9 Hz, CH_2N_3), 3.22 (t, 2H, ^3J = 6.8 Hz, CONHCH_2) 2.28 (t, 2H, ^3J = 7.5 Hz, CH_2CONH), 2.01-1.93 (m, 2H, CH_2C), 1.86-1.81 (m, 2H, CH_2CH_2C), 1.66-1.61 (m, 4H, CH_2CH_2CONH, $CH_2CH_2N_3$), 1.42-1.37 (m, 2H, $CH_2CH_2CH_2N_3$); ^{13}C NMR (150 MHz, D_2O) δ (ppm): 176.9 (CONH), 73.9 (t, $^1J_{CP}$ = 134.2 Hz, $C(PO_3)_2$), 51.0 (CH_2N_3), 40.0 ($NHCH_2$), 36.6 (CH_2CONH), 31.1 (CH_2C), 27.7 ($CH_2CH_2N_3$), 25.4 ($CH_2CH_2CH_2N_3$), 24.9 (CH_2CH_2CONH), 23.4 (t, $^3J_{CP}$ = 5.9 Hz, CH_2CH_2C); ^{31}P (242.9 MHz, D_2O) δ (ppm): 18.2 ($C(PO_3)_2$); [ESI-TOF-MS]$^-$ *m/z* calcd for $C_{10}H_{21}N_4O_8P_2$ 387.0840, found 387.0839 [M – Na]$^-$; *m/z* calcd for $C_{10}H_{20}N_4O_8P_2Na$ 409.0660, found 409.0657 [M − H]$^-$; [ESI-TOF-MS]$^+$ *m/z* calcd for $C_{10}H_{22}N_4O_8P_2Na$ 411.0816 found 411.0818 [M+H]$^+$; *m/z* calcd for $C_{10}H_{21}N_4O_8P_2Na_2$ 433.0635, found 433.0643 [M + Na]$^+$; *m/z* calcd for $C_{10}H_{20}N_4O_8P_2Na_3$ 455.0455 found 455.0465 [M − H + 2Na]$^+$; *m/z* calcd for $C_{10}H_{19}N_4O_8P_2Na_4$ 477.0274, found 477.0283 [M – 2H + 3Na]$^+$.

2.2.4. Synthesis of 1-azido-1-deoxy-ω-O-methoxypentatetracontaethylene glycol (4)

A solution of $MeOPEG_{45}OH$ (35 g, 17.375 mmol), DMAP (428 mg, 3.5 mmol) and distilled Et_3N (5.6 mL, 40.250 mmol) in CH_2Cl_2 (40 mL) was cooled to 0 °C under inert atmosphere. MsCl (2.7 mL, 35 mmol) was added dropwise over 15 min and the mixture was stirred at 0 °C during 30 min and then kept overnight at room temperature. The reaction mixture was then diluted with CH_2Cl_2 (50 mL), and washed with 5% v/v aqueous HCl solution (3 × 50 mL) and brine (50 mL). The organic phase was dried over $MgSO_4$, filtered and concentrated under reduced pressure to dryness. The solid was subsequently dissolved in dry DMF (40 mL) and NaN_3 (2.276 g, 35 mmol) was added. The mixture was stirred at 60 °C for 24 h before the solvent was rotary evaporated under high vacuum. The residue was suspended in THF (20 mL), sonicated (5 min), and filtered off. The clear organic filtrate was rotary evaporated, and the resulting solid was suspended in Et_2O (50 mL), sonicated (5 min) and filtered. The solid was dissolved in H_2O (100 mL) and extracted with CH_2Cl_2 (3 × 100 mL). The organic phases were combined, dried ($MgSO_4$) and rotary evaporated, and the residue dried under vacuum to give compound **4** (26.225 g, 12.858 mmol, 74%) as a slightly yellow powder: FT-IR (KBr) ν/cm^{-1}: 2868, 2105, 1093, 948, 842, 729; ^{1}H NMR (300 MHz, D_2O) δ (ppm): 3.96-3.93 (m, $^1J_{H,C}$ = 143.4 Hz, ^{13}C satellite peak), 3.75-3.68 (m, 176H, OCH_2CH_2O), 3.65-3.61 (m, 2H, $CH_2CH_2N_3$), 3.53-3.49 (m, 2H, CH_2N_3), 3.49-3.46 (m, $^1J_{H,C}$ = 143.4 Hz, ^{13}C satellite peak), 3.38 (s, CH_3O); ^{13}C NMR (75 MHz, D_2O) δ (ppm): 71.7 (MeOCH_2), 70.3 (OCH_2CH_2O), 70.2 (MeOCH$_2CH_2$O), 70.0 (O$CH_2CH_2N_3$), 58.8 (OMe), 50.9 (CH_2N_3).

2.2.5. Synthesis of dextran propargylcarbamate (DEX-PC, 5)

LiCl (1 g) and dextran T-40 (4 g) were pre-dried at 80 °C in a high vacuum oven for 2 days in the presence of P_2O_5. The mixture was further dried by suspension in dry toluene (50 mL) and subsequent vacuum distillation at 50 °C. This azeotropic drying process with toluene was repeated twice, and then with anhydrous DMF (1 × 50 mL) followed by evaporation of the solvent through a rotary evaporator at 60 °C under high vacuum. The dry mixture was finally dissolved in anhydrous DMF (80 mL) and stirred at 80 °C for 1.5 h. The solution was cooled down to room temperature before carbonyldiimidazole (0.972 g, 6 mmol) was added, and stirred for 2.5 h. Propargylamine (3.85 mL, 60 mmol) was then added and the mixture stirred at room temperature for 24 h. The solvent volume was reduced to 60 mL by rotary evaporation and the solution was poured into isopropanol (0.9 L). The resulting pale yellow solid was collected by filtration and dissolved in H_2O (100 mL), syringe filtered (0.45 µm) and dialyzed (12000–14000 Da MWCO) against distilled water, changing dialysate solution each 3 h until its conductivity was stable and below 1 µS/cm (3 days for final value of 0.90 µS/cm) to yield DEX-PC **5** (3.6 g) as a white solid after lyophilization: FT-IR (KBr) ν/cm^{-1}: 3420, 2930, 1709, 1639, 1530, 1461, 1419, 1346, 1264, 1156, 1041, 1014, 766, 549, 527; ^{1}H NMR (600 MHz, D_2O) δ (ppm): 5.36 (d, $^3J_{1,2}$ = 3.8 Hz, α(1→3,4) H-1), 5.21 (app bd, J_{app} = 2.8 Hz, α reducing end H-1, CH-OCONH), 5.06 (d, $^3J_{1,2}$ = 2.6 Hz, H-1^S), 5.01 (d, $^3J_{1,2}$ = 3.0 Hz, α(1→6) H-1), 4.98 (bs, H-1^S), 4.63 (d, $^3J_{1,2}$ = 7.2 Hz, β reducing end H-1), 4.02-3.93 (m, H-3,6^a, $CH_2C\equiv$), 3.78-3.73 (m, H-5,6^b), 3.60 (dd, $^3J_{1,2}$ = 3.0 Hz, $^3J_{2,3}$ = 9.7 Hz, H-2), 3.55 (t, ^3J = 9.4 Hz, H-4), 3.51 (t, ^3J = 9.9 Hz, H-4^S), 3.44 (t, ^3J = 9.5 Hz, H-4^S), 3.03 (bs, ≡CH), 2.95 (bs, ≡CH), 2.69 (app bd, J_{app} = 8.7 Hz, ≡CH); ^{13}C NMR (150 MHz, D_2O) δ (ppm): 157.9 (CO), 157.0 (CO), 99.3, 98.2, 97.7 (α(1→6) C-1), 95.6 (C-1^S), 80.4-78.8 (C≡), 76.7, 73.4 (C-3), 73.2-73.1 (≡CH), 72.0, 71.4 (C-2), 71.0, 70.2 (C-5), 69.9, 69.5 (C-4), 67.7, 65.5 (C-6), 65.2, 60.5, 30.1

($CH_2C\equiv$); Anal.: found C 40.90%, H 6.536%, N 1.42%. The number average molecular weight and the molar-mass dispersity were measured to be *Mn* = 35,240 g/mol and Đ = 1.14, respectively (Figure S14A).

2.2.6. Synthesis of DEX-ALN$_{75}$-PEG$_{25}$ (6)

Pre-dried LiCl (90 mg, 2.123 mmol) and DEX-PC **5** (350 mg, 0.0079 mmol containing 0.397 mmol of propargyl groups) were dissolved in H_2O (5 mL) and heated at 60 °C. A solution of sodium alendronate derivative **3** (127 mg, 0.298 mmol) in H_2O (2 mL) was added, followed by a suspension of $CuSO_4$ (29 mg, 0.179 mmol) and sodium ascorbate (118 mg, 0.596 mmol) in H_2O (1 mL), and the mixture was stirred at 90 °C overnight. After cooling down to room temperature, azide **4** (809 mg, 0.397 mmol) and a suspension of $CuSO_4$ (38 mg, 0.238 mmol) and sodium ascorbate (157 mg, 0.794 mmol) in H_2O (0.8 mL) were subsequently added. The mixture was stirred for 22 h at 90 °C, then diluted with H_2O (10 mL), filtered through filtering paper and then through a 0.45 μm syringe filter. Aqueous 0.1 M NaOH was added until pH ~7.0, followed by a solution of 10 mM EDTA at pH 7.0 (20 mL). The pH was then monitored and kept at ~7.0 with 0.1 M NaOH for 24 h. The mixture was again filtered through 0.45 μm syringe filter, lyophilized, re-dissolved in the minimum amount of water and dialyzed (12000–14000 Da MWCO) against distilled water, changing dialysate solution each 3 h until its conductivity was stable and below 1 μS/cm (3 days for final value of 0.60 μS/cm) to yield DEX-ALN$_{75}$-PEG$_{25}$ **6** (881 mg) as a brownish solid after lyophilization: FT-IR (KBr) ν/cm^{-1}: 3423, 2913, 2880, 1645, 1457, 1352, 1298, 1252, 1104, 1041, 952, 845, 548; ^{1}H NMR (600 MHz, D_2O) δ (ppm): 8.03 (bs, H-5-C_2HN_3), 5.35 (bs, α(1→3,4) H-1), 5.27 (bs, α reducing end H-1), 5.18 (app t, J_{app} = 5.0 Hz, C*H*-OCONH), 5.04 (bs, H-1^S), 5.00 (bs, α(1→6) H-1), 4.64 (bs, β reducing end H-1), 4.51-4.44 (m, OCH$_2$C*H*$_2$-C_2HN_3), 4.40-4.38 (m, C*H*$_2$-C_2HN_3), 4.31-4.28 (m, NHC*H*$_2$-C_2HN_3), 4.02-3.93 (m, H-5,6^a), 3.87-3.84 (m, $^1J_{H,C}$ = 140.2 Hz, ^{13}C satellite peak), 3.73 (bs, H-3,6^b, OC*H*$_2$C*H*$_2$O), 3.67-3.64 (m, OC*H*$_2$CH$_2$-C_2HN_3), 3.61-3.60 (m, H-2), 3.56-3.52 (m, H-4), 3.45 (app t, J_{app} = 9.3 Hz, H-4^S), 3.40 (s, CH_3O), 3.34-3.19 (C*H*$_2$NH), 2.88 (bs, ≡CH), 2.78 (bs, ≡CH), 2.64 (bs, ≡CH), 2.23 (bs, CH_2CO), 1.93 (bs, CH_2C), 1.77 (bs, C*H*$_2$CH$_2$C), 1.61 (C*H*$_2$CH$_2$CO, C*H*$_2$CH$_2$-C_2HN_3), 1.30-1.16 (bs, C*H*$_2$CH$_2$CH$_2$CO); ^{31}P NMR (242.9 MHz, D_2O) δ (ppm): -1.4-(-2.6) ($C(PO_3)_2$); Anal.: found C 46.24%, H 7.582%, N 2.46%; HR-ICP-MS: found P 0.81%, Na 0.103%, Cu 1.05%, Li 0.042%.

2.2.7. Synthesis of DEX-ALN$_{50}$-PEG$_{50}$ (7)

Pre-dried LiCl (90 mg, 2.123 mmol) and DEX-PC **5** (350 mg, 0.0079 mmol containing 0.397 mmol of propargyl groups) were dissolved in H_2O (5 mL) and heated at 60 °C. A solution of sodium alendronate derivative **3** (85 mg, 0.198 mmol) in H_2O (1.5 mL) was added, followed by a suspension of $CuSO_4$ (19 mg, 0.119 mmol) and sodium ascorbate (79 mg, 0.397 mmol) in H_2O (1 mL), and the mixture was stirred at 90 °C overnight. After cooling down to room temperature, azide **4** (809 mg, 0.397 mmol) and a suspension of $CuSO_4$ (38 mg, 0.238 mmol) and sodium ascorbate (157 mg, 0.794 mmol) in H_2O (0.8 mL) were subsequently added. The mixture was stirred for 22 h at 90 °C, then diluted with H_2O (10 mL), filtered through filtering paper and then through a 0.45 μm syringe filter. Aqueous 0.1 M NaOH was added until pH ~7.0, followed by a solution of 10 mM EDTA at pH 7.0 (20 mL). The pH was then monitored and kept at ~7.0 with 0.1 M NaOH for 24 h. The mixture was again filtered through 0.45 μm syringe filter, lyophilized, re-dissolved in the minimum amount of water and dialyzed (12000–14000 Da MWCO) against distilled water, changing dialysate solution each 3 h until its conductivity was stable and below 1 μS/cm (3 days for final value of 0.74 μS/cm) to yield DEX-ALN$_{50}$-PEG$_{50}$ **7** (928 mg) as a brownish solid after lyophilization: FT-IR (KBr) ν/cm^{-1}: 3429, 2917, 2881, 1645, 1457, 1352, 1253, 1103, 952, 558; ^{1}H NMR (600 MHz, D_2O) δ (ppm): 8.03 (bs, H-5-C_2HN_3), 5.35 (bs, α(1→3,4) H-1), 5.26 (bs, α reducing end H-1), 5.18 (app t, J_{app} = 5.0 Hz, C*H*-OCONH), 5.04 (bs, H-1^S), 5.00 (bs, α(1→6) H-1), 4.64 (bs, β reducing end H-1), 4.47-4.43 (m, OCH$_2$C*H*$_2$-C_2HN_3), 4.40-4.38 (m, C*H*$_2$-C_2HN_3), 4.31-4.29 (m, NHC*H*$_2$-C_2HN_3), 4.02-3.93 (m, H-5,6^a), 3.87-3.84 (m, $^1J_{H,C}$ = 140.4 Hz, ^{13}C satellite peak), 3.73 (bs, H-3,6^b, OC*H*$_2$C*H*$_2$O), 3.67-3.64 (m, OC*H*$_2$CH$_2$-C_2HN_3), 3.61-3.59 (m, H-2), 3.56-3.52 (m, H-4), 3.43 (app t, J_{app} = 10.0 Hz, H-4^S), 3.41 (s, CH_3O), 3.32-3.18 (C*H*$_2$NH), 2.88 (bs, ≡CH), 2.70 (bs, ≡CH), 2.25 (bs, CH_2CO), 1.93 (bs, CH_2C), 1.78 (bs, C*H*$_2$CH$_2$C), 1.61 (C*H*$_2$CH$_2$CO, C*H*$_2$CH$_2$-C_2HN_3), 1.26 (bs, C*H*$_2$CH$_2$CH$_2$CO); ^{31}P NMR (242.9 MHz, D_2O) δ (ppm): -1.8-(-2.9) ($C(PO_3)_2$); Anal.: found C 46.85%, H 7.769%, N 2.27%; HR-ICP-MS: found P 0.57%, Na 0.060%, Cu 0.74%, Li 0.027%. The number average molecular weight and the molar-mass dispersity were measured to be *Mn* = 83,120 g/mol and Đ = 1.36, respectively (Figure S14B).

2.2.8. Synthesis of DEX-ALN$_{25}$-PEG$_{75}$ (8)

Pre-dried LiCl (90 mg, 2.123 mmol) and DEX-PC **5** (350 mg, 0.0079 mmol containing 0.397 mmol of propargyl groups) were dissolved in H_2O (5 mL) and heated at 60 °C. A solution of sodium alendronate derivative **3** (43 mg, 0.100 mmol) in H_2O (1 mL) was added, followed by a suspension of $CuSO_4$ (10 mg, 0.060 mmol) and sodium ascorbate (40 mg, 0.200 mmol) in H_2O (1 mL), and the mixture was stirred at 90 °C overnight. After cooling down to room temperature, azide **4** (809 mg, 0.397 mmol) and a suspension of $CuSO_4$ (38 mg, 0.238 mmol) and sodium ascorbate (157 mg, 0.794 mmol) in H_2O (0.8 mL) were subsequently added. The mixture was stirred for 22 h at 90 °C, then diluted with H_2O (10 mL), filtered through filtering paper and then through a 0.45 μm syringe filter. Aqueous 0.1 M NaOH was added until pH ~7.0, followed by a solution of 10 mM EDTA at pH 7.0 (20 mL). The pH was then monitored and kept at ~7.0 with 0.1 M NaOH for 24 h. The mixture was again filtered through 0.45 μm syringe filter, lyophilized, re-dissolved in the minimum amount of water and dialyzed (12000–14000 Da MWCO) against distilled water, changing dialysate solution each 3 h until its conductivity was stable and below 1 μS/cm (2 days for final value of 0.63 μS/cm) to yield DEX-ALN$_{25}$-PEG$_{75}$ **8** (978 mg) as a brownish solid after lyophilization: FT-IR (KBr) ν/cm^{-1}: 3423, 2912, 2880, 1645, 1457, 1352, 1299, 1253, 1104, 1042, 1019, 951, 845, 550; ^{1}H NMR (600 MHz, D_2O) δ (ppm): 8.03 (bs, H-5-C_2HN_3), 5.35 (bs, α(1→3,4) H-1), 5.27 (bs, α reducing end H-1), 5.19 (app t, J_{app} = 5.0 Hz, C*H*-OCONH), 5.05 (bs, H-1^S), 5.00 (bs, α(1→6) H-1), 4.90 (bs, H-1^S), 4.64 (bs, β reducing end H-1), 4.64 (bs, OCH$_2$C*H*$_2$-C_2HN_3), 4.40-4.38 (m, C*H*$_2$-C_2HN_3), 4.31-4.28 (m, NHC*H*$_2$-C_2HN_3), 4.02-3.93 (m, H-5,6^a), 3.85-3.84 (m, $^1J_{H,C}$ = 140.4 Hz, ^{13}C satellite peak), 3.73 (bs, H-3,6^b, OC*H*$_2$C*H*$_2$O), 3.68-3.64 (m, OC*H*$_2$CH$_2$-C_2HN_3), 3.61-3.59 (m, H-2), 3.56-3.52 (m, H-4), 3.45 (app t, J_{app} = 9.6 Hz, H-4^S), 3.41 (s, CH_3O), 3.32-3.19 (C*H*$_2$NH), 3.02 (bs, ≡CH), 2.95 (bs, ≡CH), 2.23 (bs, CH_2CO), 1.93 (bs, CH_2C), 1.78 (bs, C*H*$_2$CH$_2$C), 1.61 (C*H*$_2$CH$_2$CO, C*H*$_2$CH$_2$-C_2HN_3), 1.31-1.22 (bs, C*H*$_2$CH$_2$CH$_2$CO); ^{31}P NMR (242.9 MHz, D_2O) δ (ppm): 0.5-0.1, -1.5-(-2.4) ($C(PO_3)_2$); Anal.: found C 47.86%, H 7.842%, N 2.05%; HR-ICP-MS: found P 0.26%, Na 0.092%, Cu 0.42%, Li 0.048%.

2.3. Synthesis and characterization of MIL-100(Fe) nanoMOFs

Iron trimesate nanoMOFs were synthesized using a microwave-assisted hydrothermal method as previously described (Agostoni, Anand et al., 2013; Agostoni, Chalati et al., 2013). Briefly, 30 mL of an aqueous mixture containing 6.0 mM iron chloride hexahydrate and 4.0 mM of 1,3,5-benzenetricarboxylic acid was heated at 130 °C under stirring prior to microwave irradiation at 1600 W (Mars-5, CEM, USA). The synthesized nanoMOFs were recovered by centrifugation at 10,000 g for 15 min and purified by washing six times with absolute ethanol. Their morphology was observed with a transmission electron microscope (TEM, JEOL 1400 (120 kV), Japan). Mean hydrodynamic diameters and size distributions were determined by dynamic light scattering (DLS, Malvern Nano-ZS, Zetasizer Nano series, France). NanoMOFs' Zeta potential (ZP) was measured at 25 °C using a Zetasizer Nano-ZS

instrument in a pH range of 1–10. For this, nanoMOFs were diluted to a final concentration of 100 μg/mL using a 1 mM KCl solution. The nanoMOFs specific surface area was measured by nitrogen sorption experiments at −196 °C on an ASAP 2020 (Micromeritics, USA) after sample degassing at 100 °C for 15 h under high vacuum. X-ray powder diffraction patterns (XRPD) were recorded for crystallinity characterization. NanoMOFs were stored in ethanol at room temperature and re-suspended in aqueous media whenever needed.

2.4. Surface modification of MIL-100(Fe) nanoMOFs and their characterization

2.4.1. Preparation and characterization of DEX-ALN-PEG coated nanoMOFs

NanoMOFs were centrifuged at 10,000 g for 10 min to remove the storage solvent (ethanol) and then re-dispersed in water by vortex. For coating, they were incubated overnight at room temperature with DEX-ALN-PEG solutions at mass ratios DEX-ALN-PEG: nanoMOFs of 1:4, 1:2 and 1:1. The non-attached DEX-ALN-PEG fraction was removed by centrifugation (10,000 g, 10 min). The pellets were dried and the adsorbed DEX-ALN-PEG was quantified by ICP-MS. Briefly, nanoMOFs before and after modification with DEX-ALN-PEG were digested using *aqua regia* (15 min under ultrasonic bath), and phosphorous (P) quantification was performed using an ICP-MS equipped with a triple quadrupole (Agilent 8800, Agilent Technologies, Japan). Operation conditions were daily optimized using a tuning solution. P isotope was detected using "mass shift mode" ($^{47}PO^+$) after reaction with oxygen in the cell. Conversely, scandium (Sc) (added as internal standard on samples and calibration standards solutions at a concentration of 10 μg/L)) was detected using "on mass mode" ($^{45}Sc^+$). Oxygen was introduced into the collision/reaction cell at a flow rate of 0.35 mL/min. Dwell time for each of the targeted isotopes was 1 s. P was quantified using external calibration using certified 1000 mg/L P standard solution (Merck, Germany).

The amount (*A*) of DEX-ALN-PEG associated to nanoMOFs was calculated on the basis of their P content by Eq. (1):

$$A = \frac{P1}{P2} \times 100\% \quad (1)$$

where P1 (wt%) is the phosphorous content in the coated nanoMOFs and P2 (wt%) is the phosphorous content in the synthesized DEX-ALN-PEG copolymers.

DEX-ALN-PEG coated nanoMOFs were characterized the same as the uncoated samples to determine their size distribution, morphology, porosity (BET surface area) and surface charge. The crystallinity of DEX-ALN-PEG coated nanoMOFs was studied by XRPD.

2.4.2. Colloidal stability investigation

Colloidal stabilities of DEX-ALN-PEG coated nanoMOFs were estimated by DLS after incubation in both MilliQ water and cell culture medium (DMEM complemented with 10% FBS, 1% penicillin/streptomycin (100 mg/mL) and 1% L-glutamine). Mean hydrodynamic diameters were measured at 6 h, and 1, 2, 4, 7, 9, 14, 18 and 21 d storage at 4 °C in water, and at 0, 2, 4, 6, and 8 h after incubation at 37 °C in cell culture media.

2.4.3. Effect of surface modification on drug encapsulation

MIL-100(Fe) nanoMOFs ethanolic suspension was first centrifuged (10 min, 10,000 g) to recover the sedimented nanoMOFs, which were further redispersed in pure water. For the DOX encapsulation, nanoMOFs aqueous suspension was mixed with DOX and gently stirred for 48 h at room temperature. The weight ratio between DOX and nanoMOFs was 1:5. The DOX loaded nanoMOFs were recovered by centrifugation (10,000 g, 10 min) and the supernatant was used to quantify the drug payload, which was calculated by Eq. (2):

$$Payload\ (\%) = \frac{Encapsulated\ Drug(mg)}{nanoMOFs(mg)} \times 100 \quad (2)$$

The DOX loaded nanoMOFs were further surface modified with DEX-ALN_{25}-PEG_{75} **8** by incubating the drug loaded nanoMOFs with DEX-ALN_{25}-PEG_{75} **8** aqueous solution overnight at mass ratio DEX-ALN-PEG:nanoMOFs 1:1. After surface functionalization, the DEX-ALN_{25}-PEG_{75} **8** coated drug loaded nanoMOFs were recovered again by centrifugation (10 min, 10,000 g). The supernatant was also recovered to quantify the DOX amount.

2.4.4. Human albumin adsorption studies

NanoMOFs coated or not with DEX-ALN-PEG (300 μg/mL) were incubated with HSA solutions at 100 μg/mL in 10 mM phosphate buffer (PB) at 37 °C. The samples were centrifuged at 10,000 g for 5 min to recover the nanoMOF pellets after 1, 2, 3, 4, 6, 8 and 12 h incubation. The excess of HSA in the supernatant was quantified using a bicinchoninic acid (BCA) assay.

2.4.5. "Stealth" effect of the DEX-ALN-PEG shell

A direct visualization of the MIL-100(Fe) nanoMOFs inside J774A.1 macrophages was achieved based on iron staining using a Prussian blue staining kit. In a 24-well plate (with cover slips) 1×10^5 J774A.1 macrophages were placed with RPMI complete medium and 10% FBS. Each well of macrophages was treated with 50 μg of nanoMOFs, either coated or not with DEX-ALN-PEG. The macrophages were subsequently incubated for 2 and 4 h in an incubator at 37 °C with a CO_2 concentration of 5%. Afterwards the wells were washed with complete medium and then further washed twice with PBS. Cells were fixed with 4% paraformaldehyde, washed and incubated for 10 min with 2% potassium ferrocyanide in 0.6 mM hydrochloric acid. Cells were washed again with PBS, counterstained with pararosaniline hydrochloride (0.02%) and placed on a glass slide. A drop of emersion oil was applied to each coverslip and evaluated for iron staining using light microscopy.

For Fe quantification by ICP-MS, macrophage cells (J774A.1) were seeded overnight at a density of 3.0×10^5 cells per well in 24-well plates in cell culture medium at 37 °C in 5% CO_2. Cells were then incubated with 1 mL cell culture media containing nanoMOFs coated or not with DEX-ALN-PEG for 2, 4 and 6 h (nanoMOFs concentration = 50 μg/mL). After incubation, the cells were washed with PBS for three times to eliminate the nanoMOFs which did not interact with the cells. Cells were finally dried and digested using *aqua regia* (15 min under ultrasonic bath). Fe quantification was performed using an ICP-MS equipped with a triple quadrupole (Agilent 8800). Operation conditions were daily optimized using a tuning solution. Fe and Co isotopes (added as internal standard on samples and calibration standards at a concentration of 10 μg/L) were detected using "on-mass mode" ($^{54}Fe^+$, $^{56}Fe^+$, $^{59}Co^+$). Helium was introduced into the collision/reaction cell at a flow rate of 3 mL min^{-1}. Dwell time for each of the targeted isotopes was 1 s. Fe was quantified using external calibration prepared using certified 1000 mg/L Fe standard solution (Merck, Germany).

3. Results and discussion

3.1. Synthesis and characterization of DEX-ALN-PEG copolymers

For the post-synthetic modification of the surface of MIL-100(Fe) nanoMOFs we planned to prepare DEX derivatives appended with alendronate (ALN) moieties and PEG chains. For this strategy, we first prepared alendronate and PEG azide derivatives **3** and **4**, respectively (Scheme 1). We then appended them on dextran T-40 grafted with a controlled number of therminal alkyne residues in the form of propargyl carbamate groups (DEX-PC **5**) (Scheme 2) through a Cu(I)-catalyzed azide-alkyne cycloaddition (CuAAC) reaction to yield DEX-ALN-PEG conjugates **6–8**.

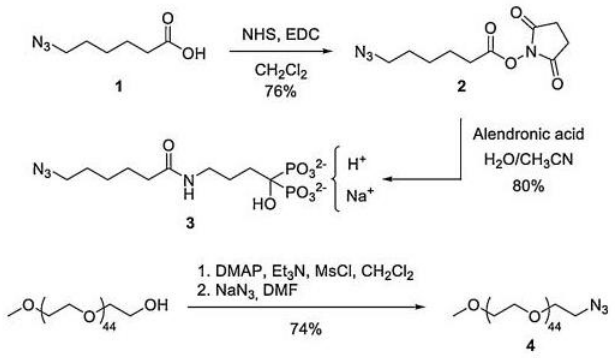

Scheme 1. Synthesis of azide derivatives **3** and **4**.

First, we synthesized azide alendronate derivative **3** (Scheme 1). The reaction between NHS-ester **2** and alendronic acid monosodium salt was performed in a MeCN:H_2O mixture keeping the pH at ~8.5 in order both to ensure the solubility of the alendronate salt and to guarantee the nucleophilic properties of the primary amine. However, precipitation of the crude after solvent evaporation with EtOH afforded product **3** with *N*-hydroxysuccinimide (NHS) byproduct, as confirmed by ^{1}H NMR spectra. Attempts to remove NHS by solid-liquid extraction using organic solvents, including EtOAc and CH_3CN, failed. Thus, compound **3** was finally isolated by column chromatography using 5:1 CH_3CN:H_2O as initial eluent until NHS was washed out of the column, and 2:1 CH_3CN:H_2O for eluting pure **3** in 80% yield after lyophilization. In the initial alkaline pH ~8.5 environment, product **3** should be most likely in a trisodium salt form (Ke et al., 2016). However, flash column chromatography probably changed the distribution curves of the species in equilibrium by partial acidification of the mixture. Indeed, negative ESI-TOF mass spectrum depicted the species $[M - Na]^-$ and $[M - H]^-$ considering M as the monosodium salt. Similarly, positive ESI-TOF mass spectrum showed $[M+H]^+$, $[M + Na]^+$, $[M - H + 2Na]^+$ and $[M - 2H + 3Na]^+$, suggesting that the alendronate derivative was obtained mainly as the monosodium salt species.

Synthesis of azido PEG chain **4** was performed in two sequential steps. Commercial $MeOPEG_{45}OH$, having a methoxy group at one end of the chain, was mesylated and used without any further purification for the reaction with sodium azide in DMF. Azido PEG **4** was isolated by two subsequent filtration processes with THF and Et_2O that yielded **4** pure enough, as confirmed by NMR analysis. It is important to remark that the broad signal observed at δ 3.65-3.61 ppm corresponding to the main chain methylene groups appeared along with ^{13}C satellites due to the ^{13}C-^{1}H coupling typically observed in high molecular weight PEG derivatives (Semple, Sullivan, Vojkovsky, & Sill, 2016).

The partial alkynylation of the dextran T-40 was achieved upon treatment with carbonyldiimidazole (CDI) and propargylamine forming propargyl carbamate groups on some of the free OH groups of the polysaccharide (Sun et al., 2011). DEX T-40 was extensively dried to minimize unwanted side reactions with water. Reaction was performed in dry DMF in the presence of anhydrous LiCl to help solubilizing the polysaccharide by interfering with its high crystallinity. DEX T-40 was then subsequently treated with 60 equivalents of CDI and an excess of propargylamine to give DEX-PC **5** (Scheme 2). Taking into account that the number of propargyl carbamate appendages directly depends on the CDI ratio, we expected these amounts to yield a maximum of 60 alkynes per DEX T-40 molecule. After dialysis and lyophilization, the composition of the obtained material was determined by elemental analysis. A mathematical model (see supplementary material) was developed to estimate the number of propargyl groups grafted on the polymer from those data. The model consistently estimated ~50 propargyl carbamate groups each time the reaction was repeated. The functionalization of the polysaccharide can be observed by ^{1}H NMR through the appearance of broad signals at δ 3.03, 2.95 and 2.69 ppm that correspond to the ethynyl proton of propargyl carbamate groups located at different positions on the glucose moieties. In addition, a set of new signals arose from the substituted glucose units, namely a doublet at δ 5.06 ppm and broad singlet δ 4.98 ppm corresponding to anomeric protons, along with two triplets at δ 3.51 and 3.44 ppm assigned to the H-4 protons. In ^{13}C NMR spectrum, signals at δ 157.9-157.0 ppm indicated the presence of carbonyl groups on the structure, while the quaternary and ternary carbons of the ethynyl group gave peaks in the range of δ 80.4-78.8 and δ 73.2-73.1 ppm, respectively.

Once DEX-PC **5** was prepared, azides **3** and **4** were conjugated using $CuSO_4$ and sodium ascorbate as catalyst system at 90 °C in water (Scheme 2). Three dextran derivatives with different ratios of ALN and PEG branches were prepared, namely DEX-ALN_{75}-PEG_{25} **6**, DEX-ALN_{50}-PEG_{50} **7** and DEX-ALN_{25}-PEG_{75} **8**, in order to study the effect of such ratio on both the stability of the coating and the "stealth" abilities of the resulting surface-modified nanoMOFs. To prevent that the different

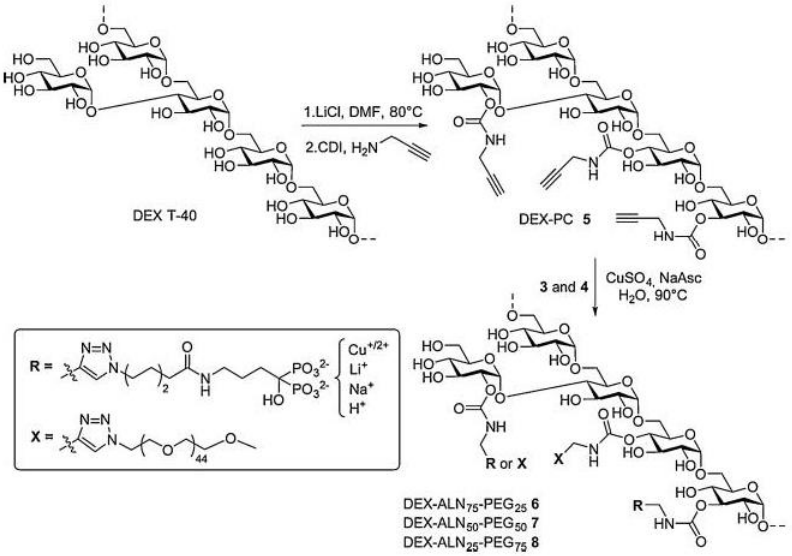

Scheme 2. Synthesis of DEX-PC **5** and DEX-ALN-PEG **6**–8. Structures of copolymers **5**–**8** are intended to simply depict different modes of carbamate attachment to the DEX chain and do not reflect either the actual spatial distribution of the appendages or the degree of substitution along the chain.

diffusion coefficients and reactivity kinetics of structurally so different azides as **3** and **4** might condition the actual ratio on **6–8**, conjugations were performed sequentially starting with the required amount of alendronate derivative **3**, followed after 8 h by addition of an excess of PEG azide **4**. It was expected that the conjugation of the short chain of alendronate in the first place would not hinder the subsequent approach of the much bulkier PEG chain in the second step, which might occur if performed in the opposite order. Purification of **6–8** was carried out by washing with a solution of EDTA at pH ~7.0 in order to chelate the excess of copper, followed by dialysis against water using 12–14 KDa MWCO membranes until stable conductivity (< 1 μS/cm) was obtained in the dialysate solution. The analysis of number average molecular weights (*Mn*) of polymers before (DEX-PC **5**) and after (DEX-ALN$_{50}$-PEG$_{50}$ **7**) chemical modification by PEG chains was achieved by SEC-MALLS. The starting material, DEX had a *Mn* value of 31,150 g/mol (Figure S14C). It was further shown that grafting ALN and PEG resulted in an expected increase of number average molecular weight (from 35,240 for DEX-PC **5** to 83,120 g/mol for DEX-ALN$_{50}$-PEG$_{50}$ **7**). This difference of around 50,000 g/mol could correspond to a ratio of 25% of PEG grafted chains of 2000 g/mol (since 50% × 2000 g/mol × 100 units = 100,000 g/mol). Nevertheless, note that this determination presents a high uncertainly notably due to the hypothesis that the refractive index increment value of DEX-ALN$_{50}$-PEG$_{50}$ **7** was equal to the one of unmodified dextran (*dn/dc* = 0.147 ml/g). Consequently, elemental analysis and HR-ICP-MS of the obtained copolymers was carried out in order to obtain a more accurate compositional profile for DEX-ALN-PEG derivatives **6–8**. The mathematical model constructed to analyze these data (see supplementary material) indicated that only 66–74% of propargyl carbamates underwent cycloaddition (Table 1). Interestingly, the average number of ALN branches appended to the polysaccharide consistently changed depending on the initial ratio of reagents although in lesser extension than foreseen, varying from ~15 in the case of DEX-ALN$_{75}$-PEG$_{25}$ **6** to ~5 for DEX-ALN$_{25}$-PEG$_{75}$ **8**. In sharp contrast, the average number of PEG branches only varies from ~26 in the case of PEG-ALN$_{75}$-PEG$_{25}$ **6** and ~32 for DEX-ALN$_{25}$-PEG$_{75}$ **8**. This fact suggests that cycloaddition of PEG azide derivative **4** onto DEX-PC **5** is mainly limited by steric hindrance of the resulting product more than the reagent amount added to the reaction. The robustness of the model is evidenced by the fact that the sum of free propargyl carbamate (*n*), ALN (*x*) and PEG (*z*) branches keeps around 50 (± 12%), which matches the estimated number of propargyl carbamate groups originally present in DEX-PC **5** starting material. It should be underlined that the model predicts the presence of at least one Cu atom per alendronate branch, along with an extra cation of Na and/or Li, even after extraction with EDTA prior dialysis. This result is not surprising since it is known that alendronate can chelate Cu(II) in a wide range of pH (Oms et al., 2016; Ostović, Stelmach, & Hulshizer, 1993), and indeed may explain the reduced cycloaddition efficiency for alendronate branches since copper cations could have been sequestered during the reaction. Although free, unbound Cu(II) has been demonstrated to be toxic for living cells (Biaglow, Manevich, Uckun, & Held, 1997), it requires concentrations as high as 78.5 μmol/L (5 mg/L) in serum for systemic toxicity in humans (Barceloux, 1999). Furthermore, the toxicity of chelated copper is remarkably lower, allowing its use to perform CuAAC reactions within living systems (Notni & Wester, 2016; Su, Li, Wang, Wang, & Zhang, 2016). We observed that copper present in DEX-ALN-PEG **6–8** did not hinder MIL-100(Fe) coating (see below) which took place through their alendronate branches, and most likely, it was displaced by iron(III) atoms from nanoMOFs surface and washed out during centrifugation isolation. The proposed structures for **6–8** were demonstrated by ^{1}H NMR spectra, where the formation of 1,2,3-triazole residues caused the appearance of a broad signal at δ 8.03 ppm in the three cases. In addition, methylene protons of PEG residues gave an intense peak at δ 3.73 ppm, while weak and broad singlets observed between δ 2.25 and 1.26 ppm evidenced the presence of alendronate branches. Furthermore, signals from non-reacted ethynyl protons were still notorious between δ 3.02 and 2.64 ppm, as the compositional model had predicted (Table 1). ^{13}C NMR experiments were strongly dominated by the high signals arising from PEG methylenes, which hindered both their acquisition and assignation. Finally, ^{31}P NMR confirmed the presence of phosphorus nuclei in the molecules with signals at δ 0.5-(-2.6) ppm.

3.2. MIL-100(Fe) nanoMOFs synthesis and surface modification

3.2.1. DEX-ALN-PEG coating and physicochemical characterization

MIL-100(Fe) nanoMOFs with a mean hydrodynamic diameter of 191 ± 23 nm and BET (Brunauer, Emmett and Teller) surface area of 1690 ± 80 $m^2 g^{-1}$ were successfully synthesized by an organic solvent-free microwave-assisted hydrothermal method. They exhibited a facetted morphology (Fig. 1C), crystalline structure (Fig. 1B) and composition in agreement with previously reported data (Agostoni, Anand et al., 2013; Agostoni, Chalati et al., 2013; Agostoni et al., 2015).

Surface modification of MIL-100(Fe) nanoMOFs with DEX-ALN-PEG was carried out through a simple, "green" (meaning organic solvent-free) method consisting on simple impregnation of nanoMOFs in aqueous solutions of the synthesized copolymers (Fig. 1A). The three copolymers with increased PEG contents, namely DEX-ALN$_{75}$-PEG$_{25}$ **6**, DEX-ALN$_{50}$-PEG$_{50}$ **7**, and DEX-ALN$_{25}$-PEG$_{75}$ **8** were used for the surface modification.

The amount of DEX-ALN-PEG associated to the nanoMOFs was determined by ICP-MS by direct quantification of the P content in the coated samples. Indeed, P is the only element present in the DEX-ALN-PEG copolymers, but not in the nanoMOFs, offering a straightforward and precise quantification method. It was found that after overnight incubation, amounts of DEX-ALN$_{75}$-PEG$_{25}$ **6**, DEX-ALN$_{50}$-PEG$_{50}$ **7**, and DEX-ALN$_{25}$-PEG$_{75}$ **8** associated to the nanoMOFs reached 29 ± 2 wt%, 27 ± 2 wt% and 32 ± 3 wt%, respectively. Interestingly, these amounts of coating material attached to the nanoMOFs were among the highest reported so far. This efficient association could be possibly attributed to: i) the strong affinity of ALN for iron site at the surface and ii) the cooperative effects of ALN moieties as schematized in Fig. 1A. As comparison, cyclodextrin (CD)-phosphate coating on the same MIL-100(Fe) nanoMOFs reached ~17 wt%. In that case, only 3–4 phosphate moieties were attached to each CD (Aykaç et al., 2017). Indeed, alendronate, used mainly for osteoporosis treatment, is known to have a strong affinity for metals. It was incorporated in nanoMOFs made of Zr-based UiO-66 NPs (Zhu et al., 2014). It was highlighted that this amino-

Table 1
Calculated (see supplementary material) number of free propargyl carbamate (*n*), alendronate (*x*) and PEG (*z*) branches from compositional profiles obtained by elemental analyses and HR-ICP-MS data.[a].

Derivative	*n* No. of propargyl groups	*x* No. of ALN groups	*z* No. of PEG chains	*n*+*x*+*z*
DEX-PC **5**	50.1	0	−0.1	50.1
DEX-ALN$_{75}$-PEG$_{25}$ **6**	16.1	14.3	26.0	56.4
DEX-ALN$_{50}$-PEG$_{50}$ **7**	13.7	10.8	30.5	55.0
DEX-ALN$_{25}$-PEG$_{75}$ **8**	17.6	4.9	32.3	54.8

[a] An error of ± 12% was estimated.

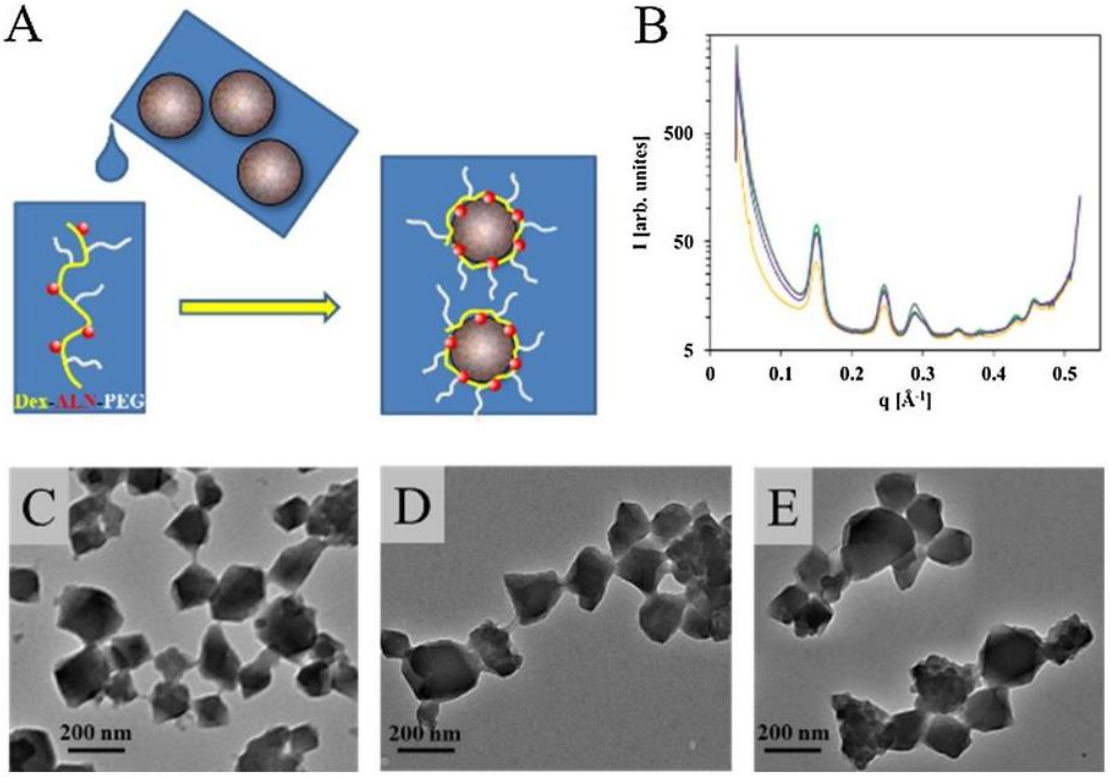

Fig. 1. Preparation and characterization of nanoMOFs coated or not with DEX-ALN-PEG. A: schematic representation of the «green» preparation of DEX-ALN-PEG coated nanoMOFs in water; For DEX-ALN-PEG, the red balls represent alendronate (ALN) moieties, dextran (DEX) is represented in yellow and poly(ethylene glycol) (PEG) chains are in white. B: XRPD patterns of nanoMOFs coated or not with DEX-ALN-PEG (green: nanoMOFs; purple: DEX-ALN_{75}-PEG_{25} **6** coated nanoMOFs; orange: DEX-ALN_{50}-PEG_{50} **7** coated nanoMOFs; gray: DEX-ALN_{25}-PEG_{75} **8** coated nanoMOFs); C-E: TEM images of uncoated nanoMOFs (C), DEX-ALN_{50}-PEG_{50} **7** coated nanoMOFs (D) and DEX-ALN_{25}-PEG_{75} **8** coated nanoMOFs (E); scale bar (200 nm). The mass ratios DEX-ALN-PEG: nanoMOFs were 1:1.

bisphosphonate was probably strongly anchored to the Zr-O clusters of the UiO NPs, thus promoting both high loading efficiencies (close to 100%) and controlled release.

These studies showed that the amount of DEX-ALN-PEG associated to the nanoMOFs was not significantly affected by the ratio of ALN used in the experiments. This suggests that a large number of ALN moieties are not required for an efficient coating of the nanoMOFs, and that DXT-ALN_{25}-PEG_{75} **8** already shows enough ALN appendages (~5) to perform the most efficient coating we could observed.

The MIL-100(Fe) nanoMOFs coated or not with DEX-ALN-PEG were characterized by a set of complementary techniques. First, XRPD studies indicated that the crystalline structure of MIL-100(Fe) nanoMOFs was preserved after surface modification (Fig. 1B) in spite of the high amounts of DEX-ALN-PEG associated to the NPs. This indicates that functionalization of DEX-ALN-PEG polymers did not disturb the crystalline structure of nanoMOFs. Second, TEM experiments showed that the nanoMOFs maintained their facetted morphology, regardless of the type of DEX-ALN-PEG adsorbed (Fig. 1C-E).

The hydrodynamic diameters of MIL-100(Fe) nanoMOFs were determined by dynamic light scattering (DLS) in water before and after surface modification. The mean hydrodynamic diameter of nanoMOFs before coating was 191 ± 23 nm. Whatever the amount and type of DEX-ALN-PEG coating material, there were no significant mean size and polydispersity variations after the coating process. Final mean diameters were in the range of 193 ± 21 nm to 209 ± 31 nm, indicating that the coating thickness was less than 10 nm and that no aggregation occurred.

Uncoated nanoMOFs had a tendency to aggregate upon storage in water (Fig. 2A), in agreement with previous studies (Agostoni et al., 2015). In contrast, nanoMOFs coated with all the DEX-ALN-PEG samples (mass ratio DEX-ALN-PEG:nanoMOFs 1:1) were stable in water up to three weeks storage, showing that their coating efficiently prevented their aggregation. However, the mass ratios DEX-ALN-PEG:nanoMOFs play an important role on the colloid stability of the nanoMOFs. For example, when reducing 4 fold the amount of DEX-ALN_{50}-PEG_{50} **7** at the nanoMOFs surface (mass ratio DEX-ALN-PEG:nanoMOFs 1:4), aggregation was observed during storage in water, as shown by a diameter increase from 193 nm to more than 400 nm in 24 h (Fig. 2A), possibly due to DEX-ALN-PEG at the surface of nanoMOFs inducing a bridging effect. Therefore this sample was excluded in the following experiments. All the nanoMOFs formulations were stable in the biological medium used in this study (DMEM complemented with 10% FBS) (Fig. 2B). No aggregation was found and the mean diameters remained constant over more than 6 h incubation at 37 °C, allowing for further biological investigations of interactions with macrophages.

To prove that the DEX-ALN-PEG copolymer did not penetrate inside the nanostructure, we performed drug encapsulation. Briefly, DOX, an anticancer drug, was used as a guest molecule for drug loading studies. DOX was efficiently loaded in uncoated nanoMOFs by host-guest interactions by adapting a previously reported procedure (Anand et al., 2014). DOX-loaded nanoMOFs were further surface-modified with DEX-ALN-PEG copolymers. It was shown that coating with DEX-ALN-PEG copolymers did not induce any DOX release (< 2 ± 0.3%), indicating that DEX-ALN-PEG copolymer did not interfere with the drug molecules located inside the porous cores.

3.2.2. Surface properties of nanoMOFs before and after functionalization

ZP measurements were performed to gain insights on the influence of the coatings on the global charge of the NPs. The ZP of the nanoMOFs, coated or not, was found to be strongly dependent upon the

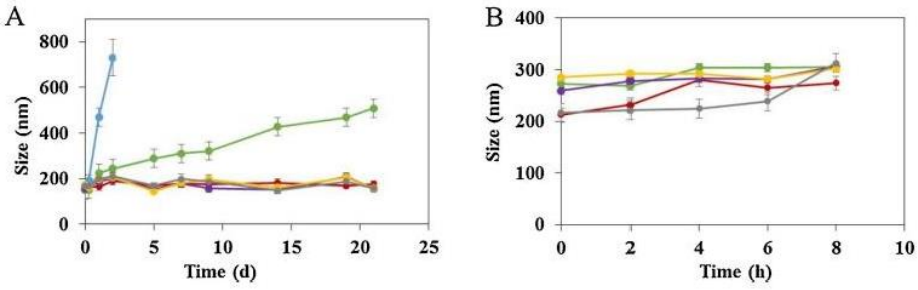

Fig. 2. Stability of nanoMOFs coated or not with DEX-ALN-PEG in water (A) and in DMEM cell culture medium (B). Green: uncoated nanoMOFs; purple: nanoMOFs coated with DEX-ALN_{75}-PEG_{25} **6** (mass ratio DEX-ALN-PEG:nanoMOFs 1:1); orange: nanoMOFs coated with DEX-ALN_{50}-PEG_{50} **7** (mass ratio DEX-ALN-PEG:nanoMOFs 1:1); gray: nanoMOFs coated with DEX-ALN_{25}-PEG_{75} **8** (mass ratio DEX-ALN-PEG:nanoMOFs 1:1); blue: nanoMOFs coated with DEX-ALN_{50}-PEG_{50} **7** (mass ratio DEX-ALN-PEG:nanoMOFs 1:4); red: nanoMOFs coated with DEX-ALN_{50}-PEG_{50} **7** (mass ratio DEX-ALN-PEG: nanoMOFs 1:2).

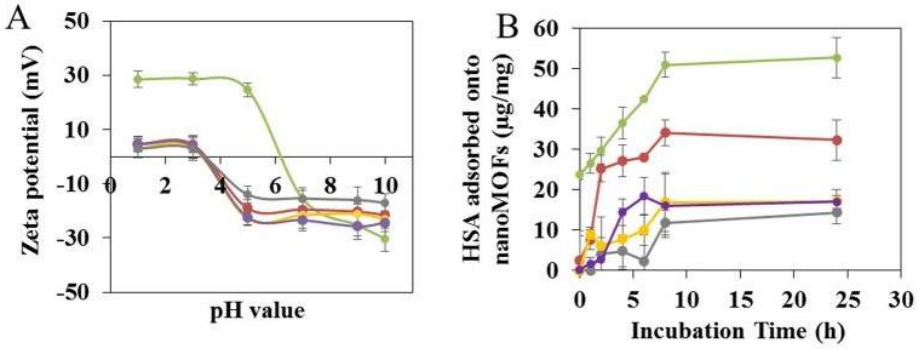

Fig. 3. Effect of surface modification of nanoMOFs by DEX-ALN-PEG copolymers on their ZP (A), amounts of HSA adsorbed (B), and a schema explaining the HSA adsorption (C). Green: uncoated nanoMOFs; purple: nanoMOFs coated with DEX-ALN_{75}-PEG_{25} **6** (mass ratio DEX-ALN-PEG: nanoMOFs 1:1); orange: nanoMOFs coated with DEX-ALN_{50}-PEG_{50} **7** (mass ratio DEX-ALN-PEG: nanoMOFs 1:1); gray: nanoMOFs coated with DEX-ALN_{25}-PEG_{75} **8** (mass ratio DEX-ALN-PEG: nanoMOFs 1:1); red: nanoMOFs coated with DEX-ALN_{50}-PEG_{50} **7** (mass ratio DEX-ALN-PEG: nanoMOFs 1:2).

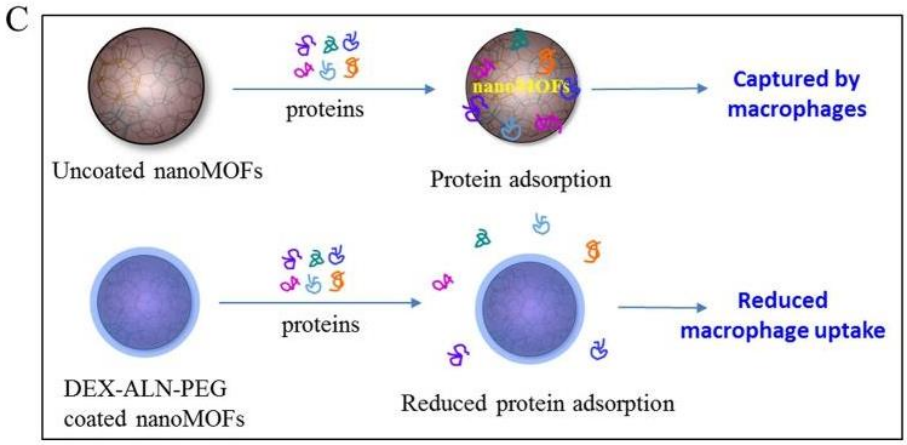

pH of the suspension medium, in a range of 1 to 10 (Fig. 3A). Typically, the ZP of uncoated nanoMOFs was positive (+23 ± 3 mV) at pH 5, whereas it shifted to negative values (-15 ± 3 mV) at pH 7. This was attributed to the presence at the nanoMOFs external surface of both uncoordinated iron sites and terminal COOH groups from the nanoMOF linker (trimesic acid, pKa's = 3.16, 3.98, and 4.85). The ZP values varied after coating with DEX-ALN-PEG copolymers (Fig. 3A). At acidic pH (< 4), the ZP was close to zero (-3 to 3 mV) indicating that the surface groups on the nanoMOFs were shielded by the coating material. At basic pH (> 7) the ZP values of -15 ± 5 mV were similar to those previously reported for DEX coatings (Lemarchand et al., 2005). Of note, there was no significant variation for ZP values obtained with the different DEX-ALN-PEG copolymers, except in the case of the copolymer with the highest PEG content (DEX-ALN_{25}-PEG_{75} **8**) whose ZP values were the closest to zero. This is in line with the protective effect of PEG shells on NPs, as previously reported (Rouzes, Gref, Leonard, Delgado, & Dellacherie, 2000).

It is well known that surface functionalization strongly influences the biodistribution of the nanocarriers (Gref et al., 1995). Indeed, after intravenous administration of NPs, plasma proteins readily adsorb on the external surface of the NPs, creating the so-called "protein corona", which considerably affects the NPs physicochemical properties and *in vivo* fate (Gref et al., 2000). To gain further understanding on protein adsorption, the interaction of nanoMOFs, coated or not with DEX-ALN-PEG, with HSA, the most abundant protein in human blood plasma, was studied here. Indeed, for many other types of NPs, HSA was used as model protein to investigate the capacity of PEG coatings to reduce protein adsorption (Gref et al., 2000). NanoMOFs coated or not with DEX-ALN-PEG copolymers were incubated with HSA aqueous solutions and the adsorbed HSA amounts, expressed as µg/mg of nanoMOFs, were determined (Fig. 3B). The experiments were carried out with fixed concentrations of nanoMOFs (300 µg/mL) and HSA (100 µg/mL) aqueous solutions. Non-adsorbed HSA was recovered in the supernatant after centrifugation, followed by quantification using a BCA assay. In the case of uncoated nanoMOFs, the amount of adsorbed HSA reached a plateau within 6 h, with around 50 µg HSA/mg nanoMOFs (Fig. 3B).

Surface modification with DEX-ALN-PEG significantly reduced HSA adsorption, with ~35 µg HSA/mg nanoMOFs for the case of DEX-ALN_{50}-PEG_{50} **7** (mass ratio DEX-ALN-PEG:nanoMOFs 1:2) coatings. This amount was further reduced to less than 20 µg HSA/mg nanoMOFs for the coatings with DEX-ALN_{75}-PEG_{25} **6**, DEX-ALN_{50}-PEG_{50} **7**, and DEX-ALN_{25}-PEG_{75} **8** (mass ratio DEX-ALN-PEG:nanoMOFs 1:1). There results clearly show that the DEX-ALN-PEG coatings are able to reduce the adsorption of the model protein HSA. This indicates that the surface modification with DEX-ALN-PEG copolymers potentially reduce the protein adsorption (e.g the opsonisation), which plays an important role on macrophage uptake (Fig. 3C).

3.2.3. Macrophage uptake of DEX-ALN-PEG surface modified nanoMOFs

The capacity of DEX-ALN-PEG coated nanoMOFs to escape macrophage uptake was evaluated on the murine macrophage J774A.1 cell line. NanoMOFs were colored using an iron staining procedure (see material and methods), allowing their identification inside cells by optical microscopy. To complete these qualitative studies, quantitative data on the amounts of nanoMOFs internalized in cells were obtained by ICP-MS, after extensive washing to remove the non-associated particles.

According to a lactic acid dehydrogenase (LDH) test previously performed to study nanoMOFs toxicity (Li et al., 2019), the particles used here coated or not with DEX-ALN-PEG shells were nontoxic for the J774A.1 cells up to 100 µg/mL, with more than 80% cell viability. This is in agreement with previously reported data showing the lack of toxicity of MIL-100(Fe) nanoMOFs (Baati et al., 2013; Bellido et al., 2015; Giménez-Marqués et al., 2018; Horcajada et al., 2010; Li et al., 2019). Internalization kinetics of nanoMOFs in J774A.1 macrophages were studied and a typical example is presented in Figure S14 (supplementary material). The amount of internalized uncoated nanoMOFs was quantified by ICP-MS, showing that after 2 h incubation ~14 µg of uncoated nanoMOFs were taken up in 3×10^5 J774A.1 macrophages, corresponding to around 1×10^7 uncoated nanoMOFs/cell and to 47% of the initial uncoated nanoMOFs (Figure S14). Moreover, this amount almost doubled after 4 h incubation, reaching 23 µg uncoated nanoMOFs/3×10^5 cells (77% of the nanoMOFs), thus demonstrating that macrophages avidly take up uncoated nanoMOFs. Remarkably, the presence of the DEX-ALN-PEG coating significantly reduced the nanoMOFs internalization, whatever the incubation time. For example, there was only less than 3 µg of coated nanoMOFs in 3×10^5 J774A.1 macrophages (corresponding to 10% of the initial coated nanoMOFs) after 2 h incubation. Even after 4 h incubation, the internalized amount of coated nanoMOFs was still less than 25%.

These direct quantification data obtained by ICP MS were supported by optical investigations of the cells after incubation with the nanoMOFs (Fig. 4). Before contact with nanoMOFs, J774A.1 cells presented a homogeneous morphology with round shapes (Fig. 4A). A typical image showing the massive uptake of uncoated nanoMOFs is presented in Fig. 4B. After 2 h incubation, the nanoMOFs appeared clustered inside the macrophages, mostly at their periphery. In contrast, after the same incubation time, the uptake of DEX-ALN_{75}-PEG_{25} **6** coated nanoMOFs was dramatically reduced (Fig. 4C).

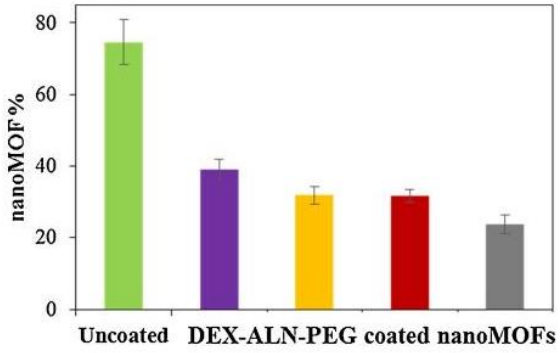

Fig. 5. *In vitro* interaction of nanoMOFs, coated or not with with a J774A.1 macrophage cell line. Purple: nanoMOFs coated with DEX-ALN_{75}-PEG_{25} **6** (mass ratio DEX-ALN-PEG:nanoMOFs 1:1); Orange: nanoMOFs coated with DEX-ALN_{50}-PEG_{50} **7** (mass ratio DEX-ALN-PEG:nanoMOFs 1:1); red: nanoMOFs coated with DEX-ALN_{50}-PEG_{50} **7** (mass ratio DEX-ALN-PEG:nanoMOFs 1:2); gray: nanoMOFs coated with DEX-ALN_{25}-PEG_{75} **8** (mass ratio DEX-ALN-PEG:nanoMOFs 1:1). 50 µg/mL nanoMOFs were incubated with 3×10^5 J774A.1 cells for 4 h, then washed to remove the loosely adhering particles. After cell lysis, the amount of internalized nanoMOFs was determined by ICP-MS and was expressed as a % of the initial amount put in contact with the cells.

The higher uptake of DEX-ALN_{75}-PEG_{25} **6** coated nanoMOFs after 4 h as compared to 2 h (Figure. S14) could be possibly due to a progressive saturation of the cells and/or a detachment of the coating in the complex biological media containing proteins or by contact with cell membranes. To further compare the different DEX-ALN-PEG coatings, an incubation time of 4 h was chosen as it corresponds to the blood circulation time of PEG-coated NPs (Gref et al., 1994). Fig. 5 shows the effect of the DEX-ALN-PEG coatings upon macrophage uptake. The nanoMOFs amounts associated to the cells were 39, 32 and 24% for DEX-ALN_{75}-PEG_{25} **6**, DEX-ALN_{50}-PEG_{50} **7**, and DEX-ALN_{25}-PEG_{75} **8**, respectively. This shows that the higher the PEG contents in the coating material, the lower the nanoMOFs uptake.

To the best of our knowledge, these are the first quantitative data on PEG-coated nanoMOFs uptake by macrophages based on a direct quantification and visualization of the Fe content in the cells. In comparison, another recent study dealt with nanoMOFs interaction with Raw 246.7 macrophages (Giménez-Marqués et al., 2018). In that case, the MIL-100(Fe) nanoMOFs were coated with PEG by GraftFast, whereas a radiolabeled drug, tritiated gemcitabine monophosphate, was incorporated into the particles. In the presence of coated particles, the detected amount of drug in the cells was reduced, as opposed to uncoated ones. However, this study did not take into account drug release during incubation with the cells, which may have influenced the quantity of drug detected as permeated into the cells (Rodriguez-Ruiz et al., 2015).

4. Conclusions

DEX-ALN-PEG copolymers were successfully synthesized,

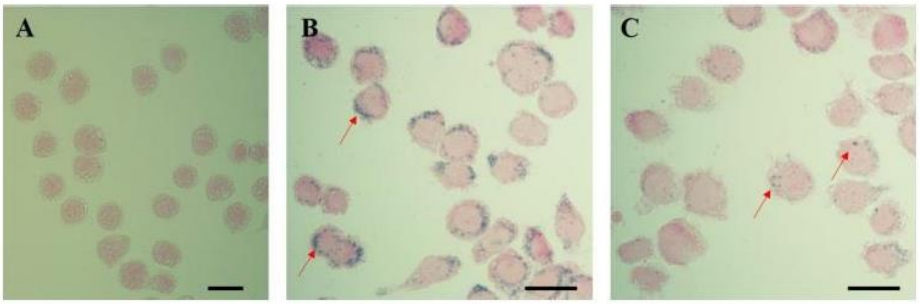

Fig. 4. Optical microscopy images showing the effect of DEX-ALN-PEG coatings on J774A.1 macrophage uptake. A: Control J774A.1 macrophages with no treatment; B: J774A.1 macrophages after 2 h incubation with 50 µg/mL uncoated nanoMOFs; C: J774A.1 macrophages after 2 h incubation with 50 µg/mL DEX-ALN_{75}-PEG_{25} **6** coated nanoMOFs (mass ratio DEX-ALN-PEG:nanoMOFs 1:1). Red arrows point out nanoMOFs stained using Prussian blue. Scale bar represents 20 µm.

controlling both the PEG and ALN grafting densities ranging from 75:25 to 25:75 ratios. They spontaneously adhered onto the external surface of MIL-100(Fe) nanoMOFs in aqueous media, forming a stable coating. In turn, the coating ensured the stability of the nanoMOFs upon storage and enabled to reduce by a 3 fold the *in vitro* uptake by macrophages. Further studies will deal with the effect on the drug release, further engineering of the coating by grafting specific ligands and/or fluorescent molecules, and coating on other metal-based MOFs (such as rare earth MOFs that can be used in biomedical applications). The *in vivo* fate of DEX-ALN-PEG functionalized nanoMOFs will be investigated.

Author contributions

The authors have made the following declarations about their contributions:

Conceived and designed the experiments: RG, AVB, DD

Performed the experiments: GC, JQ, AA, XL, MMM, DF, JMCS, BMA, JRE

Contributed reagents/materials/analysis tools: GC, AA, CL, XL, JQ, MMM, JMCS, DD, RG, AVB

Performed data analysis: GC, RG, AVB, DD, CL, XL, MMM, JMCS

Wrote the paper: RG, AVB, XL, GC

G. Cutrone and J. Qiu equally contributed to this work.

Declaration of Competing Interest

The authors declare no conflict of interest.

Acknowledgments

Financial support for this work was provided by the European Union through FP7-PEOPLE-2013-ITN (http://itn-cyclonhit.eu) project (Grant Agreement no. 608407), the French National Research Agency (ANR-14-CE08-0017 and ANR-16-CE18-0018) and the Spanish Ministry of Economy and Competitiveness (Grants CTQ2017-90050-R and CTQ2016-79412-P). This work was also supported by a public grant overseen by the French National Research Agency as part of the "Investissements d'Avenir" program (Labex NanoSaclay, ANR-10-LABX-0035). We acknowledge Dr. Doru Constantin for help with XRPD experiments. We are grateful to Ludivine Houel Renault for help with the cell culture facility in Centre Laser de l'Université Paris-Sud (CLUPS). This work has benefited from the facilities and expertise of the Liquid Chromatography Platform (Institut de Chimie de Lyon) for the characterization of polymers.

Appendix A. Supplementary data

Supplementary material related to this article can be found, in the online version, at doi:https://doi.org/10.1016/j.carbpol.2019.115085.

References

Abdelhameed, R. M., Rehan, M., & Emam, H. E. (2018). Figuration of Zr-based MOF@cotton fabric composite for potential kidney application. *Carbohydrate Polymers, 195*, 460–467.

Agostoni, V., Anand, R., Monti, S., Hall, S., Maurin, G., Horcajada, P., et al. (2013). Impact of phosphorylation on the encapsulation of nucleoside analogues within porous iron(III) metal–organic framework MIL-100(Fe) nanoparticles. *Journal of Materials Chemistry B, 1*, 4231–4242.

Agostoni, V., Chalati, T., Horcajada, P., Willaime, H., Anand, R., Semiramoth, N., et al. (2013). An improved anti-HIV activity of NRTI via metal-organic frameworks nanoparticles. *Advanced Healthcare Materials, 2*, 1630–1637.

Agostoni, V., Horcajada, P., Noiray, M., Malanga, M., Aykaç, A., Jicsinszky, L., et al. (2015). A "green" strategy to construct non-covalent, stable and bioactive coatings on porous MOF nanoparticles. *Scientific Reports, 5*, 7925.

Alemán, E. A., Pedini, H. S., & Rueda, D. (2009). Covalent bond-based immobilization approaches for single-molecule fluorescence. *ChemBiochem, 10*, 2862–2866.

Anand, R., Borghi, F., Manoli, F., Manet, I., Agostoni, V., Reschiglian, P., et al. (2014). Host-guest interactions in Fe(III)-trimesate MOF nanoparticles loaded with doxorubicin. *The Journal of Physical Chemistry B, 118*, 8532–8539.

Aykaç, A., Noiray, M., Malanga, M., Agostoni, V., Casas-Solvas, J. M., Fenyvesi, É., et al. (2017). A non-covalent "click chemistry" strategy to efficiently coat highly porous MOF nanoparticles with a stable polymeric shell. *Biochimica et Biophysica Acta - General Subjects, 1861*, 1606–1616.

Baati, T., Njim, L., Neffati, F., Kerkeni, A., Bouttemi, M., Gref, R., et al. (2013). In depth analysis of the *in vivo* toxicity of nanoparticles of porous iron(III) metal-organic frameworks. *Chemical Science, 4*, 1597–1607.

Barceloux, D. G. (1999). Copper. *Clinical Toxicology, 37*, 217–230.

Barenholz, Y. (2012). Doxil® - the first FDA-approved nano-drug: Lessons learned. *Journal of Controlled Release, 160*, 117–134.

Bellido, E., Hidalgo, T., Lozano, M. V., Guillevic, M., Simón-Vázquez, R., Santander-Ortega, M. J., et al. (2015). Heparin-engineered mesoporous iron metal-organic framework nanoparticles: Toward stealth drug nanocarriers. *Advanced Healthcare Materials, 4*, 1246–1257.

Biaglow, J. E., Manevich, Y., Uckun, F., & Held, K. D. (1997). Quantitation of hydroxyl radicals produced by radiation and copper-linked oxidation of ascorbate by 2-deoxy-D-ribose method. *Free Radical Biology & Medicine, 22*, 1129–1138.

Chen, D., Yang, D., Dougherty, C. A., Lu, W., Wu, H., He, X., et al. (2017). *In vivo* targeting and positron emission tomography imaging of tumor with intrinsically radioactive metal-organic frameworks nanomaterials. *ACS Nano, 11*, 4315–4327.

Di Nunzio, M. R., Agostoni, V., Cohen, B., Gref, R., & Douhal, A. (2014). A "ship in a bottle" strategy to load a hydrophilic anticancer drug in porous metal organic framework nanoparticles: Efficient encapsulation, matrix stabilization, and photodelivery. *Journal of Medicinal Chemistry, 57*, 411–420.

Giménez-Marqués, M., Bellido, E., Berthelot, T., Simón-Yarza, T., Hidalgo, T., Simón-Vázquez, R., et al. (2018). GraftFast surface engineering to improve MOF nanoparticles furtiveness. *Small, 14*, 1801900.

Grandjean, C., Boutonnier, A., Guerreiro, C., Fournier, J. M., & Mulard, L. A. (2005). On the preparation of carbohydrate-protein conjugates using the traceless Staudinger ligation. *The Journal of Organic Chemistry, 70*, 7123–7132.

Gref, R., Domb, A., Quellec, P., Blunk, T., Müller, R. H., Verbavatz, J. M., et al. (1995). The controlled intravenous delivery of drugs using PEG-coated sterically stabilized nanospheres. *Advanced Drug Delivery Reviews, 16*, 215–233.

Gref, R., Lück, M., Quellec, P., Marchand, M., Dellacherie, E., Harnisch, S., et al. (2000). "Stealth" corona-core nanoparticles surface modified by polyethylene glycol (PEG): Influences of the corona (PEG chain length and surface density) and of the core composition on phagocytic uptake and plasma protein adsorption. *Colloids and Surfaces B, Biointerfaces, 18*, 301–313.

Gref, R., Minamitake, Y., Peracchia, M. T., Trubetskoy, V., Torchilin, V., & Langer, R. (1994). Biodegradable long-circulating polymeric nanospheres. *Science, 263*, 1600–1603.

Horcajada, P., Chalati, T., Serre, C., Gillet, B., Sebrie, C., Baati, T., et al. (2010). Porous metal–organic-framework nanoscale carriers as a potential platform for drug delivery and imaging. *Nature Materials, 9*, 172–178.

Horcajada, P., Gref, R., Baati, T., Allan, P. K., Maurin, G., Couvreur, P., et al. (2012). Metal-organic frameworks in biomedicine. *Chemical Reviews, 112*, 1232–1268.

Hoskins, B. F., & Robson, R. (1989). Infinite polymeric frameworks consisting of three dimensionally linked rod-like segments. *Journal of the American Chemical Society, 111*, 5962–5964.

Ke, J., Dou, H., Zhang, X., Uhagaze, D. S., Ding, X., & Dong, Y. (2016). Determination of pKa values of alendronate sodium in aqueous solution by piecewise linear regression based on acid-base potentiometric titration. *Journal of Pharmaceutical Analysis, 6*, 404–409.

Kuil, J., Branderhorst, H. M., Pieters, R. J., De Mol, N. J., & Liskamp, R. M. J. (2009). ITAM-derived phosphopeptide-containing dendrimers as multivalent ligands for Syk tandem SH_2 domain. *Organic & Biomolecular Chemistry, 7*, 4088–4094.

Lemarchand, C., Gref, R., Lesieur, S., Hommel, H., Vacher, B., Besheer, A., et al. (2005). Physico-chemical characterization of polysaccharide-coated nanoparticles. *Journal of Controlled Release, 108*, 97–111.

Li, X., Semiramoth, N., Hall, S., Tafani, V., Josse, J., Laurent, F., et al. (2019). Compartmentalized encapsulation of two antibiotics in porous nanoparticles: An efficient strategy to treat intracellular infections. *Particle & Particle Systems Characterization, 36*, 1800360.

Liu, G., Li, L., Xu, D., Huang, X., Xu, X., Zheng, S., et al. (2017). Metal-organic framework preparation using magnetic graphene oxide-β-cyclodextrin for neonicotinoid pesticide adsorption and removal. *Carbohydrate Polymers, 175*, 584–591.

Notni, J., & Wester, H. J. (2016). A practical guide on the synthesis of metal chelates for molecular imaging and therapy by means of click chemistry. *Chemistry - A European Journal, 22*, 11500–11508.

Oms, O., Yang, S., Salomon, W., Marrot, J., Dolbecq, A., Rivière, E., et al. (2016). Heteroanionic materials based on copper clusters, bisphosphonates, and polyoxometalates: Magnetic properties and comparative electrocatalytic NO_x reduction studies. *Inorganic Chemistry, 55*, 1551–1561.

Ostović, D., Stelmach, C., & Hulshizer, B. (1993). Formation of a chromophoric complex between alendronate and copper (II) ions. *Pharmaceutical Research, 10*, 470–472.

Perrin, D. D., & Armarego, W. F. L. (1989). *Purification of laboratory chemicals* (3rd ed.). Oxford: Pergamon.

Rodriguez-Ruiz, V., Maksimenko, A., Anand, R., Monti, S., Agostoni, V., Couvreur, P., et al. (2015). Efficient "green" encapsulation of a highly hydrophilic anticancer drug in metal-organic framework nanoparticles. *Journal of Drug Targeting, 23*, 759–767.

Rouzes, C., Gref, R., Leonard, M., De Sousa Delgado, A., & Dellacherie, E. (2000). Surface modification of poly(lactic acid) nanospheres using hydrophobically modified dextrans as stabilizers in an o/w emulsion/evaporation technique. *Journal of Biomedical Materials Research, 50*, 557–565.

Semple, J. E., Sullivan, B., Vojkovsky, T., & Sill, K. N. (2016). Synthesis and facile end-group quantification of functionalized PEG azides. *Journal of Polymer Science Part A:*

Polymer Chemistry, 54, 2888–2895.
Simon-Yarza, M. T., Baati, T., Paci, A., Lesueur, L. L., Seck, A., Chiper, M., et al. (2016). Antineoplastic Busulfan encapsulated in metal organic framework nanocarrier: First *in vivo* results. *Journal of Materials Chemistry B, 4*, 585–588.
Simon-Yarza, T., Baati, T., Neffati, F., Njim, L., Couvreur, P., Serre, C., et al. (2016). *In vivo* behavior of MIL-100 nanoparticles at early times after intravenous administration. *International Journal of Pharmaceutics, 511*, 1042–1047.
Simon-Yarza, T., Giménez-Marqués, M., Mrimi, R., Mielcarek, A., Gref, R., Horcajada, P., et al. (2017). A smart metal-organic framework nanomaterial for lung targeting. *Angewandte Chemie International Edition, 56*, 15565–15569.
Su, Y., Li, L., Wang, H., Wang, X., & Zhang, Z. (2016). All-in-One azides: Empowered click reaction for *in vivo* labeling and imaging of biomolecules. *Chemical Communication, 52*, 2185–2188.
Sun, G., Lin, X., Wang, Z., Feng, Y., Xu, D., & Shen, L. (2011). PEGylated inulin as long-circulating pharmaceutical carrier. *Journal of Biomaterials Science Polymer Edition, 22*, 429–441.
Yuan, S., Feng, L., Wang, K., Pang, J., Bosch, M., Lollar, C., et al. (2018). Stable metal-organic frameworks: Design, synthesis, and applications. *Advanced Materials, 30*, 1–35.
Zhang, H. H., Hu, H., Zhang, H. H., Dai, W., Wang, X., Wang, X., et al. (2015). Effects of PEGylated paclitaxel nanocrystals on breast cancer and its lung metastasis. *Nanoscale, 7*, 10790–10800.
Zimpel, A., Preiß, T., Röder, R., Engelke, H., Ingrisch, M., Peller, M., et al. (2016). Imparting functionality to MOF nanoparticles by external surface selective covalent attachment of polymers. *Chemistry of Materials, 28*, 3318–3326.
Zhu, X., Gu, J., Wang, Y., Li, B., Li, Y., Zhao, W., et al. (2014). Inherent anchorages in UiO-66 nanoparticles for efficient capture of alendronate and its mediated release. *Chemical Communication, 50*, 8779–8782.

Supplementary information

Comb-like dextran copolymers: a versatile strategy to coat highly porous MOF nanoparticles with a PEG shell

Giovanna Cutrone[1,a], Jingwen Qiu[2,a], Mario Menendez-Miranda[2], Juan M. Casas-Solvas[1], Ahmet Aykaç[1], Xue Li[2], Daniel Foulkes[2], Borja Moreira-Alvarez[3], Jorge R. Encinar[3], Catherine Ladavière[4], Didier Desmaële[5], Antonio Vargas-Berenguel[1,] and Ruxandra Gref [2,*]*

[1] Department of Chemistry and Physics, University of Almería, Ctra. de Sacramento s/n, 04120 Almería, Spain

[2] Institut des Sciences Moléculaires d'Orsay, UMR CNRS 8214, Université Paris-Sud, Université Paris Saclay, 91400 Orsay, France

[3] Department of Physical and Analytical Chemistry, University of Oviedo, Julián Clavería 8, 33006 Oviedo, Spain

[4] University of Lyon, CNRS, UMR 5223, IMP, 15 bd André Latarjet, F-69622 Villeurbanne, France

[5] Institut Galien Paris-Sud, UMR 8612, CNRS, Université Paris-Sud, Faculté de Pharmacie, 5 rue JB Clément, 92296 Châtenay-Malabry, France

a These authors contributed equally.

Supplementary Material

Table of Contents

I. [1]H-NMR spectra for compounds 3-8

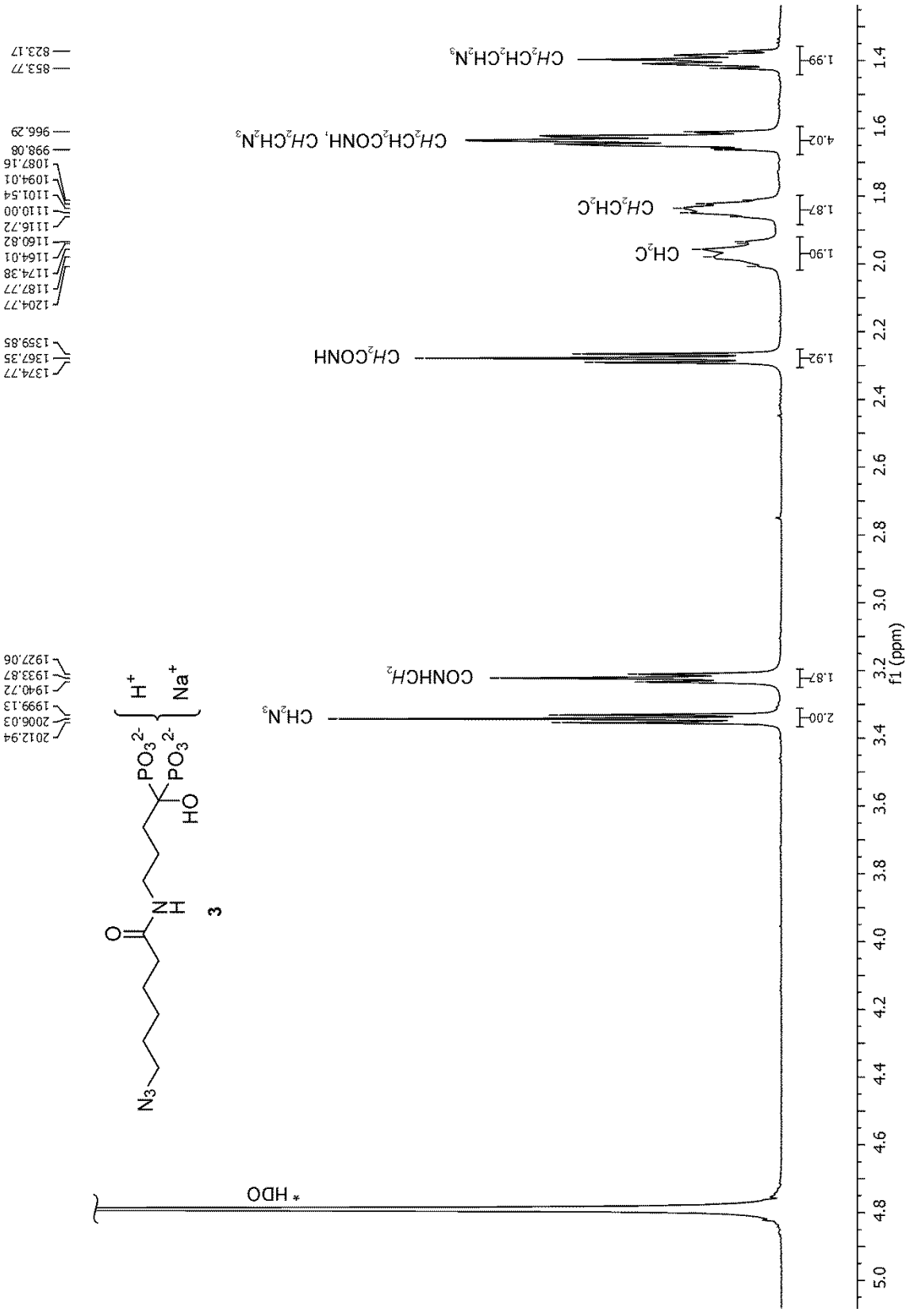

Figure S1. [1]H NMR spectrum (600 MHz, D_2O, 25 ºC) for compound **3**

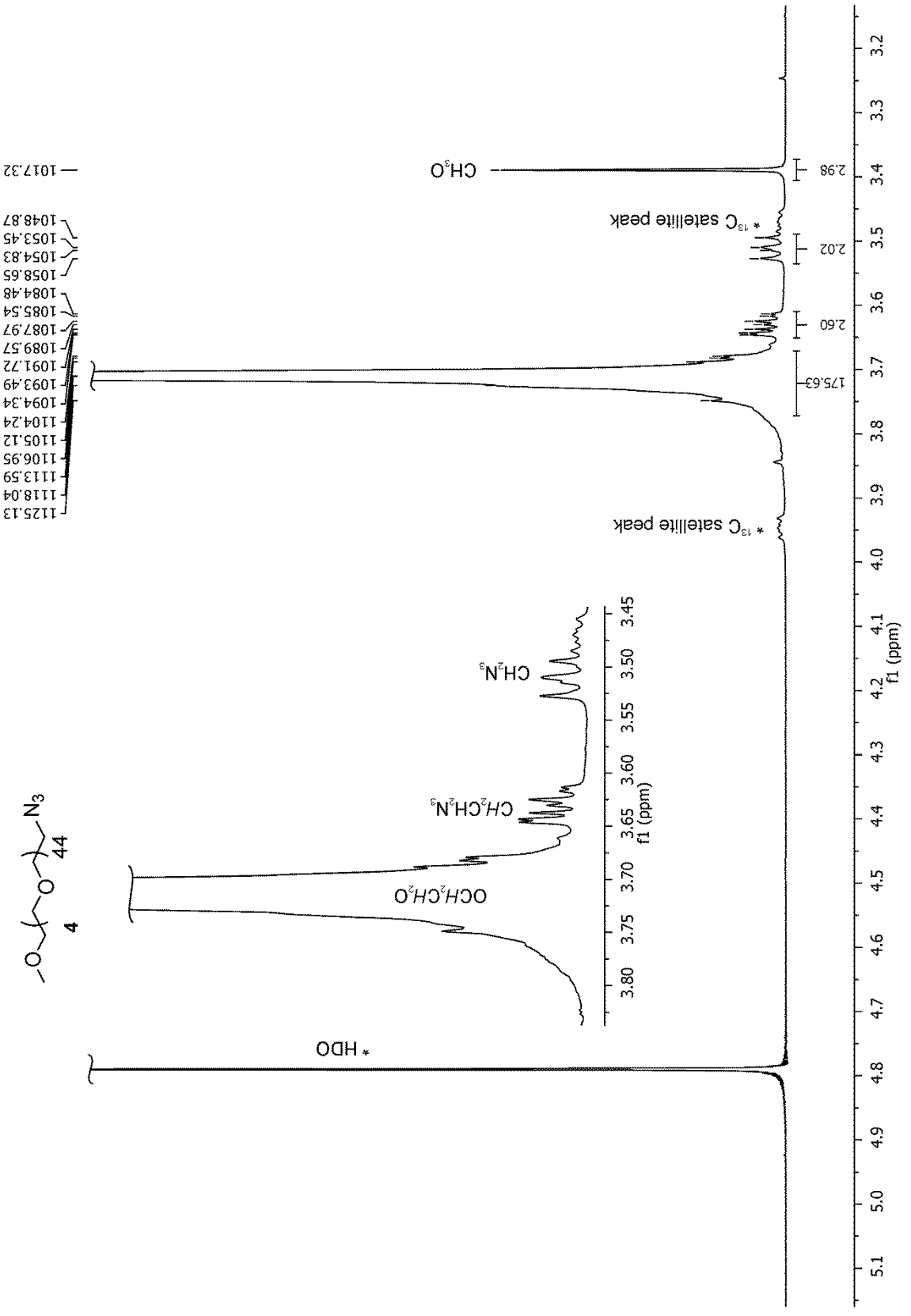

Figure S2. ^{1}H NMR spectrum (300 MHz, D_2O, 25 ºC) for compound **4**

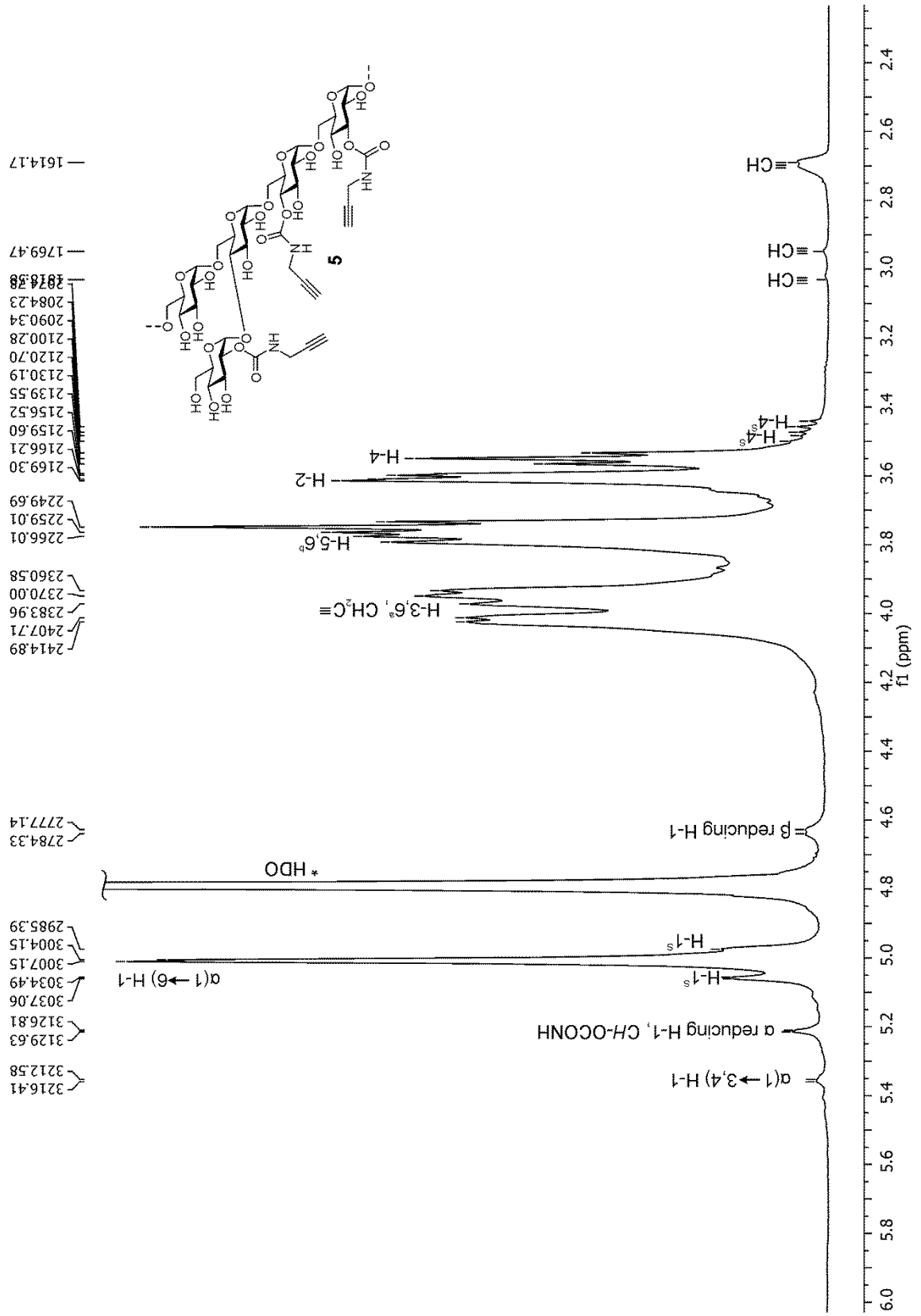

Figure S3. ^{1}H NMR spectrum (600 MHz, D_2O, 25 ºC) for DEX-PC **5**

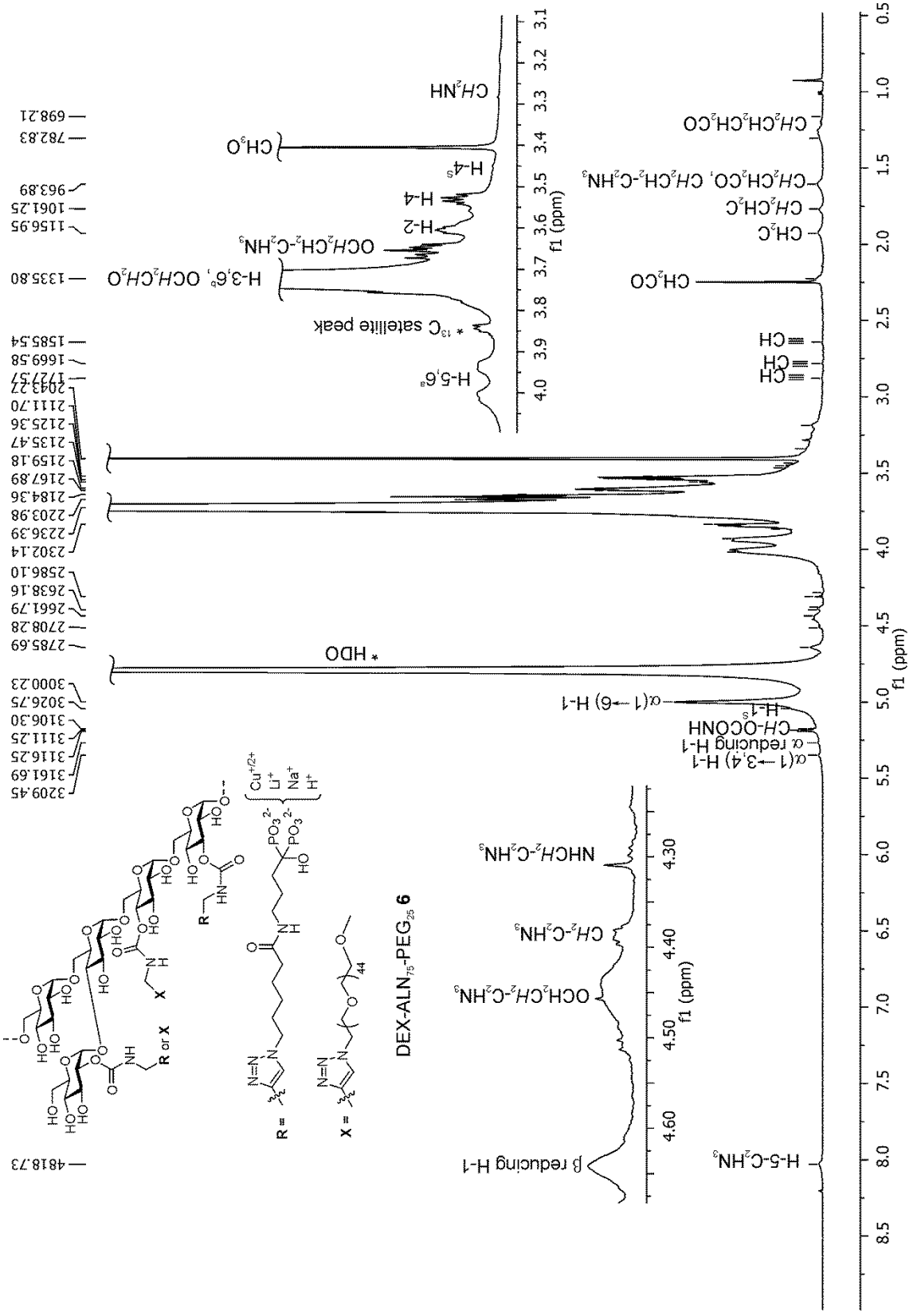

Figure S4. ^{1}H NMR spectrum (600 MHz, D_2O, 25 ºC) for DEX-ALN$_{75}$-PEG$_{25}$ **6**

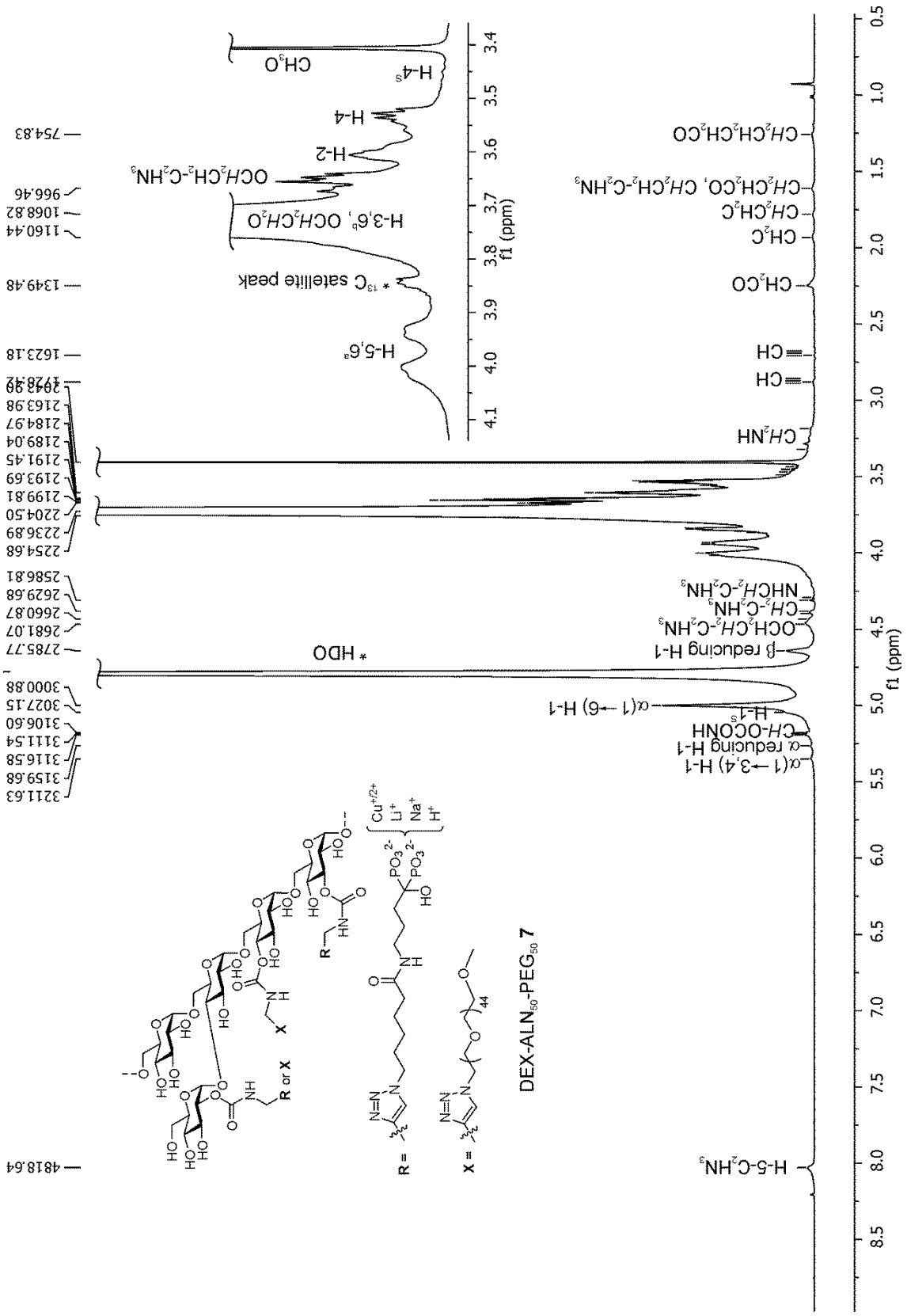

Figure S5. ^{1}H NMR spectrum (600 MHz, D_2O, 25 ºC) for DEX-ALN$_{50}$-PEG$_{50}$ **7**

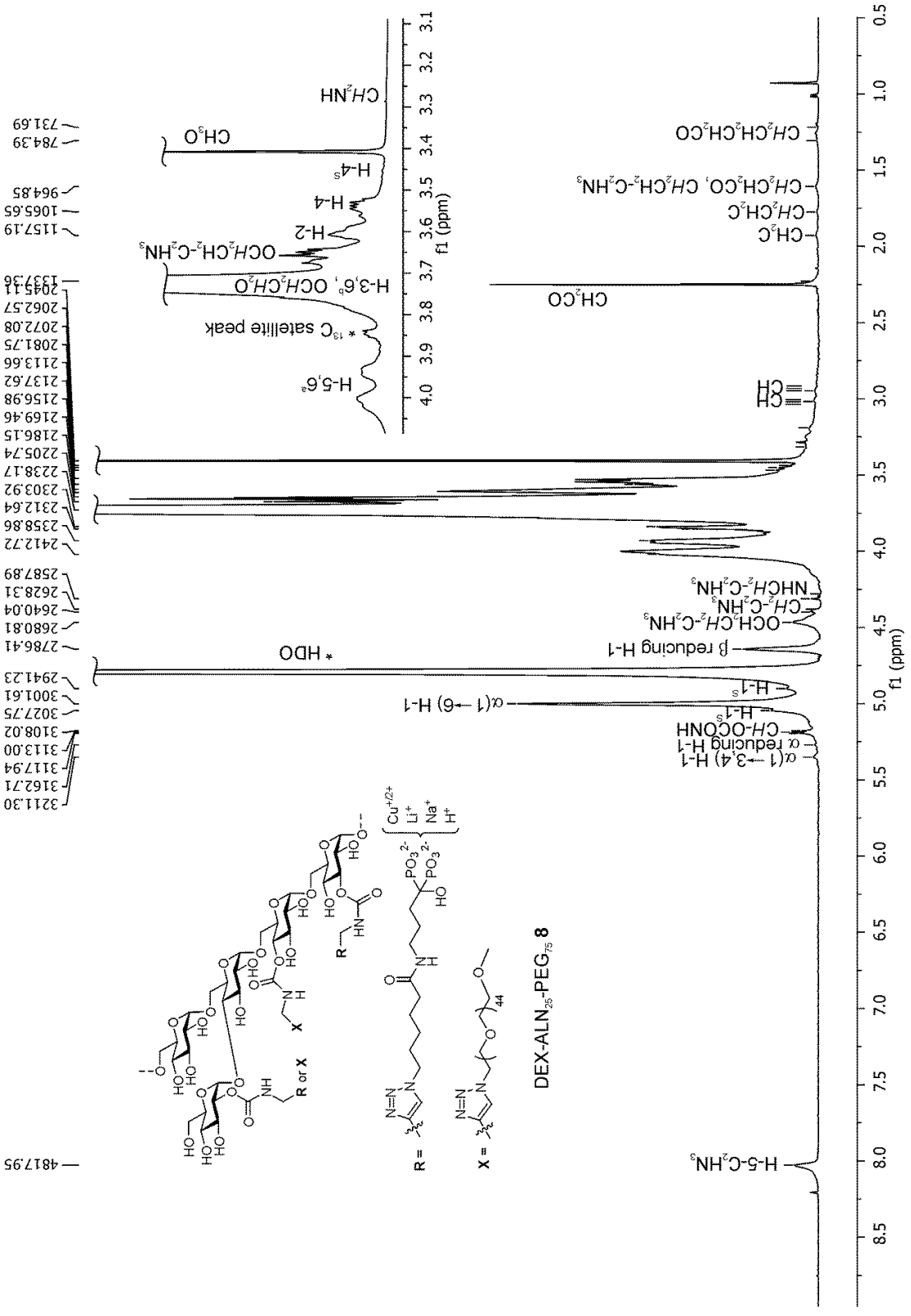

Figure S6. ^{1}H NMR spectrum (600 MHz, D_2O, 25 ºC) for DEX-ALN$_{25}$-PEG$_{75}$ **8**

II. ^{13}C-NMR spectra for compounds 3-5

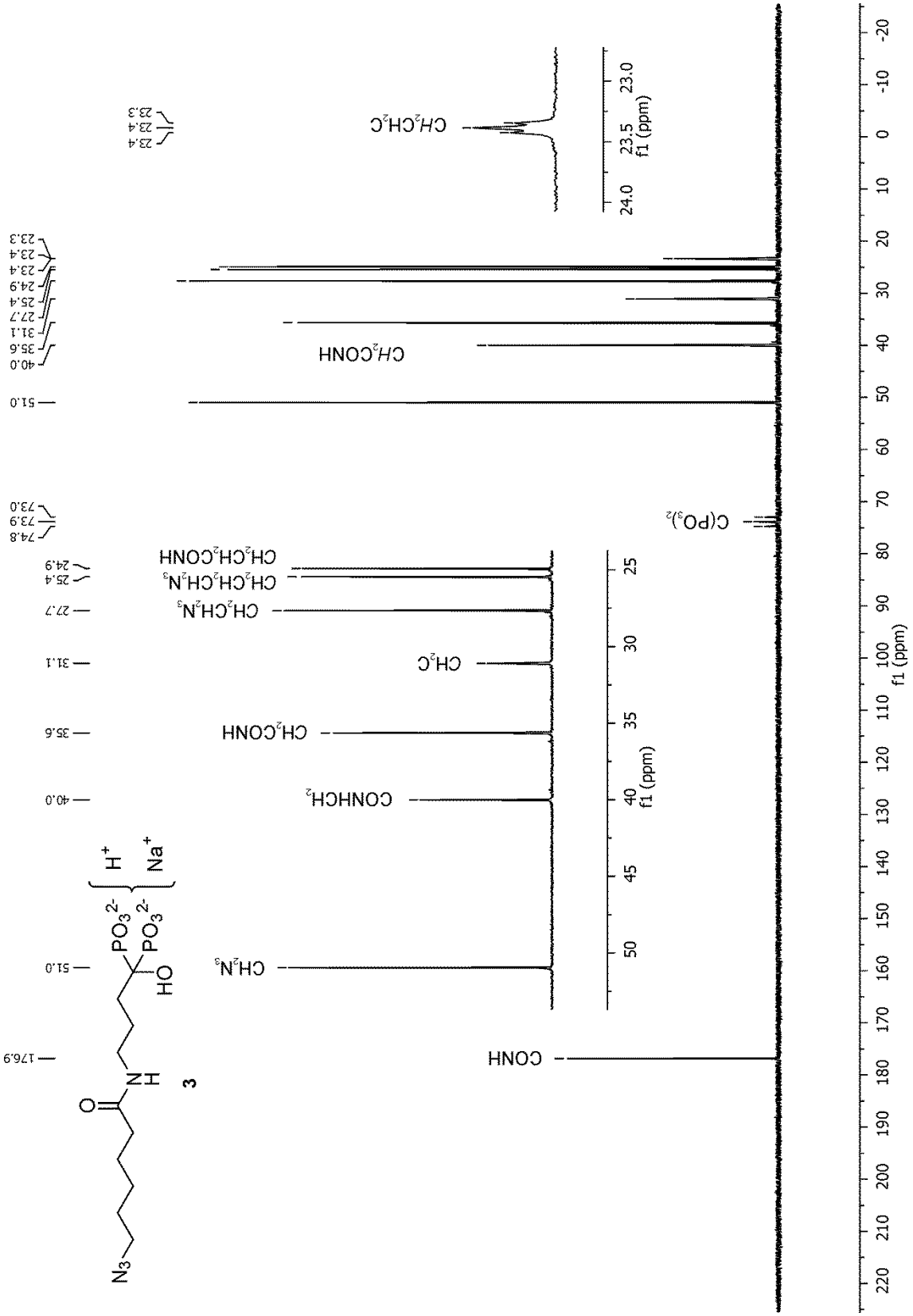

Figure S7. ^{13}C NMR spectrum (150 MHz, D_2O, 25 ºC) for compound **3**

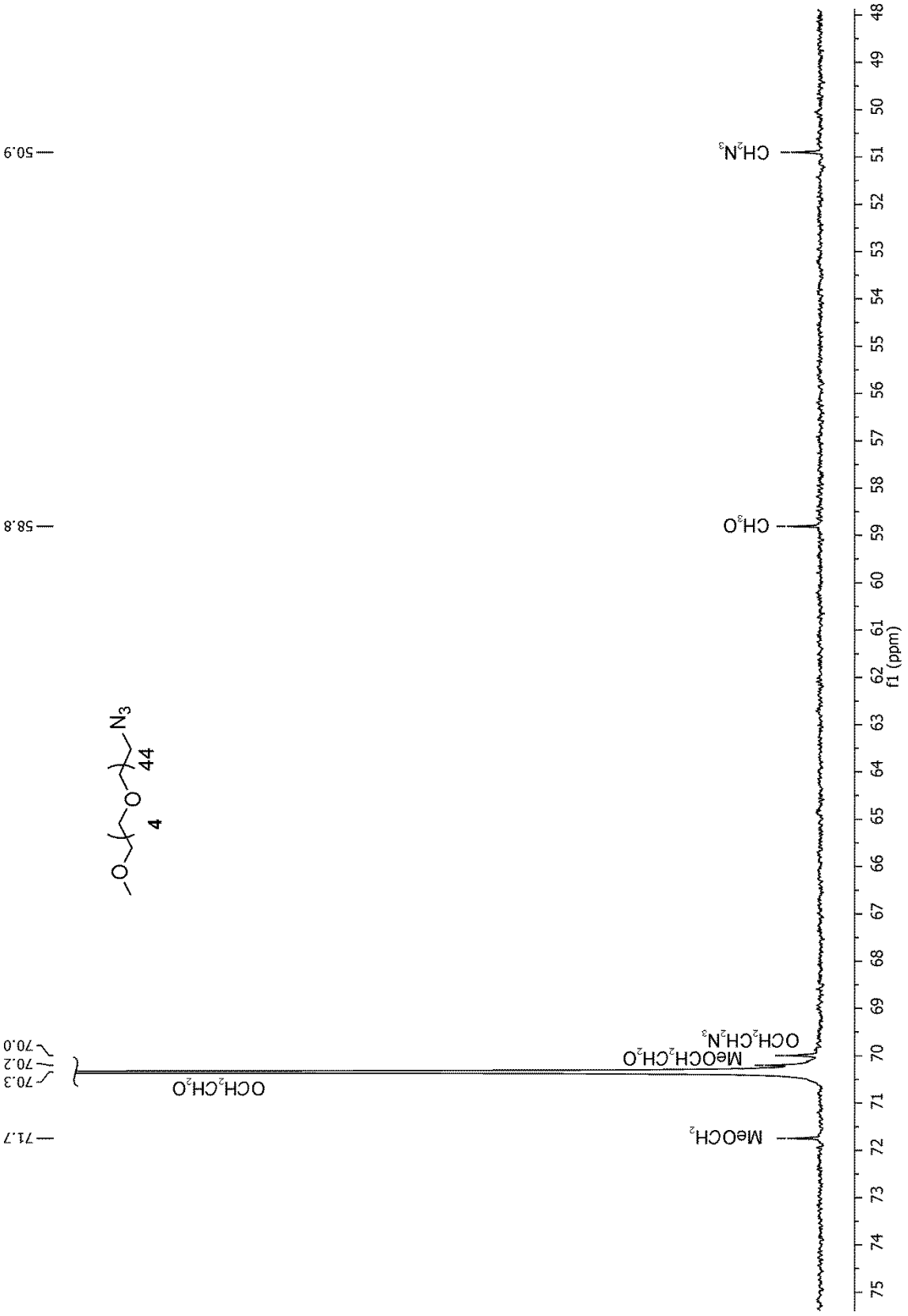

Figure S8. ^{13}C NMR spectrum (75 MHz, D_2O, 25 ºC) for compound **4**

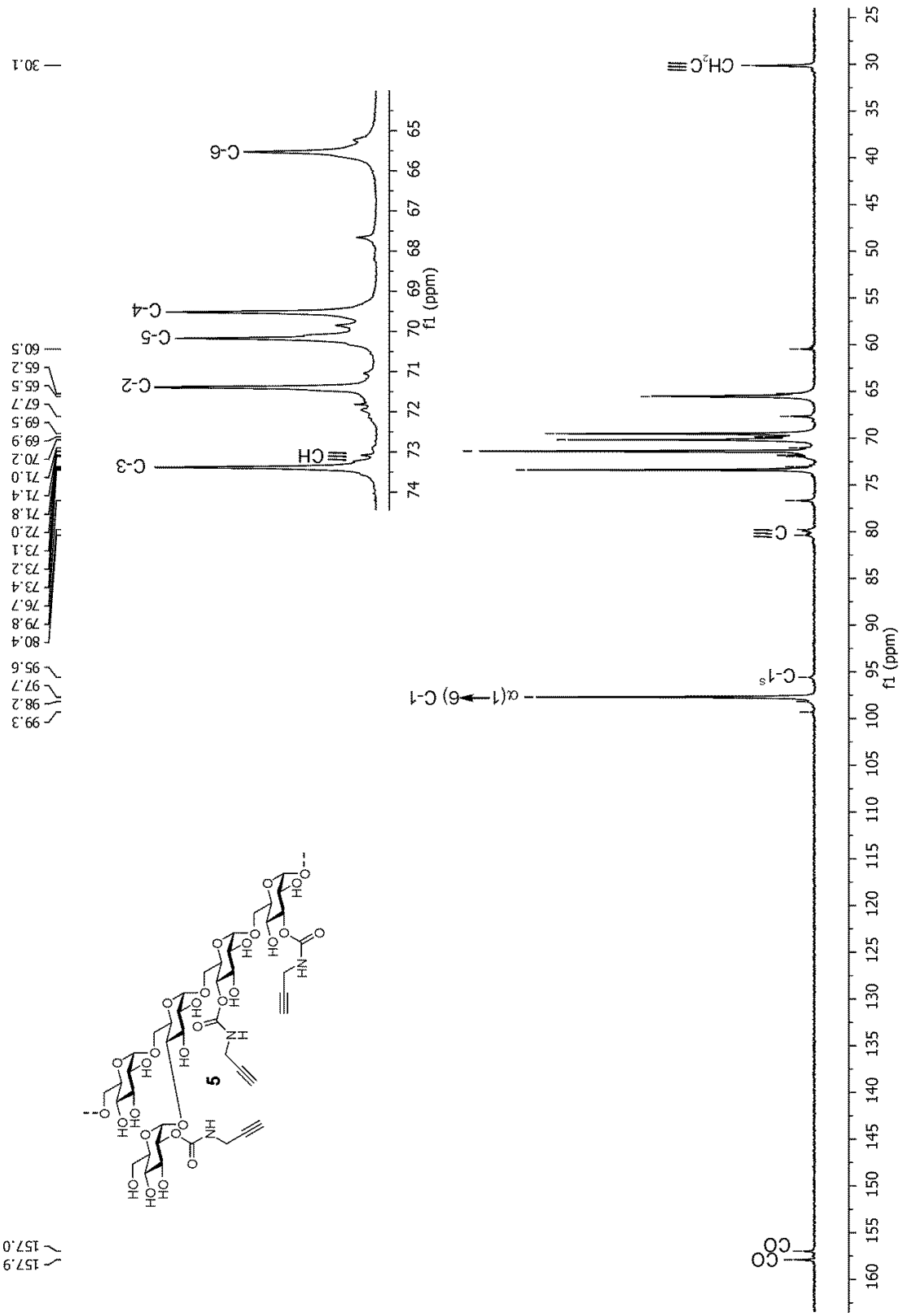

Figure S9. ^{13}C NMR spectrum (150 MHz, D_2O, 25 ºC) for DEX-PC **5**

III. ^{31}P-NMR spectra for compounds 3 and 6-8

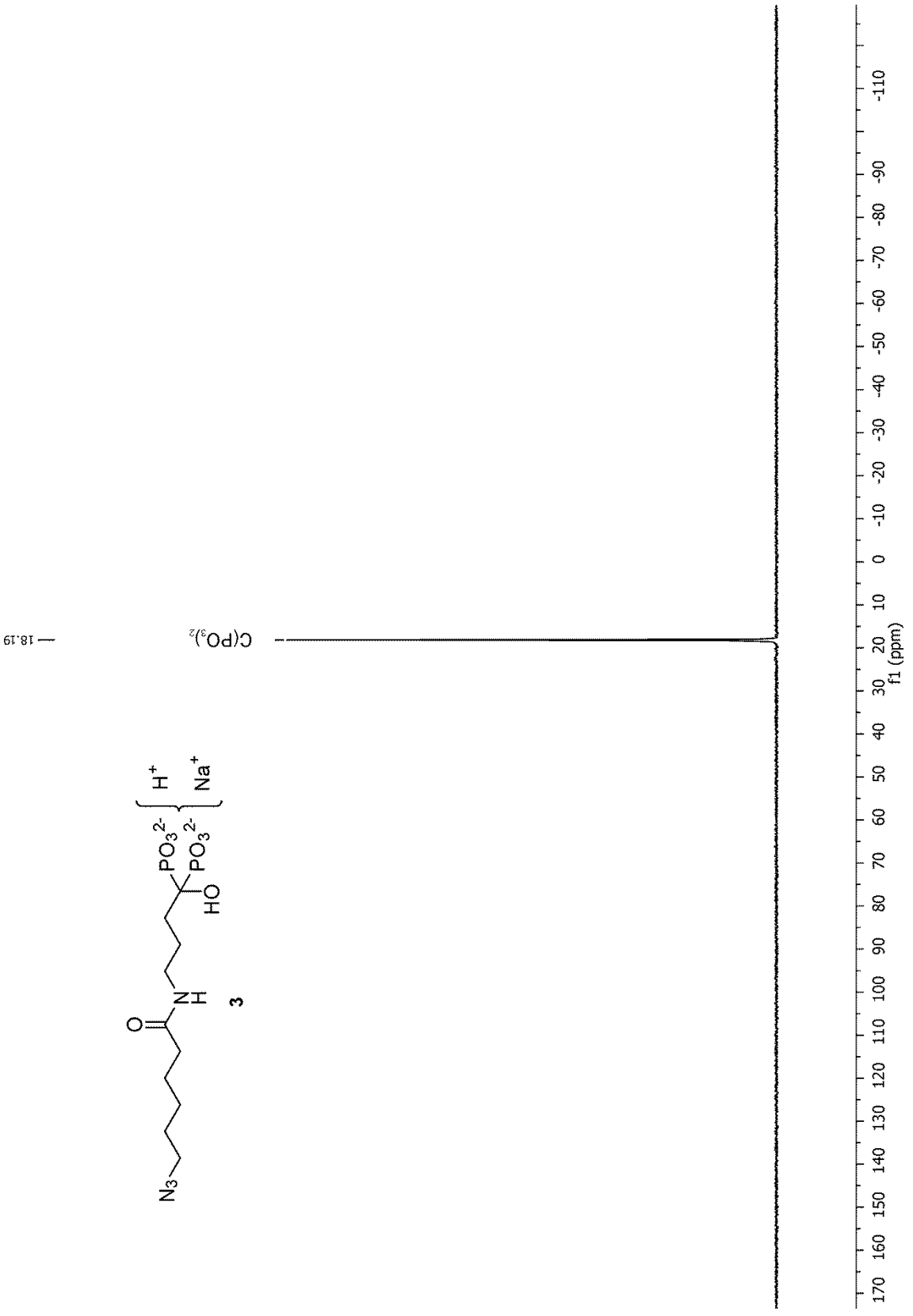

Figure S10. ^{31}P NMR spectrum (242.9 MHz, D_2O, 25 ºC) for compound **3**

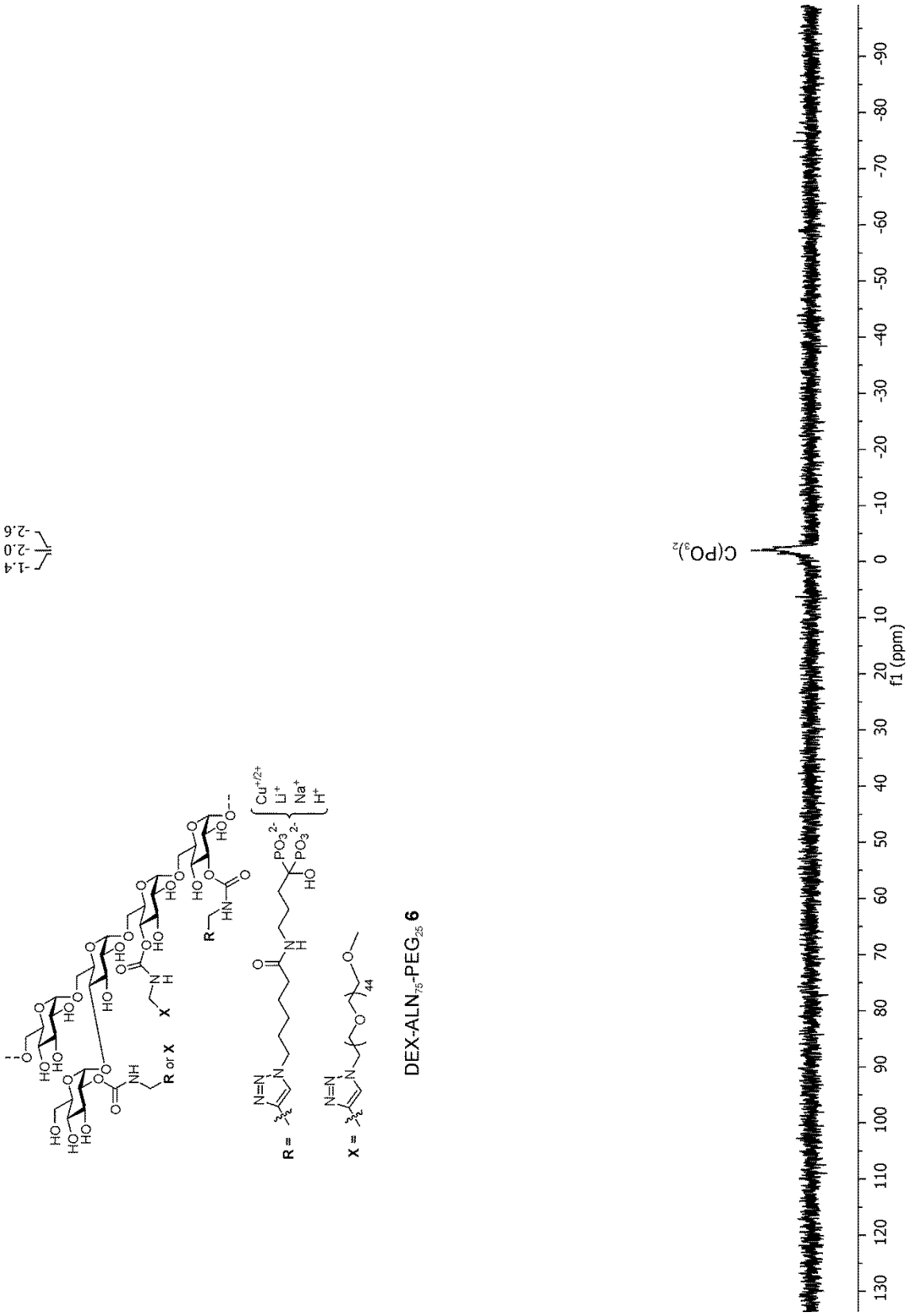

Figure S11. ^{31}P NMR spectrum (242.9 MHz, D_2O, 25 ºC) for DEX-ALN$_{75}$-PEG$_{25}$ **6**

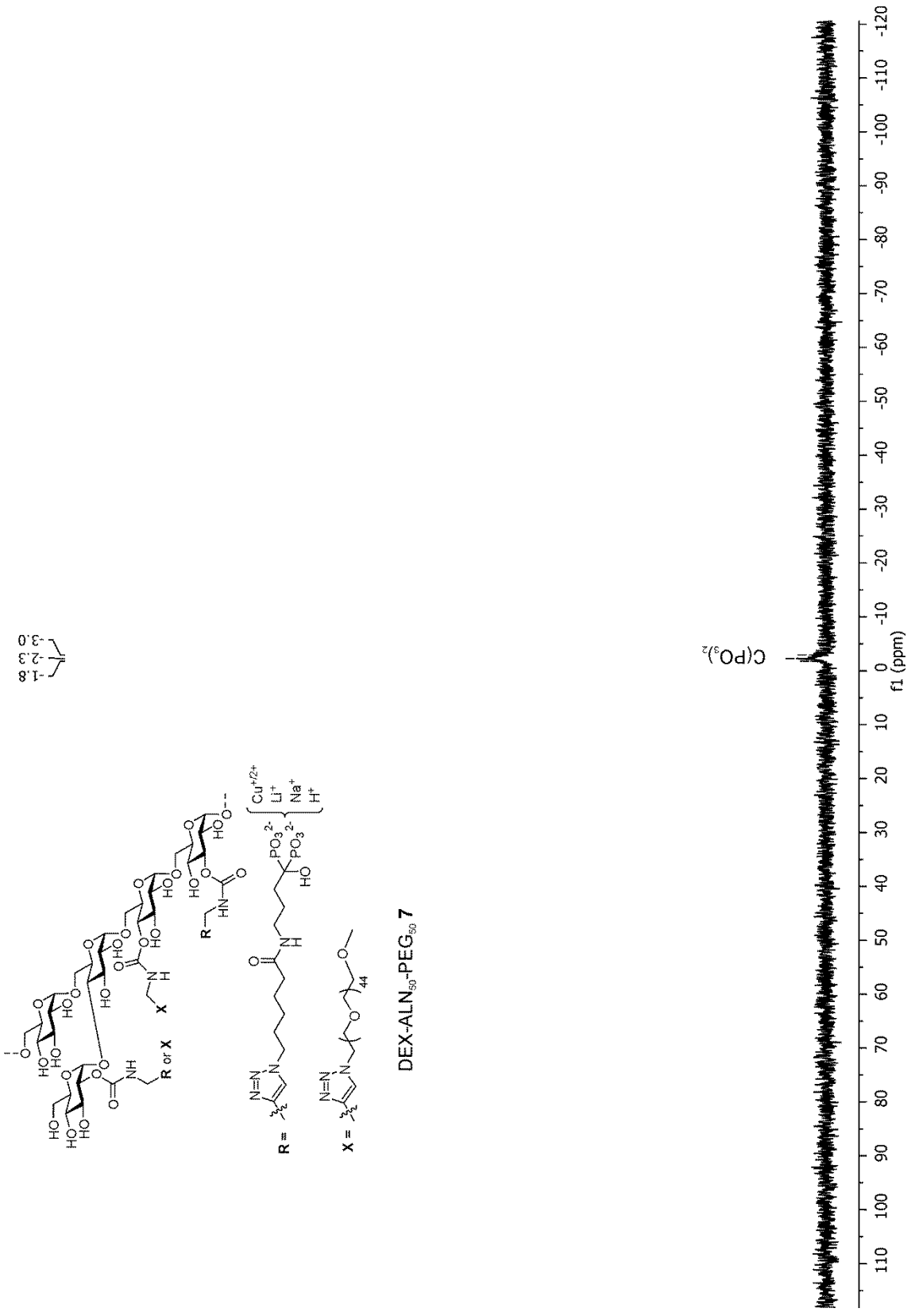

Figure S12. ^{31}P NMR spectrum (242.9 MHz, D_2O, 25 ºC) for DEX-ALN_{50}-PEG_{50} **7**

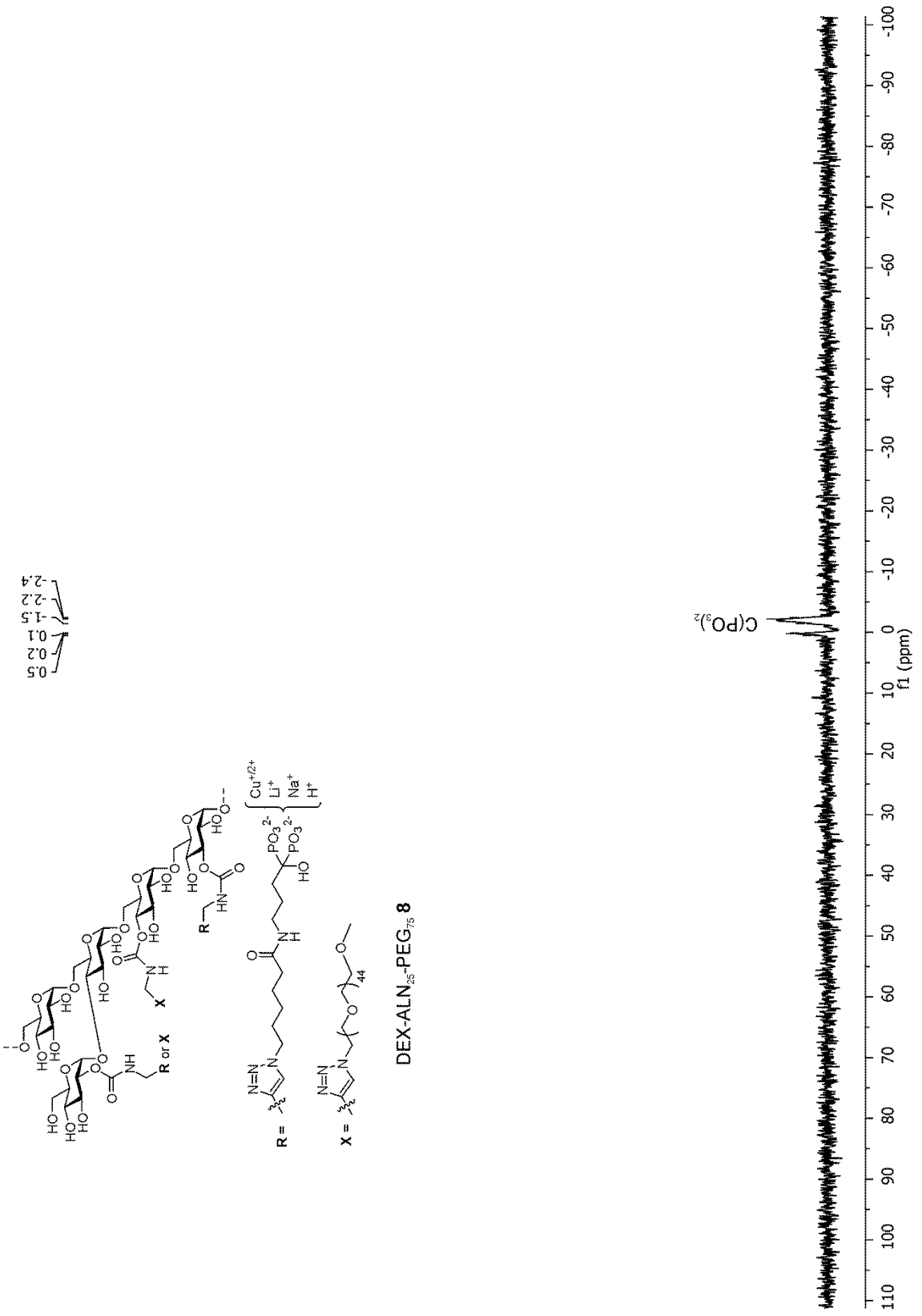

Figure S13. ^{31}P NMR spectrum (242.9 MHz, D_2O, 25 ºC) for DEX-ALN_{25}-PEG_{75} **8**

IV. Compositional model for the structural analysis of dextran derivatives 5-8

In order to analyze the structure of dextran derivatives 5-8 from compositional data obtained by elemental (for C, H and N) and HR-ICP-MS (for P, Na, Cu and Li) analyses, the following mathematical model is proposed. Although dextran presents a structure consisting of glucose moieties linked through α(1→6) glycosidic bonds with some branches mainly from α(1→3) and α(1→4) linkages, in order to simplify the model we will consider a linear, non-branched, main chain containing *k* glucose residues:

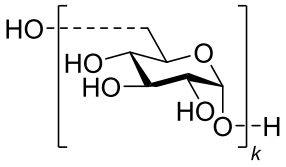

Dextran T-40 (DT40) with 40000 Da of average molecular weight was used. For that reason, the average number of glucose units for each DT40 chain (degree of polymerization) is calculated as:

$$k = \frac{(40000 - 18.02)}{162.14} = 246.59$$

where 18.02 Da is the molecular weight of the ending groups OH and H in the polymer and 162.14 Da is the molecular weight of the glucose residue ($C_6H_{10}O_5$). Thus, the molecular formula of DT40 is:

$$(C_6H_{10}O_5)k + OH + H = C_{(6k)}H_{(10k+2)}O_{(5k+1)}$$

When DT40 is propargylated by using CDI and propargylamine, a number of propargyl carbamate group are formed according to this reaction:

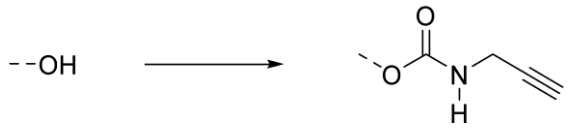

$+C_4H_3ON$

Thus, each propargyl group introduced in the polymer modifies the molecular formula of DT40 by adding C_4H_3ON.

In addition, the final product has to be considered hydrated by an undefined number of H_2O molecules (*m*), which obviously are reflected in the compositional analysis of the product. As a result, the molecular formula for DEX-PC **5** derivative, containing *n* propargyl carbamate groups and *m* hydration water molecules is:

	For *k* glucose residues	For the chain ending groups	For *n* propargyl carbamate groups	For *m* molecules of H_2O
C atoms	6*k*		4*n*	
H atoms	10*k*	2	3*n*	2*m*
O atoms	5*k*	1	*n*	*m*
N atoms			*n*	

In this analysis we assume that all nitrogen atoms present in the molecule are part of propargyl carbamate groups, and thus no imidazole carbamate groups remain on the structure. This hypothesis is based firstly on the large excess of propargylamine that was used during the reaction, and secondly on the subsequent dialysis process that should break all unreacted imidazole carbamates to the original alcohols.

DEX-PC **5** is subsequently reacted with alendronate azide derivative **3** and poly(ethylene glycol) azide **4** in the presence of LiCl and $CuSO_4$/sodium ascorbate catalyst system in order to promote CuAAC onto the propargyl carbamate groups. Those dextran OH groups that support a propargyl carbamate group which reacted with alendronate azide **3** will be then transformed into:[1]

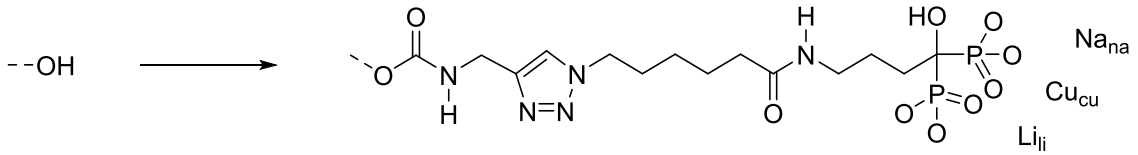

$+C_{14}H_{(25-na-cu-li)}O_9N_5P_2Na_{na}Cu_{cu}Li_{li}$

where *na* will be the number of sodium atoms, *cu* the number of copper atoms, and *li* the number of lithium atoms per alendronate branch. We will consider *x* as the number of alendronate groups per DEX molecule.

In a similar fashion, those dextran OH groups that support a propargyl carbamate group which reacted with poly(ethylene glycol) azide **4** will be then transformed into:[1]

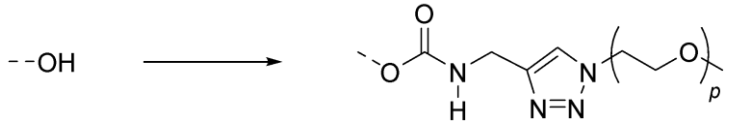

$+C_{(2p+5)}H_{(4p+6)}O_{(p+1)}N_4$

[1] Defining alendronate and poly(ethylene glycol) branches starting from original OH dextran groups instead of propargyl carbamate groups allows to redefine *n* as *free, non-reacted* propargyl carbamate groups instead of the *total* number of propargyl carbamate groups, which simplifies the analysis.

where p is the number of CH_2CH_2O moieties (degree of polymerization) of poly(ethylene glycol). Considering that we used poly(ethylene glycol) of an averaged molecular weight of 2000 Da, p can be calculated as follow:

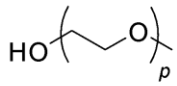

p = (2000-32.05)/44.05

Ending groups
HO MW = 17.01
CH_3 MW = 15.04
32.05

Repetitive unit
CH_2CH_2O
MW = 44.05

We will consider z as the number of poly(ethylene glycol) groups per DEX molecule.

In summary, functionalized dextran with alendronate and poly(ethylene glycol) branches will contain x alendronate groups, z PEG groups, n non-reacted propargyl groups[1] and m hydration molecules of H_2O. In addition, alendronate groups might contain na atoms of Na, cu atoms of copper and li atoms of Li. Thus, molecular formula of such derivative will be:

	For k glucose residues	For the chain ending groups	For n non-reacted propargyl carbamate groups	For m molecules of H_2O	For x alendronate groups with na atoms of Na, cu atoms of Cu and li atoms of Li	For z PEG groups
C atoms	$6k$		$4n$		$14x$	$(2p+5)z$
H atoms	$10k$	2	$3n$	$2m$	$(25-na-cu-li)x$	$(4p+6)z$
O atoms	$5k$	1	n	m	$9x$	$(p+1)z$
N atoms			n		$5x$	$4z$
P atoms					$2x$	
Na atoms					$na \cdot x$	
Cu atoms					$cu \cdot x$	
Li atoms					$li \cdot x$	

On the basis of this analysis, weight percentage of each element can be defined as follows:

$$\%C = \frac{100c_1(6k + 4n + 14x + (2p + 5)z)}{d}$$

$$\%H = \frac{100h_1(10k + 2 + 3n + 2m + (25 - na - cu - li)x + (4p + 6)z)}{d}$$

$$\%O = \frac{100o_1(5k + 1 + n + m + 9x + (p + 1)z)}{d}$$

$$\%N = \frac{100n_1(n + 5x + 4z)}{d}$$

$$\%P = \frac{100p_1(2x)}{d}$$

$$\%Na = \frac{100na_1(na \cdot x)}{d}$$

$$\%Cu = \frac{100cu_1(cu \cdot x)}{d}$$

$$\%Li = \frac{100li_1(li \cdot x)}{d}$$

where:

$d = c_1[6k + 4n + 14x + (2p + 5)z] + h_1[10k + 2 + 3n + 2m + (25 - na - cu - li)x + (4p + 6)z] + o_1[5k + 1 + n + m + 9x + (p + 1)z] + n_1(n + 5x + 4z) + p_1(2x) + na_1(na \cdot x) + cu_1(cu \cdot x) + li_1(li \cdot x)$

$k = \frac{40000-18.02}{162.14}$ $p = \frac{2000-32.05}{44.05}$ $c_1 = 12.011$

$h_1 = 1.008$ $o_1 = 15.999$ $n_1 = 14.007$

$p_1 = 30.974$ $na_1 = 22.99$ $cu_1 = 63.546$

$li_1 = 6.94$

n = number of non-reacted propargyl carbamate branches

m = number of hydration water molecules

x = number of alendronate branches

z = number of poly(ethylene glycol) branches

na = number of Na cations per alendronate branch

cu = number of Cu cations per alendronate branch

li = number of Li cations per alendronate branch

and where in addition %C + %H + %O + %N + %P + %Na + %Cu + %Li = 100

Such equation system was implemented within Wolfram Mathematica v11.0 software as follows (where carbono = %C, hidrogeno = %H, oxigeno = %O, nitrogeno = %N, fosforo = %P, cobre = %Cu, sodio = %Na and litio = %Li; values indicated for these variables in the following program correspond to those obtained for DEX-ALN$_{50}$-PEG$_{50}$ **7** derivative):

```
c1 = 12011 / 1000
h1 = 1008 / 1000
o1 = 15999 / 1000
n1 = 14007 / 1000
p1 = 30974 / 1000
cu1 = 63546 / 1000
na1 = 2299 / 100
li1 = 694 / 100
k = (40000 - (1802 / 100)) / (16214 / 100)
p = (2000 - (3205 / 100)) / (4405 / 100)
carbono = 4685 / 100
hidrogeno = 7769 / 1000
oxigeno = 41714 / 1000
nitrogeno = 227 / 100
fosforo = 57 / 100
cobre = 74 / 100
sodio = 6 / 100
litio = 27 / 1000
eqn1 =
 carbono (c1 (6 k + 4 n + 14 x + (2 p + 5) z) + h1 (10 k + 2 + 3 n + 2 m + (25 - cu - na - li) x + (4 p + 6) z) +
      o1 (5 k + 1 + n + m + 9 x + (p + 1) z) + n1 (n + 5 x + 4 z) + p1 (2 x) + cu1 (cu x) +
      na1 (na x) + li1 (li x)) - 100 c1 (6 k + 4 n + 14 x + (2 p + 5) z) == 0
eqn2 =
 hidrogeno
    (c1 (6 k + 4 n + 14 x + (2 p + 5) z) + h1 (10 k + 2 + 3 n + 2 m + (25 - cu - na - li) x + (4 p + 6) z) +
      o1 (5 k + 1 + n + m + 9 x + (p + 1) z) + n1 (n + 5 x + 4 z) + p1 (2 x) + cu1 (cu x) +
      na1 (na x) + li1 (li x)) - 100 h1 (10 k + 2 + 3 n + 2 m + (25 - cu - na - li) x + (4 p + 6) z) == 0
eqn3 =
 oxigeno (c1 (6 k + 4 n + 14 x + (2 p + 5) z) + h1 (10 k + 2 + 3 n + 2 m + (25 - cu - na - li) x + (4 p + 6) z) +
      o1 (5 k + 1 + n + m + 9 x + (p + 1) z) + n1 (n + 5 x + 4 z) + p1 (2 x) + cu1 (cu x) +
      na1 (na x) + li1 (li x)) - 100 o1 (5 k + 1 + n + m + 9 x + (p + 1) z) == 0
eqn4 =
 nitrogeno
    (c1 (6 k + 4 n + 14 x + (2 p + 5) z) + h1 (10 k + 2 + 3 n + 2 m + (25 - cu - na - li) x + (4 p + 6) z) +
      o1 (5 k + 1 + n + m + 9 x + (p + 1) z) + n1 (n + 5 x + 4 z) + p1 (2 x) + cu1 (cu x) +
      na1 (na x) + li1 (li x)) - 100 n1 (n + 5 x + 4 z) == 0
eqn5 =
 fosforo (c1 (6 k + 4 n + 14 x + (2 p + 5) z) + h1 (10 k + 2 + 3 n + 2 m + (25 - cu - na - li) x + (4 p + 6) z) +
      o1 (5 k + 1 + n + m + 9 x + (p + 1) z) + n1 (n + 5 x + 4 z) + p1 (2 x) + cu1 (cu x) +
      na1 (na x) + li1 (li x)) - 100 p1 (2 x) == 0
eqn6 =
 cobre (c1 (6 k + 4 n + 14 x + (2 p + 5) z) + h1 (10 k + 2 + 3 n + 2 m + (25 - cu - na - li) x + (4 p + 6) z) +
      o1 (5 k + 1 + n + m + 9 x + (p + 1) z) + n1 (n + 5 x + 4 z) + p1 (2 x) + cu1 (cu x) +
      na1 (na x) + li1 (li x)) - 100 cu1 (cu x) == 0
eqn7 =
 sodio (c1 (6 k + 4 n + 14 x + (2 p + 5) z) + h1 (10 k + 2 + 3 n + 2 m + (25 - cu - na - li) x + (4 p + 6) z) +
      o1 (5 k + 1 + n + m + 9 x + (p + 1) z) + n1 (n + 5 x + 4 z) + p1 (2 x) + cu1 (cu x) +
      na1 (na x) + li1 (li x)) - 100 na1 (na x) == 0
eqn8 =
 litio (c1 (6 k + 4 n + 14 x + (2 p + 5) z) + h1 (10 k + 2 + 3 n + 2 m + (25 - cu - na - li) x + (4 p + 6) z) +
      o1 (5 k + 1 + n + m + 9 x + (p + 1) z) + n1 (n + 5 x + 4 z) + p1 (2 x) + cu1 (cu x) +
      na1 (na x) + li1 (li x)) - 100 li1 (li x) == 0
Reduce[{eqn1, eqn2, eqn3, eqn4, eqn5, eqn6, eqn7, eqn8}, {n, m, x, cu, na, li, z}] //
reduce

N
valor numérico
```

From elemental and HR-ICP-MS analyses, the following data were measured:

	Experimental data							
	Elemental analysis			HR-ICP-MS				Calculated
Derivative	%C	%H	%N	%P	%Na	%Cu	%Li	%O
DEX-PC **5**	40.90	6.536	1.42	0	0	0	0	51.144
DEX-ALN_{75}-PEG_{25} **6**	46.24	7.582	2.46	0.81	0.103	1.05	0.042	41.713
DEX-ALN_{50}-PEG_{50} **7**	46.85	7.769	2.27	0.57	0.060	0.74	0.027	41.714
DEX-ALN_{25}-PEG_{75} **8**	47.86	7.842	2.05	0.26	0.092	0.42	0.048	41.428

When these data were input within the program, the following results were obtained:

	Wolfram Mathematica[a]							
Derivative	*n*	*m*	*x*	*z*	*na*	*cu*	*li*	*n*+*x*+*z*
DEX-PC **5**	50.0816	290.457	0	-0.0586	0	0	0	50.0816
DEX-ALN_{75}-PEG_{25} **6**	16.1260	277.158	14.2704	26.0495	0.34	1.26	0.46	56.4459
DEX-ALN_{50}-PEG_{50} **7**	13.7272	312.820	10.7702	30.5293	0.28	1.27	0.42	55.0297
DEX-ALN_{25}-PEG_{75} **8**	17.6461	260.918	4.9126	32.2745	0.95	1.56	0.95	54.8332

[a]An error of ±12% was estimated.

V. SEC chromatograms

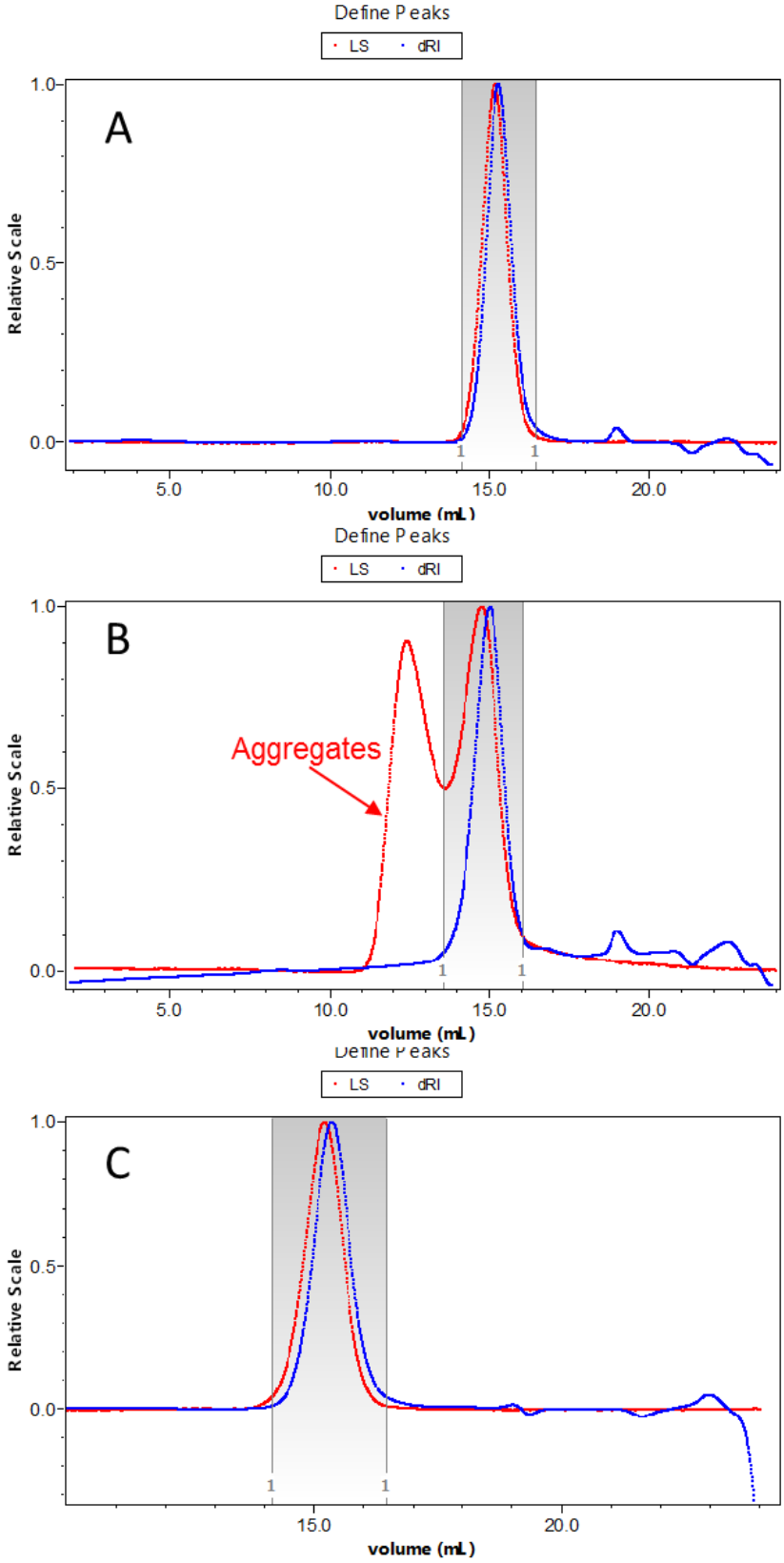

Figure S14 SEC chromatograms of DEX-PC 5 (A), DEX-ALN$_{50}$-PEG$_{50}$ 7 (B), and DEX (C)

VI. Internalization kinetics of nanoMOFs in J774 macrophages

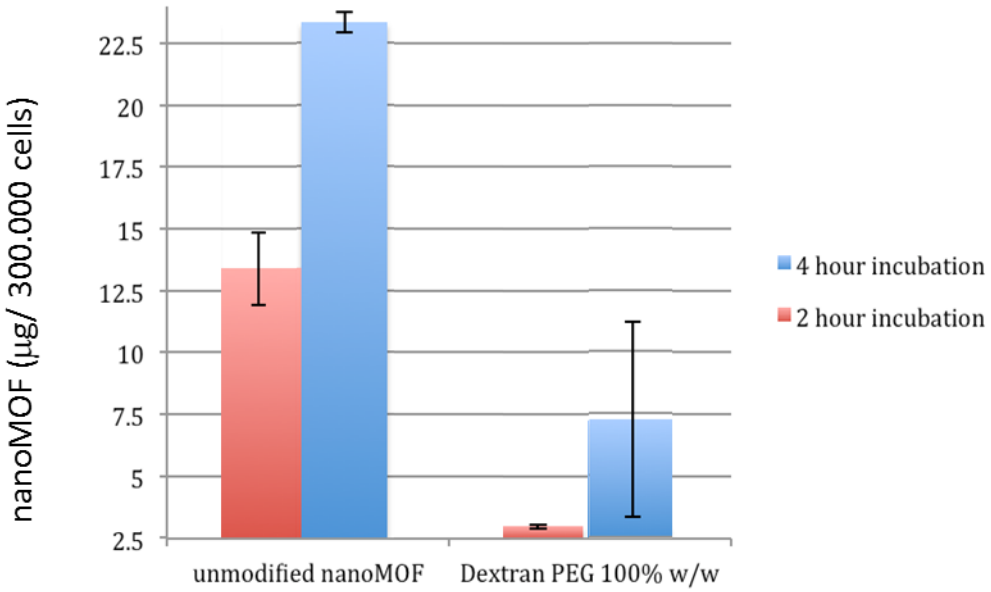

Figure S14. Interaction of nanoMOFs, coated or not with DEX-ALN$_{25}$-PEG$_{75}$ **8**, with J774 macrophages. 50 µg/mL nanoMOFs were incubated with 3×10^5 J774 cells for 2 h and 4 h, respectively.

Chapter 3 multifunctional core–shell drug loaded nanoparticles for biomedical applications

Chapter 3.1
Self-assembled multifunctional core–shell highly porous metal–organic framework nanoparticles

General Objectives and Author Contributions

Due to the special properties originating from the combination of core and shell materials, Core-shell nanoparticles (NPs) have been gaining increasing interest in the field of nanomedicine. It is well known that nanoMOFs are able to entrap a large number of drugs with high payloads. However, as previously described, it is absolutely necessary to functionalize the nanoMOFs with engineered coatings to improve the colloidal stability, enable a controllable drug release and extend the in vivo circulation time. A novel water soluble biodegradable cyclodextrin (CD)-based shell grafted or not with fluorophore were successfully synthesized in order to fulfill such challenging objective. Compared with monomeric CDs, the oligomeric CD coatings crosslinking with citric acid (γ-CD-citrate oligomers) provide better possibilities to graft functional moieties such as fluorescent molecules, spontaneously and effectively anchored on the surface of porous nanoMOFs.

We succeeded to prepare the stable core–shell NPs based on iron trimesate nanoMOFs (~200 nm) with γ-CD-citrate oligomer through a fast and "green" (without any organic solvent and surfactant) method achieved by simply mixing the two components in water. The amounts of γ-CD-citrate oligomers coated on the nanoMOFs reached up to 53 ± 8 wt%, the yield was as high as 86% in the optimized condition. In addition, fluorescence lifetime microscopy can decode the coating mechanism because of the presence of the fluorophore grafted to the shell. DOX loadings reached 48 ± 10 wt% or 65 ± 8 wt% after 1 day or 2 days incubation with the drug solution, respectively. This study paves the way toward the design of multifunctional core–shell nanoMOFs of interest for applications in the biomedical field.

International Journal of Pharmaceutics 581 (2020) 119281

Contents lists available at ScienceDirect

International Journal of Pharmaceutics

journal homepage: www.elsevier.com/locate/ijpharm

Self-assembled multifunctional core–shell highly porous metal–organic framework nanoparticles

Jingwen Qiu[a,1], Xue Li[a,1], Karine Steenkeste[a], Nadine Barroca-Aubry[b], Caroline Aymes-Chodur[b], Philippe Roger[b], Juan M. Casas-Solvas[c], Antonio Vargas-Berenguel[c], Christophe Rihouey[d], Luc Picton[d], Ruxandra Gref[a,*]

[a] Université Paris-Saclay, CNRS, Institut des Sciences Moléculaires d'Orsay, 91405 Orsay, France
[b] Université Paris-Saclay, CNRS, Institut de chimie moléculaire et des matériaux d'Orsay, 91405 Orsay, France
[c] Departamento de Química y Física, Universidad de Almería, 04120 Almería, Spain
[d] Polymères Biopolymères Surfaces, Normandie Université, UNIROUEN, Institut National des Sciences Appliquées Rouen, CNRS, UMR 6270, 76821 Mont Saint Aignan, France

ARTICLE INFO

Keywords:
Metal organic frameworks
γ-cyclodextrin-citrate oligomers
Surface modification
Doxorubicin
Self assemble

ABSTRACT

Core-shell nanoparticles (NPs) are attracting increasing interest in nanomedicine as they exhibit unique properties arising from the combined assets of core and shell materials. Porous nanoscale metal–organic frameworks (nanoMOFs) are able to incorporate with high payloads a large variety of drugs. Like other types of NPs, nanoMOFs need to be functionalized with engineered coatings to ensure colloidal stability, control *in vivo* fate and drug release. To do so, a novel biodegradable cyclodextrin (CD)-based shell was designed in this study. Water soluble γ-CD-citrate oligomers grafted or not with fluorophores were successfully synthesized using citric acid as crosslinker and efficiently anchored onto the surface of porous nanoMOFs. As compared to monomeric CDs, the oligomeric CD coatings could offer higher interaction possibilities with the cores and better possibilities to graft functional moieties such as fluorescent molecules. The amounts of γ-CD-citrate oligomers onto the nanoMOFs were as high as 53 ± 8 wt%. The yield reached up to 86% in the optimized system. These core–shell nanocomposites were stable upon storage, in contrast to the naked nanoMOFs. In addition, the presence of the coating prevented the doxorubicin (DOX)-loaded nanoMOFs from aggregation. Moreover, due to the presence of fluorophores conjugated to the shell, fluorescence-lifetime microscopy enabled deciphering the coating mechanism. DOX loadings reached 48 ± 10 wt% after 24 h incubation with the drug solution. After coating for additional 24 h, DOX loadings reached 65 ± 8 wt%.

1. Introduction

Breakthroughs in nanotechnology bring revolutionary changes in the field of life sciences, allowing diagnostics, drug delivery, and nutraceutical formulation. Particularly, core–shell nanoparticles (NPs) are attracting increasing interest as they exhibit unique properties arising from the combined assets of core and shell materials (Ghosh Chaudhuri and Paria, 2012; Khatami et al., 2018).

Although discovered recently, highly porous NPs made of metal–organic frameworks (nanoMOFs) are now widely used to incorporate high payloads of a large variety of drugs (such as antibiotics, antiviral and anticancer drugs), which are able to efficiently penetrate within their porous structures (Horcajada et al., 2010). Particularly, nanoMOFs based on iron (III) trimesate (Agostoni et al., 2013a; Li et al., 2017, 2019; Simon-Yarza et al., 2017) were considered among the most promising materials for biomedical applications, because of their biocompatibility, biodegradability, and high drug loading capacity (up to ~70 wt%). As an example, doxorubicin (DOX), one of the most powerful anthracycline anticancer drugs, was loaded in iron (III) trimesate nanoMOFs, reaching loadings of 23 wt% (Bhattacharjee et al., 2020), 16 wt% (Anand et al., 2014) and 9 wt% (Horcajada et al., 2010). DOX is largely employed in the treatment of various solid tumors and leukemia, in spite of drawbacks such as severe cardiotoxicity and possible occurrence of resistance to the treatment (Lipshultz et al., 1991; Pratt and Shanks, 1974). A strategy to circumvent these problems is the development of suitable nanocarriers to optimize its administration.

* Corresponding author.
E-mail address: ruxandra.gref@universite-paris-saclay.fr (R. Gref).
[1] These authors contributed equally.

https://doi.org/10.1016/j.ijpharm.2020.119281
Received 8 February 2020; Received in revised form 24 March 2020; Accepted 26 March 2020
Available online 07 April 2020
0378-5173/

NanoMOFs were used as DOX nanocarriers but an aggregation was observed and was attributed to drug-induced bridging of nanoMOFs (Anand et al., 2014).

In this context, surface engineering of nanoMOFs with polymers or cyclodextrins (CDs) was demonstrated to efficiently protect the nanoMOFs against aggregation in aqueous media (Agostoni et al., 2015; Cutrone et al., 2019a; Liu et al., 1999; Thatiparti et al., 2010; Wenz, 1994; Bellido et al., 2015; Giménez-Marqués et al., 2018; Cutrone et al., 2019b; Aykaç et al., 2017).

Among the shells, CDs are considered as the most versatile ones. CDs are water-soluble cyclic oligosaccharides made of 6, 7, or 8 α-1,4 linked glucose units, named as α-, β-, and γ-CD, respectively (Szejtli, 1998). Because of their unique structure with a hydrophilic exterior and a hydrophobic interior, they are inherently able to form inclusion complexes in water solution with various hydrophobic molecules *via* host–guest interaction. A variety of CD derivatives (Arima et al., 2015; Gidwani and Vyas, 2015) have been synthesized as potential DOX carriers since 1990s to improve its activity on both sensitive and multidrug-resistant cancer cell lines (Zhang et al., 2008). However, one of the main drawbacks of the CD-based drug delivery systems lies in their low drug loading capacity.

Therefore, a core–shell nanocomposite was designed in this study using iron trimesate nanoMOFs MIL-100 (Fe) (MIL stands for Materials of Institute Lavoisier) as core material and a CD-based layer as shell. Particularly, biodegradable γ-CD oligomers were synthesized using citric acid as cross linker, which plays a crucial role in anchoring the oligomers onto the surface of the nanoMOFs due to coordination with available iron sites. In addition, the versatile CD-based coatings could offer new functionalities, such as the possibilities to interact with drugs, and graft fluorescent molecules for imaging purposes, polyethylene glycol (PEG) chains for "stealth effect", and/or targeting ligands. CD-based shells might open up a wide range of biomedical applications in controlled drug release, prolonged blood circulation, imaging and targeting. As compared to monomeric CDs, the oligomeric CD coatings could offer higher interaction possibilities with the cores and better possibilities to graft functional moieties such as fluorescent molecules.

Fluorescent γ-CD citrate oligomers were synthesized for the first time to gain deep insights of the interaction between the shell and the core. In this regard, γ-CD was conjugated with the fluorescent dye cyanine 5 (Cy5) by copper (I)-catalyzed azide-alkyne cycloaddition (CuAAC) before cross-linking with citric acid (Luo et al., 2011).

Fluorescence-lifetime microscopy was employed to characterize the coating processes. As known, fluorescence lifetime is an intrinsic property of a fluorophore, independent of its concentration. However, it varies locally depending on its interaction with its environment (solvent, quenchers, NPs …). Indeed, the mean fluorescence lifetime (τ) of Cy5-γ-CD-citrate oligomers was significantly changed upon interaction with iron trimesate nanoMOFs. Compared to the conventional characterization by fluorescence quantification of the free fluorophore after separation with the attached one, fluorescence-lifetime microscopy offers a robust approach to the *in situ* characterization of the interactions between NPs and coating materials, providing important insights at the molecular level.

In a nutshell, the core–shell NPs based on iron trimesate nanoMOFs (~200 nm) with γ-CD-citrate oligomer coatings were successfully prepared by a fast and "green" (organic solvent free) method consisting in simply incubating the two components in water. Despite the simplicity of the methods, yields of 86% were obtained and as much as 53 ± 8.4 wt% coating material could be associated at the weight ratio γ-CD-citrate: nanoMOFs of 1:2, and 2:1, respectively. Moreover, the presence of fluorophores conjugated to γ-CD-citrate oligomers, allowed investigating *in situ* coating process at molecular scale based on fluorescence lifetime measurements.

2. Experimental

2.1. Materials and methods

Doxorubicin (DOX, 98%), citric acid (≥99.5%) sodium phosphate monobasic dihydrate (≥99%, $NaH_2PO_4{\cdot}2H_2O$), potassium chloride (powder, ≥99%), lithium hydride (powder, ≥95%), lithium iodide (anhydrous for synthesis), propargyl bromide (solution in toluene, 80% w/w) and copper(I) chloride (≥99.995%) were purchased from Sigma-Aldrich (Saint-Quentin-Fallavier, France). γ-CD was purchased from Cyclolab (Budapest, Hungary) and dried at 50 °C in vacuum in the presence of P_2O_5 until constant weigh. Cy5 azide ($Cy5N_3$) was obtained from Lumiprobe GmbH (Hannover, Germany). Dimethylsulfoxide (DMSO, ACS) was purchased from Panreac Applichem (Barcelona, Spain) and dried according to a literature procedure (Perrin and Armarego, 1989). Dry dimethylformamide (DMF, AcroSeal, 99.8%, over molecular sieves) was purchased from Acros (Geel, Belgium). Deuterated DMSO (DMSO-d_6, 99.8% D) and water (D_2O, 99.9% D) were obtained from Eurisotop (Gif sur Yvette, France).

Thin layer chromatography (TLC) was performed on Merck silica gel 60 F_{254} aluminum sheets and developed by UV–vis light and 5% v/v sulfuric acid in ethanol. Flash column chromatography was performed on Merck silica gel (230–400 mesh, ASTM). Melting points were measured on a Büchi B-450 melting point apparatus and are uncorrected. Optical rotations were recorded on a Jasco P-1030 polarimeter at room temperature. $[\alpha]_D$ values are given in 10^{-1} deg cm^{-1} g^{-1}. Fourier-transform infrared (FTIR) spectra were recorded on a Bruker Alpha FTIR equipped with a Bruker universal ATR sampling accessory. ^1H, ^{13}C and 2D NMR spectra for compounds **1** and **2** were recorded on a Bruker Avance III HD 600 MHz spectrometer equipped with a QCI $^1H/^{13}C/^{15}N/^{31}P$ proton-optimized quadrupole inverse cryoprobe with ^1H and ^{13}C cryochannels. Standard Bruker software was used for acquisition and processing routines. Chemical shifts (δ) are given in parts per million (ppm) and referenced to internal tetramethylsilane (TMS) signal (δ_H, δ_C 0.00). *J* values are given in hertz (Hz). MALDI-TOF mass spectra were recorded on a 4800 Plus AB SCIEX spectrometer with 2,5-dihydroxybenzoic acid (DHB) or *trans*-2-[3-(4-*tert*-butylphenyl)-2-methyl-2-propenylidene]malononitrile (DCTB) as the matrix. Syringe filtering was conducted using nylon 0.45 μm Milipore Millex® syringe-driven filter units. Dialysis was performed using Spectrum™ Spectra/Por™ Biotech Cellulose Ester (CE) 100–500 MWCO dialysis membrane tubing. A Hanna HI 98,192 EC/TDS/NaCl/Resistivity meter was employed to monitor dialysate solutions conductivity during dialysis. Freeze-drying was performed on a Telstar LyoQuest 85 lyophilizer.

Iron (III) chloride hexahydrate (98%, Alfa Aesar, Schiltigheim, France), 1,3,5-benzenetricarboxylic acid (BTC, 95%, Sigma-Aldrich, Saint-Quentin-Fallavier, France) and absolute ethanol (99%, Carlo Erba, Val-de-Reuil, France) were used for the synthesis of nanoMOFs. Water was purified by a Millipore MilliQ system.

2.2. Synthesis and characterization of γ-CD-citrate oligomers

2.2.1. Synthesis of 2^I-O-propargylcyclomaltooctaose (1)

The γ-CD (5 g, 3.855 mmol) was completely dissolved in dry DMSO (75 mL) under N_2 atmosphere before lithium hydride (54 mg, 6.746 mmol) was added to the solution. The resulting suspension was stirred at 55 °C for 24 h. Propargyl bromide (solution in toluene, 80% w/w, 430 μL, 3.855 mmol) and a catalytic amount of lithium iodide (~10 mg) were then added, and the mixture was stirred at 55 °C in the absence of light for 5 h. TLC (10:5:2 CH_3CN-H_2O-30% v/v aqueous NH_3, see supporting information) showed four spots with R_f values of 0.63, 0.52, 0.38, and 0.25, the last two corresponding to mono-2-*O*-propargylated and nonpropargylated γ-CD, respectively. The solution

was poured into acetone (700 mL) and the precipitate was filtered and washed thoroughly with acetone (2 × 300 mL). The resulting residue was transferred into a 500 mL round-bottom flask and solved in a minimum volume of water (~120 mL). Silica gel (10 g) was added and the solvent was removed under vacuum. This crude mixture was purified through a short column chromatography (20 × 5 cm) using 10:5:2 CH_3CN-H_2O-30% v/v aqueous NH_3 as the eluent to give 2^I-*O*-propargylcyclomaltooctaose **1** (1.537 g, 1.151 mmol, 30%) as a white solid after freeze-drying. Mp 205–220 °C (decomp); $[\alpha]_D^{25}$ + 128 (*c* 0.5, H_2O); R_f = 0.44 (10:5:2 CH_3CN-H_2O-30% v/v aqueous NH_3); IR (KBr): 3408, 2931, 1642, 1158, 1081, 1028, 942 cm^{-1}; ^1H NMR (600 MHz, DMSO-d_6, ppm) δ 5.94 (d, 1H, J = 2.0 Hz, OH-3^I), 5.88 (d, 1H, J = 7.0 Hz, OH), 5.82 (d, 1H, J = 2.2 Hz, OH), 5.78–5.69 (m, 10*H*, OH), 5.64 (t, 2H, J = 7.3 Hz, OH), 5.12 (d, 1H, ^3J = 3.8 Hz, H-1^I), 4.91–4.88 (m, 7H, H-1$^{II\text{-}VIII}$), 4.60 (t, 1H, J = 5.6 Hz, OH), 4.58 (d, 1H, J = 2.0 Hz, OH), 4.55–4.45 (m, 7H, OH, CHC≡), 4.40 (dd, 1H, ^2J = 15.9 Hz, ^4J = 2.4 Hz, CHC≡), 3.73 (t, 1H, ^3J = 9.6 Hz, H-3^I), 3.63–3.58 (m, 23H; H-3$^{II\text{-}VIII}$,6a$^{I\text{-}VIII}$,6b$^{I\text{-}VIII}$), 3.55–3.52 (m, 8H, H-5$^{I\text{-}VIII}$), 3.49 (t, 1H, ^4J = 2.4 Hz, ≡CH), 3.45–3.41 (m, 2H, H-2^I,4^I), 3.40–3.31 (m, H-2$^{II\text{-}VIII}$,4$^{II\text{-}VIII}$, overlapped with HDO); ^{13}C NMR (125 MHz, DMSO-d_6, ppm) δ 101.8–101.1 (C-1$^{II\text{-}VIII}$), 99.3 (C-1^I), 81.1–80.4 (C-4$^{I\text{-}VIII}$), 79.9 (C≡), 78.8 (C-2^I), 77.7 (≡CH), 73.5–71.8 (C-2$^{II\text{-}VIII}$,3$^{I\text{-}VIII}$,5$^{I\text{-}VIII}$), 60.2–59.7 (C-6$^{I\text{-}VIII}$), 58.3 (CH_2C≡); MALDI-TOF-MS: *m/z* calcd for $C_{51}H_{82}O_{40}Na$, 1357.4; found: 1357.6 $[M + Na]^+$. Column chromatography also allowed the recovery of unreacted γ-CD (1.448 g, 1.116 mmol, 29%).

2.2.2. Synthesis of 1-{6-{3-[4-(2^I-O-cyclomaltooctaosylmethyl)-1H-1,2,3-triazol-1-yl]propyl-1-amino}oxohexyl}-3,3-dimethyl-2-{(1E,3E)-5-[(E)-1,3,3-trimethylindolin-2-ylidene]penta-1,3-dien-1-yl}–3H-indol-1-ium chloride (2)

A solution of 2-O^I-propargylcyclomaltooctaose **1** (0.037 g, 0.028 mmol), Cy 5 azide (0.017 g, 0.028 mmol) and CuCl (0.002 g, 0.020 mmol) in dry DMF (3 mL) was stirred at 100 °C under N_2 atmosphere for 6 h until the starting material **1** (R_f = 0.27) was observed to vanish and a new spot (R_f = 0.43) by TLC (10:5:1 CH_3CN-H_2O-30% v/v aqueous NH_3, see supporting information). The reaction mixture was cooled down and the solvent was rotary-evaporated. The crude was dissolved in H_2O (5 mL), syringe filtered (0.45 μm) and dialyzed (100–500 Da MWCO) against distilled water, changing dialysate solution each 3 h until its conductivity was stable and below 1 μS/cm (4 days for final value of 0.98 μS/cm) to yield the entitled product (0.043 g, 0.022 mmol, 79%) as a deep blue powder after freeze-drying. IR (KBr) ν 3279, 2926, 1637, 1488, 1453, 1370, 1332, 1149, 1021, 923, 793, 704 cm^{-1}; ^1H NMR (600 MHz, DMSO-d_6, ppm) δ 8.32 (t, 2H, J = 13.0 Hz, =CH), 8.12 (s, 1H, H-5-triazole), 7.88 (t, 1H, J = 5.4 Hz, NHCO), 7.61 (d, 2H, J = 7.3 Hz, CH-indole), 7.43–7.36 (m, 4H, CH-indole), 7.26–7.23 (m, 2H, CH-indole), 6.56 (t, 1H, J = 12.3 Hz, =CH), 6.30 (d, 1H, J = 13.6 Hz, =CH), 6.25 (d, 1H, J = 13.9 Hz, =CH), 5.95 (brs, 1H, OH-3^I), 5.87 (d, 1H, J = 7.0 Hz, OH), 5.80–5.70 (m, 11*H*, OH), 5.63 (d, 1H, J = 7.5 Hz, OH), 5.60 (d, 1H, J = 7.6 Hz, OH), 5.02 (d, 1H, J = 2.9 Hz, H-1^I), 4.88 (brs, 7H, H-1$^{II\text{-}VIII}$), 4.85 (d, 1H, J = 12.5 Hz, OCH-triazole), 4.81 (d, 1H, J = 12.5 Hz, OCH-triazole), 4.70 (brs, 1H, OH), 4.60–4.47 (m, 7H, OH), 4.34 (t, 2H, J = 6.7 Hz, CH_2N-triazole), 4.09 (t, 2H, J = 6.5 Hz, CH_2N-indole), 3.75 (t, 1H, J = 8.6 Hz, H-3^I), 3.69–3.58 (m, 23H, H-3$^{II\text{-}VIII}$,6a$^{I\text{-}VIII}$,6b$^{I\text{-}VIII}$), 3.59 (s, 3H, NCH_3), 3.55–3.50 (m, 8H, H-5$^{I\text{-}VIII}$), 3.43–3.32 (m, H-2$^{I\text{-}VIII}$,4$^{I\text{-}VIII}$, overlapped with HDO), 3.03–3.00 (m, 2H, C*H*$_2$NHCO), 2.07 (t, 2H, J = 7.1 Hz, COC*H*$_2$), 1.94–1.88 (m, 2H, C*H*$_2$CH$_2$NHCO), 1.72–1.68 (m, 2H, C*H*$_2$CH$_2$N-indole), 1.68 (s, 12H, CCH_3), 1.55 (t, 2H, J = 7.3 Hz, $COCH_2CH_2$), 1.37–1.32 (m, 2H, $COCH_2CH_2CH_2$); ^{13}C NMR (150 MHz, DMSO-d_6, ppm) δ 173.2 (C_{ipso}-indole), 172.5 (C_{ipso}-indole), 172.1 (CONH), 154.9 (=CH), 143.8 (C-4-triazole), j142.8 (C-indole), 142.0 (C-indole), 141.1 (C-indole), 141.0 (C-indole), 128.5 (CH-indole), 128.4 (CH-indole), 125.4 (=CH), 124.7 (CH-indole), 124.6 (CH-indole), 124.1 (C-5-triazole), 122.4 (CH-indole), 122.3 (CH-indole), 111.0 (CH-indole), 103.2 (=CH), 103.1 (=CH), 101.8–101.1 (C-1$^{II\text{-}VIII}$), 99.5 (C-1^I), 81.1–80.3 (C-4$^{I\text{-}VIII}$), 79.3 (C-2^I), 73.4–71.8 (C-2$^{II\text{-}VIII}$,3$^{I\text{-}VIII}$,5$^{I\text{-}VIII}$), 64.3 (OCH_2-triazole), 60.2–59.8 (C-6$^{I\text{-}VIII}$), 48.9 (*C*CH$_3$), 47.2 (CH_2N-triazole), 43.3 (CH_2N-indole), 35.7 (*C*H$_2$NHCO), 35.1 (COC*H*$_2$), 31.1 (NCH_3), 29.9 (*C*H$_2$CH$_2$NHCO), 27.2 (*C*CH$_3$), 27.0 (*C*CH$_3$), 26.7 (*C*H$_2$CH$_2$N-indole), 25.7 ($COCH_2CH_2CH_2$), 24.9 ($COCH_2CH_2$); MALDI-TOF-MS: *m/z* calcd for $C_{86}H_{117}N_6O_{41}^+$ 1899.8, found 1899.7 $[M-Cl]^+$.

2.2.3. Synthesis of γ-CD-citrate oligomers

The synthetic procedure of Martel *et al.* (Martel et al., 2004) was adapted here using γ-CD monomers (native γ-CD and Cy5-γ-CD **2**) and citric acid in 1:5 M ratios. An aqueous reaction mixture was prepared by solubilizing in a 25 mL flask the catalyst (0.2 mmol $NaH_2PO_4{\cdot}2H_2O$), 0.09 mmol γ-CD, and 0.45 mmol citric acid in 2 mL water. This solution was then concentrated by evaporation for 10 min at 140 °C, and the resulting dried mixture underwent a treatment at 140 °C for 0 ~ 25 min under reduced pressure (10–15 mmHg) in a system connected to a suction pump. A yellowish polymer was obtained. Then 10 mL distilled water was added and the crude was sonicated for 5 min, followed by filtration to separate the insoluble fraction from the soluble one. The soluble fraction was recovered and dialyzed for 48 h with a cellulosic membrane (20 kDa, Spectrum Laboratories, Rancho Dominguez, USA). The solution was finally dried under reduced pressure to yield a slightly yellow powder. Fluorescent labelled γ-CD-citrate oligomers were synthesized using the same method, but 5 wt% Cy5 labelled γ-CD (**2**) was added in native γ-CD.

2.2.4. Characterization of γ-CD-citrate oligomers

The composition of synthesized γ-CD-citrate oligomers was analyzed by proton nuclear magnetic resonance (NMR) spectroscopy. ^1H NMR spectra were recorded in D_2O using a Bruker Avance 360 MHz. The citric acid: γ-CD molar ratio in the product was calculated by integrating the peaks assigned to 4 protons of the citric acid methylene group divided by 8 anomeric protons of γ-CD units. This allowed to calculate the CD wt% content in the oligomers, by taking into account the respective the molecular weights of the γ-CD (1297 g/mol) and the citrate (192 g/mol) moieties.

Fourier-transform infrared (FTIR) spectra were recorded with a Bruker apparatus (VERTEX 70).

Size-exclusion chromatography (SEC), coupled on-line with multi-angle light scattering (MALS) and refractive index (RI) detectors (SEC/MALS/RI, Wyatt Technology, Santa Barbara, USA) (Kouassi et al., 2017), was used to determine the average molecular weight values of γ-CD-citrate oligomers, using a dn/dc (referring to the rate of change of the refractive index with the concentration of a solution for a sample at a given temperature, a given wavelength, and a given solvent) value of 0.14 mL/g (Puskás et al., 2013), using two OHPAK SB 804/OHPAK SB 806 HQ columns, and 0.1 M $LiNO_3$ as eluent. Data are determined thanks to the Astra® 6.1.1 software from Wyatt Technology using Zimm order 1 between 44.8° and 140°.

2.3. Synthesis and characterization of MIL-100 (Fe) nanoMOFs

Iron trimesate MIL-100 (Fe) nanoMOFs were synthesized using a hydrothermal method assisted by microwave, as previously described (Agostoni et al., 2013a). Briefly, 30 mL of an aqueous mixture containing 2.43 g iron (III) chloride hexahydrate and 0.84 g BTC was heated at 130 °C for 6 min under stirring by microwave irradiation (Mars-5, CEM, USA). The synthesized nanoMOFs were obtained by centrifugation at 10,000 *g* for 10 min and purified by washing with absolute ethanol until the supernatant was colorless. X-ray powder diffraction patterns (XRPD) were recorded to characterize the crystallinity. Dynamic light scattering (DLS, Malvern Nano-ZS, Zetasizer Nano series, France) was used to determine the hydrodynamic diameters and size distributions. The nanoMOFs BET (Brunauer-Emmett-Teller) surface

area was measured by nitrogen sorption experiments at −196 °C using an ASAP 2020 (Micromeritics, USA) after degassing at 100 °C for 15 h under secondary vacuum. NanoMOFs were stored in ethanol at room temperature and re-dispersed in aqueous media before usage.

2.4. Surface modification of nanoMOFs with γ-CD-citrate oligomers

NanoMOFs were centrifuged at 10,000 *g* for 10 min to remove the storage solvent (ethanol) and then re-suspended in water by vortex. For the coating procedure, they were incubated at room temperature with different initial amounts of γ-CD-citrate oligomers (at the weight ratio γ-CD-citrate:nanoMOFs of 1:2 ~ 2:1). After 4 min up to 24 h incubation, the non-attached γ-CD-citrate fraction was removed by centrifugation (10,000 *g*, 10 min). The same method was employed to coat the nanoMOFs with fluorescent γ-CD-citrate.

In order to quantify the associated amount of coating material on the nanoMOFs, the non-attached γ-CD-citrate fraction recovered in the supernatant was quantified by fluorescence spectroscopy (Varian, Cary Eclipse, France) using fluorescent labelled γ-CD-citrate oligomers. The maximum excitation (λ_{ex}) and maximum emission (λ_{em}) wavelengths were 647 nm and 662 nm, respectively, in water. The calibration curve of Cy5-labeled γ-CD-citrate in water gave a linear response for a range of concentration of 10^{-2} ~ 10^{-3} mg/mL with regression factors > 0.99. The associated amount of γ-CD-citrate oligomers was calculated as the difference between the initial amounts of coating material added in the system and the amounts recovered in the supernatants and detected by the fluorimeter, after sedimentation of the coated nanoMOFs. In addition, the spectra of the coated nanoMOFs were recorded.

2.5. Characterization of γ-CD-citrate coated nanoMOFs

Morphologies of nanoMOFs, before and after surface modification were observed using a transmission electron microscope (TEM, JEOL 1400 (120 kV), Japan).

XRPD were recorded to characterize the crystallinity of nanoMOFs using a homemade setup based on a copper rotating anode generator (RU-200BEH, Rigaku Ltd., Tokyo, Japan), as previously described (Cutrone et al., 2019a, 2019b; Li et al., 2017, 2019). The X-ray beam was filtered and focused by a confocal system (CMF-12-38Cu6 from Osmic Inc., Cleveland, OH, USA). The samples were filled in round glass capillaries (1.5 mm in diameter, WJM-Glas Müller GmbH, Berlin, Germany), and mounted on an in-house motorized sample holder. The accessible scattering vector range was 0.035 ~ 0.5 $Å^{-1}$.

Colloidal stability investigation. Colloidal stabilities of γ-CD-citrate coated nanoMOFs were estimated by DLS after incubation in MilliQ water. Mean hydrodynamic diameters were measured at 0, 1, 2, 3, 7, 12, and 16 days storage at 25 °C in water.

Zeta potential (ZP) of nanoMOFs were measured at 25 °C using a Zetasizer instrument (Malvern Nano-ZS, Zetasizer Nano series, France) in a pH range of 1 to 10. For the measurements, nanoMOFs were diluted using a KCl solution (1 mM) to a final concentration of 100 μg/mL.

X-ray photon spectroscopy (XPS) was employed to investigate the surface elemental composition. Uncoated nanoMOFs, γ-CD-citrate oligomers and γ-CD-citrate coated MIL-100 nanoMOFs were deposited on a copper film. XPS measurements were performed on a K_α spectrometer (ThermoFisher), equipped with a monochromatic X-ray source (Al K_α, 1486.6 eV; spot size: 400 μm). The hemispherical analyzer was operated in Constant Analyzer Energy (CAE) mode (pass energy: 200 eV). Survey spectra acquisition was set as 1 eV/step. For the acquisition of narrow scans, pass energies of 50 eV and 100 eV and 0.1 eV/step were used. A flood gun was employed to neutralize the charge build-up. Avantage™ software was used for data treatment. The binding energies were calibrated considering the C1s binding energy set at 284.8 eV. Gaussian–Lorentzian curves (70% Gaussian character) were used to analyze the peaks.

Thermogravimetric analyses (TGA) analyses were performed to quantify the amount of coating materials using a TGA 4000 Instruments (Perkin Elmer, 100–240 V/50–60 Hz). During analysis, samples were submitted to an O_2 flow of approximately 20 mL/min. NanoMOF samples of around 10 mg were heated from 25 to 600 °C at a rate of 3 °C/min. Prior to TGA analysis, the samples were dried overnight at 60 °C to remove absorbed water. The associated amounts of γ-CD-citrate oligomers (wt%) was calculated with respect to dry MIL-100(Fe) weight.

Fluorescence lifetime measurements. The free fluorescent γ-CD citrate oligomers (500 μg/mL), and that coated on the nanoMOFs at different ratios were biphotonically excited (two-photon excitation) through an oil-immersion objective (×63, NA 1.4) at 730 nm using a pulsed titanium-sapphire laser (150 fs; 80 MHz; Chameleon, Coherent). The fluorescence signal was collected by an avalanche photodiode coupled to a PicoHarp 300 module (Picoquant, Germany) based on time-correlated single-photon counting method. A 700 nm short-pass emission filter together with a 685 nm bandpass filter (70 nm width) was used to remove any residual laser light, and the emitted fluorescence was recorded within a range of 650 to 700 nm. Instrumental response function obtained on a KI-saturated erythromycin solution was used to deconvolute the observed time-resolved decays. It was possible here to fit all of the fluorescence decays, with a sum of exponentials, giving the fluorescence lifetimes of the sample with a 100-ps time resolution (Valeur, 2002). All the results were reproducible between independent experiments, with less than 5% differences in lifetimes.

2.6. DOX encapsulation in γ-CD-citrate coated nanoMOFs

MIL-100(Fe) nanoMOFs suspension (20 mg/mL) was first centrifuged at 10,000 *g* for 10 min to recover the nanoMOFs, which were further redispersed in water. For the DOX encapsulation, 1 mL of nanoMOFs aqueous suspension (2 mg/mL) was mixed with 1 mL of DOX solution (2 mg/mL), followed by gently stirring for 24 h at room temperature. The weight ratio between DOX and nanoMOFs was 1:1. The DOX loaded nanoMOFs were recovered by centrifugation (10,000 *g*, 10 min) and the supernatant was used to quantify the drug payload, which was calculated as Eq. (1):

$$Payload\ (\%) = \frac{Encapsulated\ Drug\ (mg)}{nanoMOFs\ (mg)} \times 100 \quad (1)$$

The DOX loaded nanoMOFs were further coated with γ-CD-citrate oligomers (at the weight ratio γ-CD-citrate: nanoMOFs of 1:2), and the DOX payload were further quantified by fluorescence spectrometry with the excitation (λ_{ex}) and emission (λ_{em}) at 480 and 590 nm, respectively. DOX in the supernatant was diluted with a mixture of water and DMSO (1:1 v:v), to dissociate the complexes CD:DOX. Calibration curves of DOX were obtained between an interval of 10^{-3} to 10^{-4} $mg{\cdot}mL^{-1}$ (correlation coefficient > 0.99).

In addition, the same DOX loading method was used for nanoMOFs coated with γ-CD-citrate oligomers, except that the nanoMOFs were coated with γ-CD-citrate oligomers (at the weight ratio γ-CD-citrate: nanoMOFs of 1:2) before DOX encapsulation.

3. Results and discussions

3.1. Synthesis of γ-CD-citrate oligomers with and without fluorescent dye

The γ-CD-citrate oligomers without fluorescent dye was synthesized by adjusting a method previously reported for oligomers (Anand et al., 2013; Martel et al., 2004; Banerjee and Chen, 2007) (Scheme 1). The polymerization reaction between γ-CD and citrate acid was investigated by optimizing the heating time, under reduced pressure or at atmospheric pressure. The results are summarized in Table 1. Initially, the reaction mixture was concentrated by evaporation for 10 min at 140 °C,

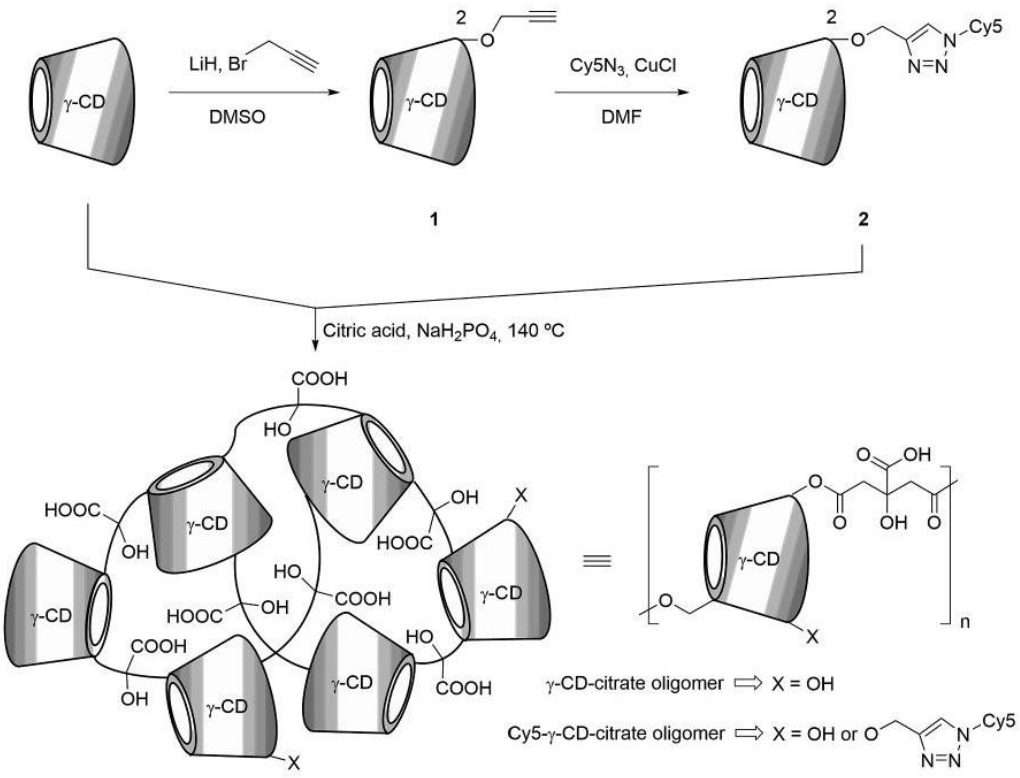

Scheme 1. Synthesis of γ-CD-citrate and Cy5-γ-CD-citrate oligomers. The structures of the oligomers depicted here are illustrative and do not reflect either the actual distribution of the cross-linking positions on the macrocycle nor the degree of Cy5 substitution in the case of Cy5-γ-CD-citrate oligomers. The molecular structures of compounds **1** and **2** can be found in the Supporting Information.

Table 1
Optimization the synthesis of γ-CD-citrate oligomers (average of 3 different batches).

Series	Mn (g/mol)	Mw (g/mol)	Đ	Yield (%)	Total heating Time (min)
1	–	–	–	2 ± 1	10
2	–	–	–	5 ± 1	15
3	9600	13,600	1.4	17 ± 3	20
4	13,600	22,000	1.6	30 ± 3	25
5	33,100	104,400	3.1	52 ± 4	30
6	14,500	42,800	2.9	37 ± 4	35
7[a]	8400	17,000	2.0	16 ± 2	25
8[a]	8500	18,500	2.2	22 ± 2	30
9[a]	10,200	23,300	2.3	28 ± 3	35

[a] The resulting dried mixture underwent an additional treatment at 140 °C for 15–25 min at atmospheric pressure.

and the resulting dried mixture underwent a treatment of 140 °C for other 0–25 min under reduced pressure in a system connected to a suction pump (entries 1–6). While the heating time was shorter than 15 min, the yield was low (less than5% for entries 1–2). With longer heating time (20 min ~ 30 min), the yield was significantly increased from 17% to 52% (entries 3–5). This indicates that longer reaction time is favorable to the esterification. However, when the heating time increased to 35 min, the yield of the soluble γ-CD-citrate oligomers decreased to 37%, which is due to the formation of a higher amount of insoluble polymers (entry 6). When the reaction took place at atmospheric pressure, lower yields were obtained, whatever the reaction time (entries 7–9). Therefore, the reaction was more efficient under reduced pressure. In addition to the yield, the polydispersity is also an important parameter for the synthesis. SEC was used to characterize the polydispersity of all the synthesized oligomers. The reaction for 30 min reached the highest yield, but unfortunately the dispersity was large (Đ = 3.1). On the contrary, the reaction for 25 min leads to acceptable dispersity (Đ = 1.6) and high yield up to 30%. As a conclusion, the best reaction condition was entry 4 (25 min heating time under reduced pressure).

In order to obtain fluorescent γ-CD-citrate oligomers, a γ-CD derivative appended with the fluorophore Cy5 was prepared for the first time (Scheme 1). First, the macrocyle was selectively monopropargylated in only one of the eight OH-2 groups present on the secondary face in 30% yield by reaction in carefully controlled stoichiometry with LiH and propargyl bromide in dry DMSO (Casas-Solvas and Vargas-Berenguel, 2008). Although several species formed during the reaction according to TLC, purification by column chromatography not only gave pure derivative **1** but also allowed us to recover 29% of the starting γ-CD pure enough to be reused. Both 1D and 2D NMR spectra unequivocally confirmed the monoalkylation of one C-2 position in compound **1**. Conjugation of **1** with the Cy5 fluorophore was carried out by copper(I)-catalyzed azide-alkyne cycloaddition (CuAAC) using commercially available Cy5-azide and CuCl in DMF. Cy5-γ-CD derivative **2** was finally obtained in 80% yield after dialysis and freeze-drying. Then, fluorescent γ-CD-citrate oligomers were synthesized under the same reaction conditions described above for non-fluorescent γ-CD-citrate oligomers, but with addition of 5% Cy5-γ-CD **2** to the native γ-CD.

The obtained γ-CD-citrate oligomers with and without fluorescent dye were characterized by FTIR, SEC and NMR. Fig. S1, shows a comparison of the FTIR spectra of γ-CD, citric acid and γ-CD-citrate oligomers. A new intense absorption band appeared at 1730 cm^{-1} for γ-CD-

citrate oligomers which was not observed in the spectra of the starting reagents. Indeed, this peak corresponds to the carbonyl stretching of the ester moiety, confirming the conversion of the carbonyl groups of the carboxylic acids (1750 and 1700 cm^{-1}) into esters functions (1730 cm^{-1}). This is in agreement with the previously reported data (Anand et al., 2013). ^{1}H-Nuclear magnetic resonance (NMR) spectroscopic technique was employed to analyze the structure of γ-CD-citrate oligomers. A typical ^{1}H NMR spectrum of γ-CD-citrate oligomer (shown in Fig. S2) displayed two sets of signals at δ 5.45–3.50 ppm and 3.10–2.70 ppm confirming the presence of the γ-CD and citric acid moieties, respectively, in the oligomer structure. The broad signal from δ 5.45 to 5.05 ppm corresponding to the γ-CD anomeric protons in the ^{1}H NMR spectrum indicated the loss of the macrocycle C_8-symmetry due to its partial acylation. The CD contents in γ-CD-citrate oligomers were found of 64% for entry 4. No significant differences were found for the Cy5-γ-CD-citrate oligomer (Fig. S3) due to the low content of Cy5, indicating that the conjugation of Cy5 did not significantly affect the polymerization.

3.2. MIL-100(Fe) nanoMOFs synthesis and surface modification with γ-CD-citrate oligomers

MIL-100(Fe) nanoMOFs with a mean hydrodynamic diameter of 235 ± 16 nm (PdI = 0.2) and BET surface area of 1720 ± 50 m^2g^{-1} were successfully synthesized. They have facetted morphology (Fig. 1A) exhibited by TEM with crystalline structure according to XRPD patterns (Fig. 1E) as previously reported (Agostoni et al., 2013b).

Surface modification of MIL-100(Fe) nanoMOFs with γ-CD-citrate oligomers was carried out by simply incubating the nanoMOFs in aqueous solutions of the synthesized oligomers, under rotative agitation, at room temperature for 5 min ~ 24 h. NanoMOFs coated with γ-CD-citrate oligomers were recovered by centrifugation and washed in order to remove the excessive γ-CD-citrate oligomers not associated to the surface. This simple coating method, devoid of the use of organic solvents, is favorable for biomedical application and for scaling up.

The amount of γ-CD-citrate oligomers associated to the nanoMOFs was determined by fluorescence spectrometry by indirect quantification of the fluorescent dye content in the supernatant after incubation. A highly efficient association (with a yield of 64%) of γ-CD-citrate oligomers was reached after only 5 min of contact time, up to 32 ± 5.3 wt% with respect to dried amount of MIL-100(Fe) nanoMOFs. It was found that the amounts of γ-CD-citrate oligomers associated to the nanoMOFs reached a plateau at 43 ± 4.5 wt% after 8 h incubation (corresponding to yield of 86%) (Fig. 2).

TGA is a direct tool to determine the amount of coating material on the surface of NPs. Uncoated nanoMOFs present typical thermograms (Fig. 1F) showing a first loss of water molecules in strong interaction with the matrices (< 200 °C) followed by loss of trimesic acid (region 300–400 °C). Finally, an inorganic Fe_2O_3 material (~38 wt%) remained in the pan at 600 °C. These experimental values are in agreement with

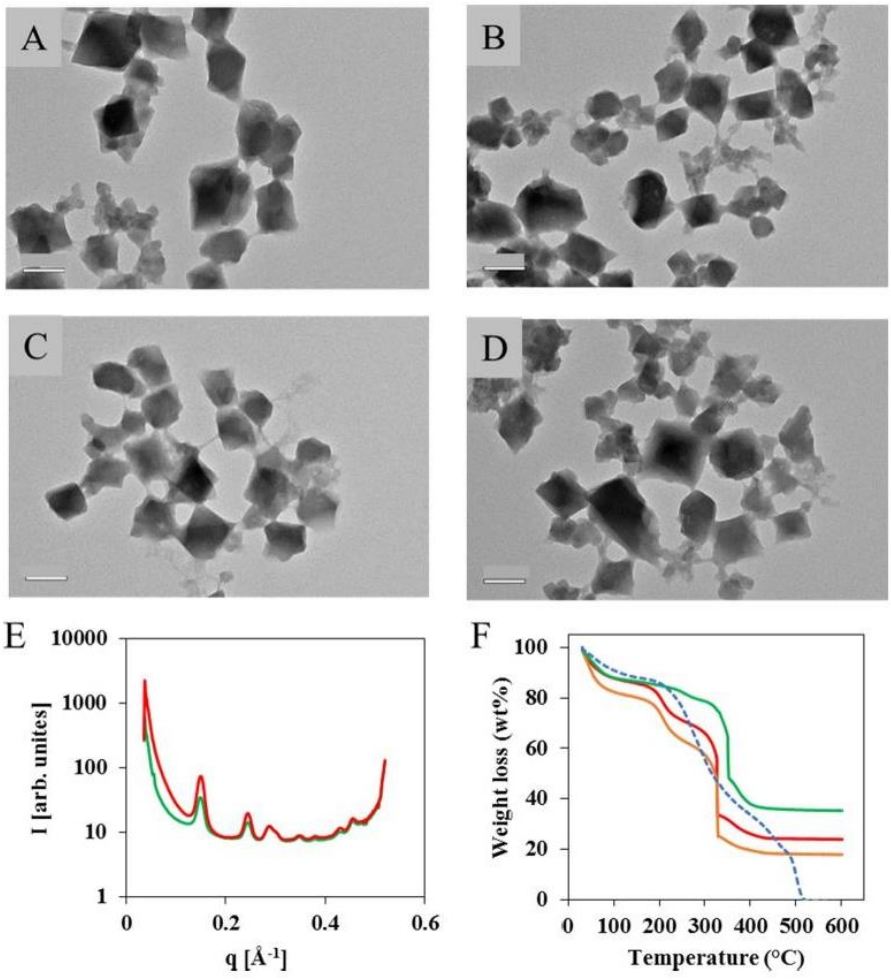

Fig. 1. TEM images of nanoMOFs, before (A) and after surface modification with different weight ratio γ-CD-citrate: nanoMOFs (B: 2:1; C: 1:1; and D: 1:1.5); scale bar: 100 nm; XRPD patterns (E) of nanoMOFs coated or not with γ-CD-citrate oligomers (green: uncoated nanoMOFs; red: nanoMOFs coated with γ-CD-citrate oligomers at weight ratio γ-CD-citrate: nanoMOFs of 2:1); TGA (F) of uncoated nanoMOFs (green), nanoMOFs coated with γ-CD-citrate oligomers (weight ratio γ-CD-citrate: nanoMOFs (red: 2:1; orange: 1:2)) and γ-CD-citrate oligomers (blue in dashed line). (For interpretation of the references to colour in this figure legend, the reader is referred to the web version of this article.)

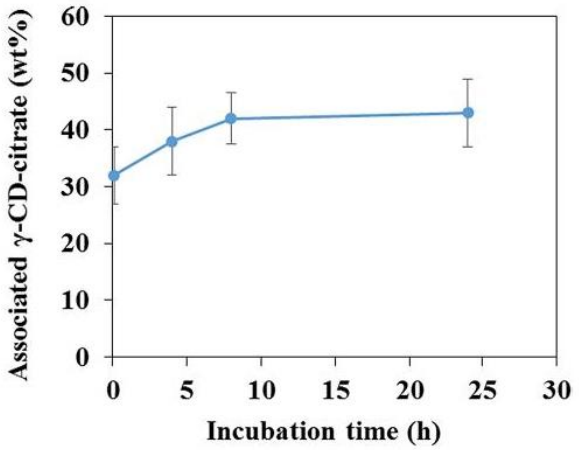

Fig. 2. Quantification of γ-CD-citrate oligomers associated to nanoMOFs by fluorescence spectrometry. Incubation kinetics (5 min ~ 24 h) at weight ratio γ-CD-citrate: nanoMOFs of 1:2.

the theoretical composition $(Fe_3OH(H_2O)_2O[(C_6H_3)\text{-}(CO_2)_3]_2$ (Hidalgo et al., 2017) of dry MIL-100(Fe) nanoMOFs, transforming at high temperature in (~36 wt% Fe_2O_3. In contrast, all the γ-CD-citrate oligomers degraded totally with no residue (blue dashed line, Fig. 1F). However, 22 wt% and 18 wt% inorganic residues were found in the case of coated nanoMOFs prepared at the weight ratio γ-CD-citrate: nanoMOFs of 1:2, and 2:1, respectively. These amounts correspond to 39 ± 8.4 wt%, and 53 ± 9.2 wt% of coating material, respectively.

To the best of our knowledge, this amount of coating material associated to the nanoMOFs is among the highest ever reported. For example, different coating materials have been investigated, including chitosan (38 wt%) (Hidalgo et al., 2017), heparin (12.5 wt%) (Elena et al., 2015), β-CD-phosphate (CD-P, 17 wt%) (Agostoni et al., 2015), CD-P monomers and polymers appended with mannose or rhodamine (20–26 wt%) (Aykaç et al., 2017), CD-P-PEG (16 wt%)(Cutrone et al., 2019a), GraftFast PEG chains (29 wt%) (Giménez-Marqués et al., 2018), and comb-like dextran copolymers (32 wt%) (Cutrone et al., 2019b).

This efficient association could be probably assigned to the strong affinity of numerous carboxyl groups for iron site on the nanoMOFs surface. As comparison, β-CD-phosphate coatings on the same nanoMOFs reached around 17 wt%. In that case, only 3–4 phosphate moieties were conjugated to each β-CD (Agostoni et al., 2015). When the β-CD-phosphate was further decorated with PEG chains, no significant difference was reported on the maximal amount of the coating materials associated to nanoMOFs. Indeed, citric acid, which has the same number of carboxyl groups as the organic linker of nanoMOFs (trimesic acid), is known to have a strong affinity for Fe sites (Abrahamson et al., 1994).

3.3. Physicochemical characterization of MIL-100(Fe) nanoMOFs coated with γ-CD-citrate oligomers

Coated nanoMOFs were characterized using a set of complementary techniques (Fig. 1). First, TEM studies illustrated that the nanoMOFs kept its size and morphology (Fig. 1B-D), despite of the high amount of the attached coating materials. XRPD patterns suggest that the crystalline structure of nanoMOFs was preserved after coating process (Fig. 1E).

Hydrodynamic diameters of nanoMOFs, coated or not, were characterized by DLS. The mean hydrodynamic diameter of uncoated nanoMOFs was 235 ± 16 nm. Whatever the amount of the coating material, there were no significant differences on the mean size and polydispersity after surface modification. Final mean diameters were in the range of 235 ± 16 nm to 247 ± 11 nm, indicating that the coating thickness was less than 10 nm and that no bridging occurred.

Colloidal stability of nanoMOFs was investigated in water before and after surface modification. As it is the case with many types of uncoated NPs, one of the main drawbacks of uncoated nanoMOFs for their biomedical application lies in their poor colloidal stability in aqueous media. Fig. 3A clearly shows that uncoated nanoMOFs underwent an aggregation in water, in agreement with previous data (Agostoni et al., 2015; Cutrone et al., 2019b). In contrast, γ-CD-citrate coated nanoMOFs were perfectly stable in aqueous media for two weeks (< 10% diameter variations). This illustrates that their coating with γ-CD-citrate oligomers efficiently prevented nanoMOFs' aggregation in water.

The influence of the coatings on the surface charge of nanoMOFs was investigated by ZP measurements. As shown in Fig. 3B, the ZP of the nanoMOFs, coated or not, was found to be strongly dependent upon the pH (in a range of 1–10) of the suspension medium, in agreement with previous reports (Cutrone et al., 2019b). Typically, the ZP of uncoated nanoMOFs was positive (+23.6 ± 2.5 mV) at pH 5, which was favorable to their colloidal stability. It shifted to negative (−14.5 ± 2.9 mV) at pH 7, where nanoMOFs immediately aggregated. In contrast, after coating with γ-CD-citrate oligomers, the ZP reached negative values (up to −45 mV) regardless of the pH values, supporting the presence of γ-CD-citrate oligomers on the surface of the nanoMOFs.

XPS was used to ascertain the presence of γ-CD-citrate oligomers within the nanoMOF top layers (~10 nm depth) and to determine the quantitative atomic surface composition. As illustrated in Fig. 4, both

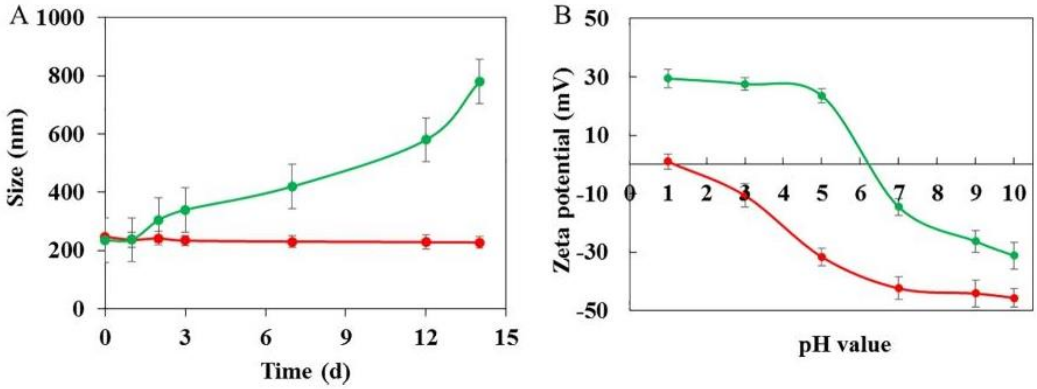

Fig. 3. Colloid stability in water (A) and zeta potential at different pH (B) of nanoMOFs before (green) and after (red) coating with γ-CD-citrate oligomers at weight ratio γ-CD-citrate: nanoMOFs of 1:2. (For interpretation of the references to colour in this figure legend, the reader is referred to the web version of this article.)

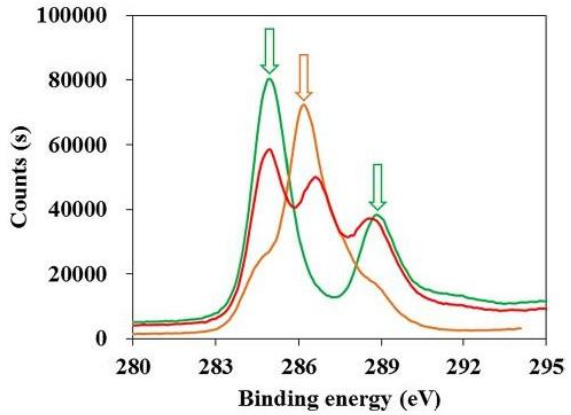

Fig. 4. XPS spectra for C1s regions of γ-CD-citrate oligomers (orange), and nanoMOFs before (green) and after (red) surface modification with γ-CD-citrate oligomers at weight ratio γ-CD-citrate: nanoMOFs of 1:2. (For interpretation of the references to colour in this figure legend, the reader is referred to the web version of this article.)

carbon C1s "fingerprints" of the carbon skeleton of nanoMOFs (284.8 and 289 eV: C-C or C-OOH, respectively) and γ-CD-citrate oligomers "fingerprint" (main contribution at 286.2 eV) were observed for nanoMOFs coated with γ-CD-citrate oligomers. The decrease of the Fe percentage in the top layers (the C/Fe atomic ratios increased from 8.3 to 29.0 before and after coating, respectively, Table S1) was indicative of the presence of γ-CD-citrate in this region.

3.4. Fluorescence lifetime measurements

The association of Cy5-γ-CD-citrate oligomer to nanoMOFs was also controlled by fluorescence lifetime measurements. Free Cy5-γ-CD-citrate oligomer fluorescence decays can be fitted by a biexponential function corresponding to fluorescence lifetimes of $\tau_1 = 1.64 \pm 0.10$ ns and $\tau_2 = 0.65 \pm 0.04$ ns respectively (Table 2). The shortest lifetime may be attributed to a population of Cy5 fluorophore interacting largely with solvent, as it is very close to the lifetime of free Cy5 in water ($\tau_2 = 0.59 \pm 0.04$ ns, Table 2). The longest lifetime is likely due to a population of Cy5 interacting with γ-CD.

Indeed, for free Cy5-γ-CD monomers, another fluorescence lifetime $\tau_1 = 1.34 \pm 0.10$ ns (Table 2) is recorded additionally to the one related to Cy5 in close vicinity to solvent. This second lifetime is linked to the presence of γ-CD. Cy5 can insert in the CD cavity either of the same or of another Cy5-γ-CD molecule, thus protecting itself from non-radiative deactivations with the solvent. This has already been observed for cyanine dyes in the presence of γ-CD (Abe et al., 2013; Fayed et al., 2002). These observations could explain the increase of the fluorescence lifetime of the Cy5 molecules. In γ-CD citrate oligomers, this second lifetime is still longer as there are more CDs that can form stronger protection from solvent than only one CD. Furthermore, the preponderance of the longer lifetime increases from Cy5-γ-CD monomers to Cy5-γ-CD-citrate oligomers, as the probability that Cy5 encounters γ-CD is higher in the oligomers than in the monomers. As a consequence, the Cy5 fluorophores are probably less exposed to water in oligomers than in monomers.

Interestingly, for the nanoMOFs coated with Cy5-γ-CD-citrate oligomer, the corresponding fluorescence decay required a third component (~0.3 ns) to be well fitted. This shorter fluorescence lifetime characterized the polymer-nanoMOF interaction inside the nanostructure and expresses a change in the fluorophore vicinity. When Cy5-γ-CD-citrate oligomer is coated on the nanoMOFs, Cy5 fluorophore does not seem to be exposed to solvent, as the lifetime corresponding to Cy5 alone (~0.6 ns) is not found (e.g. 1:4 ratio, table 2). It may be included into the nanoMOF superficial cavities and engaged in specific interactions such as hydrogen bond formations and/or in stacking complexes with their proximal constituents, which leads to reduced fluorescence lifetimes.

The weight of this picosecond fluorescence lifetime depends on the γ-CD-citrate:nanoMOFs weight ratio (Table 2). For ratios less than 1:2, the two populations corresponding to free Cy5-γ-CD-citrate practically disappeared in favor of the one corresponding to the polymer-nanoMOF complex: 96% and 90% of C5-γ-CD-citrate was adsorbed onto the surface of nanoMOFs at the weight ratio γ-CD-citrate:nanoMOFs of 1:4 and 1:2, respectively. These values correspond to ~ 45 wt% of coating material associated to the nanoMOFs, which is in good agreement with the amounts determined by both direct TGA and indirect fluorescence measurements.

At the equivalent γ-CD-citrate: nanoMOFs weight ratio approximatively the same amount of Cy5-γ-CD-citrate was associated on the nanoMOFS (45.7 ± 2.3 wt%, Table 2) and free in the system (54.3 ± 2.7%, Table2). This indicates that the maximum associated amount of Cy5-γ-CD-citrate on the nanoMOFs was around 46 wt%, which also agrees with the TGA analysis (associated γ-CD-citrate was evaluated to 53.0 ± 9.2 wt%).

However, when excessive amounts of coating material was added (weight ratios γ-CD-citrate: nanoMOFs of 1.5:1 or 2:1, Table 2), the fluorescence signal of the free Cy5-γ-CD-citrate masked the signal of the adsorbed oligomer, rendering the measurement difficulty: less than 20% fluorescent polymer-nanoMOF complexes was detected in both cases.

Table 2
Summary of the fluorescence lifetimes (τ_i) and of their corresponding populations (A_i) resulting from the multiexponential fitting of the Cy5-γ-CD-citrate fluorescence decays alone or in the presence of different amount of nanoMOFs. They are compared to the free Cy5 and free Cy5-γ-CD decays. All the results are given with 5% accuracy.

Cy5-γ-CD-citrate: nanoMOFs (weight ratio)	τ_1 (ns)	A_1 (%)	τ_2 (ns)	A_2 (%)	τ_3 (ns)	A_3 (%)	χ^2
Free Cy5	–	–	0.59	100	–	–	1.01
Free Cy5-γ-CD	1.34	10.2	0.59	89.8	–	–	1.02
free Cy5-γ-CD-citrate	1.64	38.5	0.65	61.5	–	–	1.07
1:4	1.64	4.0	–	–	0.31	96.0	1.08
1:2	1.64	1.7	0.65	7.5	0.25	90.8	1.02
1:1	1.64	10.6	0.65	43.7	0.27	45.7	1.04
1.5:1	1.64	16.7	0.65	67.1	0.28	16.1	1.09
2:1	1.64	26.4	0.65	73.5	0.28	0.1	1.04

3.5. Improved colloid stability

DOX was shown to exhibit high affinity for both MIL-100(Fe) nanoMOFs (Bhattacharjee et al., 2020; Anand et al., 2014; Horcajada et al., 2010) and γ-CD-citrate oligomers (Anand et al., 2013). Briefly, DOX payloads in the same nanoMOFs reached 23 wt% (Bhattacharjee et al., 2020), 16 wt% (Horcajada et al., 2010) and 9 wt% (Anand et al., 2014). DOX formed 1:1 and 1:2 γ-CD-citrate-DOX complexes with binding constant of $\log K_{11} = 4.4 \pm 0.1\ M^{-1}$ and $\log K_{12} = 11.1 \pm 0.1\ M^{-2}$, respectively (Anand et al., 2013). Advantageously, DOX was incorporated in a monomeric form, avoiding dimer formation and thus, drug inactivation.

In this study, the incorporation protocol was optimized to improve the DOX payload. To avoid aggregation, nanoMOFs were not dried, but transferred from ethanol to water containing the drug. Besides, the DOX concentration was increased as compared to the study by Anand et al, (Anand et al., 2013) (54.3 μg/mL previously reported *vs* 1.0 mg/mL in this study). Remarkably, in these conditions, DOX payload in nanoMOFs reached to 48 ± 10 wt% after 24 h incubation at the weight

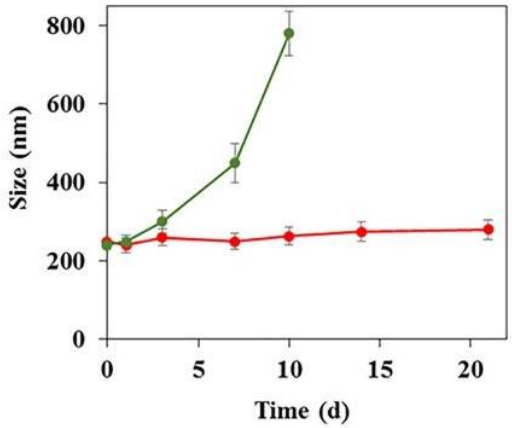

Fig. 5. Colloid stability of DOX loaded nanoMOFs before (green) and after (red) coating with γ-CD-citrate oligomers. (For interpretation of the references to colour in this figure legend, the reader is referred to the web version of this article.)

ratio of 1:1 between nanoMOFs and initial DOX (corresponding to a drug encapsulation efficiency of 48 ± 10%). After additional coating with γ-CD-citrate oligomers, DOX loading reached 65 ± 8 wt%. At a weight ratio of 4:1 between nanoMOFs and initial DOX, DOX encapsulation efficiency reached 92 ± 5%. DOX-loaded nanoMOFs underwent a progressive aggregation process (mean hydrodynamic diameter increased to > 750 nm in 10 days) (Fig. 5). In contrast, the γ-CD-citrate coatings on the nanoMOFs dramatically improved the colloid stability of DOX-loaded nanoMOFs (size variation < 10% in 3 weeks).

Further investigations will be conducted to gain insights on the localization of DOX in the core–shell nanocomposites and on the CD shell effect on drug release. In addition, it is also possible to further functionalize the CD shell with PEG chains, targeting and imaging moieties.

4. Conclusion

Water soluble γ-CD-citrate oligomers grafted or not with Cy5 fluorophore were successfully synthesized and efficiently anchored onto the surface of porous nanoMOFs, reaching up to 53 ± 8.4 wt% of coating associated to the nanoMOFs. These core–shell nanocomposites are stable upon storage, in contrast to the naked nanoMOFs. Due to the presence of the fluorophore conjugated to the shell, fluorescence lifetime microscopy enabled deciphering the coating mechanism.

By taking advantage on the versatility of CDs' chemical modifications and ability to form inclusion with a large variety of drug molecules, this study paves the way for the design of multifunctional core–shell nanoMOFs of interest for biomedical applications.

Declaration of Competing Interest

The authors declare that they have no known competing financial interests or personal relationships that could have appeared to influence the work reported in this paper.

Acknowledgements

We acknowledge Dr. Marie-Pierre Fontaine-Aupart for the useful discussion and precious comments. We are grateful for help from Ludivine Houel Renault, responsible of the platform CPBM/CLUPS/LUMAT FR2764 for confocal microscopy. We are grateful to Dr. Diana Dragoe for the XPS experiments. We acknowledge Dr. Doru Constantin for help with XRPD experiments. This research was funded by European Research Council through Cyclon Hit project (People-2013-ITN Grant Agreement 608407), by Spanish Ministry of Economy and Competitiveness (CTQ2017-90050-R), by the French National Research Agency (ANR-14-CE08-0017) and by Labex NanoSaclay (ANR-10-LABX-0035). J. Qiu acknowledges support from China Scholarship Council (CSC, N° 201708070028). The present work has benefited from Imagerie-Gif core facility supported by ANR (ANR-11-EQPX-0029/Morphoscope, ANR-10-INBS-04/FranceBioImaging; ANR-11-IDEX-0003-02/ Saclay Plant Sciences).

Appendix A. Supplementary material

Supplementary data to this article can be found online at https://doi.org/10.1016/j.ijpharm.2020.119281.

References

Abe, S., Hirota, T., Kiba, T., Miyakawa, N., Watari, F., Murayama, A., Sato, S.I., 2013. Photophysical properties of self-assembled cyanine-dye dimmer formation assisted by cyclodextrin inclusion complexation. Mol. Cryst. Liq. Cryst. 579, 22–29.

Abrahamson, H.B., Rezvani, A.B., Brushmiller, J.G., 1994. Photochemical and spectroscopic studies of complexes, of iron(III) with citric acid and other carboxylic acids. Inorganica Chim. Acta. 226, 117–127.

Agostoni, V., Chalati, T., Horcajada, P., Willaime, H., Anand, R., Semiramoth, N., Baati, T., Hall, S., Maurin, G., Chacun, H., Bouchemal, K., Martineau, C., Taulelle, F., Couvreur, P., Rogez-Kreuz, C., Clayette, P., Monti, S., Serre, C., Gref, R., 2013a. Towards an improved anti-HIV activity of NRTI via metal-organic frameworks nanoparticles. Adv. Healthc. Mater. 2, 1630–1637.

Agostoni, V., Horcajada, P., Noiray, M., Malanga, M., Aykaç, A., Jicsinszky, L., Vargas-Berenguel, A., Semiramoth, N., Daoud-Mahammed, S., Nicolas, V., Martineau, C., Taulelle, F., Vigneron, J., Etcheberry, A., Serre, C., Gref, R., 2015. A "green" strategy to construct non-covalent, stable and bioactive coatings on porous MOF nanoparticles. Sci. Rep. 5, 1–7.

Agostoni, V., Horcajada, P., Rodriguez-Ruiz, V., Willaime, H., Couvreur, P., Serre, C., Gref, R., 2013b. 'Green' fluorine-free mesoporous iron(III) trimesate nanoparticles for drug delivery. Green Mater. 1, 209–217.

Anand, R., Borghi, F., Manoli, F., Manet, I., Agostoni, V., Reschiglian, P., Gref, R., Monti, S., 2014. Host-guest interactions in Fe(III)-trimesate MOF nanoparticles loaded with doxorubicin. J. Phys. Chem. B 118, 8532–8539.

Anand, R., Malanga, M., Manet, I., Manoli, F., Tuza, K., Aykaç, A., Ladavière, C., Fenyvesi, E., Vargas-Berenguel, A., Gref, R., Monti, S., 2013. Citric acid–γ-cyclodextrin crosslinked oligomers as carriers for doxorubicin delivery. Photochem. Photobiol. Sci. 12, 1841–1854.

Arima, H., Hayashi, Y., Higashi, T., Motoyama, K., 2015. Recent advances in cyclodextrin delivery techniques. Expert Opin. 12, 1425–1441.

Aykaç, A., Noiray, M., Malanga, M., Agostoni, V., Casas-solvas, J.M., Fenyvesi, É., Gref, R., Vargas-Berenguel, A., 2017. A non-covalent "click chemistry" strategy to efficiently coat highly porous MOF nanoparticles with a stable polymeric shell. Biophys. Biochim. Acta – Gen. Subj. 1861, 1606–1616.

Banerjee, S.S., Chen, D.-H., 2007. Magnetic nanoparticles grafted with cyclodextrin for hydrophobic drug delivery. Chem. Mater. 19, 6345–6349.

Bellido, E., Hidalgo, T., Lozano, M.V., Guillevic, M., Simón-Vázquez, R., Santander-Ortega, M.J., González-Fernández, Á., Serre, C., Alonso, M.J., Horcajada, P., 2015. Heparin-engineered mesoporous iron metal-organic framework nanoparticles: toward stealth drug nanocarriers. Adv. Healthc. Mater. 4, 1246–1257.

Bhattacharjee, A., Kumar, M., Sasidhar, P., 2020. Doxorubicin loading capacity of MIL-100 (Fe): effect of synthesis conditions. J. Inorg. Organomet. Polym Mater. 100, 1–10.

Casas-Solvas, J.M., Vargas-Berenguel, A., 2008. Synthesis of a β-cyclodextrin derivative bearing an azobenzene group on the secondary face. Tetrahedron Lett. 49, 6778–6780.

Cutrone, G., Li, X., Casas-Solvas, J.M., Menendez-Miranda, M., Qiu, J., Benkovics, G., Constantin, D., Malanga, M., Moreira-Alvarez, B., Costa-Fernandez, J.M., García-Fuentes, L., Gref, R., Vargas-Berenguel, A., 2019a. Design of engineered cyclodextrin derivatives for spontaneous coating of highly porous metal-organic framework nanoparticles in aqueous media. Nanomaterials 9, 1–26.

Cutrone, G., Qiu, J., Menendez-Miranda, M., Casas-Solvas, J.M., Aykaç, A., Li, X., Foulkes, D., Moreira-Alvarez, B., Encinar, J.R., Ladavière, C., Desmaële, D., Vargas-Berenguel, A., Gref, R., 2019b. Comb-like dextran copolymers: A versatile strategy to coat highly porous MOF nanoparticles with a PEG shell. Carbohydr. Polym. 223, 115085.

Fayed, T.A., Organero, J.A., Garcia-Ochoa, I., Tormo, L., Douhal, A., 2002. Ultrafast twisting motions and intramolecular charge-transfer reaction in a cyanine dye trapped in molecular nanocavities. Chem. Phys. Lett. 364, 108–114.

Ghosh Chaudhuri, R., Paria, S., 2012. Core/shell nanoparticles: classes, properties, synthesis mechanisms, characterization, and applications. Chem. Rev. 112, 2373–2433.

Gidwani, B., Vyas, A., 2015. A comprehensive review on cyclodextrin-based carriers for delivery of chemotherapeutic cytotoxic anticancer drugs. Biomed Res. Int. 12, 1–15.

Giménez-Marqués, M., Bellido, E., Berthelot, T., Simón-Yarza, T., Hidalgo, T., Simón-Vázquez, R., González-Fernández, Á., Avila, J., Asensio, M.C., Gref, R., Couvreur, P., Serre, C., Horcajada, P., 2018. GraftFast surface engineering to improve MOF nanoparticles furtiveness. Small 14, 1–11.

Hidalgo, T., Bellido, E., Avila, J., Asensio, M.C., Salles, F., 2017. Chitosan-coated mesoporous MIL-100(Fe) nanoparticles as improved bio-compatible oral nanocarriers. Sci. Rep. 100, 1–14.

Horcajada, P., Chalati, T., Serre, C., Gillet, B., Sebrie, C., Baati, T., Eubank, J.F., Heurtaux, D., Clayette, P., Kreuz, C., Chang, J.-S., Hwang, Y.K., Marsaud, V., Bories, P.-N., Cynober, L., Gil, S., Férey, G., Couvreur, P., Gref, R., 2010. Porous metal–organic-framework nanoscale carriers as a potential platform for drug delivery and imaging. Nat. Mater. 9, 172–178.

Khatami, M., Alijani, H.Q., Sharifi, I., 2018. Biosynthesis of bimetallic and core-shell nanoparticles: their biomedical applications – A review. IET Nanobiotechnol. 12, 879–887.

Kouassi, M.C., Thébault, P., Rihouey, C., Dé, E., Labat, B., Picton, L., Dulong, V., 2017. Carboxymethylpullulan grafted with aminoguaiacol: synthesis, characterization, and assessment of antibacterial and antioxidant properties. Biomacromolecules 18, 3238–3251.

Li, X., Lachmanski, L., Safi, S., Sene, S., Serre, C., Grenèche, J.M., Zhang, J., Gref, R., 2017. New insights into the degradation mechanism of metal-organic frameworks drug carriers. Sci. Rep. 7, 1–17.

Li, X., Semiramoth, N., Hall, S., Tafani, V., Josse, J., Laurent, F., Salzano, G., Foulkes, D., Brodin, P., Majlessi, L., Ghermani, N.-E., Maurin, G., Couvreur, P., Serre, C., Bernet-Camard, M.-F., Zhang, J., Gref, R., 2019. Compartmentalized encapsulation of two antibiotics in porous nanoparticles: an efficient strategy to treat intracellular infections. Part. Part. Syst. Char. 36, 1800360.

Liu, J., Mendoza, S., Román, E., Lynn, M.J., Xu, R., Kaifer, A.E., 1999. Cyclodextrin-modified gold nanospheres. Host – guest interactions at work to control colloidal properties. J. Am. Chem. Soc. 121, 4304–4305.

Luo, S., Zhang, E., Su, Y., Cheng, T., Shi, C., 2011. A review of NIR dyes in cancer targeting and imaging. Biomaterials 32, 7127–7138.

Martel, B., Ruffin, D., Weltrowski, M., Lekchiri, Y., Morcellet, M., 2004. Water-soluble polymers and Gels from the polycondensation between cyclodextrins and poly (carboxylic acid)s: a study of the preparation parameters. J. Appl. Polym. Sci. 97, 433–442.

Perrin, D.D., Armarego, W.F.L., 1989. Purification of Laboratory Chemicals, 3rd ed. Pergamon, Oxford, UK.

Pratt, C.B., Shanks, E.C., 1974. Doxorubicin in treatment of malignant solid tumors in children. Am. J. Dis. Child. 127, 534–536.

Puskás, I., Szemjonov, A., Fenyvesi, É., Malanga, M., Szente, L., 2013. Aspects of determining the molecular weight of cyclodextrin polymers and oligomers by static light scattering. Carbohydr. Polym. 94, 124–128.

Simon-Yarza, T., Giménez-Marqués, M., Mrimi, R., Mielcarek, A., Gref, R., Horcajada, P., Serre, C., Couvreur, P., 2017. A smart metal-organic framework nanomaterial for lung targeting. Angew. Chemie Int. Ed. 56, 15565–15569.

Lipshultz, Steven E., Colan, Steven D., Gelber, Richard D., Perez-Atayde, Antonio R., Sallan, Stephen E., Sanders, Stephen P., 1991. Late cardiac effects of doxorubicin therapy for acute lymphoblastic leukemia in childhood. New Engl. J. Med. 324, 808–815.

Szejtli, J., 1998. Introduction and general overview of cyclodextrin chemistry. Chem. Rev. 98, 1743–1753.

Thatiparti, T.R., Shoffstall, A.J., von Recum, H.A., 2010. Biomaterials cyclodextrin-based device coatings for affinity-based release of antibiotics. Biomaterials 31, 2335–2347.

Valeur, B., 2002. Molecular fluorescence. principles and applications. Wiley-VCH Verlag GmbH, Weinheim, pp. 34–70.

Wenz, G., 1994. Cyclodextrins as building blocks for supramolecular structures and functional Units. Angew. Chem. Int. Ed. Engl. 33, 803–822.

Zhang, H., Peng, M.L., Cui, Y.L., Chen, C., 2008. Magnetic HP-β-CD composite nanoparticle: synthesis, characterization and application as a carrier of doxorubicin *in vitro*. Chin. J. Chem. 26, 1737–1740.

Supporting Information for

Lego-type assembly of core-shell highly porous metal-organic framework nanoparticles: a novel approach to optimize drug loading

Authors

Jingwen Qiu[1&], Xue Li[1&], Karine Steenkeste[1], Nadine Aubry-barroca[2], Caroline Aymes-chodur[2], Philippe Roger[2], Juan M. Casas-Solvas[3], Antonio Vargas-Berenguel[3], Christophe Rihouey[4], Luc Picton[4], Marie-Pierre Fontaine-Aupart[1], Ruxandra Gref[1*]

[1]Institut des Sciences Moléculaires d'Orsay, Paris Saclay, 91400 Orsay, France

[2]Institut de Chimie Moléculaire et des Matériaux d'Orsay, Université Paris- Saclay, 91405, Orsay, France

[3]Departamento de Química y Física, Universidad de Almería, 04120, Almería, Spain

[4]Laboratoire Polymères, Biopolymères, Université de Rouen, 76821 Mont Saint Aignan, France

Corresponding Author:

Dr. Ruxandra Gref

Institut Sciences Moléculaires d'Orsay, Université Paris-Saclay, 91400 Orsay, France; Tel: +33 (1) 69158234; E-mail: ruxandra.gref@universite-paris-saclay.fr.

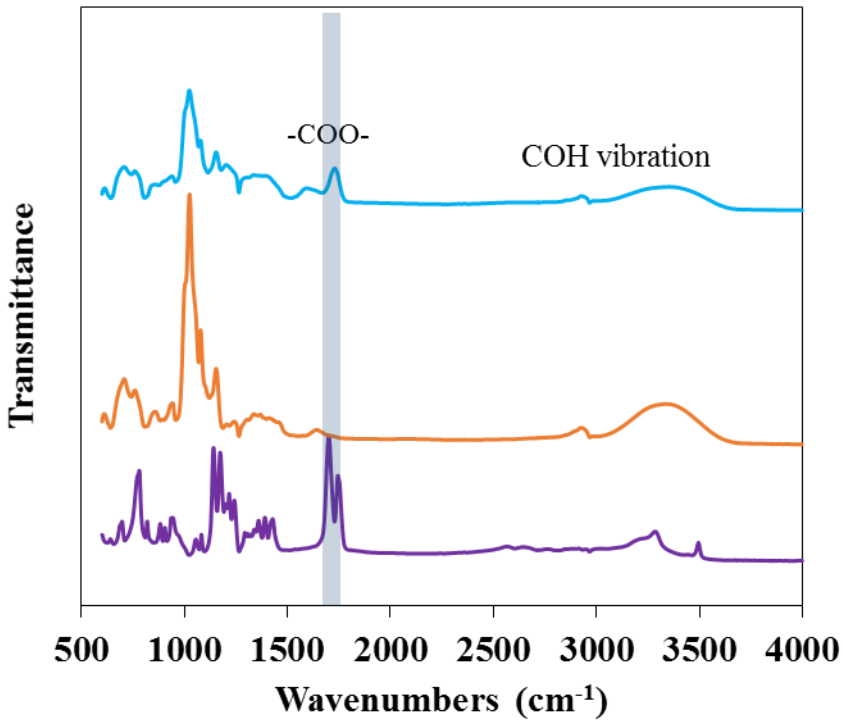

Figure S1 FTIR spectra of citric acid (purple), γ-CD (orange), Cy5-γ-CD-citrate oligomers (blue)

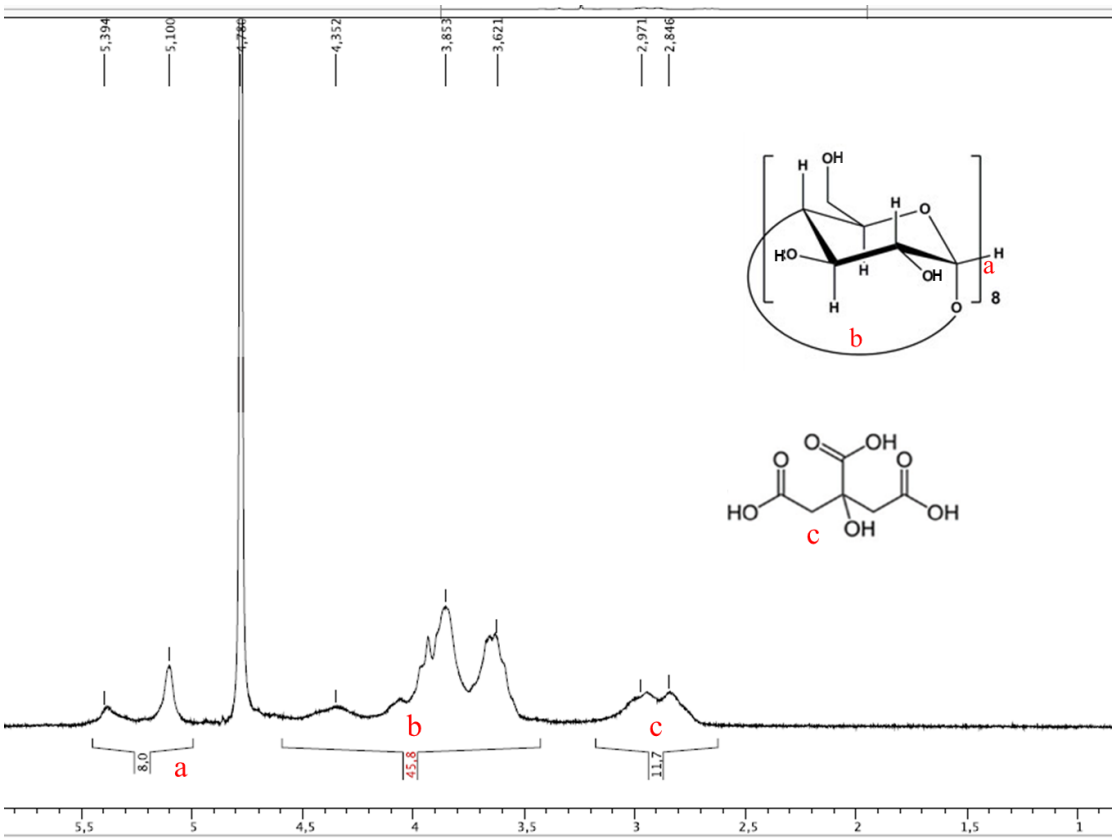

Figure S2 ^{1}H-NMR spectrum of γ-CD-citrate oligomers

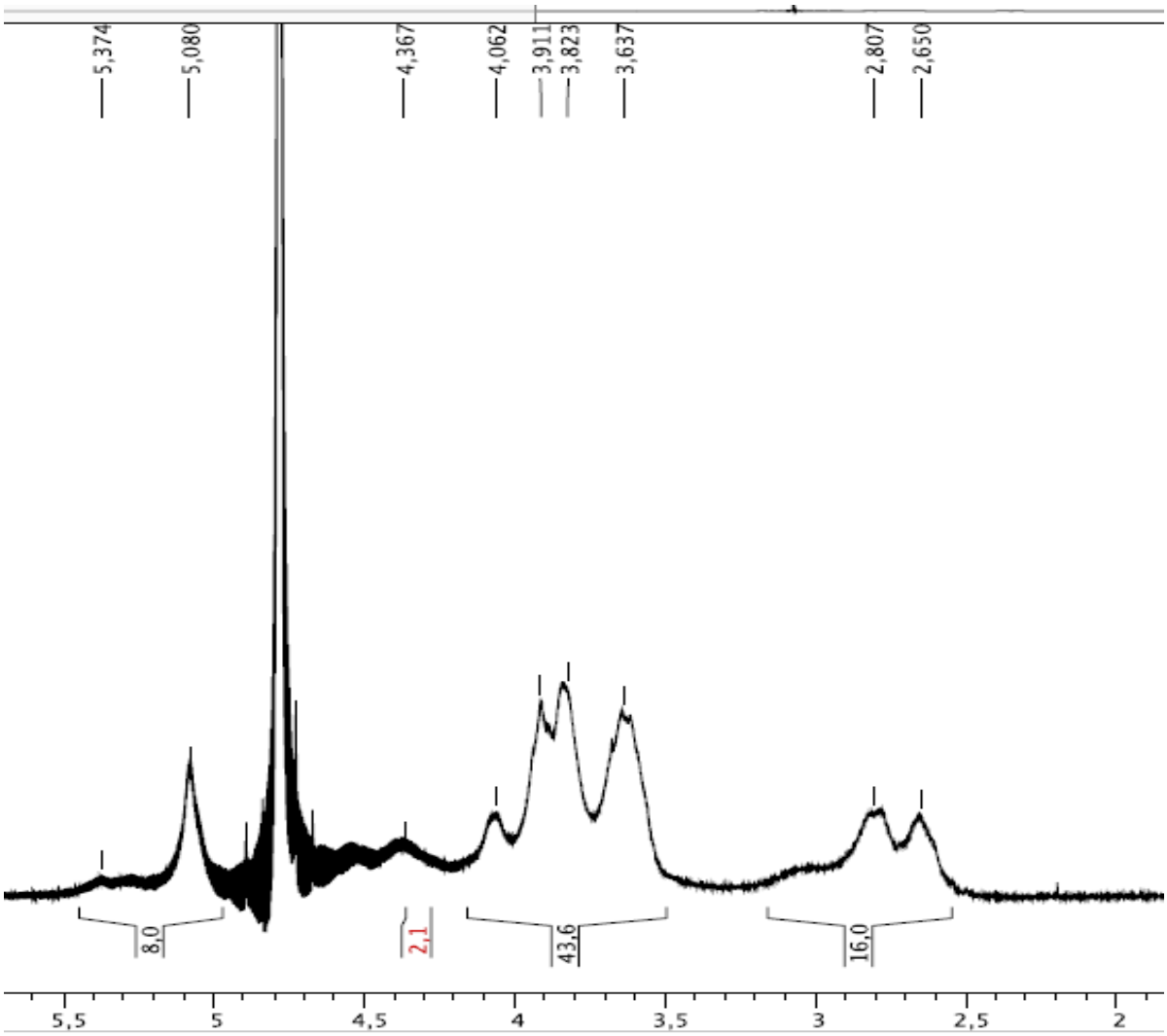

Figure S3 ^{1}H-NMR spectrum of Cy5-γ-CD-citrate oligomers

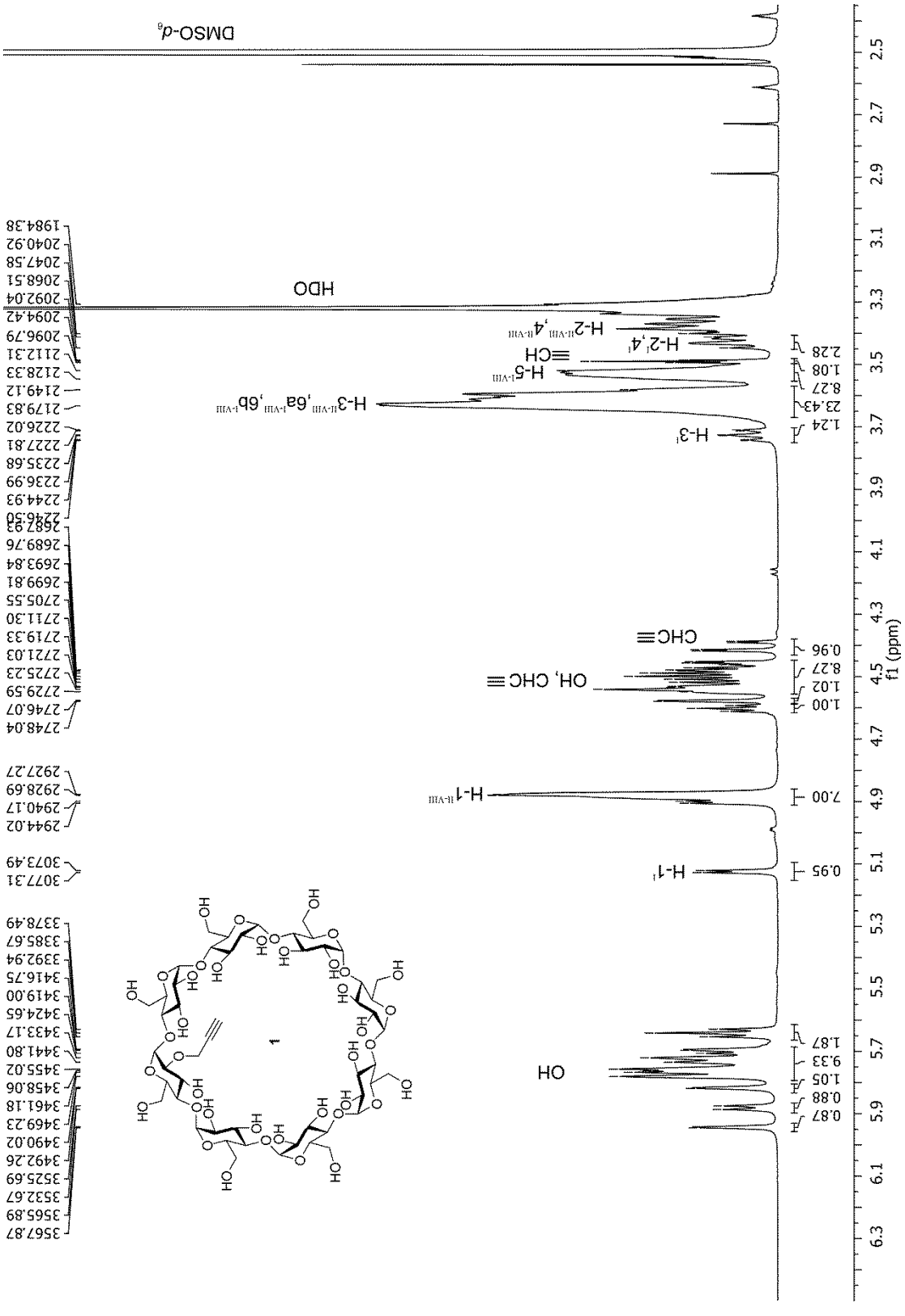

Figure S4 ^{1}H NMR spectrum (600 MHz, DMSO-d_6, 25 ºC) for derivative **1**.

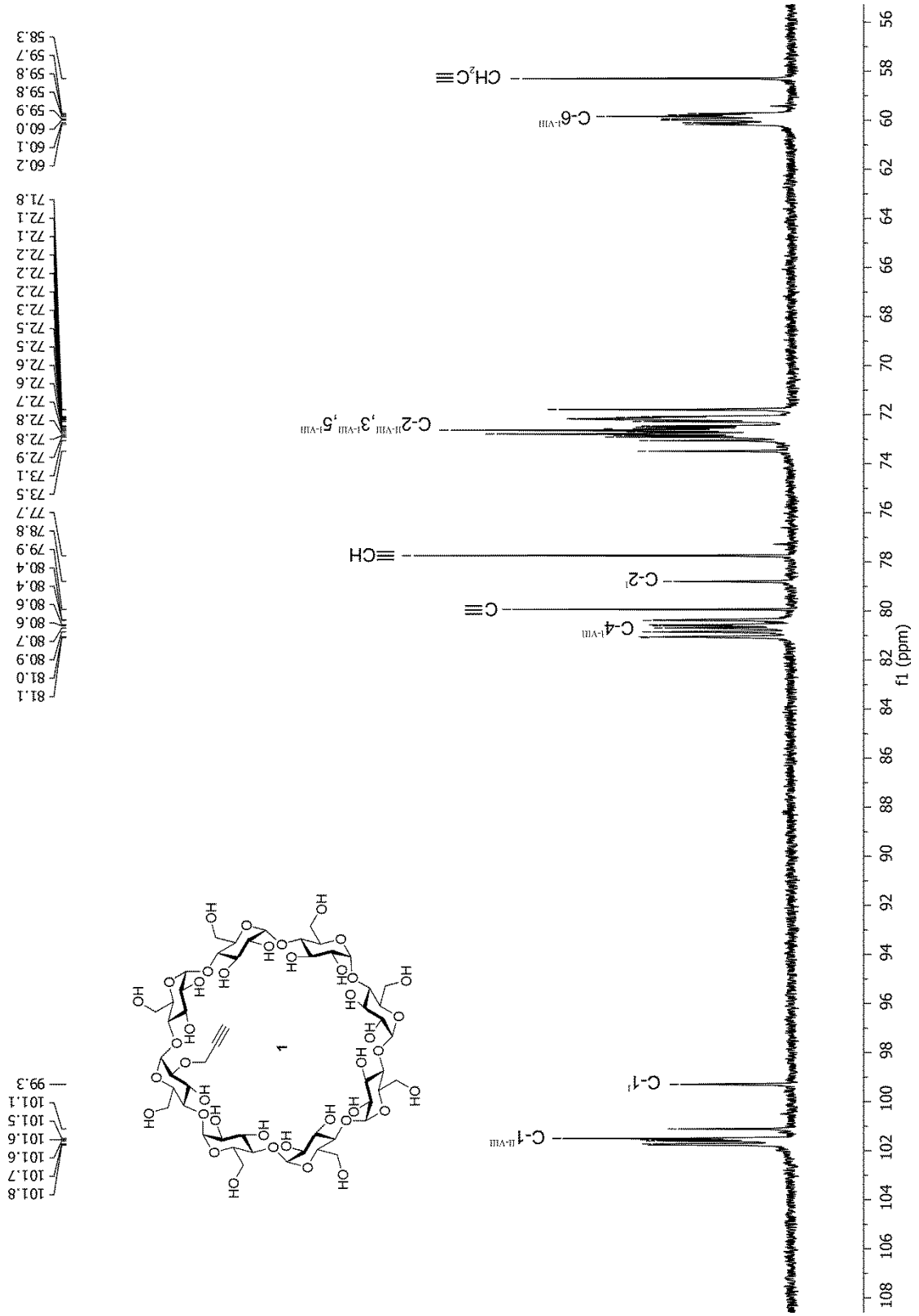

Figure S5 ^{13}C NMR spectrum (150 MHz, DMSO-d_6, 25 ºC) for derivative **1**.

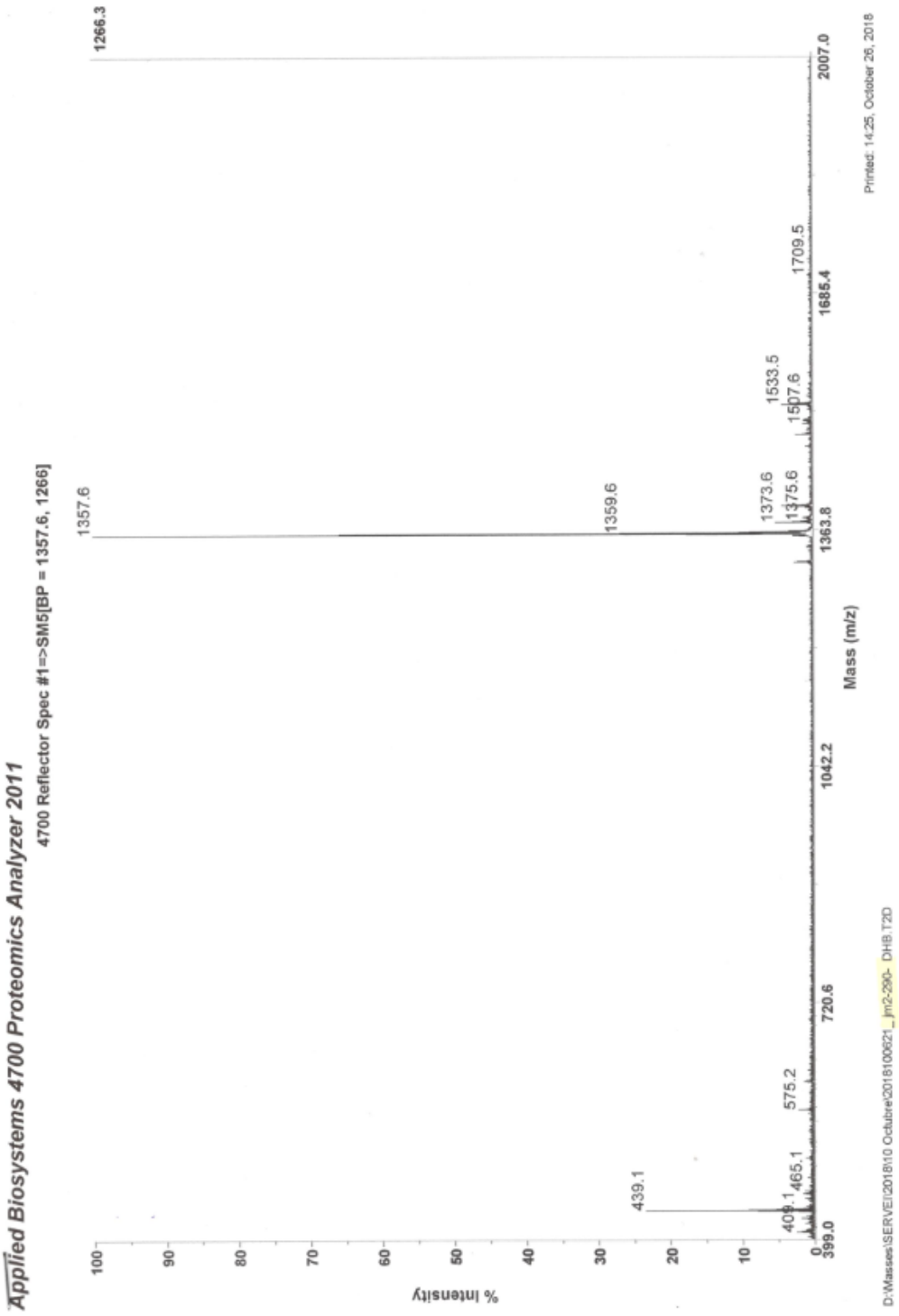

Figure S6 MALDI-TOF-MS spectrum (DHB as matrix) for derivative **1**.

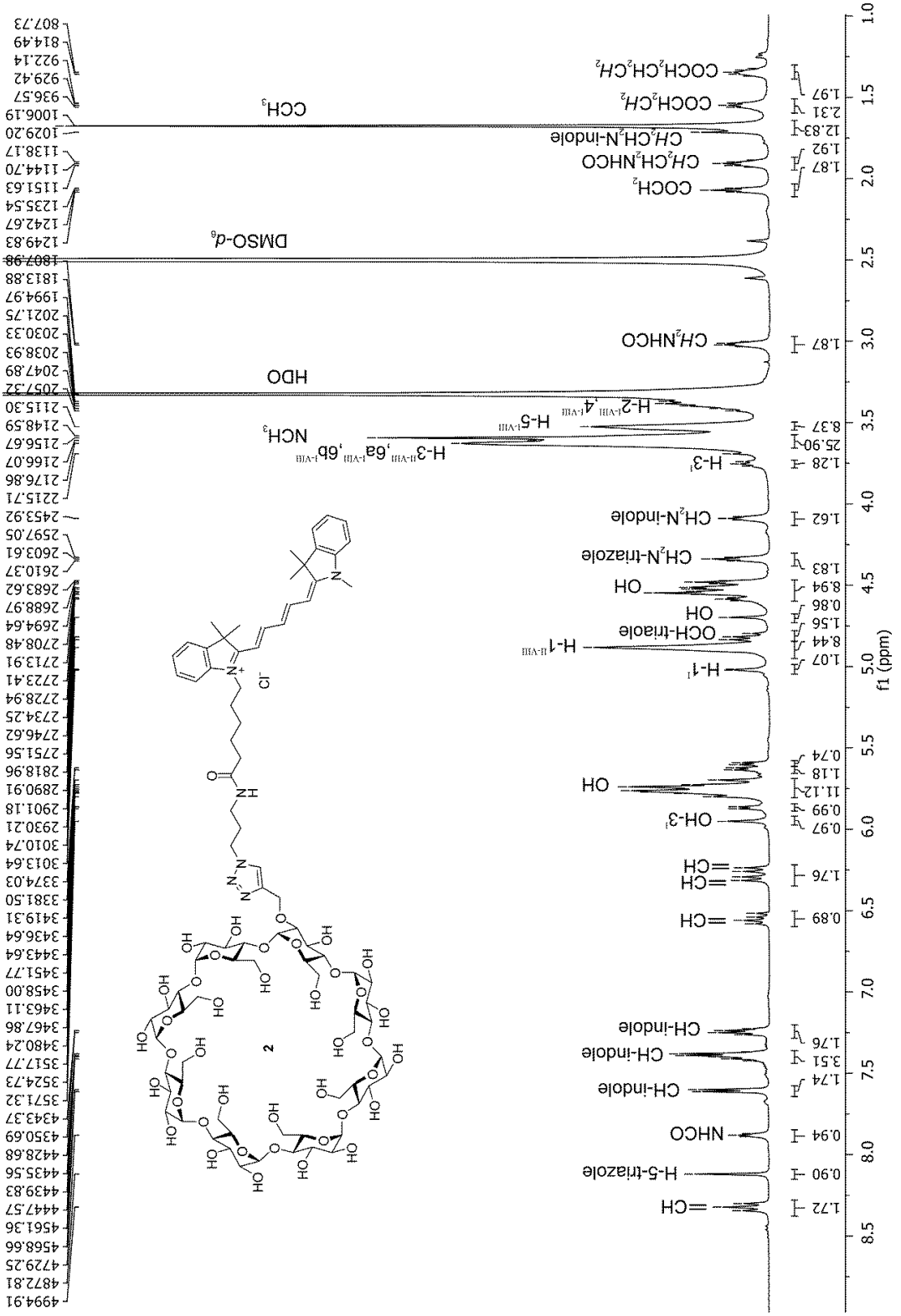

Figure S7 ^{1}H NMR spectrum (600 MHz, DMSO-d_6, 25 ºC) for derivative **2**.

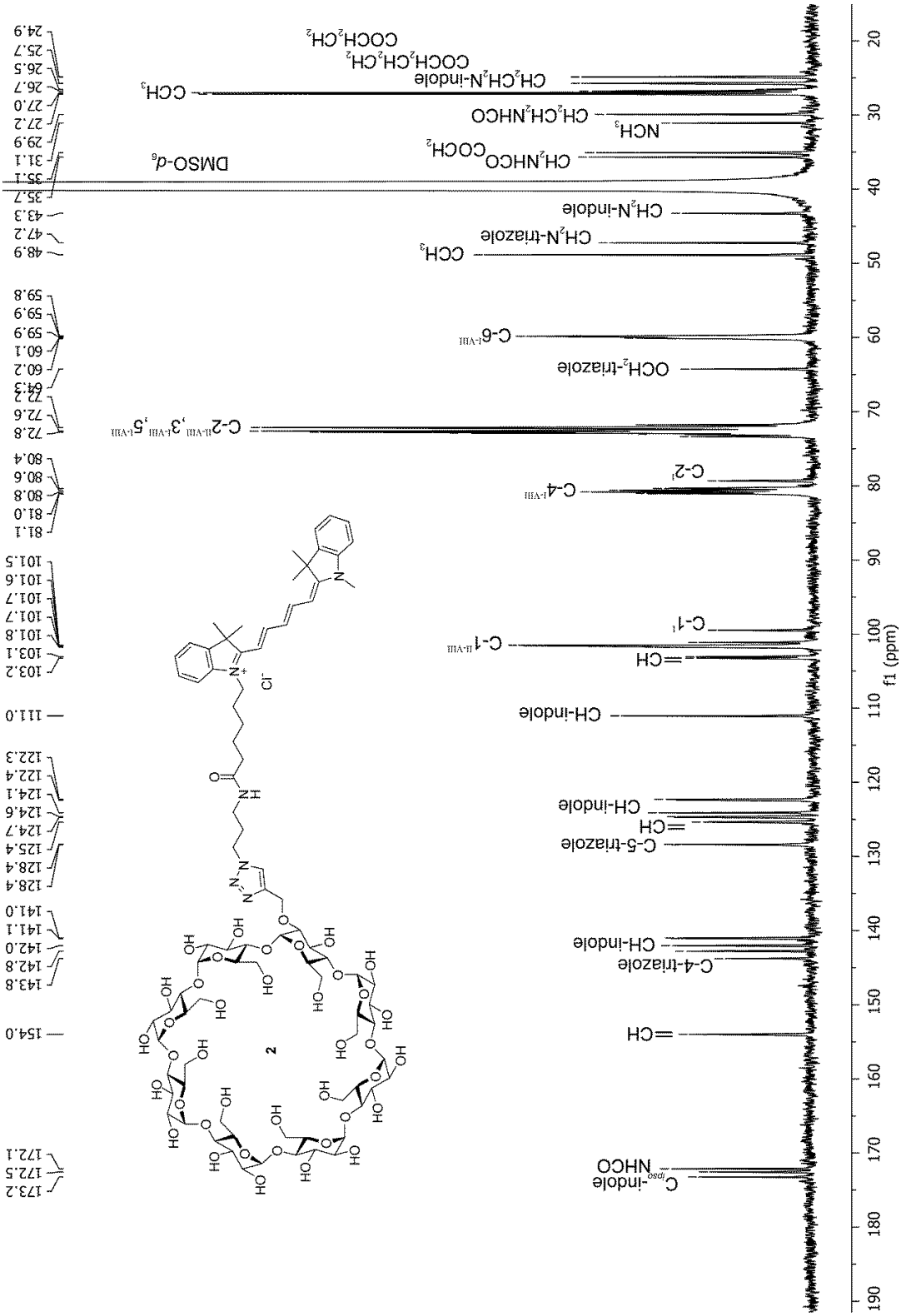

Figure S8 ^{13}C NMR spectrum (150 MHz, DMSO-d_6, 25 ºC) for derivative **2**.

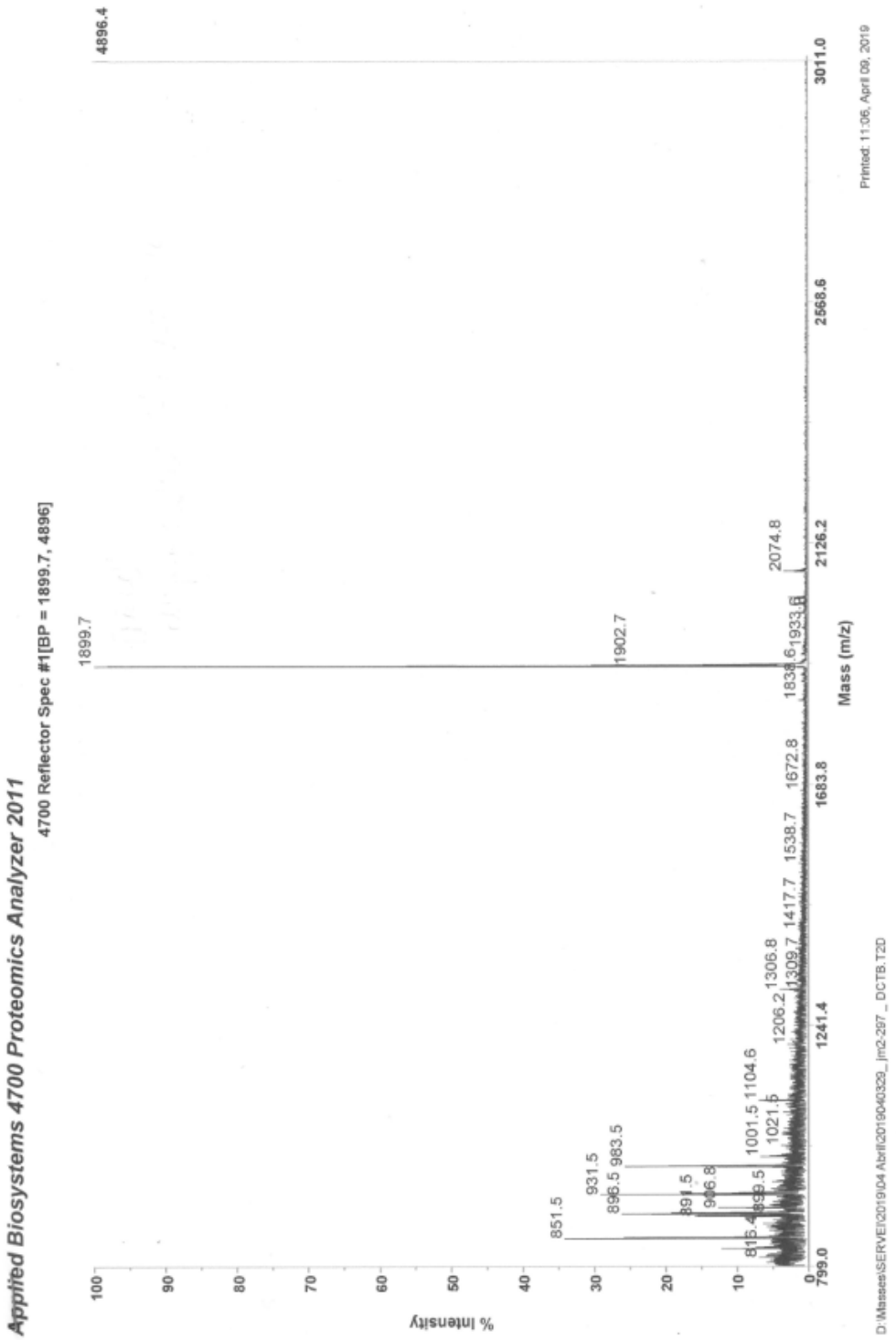

Figure S9 MALDI-TOF-MS spectrum (DCTB as matrix) for derivative **2**.

Table S1 Atomic composition (%) evaluated by XPS for γ-CD-citrate oligomers, uncoated nanoMOFs and nanoMOFs coated with γ-CD-citrate oligomers (50 wt%)

	γ-CD-citrate oligomers (%)	Uncoated nanoMOF (%)	Coated nanoMOF (%)
Fe2p	0	7	2
C1s	60	58	58
O1s	39	34	40

Chapter 3.2

Doxorubicin-loaded metal-organic frameworks nanoparticles with engineered cyclodextrin coatings: insights on drug location by solid state NMR spectroscopy

General Objectives and Author Contributions

Aluminium-based Metal-organic frameworks (Aluminium-based MOFs) were among the first synthesized and studied MOFs based on their stability and highly porous. They have been drawing an increasing interest because they can be synthesized with “green” hydrothermal method. As previously described, more recently, nanoMOFs engineered with versatile coatings are attracting numerous attention in the field of nanomedicine.

In this context, CD-based polymer (CD-CO) coated nanoMIL-100(Al) particles loaded with DOX molecules were successfully prepared and characterized. A high amount of drug was encapsulated in the nanoMOFss due to the high affinity of DOX with both the CD-CO coatings and the MOF cores. More interestingly, it was discovered that the CD-CO coatings favored the release of DOX from the cores, particularly at early stage (< 6h) and for low DOX payloads (especially TDL of 10%). Moreover, the CD-based coating accelerated the DOX loading process.

A series of high-resolution solid state nuclear magnetic resonance (ssNMR) experiments (1H-1H and 13C-27Al) were employed to obtain a deep understanding on the multiple interactions involved in the MIL-100(Al) core-shell system. To do so, 13C-labeled CD-CO oligomers were synthesized and further coated on the outer surface of the nanoMOFs. The ssNMR results clearly confirmed the high affinity of DOX with both the CD-CO shells and the nanoMOFs. The ssNMR methodology associated to the selective isotope labeling strategy demonstrated to be effective for the characterization of this system, relying on the diamagnetic character of the nanoMOFs. This study provided the grounds of a methodology to evaluate the nanoMOFs component localization at a molecular scale and to study the physicochemical properties of the nanoMOFs which play a main role on their biomedical applications.

In this study I contributed mainly with the synthesis of all the coating materials and nanoMOFs, surface modification of the nanoMOFs with coating materials, performance of DOX loading and release, and so on.

The ssNMR studies were carried on in collaboration with Dr. Charlotte Martineau-Corcos.

nanomaterials

MDPI

Article

Doxorubicin-Loaded Metal-Organic Frameworks Nanoparticles with Engineered Cyclodextrin Coatings: Insights on Drug Location by Solid State NMR Spectroscopy

Xue Li [1,†], Marianna Porcino [2,†], Jingwen Qiu [1], Doru Constantin [3], Charlotte Martineau-Corcos [2,4,*,‡] and Ruxandra Gref [1,*]

[1] Institut des Sciences Moléculaires d'Orsay, UMR CNRS 8214, Université Paris-Sud, Université Paris Saclay, 91400 Orsay, France; xue.li@universite-paris-saclay.fr (X.L.); jingwen.qiu@universite-paris-saclay.fr (J.Q.)
[2] CEMHTI UPR CNRS 3079, Université d'Orléans, F-45071 Orléans, France; marianna.porcino@cnrs-orleans.fr
[3] Laboratoire de Physique des Solides, UMR 8502, Université Paris-Sud, 91405 Orsay, France; doru.constantin@universite-paris-saclay.fr
[4] ILV UMR CNRS 8180, Université de Versailles St-Quentin en Yvelines, 78035 Versailles, France
* Correspondence: ccorcos@cortecnet.com (C.M.-C.); ruxandra.gref@universite-paris-saclay.fr (R.G.); Tel.: +33-(0)-1-30-12-11-31 (C.M.-C.); +33-(0)-1-69-15-82-34 (R.G.)
† These authors contributed equally.
‡ Current Address: CortecNet, 7 avenue du Hoggar, 91940 Les Ulis, France.

Abstract: Recently developed, nanoscale metal-organic frameworks (nanoMOFs) functionalized with versatile coatings are drawing special attention in the nanomedicine field. Here we show the preparation of core–shell MIL-100(Al) nanoMOFs for the delivery of the anticancer drug doxorubicin (DOX). DOX was efficiently incorporated in the MOFs and was released in a progressive manner, depending on the initial loading. Besides, the coatings were made of biodegradable γ-cyclodextrin-citrate oligomers (CD-CO) with affinity for both DOX and the MOF cores. DOX was incorporated and released faster due to its affinity for the coating material. A set of complementary solid state nuclear magnetic resonance (ssNMR) experiments including ^{1}H-^{1}H and ^{13}C-^{27}Al two-dimensional NMR, was used to gain a deep understanding on the multiple interactions involved in the MIL-100(Al) core–shell system. To do so, ^{13}C-labelled shells were synthesized. This study paves the way towards a methodology to assess the nanoMOF component localization at a molecular scale and to investigate the nanoMOF physicochemical properties, which play a main role on their biological applications.

Keywords: metal-organic frameworks nanoparticles; doxorubicin; cyclodextrin; solid state NMR spectroscopy

Citation: Li, X.; Porcino, M.; Qiu, J.; Constantin, D.; Martineau-Corcos, C.; Gref, R. Doxorubicin-loaded metal-organic frameworks nanoparticles with engineered cyclodextrin coatings: insights on drug location by solid state NMR spectroscopy. *Nanomaterials* **2021**, *11*, 945 https://doi.org/10.3390/nano11040945

Academic Editor: Filipe M.L. Figueiredo

Received: 23 February 2021
Accepted: 3 April 2021
Published: 8 April 2021

1. Introduction

Metal-organic frameworks (MOFs) are a class of ordered coordination network built from metal clusters as inorganic parts and organic ligands as linkers, containing potential voids [1]. Aluminum-based MOFs were among the first synthesized and studied because they are stable and highly porous. They attract a growing interest due to their "facile" hydrothermal synthesis [2]. In addition, aluminum is relatively cheap and abundant, making it an attractive metal source for mass production of MOFs. The two most reported aluminum-based MOFs are MIL (stands for materials of Institute Lavoisier) and CAU (stands for Christian–Albrechts University). Aluminum-based MOFs found useful applications in gas separation and storage, organic pollutants removal, pervaporation, and more recently, in biomedicine. Interestingly, MIL-100(Al) based metal organic gels [3] have been used as drug carriers to deliver doxorubicin (DOX). Solid-state NMR (ssNMR) spectroscopy has emerged as an essential analytical technique to achieve detailed atomic-

scale characterization of complex porous systems [4], including MOFs [5–8] The technique is non-destructive, allows probing a local scale highly complementary to diffraction and is sensitive to millisecond timescale, hence can be used to monitor dynamic processes. For instance, the activation process of MIL-100(Al) could be followed by ssNMR [9]. Although more challenging, paramagnetic MOFs can also be characterized by ssNMR spectroscopy [10].

In the field of biomedicine, ssNMR is also of particular interest [5,11–15]. Notably, ssNMR brought valuable insights on the supramolecular structure of highly porous core–shell drug nanocarriers, namely MIL-100 nanoMOFs coated with cyclodextrin-phosphate (CD-P) molecules. The first investigation [16] was performed on paramagnetic MIL-100(Fe) nanoparticle using ^{1}H solid-state magic-angle spinning (MAS) NMR analysis. The obtained ^{1}H NMR spectra revealed the interaction between the nanoMOFs and the CD-P materials by showing the close proximity between the CD-P and the paramagnetic centers on the nanoMOF external surfaces. It was thus demonstrated that cooperative interactions occurred between the coating and the core, based on phosphate-iron coordination, ensuring good shell stability in biological media. However, a large number of spinning side bands were observed due to the presence of the Fe paramagnetic center, limiting the amount of information that could be extracted from the NMR spectra. More recently, studies were carried out using the diamagnetic MIL-100 (Al) coated and loaded with phosphorus-containing species [17]. High-resolution ^{31}P-^{27}Al two-dimensional (2D) NMR experiments clearly evidenced the interactions between the nanoMOF external surfaces and the phosphorus-containing coating molecules at the molecular level. Moreover, useful information has been obtained on the interactions between the nanoMOFs and the drugs located inside their micropores [17].

In the present study, we intended to go steps beyond and take advantage of the possibilities offered by ssNMR to investigate the interactions in more complex core–shell nanoMOF systems. Recently, versatile polymeric CD-based coatings were engineered to ensure a convenient one-step surface modification of MIL-100 nanoMOFs [18]. The coatings were made of biodegradable γ-CD-citrate oligomers (CD-CO), which could be functionalized by click chemistry with fluorescent dyes [19]. Here, we took advantage of the known affinity between DOX and both the biodegradable γ-CD-citrate oligomers (CD-CO) [20] and the nanoMOFs [13] to prepare dual (core–shell) DOX-loaded nanoMOFs. Indeed, DOX was expected to be loaded both in the pores of the nanoMOFs and the γ-CD cavities located in the coating layers. The interaction of the DOX molecules with both the CD-CO shell and the MIL-100 (Al) nanoMOFs core was confirmed by a set of complementary ssNMR experiments, including 2D ^{1}H-^{1}H and ^{13}C-^{27}Al NMR. To enable this study, ^{13}C-labelled CD-CO oligomers were synthesized for the first time. DOX release in phosphate buffer saline (PBS) was investigated as a function of the drug payload, considering the possibility of DOX self-association inside the cages. This study focuses on a comprehensive understanding at a molecular scale of the drug localization and the physicochemical properties, which play an important role in the biological applications.

2. Materials and Methods

2.1. Materials and Reagents

Doxorubicin (DOX, 98%), citric acid (≥99.5%), sodium phosphate monobasic dihydrate (≥99%, $NaH_2PO_4 \cdot 2H_2O$), hydrochloric acid (HCl, 34–37%), sodium hydroxide (NaOH, ≥ 97%) potassium chloride (powder, ≥99%) and deferoxamine mesylate salt (≥92.5%) were purchased from Sigma-Aldrich (Saint-Quentin-Fallavier, France). γ-CD was purchased from Cyclolab (Budapest, Hungary). Dimethylsulfoxide (DMSO, ACS) was from Panreac Applichem (Barcelona, Spain). Deuterated DMSO (DMSO-d_6, 99.8% D) and water (D_2O, 99.9% D) were obtained from Eurisotop (Gif sur Yvette, France). 1,5-$^{13}C_2$ citric acid was obtained from CortecNet (Les Ulis, France). 1,3,5-benzenetricarboxylic acid

(BTC, 95%, Sigma-Aldrich, Saint-Quentin-Fallavier, France), aluminum nitrate nonahydrate (98%, Sigma-Aldrich, Saint-Quentin-Fallavier, France) and trimethyl trimesate (98%, Sigma-Aldrich, Saint-Quentin-Fallavier, France) and absolute ethanol (99%, Carlo Erba, Val-de-Reuil, France) were used for the synthesis of nanoMOFs. Water was purified by a Millipore MilliQ system.

Phosphate buffer saline (PBS, pH 7.4, containing 9.5 mM phosphates) was purchased from Life Technologies (Saint-Aubin, France) and was used for DOX release study.

2.2. Synthesis and Characterization of γ-CD-Citrate Oligomers

The γ-CD-citrate oligomers (CD-CO) were synthesized by adapting a previously reported method [21]. Briefly, the reaction mixture was prepared by solubilizing 0.09 mmol γ-CD, 0.45 mmol citric acid, and 0.2 mmol $NaH_2PO_4.2H_2O$ in 2 mL water. This solution was concentrated by evaporation at 140 °C for 10 min, followed by further heating at 140 °C for 15 min under reduced pressure (10–15 mmHg). Then 10 mL distilled water was added and the crude was sonicated for 5 min, followed by filtration to remove the insoluble fraction. The soluble fraction was dialyzed for 48 h using a cellulosic membrane (cut-off 20 kDa, Spectrum Laboratories, Piscataway, NJ, USA). Finally, the CD-CO and CD-^{13}CO were obtained as a solid white powder after freeze drying. To obtain CD-^{13}CO, a similar method was employed except that 1,5-$^{13}C_2$ citric acid was employed.

The composition of the synthesized CD-CO was determined by proton nuclear magnetic resonance (NMR) spectroscopy. Fourier-transform infrared (FTIR) spectra were recorded with a Bruker apparatus (VERTEX 70). The average molecular weight of the CD-CO and CD-^{13}CO was determined by size-exclusion chromatography (SEC), coupled online with multiangle light scattering (MALS) and refractive index (RI) detectors (SEC/MALS/RI, Wyatt Technology, Santa Barbara, CA, USA) [19].

2.3. Synthesis and Characterization of MIL-100 (Al) nanoMOFs

Aluminum trimesate MIL-100 (Al) nanoMOFs were synthesized as previously described [17,22]. Briefly, 20 mL of an aqueous mixture containing aluminum nitrate nonahydrate (1.43 g) and trimethyl trimesate (1.21 g) was mixed with nitric acid (4 mL, 4 m) at room temperature and then heated at 210 °C for 30 min under stirring by microwave. The synthesized MIL-100 (Al) nanoMOFs were obtained by centrifugation at 10,000× *g* for 15 min and activated by dispersing them in methanol overnight (50 mL) with vigorous stirring. The as-synthesized -MIL 100(Al) nanoMOFs were recovered by centrifugation (10,000× *g*, 15 min).

The average hydrodynamic diameters and size distributions of the nanoMOFs were determined by dynamic light scattering (DLS, Malvern Nano-ZS, Zetasizer Nano series, Orsay, France). The morphology of the nanoMOFs was investigated by transmission electron microscopy (TEM, JEOL 1400 (120 kV), Jeol Ltd., Tokyo, Japan). Powder X-ray diffraction patterns (PXRD) were recorded to characterize the crystallinity. The nanoMOFs BET (Brunauer–Emmett–Teller) surface area was measured by nitrogen sorption experiments at −196 °C using an ASAP 2020 (Micromeritics, Norcross, GA, USA) after degassing at 100 °C for 15 h under secondary vacuum. FTIR spectrum was recorded. NanoMOFs were stored in ethanol and redispersed in aqueous media before usage.

2.4. DOX Encapsulation in nanoMOFs Coated or not with CD-CO

MIL-100(Al) nanoMOFs ethanolic suspensions were first centrifuged at 10,000× *g* for 10 min to recover the nanoMOF pellets, which were further redispersed in water. For DOX encapsulation, 1 mL of nanoMOFs aqueous suspension (2 mg/mL) was mixed with 1 mL of DOX solution (0–2 mg/mL), followed by gently stirring for 1–6 days at room temperature. Theoretical drug loading (TDL), calculated as the weight ratio (%) between DOX and nanoMOFs, was in the range of 10–100%.

The same procedure was used to load DOX in MIL-100(Al) nanoMOFs coated with CD-CO (CD-CO@ MIL-100 (Al)), where the weight ratio between CD-CO and nanoMOFs was kept as 1:2 and CD-CO was added at the same time as DOX.

The DOX loaded nanoMOFs were recovered by centrifugation (10,000 × *g*, 10 min) and the supernatant was used to quantify the drug payload, as according to Equation (1):

$$Payload\ (\%) = \frac{Encapsulated\ drug\ (mg)}{Empty\ nanoMOFs\ (mg)} \quad (1)$$

taking into account the amount of nanoMOFs (mg) used for encapsulation and the amount of DOX incorporated at the end of the incubation.

Encapsulation efficiency (EE) was calculated, as according to Equation (2):

$$EE\ (\%) = \frac{\text{Encapsulated drug (mg)}}{\text{Initial Drug (mg)}} \times 100 \quad (2)$$

DOX was quantified by fluorescence spectroscopy with excitation (λ_{ex}) and emission (λ_{em}) at 480 and 590 nm, respectively. To do so, DOX in the nanoMOF supernatants was diluted with a mixture of water and DMSO (1:1 *v*:*v*), to dissociate the complexes DOX:CD before the quantification. The same loading and quantification methods were used for MIL-100 (Al) nanoMOFs, coated or not with CD-CO.

2.5. Characterization of CD-CO Coated nanoMOFs

The morphologies of nanoMOFs, loaded or not with DOX, coated or not with CD-CO, were observed using TEM. Their crystallinity was characterized by PXRD using a homemade setup based on a copper rotating anode generator (RU-200BEH, Rigaku Ltd., Tokyo, Japan), as previously described [18,23–25]. The accessible scattering vector range was 0.035–0.5 $Å^{-1}$.

Colloidal stabilities of DOX loaded nanoMOFs, coated or not with CD-CO were estimated by DLS after incubation in MilliQ water. Zeta potential (ZP) of the same nanoMOF series were measured at 25 °C using a Zetasizer instrument (Malvern Nano-ZS, Zetasizer Nano series, France) in a pH range of 1–10, adjusted using HCl or NaOH. For the measurements, nanoMOFs were diluted using a KCl solution (1 mM) to a final concentration of 100 µg/mL.

2.6. DOX Release Study

The DOX release experiments were carried out by dispersing DOX loaded nanoMOFs in PBS to reach a final nanoMOF concentration of 100 µg/mL, followed by incubation at 37 °C for 30 days under gentle shaking. The release profile was obtained by measuring both the DOX concentration in the supernatant and in the pellet at periodic time intervals. Supernatants were obtained after centrifugation at 17,000× *g* for 20 min, followed by dilution with a mixture of water and DMSO (1:1 *v*:*v*) and analyzed by fluorescence spectroscopy to determine the DOX concentrations. DOX in the pellet was extracted by degrading the DOX-loaded nanoMOFs (100 µg/mL) in 10 mg/mL of deferoxamine mesylate salt after 24 h incubation at 37 °C. The extracted DOX was further diluted with a mixture of water and DMSO (1:1 *v*:*v*) and quantified by fluorescence spectroscopy.

2.7. Solid-State NMR Spectroscopy

The ^{1}H, ^{13}C, and ^{27}Al MAS NMR spectra were recorded at a magnetic field of 9.4 T, using a Bruker 400 MHz WB NMR spectrometer and a HX 4 mm probe. The ^{1}H spectra were acquired using a Hahn echo pulse sequence, with a 90° pulse duration of 3 µs, an interpulse delay synchronized with one rotor period and a spinning rate of 10 kHz. The recycle delay was set to 3 s and 32 transients were recorded for each sample. The ^{13}C cross-polarization under MAS (CP-MAS) spectra were recorded with a contact time of 3.5 ms, a recycle delay of 3 s, and the initial 90 pulse on ^{1}H to 3 µs with a radio frequency (RF) field of 80 kHz. ^{1}H SPINAL-64 decoupling was applied during the ^{13}C acquisition. The ^{1}H and

^{13}C chemical shifts were referenced to Adamantane. For the ^{27}Al MAS NMR, the recycle delay was set to 0.3 s. The ^{27}Al chemical shifts are referenced to $Al(NO_3)_3$ solution at 0 ppm.

The ^{13}C {^{27}Al} symmetry-based resonance-echo saturation-pulse double-resonance (S-RESPDOR) [22,26–29] experiments and ^{27}Al{^{13}C} dipolar based heteronuclear multiple quantum correlation (*D*-HMQC) 2D experiments were performed under a MAS frequency of 12.5 kHz in a 4 mm probe using the same spectrometer mentioned before and a REDOR box [30]. $SR4^2_1$ [31,32] was used as the recoupling sequence in order to reintroduce ^{13}C-^{27}Al heteronuclear dipolar interactions, with different recoupling time. Recycling delay of 2.5 s was used and 8192 transients were recorded for each CP CP-RESPDOR experiment. The RF field of ^{27}Al saturation was around 85 kHz. For the HMQC, 40 t_1 slices with 6528 transients were co-added, leading to a total of experiment time of around 21 h. The states procedure provides a phase sensitive 2D NMR spectrum. All spectra were treated with 100 Hz exponential apodization in both dimensions.

The ^1H MAS and ^1H-^1H 2D MAS exchange spectroscopy (EXSY) NMR experiments were recorded on the spectrometer mentioned before and using HXY 1.3 mm probe, with a recycle delay of 3 s and a ^1H 90 pulse of 1.1 μs. Two different mixing times were used for the exchange experiments (5 ms and 15 ms) and 250 t_1 slices with 128 transients were coadded. The states procedure provided a phase sensitive 2D NMR spectrum. The samples were dried under vacuum at 40 °C before the experiments.

The ^1H{^{13}C} *D*-HMQC NMR spectra were recorded at 17.6 T using a 1.3 HXY probe in a double mode with a spinning rate of 50 kHz. The symmetry-based $SR4^2_1$ scheme was used to recouple the ^1H-^{13}C dipolar interaction at different recoupling times and a RF field of 100 kHz. Recycling delay was set at 3 s, with 320 transients, leading to a total experimental time of 15 min each.

All the samples were finely ground into powders and packed into a zirconia rotor of the appropriate size. The NMR spectra were acquired using TopSpin 3.5 Bruker Software (Bruker BioSpin GmbH, Karlsruhe, Germany) and processed with DmFit software [33].

3. Results

3.1. DOX Encapsulation in NanoMIL-100(Al)

MIL-100(Al) nanoMOFs with mean hydrodynamic diameters of 260 ± 8 nm were successfully synthesized. They exhibited facetted morphology (Figure 1A) and a crystalline structure according to TEM and PXRD investigations, respectively. The Brunauer–Emmett–Teller (BET) surface area reached 1720 ± 65 m^2/g. The nanoMOFs displayed a positive surface charge characterized by a Zeta potential of 10 ± 4 mV, and composition in agreement with previously reported data [22].

Firstly, DOX incorporation was carried out by simply incubating the nanoMOFs in aqueous DOX solutions under rotative agitation, at room temperature for 1–6 days. Figure 2 reports the kinetics of DOX encapsulation obtained by fluorescence spectroscopy. DOX incorporation kinetics were investigated at different DOX initial amounts calculated as the TDL, which is the weight ratio between DOX and nanoMOFs used in the loading process. When TDL was 10%, the DOX encapsulation efficiency (EE) reached 62.5 ± 17.5% within 1 day and plateaued in 2 days at 83.6% ± 7.4% (corresponding to a DOX payload of 8.3 ± 0.7 wt.%). At a TDL of 20%, the EE plateaued at 73.9% ± 4.2% (corresponding to a DOX payload of 14.8 ± 0.8 wt.%). At TDL of 50%, DOX payload increased to 27.4 ± 2.0 wt.% after 6 days' impregnation. This clearly shows that DOX efficiently interacted with MIL-100 nanoMOFs. In contrast, DOX payload in other type of nanoparticles (NPs) such as polymeric NPs is not as high. For example, DOX payload in poly lactic-co-glycolic acid (PLGA) NPs was less than 15 wt.%, whatever the preparation method [34]. Moreover, DOX payload in the commercial Doxil® (doxorubicin loaded liposome) was around 12 wt.% [35].

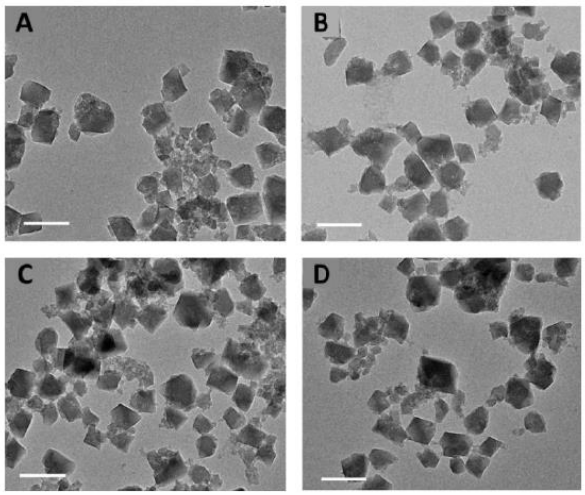

Figure 1. TEM images of MIL-100 (Al) nanoMOFs (**A**), CD-CO@ MIL-100 (Al) (**B**), DOX loaded MIL-100 (Al) (**C**) and DOX loaded CD-CO@MIL-100 (Al) (**D**) (scale bar: 200 nm).

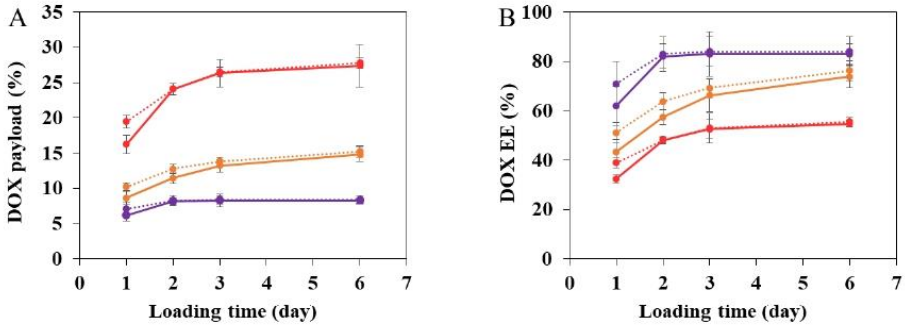

Figure 2. DOX payload (**A**) and encapsulation efficiency (EE, (**B**)) in MIL-100 (Al) nanoMOFs (continuous line) and nanoMOFs coated with CD-CO (CD-CO@nanoMOFs, dotted line) at different theoretical drug loading (TDL) (purple: 10%; orange: 20%; red: 50%).

DOX loading in MIL-100 nanoMOFs (Fe) was also investigated [13] showing DOX and nanoMOFs association constant Ka (1:1) of (1.1 ± 0.1) × 10^4 M^{-1}. The maximal DOX payload in MIL-100 (Fe) nanoMOFs was reported as 32.5 wt.% [36] at TDL of 150% after 24 h incubation, which is similar to what is observed in this study. DOX loading in MIL-100 (Al) metal organic gels (MOGs) [3] was reported to be 620 mg/g, however, no studies were carried out to investigate whether DOX was well entrapped inside the MIL-100 (Al) porosity, or if it was located on the nanoMOF surface or inside the gel network.

Noteworthy, the nanoMOFs maintained the same morphology with faceted-type structures before and after DOX encapsulation, whatever the payloads, as shown by TEM images (Figure 1C). The colloidal stability of nanoMOFs before and after drug loading was investigated. After DOX loading in nanoMOFs by impregnation, no aggregation was observed, whatever the TDL, 20% or 50%. PXRD studies showed that the crystalline structure of the MIL-100 (Al) nanoMOFs was not affected upon DOX loading (Figure 3A). However, at the highest DOX payloads, the BET surface area was dramatically reduced (1720 ± 65 m^2/g, 1245 ± 80 m^2/g, 1010 ± 65 m^2/g, and 200 ± 35 m^2/g, for nanoMOFs loaded with 0%, 8.3 ± 0.7 wt.%, 14.8 ± 0.8 wt.%, and 27.4 ± 2.0 wt.% DOX, respectively (Figure 3B),

suggesting that DOX localized inside the pores of the nanoMOFs. The presence of DOX is also confirmed by FTIR, showing the DOX peaks between 3000 and 3700 cm^{-1} on the DOX loaded particles (Figure S1).

To gain insights on the effect of DOX loading and CD-CO coating on the surface properties of nanoMOFs, Zeta potential (ZP) was measured. In agreement with previous studies, empty and uncoated nanoMOFs exhibited positive ZP (4.2 ± 2.3 mV) at pH 5, shifting to negative values (−0.5 ± 2.0 mV) at pH 7. In contrast, at maximal DOX loading (27.4 ± 2.0 wt.%), the ZP of nanoMOFs reached increased ZP values (+4.2 ± 2.3 mV and +36.4 ± 2.1 mV for empty nanoMOFs and DOX loaded nanoMOFs at pH 5, respectively) possibly due to the cationic character of DOX [37]. This tendency of positive shift decreased in basic conditions.

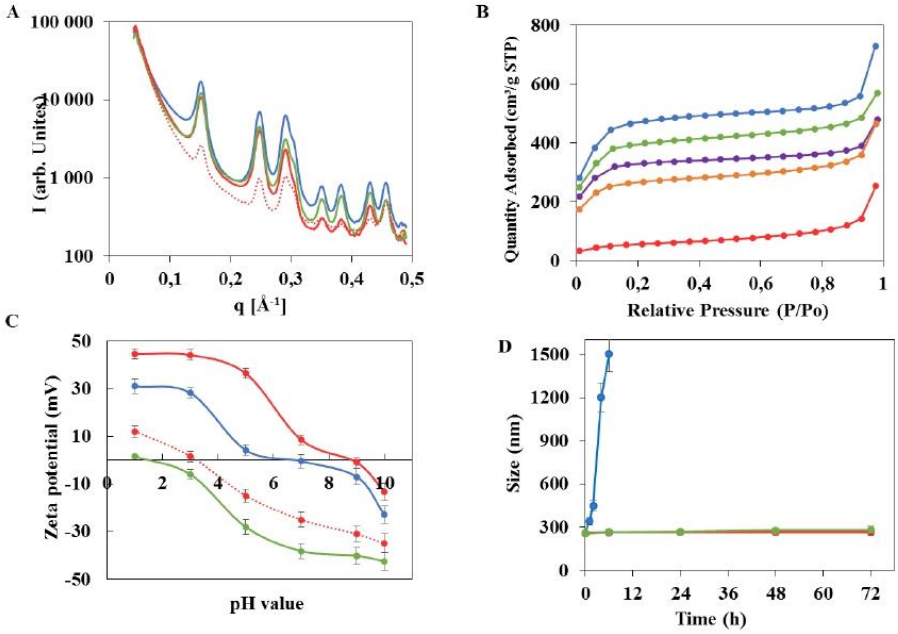

Figure 3. Characterization by PXRD (**A**) porosimetry (**B**), Zeta potential (**C**), and stability (**D**) of the particles before and after drug loading and/or surface functionalization (black: simulated PXRD patterns for MIL-100 (Al); blue: empty nanoMOFs; green: nanoMOFs coated with CD-CO; purple: nanoMOFs loaded with DOX at TDL of 10%; orange: DOX at TDL of 20%; red: DOX at TDL of 50%; red dashed line: nanoMOFs loaded with DOX at TDL of 50% and coated with CD-CO).

In an attempt to gain an understanding at the molecular level of the DOX loading processes, a ssNMR investigation on nanoMIL-100(Al) was undertaken. Indeed, ssNMR spectroscopy is well-known to provide atomic-level information about porous MOFs as drug delivery systems [4–6,9,10,31]. The ^{13}C cross-polarization under magic-angle spinning (CPMAS) NMR spectrum of DOX loaded nanoMIL-100(Al) shows the presence of the DOX molecules (Figure 4). One can notice differences between the position of some carbon resonances of the DOX loaded compared to those of pure crystalline DOX (Figure 4f). It turns out that the position of the loaded DOX is very similar to the ^{13}C chemical shift of DOX in solution (Figure 4e), notably in the 110–140 ppm region. The difference between DOX molecules in the crystalline phase and in solution is the presence of the π–π⊙interaction in the crystal that generates particular ^{13}C shifts in the aromatic region. The fact that

the DOX molecules loaded in the nanoMOFs have chemical shifts similar to that in solution indicates the absence of π–π⊛stacking once incorporated in the MOF suggesting that the drug molecules are incorporated in a molecular state.

MIL-100(Al) particles were loaded with increasing amount of DOX, from 5 to 27 wt.%. While a clear increase of the ^{13}C DOX resonance intensity is observed between the 5 and 14.8 wt. % loading (Figure 2b, c), no significant difference is observed between 14.8 and 27.4 wt. % loading (Figure 4c, d). This very likely shows that the amount of DOX that can be loaded inside the pores of the MOF is limited to around 15 wt.%. One possible explanation for the fact that the ^{13}C signal of the excess DOX molecules is not detected could be an accumulation of DOX molecules on the surface of the particles. If this external layer of DOX is amorphous, it will generate very broad ^{13}C resonances that could be difficult to detect because lying under the peaks of the crystalline phase.

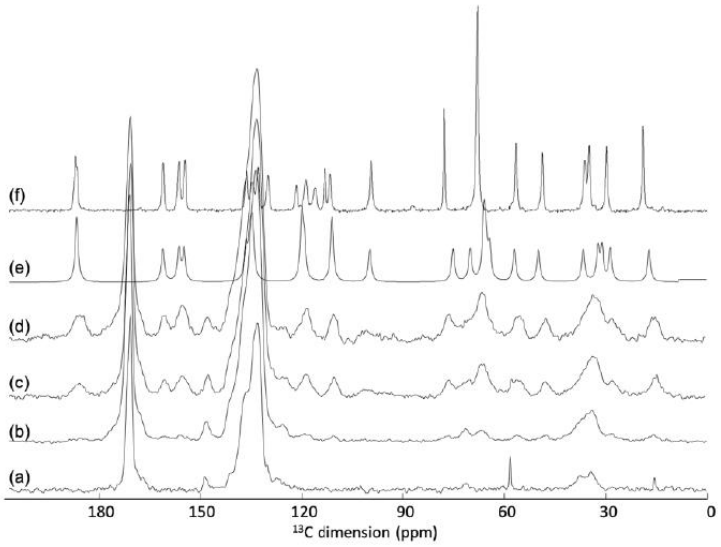

Figure 4. ^{13}C CPMAS NMR spectra of (a) MIL-100(Al) and MIL-100(Al) loaded with (b) 8.3 wt.% DOX, (c) 14.8 wt.% DOX and (d) 27.4 wt.% DOX. In (f) is shown the ^{13}C NMR spectrum of DOX in the solid-state and in (e) a simulation of the liquid-state NMR spectrum.

3.2. DOX encapsulation in nanoMIL-100(Al) coated with CD-CO

3.2.1. Surface functionalization of nanoMOFs with CD-CO

Given that the citrate moieties could efficiently interact with nanoMOFs [19] and that γ-CD has high affinity with DOX [20], the biodegradable CD-CO was chosen to functionalize nanoMIL-100 (Al). It was successfully synthesized with a yield of around 30% ± 3% using our previous methods[19]. After further characterization using ^{1}H NMR, FTIR, and SEC, it was found that the obtained CD-CO possessed an average molecular weight of 22,000 g/mol and a polydispersity (D) of 1.6, in agreement with our previous investigations [19]. Similar results were obtained for CD-^{13}CO, which exhibited Mn of 22,800 g/mol (Đ = 1.8) and a γ-CD content of 71 wt.%. This was done employing 1,5-$^{13}C_2$-citric acid in the polymer synthesis. Preparation of the labeled polymer was successful, as attested by the ^{13}C CPMAS NMR spectrum that is similar to the non-labeled polymer (Figure S2). Taking advantage of the affinity between citrate moieties in CD-CO and the Al sites in the nanoMOFs, nanoMOFs were easily functionalized with CD-CO by incubation in water at room temperature. The associated CD-CO amount was quantified by TGA, indicating that the associated CD-CO represented 8 ± 4 wt.% of the initial nanoMOFs amount (Figure S3).

The resulting CD-CO@nanoMOFs maintained their facetted structures (Figure 1B), crystallinity (Figure 3A) and BET surface area was only slightly modified (1720 ± 65 m^2/g and 1500 ± 130 m^2/g for nanoMOFs before and after surface modification, Figure 3B). This suggests that the coating material does not penetrate inside the MOF porosity. Further evidence of the presence of the coating was given by Zeta potential values, which shifted to negative values in all the studied pH range (1–10). Moreover, the presence of the coating improved the nanoMOF stability as shown in Figure 3D. Without coating nanoMOFs rapidly aggregated whereas with CD-CO shells, their main diameters remained constant over three days' incubation (less than 5% variations).

3.2.2. Interaction between DOX and CD-CO

Prior to loading DOX in CD-CO@nanoMOFs, the interaction between CD-CO and DOX was investigated by NMR. ^1H and ^{13}C MAS NMR spectra were recorded on the CD-CO citrate polymer, in order to assess the affinity of DOX with the CD-CO polymer. The ^1H MAS NMR spectrum (Figure 5B, C) was dominated by the broad peak of the CH_2 protons of the CD. The ^{13}C CPMAS NMR spectrum contains the ^{13}C resonances of both the CD (60–80 ppm region) and citrate (carboxyl atoms in the 180 ppm region, CH_2 around 40 ppm and CH-OH around 100 ppm) moieties (Figure 5(Aa)). Note that if the ^{13}C resonances of the free COOH and the ester COOCD have similar chemical shifts, a single broad resonance is observed. In order to be able to run 2D ^1H-^{13}C NMR experiments and extract more information about CD-CO and DOX interactions, we chose to enrich the citrate moieties with ^{13}C isotope (since ^{13}C natural abundance is too low at ca 1%). This choice of isotopic enrichment of the coating only (and not of the MOF linker) provides higher selectivity on the coating–MOF surface interactions of prime interest in this study.

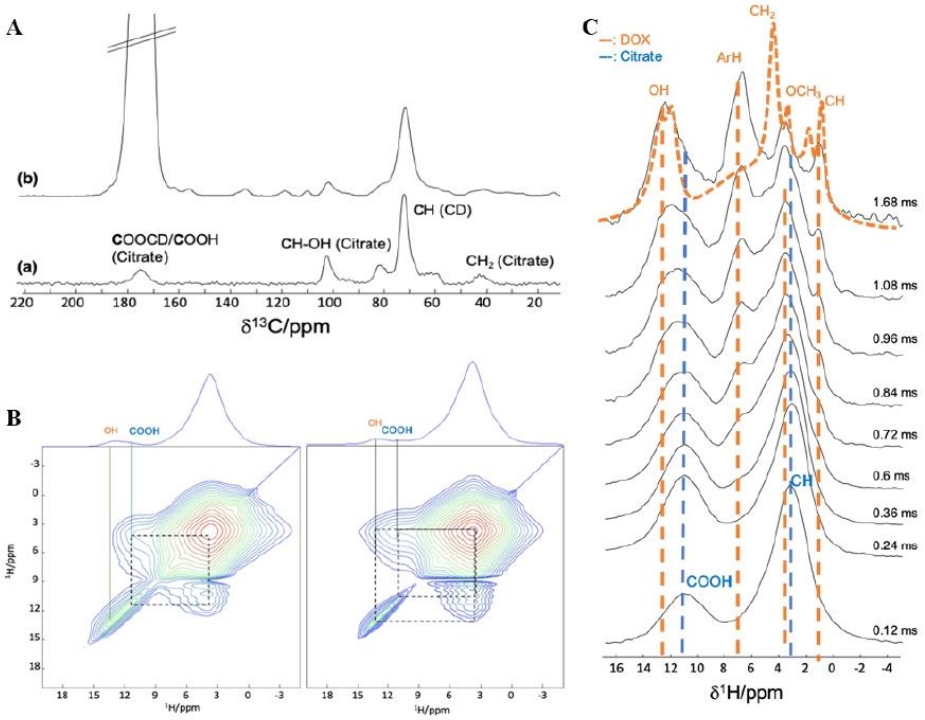

Figure 5. NMR spectra of CD-CO and DOX loaded CD-CO polymer. (**A**). ^{13}C CPMAS NMR spectra of CD-CO and DOX loaded CD-^{13}CO polymer. Small unlabeled lines correspond to the DOX signals. The strong signal of the labeled ^{13}C citrate is truncated for sake of clarity. (**B**). ^1H-^1H 2D MAS NMR spectra of DOX loaded CD-CO polymer recorded with mixing

time of 5 ms (left) and 15 ms (right) (**C**). $^{13}C\{^{1}H\}$ *D*-HMQC NMR spectrum of DOX loaded CD-CO polymer, recorded for recoupling times ranging from 0.12 to 1.68 ms. For comparison, the ^{1}H MAS NMR spectrum of DOX loaded CD-CO is shown in orange dash line. The vertical blue dash lines indicate the position of ^{13}C resonances from the CD-CO moieties, while the vertical orange dash lines indicate those of the DOX molecules.

Incorporation of the DOX molecules in the ^{13}C-labeled polymer was also achieved and at DOX loading of 14.8 wt.%, all ^{13}C resonances of the DOX are observed (Figure 5(Ab)). Although the resonances were still very broad and partially overlapping, some resolution was obtained in the ^{1}H MAS NMR spectrum of CD-CO-DOX, notably in the aromatic and OH region of the DOX (above 7 ppm). ^{1}H-^{1}H 2D MAS NMR experiments were carried out (Figure 5B) to probe spatial proximities between the protons of the CD-CO and those of the DOX. At shorter recoupling time (left spectrum), the ^{1}H-^{1}H NMR spectra shows as expected cross-correlation peaks between the unconnected COOH of the citric moieties (11 ppm) and the CH/CH_2 protons of the CO and CD (broad peak around 4 ppm). For longer recoupling time (right spectrum), one can also observe a cross-correlation peak between this CH/CH_2 peak and the peak corresponding to the OH of the DOX molecules, indicating close contact between the DOX and the CD-CO inside the particles.

Taking advantage of the ^{13}C-tag of the citrate moieties (that significantly increases the sensitivity of ^{13}C experiment), we also probed ^{13}C–^{1}H proximity. In this experiment, the magnetization of the ^{13}C-citrate was selectively chosen and transferred to its surrounding protons. The intensity of the resulting proton resonances as a function of transfer time is shown in Figure 5C. Short ^{13}C-carbon-proton spatial proximities are dominant at a short recoupling time, while longer C–H distances appear at longer transfer time. In this figure, at a short recoupling time, mostly the protons of the CD and citrate moieties are seen, as expected since the ^{13}COO belong to the citrate polymer. For longer magnetization transfer time, the protons of the DOX start also to be observed. This confirms the close mixing of the DOX molecules within the CD-CO polymer. Interestingly, the aromatic protons of the DOX have much higher intensity on the ^{1}H NMR spectrum after transfer from the ^{13}C-citrate than in the normal ^{1}H MAS NMR spectrum (orange spectrum on Figure 5C). This indicates that the aromatic parts of the DOX molecules have a preferential interaction with the ^{13}CD-CO polymer.

3.2.3. Characterization of DOX Loaded MIL-100(Al) nanoMOFs Coated with CD-CO

DOX payload: Due to this strong binding of DOX to CD-CO [20] a direct quantification of DOX in the supernatant was not possible by fluorescence measurements. Thus, a method was set up to quantify DOX, based on disruption of the inclusion complexes by adding DMSO (see the Materials and Methods). In these conditions, DOX fluorescence intensity was not influenced by the presence of CD-CO.

Interestingly, as shown in Figure 2, the presence of the CD-CO coatings accelerated the loading process. For example, at TDL of 20%, DOX payloads reached 11.5 ± 0.8 wt.% and 12.8 ± 0.7 wt.% for bare nanoMOFs and CD-CO@nanoMOFs, respectively, after 2 days' incubation (Figure 1A). This could be explained by the fact that DOX has a high affinity for both CD-CO[20] and MIL-100 (Al) nanoMOFs[13]. After 6 days' impregnation, maximal drug loading reached 14.8 ± 1.0 wt.% and 15.3 ± 0.8 wt.% for bare nanoMOFs and CD-CO@nanoMOFs, respectively (Figure 2A). Noticeably, EE reached more than 73.9% after 6 days for all the cases. When excess DOX was added in the system (TDL of 50%), DL reached 27.4 ± 2.0 wt.% and 27.8 ± 0.8 wt.% for bare nanoMOFs and CD-CO@nanoMOFs, respectively. Therefore, the CD-CO coating did not significantly change the DOX payload, but it could accelerate the loading process. For example, in the case of TDL of 50%, DOX payload of 16 ± 2.4 wt.% and 19 ± 1.9 wt.% for nanoMOFs and CD-CO@nanoMOFs was observed after 1 day of incubation.

After both the DOX loading and CD-CO coating, the crystallinity of the particles was still preserved with slight long-range changes (Figure 3A). Zeta potential was shifted to negative values compared to the empty nanoMOFs, indicating that the CD-CO coating

played a major role on the surface charge, which masked the effect of DOX molecules loaded within the pores close to the external surface.

To understand the affinity between the covering CD-CO oligomers and the MOF surface, ^{1}H, ^{27}Al, and ^{13}C MAS NMR were recorded on MIL-100(Al) nanoMOFs and CD-CO@nanoMIL-100(Al). The ^{27}Al MAS NMR of both samples is similar (Figure S4), with all Al atoms in a six-fold coordination. In the ^{13}C CPMAS NMR spectra (Figure 6A), the ^{13}C resonances corresponding to the CD-CO could be identified. Note an overlap of the carboxylic ^{13}C resonances with those of the carboxylic carbon atoms from the MOF linker in the 170–180 ppm region. Due to the small proportion of coating with respect to the nanoMOF size, the signals of the CD-CO had low intensity and it was therefore difficult to distinguish between the ester (CO-CD) and the free COOH of the citric acid moieties.

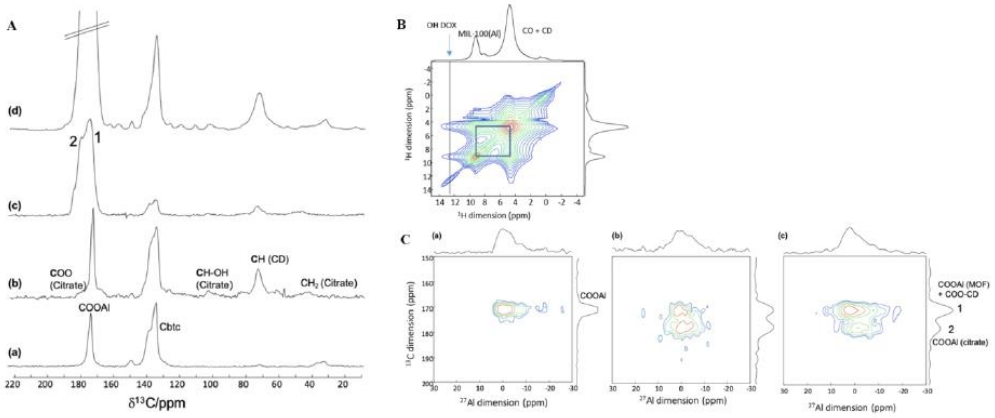

Figure 6. NMR spectra of MIL-100(Al), CD-CO@nanoMIL-100(Al), CD-^{13}CO@nanoMIL-100(Al), and DOX loaded CD-^{13}CO@nanoMIL-100(Al). (**A**). ^{13}C CPMAS NMR spectra of (a) MIL-100(Al), (b) CD-CO@nanoMIL-100(Al), (c) CD-^{13}CO@nanoMIL-100(Al), and (d) DOX loaded CD-^{13}CO@nanoMIL-100(Al). In (d), the small unlabeled peaks correspond to the DOX molecules. The intense ^{13}C resonances is truncated for sake of clarity. In (c), 1 and 2 show the two labeled carboxylic resonances. Line 2 corresponds to the ^{13}C carboxylic atoms of the CO linked to the surface aluminum sites of the MOF. Line 1 is a superimposition of COOAl carboxylic of the trimesate BTC linker and the ^{13}COO-CD of the polymer coating. (**B**). ^{1}H-^{1}H 2D MAS NMR spectrum of DOX loaded CD-^{13}CO@nanoMIL-100(Al) dried. (**C**). 2D ^{13}C-^{27}Al *D*-HMQC 2D of (a) nanoMIL-100(Al), (b) CD-^{13}CO@nanoMIL-100(Al) and (c) DOX loaded CD-^{13}CO@nanoMIL-100(Al).

^{1}H MAS NMR spectra were also recorded (Figure 6B). However, as was already observed for MIL-100(Al) nanoMOFs coated with CD-P [17], due to the presence of numerous protons both in the MOF and in the coating, no useful information could be extracted. In CD-P coated MIL-100(Al) NPs, this difficulty could be circumvented by using the heteroatoms present either in the MOF only (i.e., ^{27}Al) or in the coating only (^{31}P). This allowed clear probing of the coating-MOF interactions. In the system under study here, while the MOF still contains a heteroatom (^{27}Al), the coating only contains ^{1}H and non-abundant ^{13}C (ca. 1% natural abundance). Therefore, we chose to take advantage of the ^{13}C-labeled CD-CO polymer presented in the previous section. This way, ^{27}Al was selectively present in the MOF, while ^{13}C nucleus was present in significant quantity both in the coating (labeled ^{13}C) and in the nanoMOFs (natural abundance ^{13}C of the linker).

^{13}C CPMAS NMR spectra of the nanoMOFs coated with non-labeled or labeled CD-CO polymers are similar (Figure S2). No significant difference in the ^{1}H and ^{27}Al ssNMR spectra is noticed with the unlabeled product (Figure S5). With the higher intensity provided by the ^{13}C labeling, the carboxylic groups of the citric acid are now very visible. In particular, contrary to the CD-CO polymer shown in the previous section, two resonances, labeled 1 and 2 in Figure 6Ac, for the ^{13}C-labeled carboxylic carbon atoms of the citric moieties are observed. Since both the ^{13}COO-CD ester and the free ^{13}COOH had similar chemical shift in the pure polymer, one can infer that the new peak observed in the CD-

CO@nanoMIL-100(Al) arises from a strong interaction (maybe a chemical bond) between the citrate and the Al sites located at the surface of the nanoMOF. Such a strong interaction was already observed in the case of CD-P coating [17]. Note the absence of the COOH proton signal in the ^{1}H MAS NMR spectrum, which further support the formation of a bond between the free COOH of the CD-CO and the Al atoms located at the surface of the nanoMOF.

To understand better the interaction between the CD-CO coating and the nanoMOFs, 2D ^{13}C-^{27}Al MAS correlation NMR experiments were performed (Figure 6C). These experiments show the spatial proximity between carbon and aluminum atoms. Correlation peaks of strong intensity are observed between the CD-CO and the surface Al sites, confirming that the CD-CO polymer had high affinity with the NP surface. Note that the ^{13}C resonance at 175 ppm contains both the carboxylic group of the trimesate linker of the MOF (not labeled but present in large quantity) and the COO-CD of the CD-^{13}CO coating. ^{13}C-^{27}Al double-resonance curves were recorded (Figure S6), which give indication on relative C-Al distances. These curves show that the peak at 180 ppm (line 2) has shorter distance to the Al than the peak at 175 ppm (line 1). This supports further the hypothesis that this additional peak results from a chemical bond formed between some of the free COOH groups of the CD-CO polymers and the Al atoms located at the surface of the nanoMOFs.

In the DOX loaded CD-^{13}CO@nanoMIL-100(Al), the ^{13}C signals of the DOX molecules are seen and are similar to the solution state ^{13}C NMR spectrum of DOX, indicating the absence of π–π⊚interactions (Figure 6Ad). The ^{13}C-^{27}Al 2D MAS NMR spectrum (Figure 6Cc) shows that the coating and the NPs are still in a strong interaction. However, the relative intensity between the ^{13}CO peaks 1 and 2 is different. This indicates that, in addition to going in the pores of the MOF as shown earlier, the DOX molecules also interact significantly with the CD-CO coating. Notably, since the intensity of ^{13}C line labeled 2 has decreased, it very likely indicates that part of the ^{13}COO-Al bonds formed between the citric acid moieties and the surface Al sites have been broken after DOX incorporation.

3.3. DOX release studies

DOX release profiles in PBS at 37 °C are shown in Figure 7. At each time point, DOX released in the supernatant was recovered after centrifugation and quantified by fluorescence spectroscopy. The method was validated by DOX quantification in the pellets. To do so, several solvents and degrading agents were used. PBS was used previously in our teams [38] to extract drugs from nanoMOFs by degrading them completely, which released both the timesate linkers and the drugs. However, this method was unsuccessful in the case of DOX-loaded nanoMOFs, most probably because of the strong affinity of DOX for these matrices. Eventually, deferoxamine mesylate salt was used to erode the MOFs and extract all their drug content. Mass balance studies showed recoveries of 95% ± 5.5%.

When DOX was loaded at TDL of 20%, DOX release from bare nanoMOFs reached around 43.8% ± 1.2% within 1 h and 75.1% ± 2.0% in 2 days (Figure 7).

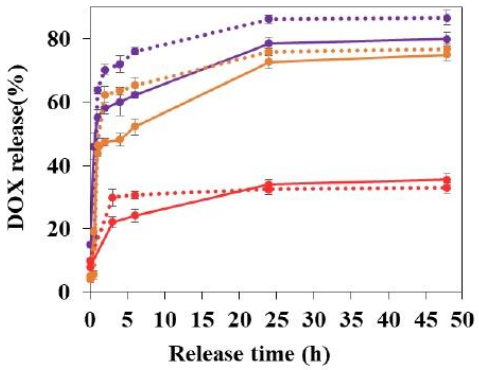

Figure 7. DOX release in PBS (pH 7.4, 9.5 mM, 37 °C). DOX loaded nanoMOFs (continuous line) and DOX loaded CD-CO@nanoMOFs (dashed line) at different TDLs (purple: 10%; orange: 20%; red: 50%).

Interestingly, the DOX release behavior was found to be dependent on the DOX payloads. When less DOX was loaded, in the case of DOX payload of 8.3 ± 0.7 wt.%, more DOX was released in the same condition (60.1% ± 4.1% and 48.2% ± 2.8% in 4 h for TDL of 10% and 20%, respectively). At high DOX loading (TDL of 50%), there was only 35.6% ± 1.9% released out in 2 days. In other words, at high DOX contents in the nanoMOFs, not all the drug is released out. Possibly, DOX self-associates inside the cages leading to incomplete release. This phenomenon has been already shown with another drug, which tends to self-associate, topotecan, which was incompletely released from MIL-100 (Fe) nanoMOFs [39].

In a nutshell, it appears that the advantage of CD coatings is to better extract DOX from the cores, especially at early times (<6 h) and for low DOX payloads (especially TDL of 10%). CD coating accelerates the loading process and facilitates DOX release.

4. Conclusions

In this study, we reported the synthesis and characterization of CD-CO coated nanoMIL-100(Al) particles loaded with DOX molecules. Due to the high affinity of DOX with both the CD-CO coating and the MOF, a high amount of drug could be loaded in the nanoparticles. High-resolution ssNMR spectroscopy was employed to characterize the core–shell nanoMOFs. In order to perform informative ^{1}H-^{13}C and ^{27}Al-^{13}C NMR experiments, the key element was to synthesize ^{13}C-labeled CD-CO oligomers, which were coated on the nanoMOF external surface. The ensemble of NMR data unambiguously confirms the high affinity of DOX with both the CD-CO moieties and the nanoMOF. Interestingly, it was found that the DOX release was dependent on the initial DOX loading rate. This finding indicates that CD coatings were promising to accelerate the loading process and facilitates DOX release.

The ssNMR methodology associated to the selective isotope labeling strategy proved efficient for the characterization of this system based on diamagnetic nanoMOF. With further technical developments and adaptation to paramagnetic system, this approach could be useful to characterize other drug delivery systems such as MIL-100(Fe) nanoMOFs.

Supplementary Materials: The following are available online at www.mdpi.com/xxx/s1, Figure S1: FTIR Characterization of the particles before and after drug loading and/or surface functionalization (blue: empty nanoMOFs; dark green: CD-CO; green: nanoMOFs coated with CD-CO; red: nanoMOFs loaded with DOX at TDL of 50%; red dashed line: nanoMOFs loaded with DOX at TDL of 50% and coated with CD-CO). Figure S2: ^{13}C CPMAS NMR spectra of (a) CD-CO coated nanoMIL-100(Al) and (b) 13C-CD-CO coated nanoMIL-100(Al), Figure S3: TGA curve of nanoMOFs (blue)

and CD-CO coated nanoMOFs (green), Figure S4: ^{27}Al MAS NRM spectrum of nanoMIL-100 (bottom) and CD-CO coated nanoMIL-100 (top), Figure S5: ^{1}H (left) and ^{27}Al (right) MAS NMR spectra of (a) CD-CO coated nanoMIL-100(Al) and (b) ^{13}C- CD-CO coated nanoMIL-100(Al), Figure S6: Left: ^{13}C-^{27}Al CP-RESPDOR NMR spectra (left) with non (green) and saturation (blue) of Al nuclei, recorded at 12.5 kHz (9.4 T) at different recoupling time. Right: RESPDOR curves of Line 2 (corresponding to COOAl (CO) and shown in orange) and Line 1 (corresponding to COOAl (MIL-100(Al)) + COOCD (CO) and shown blue).

Author Contributions: Conceived and designed the experiments: R.G., X.L., and C.M.C., Performed the experiments: X.L., M.P., J.Q., and D.C., Performed data analysis: X.L., M.P., J.Q., D.C., C.M.C., and R.G., Wrote the paper: X.L., M.P., R.G., and C.M.C. All authors have read and agreed to the published version of the manuscript.

Funding: This work was supported by a public grant overseen by the French National Research Agency (ANR) as part of the "Investissements d'Avenir" program (Labex NanoSaclay, reference: ANR-10-LABX-0035). MP thanks the Région Centre-Val de Loire for a PhD fellowship. CMC is grateful for financial support from the Institut Universitaire de France (IUF). Financial support from the IR-RMN-THC Fr3050 CNRS for conducting the research is gratefully acknowledged. This work was also supported by the Paris Ile-de-France Region—DIM "Respore".

Acknowledgments: We thank Luc Picton in Institut National des Sciences Appliquées Rouen for the SEC characterization of the synthesized CD-CO and CD-^{13}CO.

Data Availability Statement: Data is contained within the article or supplementary material. The data presented in this study are available in [insert article or supplementary material here].

Conflicts of Interest: The authors declare no conflict of interest.

References

1. Batten, S.R.; Champness, N.R.; Chen, X.-M.; Garcia-Martinez, J.; Kitagawa, S.; Öhrström, L.; O'Keeffe, M.; Suh, M.P.; Reedijk, J. Terminology of metal—Organic frameworks and coordination polymers. *Pure Appl. Chem.* **2013**, *85*, 1715–1724.
2. Stock, N. Synthesis and structures of aluminum-based metal-organic frameworks. *Metal.Org. Framew. Mater.* **2014**, 1–16, doi:10.1002/9781119951438.eibc2197.
3. Feng, Y.; Wang, C.; Ke, F.; Zang, J.; Zhu, J. MIL-100 (Al) gels as an excellent platform loaded with doxorubicin hydrochloride for pH-triggered drug release and anticancer effect. *Nanomaterials* **2018**, *8*, 1–11.
4. Martineau-Corcos, C. NMR crystallography: A tool for the characterization of microporous hybrid solids. *Curr. Opin. Colloid. Interface Sci.* **2018**, *33*, 35–43.
5. Eike Brunner, M.R. Solid-state NMR spectroscopy: An advancing tool to analyse structure and properties of metal-organic frameworks. *Chem Sci.* **2020**, *11*, 4297–4304.
6. Hoffmann, H.C.; Debowski, M.; Müller, P.; Paasch, S.; Senkovska, I.; Kaskel, S.; Brunner, E. Solid-state NMR spectroscopy of metal–organic framework compounds (MOFs). *Materials* **2012**, *5*, 2537–2572.
7. Chen, S.; Mukherjee, S.; Lucier, B.; Guo, Y.; Wong, Y.T.A.; Terskikh, V.V.; Zaworotko, M.J.; Huang, Y. Cleaving carboxyls: Understanding thermally triggered hierarchical pores in the metal − organic framework MIL-121. *J. Am. Chem. Soc.* **2019**, *141*, 14257–14271.
8. Mukherjee, S.; Chen, S.; Bezrukov, A.A.; Mostrom, M.; Terskikh, V.V.; Franz, D.; Wang, S.; Kumar, A.; Chen, M.; Space, B.; et al. Ultramicropore engineering by dehydration to enable molecular sieving of H_2 by calcium trimesate. *Angew. Chem. Int. Ed.* **2020**, *59*, 16188–16194.
9. Haouas, M.; Volkringer, C.; Loiseau, T. Monitoring the activation process of the giant pore MIL-100 (Al) by solid state NMR. *J. Phys Chem C* **2011**, *115*, 17934–17944.
10. Dawson, D.M.; Jamieson, L.E.; Mohideen, M.I.H.; McKinlay, A.C.; Smellie, I.A.; Cadou, R.; Keddie, N.S.; Morris, R.E.; Ashbrook, S.E. High-resolution solid-state 13 C NMR spectroscopy of the paramagnetic metal–organic frameworks, STAM-1 and HKUST-1. *Phys. Chem. Chem. Phys.* **2013**, *15*, 919–929.
11. Li, S.; Lafon, O.; Wang, W.; Wang, Q.; Wang, X.; Li, Y.; Xu, J.; Deng, F. Recent advances of solid-state NMR spectroscopy for microporous materials. *Adv. Mater.* **2020**, *2002879*, 1–22.
12. Mali, G. Looking into metal-organic frameworks with solid- state NMR spectroscopy. *Metal. Org. Framew.* **2016**, 1–24, doi:10.5772/64134.
13. Anand, R.; Borghi, F.; Manoli, F.; Manet, I.; Agostoni, V.; Reschiglian, P.; Gref, R.; Monti, S. Host-guest interactions in Fe(III)-trimesate MOF nanoparticles loaded with doxorubicin. *J. Phys. Chem. B* **2014**, *118*, 8532–8539.
14. Devautour-Vinot, S.; Martineau, C.; Diaby, S.; Ben-Yahia, M.; Miller, S.; Serre, C.; Horcajada, P.; Cunha, D.; Taulelle, F.; Maurin, G. Caffeine confinement into a series of functionalized porous zirconium MOFs : A joint experimental/modeling exploration. *J. Phys. Chem. C* **2013**, *117*, 11694–11704.

15. Skorupska, E.; Jeziorna, A.; Kazmierski, S.; Potrzebowski, M.J. Recent progress in solid-state NMR studies of drugs confined within drug delivery systems. *Solid. State Nucl. Magn. Reson.* **2014**, *57–58*, 2–16.
16. Agostoni, V.; Horcajada, P.; Noiray, M.; Malanga, M.; Aykaç, A.; Jicsinszky, L.; Vargas-Berenguel, A.; Semiramoth, N.; Daoud-Mahammed, S.; Nicolas, V.; et al. A "green" strategy to construct non-covalent, stable and bioactive coatings on porous MOF nanoparticles. *Sci. Rep.* **2015**, *5*, 7925.
17. Porcino, M.; Christodoulou, I.; Dang, M.; Vuong, L.; Gref, R.; Martineau-Corcos, C. New insights on the supramolecular structure of highly porous core–shell drug nanocarriers using solid-state NMR spectroscopy. *RSC Adv.* **2019**, *9*, 32472–32475.
18. Cutrone, G.; Li, X.; Casas-Solvas, J.M.; Menendez-Miranda, M.; Qiu, J.; Benkovics, G.; Constantin, D.; Malanga, M.; Moreira-Alvarez, B.; Costa-Fernandez, J.M.; et al. Design of engineered cyclodextrin derivatives for spontaneous coating of highly porous metal-organic framework nanoparticles in aqueous media. *Nanomaterials* **2019**, *9*, 1–26.
19. Qiu, J.; Li, X.; Steenkeste, K.; Barroca-Aubry, N.; Aymes-Chodur, C.; Roger, P.; Casas-Solvas, J.M.; Vargas-Berenguel, A.; Rihouey, C.; Picton, L.; et al. Self-assembled multifunctional core—Shell highly porous metal—Organic framework nanoparticles. *Int. J. Pharm.* **2020**, *581*, 119281.
20. Anand, R.; Malanga, M.; Manet, I.; Tuza, K.; Aykaç, A.; Ladavière, C.; Fenyvesi, E.; Vargas-Berenguel, A.; Gref, R.; Monti, S. Citric acid–γ-cyclodextrin crosslinked oligomers as carriers for doxorubicin delivery. *Photochem. Photobiol. Sci.* **2013**, *12*, 1841–1854.
21. Martel, B.; Ruffin, D.; Weltrowski, M.; Lekchiri, Y.; Morcellet, M. Water-soluble polymers and gels from the polycondensation between cyclodextrins and poly (carboxylic acid)s: A study of the preparation parameters. *J. Appl. Polym. Sci.* **2004**, *97*, 433–442.
22. Márquez, A.G.; Demessence, A.; Platero-Prats, A.E.; Heurtaux, D.; Horcajada, P.; Serre, C.; Chang, J.-S.; Férey, G.; De La Peña-O'Shea, V.A.; Boissière, C.; et al. Green microwave synthesis of MIL-100 (Al, Cr, Fe) nanoparticles for thin- film elaboration. *Eur. J. Inorg. Chem.* **2012**, *100*, 5165–5174.
23. Li, X.; Lachmanski, L.; Safi, S.; Serre, C.; Grenèche, J.M.; Zhang, J.; Gref, R. New insights into the degradation mechanism of metal-organic frameworks drug carriers. *Sci. Rep.* **2017**, *7*, 1–17.
24. Li, X.; Semiramoth, N.; Hall, S.; et al. Compartmentalized encapsulation of two antibiotics in porous nanoparticles: An efficient strategy to treat intracellular infections. *Part. Part. Syst. Charact.* **2019**, 1800360, doi:10.1002/ppsc.201800360.
25. Cutrone, G.; Qiu, J.; Menendez-Miranda, M.; Tafani, V.; Josse, J.; Laurent, F.; Salzano, G.; Foulkes, D.; Brodin, P.; Majlessi, L.; et al. Comb-like dextran copolymers: A versatile strategy to coat highly porous MOF nanoparticles with a PEG shell. *Carbohydr. Polym.* **2019**, *223*, 115085.
26. Gan, Z. $^{13}C/^{14}N$ heteronuclear multiple-quantum correlation with rotary resonance and REDOR dipolar recoupling. *J. Magn Reson.* **2007**, *184*, 39–43.
27. Hu, B.; Trebosc, J.P.A. Comparison of several hetero-nuclear dipolar recoupling NMR methods to be used in MAS HMQC/HSQC. *J. Magn. Reson.* **2008**, *192*, 112–122.
28. Trebosc, J.; Hu, B.; Amoureux, J.P.; Gan, Z. Through-space R3 -HETCOR experiments between spin-1/2 and half-integer quadrupolar nuclei in solid-state NMR. *J. Magn. Reson.* **2007**, *186*, 220–227.
29. Chen, L.; Wang, Q.; Hu, B.; Lafon, O.; Trebosc, J. Measurement of hetero-nuclear distances using a symmetry-based pulse sequence in solid-state NMR. *Phys. Chem. Chem. Phys.* **2010**, *12*, 9395–9405.
30. Pourpoint, F.; Aany Thankamony, S.L.; Volkringer, C.; Loiseau, T.; Trébosc, J.; Aussenac, F.; Carnevale, D.; Bodenhausen, G.; Vezin, H.; Lafon, O.; et al. Probing 27Al–13C proximities in metal–organic frameworks using dynamic nuclear polarization enhanced NMR spectroscopy. *Chem. Comm.* **2014**, *50*, 933–935.
31. Grant, D.M.; Harris, R.K.E. Encyclopedia of nuclear magnetic resonance. In *Advances in NMR*; Publisher: Wiley 2005; p. 861.
32. Brinkmann, A.; Kentgens, A.P.M. Proton-selective ^{17}O-^{1}H distance measurements in fast magic-angle-spinning solid-state NMR spectroscopy for the determination of hydrogen bond lengths. *J. Am. Chem Soc.* **2006**, *128*, 14758–14759.
33. Massiot, D.; Fayon, F.; Capron, M.; King, I.; Le Calvé, S.; Alonso, B.; Durand, J.-O.; Bujoli, B.; Gan, Z.; Hoatson, G. Modelling one- and two-dimensional solid-state NMR spectra. *Magn. Reson. Chem.* **2002**, *40*, 70–76.
34. Pieper, S.; Langer, K. Doxorubicin-loaded PLGA nanoparticles—A systematic evaluation of preparation techniques and parameters. *Mater. Today Proc.* **2017**, *4*, 188–192.
35. DOXIL® (doxorubicin HCl liposome injection) for intravenous infusion Initial U.S. Manufactured by: Ben Venue Laboratories, Inc. Bedford, OH 44146, Distributed by: Ortho Biotech Products, LP Raritan, NJ 08869-0670, Approval: 1995. 1–33.
36. Xue, T.; Xu, C.; Wang, Y.; Wang, Y.; Tian, H. Doxorubicin-loaded nanoscale metal-organic framework for tumor targeting combined chemotherapy and chemodynamic therapy. *Biomater. Sci.* **2019**, *7*, 4615–4623.
37. Munnier, E.; Tewes, F.; Cohen-Jonathan, S.; Linassier, C.; Douziech-Eyrolles, L.; Marchais, H.; Soucé, M.; Hervé, K.; Dubois, P.; Chourpa, I. On the interaction of doxorubicin with oleate ions: Fluorescence spectroscopy and liquid–liquid extraction study. *Chem. Pharm. Bull.* **2007**, *55*, 1006–1010.
38. Rodriguez-Ruiz, V.; Maksimenko, A.; Anand, R.; Monti, S.; Agostoni, V.; Couvreur, P.; Lampropoulou, M.; Yannakopoulou, K.; Gref, R. Efficient "green" encapsulation of a highly hydrophilic anticancer drug in metal-organic framework nanoparticles. *J. Drug Target.* **2015**, *23*, 759–767.
39. Di-Nunzio, M.R.; Agostoni, V.; Cohen, B.; Gref, R.; Douhal, A. A "ship in a bottle" strategy to load a hydrophilic anticancer drug in porous metal organic framework nanoparticles: Efficient encapsulation, matrix stabilization, and photodelivery. *J. Med. Chem.* **2014**, *57*, 411–420.

Supporting information

Doxorubicin-Loaded Metal-Organic Frameworks Nanoparticles with Engineered Cyclodextrin Coatings: Insights on Drug Location by Solid State NMR Spectroscopy

Xue Li [1,†], Marianna Porcino [2,†], Jingwen Qiu [1], Doru Constantin [3], Charlotte Martineau-Corcos [2,4,*,‡] and Ruxandra Gref [1,*]

[1] Institut des Sciences Moléculaires d'Orsay, UMR CNRS 8214, Paris-Sud University, Université Paris Saclay, 91400 Orsay, France; xue.li@universite-paris-saclay.fr (X.L.); jingwen.qiu@universite-paris-saclay.fr (J.Q.)
[2] CEMHTI UPR CNRS 3079, Université d'Orléans, F-45071 Orléans, France; marianna.porcino@cnrs-orleans.fr
[3] Laboratoire de Physique des Solides, UMR 8502, Université Paris-Sud, 91405 Orsay, France; doru.constantin@universite-paris-saclay.fr
[4] Université Paris Saclay, ILV UMR CNRS 8180, Université de Versailles St-Quentin en Yvelines, 78035 Versailles, France
* Correspondence: ccorcos@cortecnet.com (C.M.-C.); ruxandra.gref@universite-paris-saclay.fr (R.G.); Tel.: +33-(0)-1-30-12-11-31 (C.M.-C.); +33-(0)-1-69-15-82-34 (R.G.)
† These authors contributed equally.
‡ Current Address: CortecNet, 7 avenue du Hoggar, 91940 Les Ulis, France.

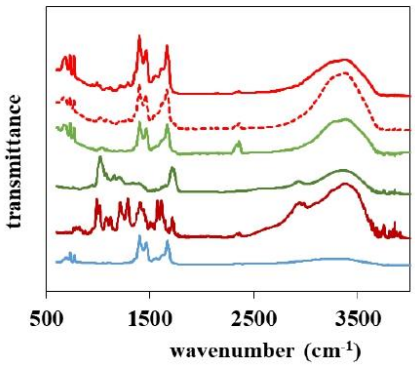

Figure S1 FTIR Characterization of the particles before and after drug loading and/or surface functionalization (blue: empty nanoMOFs; dark red: DOX; dark green: CD-CO; green: nanoMOFs coated with CD-CO; red: nanoMOFs loaded with DOX at TDL of 50%; red dashed line: nanoMOFs loaded with DOX at TDL of 50% and coated with CD-CO).

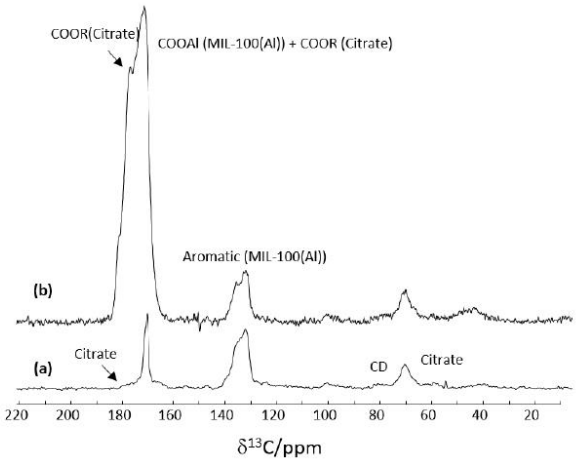

Figure S2 ^{13}C CPMAS NMR spectra of (a) CD-CO coated nanoMIL-100(Al) and (b) ^{13}C-CD-CO coated nanoMIL-100(Al)

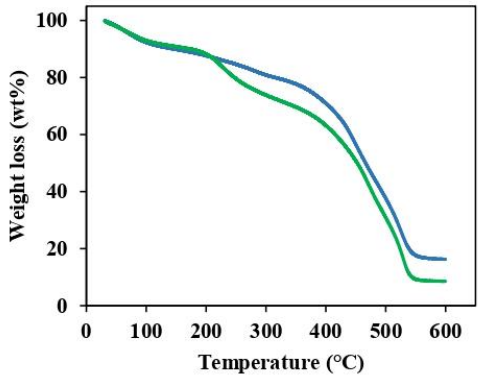

Figure S3. TGA curve of nanoMOFs (blue) and CD-CO coated nanoMOFs (green)

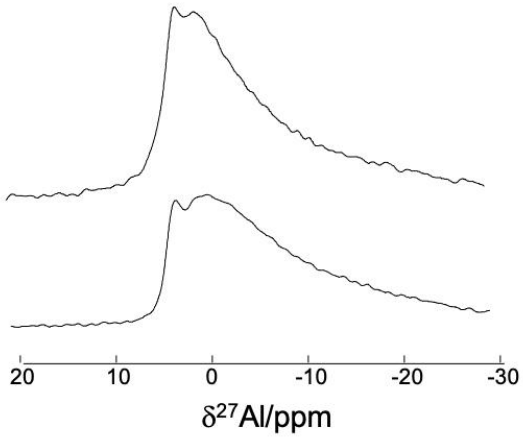

Figure S4. ^{27}Al MAS NMR spectrum of nanoMIL-100 (bottom) and CD-COcoated nanoMIL-100 (top)

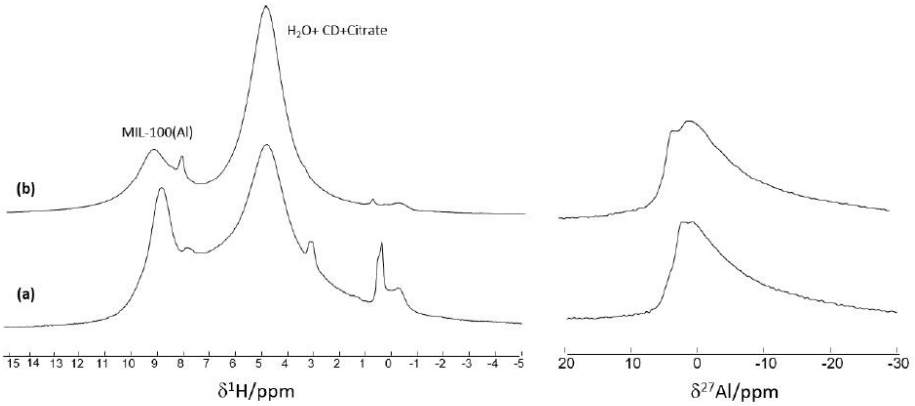

Figure S5. ^{1}H (left) and ^{27}Al (right) MAS NMR spectra of (a) CD-CO coated nanoMIL-100(Al) and (b) ^{13}C- CD-CO coated nanoMIL-100(Al)

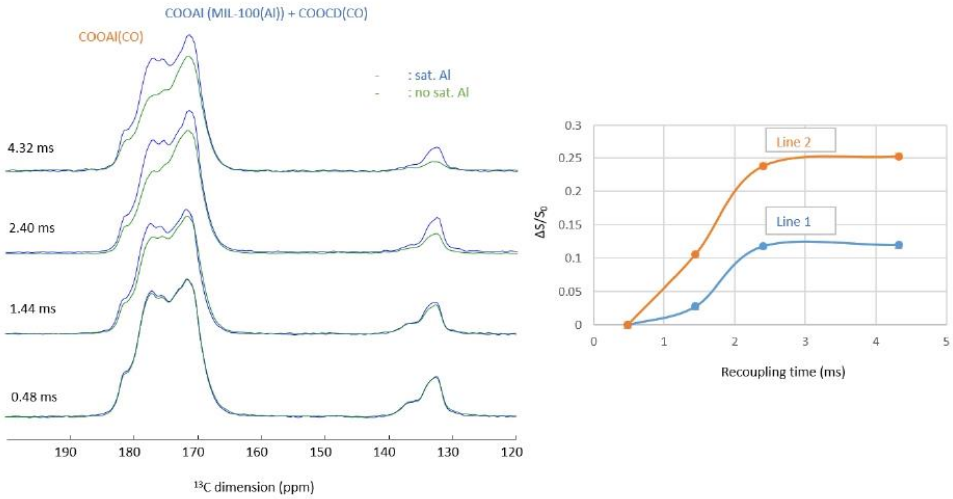

Figure S6. Left: ^{13}C-^{27}Al CP-RESPDOR NMR spectra (left) with non (green) and saturation (blue) of Al nuclei, recorded at 12.5 kHz (9.4 T) at different recoupling time. Right: RESPDOR curves of Line 2 (corresponding to COOAl (CO) and shown in orange) and Line 1 (corresponding to COOAl (MIL-100(Al)) + COOCD (CO) and shown blue)

Chapter 3.3

Porous nanoparticles with engineered shells release their drug cargo in cancer cells

In preparation

General Objectives and Author Contributions

Due to their huge surface areas and high pore volumes, MIL-100 (Fe) was demonstrated to incorporate a large number of drugs, for instance antibiotics and anticancer drugs, which are able to effectively penetrate within the porous MOF structures. Without surface modification, the uncoated nanoMOFs can be easily recognized and taken up by macrophages and removed from the blood circulation. Finally they will never reach the target sites. Therefore, it is crucial to engineer the external surface of nanoMOFs with 'stealth' properties for biomedical applications. Moreover, there are many biological barriers before achieving an efficient drug delivery. These challenges are related to the capacity to target special cells and tissues, and deliver the cargo to particular intracellular zones. Remarkably, in this study, after incorporating DOX in nanoMOFs, it is shown that DOX didn't release at pH 7.4 in both phosphate buffer saline (PBS) and cell culture medium with high payload, but released very fast and totally in artificial lysosomal fluid (ALF) at pH 4.5.

Briefly, this study included four parts:

1) Biodegradable γ-CD-citrate-PEG oligomers were successfully prepared by grafting CD-PEG monomers with citric acid by a simple one-pot reaction. The external surface of the nanoMOFs was modified with γ-CD-citrate-PEG oligomers by a green method (without any organic solvent or surfactant).

2) The anticancer drug DOX was successfully impregnated into the coated nanoMOFs with high payload up to 50wt%, the drug encapsulation was not affected by the surface modification. Moreover, DOX released very fast in artificial lysosomal fluid (ALF), compared with a slow release in PBS or cell culture medium.

3) The anticancer effect of the nanoMOFs loaded with anticancer drug and oligomers-coated was studied by MTT test and visualized by confocal investigations.

4) The PEG "brush" allowed to efficiently escape macrophage uptake, as showed by quantitative determination of the amount of internalized nanoMOFs utilizing inductively coupled plasma mass spectrometry (ICP-MS).

Porous nanoparticles with engineered shells release their drug cargo in cancer cells

Jingwen Qiu[1&], Xue Li[1&], Mahsa Rezaei[1], Gilles Patriarche[2], Juan M. Casas-Solvas[3], Jose Manuel Costa Fernandez[4], Farah Savina[1], Luc Picton[5], Antonio Vargas-Berenguel[3] and Ruxandra Gref[1]*

[1]Université Paris-Saclay, CNRS, Institut des Sciences Moléculaires d'Orsay, 91405, Orsay, France.

[2]Université Paris-Saclay, CNRS, Centre de Nanosciences et de Nanotechnologies (C2N), 91120 Palaiseau, France

[3] Department of Chemistry and Physics, University of Almería, Ctra de Sacramento s/n, 04120 Almería, Spain

[4] Department of Physical and Analytical Chemistry, University of Oviedo, Julián Clavería 8, 33006 Oviedo, Spain

[5] Polymères Biopolymères Surfaces, Normandie Université, UNIROUEN, Institut National des Sciences Appliquées Rouen, CNRS, UMR 6270, 76821 Mont Saint Aignan, France

[&]: These authors contributed equally.

Corresponding Author:

Dr. Ruxandra Gref

Université Paris-Saclay, CNRS, Institut des Sciences Moléculaires d'Orsay, 91405, Orsay, France. Tel: +33 (1) 69158234; E-mail: ruxandra.gref@universite-paris-saclay.fr.

Abstract

Highly porous nanoscale metal–organic frameworks (nanoMOFs) attract growing interest as drug nanocarriers. Engineering "stealth" nanoMOFs with poly(ethylene glycol) (PEG) coatings is challenging as the PEG chains readily penetrate inside the nanoMOFs pores. Here we address the goal of coating nanoMOFs with PEG shells by synthesizing biodegradable cyclodextrin (CD)-based oligomers with a bulky structure (larger than the nanoMOFs pores) to avoid their penetration inside the open porosity. The PEG chains were grafted by click chemistry onto the CDs which were further crosslinked by citric acid. In addition, the free citrate units allowed a spontaneous anchoring of the coatings onto the nanoMOFs by complex formation with the iron sites in the top layers. Stable coatings representing around 31 wt% were achieved. The anticancer drug doxorubicin (DOX) was successfully entrapped in the core-shell nanoMOFs with loadings up to 41 wt%. High resolution TEM (HRTEM) showed that the organized crystalline structures were preserved. Remarkably, at the highest loadings, DOX was not released out at pH 7.4, but at pH 4.5 of artificial lysosomal fluid. Confocal microscopy investigations showed that the DOX-loaded nanoMOFs penetrated inside Hela cancer cell together with their PEG shells. Then, they released the drug which further diffused inside the nucleus to eradicate the cancer cells.

1 Introduction

Metal-organic frameworks (MOFs), first reported in 1989 (Hoskins and Robson, 1989), are one of the latest classes of ordered crystalline hybrid solids. They attract growing interest because of their versatile architectures and compositions. They are tuned based on the nearly unlimited possible coordination of almost any metal and a variety of organic ligands (carboxylates, phosphonates, sulfonates or imidazolates, etc.), leading to thousands of MOFs with various pore sizes and shapes (He et al., 2021; Horcajada et al., 2012; Simon-Yarza et al., 2018). Iron(III) polycarboxylates-based nanoscale MOFs (nanoMOFs), especially MIL-100 (Fe) (MIL stands for Materials from Institut Lavoisier) are among the most studied for biomedical applications as they were proven to be biodegradable and non-toxic (Agostoni et al., 2013; Baati et al., 2013; Quijia et al., 2021); (Simon-Yarza et al., 2016, 2017). They were shown to incorporate high payloads of hydrophilic, amphiphilic and hydrophobic drugs including anticancer, antiviral and antibiotics. (Agostoni et al., 2013; Horcajada et al., 2012; Li et al., 2020b, 2019a; Rodriguez-Ruiz et al., 2015) ; (Anand et al., 2014; Chalati et al., 2011; Di Nunzio et al., 2014; Rezaei et al., 2018; Singco et al., 2016). However, as for other type of nanoparticles (NPs), the *in vivo* fate of nanoMOFs in the living body (biodistribution, pharmacokinetics and targeting abilities) strongly depends upon their surface physicochemical properties. Bare nanoMOFs can be easily taken up by macrophages and eliminated from the blood circulation, preventing them from reaching the tumor sites (Baati et al., 2013; Simon-yarza et al., 2016). Therefore, it is of outmost importance to functionalize the surface of the nanoMOFs with shells able to confer them "stealth" properties for biomedical applications.

Since long, it was revealed that surface modification with hydrophilic polymers such as poly (ethylene glycol) (PEG) in a "brush" configuration could significantly prolong the NPs' blood circulation times by reducing their recognition by the reticuloendothelial system (Gref et al., 1995, 1994). Numerous PEGylated drugs are currently used in the treatment of cancer, hepatitis

and hemophilia ("FDA approved PEGylated drugs 2021," 2021). However, there are still scarce examples of PEGylated NPs approved by the Food and Drug Administration (FDA): the first PEGylated liposome Doxil® was approved in 1995 (Barenholz, 2012), and the micellar formulation Genexol-PM made using PEG-based block copolymers was approved in 2007 in Korea and marketed in Europe (Pillai, 2014).

However, engineering the surface of porous MOFs with PEG shells remains very challenging as compared to liposomes or dense NPs made of biodegradable polymers. Indeed, the PEG chains can readily penetrate into the nanoMOF pores, releasing the encapsulated drugs in an uncontrolled manner (Agostoni et al., 2015). Recently, in order to avoid PEG penetration into the highly porous MOFs, acryl PEGs were polymerized onto the surface by a GraftFast method (Giménez-Marqués et al., 2018). However, this polymerization method does not allow a precise control of the molecular weight of the resulting PEG-based copolymers.

As an alternative, we previously developed a PEG-based shell by click chemistry (Cutrone et al., 2019b). A block copolymer was synthesized by coupling onto a dextran (DEX) backbone two types of moieties: 1) PEG chains to reduce macrophage uptake and 2) alendronate (ALN) to enable a strong coordinative interaction with the nanoMOFs' surface. Both PEG and ALE contents were well controlled by click chemistry, however, the synthesis method involved many steps and the resulting copolymers were non-biodegradable.

Herein, biodegradable shells based on PEG and γ-cyclodextrin (CD) were successfully synthesized. First, CD-PEG monomers were prepared, where each CD was linked to a PEG 2000 g/mole polymer. They were crosslinked with citric acid, leading to the formation of CD-PEG-CO oligomers. Moreover, the citrate moieties played a major role in anchoring the oligomers onto the external surface of the nanoMOFs, due to strong coordination with the available iron sites from the nanoMOFs. The bulky structure of CD-PEG-CO prevented the

PEG chains from penetrating inside the 3D nanoMOFs networks, allowing for the formation of PEG shells to evade the recognition by macrophages. What's more, the surface modification didn't influence the drug encapsulation. The drug of interest was doxorubicin (DOX), an anticancer molecule widely employed to treat many types of carcinoma, soft tissue sarcomas, and hematological malignancies (Aryal et al., 2009; Jong Oh Kim, Alexander V. Kabanov, 2009; Wang et al., 2017). As known, when administered as a free molecule, DOX lacks tumor-targeting ability resulting in poor biodistribution and low therapeutic efficacy as well as severe side effects (Lee et al., 2010; Wang et al., 2017).

Different drug delivery systems have been used to encapsulate DOX, including FDA-approved liposomal DOX formulations (Pegylated Doxil®, Lipodox® and non-pegylated Myocet®), and pre-clinical delivery platforms such as polymeric NPs, metal NPs, micelles, emulsions, gels, DNA intercalated NPs, targeted NPs etc (Zhao et al., 2018). More recently, nanoMOFs emerged as a new type of NPs for DOX encapsulation due to their high drug loading capacity (Anand et al., 2014; Bhattacharjee et al., 2020; Di Nunzio et al., 2014; Giménez-Marqués et al., 2018; Qiu et al., 2020; Zhu et al., 2016). For example, DOX loading in nanoMOF gels made of MIL-100(Al) (MIL stands for Material of Institute Lavoisier) reached up to 62 wt%. Moreover, a pH-triggered DOX release was reported, with less than 10% DOX released out in 100 h in phosphate buffer saline (PBS) at pH 7.4 and more than 90% DOX release in 50 h in PBS at pH 5.5. The biocompatible iron trimesate MIL-100 (Fe) nanoMOFs were further investigated as drug carriers for DOX and maximal reported payloads reached 65 wt% (Qiu et al., 2020). A pH responsive release was reported by Xue *et al* (Xue et al., 2019), with 66% release at pH 5.5 after 60 h, while only 37% and 30% DOX were released at pH 6.8 and 7.4 after 60 h, respectively. However, the porous nanoMOFs were not coated in these studies.

A more systematical study was carried on here, incorporating DOX at different payloads in MIL-100(Fe) nanoMOFs coated or not with CD-PEG-CO and studying its release in various

media. The optimized DOX formulations didn't release their content at pH 7.4 (PBS and cell culture medium), but rapidly released DOX in artificial lysosomal fluid (ALF) at pH 4.5. The anticancer efficacy of the drug loaded and surface-modified nanoMOFs with was evaluated. The ability of the engineered nanoMOFs to evade macrophage uptake and to get internalized in cancer cells was also investigated. Cell internalization was visualized by confocal microscopy and quantified by inductively coupled plasma mass spectrometry (ICP-MS). The core-shell nanoMOFs demonstrated a high versatility in terms of functionalities and DOX controlled release.

2 Experimental

2.1 Materials and reagents

Chemical materials. Potassium chloride (KCl, Sigma-Aldrich, ≥99%), sodium phosphate monobasic dihydrate (NaH_2PO_4. $2H_2O$, Sigma-Aldrich, ≥99%), γ-cyclodextrin (γ-CD, Cyclolab, Budapest, Hungary, ≥90%), dimethylsulfoxide (DMSO, ACS), phosphate-buffered saline (PBS, Gibco) and RPMI (Roswell Park Memorial Institute) 1640 medium (Gibco) were purchased from commercial sources and used without further purification otherwise indicated. sodium chloride (NaCl, Sigma-Aldrich, ≥99.5%), sodium hydroxide (NaOH, Emsure®, ≥99.0%), citric acid (Sigma-Aldrich, 99.0%), calcium chloride ($CaCl_2$, Sigma-Aldrich, ≥99.0%), disodium phosphate (Na_2HPO_4, Sigma-Aldrich, ≥99.0%), sodium sulfate (Na_2SO_4, abcr Gmbh, Germany, 99.0%), Magnesium chloride ($MgCl_2$, Sigma-Aldrich, ≥98.0%), glycerin (Sigma-Aldrich, ≥99.0%), citrate sodium dihydrate (Sigma-Aldrich, ≥99.0%), sodium tartrate dehydrate (abcr Gmbh, Germany, ≥99.0%), sodium pyruvate (Fluka, 99.0%) were used for the preparation of artificial lysosomal fluid (Table S1). Iron (III) chloride hexahydrate ($FeCl_3$. $6H_2O$, Alfa Aesar, Schiltigheim, France, 98%), 1,3,5-benzenetricarboxylic acid (BTC, Sigma-

Aldrich, Saint-Quentin-Fallavier, France, 95%) and absolute ethanol (EtOH, Carlo Erba, Val-de-Reuil, France, 99%) were used for the synthesis of MIL-100 (Fe). Water was purified by a Millipore MilliQ system. Doxorubicin hydrochloride (DOX, Sigma-Aldrich, 98%), and Deferoxamine mesylate salt (DFOM, Sigma-Aldrich, 92.5%), were used for drug encapsulation and drug release studies. latrunculin A (LA, Sigma-Aldrich, ≥85%) and cytochalasin D (CyD, Sigma-Aldrich, 98%) were used for inhibitors.

Cell culture. Murine macrophage cell line J774.1 *(ATCC® TIB-67™)* was grown in Dulbecco's Modified Eagle's Medium (DMEM, ThermoFisher Scientific, Villebon-sur-Yvette, France) supplemented with 10% v/v decomplemented fetal bovine serum (FBS) (ThermoFisher Scientific, Villebon-sur-Yvette, France) and 1% v/v Penicillin-Streptomycin (P/S, 5,000 U/mL, ThermoFisher Scientific, Villebon-sur-Yvette, France) at 37°C in humidified air containing 5% CO_2. HeLa cells (ATCC® CCL-2™) were cultured in DMEM supplemented with 10% v/v FBS and 1% P/S at 37°C in humidified air containing 5% CO_2. Thiazolyl blue tetrazolium bromide (MTT, Sigma-Aldrich, St. Quentin Fallavier, France) was used for toxicity evaluation of nanoMOFs.

2.2 General methods

2.2.1. Synthesis and characterization of CD-PEG-CO

Synthesis of CD-PEG-CO. The oligomers were obtained by crosslinking the CD-PEG monomers using citric acid, by adapting a previously reported procedure(Qiu et al., 2020). To find the optimal conditions, the molar ratio of monomer, citric acid and catalyst ($NaH_2PO_4 \cdot 2H_2O$) was varied over a large range (from 1:5:2 to 1:30:4).

An aqueous reaction mixture was prepared by solubilizing in a 25 mL round-bottom flask (100 mg, 0.03 mmol) CD-PEG and various amounts of catalyst, and citric acid in 2 mL water. This solution was then evaporated under magnetic stirring for 10 min at 140 °C, and the resulting

dried mixture underwent a treatment at 140 °C for 15 ~ 30 min under reduced pressure (10–15 mmHg) in a system connected to a suction pump. A yellowish product was obtained in the bottom of the flask. Then, 8 mL deionized water was added and the crude was sonicated for 3 min, followed by filtration in order to separate the insoluble fraction from the soluble part. The soluble fraction was recovered and dialyzed for 48 h with a cellulose membrane (20 kDa or 50 kDa, Spectrum Laboratories, Rancho Dominguez, US). The solution was finally dried using a freeze dryer to yield a slightly yellow powder. In addition, CD-CO and CD-CO-Cy5 were synthesized as previously reported (Qiu et al., 2020).

The compositions of synthesized CD-PEG-CO and γ-CD-citrate oligomers (CD-CO) were evaluated by proton nuclear magnetic resonance (^{1}H-NMR) spectroscopy. ^{1}H-NMR spectra were recorded in D_2O using a Bruker Avance 360 MHz. The citric acid/ CD-PEG molar ratio in the products was estimated by integrating the peaks assigned to 4 protons of the citric acid methylene group divided by 3 methyl protons of CD-PEG units. This allowed calculating the relative monomer:citrate molar ratios in the oligomers, and further have an estimation of the CD-PEG wt% contents, by taking into account the respective molecular weights of CD-PEG (3374 g/mol) and citrate (192 g/mol) moieties.

Size-exclusion chromatography (SEC), coupled on-line with multiangle light scattering (MALS) and refractive index (RI) detectors (SEC/MALS/RI, Wyatt Technology, Santa Barbara, USA), was used to determine the average molecular weight values of CD-PEG CO, using a dn/dc value of 0.14 mL/g(Puskás et al., 2013), two OHPAK SB 804/OHPAK SB806 HQ columns, and 0.1 M $LiNO_3$ as eluent. Data were determined thanks to the Astra® 6.1.1 software from Wyatt Technology using Zimm order 1 between 44.8° and 140°.

2.2.2 Synthesis and characterization of MIL-100 (Fe) nanoMOFs

Iron trimesate nanoMOFs MIL-100 (Fe) were synthesized by using a previously described

hydrothermal method assisted by microwave irradiation (Agostoni et al., 2013). Concisely, 20 mL of an aqueous mixture containing 0.84 g BTC and 2.43 g iron (III) chloride hexahydrate was heated at 130 °C for a short time (6.0 min) under stirring by microwave irradiation (Mars-5, CEM, USA). The nanoMOFs were harvested by centrifugation at 10,000 g for 10 min and purified by washing with absolute ethanol 6 times, to remove unreacted BTC and discard aggregates. The crystallinity was investigated by X-ray powder diffraction (XRPD) using a homemade setup based on a copper rotating anode generator (RU-200BEH, Rigaku Ltd., Tokyo, Japan), as previously described by our group(Li et al., 2021; Qiu et al., 2020). The samples were filled in round glass capillaries (1.5 mm in diameter, WJM-Glas Müller GmbH, Berlin, Germany). The X-ray beam was filtered and focused by a confocal system (CMF-12-38Cu6 from Osmic Inc., Cleveland, OH, USA). The accessible scattering vector range was 0.035 ~ 0.5 $Å^{-1}$.

The hydrodynamic diameters and size distributions were determined by dynamic light scattering (DLS, Malvern Nano-ZS, Zetasizer Nano series, France). The nanoMOFs BET (Brunauer-Emmett-Teller) surface area was evaluated by nitrogen sorption experiments at −196 °C using an ASAP 2020 (Micromeritics, USA) after degassing at 100 °C for 16 h under secondary vacuum. NanoMOFs were kept in EtOH at room temperature and re-suspended in aqueous media before use.

2.2.3. Surface modification of nanoMOFs with CD-PEG-CO

NanoMOFs were centrifuged at 6,000 g for 10 min to remove the storage solvent (ethanol) and then re-dispersed in water by vortex. For the coating procedure, they were incubated at room temperature with different initial amounts of CD-PEG-CO (at the weight ratio CD-PEG-CO: nanoMOFs of 1:10 ~ 1:1). After 1 day incubation, the non-attached CD-PEG-CO fraction was removed by centrifugation (10,000 g, 10 min). The same method was employed to coat the

nanoMOFs with CD-CO.

2.2.4. Characterization of CD-PEG-CO coated nanoMOFs

Morphologies of nanoMOFs, before and after surface modification and/or drug loading were investigated using a JEOL 1400 transmission electron microscope (TEM, 120 kV, Japan). The crystallinity of the particles was characterized by X-ray powder diffraction (XRPD), as previously mentioned.

STEM associated with elemental chemical energy-dispersive X-ray spectroscopy (EDX) cartography was used to evaluate the elemental (C, O, N, S, Cl and Fe) distribution in the particles. The MIL-100 (Fe) nanoMOFs coated or not with CD-PEG-CO and loaded or not with DOX were placed on a copper grid covered with a pure carbon membrane. The STEM observations were made on a Titan Themis 200 microscope (FEI/Thermo Fischer Scientific) equipped with a geometric aberration corrector on the probe. This microscope was also equipped with the "Super-X" systems for EDX analysis with a detection angle of 0.9 sr. The observations were made at 200 kV with a probe current of about 70 pA and a half-angle of convergence of 24 mrad. High-angle annular dark-field (HAADF)-STEM images were acquired with a camera length of 110 mm (inner/outer collection angles were respectively 69 mrad and 200 mrad).

Colloidal stability investigation. Colloidal stabilities of CD-PEG-CO coated nanoMOFs in water were evaluated by DLS. Mean hydrodynamic diameters were measured at 0, 1, 2, 6, 10, and 14 days storage at 25 °C. Zeta potential (ZP) of nanoMOFs were determined at 25 °C using a Zetasizer instrument (Malvern Nano-ZS, Zetasizer Nano series, France) in a pH range of 1 to 10. For the measurements, nanoMOFs were diluted using a KCl solution (1 mM) to a final concentration of 100 μg/mL.

Thermogravimetric analyses (TGA) analyses were used to quantify the amount of coating materials attached on the surface of nanoMOFs using a TGA 4000 Instruments (Perkin Elmer, 100–240 V/50–60 Hz) using our previous protocol(Qiu et al., 2020). During analysis, samples were submitted to an O_2 flow of approximately 20 mL/min. Around 10 mg of nanoMOF samples, coated or not, were heated from 25 to 600 °C at a rate of 3 °C/min. Prior to the TGA analysis, the samples were dried overnight at 60 °C to remove the absorbed water. The associated amounts of CD-PEG-CO (wt%) were calculated with respect to dry MIL-100(Fe) nanoMOFs weight.

2.2.5 DOX encapsulation in CD-PEG-CO or CD-CO coated nanoMOFs

MIL-100(Fe) nanoMOFs suspension (8 mg/mL) was first centrifuged at 10,000 g for 10 min to recover the nanoMOFs, which were further re-suspended in water. For the DOX encapsulation, 0.25 mL of nanoMOFs aqueous suspension (4 mg/mL) was mixed with different volumes of DOX solution (5 mg/mL), with or without 125 μL CD-PEG-CO (4 mg/mL) or CD-CO (4 mg/mL). The final volume was adjusted to 1 mL. Theoretical drug loading (TDL), calculated as the weight ratio (%) between DOX and nanoMOFs, was in the range of 10–100%. The resulting suspensions were gently stirred for 1 to 6 days at room temperature to allow DOX incorporation. Then, 1 mL of nanoMOF suspensions were centrifuged (17,000 g, 15 min) and both supernatants and pellets were recovered to assess the amounts of incorporated DOX.

The supernatants were used to quantify the drug payload, which was calculated as Eq. (1):

$$Payload\ (\%) = \frac{\text{Encapsulated Drug (mg)}}{\text{NanoMOFs (mg)}} \times 100 \qquad (1)$$

Encapsulation efficiency (EE) was calculated, as according to Equation (2):

$$EE\ (\%) = \frac{\text{Encapsulated Drug (mg)}}{\text{Initial Drug (mg)}} \times 100 \qquad (2)$$

DOX quantification was performed using fluorescence spectrometry with the excitation (λ_{ex})

and emission (λ_{em}) at 500 and 590 nm, respectively. DOX in the supernatant was diluted with a water/DMSO mixture (1:1 v/v), to dissociate the complexes γ-CD: DOX. Calibration curves of DOX were obtained between an interval of 10^{-3} to 10^{-4} mg·mL^{-1} (correlation coefficient > 0.999). Pellets were digested in 1 mL of DFOM (10 mg/mL in PBS), then incubated at 37ºC in a rotator with a rotational speed of 200 rpm for overnight, then diluted with a water/DMSO mixture (1:1 v/v) to determine DOX payloads.

2.2.6 Release of DOX from MIL−100 (Fe)

The DOX release experiments were performed by incubating the nanoMOFs in different media (PBS, RPMI, AFL and water) at 37 °C in a rotator with a rotational speed of 200 rpm. At periodic time intervals, 1 mL of the suspensions (100 μg/mL) were centrifuged (17,000 g, 15 min) and the supernatants were recovered for DOX quantification.

The DOX concentration in the supernatant media was analyzed by fluorescence spectrometry. The percentage of the released DOX was calculated as Eq. (3):

$$Released\ DOX\ (\%) = \frac{\text{DOX amount in the supernantant}}{\text{DOX amount loaded in nanoMOFs}} \times 100 \quad (3)$$

The release study was further confirmed by digesting the pellet in 1mL of DFOM (10 mg/mL in PBS), then incubated at 37ºC in a rotator with a rotational speed of 200 rpm for overnight, after that diluted with water/DMSO mixture (1:1 v/v) to determine the amount of DOX in the pellets.

2.2.7 NanoMOF interaction with macrophages

NanoMOFs quantification inside cells using ICP-MS. The amounts of nanoMOFs internalized inside the cells were determined by iron quantification using ICP-MS. Briefly, macrophage cells (J774A.1) were seeded as previously described. Cells treated or not with

inhibitors were then incubated with 50 µg/mL nanoMOFs coated or not with CD-PEG-CO or CD-CO for 4 h. Then, the cells were washed with PBS for three times to eliminate the nanoMOFs in the medium. Four different wells were used to prepare the cells at one condition, where the cells in one well were counted and the cells in other three wells were finally dried at 60°C for 2 h and digested using *aqua regia* (15 minutes under sonication) for Fe quantification. Fe quantification was carried out by ICP-MS (Agilent 8800) as previously reported (Cutrone et al., 2019b, 2019a; Li et al., 2020b). Co was added at a concentration of 10 µg/L as internal standard. Fe and Co isotopes were detected using "on-mass mode" ($54Fe^+$, $56Fe^+$, $59Co^+$). Fe was finally quantified using external calibration prepared from certified 1000 mg/L Fe standard solution (Merck, Germany).

2.2.8 Anticancer efficacy of drug loaded particles evaluated on Hela cells

Confocal visualization. Hela cells were seed at the density of 3.0×10^4 cells/well on sterile glass slides placed at the bottom of each well and let incubate overnight. Then, nanoMOFs empty or loaded with DOX (at TDL of 20%, and 50%) and coated or not with CD-CO-Cy5 and CD-PEG-CO (50 wt%) were added at a concentration of 50 µg/mL in each well. By simply mixing with CD-PEG-CO, the nanoMOFs were efficiently labelled after incubation overnight. After incubation with living cells for 2 h, 6 h, and 24 h, cells were washed three times with PBS to remove free particles. The living cells were visualized using a confocal microscope (LEICA SP5 system), equipped with a CO_2 regulated (5% CO_2) and a thermostatically controlled chamber (37°C). DOX and Cy5 were excited at 488 nm and 614 nm, respectively. The emissions from 550-650 nm and 650-750 nm were collected for DOX and Cy5, respectively. The images were processed with the Image J software.

NanoMOFs internalization in Hela cells quantified by ICP-MS. The same protocol for J774A.1 cells was used for Hela cells, but no inhibitor was used. The internalized nanoMOFs were directly quantified by ICP-MS as described in section 2.2.7.

Cytotoxicity assays. The cytotoxicity of nanoMOF samples, with and without coatings and loaded or not with DOX was evaluated by MTT. First, Hela cells were seeded in 96 well plates at the density of 1.0×10^4 cells/well and incubated overnight. Then, the Hela cells were exposed to various concentrations (0-100 µg/mL) of nanoMOFs coated or not with CD-CO/CD-PEG-CO and/or loaded with DOX (at TDL of 20%). After 24 h incubation, all the medium in the wells was removed and excess unbounded nanoMOFs were discarded by rinsing two times with PBS. Then, the cells were incubated for another 4 h with an MTT solution (100 µl, 500 µg/mL). Finally, 100 µl DMSO was introduced in each well to dissolve the formazan crystals followed by absorbance detection using a plate reader (GloMax® Discover Microplate Reader, Promega) at the wavelength of 490 nm.

3 Results and discussion

3.1 Synthesis and characterization of CD-PEG oligomers

Synthesis of CD-PEG oligomers.

Prior to CD-PEG oligomers synthesis, the CD-PEG monomer was successfully synthesized by click chemistry.

The CD-PEG oligomers were synthesized by adjusting a previous method reported for CD-CO (Qiu et al., 2020) (Scheme 1). The polymerization reaction between CD-PEG and citric acid was investigated by optimizing the heating time and the molar ratio between CD-PEG, citrate acid and catalyst. The different synthesis conditions are summarized in Table 1.

Table 1. Optimization of the CD-PEG-CO synthesis conditions. Influence of the molar ratio of the reactants and the catalyst on the average weight and number molar masses Mw and Mn, and

on the polydispersity Đ and polymerization yield.

Series	CD-PEG:citric acid: catalyst (molar ratio)	Total heating time (min)	M_n (g/mol)	M_w (g/mol)	Đ	Yield (%)
1	1:5:2	25	7500	13000	1.7	35
2	1:5:2	30	7600	36800	4.8	30
3	1:5:2	35	8400	29200	3.5	33
4	1:5:2	40	11200	52600	4.7	35
5	1:10:2	25	10000	14300	1.4	35
6	1:10:4	25	12900	22100	1.7	33
7	1:15:4	25	19000	33600	1.8	34
8	1:20:4	25	14700	23000	1.6	30
9	1:30:4	25	9600	37500	3.9	32
10	1:10:10	25	13800	24300	1.7	35
11	1:15:15	25	25300	160000	6.3	32
12	1:15:4	25	30700	53400	1.7	23
13	1:20:4	25	24200	35600	1.5	22
14	1:10:4	25	21300	35100	1.6	21
15	1:10:10	25	21600	50300	2.3	20

20 kDa and a 50 kDa cut-off dialysis membrane were used for the dialysis of entries 1-11 and 12-15, respectively.

Initially, the reaction mixture was concentrated by evaporation, and the resulting dried mixture was heated at 140 °C for other 15–30 min under reduced pressure (entries 1–4). The average molar masses (Mn) increased with the heating time from 7500 to 11200 g/mole for 25 min and

40 min, respectively, whereas the polymerization yield was practically unchanged (30-35 %).

However, the polydispersity increased from 1.7 (25 min) to 4.7 (40 min) (entries 1–4,) which could be possibly explained by random crosslinking in between the CD-PEG monomers in the viscous reaction mixture. Therefore, to maintain low polydispersity values, the total heating time was fixed at 25 min, and the molar ratio among CD-PEG, citrate acid and catalyst was systematically investigated (entries 5–11). It is found that when the molar ratio among CD-PEG, citrate acid and catalyst was 1:15:4, the Mw was high (33,600 g/mole), with acceptable polydispersity (Đ=1.8) (entry 7). Furthermore, the oligomers with the lowest molar masses were removed by purification by dialysis using a membrane with a cutoff of 50 kDa, resulting in a series of copolymers with large Mw (entries 12-15; SEC chromatograms can be found in Fig. S1). The best condition was entry 12, corresponding to a Mw of 53400 g/mole and Đ=1.7. The composition of this CD-PEG-CO copolymer and of the corresponding CD-PEG monomer were assessed by ^{1}H-NMR spectroscopy (Figs. S2-S3). Fig. S3 shows that as expected, the composition of CD-PEG corresponds to one PEG chain grafted to each CD unit, in average.

In the case of CD-PEG-CO, the characteristic peak of citric acid (f) was well observed, indicating its efficient incorporation in the copolymers (Fig. S3). The citric acid/CD-PEG molar ratio was estimated by integrating the peaks assigned to the 4 protons of the citric acid methylene groups (f) and the three methyl (a) protons of the CD units. The molar ratio: citric acid/CD-PEG was found as 5.9, corresponding to a CD-PEG-CO with an average composition $(CD\text{-}PEG)_{12}$ $(citrate)_{72,}$ with high PEG contents (45 wt%).

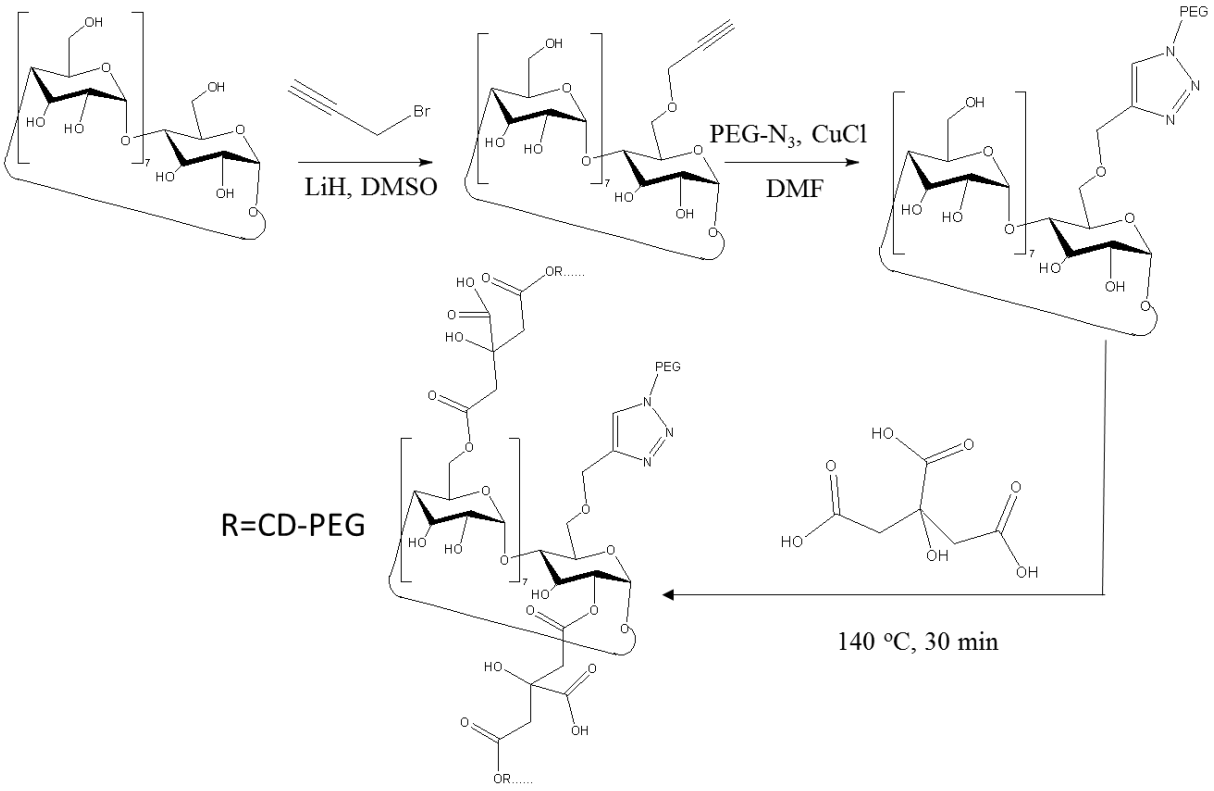

Scheme 1: Synthesis of CD-PEG monomer and CD-PEG-CO.

The optimized copolymer (entry 12) was further used in all the coating studies. Besides, in order to track the localization of nanoMOFs in cells using confocal microscopy, a fluorescent CD-CO-Cy5 copolymer was synthesized to allow stable fluorescent coating onto the nanoMOFs, as previously described (Qiu et al., 2020). Made by crosslinking CD-Cy5 monomers with citric acid, it had an average molar mass of 31050 g/mol, and a polydispersity Đ=1.6.

3.2 Surface modification of MIL-100(Fe) nanoMOFs with CD-PEG-CO and their physicochemical characterizations

The porous nanoMOFs were successfully synthesized with a mean hydrodynamic diameter of 255 ± 14 nm and a BET surface area of 1750 ± 45 m^2g^{-1}. They exhibited a facetted morphology (Fig. 1A) as previously reported (Agostoni et al., 2013) and were well crystallized according to

XRPD patterns (Fig. 1E). Furthermore, high resolution STEM investigations clearly evidenced the crystalline structures with well delimited planes (Fig.2). It was possible to access to the nanoMOFs' 6-fold symmetry and interplanar spacings (Fig. S4). The obtained values of 2.61 and 1.52 nm correspond well to the 220 (2.55 nm) and 422 (1.48 nm) crystalline planes of the cubic structure of the MIL100 Fe (a: 0.7234 nm) (Agostoni et al., 2013; Horcajada et al., 2007).

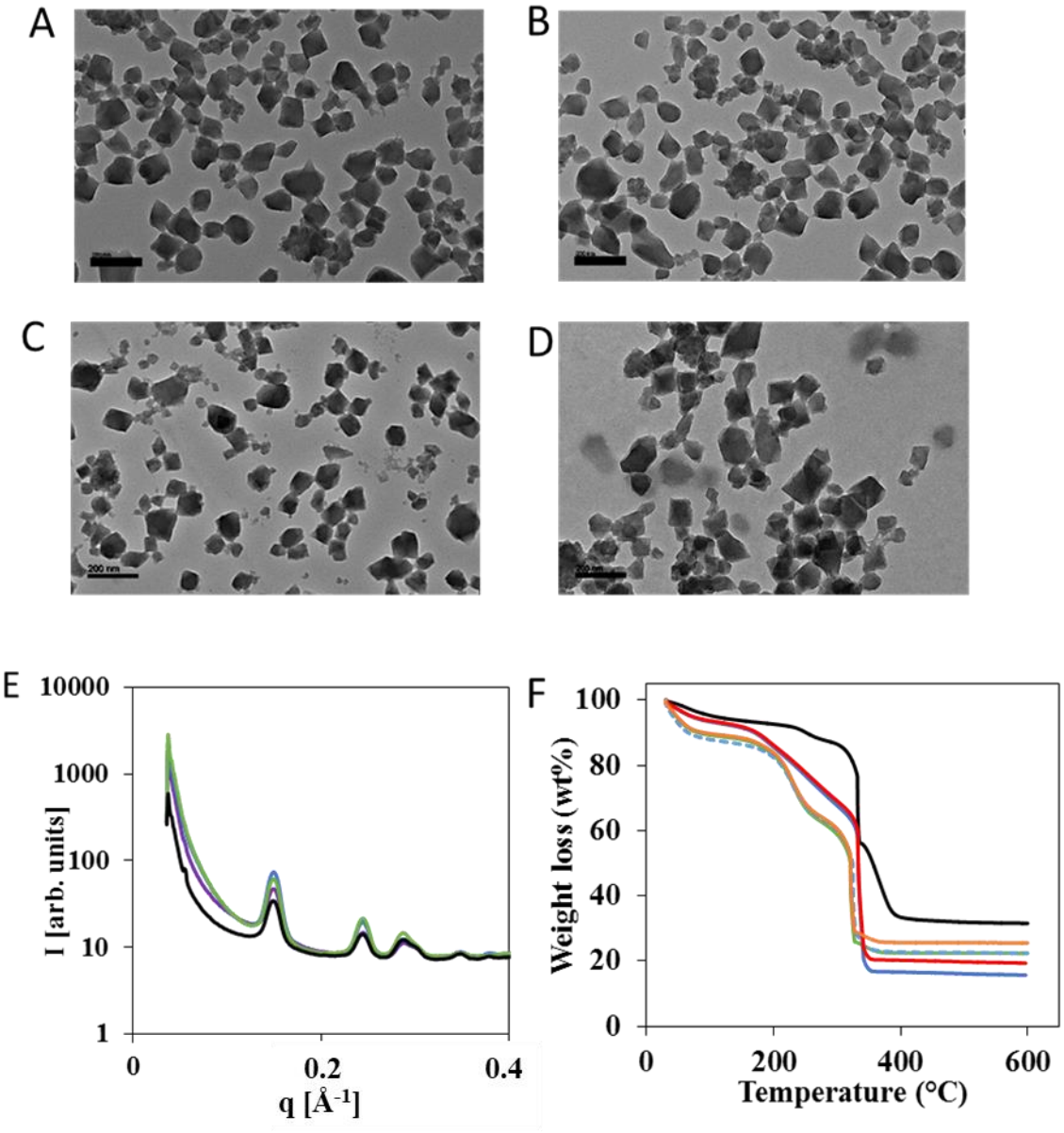

Figure 1 TEM images of nanoMOFs, before (A) and after (B) surface modification with 29 wt% CD-PEG-CO; loaded with 18 wt% DOX (C); coated with 29 wt% CD-PEG-CO and loaded with 18 wt% DOX (D); scale bar: 200 nm; XRPD patterns of uncoated nanoMOFs (black solid

line), loaded with 18 wt% DOX (purple in solid line), coated with 29 wt% CD-PEG-CO (blue line), coated with 29 wt% CD-PEG-CO and loaded with 18 wt% DOX (green solid line) XRPD patterns (E), and TGA (F) of uncoated nanoMOFs (black), nanoMOFs coated with CD-PEG-CO (orange: 24 wt%, blue dotted line : 29 wt%; green: 32 wt%), 42% DOX loaded nanoMOFs (red), coated with 29 wt% CD-PEG-CO and loaded with 42 wt% DOX (blue).

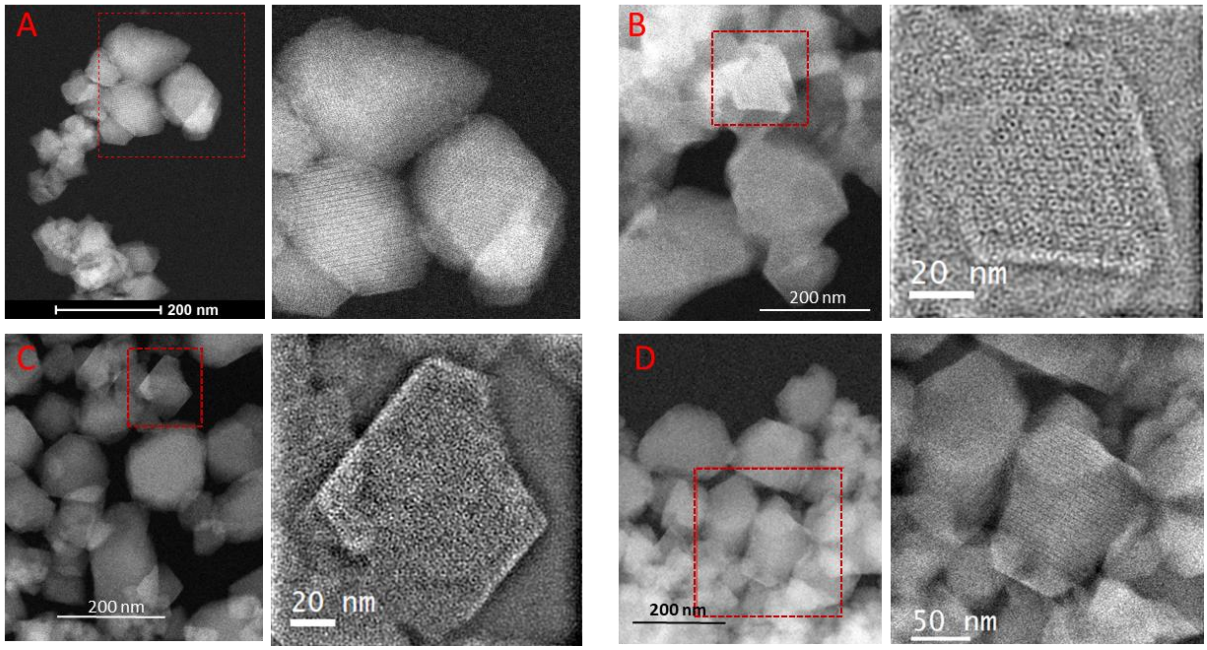

Figure 2 STEM images of nanoMOFs: empty nanoMOFs (A); MOFs loaded with 18 wt% DOX (B); MOFs loaded with 18 wt% DOX and coated with 29 wt% CD-PEG-CO (C); MOFs loaded with 42 wt% DOX (D).

Surface modification of nanoMOFs with CD-PEG-CO was achieved by a "green" method (free of organic solvents and surfactants), consisting in a one-step incubation at room temperature of the nanoMOFs in an aqueous solution of the synthesized oligomers. The procedure was similar to the one described to coat similar MIL-100(Fe) nanoMOFs with CD-CO oligomers (Qiu et al., 2020) or with phosphorylated CD derivatives (Agostoni et al., 2015). After overnight incubation, CD-PEG-CO coated nanoMOFs were harvested by centrifugation and the amount

of CD-PEG-CO associated to the nanoMOFs was determined by TGA (Fig. 1F). In the thermograms of the uncoated nanoMOFs, it can be observed that a residual inorganic Fe_2O_3 material (~35 wt%) remained at 600 °C, in agreement with our previous reports (Qiu et al., 2020). The amount of residual material was diminished in the case of CD-PEG-CO coated nanoMOFs, to 25±2 wt%, 26±2 wt% and 27±2 wt% when the CD-PEG-CO: nanoMOFs weight ratio in the coating procedure was 1:1, 1:2 and 1:3, respectively. This correspond to CD-PEG-CO associated amounts of 32±2, 29±2 and 24±2 wt%, respectively.

In conclusion, the maximal amount of CD-PEG-CO associated to the nanoMOFs in these studies reached to around 32 wt%, which is in the same order of magnitude as in the case of other PEGylated coatings such as those obtained by GraftFast (29 wt%)(Giménez-Marqués et al., 2018), and by using comb-like PEGylated dextran copolymers (32 wt%)(Cutrone et al., 2019b). Noteworthy, the amount is twice higher than for CD-Phosphate-PEG coatings (16 wt%)(Cutrone et al., 2019a). The strong affinity of numerous carboxyl groups in CD-PEG-CO for the iron sites on the nanoMOFs' surface most probably accounts for this efficient association. There is no significant difference in terms of the CD-PEG-CO associated amount between the samples prepared at weight ratio CD-PEG-CO: nanoMOFs of 1:1 and 1:2, however, the coating yields were 32% and 58%, respectively. Therefore, the coating condition was fixed to a weight ratio CD-PEG-CO: nanoMOFs of 1:2 for the following studies.

Remarkably, the CD-PEG-CO coated nanoMOFs maintained their size, facetted morphology (Fig. 1B) and crystalline structure (Fig. 1E) despite the high amounts of associated coatings. There was a slight size increase in hydrodynamic diameters, from 255 ± 14 nm to 268 ± 15 nm, before and after CD-PEG-CO coating, respectively (Fig. S5) which could be due to the presence of the shell.

Furthermore, in contrast to the uncoated nanoMOFs, the CD-PEG-CO coated ones were stable upon storage up to 2 weeks (less than 15% size variation, Fig. S5). The presence of the CD-

PEG-CO coating was further supported by the significant ZP variations as compared to uncoated particles (Fig. 3B). The first observation was that the ZP of the nanoMOFs, before and after surface modification, was strongly dependent upon the pH (in a range of 1~10) of the suspension media, in agreement with previous reports (Li et al., 2019a). The ZP of as-synthesized nanoMOFs was positive (+24±2 mV) at pH 5, but shifted to negative values (-15±3 mV) at the same pH value after coating with CD-PEG-CO. This is possibly due to the presence of citrate-based coatings with a negative charge, as reported in previous studies (Cutrone et al., 2019b).

3.3 DOX encapsulation and drug release

After the successful surface functionalization, DOX was encapsulated as drug of interest to evaluate if the core-shell NPs are able to encapsulate and release drug cargoes. First of all, DOX encapsulation was performed by simply incubating the nanoMOFs in aqueous DOX solutions under gentle rotating agitation at room temperature. Fig. 3 A indicates the kinetics of DOX incorporation in 6 days quantified by fluorescence spectroscopy. Briefly, DOX loading kinetics were studied at different DOX initial amounts while the TDL of DOX was 10%, 20%, and 50%. When TDL was 10%, the DOX payload reached 9±0.2 wt% within 1 day and plateaued in 2 days at 9.6±0.2 wt%, indicating the excellent DOX encapsulation efficiency up to 96%. When TDL was increased to 20%, the DOX payload plateaued in 3 days at 19±1.0 wt%, corresponding to more than 95% of DOX encapsulation efficiency. Remarkably, the DOX payload reached up to 32±1.5 wt% after 1 day impregnation when TDL was 50%. It further mounted to 41±2 wt% after 6 days impregnation. Complementary TGA experiments confirmed these findings (Fig. 1F) showing a 42±2 wt% DOX payload.

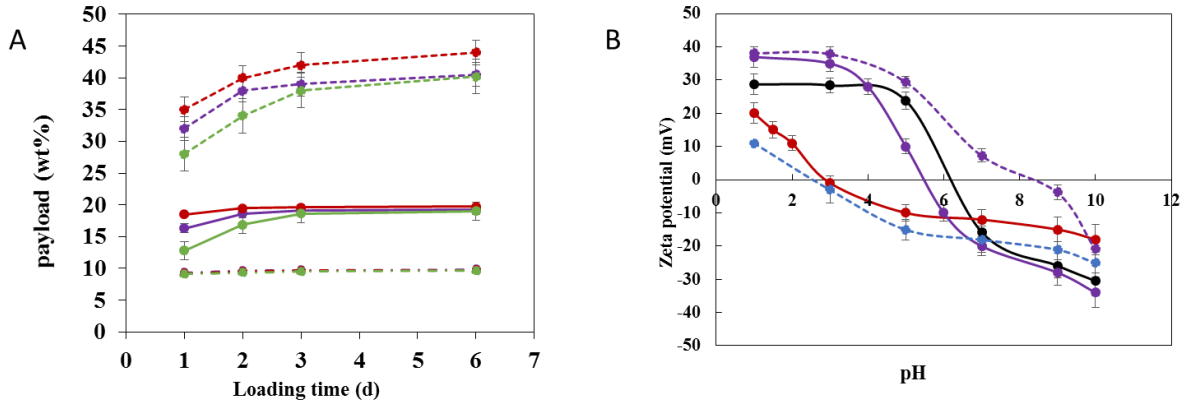

Figure 3 DOX loading and surface charge of DOX loaded nanoMOFs, coated or not with CD-CO/CD-PEG-CO. A: DOX loading kinetics in bare nanoMOFs (purple), and nanoMOFs coated with CD-PEG-CO (green) or CD-CO (red) when TDL was 50 wt% (dashed line ----), 20 wt% (continuous line) and 10 wt% (dashed line – · – · ·). B: Zeta potential of empty nanoMOFs (black), 19±1 wt% DOX loaded nanoMOFs (purple solid line), 41±2 wt% DOX loaded nanoMOFs (purple dashed line) and 29 wt% CD-PEG-CO coated nanoMOFs 19±1 wt% DOX loaded (red solid line) or not (blue dashed line) with DOX. The same color code is used in A and B.

These results clearly showed that MIL-100(Fe) nanoMOFs act as "nanosponges", effectively adsorbing DOX in their cages. Surprisingly, when the TDL was increased to 100%, the DOX payload reached up to 65±3.0 wt% (Fig. S6), which is similar to the reported DOX loading (62 wt%) in MIL-100 (Al) metal-organic gels (Feng et al., 2018). However, this DOX loaded amount is theoretically larger than the available nanoMOF pore volume (Agostoni et al., 2013), suggesting that DOX most probably be located both inside the pores and on the surface of the nanoMOFs. This hypothesis was supported by ZP investigations, before and after DOX loading (Fig. 3B).

At the DOX payload of 19±1 wt%, there was no significant ZP variation between loaded and unloaded nanoMOFs in the pH range from 7 to 10. On the contrary, ZP significantly shifted to more positive values when DOX payload increased to 41±2 wt%. As an example, ZP values were -16±4 mV and +7±2 mV for empty nanoMOFs and DOX loaded nanoMOFs, respectively, at a pH of 7. This could possibly be attributed to the cationic character of DOX located at the nanoMOFs' surface (Unnier et al., 2007). This supports the hypothesis of DOX location in the nanoMOFs' top layers at highest (41 ± 2 %) drug loadings as compared to 19±1wt%.

The maximal DOX payload in MIL-100 (Fe) nanoMOFs reported in the literature was 33 wt% (Xue et al., 2019) but in these studies, only a one day impregnation time was investigated. The DOX loading in other type of NPs was much lower. For instance, DOX payload in the commercial Doxil® (DOX-loaded liposomes) (Barenholz, 2012) and poly-lactic-co-glycolic acid (PLGA) (Pieper and Langer, 2017) was less than 15 wt%. Altogether, these data highlight the affinity of DOX for MIL-100(Fe) nanoMOFs.

Noteworthy, whatever the DOX loadings, the nanoMOFs' faceted morphology was preserved, before and after DOX encapsulation, as shown by TEM investigations (Fig. 1C). In addition, at the highest DOX loading (42 wt%), the cages of the nanoMOFs were well observed (Fig. 2B and 2D). PXRD patterns of DOX-loaded nanoMOFs demonstrated that the crystalline structure of the MIL-100 (Fe) nanoMOFs was maintained despite of their unprecedented DOX payloads (Fig. 1E). Advantageously, regardless of their DOX loading, all the nanoMOFs samples were stable for at least two weeks. (Fig. S5).

Interestingly, the surface modification with CD-CO and CD-PEG-CO didn't significantly affect the DOX loading (Fig. 3A). Due to the guest-host inclusion between DOX and γ-CD, CD-CO accelerated the drug loading process, in agreement with our previous investigations (Qiu et al., 2020).

Finally, there were no significant differences in the drug loading values, at the plateau reached after 6 days impregnation. When the DOX TDL was 50%, the measured DOX loadings were 41±2 wt%, 44±3 wt%, and 40±2 wt% for bare nanoMOFs, nanoMOFs coated with CD-CO, and CD-PEG-CO, respectively.

Similarly, when the DOX TDL was 20%, the DOX payloads were 15±2% and 17±3%, for nanoMOFs coated or not with CD-PEG-CO. Moreover, despite the high drug loading and surface modification with CD-PEG-CO, the nanoMOFs maintained their crystalline structures (Fig. 1E) and facetted morphologies (Fig. 2C). Complementary investigations were carried out by EDX to gain further insights on DOX distribution within the nanoMOFs and to estimate the individual nanoMOFs drug loadings. To track the drug, EDX mappings of Cl and N elements specific of DOX and not present in nanoMOFs were performed (Fig. 4). Only Cl mapping gave reliable information, as the N signal was shielded by the large signals arising from C and O. Table 2 summarizes the estimated drug loadings of randomly chosen nanoMOFs. In average, the DL was 15.7±1.9 and 15.2±3.9 wt% for the uncoated and CD-PEG-CO coated nanoMOFs, respectively. The EXD data are just estimations of the loadings, but the results clearly prove that the nanoMOFs are homogeneous in terms of composition and that the presence of the CD-PEG-CO coatings do not influence the drug loading.

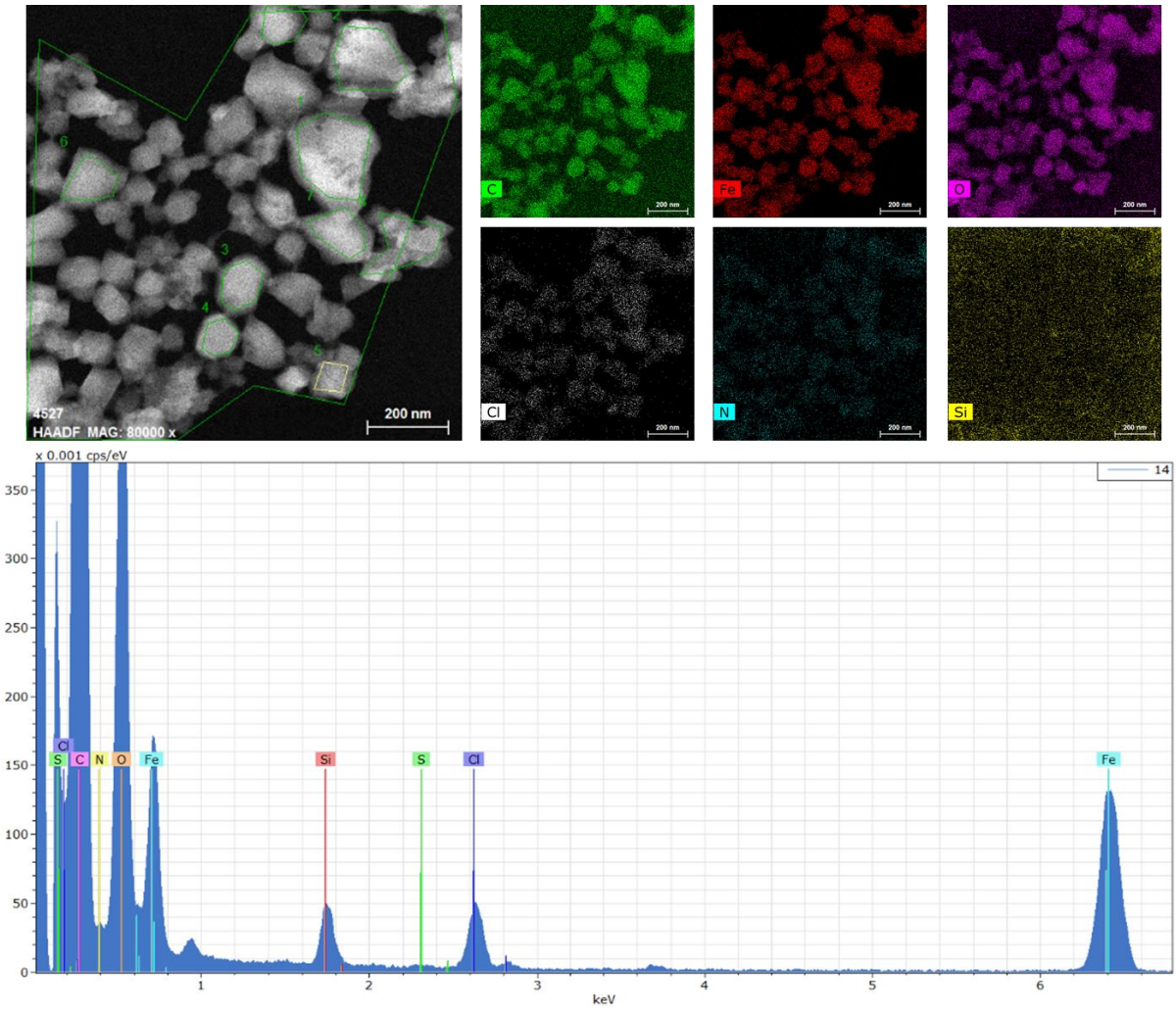

Figure 4 STEM-EDX images of DOX-loaded nanoMOFs (18 wt%) coated by CD-PEG-CO (29 wt%). Mapping of the constitutive C, Fe, O, Cl and N elements. Si signal arises from the support.

Table 2 Experimental Fe/Cl weight ratios of a series of DOX-loaded nanoMOFs; 1.1-1.9 are DOX loaded nanoMOFs (18 wt%), 2.1-2.9 are DOX loaded (18 wt%) and CD-PEG-CO (29 wt%) coated nanoMOFs

series	Fe/Cl (wt%)	DOX payload (%)
1.1	10.6	21.0
1.2	11.0	19.5
1.3	11.1	19.1
1.4	11.5	16.6
1.5	11.5	16.6
1.6	11.7	16.2
1.7	11.7	16.2
1.8	11.8	16.0
1.9	14.5	13.6
Average	11.7±1.2	15.7±1.9
2.1	10.4	21.3

2.2	10.5	21.1
2.3	11.6	16.4
2.4	12.2	15.6
2.5	13.1	14.6
2.6	14.4	13.7
2.7	15.4	12.7
2.8	17.1	11.1
2.9	17.8	10.5
Average	13.6±2.7	15.2±3.9

DOX release studies were further carried out systematically in different media, i.e. simulated physiological medium (PBS buffer), cell culture medium (RPMI), and simulated intracellular medium (ALF). As shown in Fig. 5, the DOX release is dependent on the drug loading. At low DOX payload (9.6±0.2 wt%), DOX release in both PBS (pH = 7.4) and RPMI (pH = 8.0) approached 12 ± 1.2% within 6 h, and it reached 88 ± 2.3% and 70 ± 2.2% in 1 month (Fig. 5 A and B).

When the DOX payload increased to 19 ± 1.0 wt%, DOX released amounts were reduced. For example, only 9 ± 0.4% and 60 ± 2.0% DOX amounts were released in PBS in 6 h and 1 month, respectively. Similar release profiles were found for DOX release in RPMI (9 ± 1.0% and 38 ± 3.0% for DOX release in 6 h and 1 month, respectively). At high DOX payload of 41 ± 2.1 wt%, DOX didn't release in both PBS and RPMI within 48 h (<1%) and there were only 16 ± 3.2% and 12 ± 1.0% released in 1 month in PBS and RPMI, respectively. These results were confirmed by quantifying the DOX amount in the pellet, For instance, when the DOX payload was 19±1.0 wt%, only 9.2±0.3% and 61±1.8.0% DOX amounts were released in PBS in 6 h and 1 month, respectively.

The incomplete DOX release at high loadings could be explained by the self-association of the drug molecules confined inside the nanoMOFs cages. Similar results were reported in the case of topotecan-loaded MIL-100(Fe) nanoMOFs (Di Nunzio et al., 2014). When concentrated inside the cages, topotecan was prone to aggregate by π-stacking and the formed cluster were too large to be released out.

In contrast, the DOX release rate was remarkably increased in ALF (pH = 4.5) for all the studied cases (Fig. 5C, and Fig. S7). For instance, there was around 90±3% and 94±2% DOX release in 6 h and 24 h when loaded at 9.6±1 wt% (Fig. S7). Even at DOX loading of 41±2 wt%, a very high DOX release up to 86±3% was observed in 24 h (Fig. 5C). Interestingly, the "burst" effect was significantly reduced when the DOX-loaded nanoMOFs were coated with CD-CO or CD-PEG-CO (64±1%, 46±1% and 42±3% was released in 1 h from bare nanoMOFs, nanoMOFs coated with CD-CO, and CD-PEG-CO, respectively). However, all the samples reached a similar plateau (80-90% release) in 24 h. Noteworthy, non-released DOX could be extracted from the nanoMOFs using DFOM, after the plateau was reached. Results were in agreement with HPLC data, confirming that the release was not complete.

These drug release profiles clearly show that the DOX release behavior can be controlled by the amount of entrapped drug molecules and by the composition of the release media. Such a behavior is of interest in the design of DOX nanocarriers for cancer treatment (Aryal et al., 2009; Jong Oh Kim, Alexander V. Kabanov, 2009; Lee et al., 2010; Wang et al., 2017). Indeed, if administered by intravenous injection, the DOX-loaded nanoMOFs developed here could preserve their DOX payloads in physiological media at pH 7.4, contributing to significantly decrease the DOX side effects in normal tissues, especially heart. In contrast, DOX would be released out of the nanoMOFs once they get internalized in the targeted cells. Indeed, it was shown here that, once the DOX loaded nanoMOFs were internalized in the cells most probably by endocytosis, DOX was rapidly released out and efficiently killed the cancer cells. Moreover, to the best of our knowledge, it is the first time to report that DOX at high loading can be released out (>85%) from nanoMOFs in 24 h.

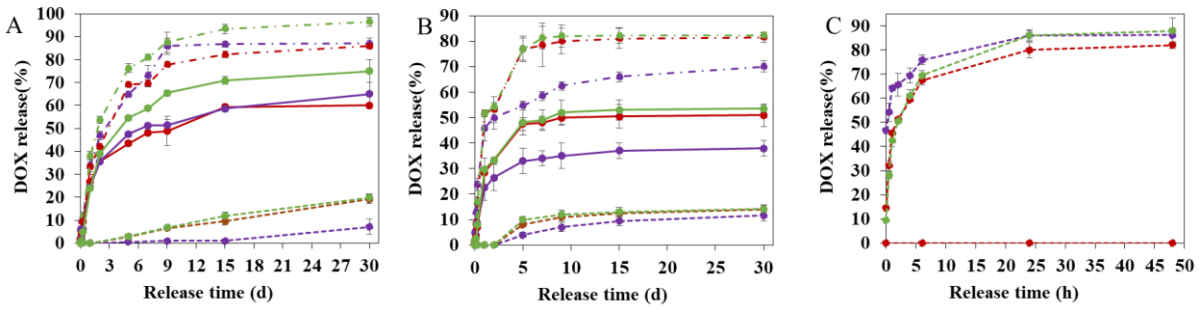

Figure 5 DOX release in PBS (A); in RPMI (B); in artificial lysosomal fluid (C) : DOX in bare nanoMOFs (purple), and nanoMOFs coated with CD-PEG-CO (green) or CD-CO (red) when TDL was 50% (dashed line ----), TDL was 20% (straight line), and TDL was 10% (dashed line – · –). DOX loadings were 41±2 wt%, 44±3 wt%, and 40±2 wt% for bare nanoMOFs, nanoMOFs coated with CD-CO, and CD-PEG-CO (dashed line ----); 19.2±0.9 wt%, 19.7±1 wt%, and 19±0.6 wt% for bare nanoMOFs, nanoMOFs coated with CD-CO, and CD-PEG-CO (straight line); 9.8±0.2 wt%, 9.7±0.2 wt%, and 9.6±0.2 wt% for bare nanoMOFs, nanoMOFs coated with CD-CO, and CD-PEG-CO (dashed line – · –).

After the systematic characterization of DOX loading, surface functionalization, and drug release, we investigated the biological effect of the prepared formulations. Firstly, the stealth effect of CD-PEG-CO modified nanoMOFs was evaluated *in vitro* on macrophages (J774A.1 cells). The quantity of nanoMOFs internalized in the J774 was determined using ICP-MS as previously described (Cutrone et al., 2019b). This quantification of iron content in cells was performed to study the nanoMOFs cellular uptake. Around 75% uncoated nano-MOFs/3×10^5 cells were taken up by J774A.1 cells after 4 h incubation, thus showing that macrophages avidly took up uncoated nanoMOFs, in agreement with our previous results (Cutrone et al., 2019a, 2019b; Li et al., 2020b). There was about 70% CD-CO coated nanoMOFs internalized in macrophages, meaning that the CD-CO coating didn't have stealth effect. Interestingly, the presence of the CD-PEG-CO coating reduced the nanoMOFs internalization to 50% at the same

incubation time. What's more, the internalized amount of CD-PEG-CO coated nanoMOFs was further reduced to 35% and 40% in the presence of the inhibitors latrunculin A and cytochalasin D, respectively (Fig. S8), which block actin polymerization and hence disrupt microfilament-mediated internalization, manifesting the role of phagocytosis. These results are agreement with our previous studies (Li et al., 2019a).

3.4 Cytotoxicity assays of nanoMOFs on cervical cancer cells

All the studied nanoMOFs, coated or not, were nontoxic for the Hela cervical cancer cells up to 100 µg/mL (Fig. 6A), with more than 87% cell viability after 24 h incubation, which is in line with previous reports (Baati et al., 2013; Bellido et al., 2015; Giménez-marqués et al., 2018; Horcajada et al., 2010; Li et al., 2019a). Noteworthy, the newly synthesized CD-CO and CD-PEG-CO oligomers were not toxic neither, up to 100 µg/mL. In contrast, as expected, the anticancer drug DOX (Fig. 6B, blue histograms) exerted a cytotoxic effect with 67% cell viability at 1 µg/mL, which further diminished to 33% at 5 µg/mL. Indeed, free DOX molecules are efficient in eradicating cancer cells, since they can easily pass through their cell membrane and reach the nuclei. In this context, the engineered nanoMOFs could play a role *in vivo*, acting as nanocarriers which maintain their DOX cargo until they reach the cancer cells, where they would release DOX, thus reducing DOX toxicity in healthy organs. Keeping these aspects in mind, preliminary *in vitro* studies were carried on here. The cytotoxicity of DOX-loaded nanoMOFs was dependent on their internalization inside the cancer cells (Fig. 7). According to ICP-MS quantifications, around 15% of the nanoMOFs put in contact with the Hela cells were internalized after 24 h incubation. For example, when DOX loaded nanoMOFs was incubated with Hela cells at DOX concentration of 5 µg/mL, the internalized DOX was around 0.75 µg/mL. Taking into account the amount of internalized nanoMOFs, the DOX loaded nanoMOFs didn't significantly affect the DOX efficacy (60% and 67% for DOX loaded nanoMOFs at 5 µg/mL and free DOX at 1 µg/mL, respectively). These results are in agreement

with reported data (Xue et al., 2019), where around 65% cell viability was observed for MCF-7 cells after 24 h incubation with DOX-loaded MIL-100(Fe) nanoMOFs.

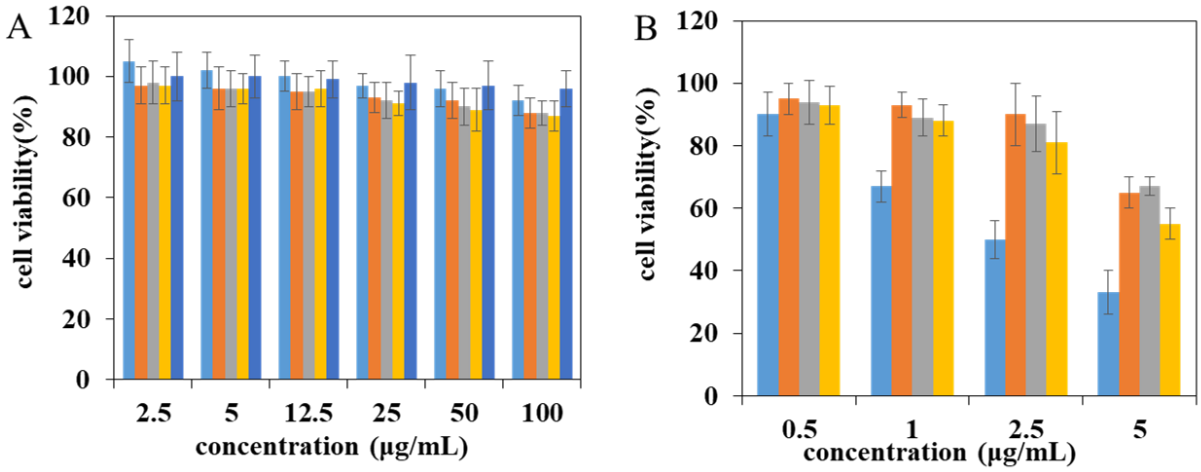

Figure 6 A: A: Cell viability of HeLa cells incubated for 24 h with CD-PEG-CO (light blue), CD-CO (orange), 29 wt% CD-PEG-CO coated nanoMOFs (grey), 42 wt% CD-CO coated nanoMOFs (yellow) and nanoMOFs (dark blue). Component concentrations were 2.5 µg/mL, 5 µg/mL, 12.5 µg/mL, 25 µg/mL, 50 µg/mL, and 100 µg/mL; B: Cell viability of HeLa cells incubated 24 h with free DOX (light blue), 18 wt% DOX loaded nanoMOFs (orange), 42 wt% CD-CO coated and 18 wt% DOX loaded nanoMOFs (grey), 29 wt% CD-PEG-CO coated and 18 wt% DOX loaded nanoMOFs (yellow). The equivalent DOX concentrations in all samples were 0.5µg/mL, 1 µg/mL, 2.5 µg/mL and 5 µg/mL.

The amounts of internalized nanoMOFs (15%) in Hela were in agreement with previous studies showing the efficient internalization of nanoMOFs coated or not, in pancreatic, breast, ovarian or bladder cancer cell lines (Li et al., 2020b, 2019a; Rodriguez-Ruiz et al., 2015; Wuttke et al., 2015). It was shown that nanoMOFs acted as “Trojan horses” by internalizing inside the cancer cells, carrying their drug cargo to eradicate cancer cells (Li et al., 2019b). In this study it was shown that interestingly, the presence of a CD-based coating (PEGylated or not) did not reduce the nanoMOF anticancer efficacy on Hela cells.

3.5 Localization of nanoMOF in Hela cells

The internalization of nanoMOF in Hela cells was further investigated using confocal microscopy. To do so, fluorescent CD-CO was synthesized as previously described by crosslinking CD-Cy5 with citric acid (Qiu et al., 2020) and was used as coating to track the nanoMOF internalization and intracellular stability of the coating material. The fluorescent dye Cy5 with Ex/Em of 647/666 was chosen in order to avoid overlapping with the signal rising from DOX molecules (Ex/Em=470/593). The CD-CO-Cy5 coating showed a low detachment from the nanoMOFs in cell culture medium (< 25% after 24 h incubation). Thus, taking advantage of the fluorescent DOX molecules and the low drug release in cell culture medium (< 10% in 24 h, Fig. 5), the drug localization was also visualized simultaneously with the coating.

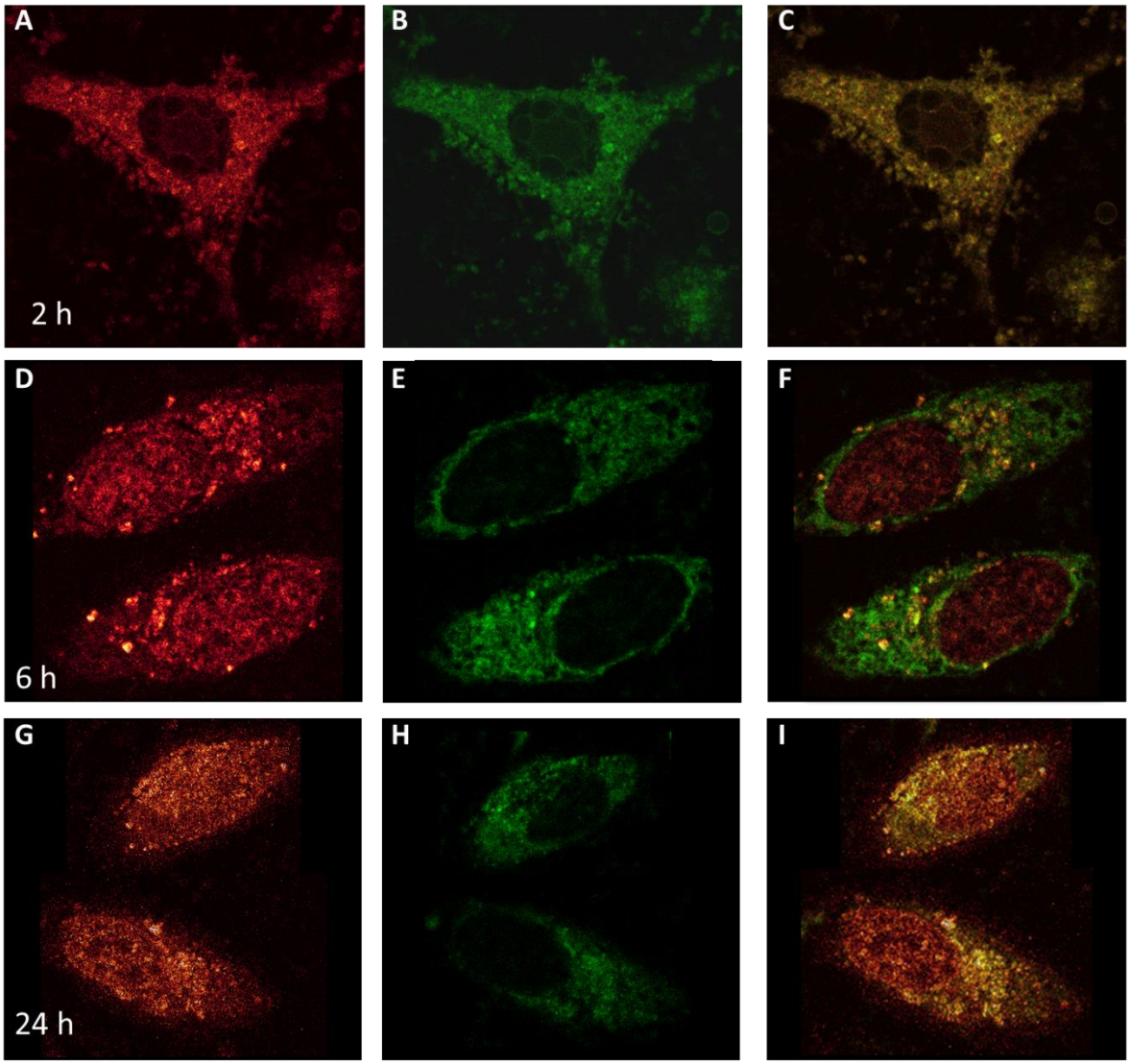

Figure 7 Confocal images of Hela cells incubated with DOX loaded nanoMOFs coated with CD-CO-Cy5 and CD-PEG-CO after 2 h (A-C), 6 h (D-F), and 24 h (G-I) incubation. The signal of DOX was recorded in red (left pannel), Cy5 in green (middle pannel), and the overlay was shown in the right pannel.

As shown in Fig. 7, after 2 h incubation, the nanoMOFs were efficiently internalized inside Hela cells maintaining their coatings and the encapsulated DOX. Indeed, the green (Cy5-labelled coating) and red (DOX) signals were colocalized (Fig. 7C). The nanoMOFs preferentially located in the cytoplasm at early stage, and no fluorescent signal was found in

the nuclei. These findings suggest that the nanoMOFs' coatings were intact bearing and the incorporated DOX was not released. This is in agreement with the reported confocal images in the case of DOX loaded mesoporous silica NPs modified with poly acrylic acid(Minati et al., 2013), where DOX signal was observed only in cytoplasm after 2 h incubation. However, the coating material was not labelled in this case.

In the case of DOX-loaded MIL-100 nanoMOFs with CD-PEG-CO coating, after 6 h incubation, the situation was totally different and the two fluorescent signals were not colocalized anymore: DOX diffused into the nucleus but the coating material remained in the cytoplasm (Fig. 7F). This suggests that the coating materials most probably detached from nanoMOFs. This is in agreement with previous reports that nanoMOFs didn't penetrate inside the cell nuclei (Li et al., 2020a) and that nanoMOFs were prone to degraded within a few hours inside cells (Li et al., 2019a), releasing the drug cargos. Similar phenomenon was observed in the case of DOX loaded nanoassemblies composed of poly (ethylene glycol)-β-cyclodextrin and a disulfide-containing adamantine-terminated doxorubicin prodrug (Xiong et al., 2018). DOX started to penetrate inside the cell nuclei after 8 h incubation with HepG2 cells. In the case of DOX-loaded mesoporous silica NPs coated with poly acrylic acid, the authors reported that DOX was mainly located in cell nuclei after 17 h incubation. However, no intermediate incubation times were investigated between 2 and 17 h (Minati et al., 2013).

Presumably, in the case studied here, the DOX molecules released out of the nanoMOFs exerted their cytotoxic effect in the nucleus by the well-known mechanisms consisting in intercalating within DNA base pairs, causing breakage of DNA strands and inhibition of both DNA and RNA synthesis (Johnson-arbor and Dubey, 2020). Indeed, after 24 h interaction with the DOX-loaded nanoMOFs, the Hela cells were practically all eradicated, and the few remaining cells showed shrinked morphologies and reduced nuclei sizes. In addition, the Cy5 also started to quench, exhibiting a much less bright fluorescent intensity. In a nutshell, these studies demonstrates that

nanoMOFs localized in the cytoplasm where they degraded, releasing the coating materials from the shell and the DOX molecules from the core. The detached coating shell remained in the cytoplasm, whereas the released DOX diffused inside the nucleus, causing DNA damage.

4. **Conclusion**

A series of CD-PEG-CO water-soluble oligomers were successfully synthesized, reaching molecular weights up to 53 kD and low polydispersities of 1.7. They spontaneously anchored onto the surface of MIL-100(Fe) nanoMOFs in aqueous media forming stable coatings. The surface modification didn't significantly affect the nanoMOFs' DOX loading capacity. DOX loadings reached 64±3%, and the presence of the shell didn't interfere with the nanoMOF incorporation capacity. Remarkably, DOX didn't release out (<1%) at pH 7.4 from the formulation of TDL of 50% DOX loaded nanoMOFs coated or not with CD –PEG-CO oligomer in two days, whereas it rapidly released out in ALF at pH 4.5. Confocal investigations showed that the DOX loaded nanoMOFs penetrated inside cancer cell together with their PEG-based shells, followed by DOX release and diffusion inside the nucleus to eradicate the cancer cells. Noteworthy, the shell was released inside the cells, but not in the outer medium.

These studies pave the way to the design of engineered core-shell nanoMOFs that do not release their drug content in biological media, but only in intracellular environment. Further studies will concern nanoMOF surface modifications with CD-PEG-CO coatings bearing targeting moieties.

Acknowledgements

We are grateful for help from Ludivine Houel Renault, responsible of the platform CPBM/CLUPS/LUMAT FR2764 for confocal microscopy. We acknowledge Dr. Doru

Constantin (LPS Orsay) for help with XRPD experiments. We thank Dr. Borja Moreira-Alvarez, Dr. Jorge R. Encinar for ICP-MS. We acknowledge Dr. Christophe Rihouey and Dr. Tony Varacavoudin for the GPC investigations. This research received support from the French National Research Agency (ANR-14-CE08-0017 and ANR-20-CE19-0020) and by Labex NanoSaclay (ANR-10-LABX-0035). J. Qiu acknowledges support from China Scholarship Council (CSC, N° 201708070028). The present work has benefited from Imagerie - Gif core facility supported by ANR (ANR-11-EQPX-0029/Morphoscope, ANR-10-INBS-04/FranceBioImaging; ANR - 11 - IDEX - 0003 - 02/ Saclay Plant Sciences).

Appendix A. Supplementary material

Supplementary data to this article can be found online at https://doi.org/10.1016/xxxxxx.

References

Agostoni, V., Chalati, T., Horcajada, P., Willaime, H., Anand, R., Semiramoth, N., Baati, T., Hall, S., Maurin, G., Chacun, H., Bouchemal, K., Martineau, C., Taulelle, F., Couvreur, P., Rogez-Kreuz, C., Clayette, P., Monti, S., Serre, C., Gref, R., 2013. Towards an improved anti-HIV activity of NRTI via metal-organic frameworks nanoparticles. Adv. Healthc. Mater. 2, 1630–1637.

Agostoni, V., Horcajada, P., Noiray, M., Malanga, M., Aykaç, A., Jicsinszky, L., Vargas-Berenguel, A., Semiramoth, N., Daoud-Mahammed, S., Nicolas, V., Martineau, C., Taulelle, F., Vigneron, J., Etcheberry, A., Serre, C., Gref, R., 2015. A "green" strategy to construct non-covalent, stable and bioactive coatings on porous MOF nanoparticles. Sci. Rep. 5, 7925.

Anand, R., Borghi, F., Manoli, F., Manet, I., Agostoni, V., Reschiglian, P., Gref, R., Monti, S., 2014. Host-guest interactions in Fe(III)-trimesate MOF nanoparticles loaded with

doxorubicin. J. Phys. Chem. B 118, 8532–8539.

Aryal, S., Grailer, J.J., Pilla, S., Steeber, A., Gong, S., 2009. Doxorubicin conjugated gold nanoparticles as water-soluble and pH-responsive anticancer drug nanocarriers. J. Mater. Chem. 19, 7879–7884.

Baati, T., Njim, L., Neffati, F., Kerkeni, A., Bouttemi, M., Gref, R., Najjar, M.F., Zakhama, A., Couvreur, P., Serre, C., Horcajada, P., 2013. In depth analysis of the in vivo toxicity of nanoparticles of porous iron(iii) metal-organic frameworks. Chem. Sci. 4, 1597–1607.

Barenholz, Y., 2012. Doxil® - The first FDA-approved nano-drug: lessons learned. J. Control. Release 160, 117–134.

Bellido, E., Hidalgo, T., Lozano, M.V., Guillevic, M., Simón-Vázquez, R., Santander-Ortega, M.J., González-Fernández, Á., Serre, C., Alonso, M.J., Horcajada, P., 2015. Heparin-engineered mesoporous iron metal-organic framework nanoparticles: toward stealth drug nanocarriers. Adv. Healthc. Mater. 4, 1246–1257.

Bhattacharjee, A., Kumar, M., Sasidhar, P., 2020. Doxorubicin loading capacity of MIL - 100 (Fe): effect of synthesis conditions. J. Inorg. Organomet. Polym. Mater. 100, 1–10.

Chalati, T., Horcajada, P., Couvreur, P., Serre, C., Ben Yahia, M., Maurin, G., Gref, R., 2011. Porous metal organic framework nanoparticles to address the challenges related to busulfan encapsulation. Nanomedicine 6, 1683–1695.

Cutrone, G., Li, X., Casas-Solvas, J.M., Menendez-Miranda, M., Qiu, J., Benkovics, G., Constantin, D., Malanga, M., Moreira-Alvarez, B., Costa-Fernandez, J.M., García-Fuentes, L., Gref, R., Vargas-Berenguel, A., 2019a. Design of engineered cyclodextrin derivatives for spontaneous coating of highly porous metal-organic framework nanoparticles in aqueous media. Nanomaterials 9, 1–26.

Cutrone, G., Qiu, J., Menendez-Miranda, M., Casas-Solvas, J.M., Aykaç, A., Li, X., Foulkes, D., Moreira-Alvarez, B., Encinar, J.R., Ladavière, C., Desmaële, D., Vargas-Berenguel,

A., Gref, R., 2019b. Comb-like dextran copolymers: A versatile strategy to coat highly porous MOF nanoparticles with a PEG shell. Carbohydr. Polym. 223, 115085.

Di Nunzio, M.R., Agostoni, V., Cohen, B., Gref, R., Douhal, A., 2014. A “ship in a bottle” strategy to load a hydrophilic anticancer drug in porous metal organic framework nanoparticles: Efficient encapsulation, matrix stabilization, and photodelivery. J. Med. Chem. 57, 411–420.

FDA approved PEGylated drugs 2021 [WWW Document], 2021. . Biochem. Sci. Inc.

Feng, Y., Wang, C., Ke, F., Zang, J., Zhu, J., 2018. MIL-100 (Al) gels as an excellent platform loaded with doxorubicin hydrochloride for pH-triggered drug release and anticancer effect. Nanomaterials 8, 1–11.

Giménez-marqués, M., Bellido, E., Berthelot, T., Simón-yarza, T., Hidalgo, T., Simón-vázquez, R., González-fernández, Á., Avila, J., Asensio, M.C., Gref, R., Couvreur, P., Serre, C., Horcajada, P., 2018. GraftFast Surface Engineering to Improve MOF Nanoparticles Furtiveness. small 14, 1–11.

Giménez-Marqués, M., Bellido, E., Berthelot, T., Simón-Yarza, T., Hidalgo, T., Simón-Vázquez, R., González-Fernández, Á., Avila, J., Asensio, M.C., Gref, R., Couvreur, P., Serre, C., Horcajada, P., 2018. GraftFast surface engineering to improve MOF nanoparticles furtiveness. Small 14, 1801900.

Gref, R., Domb, A., Quellec, P., Blunk, T., Müller, R.H., Verbavatz, J.M., Langer, R., 1995. The controlled intravenous delivery of drugs using PEG-coated sterically stabilized nanospheres. Adv. Drug Deliv. Rev. 16, 215–233.

Gref, R., Minamitake, Y., Peracchia, M.T., Trubetskoy, V., Torchilin, V., Langer, R., 1994. Biodegradable long-circulating polymeric nanospheres. Science (80-.). 263, 1600–1603.

He, S., Wu, L., Li, X., Sun, Hongyu, Xiong, T., Liu, J., Huang, C., Sun, Huimin, Chen, W., Gref, R., Zhang, J., 2021. Metal-organic frameworks for advanced drug delivery. Acta

Pharm. Sin. B 1–89.

Horcajada, P., Chalati, T., Serre, C., Gillet, B., Sebrie, C., Baati, T., Eubank, J.F., Heurtaux, D., Clayette, P., Kreuz, C., Chang, J.-S., Hwang, Y.K., Marsaud, V., Bories, P.-N., Cynober, L., Gil, S., Ferey, G., Couvreur, P., Gref, R., 2010. Porous metal-organic-framework nanoscale carriers as a potential platform for drug delivery and imaging. Nat. Mater. 9, 172–178.

Horcajada, P., Gref, R., Baati, T., Allan, P.K., Maurin, G., Couvreur, P., 2012. Metal-organic frameworks in biomedicine. Chem. Rev. 112, 1232–1268.

Horcajada, P., Surble, S., Serre, C., Hong, D., Seo, Y., Chang, J., Grene, J., 2007. Synthesis and catalytic properties of MIL-100 (Fe), an iron (III) carboxylate with large pores. Chem. Commun 100, 2820–2822.

Hoskins, B.F., Robson, R., 1989. Infinite polymeric frameworks consisting of three dimensionally linked rod-like segments. J. Am. Chem. Soc. 111, 5962–5964.

Johnson-arbor, K., Dubey, R., 2020. Doxorubicin [WWW Document]. StatPearls [Internet]. Treasure Isl. StatPearls Publ.

Jong Oh Kim, Alexander V. Kabanov, T.K.B., 2009. Polymer micelles with cross-linked polyanion core for delivery of a cationic drug doxorubicin. J. Control. Release 138, 197–204.

Lee, C., Cheng, S., Huang, I., Souris, J.S., Yang, C., Mou, C., Lo, L., 2010. Intracellular pH-responsive mesoporous silica nanoparticles for the controlled release of anticancer chemotherapeutics. Angew. Chem. Int. Ed 49, 8214–8219.

Li, X., Porcel, E., Menendez-miranda, M., Qiu, J., Yang, X., 2020a. Highly porous hybrid metal – organic nanoparticles loaded with gemcitabine monophosphate : a multimodal approach to improve chemo- and radiotherapy. ChemMedChem 15, 274–283.

Li, X., Porcino, M., Qiu, J., Constantin, D., Martineau-corcos, C., Gref, R., 2021.

Doxorubicin-loaded metal-organic frameworks nanoparticles with engineered cyclodextrin coatings : insights on drug location by solid state NMR spectroscopy. Nanomaterials 11, 1–15.

Li, X., Salzano, G., Qiu, J., Menard, M., Berg, K., Theodossiou, T., Ladavière, C., Gref, R., 2020b. Drug-loaded lipid-coated hybrid organic-inorganic " stealth " nanoparticles for cancer therapy. Front. Bioeng. Biotechnol. 8, 1–12.

Li, X., Semiramoth, N., Hall, S., Tafani, V., Josse, J., Laurent, F., Salzano, G., Foulkes, D., Brodin, P., Majlessi, L., Ghermani, N.-E., Maurin, G., Couvreur, P., Serre, C., Bernet-Camard, M.-F., Zhang, J., Gref, R., 2019a. Compartmentalized encapsulation of two antibiotics in porous nanoparticles: an efficient strategy to treat intracellular infections. Part. Part. Syst. Charact. 36, 1–9.

Li, X., Serre, C., Porcel, E., Menendez-Miranda, M., Qiu, J., Yang, X., Pastor, A., Desmaële, D., Lacombe, S., Gref, R., 2019b. Highly porous hybrid metal-organic nanoparticles loaded with gemcitabine-monophosphate: a multimodal approach to improve chemo and radiotherapy. ChemMedChem 1–10.

Minati, L., Antonini, V., Serra, M.D., Speranza, G., Enrichi, F., Riello, P., 2013. pH-activated doxorubicin release from polyelectrolyte complex layer coated mesoporous silica nanoparticles. Microporous Mesoporous Mater. 180, 86–91.

Pieper, S., Langer, K., 2017. Doxorubicin-loaded PLGA nanoparticles - a systematic evaluation of preparation techniques and parameters. Mater. Today Proc. 4, S188–S192.

Pillai, G., 2014. Nanomedicines for cancer therapy : an update of FDA approved and those under various stages of development. SOJ Pharm. Pharm. Sci. 1, 1–13.

Puskás, I., Szemjonov, A., Fenyvesi, É., Malanga, M., Szente, L., 2013. Aspects of determining the molecular weight of cyclodextrin polymers and oligomers by static light scattering. Carbohydr. Polym. 94, 124–128.

Qiu, J., Li, X., Steenkeste, K., Barroca-aubry, N., Aymes-chodur, C., Roger, P., Casas-solvas, J.M., Vargas-berenguel, A., Rihouey, C., 2020. Self-assembled multifunctional core – shell highly porous metal – organic framework nanoparticles. Int. J. Pharm. 581, 119281.

Quijia, C.R., Lima, C., Silva, C., Alves, R.C., 2021. Application of MIL-100(Fe) in drug delivery and biomedicine. J. Drug Deliv. Sci. Technol. 100, 102217.

Rezaei, M., Abbasi, A., Varshochian, R., Dinarvand, R., Jeddi-tehrani, M., 2018. NanoMIL-100 (Fe) containing docetaxel for breast cancer therapy. Artif. Cells, Nanomedicine, Biotechnol. 46, 1390–1401.

Rodriguez-Ruiz, V., Maksimenko, A., Anand, R., Monti, S., Agostoni, V., Couvreur, P., Lampropoulou, M., Yannakopoulou, K., Gref, R., 2015. Efficient “green” encapsulation of a highly hydrophilic anticancer drug in metal-organic framework nanoparticles. J. Drug Target. 23, 759–767.

Simon-Yarza, M.T., Baati, T., Paci, A., Lesueur, L.L., Seck, A., Chiper, M., Gref, R., Serre, C., Couvreur, P., Horcajadab, P., 2016. Antineoplastic Busulfan encapsulated in Metal Organic Framework nanocarrier: first in vivo results M.T. J. Mater. Chem. B 4, 585–588.

Simon-yarza, T., Baati, T., Neffati, F., Njim, L., Couvreur, P., Serre, C., Gref, R., Najjar, M.F., Zakhama, A., Horcajada, P., 2016. In vivo behavior of MIL-100 nanoparticles at early times after intravenous administration. Int. J. Pharm. 511, 1042–1047.

Simon-Yarza, T., Giménez-Marqués, M., Mrimi, R., Mielcarek, A., Gref, R., Horcajada, P., Serre, C., Couvreur, P., 2017. A Smart Metal–Organic Framework Nanomaterial for Lung Targeting. Angew. Chemie - Int. Ed. 56, 15565–15569.

Simon-Yarza, T., Mielcarek, A., Couvreur, P., Serre, C., 2018. Nanoparticles of metal-organic frameworks: on the road to in vivo efficacy in biomedicine. Adv. Mater. 30, 1–15.

Singco, B., Liu, L., Chen, Y., Shih, Y., Huang, H., 2016. Approaches to drug delivery: Confinement of aspirin in MIL-100(Fe) and aspirin in the de novo synthesis of metal-

organic frameworks. Microporous Mesoporous Mater. 15, 254–260.

Unnier, E.M., Ewes, F.T., Onathan, C.O., Inassier, C.L., Yrolles, L.D.O., Archais, H.M., Oucé, M.S., Ervé, K.H., 2007. On the interaction of doxorubicin with oleate ions : fluorescence spectroscopy and liquid – liquid extraction study. Chem. Pharm. Bull 55, 1006–1010.

Wang, J., Bhattacharyya, J., Mastria, E., Chilkoti, A., 2017. A quantitative study of the intracellular fate ofpH-responsive doxorubicin- polypeptide nanoparticles. J. Control. Release 260, 100–110.

Wuttke, S., Braig, S., Preiß, T., Zimpel, A., Sicklinger, J., Bellomo, C., Radler, J.O., Vollmarb, A.M., Bein, T., 2015. MOF nanoparticles coated by lipid bilayers and their uptake by cancer cells. Chem commun 100, 2–5.

Xiong, Q., Cui, M., Yu, G., Wang, J., Song, T., Wang, J., 2018. Facile Fabrication of Supramolecular Nanoassemblies for Co-delivery of Doxorubicin and Sorafenib toward Hepatoma Cells. Front. Pharmacol. 9, 1–11.

Xue, T., Xu, C., Wang, Yu, Wang, Yanbing, Tian, H., Zhang, Y., 2019. Doxorubicin-loaded nanoscale metal-organic framework for tumor targeting combined chemotherapy and chemodynamic therapy. Biomater. Sci. 7, 4615–4623.

Zhao, N., Woodle, M.C., Mixson, A.J., 2018. Advances in delivery systems for doxorubicin. J. Nanomed. Nanotechnol. 9, 1–9.

Zhu, Y., Chen, S., Zhao, H., Yang, Y., Chen, X., Sun, J., Fan, H., Zhang, X., 2016. PPy @ MIL-100 nanoparticles as a pH- and near-IR-irradiation- responsive drug carrier for simultaneous photothermal therapy and chemotherapy of cancer cells. ACS Appl. Mater. Interfaces 2016, 8, 34209−34217.

Supporting Information for

Porous nanoparticles with engineered shells release their drug cargo in cancer cells

Jingwen Qiu[1&], Xue Li[1&], Mahsa Rezaei[1], Gilles Patriarche[2], Juan M. Casas-Solvas[3], Jose Manuel Costa Fernandez[4], Farah Savina[1], Luc Picton[5], Antonio Vargas-Berenguel[3] and Ruxandra Gref[1]*

[1]Université Paris-Saclay, CNRS, Institut des Sciences Moléculaires d'Orsay, 91405, Orsay, France.

[2]Université Paris-Saclay, CNRS, Centre de Nanosciences et de Nanotechnologies (C2N), 91120 Palaiseau, France

[3] Department of Chemistry and Physics, University of Almería, Ctra de Sacramento s/n, 04120 Almería, Spain

[4] Department of Physical and Analytical Chemistry, University of Oviedo, Julián Clavería 8, 33006 Oviedo, Spain

[5] Polymères Biopolymères Surfaces, Normandie Université, UNIROUEN, Institut National des Sciences Appliquées Rouen, CNRS, UMR 6270, 76821 Mont Saint Aignan, France

[&]: These authors contributed equally.

Corresponding Author:

Dr. Ruxandra Gref

Université Paris-Saclay, CNRS, Institut des Sciences Moléculaires d'Orsay, 91405, Orsay, France. Tel: +33 (1) 69158234; E-mail: ruxandra.gref@universite-paris-saclay.fr.

Table S1 Composition of the artificial lysosomal fluid. Weight and concentrations of products used to prepare a total volume of 250 mL.

Compound	Concentration (mg/mL)	Weight (mg)
Sodium chloride	3.2	800
Sodium hydroxide	6.0	1500
Citrate acid	21	5250
Calcium chloride	0.10	25
Disodium phosphate	0.18	24
Sodium sulfate	0.039	10
Magnesium chloride	0.11	13
Glycerin	0.059	15
Citrate sodium dihydrate	0.077	19
Sodium tartrate dehydrate	0.090	22.5
Sodium pyruvate	0.086	21.5

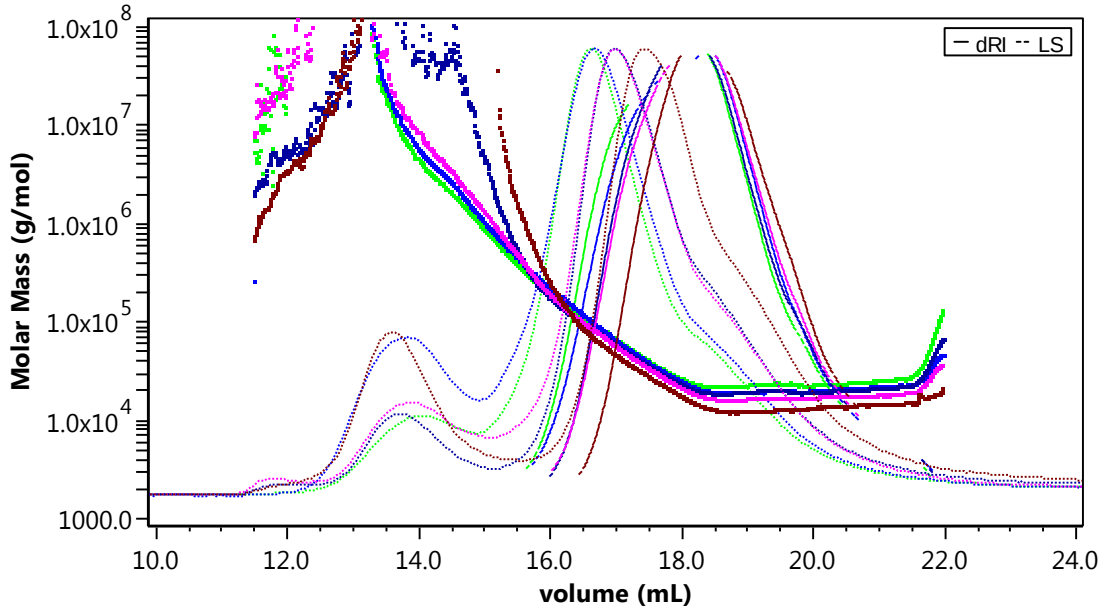

Figure S1 Elution profiles and molar mass distributions of CD-PEG-CO after purification by dialysis. Samples are named according to Table 1: entry 10 (brown), entry 12 (green), entry 13 (dark blue), entry 14 (pink), entry 15 (light blue). Signals are from differential refractometric detector (dRI) : solid line, and light scattering (LS) detector: dotted line.

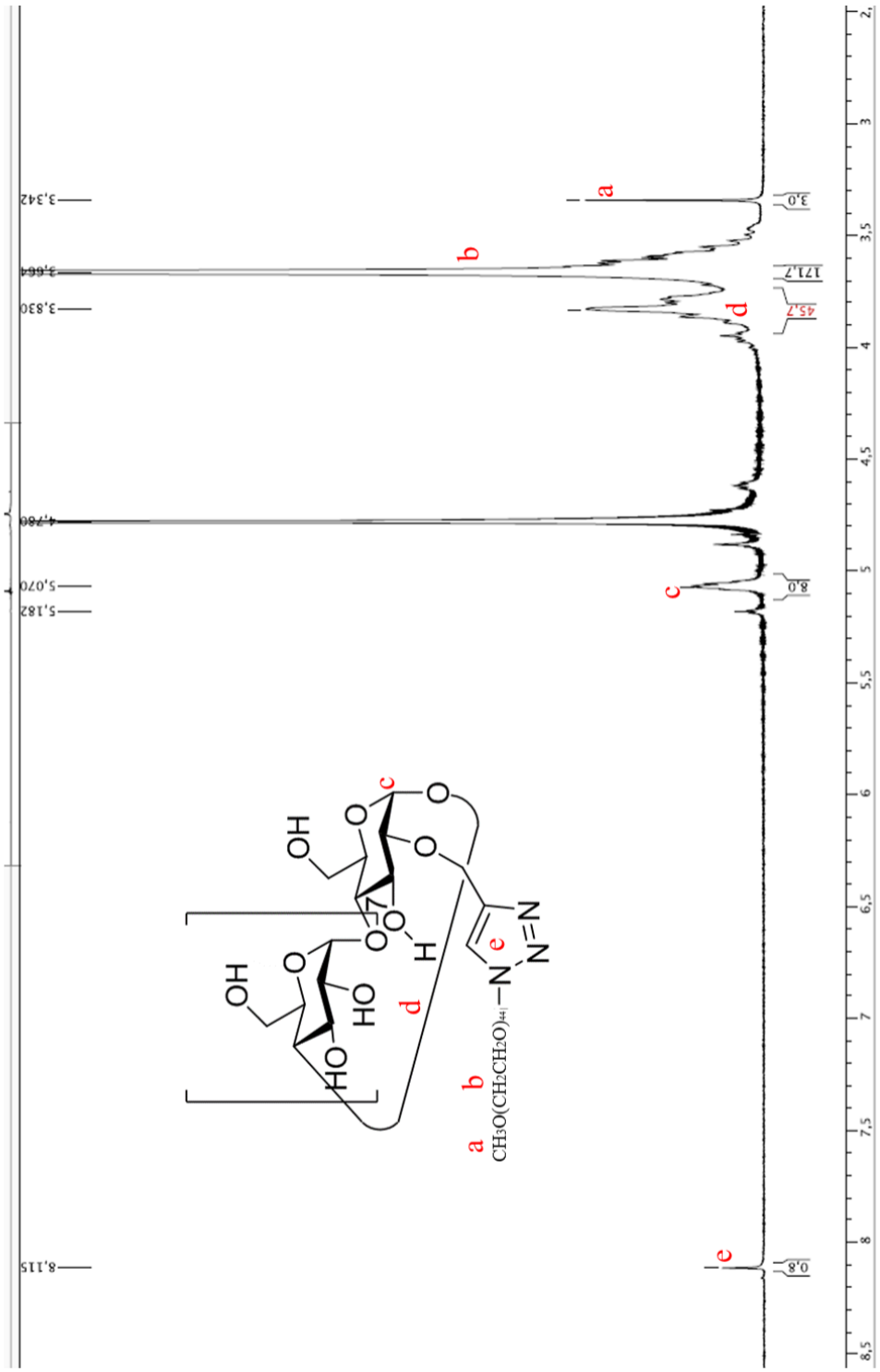

Figure S2 ^{1}H-NMR spectrum of CD-PEG monomer: The PEG-2000/CD molar ratio in the compound was estimated by integrating the peaks assigned to the 3 protons of the PEG-2000 methyl group (a) divided by 8 anomeric protons (d) of the CD units. The ratio PEG/CD=(3/3)/(8/8)=1,0; meaning that one CD was linked with one PEG. For the part of PEG-2000, the calculated proton amount of the CH_2CH_2 is 172, which is very close to the theoretical value (44×4=176).

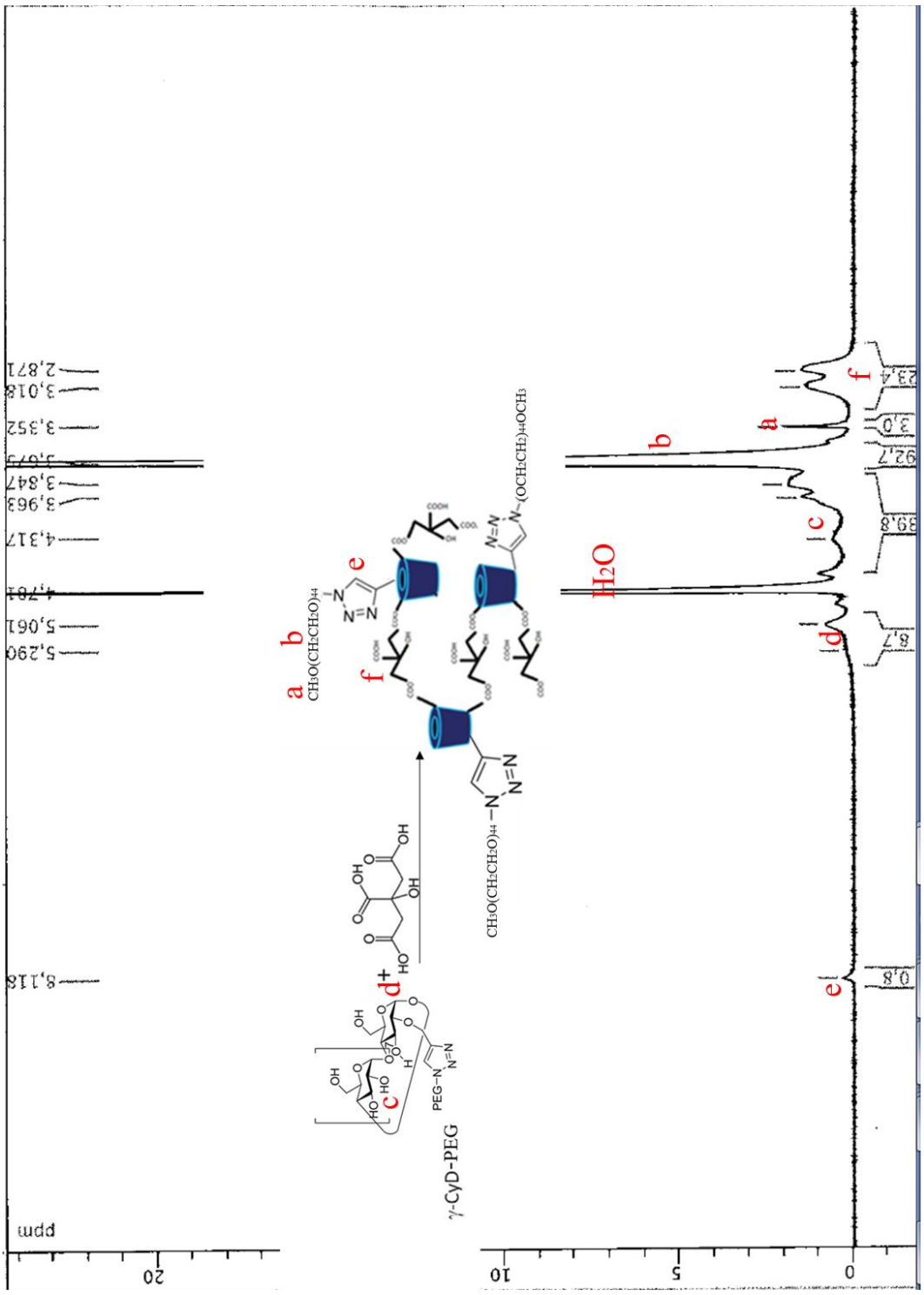

Figure S3 [1]H-NMR spectrum of CD-PEG-CO. The citric acid/CD-PEG molar ratio in the copolymer was estimated by integrating the peaks assigned to the 4 protons of the citric acid methylene groups (f) and the three methyl (a) protons of the CD units. The ratio gave the molar ratio: citric acid/CD-PEG of 6.0; considering that the Mw was around 53400 g/mole, this means 174

that the composition of the copolymer is $(CD\text{-}PEG)_{12}$ $(citrate)_{72}$.

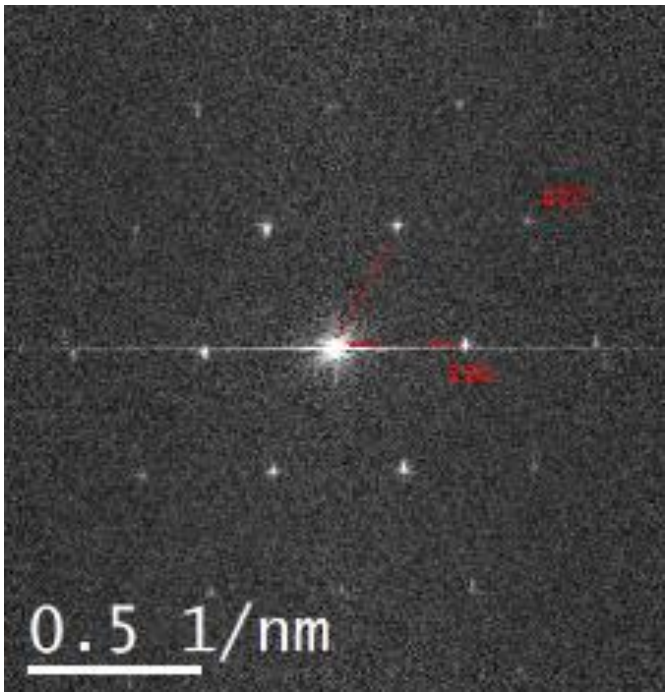

Figure S4 X-Ray diffraction pattern of empty MIL-100 (Fe) nanoMOFs highlighting their ordered structure.

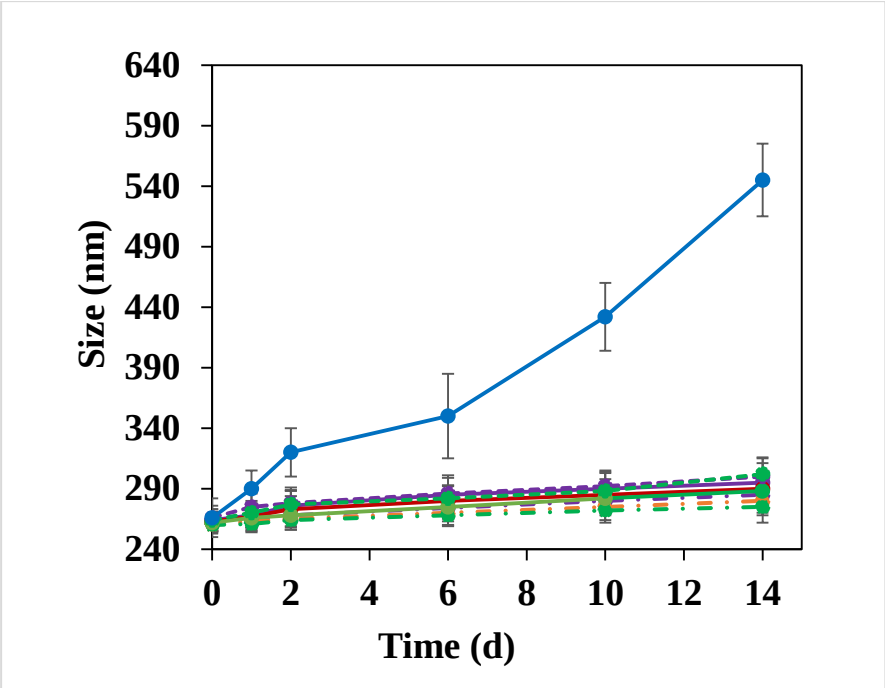

Figure S5 Colloid stability of DOX-loaded nanoMOFs before and after surface modification. Uncoated nanoMOFs (blue), DOX in bare nanoMOFs (purple), and nanoMOFs coated with CD-PEG-CO (green) or CD-CO (red) at DOX TDL of 50% (dashed line ----), TDL of 20% (straight line), and TDL of 10% (dashed line — · –).

Figure S6 DOX payload in nanoMOFs coated with CD-CO at TDL of 100% using different loading methods (A: one pot loading; B: loading first then coating; C: coating first and then loading; D: bare nanoMOFs without coating).

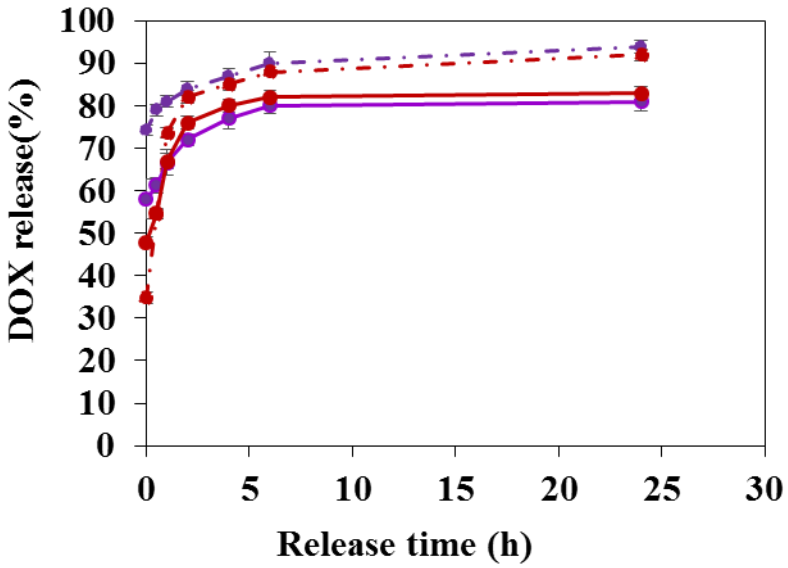

Figure S7 DOX release in ALF : DOX in bare nanoMOFs (purple), and nanoMOFs coated with CD-CO (red) at DOX:nanoMOFs weight ratio of 1:5 (straight line), and 1:10 (dashed line).

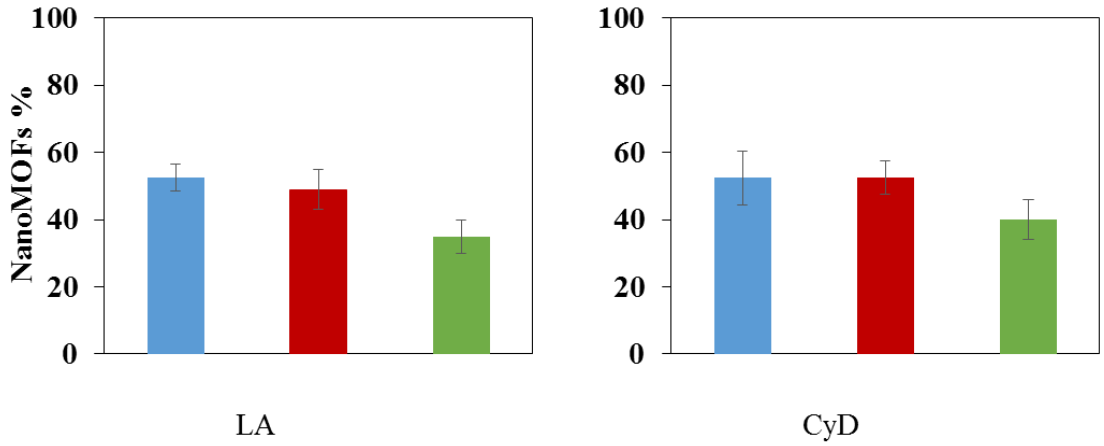

Figure S8 NanoMOFs internalization in cells quantified by ICP-MS: nanoMOFs coated with 29 wt% CD-PEG-CO (green), nanoMOFs coated with 42 wt% CD-CO (red), and uncoated nanoMOFs (Fe) (blue).

General Discussion and Perspectives

Recent developments in the field of nanomedicine have demonstrated that the surface modification of nanoparticle (NPs) plays an important role in the drug efficacy, being a key point for their successful biomedical application[1,2]. Among an increasing number of drug nanocarriers developed so far, nanoscale hybrid iron carboxylate Metal-Organic Frameworks (nanoMOFs) have been reported as one of the most promising drug carriers[1–6] based on: i) their adjustable porosity and versatile composition, , ii) low *in vivo* toxicity[7], iii) unprecedented loading capacities of a variety of drugs together with iv) the ability to achieve controlled release under physiological conditions and v) their biocompatibility and biodegradability.

It was reported that surface modification with hydrophilic PEG chains in a "brush" configuration could dramatically prolong the blood circulation times of NPs by reducing their recognition by the reticuloendothelial system[8,9]. However, up to now, only a few number of cases have been reported on engineering the surface of nanoMOFs with PEG shells[10,11]. Indeed, it is more challenging to functionalize the porous surface of MOFs, as compared for example, to dense NPs composed of biodegradable polymers or to liposomes. Indeed, it has been reported that PEG chains can penetrate into the MOF pores, decrease the drug loading capacity, and lead to uncontrolled drug release[10]. In order to prevent the PEG from penetrating into the highly porous MOFs, the method of GraftFast was employed to form PEG-based shells. This method was based on polymerization of acryl PEGs[11]. However, the molecular weight of the resulting PEG-based copolymer could not be effectively controlled.

Therefore, there is an urgent need to develop an engineered PEG coating which can efficiently decrease reticuloendothelial sequestration of nanoMOFs. Herein we employed two strategies to engineer nanoMOFs surface-modified with PEG chains. The first strategy is to use the bulky macromolecule DEX as a backbone, followed by coupling two types of moieties: i) PEG chains to reduce macrophage uptake and ii) alendronate (ALN) to spontaneously coordinate to the external surface of nanoMOFs (chapter 2). The second strategy is to synthesize oligomers based on the cage molecule "CDs" coupled with PEG chains (chapter 3). The first strategy adopted mainly click chemistry to "click" different functional moieties to the backbone whereas the second strategy was to "click" PEG chains to CDs, followed by crosslinking the CD-PEG units. These two strategies share common characteristics and at the same time both of them have their own advantages and disadvantages.

1. First strategy: synthesis of DEX-ALN-PEG

In chapter 2, both PEG and ALN were successfully grafted onto the DEX backbone and the number of grafted units was controlled. Three dextran derivatives with different molar ratios of ALN and PEG branches were synthesized, namely DEX-ALN_{75}-PEG_{25}, DEX-ALN_{50}-PEG_{50} and DEX-ALN_{25}-PEG_{75}, which were confirmed by ^{1}H NMR, ^{13}C NMR and ^{31}P NMR spectroscopies. MIL-100(Fe) nanoMOFs with a mean hydrodynamic diameter around 200 nm were successfully synthesized by a green method, without organic solvents, assisted by microwave and within a short time. The three copolymers with increased PEG contents were used as coating materials for the surface modification of nanoMOFs, following a fast, green method (without any organic solvent or surfactant) consisting of simply soaking nanoMOFs in aqueous solutions of the prepared copolymers. This facile coating protocol, devoid of the use of any organic solvents or surfactant, is beneficial for the applications in biomedical field and for scaling up.

It was found that after overnight impregnation, the amounts of DEX-ALN_{75}-PEG_{25}, DEX-ALN_{50}-PEG_{50}, and DEX-ALN_{25}-PEG_{75} associated onto the surface of nanoMOFs reached 29 ± 2 wt%, 27 ± 2 wt% and 32 ± 3 wt%, respectively. These amounts were determined by ICP-MS by direct quantification of the P content in the coated nanoMOFs. The nanoMOFs coated or not with DEX-ALN-PEG were characterized by a series of complementary techniques. XRPD studies demonstrated that the coating materials based on DEX-ALN-PEG polymers did not disturb the crystalline structure of nanoMOFs, despite the high amounts of DEX-ALN-PEG associated to the NPs. Besides, TEM experiments indicated that the facetted morphology of the nanoMOFs was not affected after surface modification. Uncoated nanoMOFs aggregated during storage in water, whereas on the contrary, the colloid stability of nanoMOFs was greatly improved after coating with all the DEX-ALN-PEG samples (mass ratio DEX-ALN-PEG:nanoMOFs 1:1), illustrating that their coating effectively prevent nanoMOFs from aggregation.

In order to gain deep insights on protein adsorption, the interaction of nanoMOFs, coated or not with copolymers, with HSA, the most abundant protein in human blood plasma, was investigated. The optimized DEX-ALN-PEG coatings could reduce five times the adsorption of the model protein HSA. There results clearly reveal that the DEX-ALN-PEG coating materials greatly decrease protein adsorption, which plays an important role on macrophage

uptake.

The ability of DEX-ALN-PEG coated nanoMOFs to evade macrophage uptake was assessed on the murine macrophage J774A.1 cell line. After 2 h incubation, the optical microscopy images illustrated that a large amount of nanoMOFs clustered inside the macrophages. On the contrary, with the same incubation time, the uptake of DEX-ALN_{25}-PEG_{75} coated nanoMOFs was dramatically decreased. To further quantify the macrophage uptake, ICP-MS was employed in this study. These results reveals the efficacy of the DEX-ALN-PEG coatings upon macrophage uptake. After 4 h incubation, the nanoMOFs amounts internalized in the cells were 77, 39, 32 and 24% for control (uncoated nanoMOFs), DEX-ALN_{75}-PEG_{25}, DEX-ALN_{50}-PEG_{50}, and DEX-ALN_{25}-PEG_{75}, respectively. This demonstrates that the higher the PEG contents in the functionalized material, the lower the nanoMOFs uptake. To the best of our knowledge, these are the first quantitative results on PEG-coated nanoMOFs uptake by macrophages based primarily on a direct quantification and visualization of the iron content in the cells.

In spite of all their advantages (easy to click a series of functional moieties, stealth effect, green method for coating procedure, etc), the DEX-ALN-PEG copolymers are not biodegradable, involve multiple synthesis steps, and therefore their synthesis is not easy to scale up. This can hamper their application in the biomedical field.

2. Second strategy: synthesis of CD-PEG-CO

To improve the biodegradability of the PEG-based coating materials, our second strategy was to synthesize oligomers based on CDs. It is recognized that CDs possess excellent properties to form host-guest inclusion complexes in aqueous solutions with various hydrophobic active molecules, due to their peculiar structure with a hydrophobic interior and a hydrophilic exterior. Therefore, we employed CDs in the shells to elaborate versatile coating materials. As shown in chapter 3.1, a core–shell nanomaterial was devised using MIL-100 (Fe) nanoMOFs as the core and a CD-based layer as the shell.

2.1 Synthesis of CD-CO

First of all, biodegradable CD-CO (with and without fluorescent dye) were prepared adopting citric acid as cross linker, which plays an important role in anchoring the oligomers onto the surface of the nanoparticles due to the coordination between the citric acid and the available iron sites from MIL-100 (Fe). As far as we know, it is the first reported case that fluorescent

CD-CO were synthesized to further understand the interaction between the shell and the core. The synthesized CD-CO with and without fluorescent dye were characterized by a set of complementary techniques, including FTIR, SEC and NMR spectroscopies.

Similar to the DEX-ALN-PEG coated nanoMOFs, the CD-CO coated nanoMOFs was performed by easily impregnating the nanoMOFs in aqueous solutions of the synthesized CD-CO. The facetted morphology of nanoMOFs visualized by TEM and the XRPD crystalline structure were preserved after surface functionalization[10]. The amount of γ-CD-citrate oligomers anchoring on the surface of nanoMOFs was determined both by fluorescence spectroscopy and by TGA, an indirect tool to measure the fluorescent dye content in the supernatant after impregnation and a direct quantification of the amount of coating material on the surface of NPs, respectively. The two set of values obtained from these two different techniques were in good agreement with each other. There was 53 ± 9 wt% of CD-CO associated to the nanoMOFs, which was almost twice the amount of the attached DEX-ALN_{25}-PEG_{75} (32 ± 3 wt%). This effective association could be probably related to the strong coordination of the abundant carboxyl groups for the iron sites located at the external surface of the nanoMOFs. Indeed, citric acid, possessing the same number of carboxyl groups as trimesic acid (the organic linker of nanoMOFs), is well recognized to have a strong affinity to Fe sites.

In addition to the conventional techniques, such as TEM, XRD, TGA and DLS, XPS was employed to assess the presence of CD-CO within the nanoMOFs' top layers (~10 nm depth) and to quantify the atomic surface composition. Both "fingerprint" of CD-CO (main contribution at 286.2 eV) and carbon C1s ''fingerprint'' of the carbon skeleton of nanoMOFs (284.8 and 289 eV: C-C or C-OOH, respectively) were well observed for CD-CO coated nanoMOFs, confirming that the surface of nanoMOFs was well shielded with CD-CO.

The other novelty in this study was the use of fluorescence-lifetime microscopy to characterize the coating processes. It is well recognized that fluorescence lifetime is an inherent property of a fluorophore, no matter of its concentration. However, it could change partially according to its interaction with its environment (solvent, quenchers, NPs, etc). Indeed, the mean fluorescence lifetime (τ) of fluorescent CD-CO was remarkably modified upon interaction with nanoMOFs. Fluorescence-lifetime microscopy provided a straightforward method for an *in situ* characterization of the interactions between nanoMOFs and their coating materials, playing an important role to gain deep insights at the molecular level.

In the subchapter 3.1, DOX payload in nano-MOFs reached up to 48 ± 10 wt% after 24 h incorporation when the nanoMOFs and DOX were incubated at a weight ratio of 1:1 . DOX-loaded nanoMOFs had a tendency to aggregate (mean hydrodynamic diameter raised to > 750 nm in 10 days). On the contrary, the colloid stability of DOX-loaded nanoMOFs was dramatically improved (size variation <10% in 3 weeks) after coating with CD-CO.

ssNMR spectroscopy has been used to characterize the DOX localization in CD-CO coated nanoMOFs,. It emerged as an indispensable analytical technique to obtain a comprehensive atomic-scale characterization of complex porous materials, such as MOFs. ssNMR was a powerful tool to investigate the supramolecular structure of highly porous core–shell drug nanocarriers, namely, CD-phosphate (CD-P) coated MIL-100 nanoMOFs. The first case of reported investigation was carried on paramagnetic MIL-100(Fe) nanoparticle employing ^{1}H solid-state magic-angle spinning (MAS) NMR analysis. The resulting ^{1}H NMR spectra showed that cooperative interactions took place between the shell and the core, based on phosphate-iron coordination, improving the colloidal stability of the core-shell nanoMOFs. However, numerous spinning side bands were detected due to the presence of the Fe paramagnetic center, restricting the volume of information that could be drawn from the NMR spectra. In the subchapter 3.2, we synthesized MIL-100(Al) nanoMOFs with hydrodynamic diameter of around 260 nm for NMR characterization.

Prior to the NMR study, DOX impregnation kinetics were studied at different DOX initial amounts (TDL of 10%, 20%, 50%). The maximum DOX payload was around 28 wt% after 6 days incubation, which obviously demonstrates that there is a strong interaction between DOX and the MIL-100 nanoMOFs. The morphology with faceted-type structures and the XRPD crystalline structure of the MIL-100 (Al) nanoMOFs were not affected after DOX encapsulation. Remarkably, with the highest DOX payloads, the BET surface area were greatly decreased (1720 ± 65 m^2/g, and 200 ± 35 m^2/g, for nanoMOFs before and after DOX loading (27±2.0 wt%), respectively, indicating that DOX penetrated inside the pores of the nanoMOFs. Meanwhile, the CD-CO(^{13}C) was successfully synthesized to track the localization of CD-CO in nanoMOFs and the interaction between CD-CO and DOX. Similarly to MIL-100 (Fe) nanoMOFs, MIL-100 (Al) nanoMOFs were easily modified with CD-CO (^{13}C) by soaking in water at room temperature. The morphology and crystallinity of the nanoMOFs was preserved after surface modification. BET surface area was only slightly lowered (1720 ± 65 m2/g &1500 ± 130 m2/g for nanoMOFs before and after surface modification), which demonstrates that the

coatings mainly remained on the surface of the nanoMOFs.

Interestingly, the ^{1}H-^{1}H NMR spectra showed close contact between the DOX and the CD-CO inside the particles. The aromatic protons of the DOX have much higher intensity on the 1H NMR spectrum after transfer from the ^{13}C-citrate than in the normal 1H MAS NMR spectrum. This indicates that the aromatic parts of the DOX molecules have a preferential interaction with the 13CD-CO polymer.

Interestingly, DOX release was highly dependent on the DOX payloads. At the highest DOX loading, DOX release was much reduced. For example, 60±4%, 48±3%, and 22±2% DOX was released in 4 h for DOX loaded nanoMOFs with TDL of 10%, 20% and 50%, respectively. Therefore, not all the drug was released out at high DOX contents in the nanoMOFs. Possibly, DOX self-associates inside the cages causing the incomplete release, as it was previously been shown with another drug, topotecan (ref). What is more, it appears that one additional advantage of CD coatings is to better release DOX out from the cores, in particular, at early phases (< 6h) and for low DOX payloads (particularly TDL of 10%). In conclusion, CD coating speeds up the loading process and promotes DOX release.

One novelty was the use of ssNMR spectroscopy to characterize the core-shell nano-MOFs. ^{13}C-labeled CD-citrate oligomers were successfully synthesized and coated on the nanoMOFs outer surface to perform informative ^{1}H-^{13}C and ^{27}Al-^{13}C NMR experiments. The ssNMR methodology related to the selective isotope labeling approach proved to be effective for the characterization of this system based on diamagnetic nanoMOF.

In a nutshell, biodegradable CD-CO (with and without fluorescent dye) were successfully synthesized with a facile green method, DOX was well incorporated into the pores of nanoMOFs with high drug payload, the external surface of DOX loaded nanoMOFs was successfully engineered with CD-CO. Interestingly, CD coatings have also potential capability to interact with drugs.

2.2 Synthesis of CD-PEG-CO

The CD-PEG-CO was synthesized by a two-step procedure: the first step was to click PEG on CD followed by the second step of crosslinking. Every CD molecule was linked with one PEG chain and then, linked with citric acid. The PEG density in the synthesized CD-PEG-CO was around 9% (grafted glucopyrano. Compared to the DEX-ALN-PEG copolymers, CD-PEG-CO have the advantage of biodegradability due to the degradable ester bonds. However, the PEG

density in CD-PEG-CO was slightly lower than that in DEX-ALN-PEG (around 13% of units were grafted).

After the successful synthesis of CD-PEG-CO, the surface modification of nanoMOFs was performed using the same “green” strategy (no organic solvents, no surfactant) as in the case of DEX-ALN-PEG. The maximal amount of associated CD-PEG-CO was up to around 30 wt% measured by TGA analysis, similar to that of DEX-ALN-PEG (32 wt%). Moreover, the drug loading capacity remained unaffected after surface modification. For example, the DOX payloads of the CD-PEG-CO-coated or the bare nanoMOFs were 40 ± 3 wt% and 41 ± 2 wt% respectively, after 6 days impregnation. One other novelty in this study was the use of high-resolution STEM to characterize the bare or coated nanoMOFs. The images clearly revealed the crystalline structures before and after drug loading. Remarkably, the incorporated DOX didn’t release out at physiological pH 7.4, whereas it released out immediately in artificial lysosomal fluid (ALF). Confocal microscopy investigations were in good agreement with these findings: when nanoMOFs were put in contact with cancer cells (Hela cell line), DOX was not released in the extracellular medium, but only inside the cells. Noteworthy, the engineered nanoMOFs penetrated inside the cells together with their coatings, and then degraded intracellularly, releasing both their coatings and their active dug cargo, which in turn eradicated the cancer cells. However, despite their biodegradable character, the CD-CO and CD-CO-PEG coatings were less effective to reduce the macrophage uptake than the DEX-ALN-PEG ones, presumably because of lower PEG contents or unfavorable PEG orientation to form a protective “brush” at the nanoMOFs’ surface.

In a nutshell, "click" chemistry enabled successfully to produce both DEX-ALN-PEG and CD-PEG-CO copolymers. It is a well-known powerful tool, able to conjugate functional groups to DEX backbone or to CDs. Despite their different synthesis procedures, both DEX-ALN-PEG and CD-PEG-CO adsorbed spontaneously and efficiently onto the external surface of nanoMOFs, enabling reaching high coating amounts, up to around 30 wt%. The presence of the coating materials didn’t significant influence the drug loading. In the case of DEX-ALN-PEG with highest PEG density, the best “stealth” effect was observed, possibly due to the stronger anchoring interaction between ALN and Fe sites. However, the DEX-ALN-PEG is a bulky linear molecule, prone to induce bridging effects in between the nanoMOFs. This explains why large amounts (weight ratio between nanoMOFs and the coating material of 1:1) of DEX-ALN-PEG copolymer was required for the surface modification. In the case of lower molecular

weight CD-PEG-CO, the bridging effect was negligible. Indeed, regardless of the weight ratio between nanoMOFs and CD-PEG-CO, no aggregation was observed after surface modification.

By applying the "camouflaging" technique on nanoMOFs, the macrophage uptake of the nanomaterials was significantly reduced, indicating the success in escaping the recognition by these immune cells. . As perspective, ligands for active targeting could be further conjugated to the PEG chains. The resulting copolymers could be similarly adsorbed onto the nanoMOFs endowing them with active targeting abilities. The potential targeting ligands include small molecules, peptides, antibodies, engineered proteins, or nucleic acid aptamers. More specific examples are the antibody Trastuzumab for HER2 receptor and folic acid.. After conjugating with the active targeting ligand, the cancer cellular uptake is expected to further increase by receptor-mediated endocytosis, contributing to increased drug accumulation in cancer cells. This mechanism relies on the interaction between tumor ligands conjugated on the surface of nanoMOFs and the overexpressed receptors/antigens on cancer cell surfaces.

It is recognized that targeting drug delivery systems exhibit several advantages over the conventional chemotherapeutic drugs, particularly in regard to decrease of side effects and enhancement of drug efficacy and safety. Nevertheless, one main disadvantage of many active targeting drug delivery system lies in the expensive and sophisticated technology required for their production. Coatings on nanoMOFs by simple incubation with preformed functionalized copolymers could offer simple and reproducible strategies of interest to be explored in the future. - Therefore, the selection of the targeting ligand will be of upmost importance for the successful coating. Besides, it will be interesting to further explore drug incorporation into functionalized core-shell NPs, as well as shell stabilities in biological media. The strategies presented here could be employed to form coating based on other materials, such as hyaluronic acid, or chitosan. Last, the coating strategies could be applied to other types of biodegradable MOFs, such as UIO-66 and ZIF-8.

The new biomaterials engineered here could find many other biomedical applications in preparing drug nanocarriers, implants or gels to deliver drugs in a controlled manner. The versatile family of biomaterials synthesized here open new fascinating fields of investigation and their *in vitro/in vivo* toxicity and (bio)degradation is worthwhile to be further deeply investigated.

Reference:

1. Horcajada, P. *et al.* Metal-Organic Frameworks in biomedicine. *Chem. Rev.* **112**, 1232–1268 (2012).

2. Simon-Yarza, T., Mielcarek, A., Couvreur, P. & Serre, C. Nanoparticles of Metal-Organic Frameworks: On the Road to In Vivo Efficacy in Biomedicine. *Adv. Mater.* **30**, 1–15 (2018).

3. He, S. *et al.* Metal-organic frameworks for advanced drug delivery. *Acta Pharm. Sin. B* 1–89 (2021). doi:10.1016/j.apsb.2021.03.019

4. Yang, J. & Yang, Y. Metal – Organic Frameworks for Biomedical Applications. *Small* **1906846**, 1–24 (2020).

5. Zhu, W. *et al.* Versatile Surface Functionalization of Metal – Organic Frameworks through Direct Metal Coordination with a Phenolic Lipid Enables Diverse Applications. *Adv. Funct. Mater.* **1705274**, 1–12 (2018).

6. He, C., Liu, D. & Lin, W. Nanomedicine Applications of Hybrid Nanomaterials Built from Metal-Ligand Coordination Bonds: Nanoscale Metal-Organic Frameworks and Nanoscale Coordination Polymers. *Chem. Rev.* **115**, 11079–11108 (2015).

7. Tarek Baati, Leila Njim, Fadoua Neffati, Abdelhamid Kerkeni, Muriel Bouttemi, Ruxandra Gref, Mohamed Fadhel Najjar, Abdelfateh Zakhama, Patrick Couvreur, C. S. and P. H. In depth analysis of the in vivo toxicity of nanoparticles of porous iron(III) metal–organic frameworks. *Chem. Sci.* **4**, 1597–1607 (2013).

8. Gref, R. *et al.* Biodegradable long-circulating polymeric nanospheres. *Science (80-.).* **263**, 1600–1603 (1994).

9. Gref, R. *et al.* The controlled intravenous delivery of drugs using PEG-coated sterically stabilized nanospheres. *Adv. Drug Deliv. Rev.* **16**, 215–233 (1995).

10. Agostoni, V. *et al.* A “green” strategy to construct non-covalent, stable and bioactive coatings on porous MOF nanoparticles. *Sci. Rep.* **5**, 7925 (2015).

11. Giménez-Marqués, M. *et al.* GraftFast Surface Engineering to Improve MOF Nanoparticles Furtiveness. *Small* **14**, 1801900 (2018).

12. Anand, R. *et al.* Citric acid–γ-cyclodextrin crosslinked oligomers as carriers for doxorubicin delivery. *Photochem. Photobiol. Sci.* **12**, 1841–1854 (2013).

General Conclusion

In this study, two different types of carbohydrate polymers were used to functionalize highly porous iron trimesate nanoMOFs MIL-100 (Fe) in view of possible biomedical application.

1. DEX-ALN-PEG copolymers were successfully synthesized by click chemistry with high yields in each step. Both PEG and ALN grafting densities were controlled, and the PEG:ALN molar ratios ranged from 75:25 to 25:75. The colloidal stability of the nanoMOFs was greatly improved after their external surface modification. The copolymers were firmly anchored in aqueous media by a "green" (organic solvent-free) method. More importantly, the DEX-ALN-PEG coatings were able to decrease 3 times the *in vitro* uptake by macrophages.
2. Biodegradable CD-CO grafted or not with Cy5 fluorophore was successfully synthesized and effectively adsorbed onto the surface of porous nanoMOFs, achieving up to 53 ± 8 wt% of coating material associated with the nanoMOFs. Compared with the bare nanoMOFs, these core–shell nanoMOFs were very stable upon storage. taking advantage of the presence of a fluorophore conjugated to CD-CO, fluorescence lifetime microscopy was employed to decipher the coating mechanism. Taking advantage of the high versatility of CDs' chemical modifications and capacity to form "host-guest" inclusion with a wide range of drug molecules, we successfully encapsulated DOX in the core-shell nanoMOFs.
3. In order to characterize the drug localization in the core-shell nanoMOFs, high-resolution ssNMR spectroscopy was employed. ^{13}C-labeled CD-CO was synthesized to perform informative ^{1}H-^{13}C and ^{27}Al-^{13}C NMR experiments. CD-^{13}CO coated MIL-100(Al) nanoMOFs loaded with DOX were successfully synthesized. A set of NMR data clearly confirmed the high association of DOX with both the nanoMOF and the CD-CO moieties. CD coatings were found to be promising in accelerating the loading process and in promoting DOX release. The ssNMR methodology related to the selective isotope labeling strategy was proven to be effective for the characterization of this system based on diamagnetic nanoMOF.
4. The coating material CD-PEG-CO was finally synthesized with Mw of 53 kDa, and it spontaneously associated onto the surface of MIL-100(Fe) nanoMOFs in aqueous media. The drug loading capacity remained unaffected after surface modification. Remarkably, the incorporated DOX didn't release out at physiological pH 7.4, whereas it released out immediately in artificial lysosomal fluid (ALF). Confocal microscopy

investigations were in good agreement with these findings: when nanoMOFs were put in contact with cancer cells (Hela cell line), DOX was not released in the extracellular medium, but only inside the cells. Noteworthy, the engineered nanoMOFs penetrated inside the cells together with their coatings, and then degraded intracellularly, releasing both their coatings and their active dug cargo, which in turn eradicated the cancer cells. However, despite their biodegradable character, the CD-CO and CD-CO-PEG coatings were less effective to reduce the macrophage uptake than the DEX-ALN-PEG ones, presumably because of lower interactions with the iron trimesate cores.

In a nutshell, these studies reveal the potential of coatings based on carbohydrate copolymers to produce core-shell nanoMOFs for biomedical applications, paving the way for applications particularly in the field of cancer treatment. Further studies will deal with ligand grafting onto the shells for targeting cancer cells.

Annex I: Drug-Loaded Lipid-Coated Hybrid Organic-Inorganic “Stealth” Nanoparticles for Cancer Therapy

frontiers in Bioengineering and Biotechnology

ORIGINAL RESEARCH
published: 15 September 2020
doi: 10.3389/fbioe.2020.01027

Drug-Loaded Lipid-Coated Hybrid Organic-Inorganic "Stealth" Nanoparticles for Cancer Therapy

*Xue Li[1], Giuseppina Salzano[1], Jingwen Qiu[1], Mathilde Menard[2], Kristian Berg[2], Theodossis Theodossiou[2], Catherine Ladavière[3] and Ruxandra Gref[1]**

[1] Université Paris-Saclay, CNRS UMR 8214, Institut des Sciences Moléculaires d'Orsay, Orsay, France, [2] Department of Radiation Biology, Institute for Cancer Research, Oslo University Hospital, Oslo, Norway, [3] University of Lyon, CNRS, UMR 5223, IMP, Villeurbanne, France

OPEN ACCESS

Edited by:
Gang Liu,
Xiamen University, China

Reviewed by:
Paolo Bigini,
Mario Negri Institute for Pharmacological Research (IRCCS), Italy
Clara Mattu,
Politecnico di Torino, Italy

***Correspondence:**
Ruxandra Gref
ruxandra.gref@universite-paris-saclay.fr;
ruxandra.gref@u-psud.fr

Specialty section:
This article was submitted to Nanobiotechnology, a section of the journal Frontiers in Bioengineering and Biotechnology

Received: 28 May 2020
Accepted: 06 August 2020
Published: 15 September 2020

Citation:
Li X, Salzano G, Qiu J, Menard M, Berg K, Theodossiou T, Ladavière C and Gref R (2020) Drug-Loaded Lipid-Coated Hybrid Organic-Inorganic "Stealth" Nanoparticles for Cancer Therapy. Front. Bioeng. Biotechnol. 8:1027. doi: 10.3389/fbioe.2020.01027

Hybrid porous nanoscale metal organic frameworks (nanoMOFs) made of iron trimesate are attracting increasing interest as drug carriers, due to their high drug loading capacity, biodegradability, and biocompatibility. NanoMOF surface modification to prevent clearance by the innate immune system remains still challenging in reason of their high porosity and biodegradable character. Herein, FDA-approved lipids and poly(ethylene glycol) (PEG)-lipid conjugates were used to engineer the surface of nanoMOFs by a rapid and convenient solvent-exchange deposition method. The resulting lipid-coated nanoMOFs were extensively characterized. For the first time, we show that nanoMOF surface modification with lipids affords a better control over drug release and their degradation in biological media. Moreover, when loaded with the anticancer drug Gem-MP (Gemcitabine-monophosphate), iron trimesate nanoMOFs acted as "Trojan horses" carrying the drug inside cancer cells to eradicate them. Most interestingly, the PEG-coated nanoMOFs escaped the capture by macrophages. In a nutshell, versatile PEG-based lipid shells control cell interactions and open perspectives for drug targeting.

Keywords: metal organic frameworks, nanoparticles, lipids, poly(ethylene glycol), stealth, sustained drug release

INTRODUCTION

Despite progresses in drug development and cancer biology, cancer mortality rate remains over 30%, and the morbidity much higher. Nanomedicine has shown great promise through drug delivery by achieving drug transcytosis, drug targeting and theranostics (Rosenblum et al., 2018; Senapati et al., 2018). Nanoscale metal organic frameworks (nanoMOFs) recently emerged as an attracting class of hybrid nanomaterials for biomedical applications due to their biodegradability, biocompatibility, elevated drug loading capacity and high versatility in terms of architecture and physico-chemical properties (Horcajada et al., 2010, 2012; He et al., 2015; Rojas et al., 2019). NanoMOFs are formed by the self-assembly of metal centers and organic ligands, leading to the formation of open crystalline structures with regular and high porosities.

Iron (III) trimesate nanoMOFs (**Figure 1** upper panel) are among the most widely studied MOFs for drug delivery (Horcajada et al., 2010; Agostoni et al., 2013; Baati et al., 2013; Simon-Yarza et al., 2016; Li et al., 2019a). Recently, they were shown to display several intrinsic properties of main interest in the nanomedicine field: radio-enhancement properties when submitted to γ-irradiation (Li et al., 2019a); they behaved as T_2-weighted MRI imaging contrast agents (Horcajada et al., 2010) and they had intrinsic antibacterial effects killing intracellular bacteria (Li et al., 2019b).

In addition, iron trimesate nanoMOFs MIL-100 (Fe) (MIL stands for Material from Institut Lavoisier) exhibited high drug loading capacity soaking a variety of drugs from their aqueous solutions with yields close to 100%. In the case of Gemcitabine-monophosphate (Gem-MP), the drug payload reached ∼30 wt% with >98% drug loading efficiency (Rodriguez-Ruiz et al., 2015). Gem-MP, the active intermediate of Gem, is widely used in various carcinomas, including pancreatic cancer, bladder cancer, and non-small cell lung cancer. The administration of Gem-MP is of high interest for resistant cancer treatment since the phosphorylation of Gem can be a rate-limiting step especially difficult for resistant cancer cells. However, Gem-MP administration is hampered by its poor stability in biological media and low cellular uptake (Bouffard et al., 1993). In this challenging context, some of us showed that Gem-MP could be protected against degradation with increased cellular uptake by encapsulation in nanoMOFs (Rodriguez-Ruiz et al., 2015).

Surface modifications are essential to control drug release and modulate the *in vivo* fate of nanoMOFs in the living body. Silica coatings were employed in an attempt to control the release of loaded molecules from nanoMOFs MIL-101 (Taylor-Pashow et al., 2009). NanoMOFs were coated with lipid bilayers to improve their uptake by cancer cells (Wuttke et al., 2015) or with chitosan to increase their intestinal permeability (Hidalgo et al., 2017). Heparin coatings endowed the nanoMOFs with longer-blood circulation time (Bellido et al., 2015).

Poly(ethylene glycol) (PEG) based materials remain the most employed ones to engineer coatings able to prevent nanoparticles (NPs) clearance by the innate immune system, which is a prerequisite for biomedical applications (Gref et al., 1994, 1995). However, as compared to dense polymeric NPs, the porous nanoMOFs are more challenging to be coated with PEG, because these linear chains readily penetrate within their porosity, inducing an uncontrolled "burst" drug release (Agostoni et al., 2015). There are still scarce examples of successful PEGylated nanoMOF formulations. PEG was crosslinked onto the nanoMOF's surface to avoid its penetration inside the porous cores (Giménez-marqués et al., 2018) but resulted in a non-biodegradable coating. Alternatively, nanoMOFs were coated with inclusion complexes consisting of functionalized

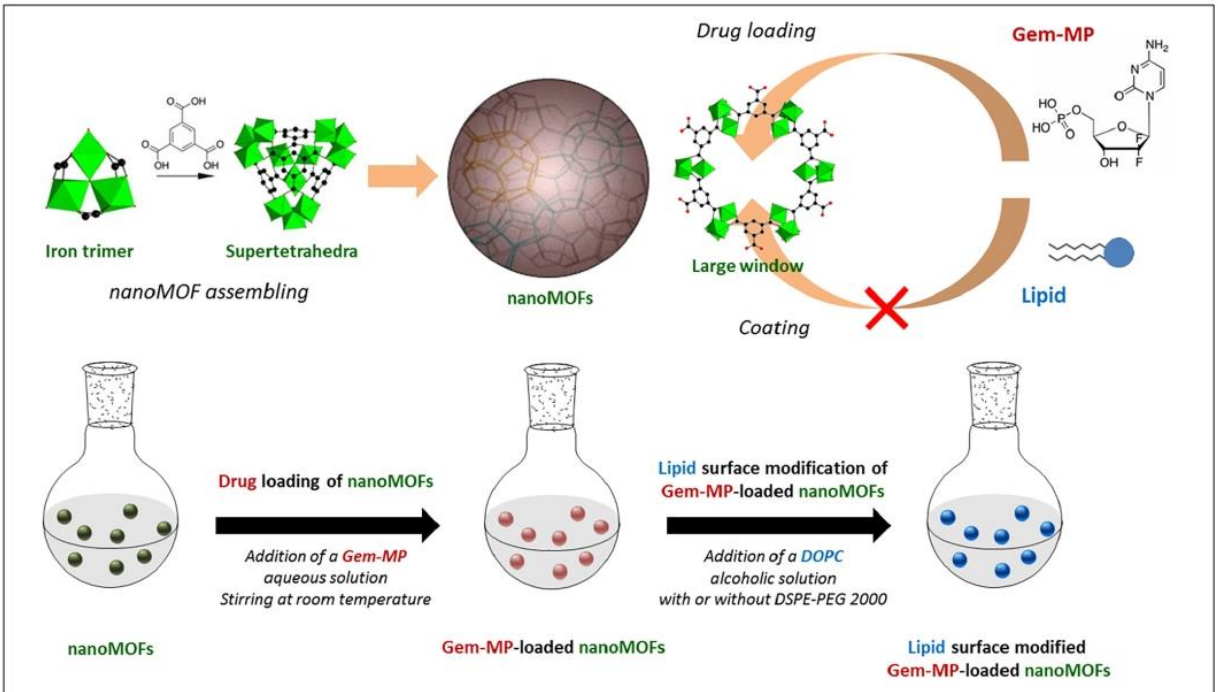

FIGURE 1 | Upper panel: Schematic representation of the MIL-100(Fe) nanoMOF assembly from iron trimers and trimesic acid. Gem-MP was loaded by impregnation from aqueous solutions, penetrating inside the nanoMOFs through their largest windows (approx. 9 Å in size). Lipid molecules (DOPC and DSPE-PEG 2000) with larger molecular dimensions than the large windows were used to coat the nanoMOFs. **Lower panel**: Preparation steps of lipid-coated nanoMOFs. First, Gem-MP was loaded, into the nanoMOFs followed by their coating with lipid shells and PEG-lipid conjugates.

cyclodextrins (CDs) and PEG chains coupled to adamantine (Agostoni et al., 2015; Aykac et al., 2017; Cutrone et al., 2019a). Finally, comb-like copolymers consisting of polysaccharides grafted with moieties able to coordinate to the nanoMOFs and PEG chains were synthesized and anchored onto the nanoMOFs (Cutrone et al., 2019b). However, all these coatings imply sophisticated chemistry strategies and/or several preparation steps, which might restrict their further applications. Moreover, all the PEGylated (macro) molecules used in the previous studies are not approved by Food and Drug Administration (FDA).

In this context, we propose to engineer for the first time PEGylated coatings on nanoMOFs by using only FDA-approved materials using a convenient one-step method. To date, Doxil R and Onivyde R represent the only FDA-approved PEGylated NPs (Barenholz, 2012), where DSPE-PEG 2000 (1,2-distearoyl-*sn*-glycero-3-phosphoethanolamine-N-[amino (polyethylene glycol)-2000] sodium salt) were used in both cases. Herein, DSPE-PEG 2000 was used in combination with DOPC (1,2-dioleoyl-*sn*-glycero-3-phosphocholine) to functionalize the surface of iron trimesate MOFs (**Figure 1** lower panel). Moreover, we show that the PEG-based coating have an impact on both drug release and nanoMOFs degradation, which was not the case with the coatings used so far. Finally, the coatings were able not only to reduce macrophage uptake *in vitro* but also to kill cancer cells.

MATERIALS AND METHODS

Materials

Iron (III) chloride hexahydrate (98%) was purchased from Alfa Aesar (Schiltigheim, France). 1,3,5-benzenetricarboxylic acid (BTC, 95%) and absolute ethanol (99%) were from Sigma-Aldrich (Saint-Quentin-Fallavier, France). These materials were used for the synthesis of nanoMOFs. Amoxicillin (Amox) from Sigma-Aldrich (Saint-Quentin-Fallavier, France) and 2′,2′-difluorodeoxycytidine monophosphate (Gem-MP) from Toronto Research Chemicals (North York, Canada) were the drugs used in this study. 1,2-dioleoyl-sn-glycero-3-phosphocholine (DOPC) and (1,2-distearoyl-*sn*-glycero-3-phosphoethanolamine-N-[amino(polyethylene glycol)-2000] sodium salt (DSPE-PEG 2000) were ordered from Avanti Polar Lipids (Alabama, United States) as coating materials. 3-(4,5-Dimethyl-2-thiazolyl)-2,5-diphenyl-2H-tetrazolium bromide (MTT, Sigma-Aldrich, Oslo, Norway) was used for toxicity evaluation of nanoMOFs. All the chemicals were used without further purification.

Cell Culture

Murine macrophage cell line J774A.1, *CelluloNet biobank BB-0033-00072*, were grown in RPMI-1640 medium (Thermo Fisher Scientific, Villebon-sur-Yvette, France) supplemented with 10% v/v decomplemented fetal bovine serum (FBS, Thermo Fisher Scientific, Villebon-sur-Yvette, France), 1% L-Gluthamine (Sigma-Aldrich, Oslo, Norway), and 1% (P/S, Sigma-Aldrich, Oslo, Norway) at 37°C in humidified air containing 5% CO_2. SKOV3 ovarian cancer cell were cultivated in a RPMI-1640 media without phenol red supplemented with 10% FBS, 5% L-Gluthamine and 5% penicillin/streptomycin (P/S) at 37°C in a 5% CO_2 humidified atmosphere.

Synthesis and Characterization of MIL-100(Fe) NanoMOFs

Iron trimesate nanoMOFs was synthesized by microwave assisted hydrothermal reaction as previously described [6]. Briefly, 20 mL of aqueous mixture containing 6.0 mM of iron chloride hexahydrate and 4.02 mM of trimesic acid (TA, 1,3,5-benzenetricarboxylic acid) was heated at 130°C for 6 min under stirring. The reaction was carried out with the power of 1600 W (Mars-5, CEM, United States). The as-synthesized nanoMOFs were harvested by centrifugation (10,000 *g*, 15 min) and washed with absolute ethanol to remove the excessive TA until the supernatant became colorless. NanoMOFs were stored in ethanol at room temperature for further usage at the concentration of 18.2 mg/mL.

SEM images were acquired on a Zeiss SUPRA 55 VP field emission gun scanning electron microscope fitted with an EDAX EDS analytical system. It was set to a low voltage (1 kV) and low current (a few pA) in order not to damage the samples and to avoid any conductive coating that could bother direct observation of the samples. Secondary electron type detector was used to record the images.

Dynamic light scattering (DLS) measurements were performed at 25°C on a Malvern Zetasizer Nano-ZS instrument at 90° angle. The mean hydrodynamic diameter of the particles was determined in a diluted aqueous suspension at 50 μg/mL.

Nanoparticle tracking analysis (NTA) was performed on Malvern NanoSight (LM10 Instrument, Malvern Instruments Ltd., Orsay, France), which combines a conventional optical microscope with a laser to illuminate the NPs in Brownian motion. It is used to individually follow nanoMOFs to gain insight into their size distribution and concentration.

Zeta potential (ZP) of nanoMOFs were measured at 25°C using a Zetasizer Nano-ZS instrument at different pH ranging from 3 to 10. NanoMOFs was diluted to 100 μg/mL with 1 mM KCl. Measured electrophoretic mobilities were converted to zeta potential values according to the Smoluchowski equation. Nitrogen sorption measurements were performed on a Micromeritics Instruments ASAP 2020 at 77 K. Samples were degassed at 100°C for 15 h. BET surface area was calculated in the partial pressure range of 0.05 – 0.20 P/P_0.

Drug Encapsulation in NanoMOFs

Drugs (Gem-MP and Amox) were loaded within nanoMOFs simply by impregnation of drug(s) aqueous solutions and nanoMOFs. Practically, nanoMOFs suspension (1.0 mg) were centrifuged for 10 min at 10,000 *g* and re-suspended in 1 mL of aqueous drug solutions (0.125 ∼ 1 mg/mL for Amox and 0.08 ∼ 0.2 mg/mL for Gem-MP) or water as a control. Different drug concentrations were used to optimize the drug encapsulation. After incubation at room temperature under gentle stirring for several hours (12 h for Amox and 4 h for Gem-MP), the nanoMOFs were recovered by centrifugation at 10,000 *g* for 10 min. The non-encapsulated drug in the supernatant was

quantified by adapting previously described High Performance Liquid Chromatography (HPLC) methods (Li et al., 2019a,b). Specifically, HPLC analysis was performed on an Agilent system using a tunable UV absorbance detector. The injection volume of AMOX was 10 μL followed by eluant flow at a rate of 0.5 mL/min through a C18 Silica column (4.6 × 250 mm, 5 μm; Phenomenex) maintained at 30°C. The mobile phase consisted of 30% (v/v) methanol containing 5.2 mg/mL of sodium dihydrogene phosphate monohydrate. The pH was adjusted to 5 using phosphoric acid solution. AMOX were detected at 247 nm and retention times were 4.6 min. Similarly, Gem-MP was detected using the same Agilent system and column. The mobile phase was composed of 84% buffer [0.2 M (TEAA)]: 16% methanol. It was detected at 254 nm with an injection volume of 10 μl. The drug payload was calculated as Equation (1):

$$Payload\ \ (\%) = \frac{Encapsulated\ \ Drug(mg)}{nanoMOFs(mg)} \times 100 \qquad (1)$$

Surface Modification of NanoMOFs With DOPC Lipids and PEG-Lipid Conjugates

Surface modification was performed using a "green" method. To prepare DOPC coated nanoMOFs, 60 μl of nanoMOFs were mixed with 40 μl of DOPC alcoholic solution containing 100 μg of DOPC. Subsequently, 900 μl of water were rapidly added using an electronic pipette. The weight ratio between DOPC and nanoMOF was in the range of 1:20 ~ 1:1. In the case of PEG-lipid conjugates coated nanoMOFs, 20 wt% of DOPC was replaced by DSPE-PEG 2000.

Characterization of Lipid Coated NanoMOFs

Lipid Quantification

DOPC quantification was performed by a colorimetric, enzymatic method (BIOLABO, Maizy, France) which is commonly used to determine the phospholipid amount in serum. This titration is based on the assay of the choline moiety of phospholipids. To do this, 10 μL of specimens or a standard solution were mixed with the reagents in the BIOLABO titration kit. The mixtures were stirred 10 min. at 37°C. Then, the absorbance at 500 nm of all samples was measured. The DOPC concentration was finally calculated as Eq. (2):

$$DOPC\ concentration = Standard\ concentration \times \frac{Abs(specimen)}{Abs(standard)} \times 100 \qquad (2)$$

NPs Concentration Measurements by NP Tracking Analysis (NTA)

The concentration of nanoMOFs modified with DOPC or PEG-lipid conjugates at different weight ratios was investigated by Nanosight (LM10 Instrument, Malvern Instruments Ltd., Orsay, France), which combines a conventional optical microscope with a laser to illuminate the NPs in Brownian motion. Of main interest here, the size distribution and concentration could be determined simultaneously. Results are expressed as means of five independent measurements.

Colloid Stability Characterization by DLS

The colloid stability of the nanoMOFs before and after lipid surface modification was monitored in water every day during 3 weeks' storage at 4°C. The stability in biological medium, including cell culture medium and phosphate buffer saline (PBS) used in this study, was also measured at 0, 0.5, 1, 2, 4, 6, and 8 h after incubation at 37°C.

Drug Release and Degradation of nanoMOFs

Drug release was performed in PBS of different concentrations at 37°C. Briefly, drug loaded nanoMOFs were centrifuged at 10,000 *g* for 10 min and the pellet was re-dispersed in 1 mL water by vortex. Aliquots of 100 μL were taken and mixed with 900 μl of the media used for release. The final concentration of PBS was 1, 3, and 6 mM and nanoMOFs of 2.0 mg/mL. After different incubation times (30 min, 1 h, 2 h, 4 h, 6 h and 24 h), the suspensions were centrifuged and the supernatants were assessed by HPLC as previously described to determine the amount of released drug. Moreover, the trimesate release was also evaluated by HPLC. Briefly, trimesate was analyzed with a mobile phase consisting of 90% buffer (5.75 g/L of $NH_4H_2PO_4$): 10% Acetonitrile containing 5 mM TBAP. The injection volume was 5 μl and the detection wavelength was set at 220 nm.

Human Plasma Protein Adhesion Tests

Human serum albumin (HSA) was used in this study. NanoMOFs modified or not (300 μg/mL) were incubated with HSA at 100 μg/mL in 10 mM phosphate buffer at 37°C. The samples were centrifuged at 10,000 *g* for 5 min to remove the nanoMOFs after 1, 2, 4, 6, 8 and 12 h incubation. The excessive amounts of HSA in the supernatant were quantified using a bicinchoninic acid (BCA) assay.

NanoMOF Internalization in Macrophage

NanoMOF internalization was quantified by Inductively Coupled Plasma Mass Spectrometry (ICP-MS). Macrophage cells (J774A.1) were seeded at a density of 2.0×10^5 cells per well in 24-well plates. Cells were cultured at 37°C in 5% CO_2 overnight for attachment. Cells were then incubated with 1 mL cell culture media containing nanoMOFs coated or not with lipids (nanoMOF concentration = 50 μg/mL). At the end of the 4 h incubation, the cells were washed with PBS for three times to eliminate the excess of MOFs. Cells were finally dried and digested using aqua regia (15 min under ultrasonic bath), Fe quantification was performed using an ICP-MS equipped with a triple quadrupole (Agilent 8800, Agilent Technologies, Japan). Fe and Co were added as internal standard on samples and calibration standards solution at a concentration of 10 μg/L. Isotopes were detected using "on-mass mode" ($^{54}Fe^+$, $^{56}Fe^+$, $^{59}Co^+$). Helium was introduced into the collision/reaction cell at a flow rate of 3 mL/min. Dwell time for each of the targeted isotopes was 1 s. Fe was quantified using external calibration prepared using certified 1000 mg/L Fe standard solution (Merck, Germany). Operation conditions were daily optimized using a tuning solution.

Cytotoxicity Assessment

MTT assays were carried out on SKOV3 ovarian cancer cell line to investigate the cytotoxicity of NPs. The cells were plated in 96 well plates at a concentration of 10,000 cells per well. The media was removed after 24 h incubation and replaced by fresh media containing the MOFs nanoparticles at different concentrations. The cytotoxicity was assessed by MTT assay at 24, 48 and 72 h following the incubation of the cells with the MOFs. In brief, 100 μL of complete media containing 0.5 mg/mL of MTT were added to cells and incubated for 2 h at 37°C in a 5% CO_2 humidified atmosphere. Subsequently, the MTT media were removed and replaced by 100 μL of DMSO per well to dissolve the MTT-formazan crystals. The plates were shaken for 10 min at 350 rpm in a Heidolph Titramax 101 orbital shaker, and the absorbance at 595 nm was measured with the Tecan spark M10 plate reader. Each MTT experiment was reproduced three times.

RESULTS AND DISCUSSION

MIL-100 (Fe) nanoMOF Surface Modification and Characterization of Functionalized NanoMOFs

Iron trimesate nanoMOFs with mean diameters of 232 ± 14 nm and Brunauer–Emmett–Teller (BET) surface areas of 1519 ± 50 $m^2.g^{-1}$ were successfully synthesized by a "green" organic solvent-free hydrothermal method exempt of toxic additives such as hydrofluoric acid (Agostoni et al., 2013). They were crystalline and exhibited a facetted morphology (**Figure 2A**) in agreement with previously reported data (Cutrone et al., 2019a,b).

In an attempt to achieve "stealth" NPs, the as-synthesized nanoMOF were surface functionalized with PEG-lipid conjugates in a one-step procedure using a mixture of DSPE-PEG 2000 and DOPC. Lipids were associated within less than 2 min at room temperature by dispersing the nanoMOFs in an ethanolic aqueous solution containing both DSPE-PEG 2000 and DOPC, followed by a quick addition of water to favor lipid deposition onto the nanoMOF surface. Indeed, lipids were freely soluble in ethanol/water mixtures, but they readily precipitated upon progressive addition of water which drastically reduced their solubility, leading to precipitation onto the nanoMOF surfaces (Wuttke et al., 2015). DOPC-coated nanoMOFs were prepared as controls using the same method. The bare and coated nanoMOFs were characterized by a set of complementary methods.

Firstly, SEM images show that the lipid-coated nanoMOFs displayed similar shapes but with more rounded edges (**Figure 2B**) as compared to the uncoated ones (**Figure 2A**), possibly because surface modification. No significant differences were observed for the coated nanoMOFs with or without PEG-lipid conjugates (**Figure 2C**). Secondly, EDX experiments were performed to detect the presence of elements specific to the MOF cores (C, O, Fe) and to the shells (C, O, N) in the top layers of the NPs (around 10 nm depth). The presence of the DOPC coating was evidenced by the detection of an N peak characteristic of DOPC which was not found with bare nanoMOFs (**Supplementary Figure S1**). Interestingly, in the PEG shells obtained with the lipid mixtures, the relative O content was increased by a factor of 4 as compared to DOPC coatings (**Supplementary Figure S1**) possibly due to the presence of PEG chains in the nanoMOFs' top layers, as PEG has the highest O content from all the nanoMOF components. These data offer a straightforward proof for both the presence of DOPC and PEG-lipid conjugates in the nanoMOF top layers.

The amount of DOPC in the nanoMOFs was quantified by using a colorimetric enzymatic method. For this, the DOPC:nanoMOF weight ratio in the preparation procedure was varied from 1:20 to 1:1. As shown in **Figure 3A**, the amount of lipids associated to the nanoMOFs increased with the amount of lipids used in the coating procedure. A plateau was reached at a DOPC: nanoMOF weight ratio of 1:3, corresponding to 25 ± 4 wt% lipids associated to the nanoMOFs. These quantities of coating material are among the highest reported so far (Horcajada et al., 2010; Agostoni et al., 2015; Bellido et al., 2015; Hidalgo et al., 2017; Giménez-marqués et al., 2018; Cutrone et al., 2019a,b). As comparison, phosphorylated cyclodextrin (CD-P) coatings on same iron trimesate nanoMOFs reached ∼ 17 wt% (Agostoni et al., 2015). The important lipid association could be possibly due to: i) the fast precipitation of lipids at the hydrophobic surface of nanoMOFs, and ii) the strong affinity of the phosphate groups in the lipids for the iron sites at the nanoMOFs' surface.

The nanoMOFs, coated or not, were characterized by a set of complementary methods. First, X-ray powder diffraction

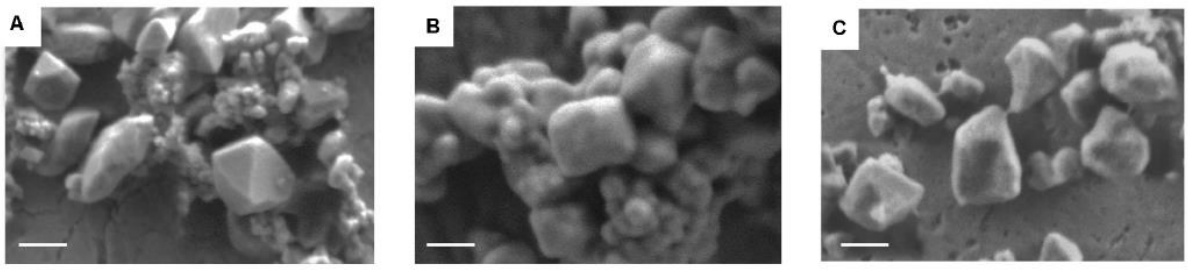

FIGURE 2 | Representative scanning electron microscope (SEM) images of nanoMOFs before and after lipid modification. **(A)** nanoMOFs; **(B)** nanoMOFs after modification with DOPC; **(C)** nanoMOFs after modification with DOPC and DSPE-PEG 2000. Scale bar: 100 μm.

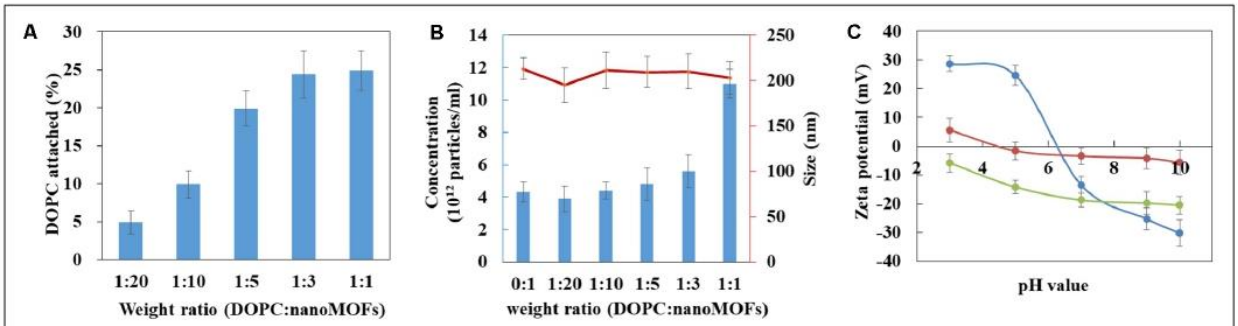

FIGURE 3 | Characterization of lipid-coated nanoMOFs. **(A)** Quantification of the amount of DOPC in the nanoMOFs; **(B)** Mean hydrodynamic diameter (red) and concentration (blue) of DOPC-coated nanoMOFs determined by NTA. **(C)** Zeta potential of nanoMOFs as a function of pH before (blue) and after lipid coating with (red) or without (green) the addition of DSPE-PEG 2000.

(XRPD) showed that the crystalline structure of the nanoMOFs was preserved after surface modification (**Supplementary Figure S2**). Dynamic light scattering (DLS) proved that there were no significant differences between the mean hydrodynamic diameters of nanoMOFs before and after surface functionalization (232 ± 14 nm, 241 ± 17 nm and 238 ± 11 nm for uncoated nanoMOFs, lipid coated nanoMOFs at a DOPC: nanoMOF weight ratio of 1:3, with and without DSPE-PEG 2000, respectively). Moreover, the BET surface areas were not affected by surface modification with lipids (1519 ± 50 $m^2.g^{-1}$, 1486 ± 70 $m^2.g^{-1}$, and 1547 ± 80 $m^2.g^{-1}$ for uncoated nanoMOFs, lipid coated nanoMOFs with and without DSPE-PEG 2000, respectively), suggesting that the bulky lipids were located onto the nanoMOF's external surfaces rather than into their porosity.

Before surface modification, the nanoMOF concentration was around (4 ± 0.8) × 10^{12} particles/mL, as determined by Nanoparticle Tracking Analysis (NTA). Interestingly, the nanoMOF particle concentration did not change upon modification with lipids (**Figure 3B**, blue histograms), suggesting that the lipids adhered at their surface and did not remain into the suspension medium. Indeed, at DOPC:nanoMOFs weight ratios from 0:1 up to 1:3, both particle concentrations and mean hydrodynamic diameters were unaffected [(5.6 ± 0.8) × 10^{12} particles/mL, and 210 ± 23 nm, respectively]. To support this hypothesis, DLS analysis of supernatants (**Supplementary Table S1**) after particle centrifugation revealed that they were devoid of any lipid vesicles (<1% particles free).

However, addition of excess lipids (weight DOPC:nanoMOF ratio of 1:1) resulted in a dramatic increase of total particle concentration [from (4 ± 0.8) × 10^{12} to (1.1 ± 0.4) × 10^{13} particles/mL], presumably because the nanoMOF surfaces were saturated with lipids. Of note, the mean hydrodynamic diameter of the nanoMOFs was unaffected, only the polydispersity index (PdI) increased from 0.15 to 0.25, possibly because of the presence of lipid vesicles in excess. Note that the association of DSPE-PEG 2000 didn't significantly influence the mean hydrodynamic diameter, nor the nanoMOF's concentration (less than 10% variations) suggesting that the PEGylated lipids also attached onto the nanoMOFs. In conclusion, lipids were associated up to 25 ± 4 wt% without inducing any changes in nanoMOF porosities, size distribution, and crystallinity.

Interestingly, the presence of the coatings affected the nanoMOFs electrophoretic mobility, as shown by Zeta potential (ZP) investigations in **Figure 3C**. Indeed, the ZP of the uncoated nanoMOFs was strongly dependent upon the pH of the suspension medium, shifting from positive values (+ 23 ± 3 mV) at pH lower than 5 to negative values (−15 ± 3 mV) at basic pH. This could be probably due to the presence of both uncoordinated iron sites and terminal carboxyl groups of the trimesate ligands at the external nanoMOFs surface (Cutrone et al., 2019b). The ZP values were dramatically altered after surface modification (**Figure 3C**). DOPC-coated nanoMOFs displayed negative ZP values (−6 to −20 mV) whatever the pH in the range of 3 to 10, in line with data reported for DOPC liposomes (Chibowski and Szcześ, 2016). These results support the presence of DOPC lipid layers onto the nanoMOFs which shield their charged surface moieties. Interestingly, when the nanoMOFs were surface-functionalized with PEG chains, their ZP values were shifted to neutral (–1.6 ± 3.4 mV). This is in good agreement with other studies on PEG-coated NPs (Gref et al., 1995; Thevenot et al., 2007; Troutier and Ladavière, 2007; Troutier-Thuilliez et al., 2009; Bugnicourt et al., 2019).

Effect of the Coatings on the Colloidal Stability of NanoMOFs in Biological Media

As the majority of uncoated NPs, nanoMOFs suffer from poor stability in biological media, which hampers their biomedical applications. **Figure 4** clearly shows that uncoated nanoMOFs undergo a fast aggregation in both phosphate buffer saline (PBS, pH = 7.4, 10 mM) and cell culture medium DMEM (Dulbecco's Modified Eagle Medium) without fetal bovine serum (FBS), with the mean hydrodynamic diameters rapidly increasing to more than 1 μm within only 6 h at 37°C (**Figure 4**). No significant variation was observed for the mean hydrodynamic diameter of uncoated nanoMOFs in water in the first 1 h, however, they tended to aggregate upon storage (**Supplementary Figure S3**). They were stable only in DMEM supplemented with 10% (v/v)

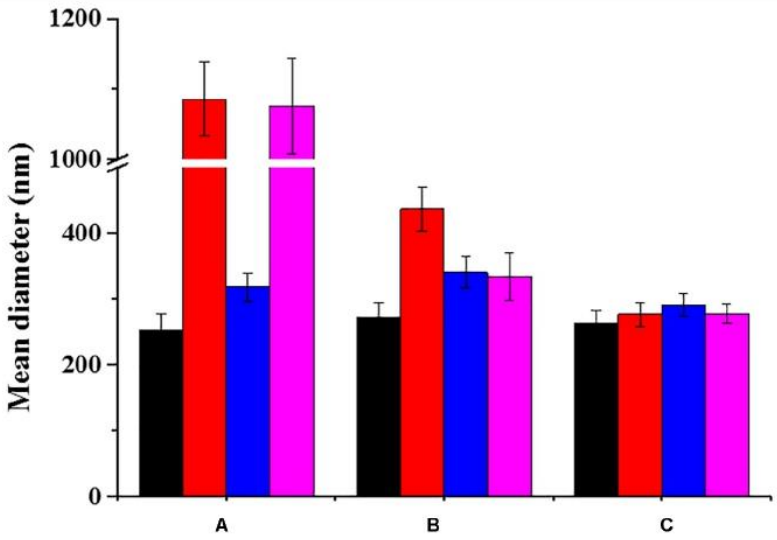

FIGURE 4 | Colloidal stability of nanoMOFs in different media, before **(A)** and after surface functionalization with DOPC **(B)** or PEG-lipid conjugates **(C)**. Mean hydrodynamic diameters of nanoMOF suspensions at 100 μg/mL were determined by DLS after 6 h incubation at 37°C. (Black: water; red: PBS; blue: DMEM supplemented with 10v/v% FBS; pink: DMEM without FBS).

FBS, possibly due to the formation of a protein corona at their surface preventing their aggregation (see section "Effect of surface functionalization of nanoMOFs on protein adsorption and macrophage uptake").

In contrast, DOPC coated nanoMOFs were stable both in water and DMEM. No aggregation was observed even after 3 weeks storage. However, they still underwent aggregation in PBS (**Figure 4**). Remarkably, PEGylation allowed circumventing stability issues, whatever the suspension media (less than 10% diameter variation in PBS).

As all the coated and uncoated nanoMOFs were stable in DMEM supplemented with 10% (v/v) FBS, it was possible to explore further their cytotoxicity and interactions with cancer cell lines and macrophages. The PEGylated nanoMOFs exhibited excellent colloidal stability in all the tested biological media and thus appeared as optimal candidates for biological applications.

Control of Degradation and Drug Release by Lipid Coating

There is a general agreement on the fact that once the nanomaterials release their drug cargo, they should degrade to avoid accumulation inside the body (Horcajada et al., 2012). However, Fe-based nanoMOFs are reported to degrade rapidly in the biological media, because of coordination of various ions (phosphates, sulfates, etc.) to their iron sites, sometimes leading to uncontrolled "burst" drug release (Agostoni et al., 2013; Li et al., 2017, 2019b). It was therefore interesting to investigate if the hydrophobic lipid coatings could interfere with the rapid penetration of the aqueous degrading media inside the pores, thus allowing gaining better control upon the release and degradation mechanisms.

Degradation of nanoMOFs is generally monitored by the release of the constituting ligand trimesate (Agostoni et al., 2013; Rodriguez-Ruiz et al., 2015; Li et al., 2017). The degradation of the lipid-coated or bare nanoMOFs was studied by assaying ligand trimesate by HPLC in PBS (**Figure 5A**). In PBS 1 mM, uncoated nanoMOFs (blue curve, **Figure 5A**) underwent a fast degradation in the first 1 h at 37°C with around 15.5 ± 1.1% trimesate released, in agreement with previous reports (Li et al., 2017). It was discovered that in the same conditions, the lipid-coated nanoMOFs, with (red curve, **Figure 5A**) or without PEG-lipids conjugates (green curve, **Figure 5A**), exhibited much slower degradation profiles than the uncoated nanoMOFs, with only 10 ± 0.2% trimesate release in the first 1 h. This suggests a more progressive diffusion of the phosphate ions into the coated nanoMOFs, slowing down their degradation. However, the same plateau was reached after 24 h incubation, corresponding to a total complexation of the phosphates in the medium (Li et al., 2017). In conclusion, the shell efficiently delayed the degradation process.

Then, the effect of lipid coatings on drug release was studied. Selected drug of interest was Gem-MP, a hydrophilic drug with low cell permeability. NanoMOFs acted as efficient "nanosponges", soaking Gem-MP from their aqueous solution with almost perfect efficiency (>98%). Maximal loadings reached 25 wt% reflecting the strong interaction between the drug and the iron trimesate matrices. Advantageously, the lipid coating process didn't induce any significant drug release (less than 3% variations before and after coating).

Gem-MP release is governed by a competition of coordination between the phosphate moieties in Gem-MP and free phosphates in PBS for the iron(III) Lewis acids

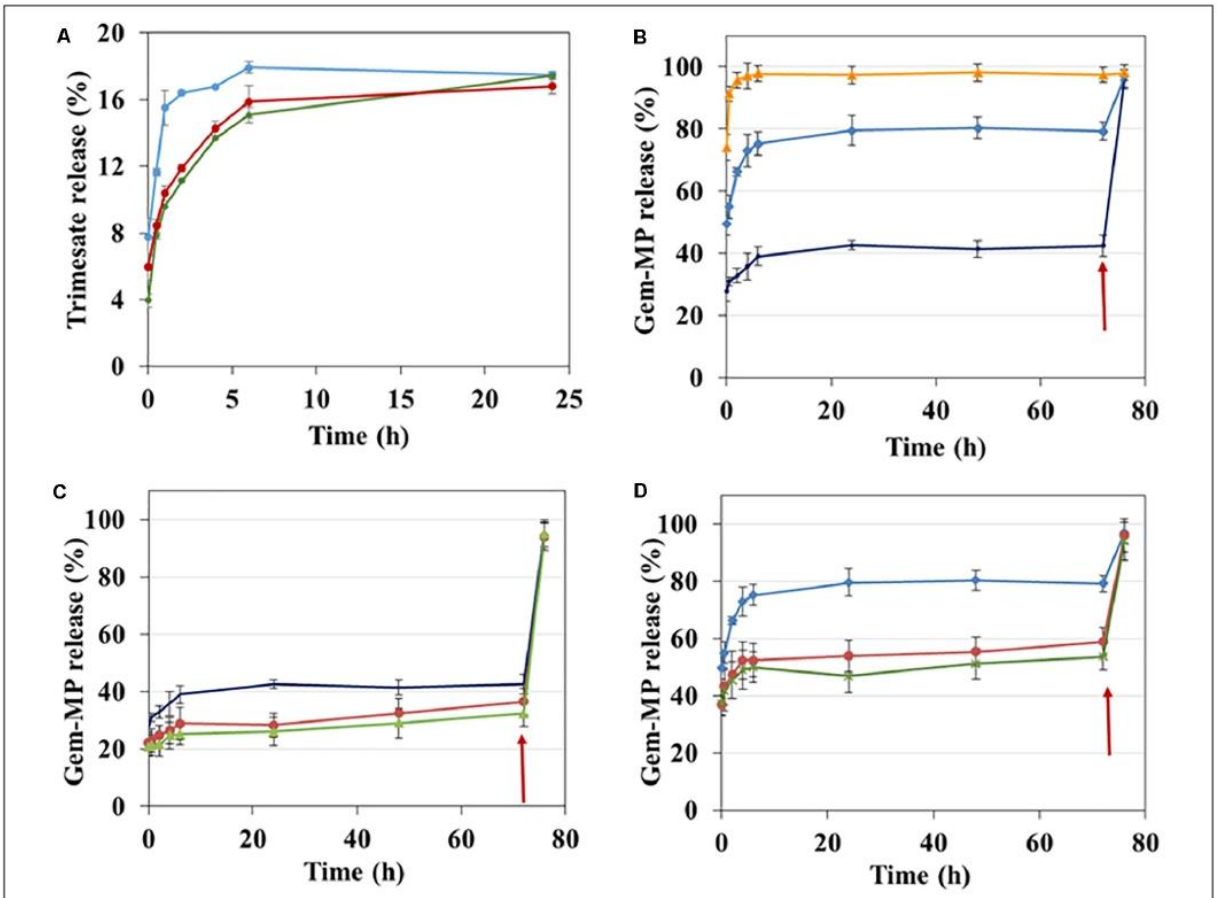

FIGURE 5 | Effect of surface modification on Gem-MP and trimesate release analyzed by HPLC. **(A)** Trimesate release in 1 mM PBS from nanoMOFs before (blue) and after lipid coating with (red) or without (green) coating with PEG-lipid conjugates after incubation at 37°C. **(B)** Gem-MP release from uncoated nanoMOFs in PBS with different molarities (orange: 6 mM, blue: 3 mM; dark blue: 1 mM). Gem-MP release in 1 mM **(C)** or 3 mM **(D)** PBS from nanoMOFs before (blue/dark blue) and after lipid coating with (red) or without (green) coating with PEG-lipid conjugates. In all cases **(B–D)**, phosphate concentration was adjusted to 10 mM after 72 h incubation at 37°C (red arrows), followed by further incubation for 4 h at 37°C.

of nanoMOFs (Agostoni et al., 2013, 2015; Rodriguez-Ruiz et al., 2015). As expected, it was found that the higher the amount of phosphates, the higher the amount of drug released (**Figure 5B**). At low phosphate concentrations (PBS 1 mM or 3 mM), a plateau (around 40% or 80% Gem-MP release) was reached in 24 h, when all the phosphate molecules present in the release medium were complexed to the iron sites, as previously reported (Agostoni et al., 2013, 2015; Rodriguez-Ruiz et al., 2015). When additional phosphates were added in the release medium, all the drug still remaining in the nanoMOFs was immediately released (**Figure 5B**, arrow). Gem-MP release was well correlated with particle degradation, resulting in trimesate release (**Supplementary Figure S4**).

The presence of the lipid coating reduced the drug release from the nanoMOFs (**Figure 5C**). For instance, after 6 h incubation in PBS 1 mM, around 30% Gm-MP was released from the coated nanoMOFs, in comparison to 40% with the uncoated ones. This is possibly due to the restricted diffusion of phosphates into the nanoMOFs because of the lipid coating. Similarly, after 6 h incubation in PBS 3 mM, around 50% Gem-MP was released from the coated nanoMOFs, in comparison to 78% with the uncoated ones (**Figure 5D**). The Gem-MP release from coated nanoMOFs gradually increased in a sustained manner in the following days (**Figures 5C,D**). All the remained drugs could be released out after 4 h incubation in concentrated phosphate buffer (10 mM PBS).

Similar results were found with another drug, amoxicillin (Amox). The amount of Amox released in the first hour of incubation release was reduced by a factor of two in the case of lipid-coated nanoMOFs as compared to the naked ones (**Figure 6A**), confirmed by different dilution factors at 10, 20, and 40 (**Figure 6B**). However, in the presence of strongly

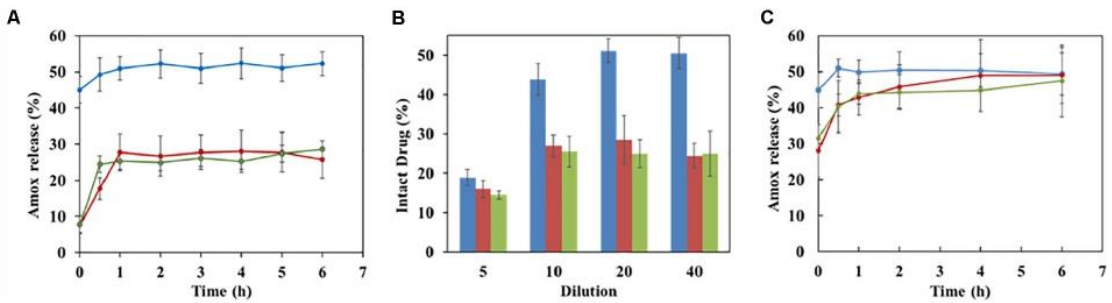

FIGURE 6 | Effect of coating on Amox release in water **(A,B)** and in PBS **(C)**. **(A)** Release kinetics of Amox in water from nanoMOFs (1 mg/mL) before or after coating, with a dilution factor of 20; **(B)** Effect of dilution factor on Amox release after 4 h incubation at 37°C in water (Blue: uncoated nanoMOFs; red: DOPC coated nanoMOFs; Green: DOPC and PEG-lipid conjugate coated nanoMOFs).

complexing phosphates, the degradation was only delayed, but not avoided (**Figure 6C**).

Cytotoxicity Assays of nanoMOFs on Ovarian Cancer Cells

All the studied nanoMOFs were non-toxic for the SKOV3 ovarian cancer cells up to 100 μg/mL (**Figure 7A**, blue histograms), with more than 98% cell viability in 24 h, which is in agreement with the previously reported lack of toxicity of these materials (Horcajada et al., 2010; Baati et al., 2013; Bellido et al., 2015; Giménez-marqués et al., 2018; Li et al., 2019b). In contrast, as expected, the anticancer drug Gem-MP (20 μg/mL, **Figure 7A**, brown histograms) exerted a cytotoxic effect with 45% cell viability after 48 h incubation, which further diminished to 29% in 72 h. Remarkably, Gem-MP loaded nanoMOFs showed a strong *in vitro* activity on SKOV3 ovarian cancer cells, higher than the free drug (**Figure 7**). At equivalent Gem-MP concentrations, whatever the drug loading (8 or 20 wt%) and the amount of nanoMOF in contact with the cells (10 to 100 μg/mL), the drug-loaded nanoMOFs outperformed the free drug in terms of toxicity on cancer cells (**Figure 7** and **Supplementary Figure S5**).

This is in line with previous studies showing the efficient internalization of nanoMOFs bearing or not a lipid coating in pancreatic, breast, or bladder cancer cell lines (Rodriguez-Ruiz et al., 2015; Wuttke et al., 2015; Li et al., 2019a). It was recently shown that nanoMOFs acted as "Trojan horses" internalized by cancer cells, carrying their Gem-MP cargo to interfere with DNA (Li et al., 2019a). In this study it was shown that interestingly, the presence of a lipid coating (PEGylated or not) did not reduce the nanoMOF anticancer efficacy on SKOV3 ovarian cancer cells.

Effect of Surface Functionalization of NanoMOFs on Protein Adsorption and Macrophage Uptake

It is well known that intravenously administered NPs are readily covered by plasma proteins, creating the so-called "protein corona", which plays a crucial role on the NPs' biodistribution and *in vivo* fate (Gref et al., 2000). To gain insight on the influence of lipid coating of nanoMOFs on protein adsorption, HSA (human serum albumin), the most abundant protein in human blood plasma, was selected for this study.

NanoMOFs coated or not with DOPC lipids and PEG-lipid conjugates were incubated for 4 h at 37°C with HSA. After separation of the supernatants by centrifugation, the amount of non-adsorbed HSA was quantified using a BCA titration in order to determine the adsorbed HSA amounts onto nanoMOFs, lipid-modified or not. These amounts, expressed as μg/mg of nanoMOFs, are reported in **Figure 8A**. In the case of uncoated nanoMOFs (**Figure 8A**, blue curve), the amount of adsorbed HSA reached a plateau within 6 h, with around 50 μg HSA/mg nanoMOFs. Interestingly, lipid coating dramatically reduced HSA adsorption, to only ~5 μg HSA/mg nanoMOFs (**Figure 8A**, green curve), regardless of the addition of DSPE-PEG 2000 (**Figure 8A**, red curve). To the best of our knowledge, these adsorbed HSA amounts are among the lowest reported with MIL-100 (Fe) nanoMOFs (Gref et al., 2000; Cutrone et al., 2019b), suggesting that lipid-based coating on nanoMOFs is efficient to avoid albumin adsorption.

The potential "stealth" effect of the lipid-coated nanoMOFs, PEGylated or not, was evaluated on the murine macrophage cell line J774. Quantitative data on the amounts of nanoMOFs internalized by cells were obtained by ICP-MS, after extensive washing to remove the non-associated particles. An incubation time of 4 h was chosen as it corresponds to the typical blood circulation time of PEG-coated NPs (Cutrone et al., 2019b). Interestingly, the DOPC coating of nanoMOFs reduced their macrophage uptake by a factor of 2.4, from 75 ± 6% to 31 ± 3% (**Figure 8B**). The nanoMOF functionalization with PEG chains was even more effective, reducing their interactions with macrophage to 21 ± 2%. Despite these great *in-vitro* results, it is widely known that numerous complex interactions can occur after NP administration in multicellular organisms. Therefore, *in vivo* studies need to be carried on to demonstrate the efficacy of the PEG coating to reduce reticuloendothelial system (RES) uptake.

Nevertheless, it has to be noted that, in similar experimental conditions, other coating materials showed higher interactions with macrophages, for instance, 41 ± 3% for CD-P coating, and

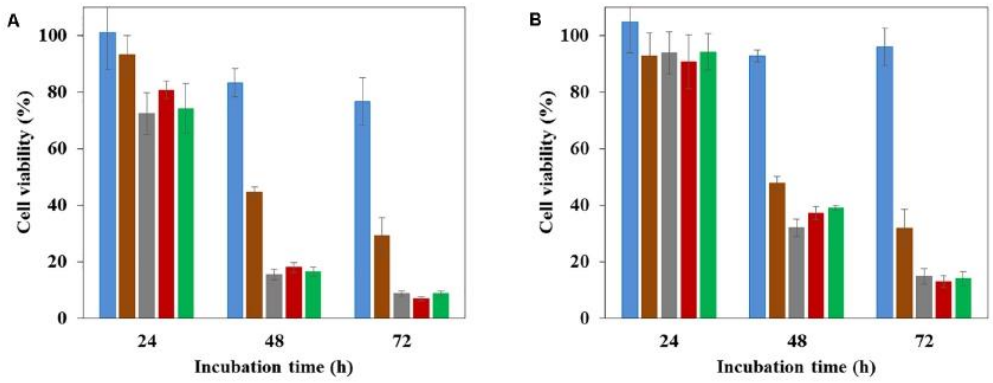

FIGURE 7 | Cytotoxcity measured by MTT assays of nanoMOFs (blue), anticancer efficacy of Gem-MP (brown), Gem-MP loaded nanoMOFs before (gray) and after coating with DOPC (red) or PEG-lipid conjugates (green). The experiments were performed on SKOV3 ovarian cancer cells, at different incubation times, with different concentrations nanoMOFs. **(A)** 100 μg/mL; **(B)** 30 μg/mL. Gem-MP loading was 20 wt%.

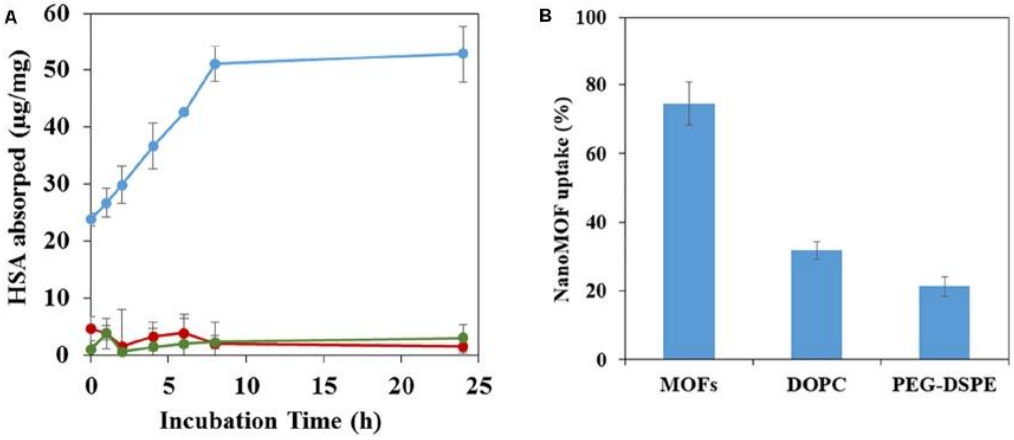

FIGURE 8 | HSA adsorption assayed by BCA assay **(A)** and J774 murine macrophage uptake **(B)** of nanoMOFs before and after lipid surface functionalization. **(A)** HSA adsorption by nanoMOFs before (blue) and after lipid coating with (red) or without (green) the addition of DSPE-PEG 2000. **(B)** NanoMOFs (before and after lipid coating, with or without addition of DSPE-PEG 2000) internalization inside murine macrophage J774 cells. 50 μg/mL nanoMOFs were incubated with 3×10^5 J774 cells for 4 h, and the amount of internalized nanoMOFs was determined by ICP-MS and expressed as a% of the initial nanoMOF amount in contact with the cells. Significant difference was observed for nanoMOFs before and after surface modification ($p < 0.01$).

39 ∼ 24% for comb-like copolymers (Cutrone et al., 2019a,b). The advantage of lipid coating, demonstrated in this work, is a straightforward method, leading to efficient and stable coatings based on already FDA-approved materials. Lipid coatings on NPs are considered to be a promising strategy for the treatment of severe pathologies such as cancer (Luchini and Vitiello, 2019). In this study, the lipid coating not only afforded a control upon cell interaction but also provided a biocompatible protective barrier, modulating drug release and nanoMOF degradation. Of note, the nanoMOFs used in this study were shown to be biocompatible after intravenous administration in rats (Baati et al., 2013). However, the biocompatibility of the supermolecules assembled resulting from nanoMOFs coating with lipids has to be demonstrated *in vivo*.

CONCLUSION

The surface of iron trimesate nanoMOFs was successfully modified with FDA approved DSPE-PEG 2000 in combination with DOPC by a fast solvent-exchange deposition method. We described herein the preparation and comprehensive characterization of the lipid modified NPs. We showed, for the first time, that the lipid surface modification of porous nanoMOFs reduced their tendency to degrade rapidly in PBS. Moreover, the coating of nanoMOFs with PEG-lipid conjugates successfully decreased their uptake by macrophages *in vitro* by a factor of 3.6. Finally, nanoMOFs acted as "Trojan horses" internalizing inside the cancer cells, and carrying their Gem-MP cargo to interfere with DNA.

DATA AVAILABILITY STATEMENT

The datasets generated for this study are available on request to the corresponding author.

AUTHOR CONTRIBUTIONS

RG conceived the study. RG, XL, and GS designed the experiments. XL, GS, and JQ preformed the experiments. CL contributed to the lipid investigations. XL and RG wrote the manuscript. MM, KB, and TT contributed to the biological evaluations. All authors approved the submitted version.

FUNDING

Financial support for this work was provided the French National Research Agency (ANR-14-CE08-0017 and ANR-16-CE18-0018) and Euronanomed III (project PCInano). This work was also supported by a public grant overseen by the French National Research Agency as part of the "Investissements d'Avenir" program (Labex NanoSaclay, ANR-10-LABX-0035).

ACKNOWLEDGMENTS

We acknowledge Dr. B. Moreira-Alvarez and Dr. J. R. Encinar for their kind help with ICP-MS analysis. We also thank Dr. D. Constantin for help with XRPD experiments.

SUPPLEMENTARY MATERIAL

The Supplementary Material for this article can be found online at: https://www.frontiersin.org/articles/10.3389/fbioe.2020.01027/full#supplementary-material

REFERENCES

Agostoni, V., Chalati, T., Horcajada, P., Willaime, H., Anand, R., Semiramoth, N., et al. (2013). Towards an improved anti-HIV activity of NRTI via Metal-Organic Frameworks nanoparticles. *Adv. Healthc. Mater.* 2, 1630–1637. doi: 10.1002/adhm.201200454

Agostoni, V., Horcajada, P., Noiray, M., Malanga, M., Aykaç, A., Jicsinszky, L., et al. (2015). A "green" strategy to construct non-covalent, stable and bioactive coatings on porous MOF nanoparticles. *Sci. Rep.* 5:7925. doi: 10.1038/srep07925

Aykac, A., Noiray, M., Malanga, M., Agostoni, V., Casas-Solvas, J. M., Fenyvesi, E., et al. (2017). A non-covalent "click chemistry" strategy to efficiently coat highly porous MOF nanoparticles with a stable polymeric shell. *BBA Gen. Subj.* 1861, 1606–1616. doi: 10.1016/j.bbagen.2017.01.016

Baati, T., Njim, L., Neffati, F., Kerkeni, A., Bouttemi, M., Gref, R., et al. (2013). In depth analysis of the in vivo toxicity of nanoparticles of porous iron(iii) metal-organic frameworks. *Chem. Sci.* 4, 1597–1607. doi: 10.1039/c3sc22116d

Barenholz, Y. (2012). Doxil® - The first FDA-approved nano-drug: lessons learned. *J. Control. Release* 160, 117–134. doi: 10.1016/j.jconrel.2012.03.020

Bellido, E., Hidalgo, T., Lozano, M. V., Guillevic, M., Simón-Vázquez, R., Santander-Ortega, M. J., et al. (2015). Heparin-engineered mesoporous iron Metal-Organic Framework nanoparticles: toward stealth drug nanocarriers. *Adv. Healthc. Mater.* 4, 1246–1257. doi: 10.1002/adhm.201400755

Bouffard, D. Y., Laliberté, J., and Momparler, R. L. (1993). Kinetic studies on 2',2'-difluorodeoxycytidine (gemcitabine) with purified human deoxycytidine kinase and cytidine deaminase. *Biochem. Pharmacol.* 45, 1857–1861. doi: 10.1016/0006-2952(93)90444-2

Bugnicourt, L., Peers, S., Dalverny, C., and Ladavière, C. (2019). Tunable morphology of lipid/chitosan particle assemblies. *J. Colloid Interface Sci.* 534, 105–109. doi: 10.1016/j.jcis.2018.08.098

Chibowski, E., and Szcześ, A. (2016). Zeta potential and surface charge of DPPC and DOPC liposomes in the presence of PLC enzyme. *Adsorption* 22, 755–765. doi: 10.1007/s10450-016-9767-z

Cutrone, G., Li, X., Casas-Solvas, J. M., Menendez-Miranda, M., Qiu, J., Benkovics, G., et al. (2019a). Design of engineered cyclodextrin derivatives for spontaneous coating of highly porous Metal-Organic Framework nanoparticles in aqueous media. *Nanomaterials* 9, 1–26. doi: 10.3390/nano9081103

Cutrone, G., Qiu, J., Menendez-Miranda, M., Casas-Solvas, J. M., Aykaç, A., Li, X., et al. (2019b). Comb-like dextran copolymers: a versatile strategy to coat highly porous MOF nanoparticles with a PEG shell. *Carbohydr. Polym.* 223:115085. doi: 10.1016/j.carbpol.2019.115085

Giménez-marqués, M., Bellido, E., Berthelot, T., Simón-yarza, T., Hidalgo, T., Simón-vázquez, R., et al. (2018). GraftFast surface engineering to improve MOF nanoparticles furtiveness. *Small* 14, 1–11. doi: 10.1002/smll.201801900

Gref, R., Domb, A., Quellec, P., Blunk, T., Müller, R. H., Verbavatz, J. M., et al. (1995). The controlled intravenous delivery of drugs using PEG-coated sterically stabilized nanospheres. *Adv. Drug Deliv. Rev.* 16, 215–233. doi: 10.1016/0169-409x(95)00026-4

Gref, R., Lück, M., Quellec, P., Marchand, M., Dellacherie, E., Harnisch, S., et al. (2000). "Stealth" corona-core nanoparticles surface modified by polyethylene glycol (PEG): Influences of the corona (PEG chain length and surface density) and of the core composition on phagocytic uptake and plasma protein adsorption. *Colloids Surfaces B Biointerfaces* 18, 301–313. doi: 10.1016/s0927-7765(99)00156-3

Gref, R., Minamitake, Y., Peracchia, M. T., Trubetskoy, V., Torchilin, V., and Langer, R. (1994). Biodegradable long-circulating polymeric nanospheres. *Science* 263, 1600–1603. doi: 10.1126/science.8128245

He, C., Liu, D., and Lin, W. (2015). Nanomedicine applications of hybrid nanomaterials built from Metal-Ligand Coordination bonds: Nanoscale Metal-Organic Frameworks and Nanoscale Coordination Polymers. *Chem. Rev.* 115, 11079–11108. doi: 10.1021/acs.chemrev.5b00125

Hidalgo, T., Bellido, E., Avila, J., Asensio, M. C., and Salles, F. (2017). Chitosan-coated mesoporous MIL-100 (Fe) nanoparticles as improved bio-compatible oral nanocarriers. *Sci. Rep.* 100, 1–14. doi: 10.1038/srep43099

Horcajada, P., Chalati, T., Serre, C., Gillet, B., Sebrie, C., Baati, T., et al. (2010). Porous Metal-Organic-Framework nanoscale carriers as a potential platform for drug delivery and imaging. *Nat. Mater.* 9, 172–178. doi: 10.1038/nmat2608

Horcajada, P., Gref, R., Baati, T., Allan, P. K., Maurin, G., and Couvreur, P. (2012). Metal-Organic Frameworks in biomedicine. *Chem. Rev.* 112, 1232–1268. doi: 10.1021/cr200256v

Li, X., Lachmanski, L., Safi, S., Sene, S., Serre, C., Grenèche, J. M., et al. (2017). New insights into the degradation mechanism of Metal-Organic Frameworks drug carriers. *Sci. Rep.* 7, 1–17. doi: 10.1038/s41598-017-13323-1

Li, X., Porcel, E., Menendez-Miranda, M., Qiu, J., Yang, X., Pastor, A., et al. (2019a). Highly porous hybrid metal-organic nanoparticles loaded with gemcitabine-monophosphate: a multimodal approach to improve chemo and radiotherapy. *ChemMedChem* 15, 274–283. doi: 10.1002/cmdc.201900596

Li, X., Semiramoth, N., Hall, S., Tafani, V., Josse, J., Laurent, F., et al. (2019b). Compartmentalized encapsulation of two antibiotics in porous nanoparticles: an efficient strategy to treat intracellular infections. *Part. Part. Syst. Charact.* 36, 1–9. doi: 10.1002/ppsc.201970009

Luchini, A., and Vitiello, G. (2019). Understanding the nano-bio interfaces: lipid-coatings for inorganic nanoparticles as promising strategy for biomedical applications. *Front. Chem.* 7:343. doi: 10.3389/fchem.2019.00343

Rodriguez-Ruiz, V., Maksimenko, A., Anand, R., Monti, S., Agostoni, V., Couvreur, P., et al. (2015). Efficient "green" encapsulation of a highly hydrophilic anticancer drug in Metal-Organic Framework nanoparticles. *J. Drug Target.* 23, 759–767. doi: 10.3109/1061186x.2015.1073294

Rojas, S., Arenas-Vivo, A., and Horcajada, P. (2019). Metal-Organic Frameworks: a novel platform for combined advanced therapies. *Coord. Chem. Rev.* 388, 202–226. doi: 10.1016/j.ccr.2019.02.032

Rosenblum, D., Joshi, N., Tao, W., Karp, J. M., and Peer, D. (2018). Progress and challenges towards targeted delivery of cancer therapeutics. *Nat. Commun.* 9, 1–12. doi: 10.1038/s41467-018-03705-y

Senapati, S., Mahanta, A. K., Kumar, S., and Maiti, P. (2018). Controlled drug delivery vehicles for cancer treatment and their performance. *Signal Transduct. Target. Ther.* 3, 1–19. doi: 10.1038/s41392-017-0004-3

Simon-Yarza, M. T., Baati, T., Paci, A., Lesueur, L. L., Seck, A., Chiper, M., et al. (2016). Antineoplastic busulfan encapsulated in Metal Organic Framework nanocarrier: first in vivo results. *J. Mater. Chem. B* 4, 585–588. doi: 10.1039/c5tb02084k

Taylor-Pashow, K. M. L., Della Rocca, J., Xie, Z., Tran, S., and Lin, W. (2009). Postsynthetic modifications of iron-carboxylate nanoscale Metal-Organic Frameworks for imaging and drug delivery. *J. Am. Chem. Soc.* 131, 14261–14263. doi: 10.1021/ja906198y

Thevenot, J., Troutier, A., David, L., Delair, T., and Ladavière, C. (2007). Steric stabilization of lipid/polymer particle assemblies by poly (ethylene glycol)-lipids. *Biomacromolecules* 8, 3651–3660. doi: 10.1021/bm700753q

Troutier, A., and Ladavière, C. (2007). An overview of lipid membrane supported by colloidal particles. *Adv. Colloid Interface Sci.* 133, 1–21. doi: 10.1016/j.cis.2007.02.003

Troutier-Thuilliez, A. L., Thevenot, J., Delair, T., and Ladavière, C. (2009). Adsorption of plasmid DNA onto lipid/polymer particle assemblies. *Soft. Matter.* 5, 4739–4747. doi: 10.1039/b911260j

Wuttke, S., Braig, S., Preiß, T., Zimpel, A., Sicklinger, J., Bellomo, C., et al. (2015). MOF nanoparticles coated by lipid bilayers and their uptake by cancer cells. *Chem. Commun.* 51, 15752–15755. doi: 10.1039/c5cc06767g

Conflict of Interest: The authors declare that the research was conducted in the absence of any commercial or financial relationships that could be construed as a potential conflict of interest.

Supplementary Material

Drug-loaded lipid-coated hybrid organic-inorganic "stealth" nanoparticles for cancer therapy

Xue Li[1], Giuseppina Salzano[1], Jingwen Qiu[1], Mathilde Menard[2], Kristian Berg[2], Theodossis Theodossiou[2], Catherine Ladavière[3], Ruxandra Gref [1]*

[1] Université Paris-Saclay, CNRS UMR 8214, Institut des Sciences Moléculaires d'Orsay, 91405, Orsay, France.

[2] Department of Radiation Biology, Institute for Cancer Research, Norwegian Radium Hospital, Oslo University Hospital, 0372, Oslo, Norway.

[3] University of Lyon, CNRS, UMR 5223, IMP, 15 bd André Latarjet, F-69622, Villeurbanne, France

*** Correspondence:**
Ruxandra Gref
ruxandra.gref@universite-paris-saclay.fr

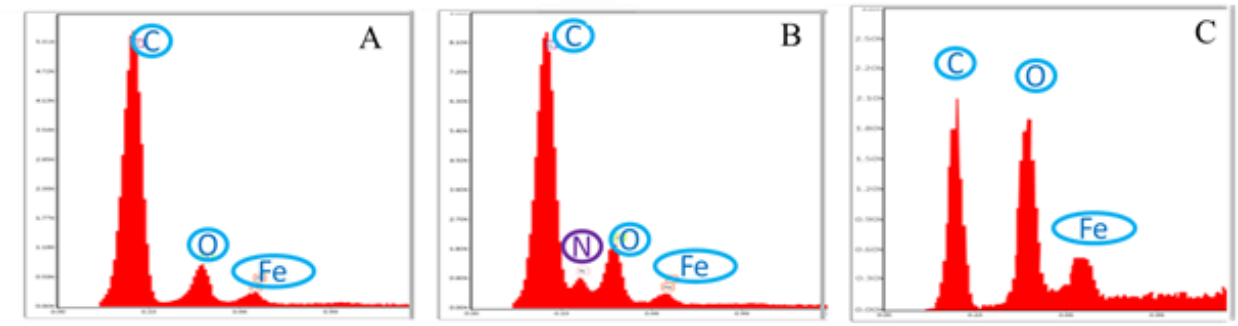

Figure S1. EDX spectra of nanoMOFs before and after lipid surface modification. A: Uncoated nanoMOFs; B: DOPC coated nanoMOFs; C: lipid coated nanoMOFs with the addition of DSPE-PEG 2000

Table S1 Mean hydrodynamic diameters of the NPs (characterized by DLS) in the supernatants obtained after centrifugation at 10,000 g for 10min of DOPC-coated nanoMOFs.

No.	DOPC:nanoMOFs	Mean hydrodynamic diameter (nm)	Attenuator[a]
1	1:1	268 ± 26.4	9
2	1:3	153 ± 23.1	11
3	1:5	139 ± 25.3	11
4	1:10	146 ± 21.4	11
5	1:20	131 ± 24.3	11
6	0:1	143 ± 17.9	11

[a] 11 is the maximal value of the attenuator

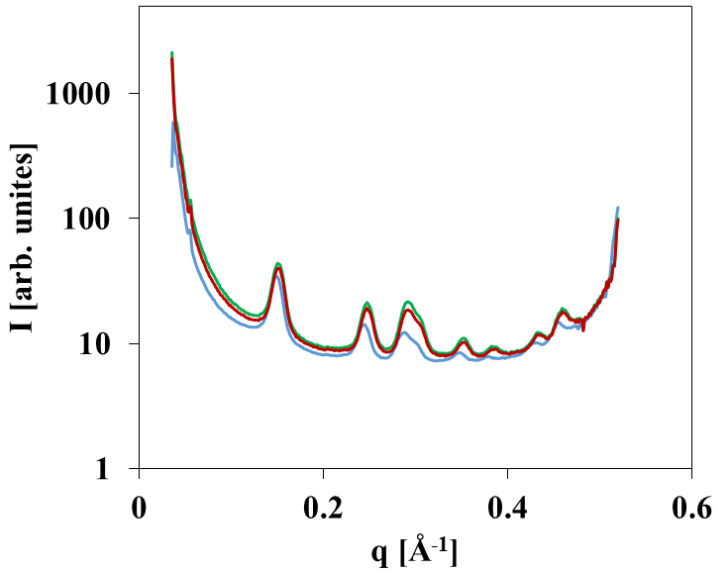

Figure S2 Crystallinity of nanoMOFs before and after lipid surface modification. XRPD patterns of uncoated nanoMOFs (blue), DOPC-coated nanoMOFs (green), and DOPC-coated nanoMOFs with the addition of DSPE-PEG 2000 (red).

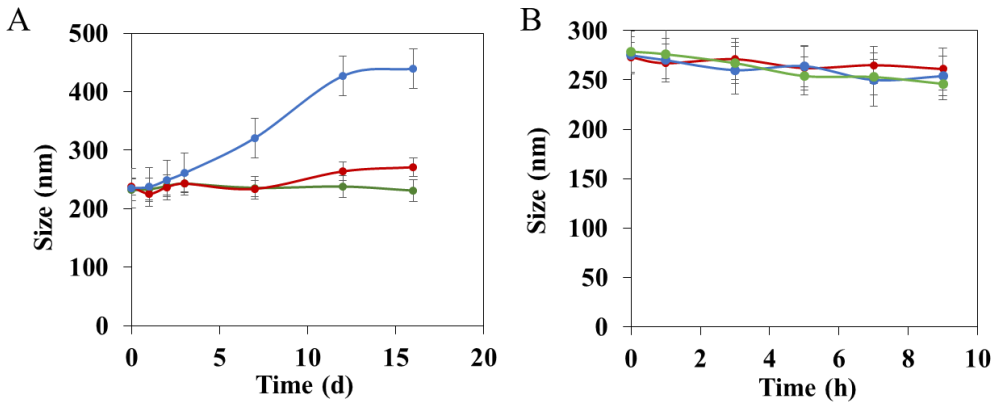

Figure S3. Colloidal stability in water (A) and in cell culture medium (B) of nanoMOFs coated or not with lipids. Blue: Uncoated nanoMOFs; Green: DOPC-coated nanoMOFs; Red: DOPC-coated nanoMOFs with the addition of DSPE-PEG 2000.

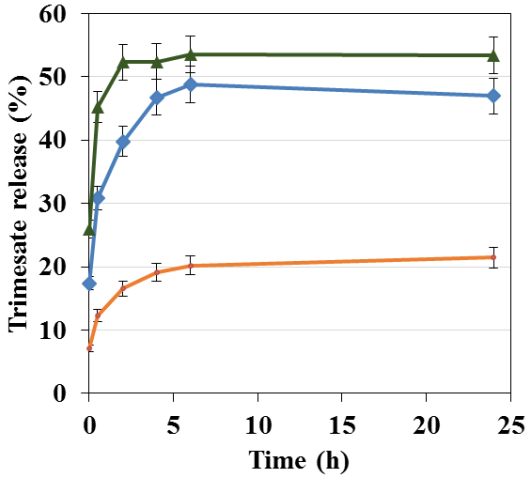

Figure S4. Trimesate release of Gem-MP loaded nanoMOFs in PBS (green: 6 mM; blue: 3 mM; orange: 1 mM)

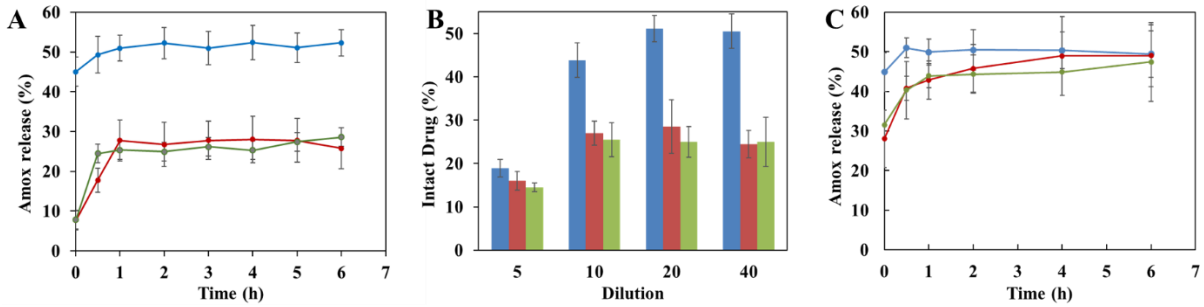

Figure S5. Effect of coating on Amox release in water (A, B) and in PBS (C). A: Release kinetics of Amox in water from nanoMOFs (1mg/mL) before or after coating, with a dilution factor of 20; B: Effect of dilution factor on Amox release after 4 h incubation at 37°C in water; (Blue: uncoated nanoMOFs; red: DOPC coated nanoMOFs; Green: DOPC and PEG-lipid conjugate coated nanoMOFs)

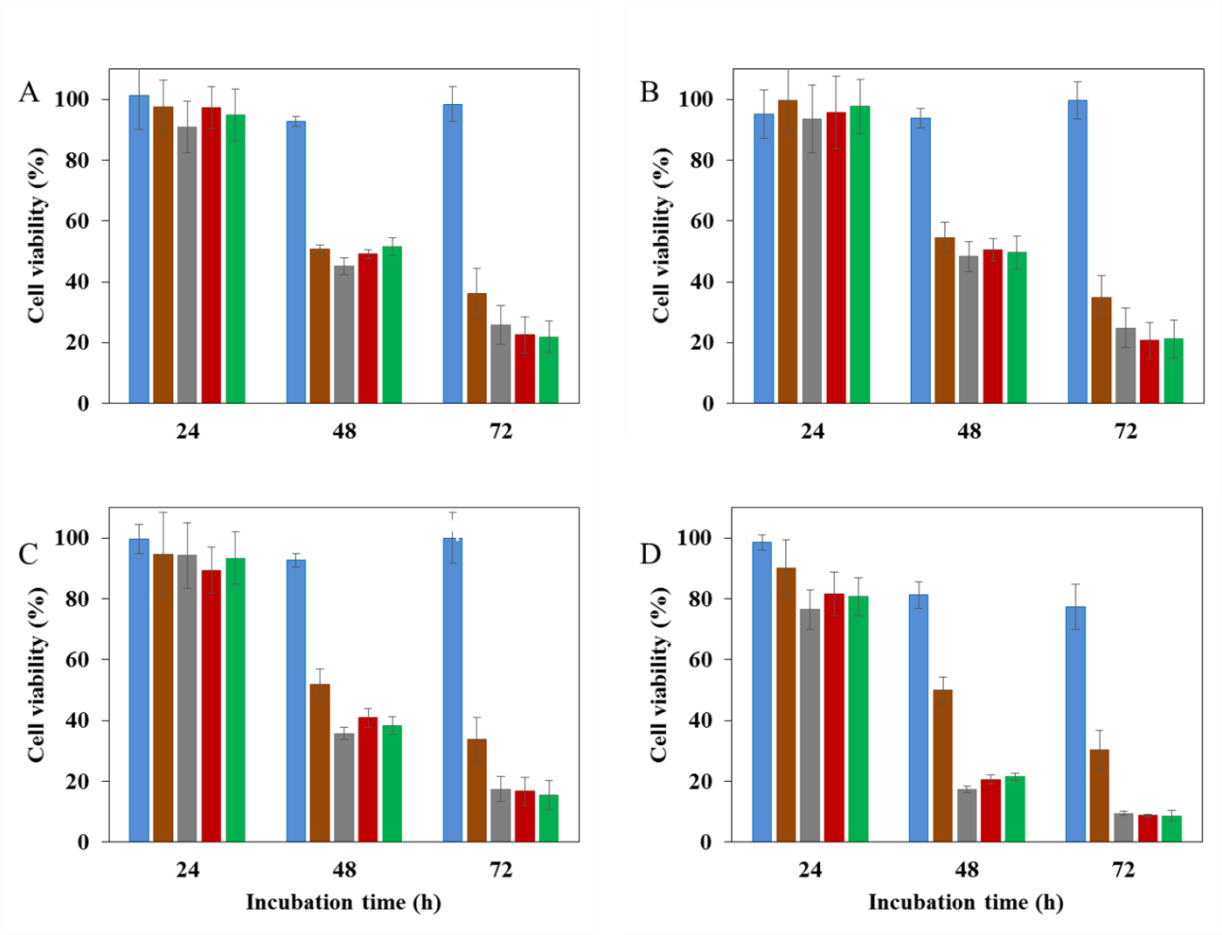

Figure S6 Cytotoxicity of nanoMOFs (blue), anticancer efficacy of Gem-MP (orange), Gem-MP loaded nanoMOFs before (grey) and after coating with DOPC (red) or DOPC with PEG-lipid conjugates (green). The experiments were performed on SKOV3 ovarian cancer cells. A: 10 µg/mL of 20% Gem-MP loaded nanoMOFs; B: 10 µg/mL of 8% Gem-MP loaded nanoMOFs; C: 30 µg/mL of 8% Gem-MP loaded nanoMOFs; D: 100 µg/mL of 8% Gem-MP loaded nanoMOFs.

Annex 2: Highly Porous Hybrid Metal–Organic Nanoparticles Loaded with Gemcitabine Monophosphate: a Multimodal Approach to Improve Chemo- and Radiotherapy

ChemPubSoc Europe

DOI: 10.1002/cmdc.201900596

CHEMMEDCHEM Full Papers

Highly Porous Hybrid Metal–Organic Nanoparticles Loaded with Gemcitabine Monophosphate: a Multimodal Approach to Improve Chemo- and Radiotherapy

Xue Li,[a] Erika Porcel,[a] Mario Menendez-Miranda,[a] Jingwen Qiu,[a] Xiaomin Yang,[a] Christian Serre,[b] Alexandra Pastor,[c] Didier Desmaële,[c] Sandrine Lacombe,*[a] and Ruxandra Gref*[a]

Nanomedicine recently emerged as a novel strategy to improve the performance of radiotherapy. Herein we report the first application of radioenhancers made of nanoscale metal-organic frameworks (nanoMOFs), loaded with gemcitabine monophosphate (Gem-MP), a radiosensitizing anticancer drug. Iron trimesate nanoMOFs possess a regular porous structure with oxocentered Fe trimers separated by around 5 Å (trimesate linkers). This porosity is favorable to diffuse the electrons emitted from nanoMOFs due to activation by γ radiation, leading to water radiolysis and generation of hydroxyl radicals which create nanoscale damages in cancer cells. Moreover, nanoMOFs act as "Trojan horses", carrying their Gem-MP cargo inside cancer cells to interfere with DNA repair. By displaying different mechanisms of action, both nanoMOFs and incorporated Gem-MP contribute to improve radiation efficacy. The radiation enhancement factor of Gem-MP loaded nanoMOFs reaches 1.8, one of the highest values ever reported. These results pave the way toward the design of engineered nanoparticles in which each component plays a role in cancer treatment by radiotherapy.

Introduction

Despite advances and refinements in cancer early detection and treatment, the vast majority of human malignancies are not effectively eradicated and there is a clear need to develop more efficient treatments based on combined modalities. Chemoradiation, the combination of chemotherapy and radiotherapy, is now the standard of care for many of solid tumors, including lung, esophageal, head and neck cancers.[1–3] Advantageously, synergistic effects were reported in chemoradiation, since some anticancer drugs not only interfere with cell metabolism, but they also make cancer cells more sensitive to radiotherapy.[4] In clinical studies, gemcitabine (Gem) showed improved therapeutic effects in combination with irradiation even at very low dosages (less than 50 mg/m^2 per week).[5]

Gem is a prodrug which relies on the intracellular enzyme deoxycytidine kinase to form its active intermediates: mono-, di-, and triphosphate derivatives.[6] It has been shown both *in vitro* and *in vivo* that after phosphorylation this drug exerts its cytotoxic effects and induces radiosensitization mainly through inhibition of DNA synthesis.[7] However, the first intracellular phosphorylation of Gem is the rate-limiting step and especially difficult for resistant cancer cells.[6,8] The administration of Gem monophosphate (Gem-MP) is hampered by its poor stability in biological media and poor cellular uptake.[6] Moreover, because of lack of tumor targeting and specificity, healthy-tissue toxicity of this drug is the major drawback.[5,9] In this challenging context, some of us have shown that Gem-MP could be protected against degradation with increased cellular uptake by encapsulation in nanoparticles (NPs).[10] Nanotechnology has proven the effectiveness to target tumors, strategy of particular interest for drug delivery by achieving drug transcytosis, drug targeting and theranostics.[11,12] In addition to the benefits of NPs for drug delivery, the potential value of metal based NPs as radioenhancers has been discovered in 2000.[13,14] Currently, there are several types of high-Z NPs in clinical development, including Au NPs, Gd NPs, and crystalline HfO_2 NPs endowed with a targeting coating.[15] More recently, porous Hf based nanoscale metal-organic frameworks (nanoMOF) outperformed dense HfO_2 NPs.[16–18] The combination of nanoMOFs mediated radiotherapy with checkpoint blockade has been shown as a promising strategy to broaden the application of immunotherapy.

[a] Dr. X. Li, Dr. E. Porcel, Dr. M. Menendez-Miranda, J. Qiu, X. Yang, Dr. S. Lacombe, Dr. R. Gref
Institut de Sciences Moléculaires d'Orsay
UMR CNRS 8214
Université Paris-Sud
Université Paris-Saclay
Rue André Rivière
91405 Orsay Cedex (France)
E-mail: ruxandra.gref@u-psud.fr
sandrine.lacombe@u-psud.fr

[b] Dr. C. Serre
Institut des Matériaux Poreux de Paris, FRE 2000
Ecole Normale Supérieure de Paris
Ecole Supérieure de Physique et de Chimie Industrielles de Paris, PSL Research University
24 rue Lhomond
75005 Paris (France)

[c] A. Pastor, Dr. D. Desmaële
Institut Galien,
UMR CNRS 8612, Université Paris-Sud, Université Paris-Saclay,
5 Rue Jean-Baptiste Clément
92290 Châtenay-Malabry (France)

Supporting information for this article is available on the WWW under https://doi.org/10.1002/cmdc.201900596

However, there are still no examples of NPs engineered to act both as radioenhancers and nanocarriers to target anticancer drugs to the tumors. We developed here this concept using porous nanoMOF loaded with Gem-MP. Iron (III) trimesate nanoMOFs MIL-100(Fe) (MIL stands for Materials from Institut Lavoisier) were shown to be biodegradable and devoid of toxicity *in vivo*.[19–21] Furthermore, they act as efficient contrast agents for Magnetic Resonance Imaging (MRI) constituting promising devices for theragnostic applications.[22] NanoMOFs' surfaces can also be engineered for cancer cell targeting and for long blood circulation purposes.[22–26] Due to their hydrophilic/hydrophobic character and high surface areas up to 1700 m^2/g,[27] iron(III) trimesate nanoMOFs were successfully loaded with unprecedented amounts (up to 20–70 wt%) of a large variety of drugs able to penetrate within their open porous MOF structures.[27–29] For instance, phosphorylated drugs such as Gem-MP,[10] AZT-MP,[30] and AZT-TP[30,31] were loaded with efficiencies close to 100%.

MIL-100(Fe) nanoMOFs are assembled up from Fe(III) oxocentered trimers of octahedra and trimesate linkers (1,3,5-benzene tricarboxylate) that self-assemble to build a 3D porous architecture delimiting large (29 Å) and small (24 Å) mesoporous cages (Figure 1A). These cages are accessible for drug adsorption in the 3D-porosity through pentagonal (5.6 Å) and hexagonal windows (8.6 Å).[27] Iron trimesate nanoMOFs were also shown to be non-toxic and to generate in biological media reactive oxygen species (ROS).[29,32] In summary, Gem-MP loaded nanoMOFs exhibit potentially favorable characteristics for multimodal cancer treatment: i) they efficiently load and protect Gem-MP; ii) their surface can be functionalized in a versatile manner to control the interactions with biological systems and iii) they are non-toxic, biodegradable, and potentially allow monitoring by MRI accumulation at the tumor and disease evolution (theranostics).

Here we demonstrate *in vitro* that nanoMOFs amplify the effect of γ-rays on tumor cells killing, and for the first time, we combine radiotherapy and chemotherapy using Gem-MP loaded nanoMOFs. As a whole, this confers to these new type of nanoagents the unique synergistic effect to enhance by a factor of 1.8 the radiotoxicity of the treatment.

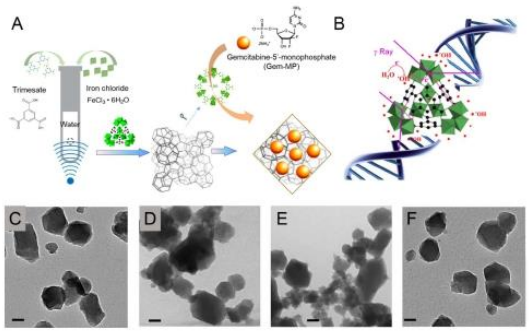

Figure 1. Schematic representation of the "green" hydrothermal synthesis of nanoMOFs and Gem-MP encapsulation (A); Fast processes ($t < 10^{-12}$ s) involved in nanoMOF excited by γ radiations (B), including the secondary electron generation and ROS production. The porous 3D structure of nanoMOF is prone to facilitate ROS diffusion. Morphology of as-synthesized nanoMOFs (C), Gem-MP loaded nanoMOF before (D) and after (E) 24 h incubation in water; and irradiated nanoMOFs (F); scale bar in C–F: 50 μm.

Results and Discussion

NanoMOFs Synthesis and Drug Incorporation

Several methods have been described for the synthesis of MIL-100(Fe) nanoMOFs[33—38] among which microwave-assisted solvent-free "green" hydrothermal techniques are the most effective to obtain high yields of nanoMOFs with controlled sizes.[34] The nanoMOFs are crystalline (Figure S1) with diffraction patterns in agreement with previous studies.[39,40] They possessed a facetted morphology (Figure 1C) and their hydrodynamic diameters, characterized by dynamic light scattering (DLS) and NP tracking analysis (NTA), were 217 ± 25 nm and 200 ± 64 nm, respectively (Figure S2). NTA tracks all the individual NPs in their Brownian motion and thus gives the size distribution based on number, whereas DLS measures the fluctuations of the scattered light and is more sensitive to largest particles. A good agreement was found between the complementary DLS and NTA methods (less than 10% differences) as previously reported with other types of NPs.[41] NanoMOFs displayed a BET (Brunauer-Emmett-Teller) specific surface of $1740 \pm 100\ m^2 \cdot g^{-1}$, in agreement with previously reported data.[39,40]

Due to the strong coordination between phosphate groups and the unsaturated iron(III) Lewis acid sites from their framework, nanoMOFs acted as efficient "molecular nanosponges", soaking up Gem-MP from its aqueous solution within the large mesoporous cages (29 Å). Almost a perfect loading efficiency (> 98%) was obtained, confirming the strong interaction between Gem-MP and nanoMOFs due to coordination of the phosphate moiety of Gem with the Fe trimers which possesses two accessible unsaturated metal sites per trimer.[10,30] Encapsulation of Gem-MP did not affect the integrity of the 3D crystalline nanoMOF structures as demonstrated by (i) morphology and size unaffected (Figure 1D) (ii) similar PXRD (Figure S1) and DLS mean diameters (221 ± 18 nm versus 217 ± 25 nm, Figure S2) as well as (iii) less than 1% release of their constitutive ligand, trimesate. NanoMOF suspensions loaded with 10 wt% Gem-MP were also stable in water during storage, with preserved morphology (Figure 1E) and neither detectable (<1%) Gem-MP release nor ligand detachment (<1%) over one day, in agreement with our previous study.[10] Gem-MP release studies were also conducted in DMEM cell culture media. Hydrodynamic diameter didn't change after 6 h incubation (Figure S2). As expected, nanoMOFs progressively degraded, which resulted in around 15% of Gem-MP release in the suspension media after 6 h incubation. This degradation is triggered by the phosphates from the media that coordinate to the iron sites leading to ligand and drug release.[42] In our case, Gem-MP release remained lower than 20% after 24 h incubation in cell culture medium. (Figure S3). The efficient drug

encapsulation and the stable formulation built the foundation for biological evaluation.

Toxicity of nanoMOF, Gem-MP, and Gem-MP Loaded nanoMOF

These studies were completed by toxicity investigations of nanoMOFs loaded or not with Gem-MP on HeLa cells used as cellular probes. The cells were incubated with the products in the same conditions as the ones used for irradiation studies (Figure S4). As expected, free Gem-MP induced a cytotoxic effect killing 50% of cells after 6 h incubation at concentrations of 1.7 μg/mL. In contrast, no significant toxicity (>95% cell viability) was observed with unloaded nanoMOF at concentrations of 17 μg/mL. At equivalent concentrations, the toxicity of Gem-MP was similar whether the drug was free or incorporated in the nanoMOFs (cell viability of 53±6.4% for Gem-MP and 52±8.1% for Gem-MP loaded nanoMOFs). The lack of toxicity of nanoMOFs in the irradiation conditions set up the basis for the further biological investigation.

Localization and Quantification of nanoMOF in HeLa Cells

Prior to irradiation experiments, the internalization of nanoMOF in HeLa cells was investigated using confocal microscopy. This tool allows detecting optical sections within cells, thus unravelling the location of the NPs. However, confocal microscopy requires labelling of the NPs with fluorescent dyes. Iron based nanoMOFs are challenging to be labelled because of dye fluorescence quenching in the pores or desorption from the surface once in contact with biological media. Figure 2A illustrates these issues: fluorescein,[24] one of the most widely employed dyes, can penetrate inside the porous 3D nanoMOF structure but its fluorescence was quenched. In contrast, Rhodamine (Rhod) with bulkier structure, unable to enter in the pores of the MOF, was efficiently associated to the coating of the outer surface of the nanoMOFs up to 8.2±0.2 wt%, thus allowing a successful labelling. However, around 43 wt% of Rhod was immediately released within 5 minutes ("burst release") upon incubation in cell culture medium (Figure 2B).

In this context, to achieve an efficient Rhod labelling, stable in biological media, a new Rhod derivative functionalized with a hydrophobic anchor was synthesized. Adamantane (Ada) was chosen as lipophilic anchoring agent as its molecular size is well adapted to insert as a guest into the cages at the nanoMOFs surface, whereas the bulky hydrophilic Rhod would deploy in the suspension medium, avoiding quenching. 1-Adamantane acetic acid was successfully attached to Rhod *via* a short covalent linker as depicted in Figure S5. Briefly, an excess of 2,2′-(ethylendioxy)bis(ethylamine) (1) was reacted with 1-adamantane acetyl chloride to give the corresponding mono amide (2), which was further acylated with succinic anhydride to provide the carboxylic acid (3). Rhod-Ada (5) was obtained by reaction with rhodamine piperazine (4) using EDCI as coupling agent by adapting a published procedure.[43] The purified Rhod-Ada had similar fluorescence spectrum as Rhod, showing Excitation/Emission = 566 nm/589 nm (Figure S6A).

Rhod-Ada was efficiently adsorbed on the surface of nanoMOFs by a simple solvent-free method, consisting in 12 h incubation under gentle stirring of nanoMOF aqueous suspensions containing Rhod-Ada. The amount of associated Rhod-Ada reached 7.1±0.1 wt% and a blue shift of 2–3 nm was observed for Rhod-Ada emission after adsorption on the surface of nanoMOFs (Figure S6B). In contrast with parent Rhod which detached readily from nanoMOFs (Figure 2B), Rhod-Ada showed a low release from the nanoMOFs in cell culture media, i.e. less than 10% after 6 h incubation (Figure 2C). As a conclusion, the newly synthesized Rhod-Ada ensures stable coatings for biological evaluations such as the study of the interactions between nanoMOFs and HeLa cells using confocal microscopy.

As shown in Figure 3 and the video in Supporting Information, the confocal images showed high intensity inside the cytoplasm, despite extensive washing to remove loosely adhered nanoMOFs. This demonstrates that nanoMOFs local-

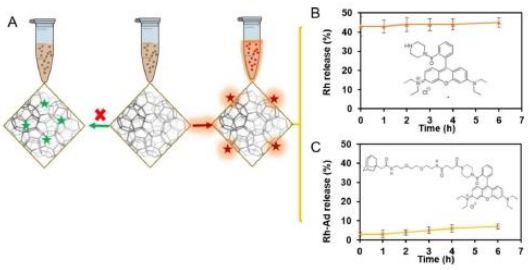

Figure 2. NanoMOF labeling with fluorescent dyes. A. Schematic representation of two strategies for nanoMOF labeling: i) fluorescent dyes which penetrate inside the porous structure of nanoMOFs, such as fluorescein, eventually quenched; ii) nanoMOFs labeled by adsorption of fluorescent dyes (Rhod, Rhod-Ada) on the surface maintain their fluorescence (red star). Rhod (B) and Rhod-Ada (C) release kinetics in cell culture medium.

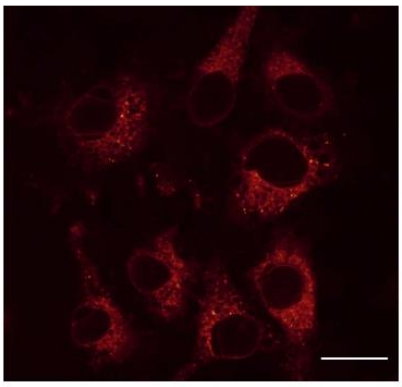

Figure 3. Confocal images of nanoMOF internalization in HeLa cells. Confocal images of HeLa cells after 6 h incubation with Rhod-Ada labeled nanoMOFs (100μg/mL) followed by intensive washing with PBS. (scale bar 25 μm).

ized in the cytoplasm but not in the nucleus. The surface modification of nanoMOFs with Rhod-Ada could affect cellular uptake and distribution, therefore the quantification of intracellular nanoMOFs with or without Rhod-Ada was performed.

The quantity of nanoMOFs internalized in the cells was determined using a procedure based on iron staining with potassium ferrocyanide.[25] This quantification of iron content in cells was performed for concentrations ranging from 25 to 200 μg/mL nanoMOFs added to HeLa cells for 6 h incubation. Prior to the iron dosage, the cells were washed to remove non adhered particles and then digested. As shown in Figure 4, the amount of nanoMOFs internalized in HeLa cells increased almost linearly as a function of the nanoMOF concentration. This calibration curve was used to determine the amount of internalized nanoMOFs at the concentration of 17 μg/mL where there was no toxicity observed. It was found that around 8 pg nanoMOFs were associated per cell, corresponding to 1.5 pg Fe/cell, either internalized or firmly attached on the cell membrane.

Impact of nanoMOFs, Gem-MP, and Gem-MP Loaded nanoMOFs on Radiation Effects

Prior to irradiation studies, the stability of nanoMOFs, loaded or not with Gem-MP and Gem-MP alone was investigated upon radiation using doses ranging from 4 to 6.5 Gy.

Noteworthy, even at the highest dose, nanoMOFs kept similar facetted morphology as non-irradiated samples (Figures 1A and 1F) with neither significant size variation after irradiation, as shown by NTA and DLS methods (Figure S2), nor degradation as indicated by the negligible loss of their constitutive ligand, trimesate (<1%, Table S1). Gem-MP was not degraded either, at the highest irradiation dose. Remarkably, nanoMOFs did not lose their Gem-MP content upon irradiation (Table S1), as indicated by negligible release of Gem-MP. These data further confirm the strong interaction between Gem-MP and nanoMOFs.

Clonogenic assay was then used to investigate the impact of nanoMOF, Gem-MP, and Gem-MP loaded nanoMOFs on cell killing induced by radiation. The colony-forming potential of cells were assessed after treatment with nanoMOFs, Gem-MP, and Gem-MP loaded nanoMOFs using a standardized procedure, where the radiation dose was fixed in the range of 1~6.5 Gy, comparable to the clinical dosage.[44,45]

The survival curves of HeLa cells in the presence or not of Gem-MP, nanoMOFs and Gem-MP loaded nanoMOFs, irradiated with γ-rays, are presented in Figure 5. The cell survival fractions (SF) decreased exponentially with the increase of the radiation dose, in agreement with previous reports.[45–48] Interestingly, the bare nanoMOFs activated by γ-rays decreased significantly the cell survival. The efficiency of nanoMOFs to amplify radiation-induced cell death was evaluated by calculating the dose enhancement factor (DEF) and the radiation enhancement factor (REF)[15] defined by the equations (1) and (2).

$$DEF_{(D)} = SF^{D}{}_{control}/SF^{D}{}_{nanoMOFs} \quad (1)$$

where $SF_{control}$ and $SF_{nanoMOFs}$ correspond to SF of the control and SF of treated cells at a certain dose D, respectively.

$$REF = D^{10}{}_{control}/D^{10}{}_{nanoMOFs} \quad (2)$$

where $D^{10}{}_{nanoMOFs}$ and $D^{10}{}_{control}$ correspond to the radiation doses used to reach 10% of cell survival fraction in the samples treated with nanoMOFs and in the controls, respectively.

As reported in Table 1, REF value of nanoMOF alone reached 1.2. The DEF (2 Gy) and DEF (4 Gy) of nanoMOF alone were found close to 1.3 and 1.5, respectively. This is comparable to the effects observed by Mazur *et al.* with iron oxide NPs, showing DEF (1-4 Gy) values in the range of 1.1–1.6.[49,50] This clearly indicates that nanoMOFs enhance radiation effects. Remarkably, the equivalent iron concentration in the nanoMOFs used in this study was much lower than the one reported in previous studies with other iron oxide NPs (nanoMOFs contain

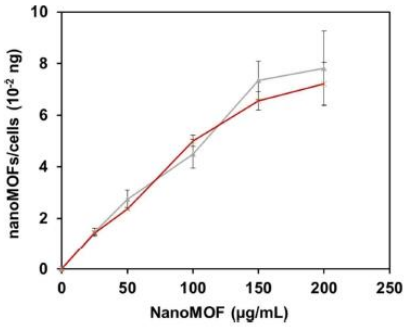

Figure 4. Quantification of nanoMOFs internalized in HeLa cells. Gray: as-synthesized nanoMOFs; red: Rhod-Ada labelled nanoMOFs. NanoMOFs with different concentrations (25, 50, 100, 150 and 200 μg/mL) were incubated with 2×105 HeLa cells in 24 well plates for 6 h, and the mass of internalized nanoMOFs was determined respectively.

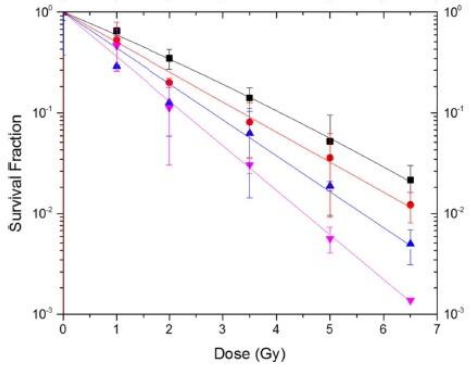

Figure 5. The effect of nanoMOFs and Gem-MP on irradiation enhancement. Survival fractions of HeLa cells irradiated by γ rays, in the presence of nanoMOF (red), Gem-MP (blue), Gem-MP loaded nanoMOF (pink), and in the control (black).

Table 1. Summary of REF (radiation enhancement factor), DEF(2Gy) (dose enhancement factor at 2Gy), and DEF(4Gy) obtained with HeLa cells irradiated by γ source, in the presence of nanoMOFs, Gem-MP, Gem-MP loaded nanoMOFs. Control sample was HeLa cells treated by only γ irradiation.

Sample	REF	DEF(2Gy)	DEF(4Gy)
control	1	1	1
nanoMOF	1.19	1.30	1.53
Gem-MP	1.35	1.58	2.23
Gem-MP loaded nanoMOF	1.83	2.68	6.47

56 μM Fe compared to iron oxide NPs containing 3.6 mM ~17.9 mM Fe[49,50]). Moreover, the incubation time was also much shorter (6 h for nanoMOFs in comparison with 72 h for iron oxide NPs[49,50]). The amount of Fe internalized in cells in the case of iron oxide NPs reached up to 40 pg/cell, whereas in this study, it was only 1.5 pg/cell. As a conclusion, the porous iron trimesate nanoMOFs are much more efficient to amplify radiation effects of γ-rays than solid iron oxide NPs. To the best of our knowledge, this is the first time that a radioenhancing effect of Fe-based porous material is reported.

The radioenhancement effect is due to the succession of physicochemical processes as described elsewhere for high-Z compounds and dense NPs.[15] Of note we present here a radioenhancement effect with porous low density NPs containing iron.[15] Briefly, the radioenhancement observed with the nanoMOFs may be explained by the activation of Fe atoms interacting with γ rays, followed by de-excitation and emission of electrons. The interaction of emitted electrons with surrounding water molecules is responsible for the production of hydroxyl radicals, which are toxic for the cells.[15] Thus, the toxicity of a radiation treatment increases with the number of electrons interacting with water molecules. Therefore it is expected that the surface area of the NPs plays an important role[51] because the production of radicals increases with the porosity of the agent. Inversely, the number of electrons is expected to decrease when electrons do not travel to the surface, which is the case for increasing diameter of the solid particle. Advantageously, MIL-100(Fe) nanoMOFs possess a high specific BET surface area up to 1740 $m^2 \cdot g^{-1}$. Moreover, their regular 3D structure with well dispersed Fe centers separated by distances of around 5 Å (trimesate linkers), is favorable for a better electron traveling through the interconnected network to enhance hydroxyl radical generation and facilitate their fast diffusion in the surrounding biological medium. As a consequence, nanoMOFs act efficiently as radioenhancers despite the relatively low electron density of the emitting atoms (Fe with Z of 26), as compared to Gd (64), Au (79), Pt (78) or Hf (72).

To characterize the type of lesions amplified by nanoMOFs, SF curves were fitted using the linear quadratic law (Eq. (3)):[45]

$$SF(D) = \exp-(\alpha D + \beta D^2) \quad (3)$$

where D is the dose of irradiation. The coefficient α corresponds to the contribution of directly-lethal lesions, whereas β is attributed to the contribution of additive sub-lethal lesions. The values of α and β determined by the fitting procedure are reported in Table 2. The presence of nanoMOFs alone induces an increase in α (0.30 for nanoMOFs and 0.22 for the control). This indicates an enhancement of the direct lethality of the radiation treatment in the presence of nanoMOFs.

The same data analysis was performed for cells treated with Gem-MP. We found that Gem-MP amplified cell death by DEF (4 Gy) of 2.23 and REF of 1.35. The increase of α (from 0.22 for the control to 0.36) shows that direct lethal damages are increased. This corresponds to the well-known effect of the drug, which agrees with former studies.[10] Thus, upon irradiation, the agent induces radiosensitization of the cells, namely an amplification of radiation effect due to perturbation of a metabolic pathway. Gem-MP is responsible for: i) induction of early S phase block[52] via DNA inhibition at the moment of irradiation, contributing to more pronounced radiosensitizing effect; ii) inhibition of RAD51-dependent repair for DNA breaks induced by irradiation.[53] This effect is distinct from the "radioenhancement" presented above (which is related to early stage electronic processes).

For Gem-MP loaded nanoMOF, an unprecedented effect was observed. In this case, cell killing drastically increased as witnessed by the REF of 1.83 (as compared to 1.19 for nanoMOF, and 1.35 for Gem-MP alone) and by the DEF (4 Gy) up to 6.47 (as compared to 1.53 for nanoMOF and 2.23 for Gem-MP). To the best of our knowledge, the REF obtained with high-Z NPs is in the range of 1.1 to 1.6.[15,56] Thus, the amplification effect obtained by Gem-MP loaded nanoMOF is among the highest ever reported. This is associated with a doubling of the directly lethal damage as illustrated by an increase from 0.22 (for the control) up to 0.44 with Gem-MP loaded nanoMOF, much higher than that of nanoMOFs (0.30) and Gem-MP (0.36) alone. This demonstrates for the first time that the use of drug carried nanocages (Gem-MP loaded nanoMOFs) are able to combine radioenhancement and radiosensitization, which results in a much higher amplification of radiation effects superior to each element (nanoMOF and Gem-MP) considered separately. This may be explained as follows. When Gem-MP loaded nanoMOFs were incubated with HeLa cells, Gem-MP probably inhibited DNA synthesis and induced cell block in early S phase, which is more sensitive to irradiation.[52] Upon irradiation, nanoMOFs amplified the radiation effect by generating high amounts of ROS, which generated DNA damages. Gem-MP hindered reparation of DNA double-strand breaks in particular. Moreover, as previously shown, when Gem-MP loaded nanoMOFs were incubated with HeLa cells, they penetrated inside the cells, thus promoting

Table 2. Calculated coefficients α and β for HeLa cells irradiated by γ source, in the presence of nanoMOF, Gem-MP, Gem-MP loaded nanoMOF, and in the control (HeLa cells treated by only γ irradiation). The dependency R^2 values are reported in the last column.

Sample	α (Gy^{-1})	β (Gy^{-2})	R^2
control	0.22 ± 0.01	0.006 ± 0.002	0.9995
nanoMOF	0.30 ± 0.01	0	0.9979
Gem-MP	0.36 ± 0.01	0	0.9933
Gem-MP loaded nanoMOF	0.44 ± 0.01	0	0.9989

interaction between the drug and the cells as compared with free drug unable to bypass cell membranes. This could be another reason for the improved anticancer activity after irradiation of encapsulated drug that is of high interest for clinical applications. In conclusion, radiosensitization of Gem-MP and radioenhancement of nanoMOFs complement each other to improve irradiation performance, synergistically contributing to eradicate cancer cells upon irradiation.

Nanoscale Impact of nanoMOFs

To gain further insights onto the physicochemical effects induced on biological molecules by nanoMOFs activated by radiation, we used plasmids as molecular nanoprobes to quantify the induction of nanosize (complex) damages.[44,54] In particular, we quantified double strand breaks (DSBs), which are separated by more 2 nm (distance between two strands), to probe the effect of nanoMOFs on the induction of nanosize damages (Figure 1B). The addition of nanoMOFs alone (without irradiation) did not induce any damage. Upon irradiation, the number of single strand breaks (SSB) kept constant (less than 5% variation) in comparison to control, whereas DSBs increased with the dose, indicating that nanosize damages were induced. The effect of nanoMOFs on DSB is illustrated in Figure 6, where the nanoprobe was mixed with nanoMOFs and irradiated at a dose ranging from 0 up to 115 Gy. The yield of DSB, defined as the number of breaks induced per plasmid and per gray, corresponds to the slope of the dose response curves.[45] Remarkably, when the ratio of nanoprobe over nanoMOFs was close to 200:1, the induction of DSBs was dramatically enhanced (Figure 6). In the dose range of 0~70 Gy, DSB increased linearly with the dose, in agreement with previously reported studies with Gd-based NPs.[45] The yield of DSB increased 2.33 times (0.003 for the control and 0.007 with the addition of nanoMOFs). In the dose range 70~115 Gy, DSB increased in an exponential manner (Fitting: $DSB = 4\times10^{-5}x^2 - 0.0045x + 0.1831$, x = dose). DSB increased by a factor of 5 at 115 Gy.

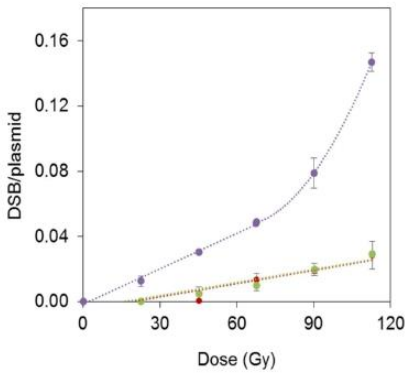

Figure 6. Yields of nanosize lesions in nanoprobes (plasmids) upon γ rays irradiation in the presence of nanoMOFs for different plasmid:nanoMOFs ratio (red: plasmids control; green: plasmid:nanoMOFs (number ratio) = 2000:1; purple: plasmid:nanoMOFs (number ratio) = 200:1).

These results suggest the activation of physicochemical processes including the emission of electrons and consecutive production of water radicals, responsible for the induction of nanosize damages as explained before. In particular, the emission of electrons in water and therefore the production of reactive radicals are facilitated by the porous structure of the nanoMOFs. It thus confirms that nanoMOFs amplify the induction of nanosize damage due to physicochemical effects and to the porous character of this agent.

Conclusions

Here we report the first proof of concept of nanoMOFs loaded with an anticancer drug to eradicate tumor cells upon irradiation. Whereas free Gem-MP is a powerful radiosensitizer, iron trimesate nanoMOFs were shown to possess intrinsic radioenhancement properties taking advantage of the ordered porous 3D structure. This approach could be extended to other drugs, provided that they are not subject to degradation upon irradiation. Non-toxic nanoMOFs acted as "Trojan horses" significantly penetrating inside cancer cells, thus promoting the cytotoxic action of entrapped Gem-MP. By displaying different mechanisms of action, both nanoMOFs activated by radiation and their Gem-MP cargo synergistically contributed to kill cancer cells. Given that nanoMOFs could act as contrast agent for MRI imaging, this opens a new perspective for imaging guided chemoradiotherapy, paving the way toward a new paradigm of NPs aided radiotherapy using drug loaded radio-enhancing carriers to synergistically play on different modes of action and improve cancer treatments.

Experimental Section

Materials

Chemical materials. Iron (III) chloride hexahydrate (98%, Alfa Aesar, France), and 1,3,5-benzenetricarboxylic acid (trimesate, 95%, Sigma-Aldrich, France) were used for the synthesis of nanoMOFs. Absolute ethanol (99%, Carlo Erba, France) was used to purify the nanoMOFs. 2′,2′-difluorodeoxycytidine monophosphate (Gem-MP) was purchased from Toronto Research Chemicals (Canada). Triethylamine acetate and methanol (HPLC grade) were purchased from Sigma-Aldrich (France) as mobile phase for detection of Gem-MP.

For Rhod-Ada synthesis, diethyl ether and tetrahydrofuran (THF) were distilled from sodium/benzophenone ketyl. *N,N*-Dimethylformamide (DMF), and dichloromethane (CH_2Cl_2) were distilled from calcium hydride, under nitrogen atmosphere. All reactions involving air- or water-sensitive compounds were routinely conducted in glassware which was flame-dried under a positive pressure of nitrogen or argon. 1-Adamantane acetic acid, oxalyl chloride, succinic anhydride, 1-ethyl-3-(3-dimethylaminopropyl)-carbodiimide (EDCI), hydroxybenzotriazole (HOBt), ethyl ether (Et_2O), sodium hydroxide (NaOH) and 2,2′-(ethylendioxy)bis(ethylamine) were obtained from Sigma-Aldrich (France). Rhodamine piperazine was obtained according to T. Nguyen et al.[43] Chemicals

obtained from commercial suppliers were used without further purification.

Cell culture. HeLa cells were grown in DMEM medium (Life Technologies, France) supplemented with 10% v/v decomplemented fetal bovine serum (FBS) (Life Technologies, France) and 1% Penicillin/Streptomycin (Life Technologies, France) at 37 °C in humidified air containing 5% CO_2.

Synthesis and Characterization of MIL-100(Fe) nanoMOFs

MIL-100(Fe) nanoMOFs were synthesized as previously described by microwave assisted hydrothermal reaction.[34] Briefly, 30 mL of aqueous mixture containing 6.0 mM of iron chloride hexahydrate and 4.02 mM of trimesic acid was heated by microwave at 130 °C for 6 min under stirring with power of 1600 W (Mars-5, CEM, USA). The as-synthesized nanoMOFs were recovered by centrifugation at 10,000 g for 15 min and washed six times with absolute ethanol to remove unreacted trimesate. The dynamic diameter of nanoMOFs was characterized by dynamic light scattering (DLS; Malvern Nano-ZS, Zetasizer Nano series, France). The porous surface area was measured by nitrogen sorption experiments at −196 °C on an ASAP 2020 (Micromeritics, USA) after sample degassing at 100 °C for 15 h under vacuum. NanoMOFs were stored in ethanol at room temperature until further usage.

Drug Loading and Release Studies

NanoMOFs suspensions in ethanol (1.0 mg) were centrifuged at 10,000 g for 10 min, supernatants were discarded and the pellets were re-dispersed in 1.0 mL of Gem-MP aqueous solution (100 μg/mL). After gently stirring overnight, the drug-loaded nanoMOFs were recovered by centrifugation (10,000 g, 10 min) and the supernatant was analyzed by HPLC to determine the amount of non-encapsulated Gem-MP. For the release studies, the Gem-MP loaded nanoMOFs (1.0 mg/mL) were centrifuged (10,000 g, 10 min) and redispersed in cell culture medium Dulbecco Modified Eagle Medium (DMEM) supplemented with 10% Fetal Bovine Serum (FBS), 1% penicillin/streptomycin (100 mg/mL), and 1% L-Glutamine. Drug release studies were performed at 37 °C with nanoMOFs concentrations of 2.5 mg/mL. After different incubation times (30 min, 2 h, 4 h, 6 h, and 8 h), the samples were centrifuged (10,000 g, 10 min). The pellets were redispersed in 10 mM phosphate buffered saline (PBS) by vortex to totally degrade the nanoMOFs. Extracted Gem-MP was assessed by HPLC to determine the nanoMOF drug loadings.

HPLC methods. Detection of Gem-MP and TA was carried out by HPLC (Agilent 1100, USA) using a Phenomenex C_{18} column (4.6× 250 mm, 5 μm) at a flow rate of 1.0 mL/min. A mobile phase consisting of 84% buffer (0.2 M Triethylamine Acetate): 16% methanol was used. Compounds were detected at 254 nm with an injection volume of 20 μL. Retention times of trimesate and Gem-MP were 2.67 and 3.08 min, respectively.

Stability of nanoMOF, Gem-MP, and Gem-MP Loaded nanoMOF Upon Irradiation

NanoMOF, Gem-MP, and Gem-MP loaded nanoMOF were prepared at the concentration of 17 μg/mL, 1.7 μg/mL, and 17 μg/mL for nanoMOF, Gem-MP and Gem-MP loaded nanoMOFs with 10 wt% drug loading, respectively. All the samples were incubated in water at 37 °C for 6 h, followed by irradiation at 4, and 6.5 doses using a Cs-137 gamma source (energy = 0.6617 MeV (γ)) generated by GSR-D1 gamma irradiator at Institut Curie in Orsay, France. The supernatants of all samples after irradiation were recovered after centrifugation at 17,000 g for 20 min and analyzed by HPLC to quantify the amount of released TA and Gem-MP.

Fluorescent Labelling of nanoMOFs

Rhod-Ada conjugate was synthesized in order to efficiently label the nanoMOFs.

General

IR spectra were obtained as solid or neat liquid on a Fourier Transform Bruker Vector 22 spectrometer. Only significant absorptions are listed. The ^1H and ^{13}C NMR spectra were recorded on Bruker Avance 300 (300 MHz and 75 MHz, for ^1H and ^{13}C, respectively) or Bruker Avance 400 (400 MHz and 100 MHz, for ^1H and ^{13}C, respectively) spectrometers. Recognition of methyl, methylene, methine, and quaternary carbon nuclei in ^{13}C NMR spectra rests on the J-modulated spin-echo sequence. Mass spectra were recorded on a Bruker Esquire-LC. Analytical thin-layer chromatography was performed on Merck silica gel 60F254 glass precoated plates (0.25 mm layer). Column chromatography was performed on Merck silica gel 60 (230–400 mesh ASTM). These methods were used for all the following compounds.

Synthesis of 2-(Adamantan-1-yl)-N-{2-[2-(2-aminoethoxy)ethoxy] ethyl}acetamide (2). To a solution of 1-adamantane acetic acid (280 mg, 1.44 mM) in CH_2Cl_2 (3 mL) was added a drop of DMF and oxalyl chloride (202 mg, 1.58 mmol). The reaction mixture was stirred 2 h at 20 °C and then concentrated *in vacuo*. The residue was taken up into CH_2Cl_2 (10 mL) and slowly added over three hours to 2,2′(ethylendioxy)bis(ethylamine) (2.13 g, 14.4 mmol) in CH_2Cl_2 (20 mL). The reaction mixture was stirred at room temperature for 12 h and concentrated under reduced pressure. The residue was treated with 0.5 N NaOH (10 mL) and extracted with Et_2O (2×5 mL). The organic layer was discarded, and the aqueous phase was extracted with CH_2Cl_2 (5×10 mL). The combined organic phases were dried over $MgSO_4$ and concentrated to leave a pale yellow oil which used directly in the next step (262 mg, 56%).

IR (neat, cm^{-1}) *n* 3330 (br), 2929, 2899, 2846, 1640, 1510, 1480, 1347, 1336, 1315, 1293, 1275, 1243, 1203, 1156, 1139, 1103, 1096, 989, 925, 906, 883, 725; ^1H NMR (300 MHz, $CDCl_3$) δ 6.10 (br s, 1H, CONH), 3.58 (s, 4H, OCH_2CH_2O), 3.55–3.45 (m, 4H, $CH_2OCH_2CH_2OCH_2$), 3.45–3.35 (m, 2H, $HNCH_2CH_2O$), 2.87 (br s, 2H), 2.19 (br s, 2H, NH_2), 1.95–1.88 (m, 5H, CH_2CON, H-3, H-5, H-7), 1.75–1.60 (m, 12H, H-2, H-4, H-6, H-8, H-9, H-10) ppm; ^{13}C NMR (75 MHz, $CDCl_3$) δ 171.1 (C, CON), 73.3 (CH_2, CH_2O), 70.3 (CH_2, CH_2O), 70.2 (CH_2, CH_2O), 70.1 (CH_2, CH_2O), 51.7 (CH_2, AdaCH$_2$CON), 42.7 (3CH_2, C-2, C-8, C-9), 41.8 (CH_2, CH_2N), 39.1 (CH_2, $CONCH_2$), 36.9 (3CH_2, C-4, C-6, C-10), 32.8 (C, C-1), 28.7 (3CH, C-3, C-5, C-7) ppm; MS (ESI+): m/z (%) = 325.3 (100) [M^-].

3-{[2-(2-{2-[2-(Adamantan-1-yl)acetamido]ethoxy}ethoxy)ethyl]carbamoyl}propanoic acid (3) synthesis. A mixture of amine **2** (124 mg, 0.38 mmol) and succinic anhydride (50 mg, 0.51 mmol) in THF (3 mL) was heated at 40 °C for 16 h. The mixture was concentrated *in vacuo* and the residue was chromatographed on silica gel eluting with CH_2Cl_2/MeOH, 20:1 to leave the acid **3** as a colorless oil (113 mg, 70%). IR (neat, cm^{-1}) *n* 3300 (br), 3080 (br), 2930, 2901, 2846, 1720, 1645, 1619, 1540, 1454, 1347, 1335, 1242, 1203, 1173, 1157, 1140, 1103, 1095, 1078, 1045, 990, 882; ^1H NMR (300 MHz, MeOH-d_4) δ 3.61 (s, 4H, OCH_2CH_2O), 3.54 (t, *J* = 5.4 Hz, 4H, $CH_2OCH_2CH_2OCH_2$), 3.36 (t, *J* = 5.4 Hz, 4H, $CONHCH_2CH_2O$), 2.61–2.55 (m, 2H, CH_2CO_2H), 2.51–2.45 (m, 2H, $NCOCH_2$), 1.95 (s, 5H, CH_2CON, H-3, H-5, H-7), 1.80–1.60 (m, 12H, H-2, H-4, H-6, H-8, H-9, H-10) ppm; ^{13}C NMR (75 MHz, MeOH-d_4) δ 176.0 (C, CO_2H), 174.5 (C, CON), 173.8 (C, CON), 71.3 (CH_2, CH_2O), 71.2 (CH_2, CH_2O), 70.6 (CH_2, CH_2O), 70.5

(CH_2, CH_2O), 51.8 (CH_2, $AdaCH_2CON$), 43.7 ($3CH_2$, C-2, C-8, C-9), 40.3 (CH_2, CH_2NCO), 40.1 (CH_2, $CONCH_2$), 37.9 ($3CH_2$, C-4, C-6, C-10), 33.7 (C, C-1), 31.5 (CH_2, $CH_2CH_2CO_2H$), 30.3 (CH_2, $CH_2CH_2CO_2H$), 30.17 (3CH, C-3, C-5, C-7) ppm; MS (ESI-): m/z (%) = 423.3 (100) [M^-].

9-{2-[4-(3-{[2-(2-{2-[2-(adamantan-1-yl)acetamido]ethoxy}ethoxy) ethyl] carbamoyl} propanoyl) piperazine-1-carbonyl]phenyl}-6-(diethylamino)-N,N-diethyl-3H-xanthen-3-iminium chloride (Rhod-Ada, 5). To a mixture of rhodamine piperazine (120 mg, 0.22 mmol) and acid 3 (113 mg, 0.26 mmol) in DMF (3 mL) was sequentially added HOBt (10 mg, 0.07 mmol), EDCI (56 mg, 0.29 mmol) and Hünig's base (148 mg, 1.15 mmol). The reaction mixture was stirred at 20 °C for 24 h and concentrated under reduce pressure. The residue was taken up into HCl 0.1 N (5 mL) and extracted with CH_2Cl_2 (3× 10 mL). The combined organic phases were dried over $MgSO_4$ and concentrated to leave a dark red oil which was chromatographed over silica gel eluting with CH_2Cl_2/MeOH, 20:1 and then 10:1 to give the rhodamine adamantane conjugate 5 as a dark red solid (79 mg, 47%). ^{1}H NMR (300 MHz, $CDCl_3$) δ 7.90–7.67 (m, 5H, 2 NH, H-3′$_{Rhod}$, H-5′$_{Rhod}$, H-6′$_{Rhod}$), 7.55–7.50 (m, 1H, H-4′$_{Rhod}$), 7.29 (d, J = 9.3 Hz, 2H, H-1$_{Rhod}$, H-8$_{Rhod}$), 7.07 (dd, J = 9.3 Hz, J = 2.4 Hz, 2H, H-2$_{Rhod}$, H-7$_{Rhod}$), 6.97 (d, 1H, J = 2.4 Hz, 2H, H-4$_{Rhod}$, H-5$_{Rhod}$), 3.69 (q, J = 7.0 Hz, 8H, $N(CH_2CH_3)_2$), 3.60 (s, 4H, OCH_2CH_2O), 3.57-3.30 (m, 16H, $CH_2CH_2OCH_2CH_2OCH_2CH_2$, $CON(CH_2CH_2)_2NCO$), 2.65-2.55 (m, 2H, CH_2CON), 2.50–2.42 (m, 2H, CH_2CON), 2.00-1.90 (m, 5H, CH_2CON, H-3$_{Ada}$, H-5$_{Ada}$, H-7$_{Ada}$), 1.80-1.60 (m, 12H, H-2$_{Ada}$, H-4$_{Ada}$, H-6$_{Ada}$, H-8$_{Ada}$, H-9$_{Ada}$, H-10$_{Ada}$), 1.31 (t, J = 7.0 Hz, 12H, $N(CH_2CH_3)_2$) ppm; ^{13}C NMR (75 MHz, $CDCl_3$) δ 174.7 (C, CO), 173.9 (C, CO), 172.7 (C, CO), 169.6 (C, CO$_{Rhod}$), 159.3 (2 C, C-3$_{Rhod}$, C-6$_{Rhod}$), 157.2 (2 C, C-4a$_{Rhod}$, C-4b$_{Rhod}$), 157.0 (C, C-1′$_{Rhod}$), 136.5 (CH, C-5′$_{Rhod}$), 133.2 (2CH, C-1$_{Rhod}$, C-8$_{Rhod}$), 132.7 (C, C-9$_{Rhod}$), 131.8 (CH, C-6′$_{Rhod}$), 131.3 (C and CH, C-2′$_{Rhod}$, C-3′$_{Rhod}$), 128.9 (CH, C-4′$_{Rhod}$), 115.4 (2CH, C-2$_{Rhod}$, C-7$_{Rhod}$), 114.8 (2 C, C-8a$_{Rhod}$, C-8b$_{Rhod}$), 97.3 (2CH, C-4$_{Rhod}$, C-5$_{Rhod}$), 71.3 (CH_2, CH_2O), 71.2 (CH_2, CH_2O), 70.7 (CH_2, CH_2O), 70.6 (CH_2, CH_2O), 51.8 (CH_2, $AdaCH_2CON$), 46.9 ($4CH_2$, $N(CH_2CH_3)_2$), 43.7 ($3CH_2$, C-2$_{Ada}$, C-8$_{Ada}$, C-9$_{Ada}$), 43.2-42.6 (m, $4CH_2$, $N(CH_2CH_2)_2N$), 40.3 (CH_2, CH_2NCO), 40.1 (CH_2, $CONCH_2$), 37.9 ($3CH_2$, C-4$_{Ada}$, C-6$_{Ada}$, C-10$_{Ada}$), 33.8 (C, C-1$_{Ada}$), 31.5 (CH_2, $NCOCH_2CH_2CON$), 30.2 (3CH, C-3$_{Ada}$, C-5$_{Ada}$, C-7$_{Ada}$), 29.0 (CH_2, $NCOCH_2CH_2CON$), 12.8 ($4CH_3$, $N(CH_2CH_3)_2$) ppm; MS (ESI+): m/z (%) = 917.6 (100) [M–Cl]$^+$, 553.3 (15), 539.3 (14), 470 (80) [M–Cl +Na]$^{2+}$.

NanoMOFs Labeling with Rh-Ad

Rh–Ad was dissolved in water at a concentration of 1 mM and incubated overnight with nanoMOFs at a weight ratio of 1:10 (Rhod-Ad: nanoMOFs). Rhod-Ad labelled nanoMOFs were washed with water until no free Rhod-Ad was found in the washing solution (concentration < 0.05 μg/mL). Because of quenching effect of nanoMOFs, Rhod adsorption on the surface of nanoMOFs could not be directly quantified. Indirect methods were applied consisting in quantifying the initial Rhod amount added to nanoMOFs and the free Rhod in the supernatants after extensive washings of the nanoMOFs using a fluorescence spectrophotometer (VARIAN, Cary Eclipse). Rhod-Ad adsorption was calculated as the weight ratio (%) between the adsorbed Rhod-Ad and the nanoMOFs. Rhod-Ad release was measured in cell culture medium. After incubation at 37 °C for 1, 2, 4, and 6 h, the samples were collected by centrifugation and the detached Rhod-Ad was measured using a fluorimeter. Rhod labelling was performed in the same way as control samples.

Visualization by confocal microscopy. 3.0×10^4 HeLa cells were seed on sterile glass slides. After incubating overnight for the cells to get attached, nanoMOFs labelled with Rhod or Rhod-Ad were incubated with living cells for 6 h. After washing three times with PBS to remove free nanoMOFs, living cells were visualized using a LEICA SP5 confocal system, equipped with a thermostatically controlled and CO_2 regulated chamber (Centre de photonique BioMédicale, Centre Laser Université Paris Sud, France). Rhod and Rhod-Ad were excited at 514 nm and the emission from 560–600 nm were collected. The images were processed with the Image J software.

Fe quantification was performed by adjusting a previous reported iron staining protocol.[25] Briefly, 2.0×10^5 cells were plated in 24 wells plates and incubated for 24 h for cell adherence. Then the cells were incubated for 6 h with 1 mL of DMEM 10% FBS or 1 mL of culture media containing nanoMOFs labelled or not with Rhod-Ad (nanoMOF concentration = 0 ~ 200 μg/mL). Cells were prepared in four wells for each condition. At the end of the incubation, the cells were washed three times with PBS to eliminate non interacting MOFs. Cells were detached using trypsin and then counted with Luna counting (LUNA™, Logos Biosystem, Korea). Cells in four other wells cultured in the same conditions were digested with 100 μL HCl (5 M) at 60 °C for 2 h. At the end of the incubation, 100 μL of 4% potassium ferrocyanide was added in each well. The plates were further incubated at room temperature in the dark for 30 min. The absorbance of the treated samples was measured at 690 nm. Calibration curves were obtained with nanoMOFs suspensions with known concentrations (0 ~ 250 μg/mL). The internalized nanoMOFs was quantified using HeLa cells without nanoMOFs as control.

Effect of Gem-MP and nanoMOFs on SF of HeLa Cells Upon Irradiation

HeLa cells were cultured using DMEM media supplemented with 10% FBS, 1% penicillin/streptomycin (100 mg/mL), and 1% L-Glutamine. Cells were maintained at 37 °C in a 5% CO_2 incubator. Growing cells at a density of 2×10^5 were seeded in flasks (25 cm^3) 12 h before irradiation. NanoMOFs loaded or not with Gem-MP were added to the cell culture medium at an equivalent Fe concentration of 56 μM. After 6 h incubation, the compounds (nanoMOFs, Gem-MP, and Gem-MP loaded nanoMOFs) were removed and the cells were irradiated using the same Cs-137 gamma source as for the stability investigation. The cells were irradiated at ambient conditions with doses of 1, 2, 3.5, 5, and 6.5 Gy. The effect of radiation, nanoMOFs and Gem-MP on cells was quantified by clonogenic assay. Briefly, cells were detached with trypsin (0.05%) and plated onto Petri dishes (100 mm) at a density of 100 surviving cells/dish. The plating efficiency was close to 39% for HeLa cells, whatever they interacted or not with nanoMOFs. When Gem-MP was used, the plating efficiency was close to 28%. After 2 weeks of incubation, the formed cell colonies were washed twice with PBS and stained with 0.5% methylene blue in methanol. The colonies were finally counted to determine the surviving fractions.

Effect of Gem-MP and nanoMOFs on DNA Damage Induced by Irradiation

Plasmids. The commercial pBR322 (p stands for "plasmid," and BR for "Bolivar" and "Rodriguez") DNA (Molecular biology, France) composed of 4361 base pairs and diluted in Tris-EDTA buffer (0.5 μg/mL) was used. NanoMOFs were considered as spheres with diameter of 200 nm and the weight of the single NP were theoretically calculated. The effect of nanoMOFs was investigated using a DNA:nanoMOFs number ratio ranging from 2000:1 to 200:1. Plasmids were irradiated with γ source from Co-60 (energy = 1.25 MeV (γ), dose rate = 4.51 Gy/min) in Orsay, France. After irradiation at the dose range of 0–115 Gy, agarose gel electrophoresis was performed to analyze the samples. Briefly, the three conformers of the plasmid were separated by migration in agarose gel (1.0 wt%) under electrophoresis at an electric intensity of 80 mA

for 3 h. After quantification of the three band intensities (S, R, and L) by Image J, the respective yields of SSB and DSB were determined as previously reported.[55] Given the fact that the S forms bind 1.47-times less ethidium bromide than R and L conformations, which was calculated based on the binding constant of R, S, and L to ethidium bromide,[56] the fraction of R (R'), S (S'), and L (L') was calculated as following:

$$\text{Total} = 1.47 \times S + R + L$$

$$R' = R/\text{Total}$$

$$S' = 1.47 \times S/\text{Total}$$

$$L' = L/\text{Total}$$

The induction of SSBs and DSBs per plasmid was determined using Poisson law statistics,[55] which is based on the discrete probability distribution that expresses the probability of a given number of events occurring in a fixed space:

$$\text{SSB yield (breaks per plasmid)} = \ln[(1-L')/S']$$

$$\text{DSB yield (breaks per plasmid)} = L'/(1-L')$$

Acknowledgements

We acknowledge support from the Université Paris Saclay for the "Inititative de Recherche Stratégique" IRS NanoTheRad project. This research was funded by European Research Council through Cyclon Hit project (People-2013-ITN Grant Agreement 608407), by the French National Research Agency (ANR) grant ANR-14-CE08-0017 and the ARGENT project, Grant Agreement 608163. This work is supported by a public grant overseen by the French ANR as part of the "Investissements d'Avenir" program (Labex NanoSaclay, reference: ANR-10-LABX-0035). It was also supported by the China Scholarship Council through a PhD grant. We acknowledge help from Ludivine Houel Renault, responsible of the platform CPBM/CLUPS/LUMAT FR2764 for cell culture and confocal microscopy.

Keywords: metal–organic frameworks · nanoparticles · radioenhancers · radiosensitization · synergistic effect

[1] B. Pauwels, A. E. C. Korst, F. Lardon, J. B. Vermorken, *Oncologist* **2005**, *10*, 34.
[2] T. Song, M. Fang, S. Wu, *Clin. Interventions Aging* **2018**, *13*, 2275.
[3] F. Lim, R. Glynne-Jones, *Cancer Treat. Rev.* **2011**, *37*, 520.
[4] R. Roy, A. Maraveyas, *Oncologist* **2010**, *15*, 259.
[5] O. M. Vanderveken, P. Szturz, P. Specenier, M. C. Merlano, M. Benasso, D. Van Gestel, K. Wouters, C. Van Laer, D. Van den Weyngaert, M. Peeters, *Oncologist* **2016**, *21*, 59.
[6] D. Y. Bouffard, J. Laliberté, R. L. Momparler, *Biochem. Pharmacol.* **1993**, *45*, 1857.
[7] C. H. Hsu, *Mol. Pharmacol.* **2004**, *67*, 806.
[8] A. M. Bergman, H. M. Pinedo, G. J. Peters, *Drug Resist. Updates* **2002**, *5*, 19.
[9] A. M. Allen, M. M. Zalupski, J. M. Robertson, F. E. Eckhauser, D. Simone, D. Brown, G. Hejna, D. Normolle, T. S. Lawrence, C. J. McGinn, *Int. J. Radiat. Oncol. Biol. Phys.* **2004**, *59*, 1461.
[10] V. Rodriguez-Ruiz, A. Maksimenko, R. Anand, S. Monti, V. Agostoni, P. Couvreur, M. Lampropoulou, K. Yannakopoulou, R. Gref, *J. Drug Targeting* **2015**, *23*, 759.
[11] D. Rosenblum, N. Joshi, W. Tao, J. M. Karp, D. Peer, *Nat. Commun.* **2018**, *9*, 1.
[12] S. Senapati, A. K. Mahanta, S. Kumar, P. Maiti, *Signal Transduct. Target. Ther.* **2018**, *3*, 7.
[13] D. Kwatra, A. Venugopal, S. Anant, *Transl. Cancer Res.* **2013**, *2*, 330.
[14] D. M. Herold, I. J. Das, C. C. Stobbe, R. V. Iyer, J. D. Chapman, *Int. J. Radiat. Biol.* **2000**, *76*, 1357.
[15] Z. Kuncic, S. Lacombe, *Phys. Med. Biol.* **2018**, *63*, 1.
[16] K. Lu, C. He, N. Guo, C. Chan, K. Ni, G. Lan, H. Tang, C. Pelizzari, Y. X. Fu, M. T. Spiotto, *Nat. Biomed. Eng.* **2018**, *2*, 600.
[17] K. Ni, G. Lan, C. Chan, B. Quigley, K. Lu, T. Aung, N. Guo, P. La Riviere, R. R. Weichselbaum, W. Lin, *Nat. Commun.* **2018**, *9*, 1.
[18] K. Ni, G. Lan, S. S. Veroneau, X. Duan, Y. Song, W. Lin, *Nat. Commun.* **2018**, *9*, 1.
[19] T. Baati, L. Njim, F. Neffati, A. Kerkeni, M. Bouttemi, R. Gref, M. F. Najjar, A. Zakhama, P. Couvreur, C. Serre, *Chem. Sci.* **2013**, *4*, 1597.
[20] T. Simon-Yarza, T. Baati, F. Neffati, L. Njim, P. Couvreur, C. Serre, R. Gref, M. F. Najjar, A. Zakhama, P. Horcajada, *Int. J. Pharm.* **2016**, *511*, 1042.
[21] T. Simon-Yarza, M. Giménez-Marqués, R. Mrimi, A. Mielcarek, R. Gref, P. Horcajada, C. Serre, P. Couvreur, *Angew. Chem. Int. Ed.* **2017**, *56*, 15565.
[22] P. Horcajada, T. Chalati, C. Serre, B. Gillet, C. Sebrie, T. Baati, J. F. Eubank, D. Heurtaux, P. Clayette, C. Kreuz, *Nat. Mater.* **2010**, *9*, 172.
[23] M. Giménez-marqués, E. Bellido, T. Berthelot, T. Simón-yarza, T. Hidalgo, R. Simón-vázquez, Á. González-Fernández, J. Avila, M. C. Asensio, R. Gref, *Small* **2018**, *14*, 1801900.
[24] T. Hidalgo, M. Giménez-Marqués, E. Bellido, J. Avila, M. C. Asensio, F. Salles, M. V. Lozano, M. Guillevic, R. Simón-Vázquez, A. González-Fernández, *Sci. Rep.* **2017**, *7*, 1.
[25] S. Wuttke, S. Braig, T. Preiß, A. Zimpel, J. Sicklinger, C. Bellomo, J. O. Rädler, A. M. Vollmar, T. Bein, *Chem. Commun.* **2015**, *51*, 15752.
[26] V. Agostoni, P. Horcajada, M. Noiray, M. Malanga, A. Aykaç, L. Jicsinszky, A. Vargas-Berenguel, N. Semiramoth, S. Daoud-Mahammed, V. Nicolas, *Sci. Rep.* **2015**, *5*, 7925.
[27] E. Bellido, T. Hidalgo, M. V. Lozano, M. Guillevic, R. Simón-Vázquez, M. J. Santander-Ortega, Á. González-Fernández, C. Serre, M. J. Alonso, P. Horcajada, *Adv. Healthcare Mater.* **2015**, *4*, 1246.
[28] G. Férey, C. Mellot-Draznieks, C. Serre, F. Millange, J. Dutour, S. Surblé, I. Margiolaki, *Science* **2005**, *309*, 2040.
[29] P. Horcajada, R. Gref, T. Baati, P. K. Allan, G. Maurin, P. Couvreur, *Chem. Rev.* **2012**, *112*, 1232.
[30] X. Li, N. Semiramoth, S. Hall, V. Tafani, J. Josse, F. Laurent, G. Salzano, D. Foulkes, P. Brodin, L. Majlessi, *Part. Part. Syst. Charact.* **2019**, *36*, 1.
[31] V. Agostoni, R. Anand, S. Monti, S. Hall, G. Maurin, P. Horcajada, C. Serre, K. Bouchemal, R. Gref, *J. Mater. Chem. B* **2013**, *1*, 4231.
[32] V. Agostoni, T. Chalati, P. Horcajada, H. Willaime, R. Anand, N. Semiramoth, T. Baati, S. Hall, G. Maurin, H. Chacun, *Adv. Healthcare Mater.* **2013**, *2*, 1630.
[33] R. Grall, T. Hidalgo, J. Delic, A. Garcia-marquez, S. Chevillard, P. Horcajada, *J. Mater. Chem. B* **2015**, *3*, 8279.
[34] M. N. Martin, A. J. Allen, R. I. Maccuspie, V. A. Hackley, *Langmuir* **2014**, *30*, 11442.
[35] V. Agostoni, P. Horcajada, V. Rodriguez-Ruiz, H. Willaime, P. Couvreur, C. Serre, R. Gref, *Green Mater.* **2013**, *1*, 209.
[36] F. Jeremias, S. K. Henninger, C. Janiak, *Dalton Trans.* **2016**, *45*, 8637.
[37] Y. Xu, L. Xu, S. Qi, Y. Dong, Z. U. Rahman, H. Chen, X. Chen, *Anal. Chem.* **2013**, *85*, 11369.
[38] F. Zhang, J. Shi, Y. Jin, Y. Fu, Y. Zhong, W. Zhu, *Chem. Eng. J.* **2015**, *259*, 183.
[39] I. Levy, I. Sher, E. Corem-Salkmon, O. Ziv-Polat, A. Meir, A. J. Treves, A. Nagler, O. Kalter-Leibovici, S. Margel, Y. Rotenstreich, *J. Nanobiotechnol.* **2015**, *13*, 34.
[40] S. R. Miller, D. Heurtaux, T. Baati, P. Horcajada, J.-M. Grenèche, C. Serre, *Chem. Commun.* **2010**, *46*, 4526.
[41] X. Li, G. Salzano, J. Zhang, R. Gref, *J. Pharm. Sci.* **2017**, *106*, 395.
[42] X. Li, L. Lachmanski, S. Safi, S. Sene, C. Serre, J. M. Grenèche, J. Zhang, R. Gref, *Sci. Rep.* **2017**, *7*, 1.
[43] T. Nguyen, M. B. Francis, *Org. Lett.* **2003**, *5*, 3245.
[44] E. Porcel, S. Liehn, H. Remita, N. Usami, K. Kobayashi, Y. Furusawa, C. Le Sech, S. Lacombe, *Nanotechnology* **2010**, *21*, 1.
[45] E. Porcel, O. Tillement, F. Lux, P. Mowat, N. Usami, K. Kobayashi, Y. Furusawa, C. Le Sech, S. Li, S. Lacombe, *Nanomedicine Nanotechnology, Biol. Med.* **2014**, *10*, 1601.
[46] M. Guo, Y. Sun, X.-D. Zhang, *Appl. Sci.* **2017**, *7*, 232.
[47] S. Shrestha, L. N. Cooper, O. A. Andreev, Y. K. Reshetnyak, M. P. Antosh, *Jacobs J. Radiat. Oncol.* **2016**, *3*, 26.

[48] A. S. Wozny, M. T. Aloy, G. Alphonse, N. Magné, M. Janier, O. Tillement, F. Lux, M. Beuve, C. Rodriguez-Lafrasse, *Nanomedicine:NBM.* **2017**, *13*, 2655.
[49] C. M. Mazur, R. R. Strawbridge, E. S. Thompson, A. A. Petryk, D. J. Gladstone, P. J. Hoopes, *Prog. Biomed. Opt. Imaging - Proc. SPIE* **2015**, *9326*, 1.
[50] C. M. Mazur, J. A. Tate, R. R. Strawbridge, D. J. Gladstone, P. J. Hoopes, *Proc. SPIE-Int. Soc. Opt. Eng.* **2013**, *26*, 1.
[51] P. Retif, S. Pinel, M. Toussaint, C. Frochot, R. Chouikrat, T. Bastogne, M. Barberi-Heyob, *Theranostics* **2015**, *5*, 1030.
[52] B. Pauwels, A. E. C. Korst, G. G. O. Pattyn, H. A. J. Lambrechts, D. R. Van Bockstaele, K. Vermeulen, M. Lenjou, C. M. J. De Pooter, J. B. Vermorken, F. Lardon, *Int. J. Radiat. Oncol. Biol. Phys.* **2003**, *57*, 1075.
[53] S. Kobashigawa, K. Morikawa, H. Mori, G. Kashino, *Anticancer Res.* **2015**, *35*, 2731.
[54] C. Le Sech, H. Frohlich, C. Saint-Marc, M. Charlier, *Radiat. Res.* **2006**, *145*, 632.
[55] M. Spotheim-Maurizot, M. Charlier, R. Sabattier, *Int. J. Radiat. Biol.* **1990**, *57*, 301.
[56] Y. A. Hiroyuki Tomita, M. Kai, T. Kusama, *J. Radiat. Res.* **1995**, *36*, 46.

Manuscript received: October 23, 2019
Revised manuscript received: November 18, 2019
Accepted manuscript online: November 25, 2019
Version of record online: December 17, 2019

CHEMMEDCHEM

Supporting Information

Highly Porous Hybrid Metal–Organic Nanoparticles Loaded with Gemcitabine Monophosphate: a Multimodal Approach to Improve Chemo- and Radiotherapy

Xue Li, Erika Porcel, Mario Menendez-Miranda, Jingwen Qiu, Xiaomin Yang, Christian Serre, Alexandra Pastor, Didier Desmaële, Sandrine Lacombe,* and Ruxandra Gref*

I.1 X-ray powder diffraction (XRPD) characterization

XRPD experiments were performed to investigate the effect of drug loading on crystalline structure of nanoMOFs. As shown in Figure S1, the XRPD patterns of Gem-MP loaded MOFs were very similar to those of empty nanoMOFs, suggesting that drug incorporation didn't affect the crystallinity of the nanoMOFs.

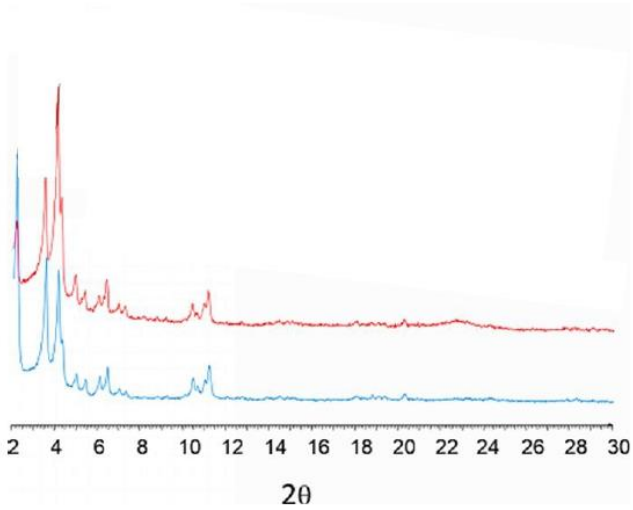

Figure S1. XRPD patterns of MIL-100(Fe) nanoMOFs before (blue) and after (red) drug encapsulation of 10wt% Gem-MP

I.2 Size characterization by NTA and DLS

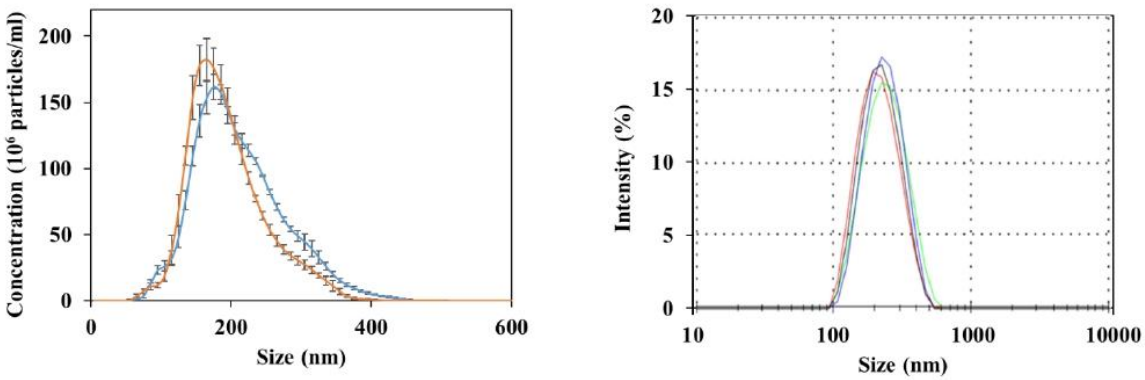

Figure S2. Size distribution of nanoMOFs characterized by NTA (left: blue: as-synthesized nanoMOFs; orange: nanoMOFs irradiated at 6.5 Gy) and DLS (right: blue: as-synthesized

nanoMOFs; red: nanoMOFs degraded in 1 mM PBS at 37°C for 12 h; green: nanoMOFs loaded with 10 wt% Gem-MP; Gray: nanoMOF irradiated at 6.5Gy)

I.3 Gem-MP release in cell culture medium

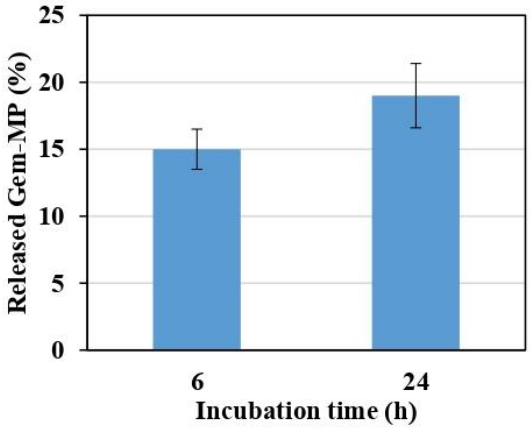

Figure S3. Gem-MP release from nanoMOFs in DMEM supplemented with 10% (v/v) FBS after incubation at 37°C for 6 h and 24 h. Drug loading was10 wt%. Non-released Gem-MP was extracted from the nanoMOFs by centrifugation (10,000 g, 15 min) and degradation of the resulting pellets in 10mM PBS for 4 h at 37°, followed by HPLC quantification.

I.4 Stability of nanoMOF and Gem-MP upon irradiation

Table S1 Stability of nanoMOF (17 µg/mL), Gem-MP (1.7µg/mL), and nanoMOF loaded with 10 wt% Gem-MP (containing 17 µg/mL nanoMOFs and 1.7 µg/mL Gem-MP) upon irradiation at doses of 4 and 6.5 Gy after incubation in DMEM supplemented with 10% (v/v) FBS at 37°C for 6 h.

Sample	Incubation (h)	Dose(Gy)	Trimesate release (%)	C(Gem-MP. µg/mL)
NanoMOF	0	0	<1	-
	6	0	<1	-
	6	4	<1	-
	6	6.5	<1	-
Gem-MP	0	0	-	1.78 ±0.09
	6	0	-	1.81 ±0.12
	6	4	-	1.74 ±0.07
	6	6.5	-	1.69 ± 0.08
Gem-MP loaded nanoMOFs	0	0	<1	< 0.5
	6	0	<1	< 0.5
	6	4	<1	< 0.5
	6	6.5	<1	< 0.5

I.5 Cytotoxic effect of nanoMOFs, Gem-MP and Gem-MP loaded nanoMOFs on Hela cells

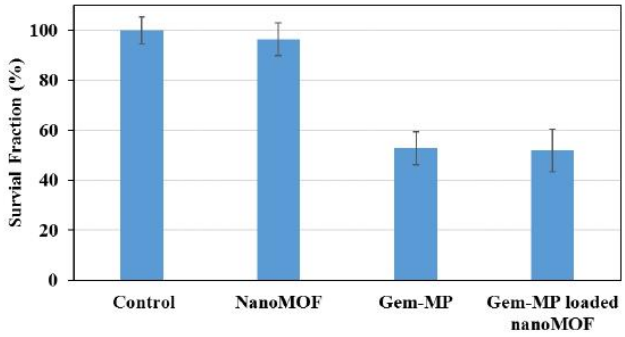

Figure S4. Cell survival of Hela cells incubated 6 h at 37°C with, respectively, nanoMOFs (17µg/mL), Gem-MP (1.7µg/mL) and nanoMOFs loaded with 10 wt% Gem-MP (17µg/mL nanoMOFs containing an equivalent amount of 1.7 µg/mL Gem-MP) . The clonogenic assay was performed by seeding 100 surviving cells, treated or not, in petri dishes for two weeks for colony formation followed by colony staining and counting. Survival fractions were calculated as the colony numbers obtained for the treated groups over the colony number observed for the control.

I.6 Synthesis of Rh-Ad for nanoMOF labeling

Rh-Ad was synthesized as shown in Figure S4. Briefly, an excess of 2,2'(ethylendioxy)bis(ethylamine) (1) was reacted with 1-adamantane acetyl chloride in methylene chloride to give the corresponding mono amide 2 in 56% yield together with some bis-amide derivative. The former compound was acylated with succinic anhydride to provide the carboxylic acid 3 in 70% yield. Amide bond formation with rhodamine piperazine (4) easily available from rhodamine B base using EDCI as coupling agent delivered the desired Rh-Ad (5) in 47% yield.

The excitation and emission wavelengths were 566 nm and 589 nm, respectively (Figure S5A). After adsorption on the surface of nanoMOFs, a blue shift of Rh-Ad emission was observed (Figure S5B).

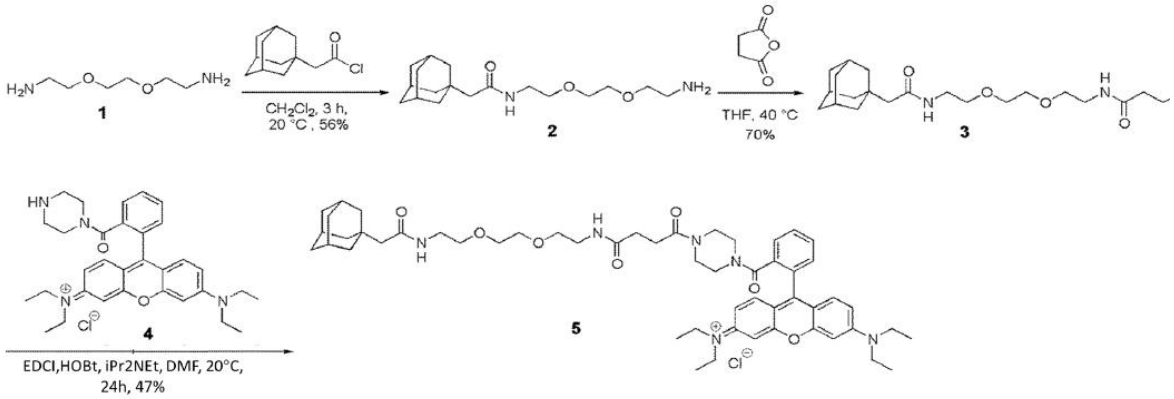

Figure S5 Synthetic route for the synthesis of Rh-Ad. 1): 2,2'(ethylendioxy)bis(ethylamine); 2): 2-(Adamantan-1-yl)-N-{2-[2-(2-aminoethoxy)ethoxy]ethyl}acetamide; 3): 3-{[2-(2-{2-[2-(Adamantan-1-yl) acetamido]ethoxy}ethoxy)ethyl]carbamoyl}propanoic acid; 4): rhodamine piperazine; 5): 9-{2-[4-(3-{[2-(2-{2-[2-(adamantan-1-yl)acetamido]ethoxy}ethoxy)ethyl]carbamoyl} propanoyl) piperazine-1-carbonyl]phenyl}-6-(diethylamino)-*N,N*-diethyl-3H-xanthen-3-iminium chloride.

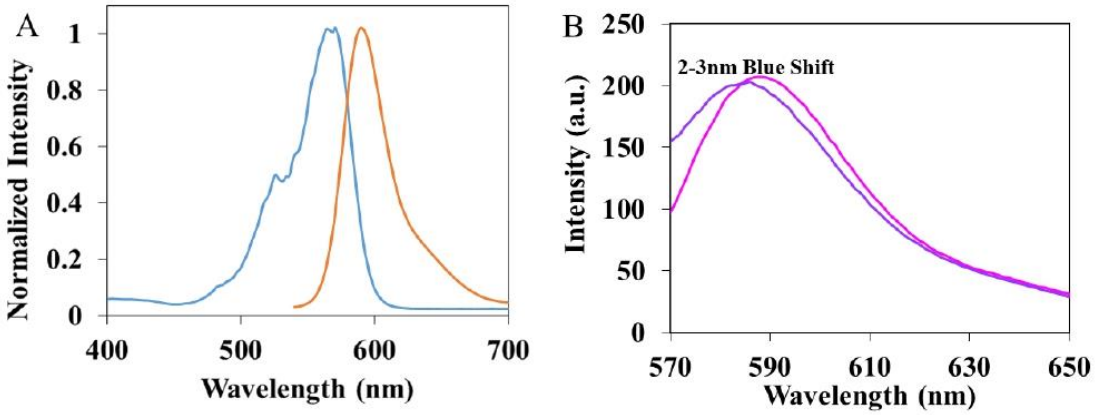

Figure S6 A. Excitation and Emission Spectra of Rh-Ad, showing Ex/Em=566nm/589nm; B. Emission spectra of free Rh-Ad (pink) and Rh-Ad labeled nanoMOFs (purple).

Annex 3: Design of Engineered Cyclodextrin Derivatives for Spontaneous Coating of Highly Porous Metal-Organic Framework Nanoparticles in Aqueous Media

nanomaterials

MDPI

Article

Design of Engineered Cyclodextrin Derivatives for Spontaneous Coating of Highly Porous Metal-Organic Framework Nanoparticles in Aqueous Media

Giovanna Cutrone [1], Xue Li [2], Juan M. Casas-Solvas [1], Mario Menendez-Miranda [2], Jingwen Qiu [2], Gábor Benkovics [3], Doru Constantin [4], Milo Malanga [3], Borja Moreira-Alvarez [5], José M. Costa-Fernandez [5], Luis García-Fuentes [1], Ruxandra Gref [2,*] and Antonio Vargas-Berenguel [1,*]

1 Department of Chemistry and Physics, University of Almería, Crta. de Sacramento s/n, E-04120 Almería, Spain
2 Institut des Sciences Moléculaires d'Orsay, UMR CNRS 8214, Université Paris-Sud, Université Paris Saclay, 91400 Orsay, France
3 CycloLab R&D Ltd., Illatos út 7, H-1097 Budapest, Hungary
4 Laboratoire de Physique des Solides, UMR 8502, Université Paris-Sud, 91405 Orsay, France
5 Department of Physical and Analytical Chemistry, University of Oviedo, Julián Clavería 8, 33006 Oviedo, Spain
* Correspondence: ruxandra.gref@u-psud.fr (R.G.); avargas@ual.es (A.V.-B.)

Received: 23 July 2019; Accepted: 30 July 2019; Published: 1 August 2019

Abstract: Nanosized metal-organic frameworks (nanoMOFs) MIL-100(Fe) are highly porous and biodegradable materials that have emerged as promising drug nanocarriers. A challenging issue concerns their surface functionalization in order to evade the immune system and to provide molecular recognition ability, so that they can be used for specific targeting. A convenient method for their coating with tetraethylene glycol, polyethylene glycol, and mannose residues is reported herein. The method consists of the organic solvent-free self-assembly on the nanoMOFs of building blocks based on β-cyclodextrin facially derivatized with the referred functional moieties, and multiple phosphate groups to anchor to the nanoparticles' surface. The coating of nanoMOFs with cyclodextrin phosphate without further functional groups led to a significant decrease of macrophage uptake, slightly improved by polyethylene glycol or mannose-containing cyclodextrin phosphate coating. More notably, nanoMOFs modified with tetraethylene glycol-containing cyclodextrin phosphate displayed the most efficient "stealth" effect. Mannose-coated nanoMOFs displayed a remarkably enhanced binding affinity towards a specific mannose receptor, such as Concanavalin A, due to the multivalent display of the monosaccharide, as well as reduced macrophage internalization. Coating with tetraethylente glycol of nanoMOFs after loading with doxorubicin is also described. Therefore, phosphorylated cyclodextrins offer a versatile platform to coat nanoMOFs in an organic solvent-free, one step manner, providing them with new biorecognition and/or "stealth" properties.

Keywords: metal-organic frameworks; MIL-100(Fe); β-cyclodextrin; mannose; molecular recognition; "stealth" effect; multivalent effect; isothermal titration calorimetry; macrophage

1. Introduction

Metal-organic frameworks (MOFs) are currently among the most versatile materials, with crystalline porous structures built using organic linkers and metal cations. Since they were discovered [1], their applications were focused on biosensing, gas storage, separation, heterogeneous catalysis, and imaging [2–8]. More recently, their innovative biomedical applications as potential drug

delivery nanocarriers are gaining increasing interest for the treatment of a variety of diseases [9–12]. These materials allow tuning pore sizes and shapes by varying both metal cations and organic linkers, and thus drug interactions with the matrix can be optimized [13]. The opportunity to confer ad hoc chemical and structural features in addition to the peculiar properties of the internal porous volume make MOFs promising drug delivery systems (DDS) for a large variety of guest molecules [14].

Among the large MOFs family, nanosized metal-organic frameworks MIL-100(Fe) (MIL standing for materials of Institute Lavoisier) are a biodegradable material easily synthesized by a "green" microwave assisted hydrothermal method, made of spontaneous coordination between iron(III) cations and trimesate linkers (1,3,5-benzene tricarboxylate) generating a porous architecture. The structure is accessible through mesoporous windows of two different sizes (5.6 and 8.6 Å), and forms internal cages of 24 and 29 Å available for drug incorporation [15]. MIL-100(Fe) nanoMOFs could entrap a wide range of therapeutic molecules providing high loadings up to 20–70 wt% [9], and were well tolerated in vivo in rats since doses up to 220 mg Kg^{-1} did not trigger any toxicity signs up to one week after injection [11,12,16]. Although iron concentration increased in both liver and spleen upon administration, levels remained far from those able to cause liver malfunction, and iron excess was excreted by urine and feces after 15 days [16]. However, appropriate coating of the nanoMOF surface is desirable for several reasons: (i) An adequate coating may overcome nanoMOFs' tendency to aggregate in aqueous media thus providing colloidal stability to the system; (ii) it could control and modulate drug release; and (iii) it could confer the nanoMOFs with biorecognition and targeting abilities to reach their biological targets through recognition of specific receptors. In order to achieve these goals, one strategy is to employ a noncovalent coating using saccharide derivatives that are large enough to avoid penetration within the nanoMOF's pores while conferring colloidal stability and modulated drug release. Recently, we have reported a postsynthetic strategy using phosphorylated β-cyclodextrin (β-CD) building-blocks for the preparation of a biocompatible nanoMOFs system [15,17]. Noncovalent coatings were developed by attaching phosphate groups to the macrocycle that subsequently bind the metallic sites on the nanoparticle surface. Advantageously, the procedure was carried out directly in water in one step without using any toxic additives and led to coatings stable enough under physiological conditions. β-CD was chosen because its dimensions are, as needed, large enough to avoid penetration within the MIL-100(Fe) nanoMOFs pores [18], and their numerous free OH are very suitable for introducing functional groups in the primary or/and secondary rims. In addition, β-CD coatings were able to improve suspension stability and could be further functionalized with fluorescent dyes.

Additionally, application of nanoparticles in biological media is strongly affected by their interaction with proteins from the medium. When nanoparticles are exposed to a biological environment, a fast adsorption of proteins onto their surfaces takes place, thus forming a NP-protein complex corona. This so-called "protein corona" modifies the nanoparticles "identity" and triggers various biological processes towards the nanoparticles including blood clearance and immunity response [19]. A potential drug nanocarrier must avoid rapid clearance during the circulation time and should prevent fast cellular uptake. In this regard, long chain polyethylene glycol (PEG) shells are used as a molecular barrier that shields nanoparticles against protein adsorption and fast recognition by the immune system, as it is proved that PEG has one of the lowest levels of protein absorption among all known polymers [20]. Such PEG brushes confer "stealth" properties to the drug delivery systems and lead to a decrease in cellular uptake. However, whereas PEG surface modification has been widely documented in the case of liposomes and polymeric nanoparticles, only a few attempts have been made so far to modify MIL-100(Fe) nanoMOFs with PEG [15,21].

A challenging issue concerning the development of MOF-based nanocarriers is their surface functionalization with molecular recognition properties, so they can be used for specific targeting. In this regard, biomolecules involved in biological recognition processes such as carbohydrates present several advantages over other biomolecules [22,23]. In addition to contributing to the nanoparticle biocompatibility and stability in aqueous media preventing aggregation, they are available on a large

scale and relatively easy to chemically modify. Furthermore, they have been proven to provide "stealth" properties comparable to those conferred by PEGylation, while barely affecting the molecular recognition properties [24,25]. However, the interaction between carbohydrates and their specific protein receptors, called lectins, are typically very weak when compared with other biological binding events [26]. Nature uses a well-known strategy, named multivalent effect, to increase this low affinity by gathering multiple copies of sugars to achieve a global binding potency toward their receptors higher than that for the sum of the monovalent interactions [27]. Inspired by this natural approach, a vast number of structures decorated with multiple carbohydrate moieties have been tested as potential theranostic agents in biosensing and biomedicine [22,28,29].

Lectins are overexpressed in some tumor cells [30,31]. Thus, decorating nanoparticles of different types with carbohydrates is an efficient approach to increase the local concentration of anticancer drugs near tumor cells, facilitating specific cellular uptake through the specific binding between the carbohydrate ligand and the overexpressed specific lectin [32,33]. Among this family of proteins, mannose-binding lectins (MBLs) are overexpressed by many human cancer cells and may be used as therapeutic targets [30]. Mannose has been used to target cells of the immune system such as macrophages, dendritic cells, or Langerhans cells, as well as pathogenic microorganisms [34–36] and cancer cells including retina, breast, and prostate, due to its high specificity to lectin receptors [37–39]. Moreover, it has been recently reported that PEGylated silicon nanoparticles (SiNPs) anchored with mannose had a better "stealth" effect compared to PEGylated SiNPs in vivo [24]. Furthermore, hydroxyethyl starch nanocarriers PEGylated and mannose-functionalized on the outer PEG layer not only showed an efficient "stealth" effect, but also that the targeting moieties were accessible to the biological receptors [25]. However, to the best of our knowledge, only a few examples of nanoMOFs functionalized with mannose have previously been reported by some of us [15,17].

In this context, we describe a convenient preparation of tetraethylene glycol (TEG)-, PEG-, and mannose-surface functionalized MIL-100(Fe) nanoMOFs. The preparation involved, first, the synthesis of a series of phosphorylated β-CD scaffolds displaying motifs of mannose and/or TEG or PEG (average MW ~2000) as coating building blocks, followed by a postsynthetic modification of MIL-100(Fe) nanoMOFs by spontaneous self-assembly of the building blocks on their surfaces. We compare the "stealthy" capacity of the surface-modified nanoMOFs to reduce the cellular uptake and to enhance the retention time, avoiding capture by phagocytic cells. Mannosylated nanoparticles exhibit enhanced binding affinity towards a model mannose-specific lectin concanavalin A (ConA) due to the globular multivalent display of the mannose moieties on their surface, much like the glycocalyx [40]. Moreover, we demonstrate that the coating method can be applied to drug-loaded MIL-100(Fe) nanoMOFs, using anticancer drug doxorubicin (DOX).

2. Materials and Methods

2.1. Materials

Thin layer chromatography (TLC) was performed on Merck silica gel 60 F_{254} aluminum sheets and developed by UV–vis light, iodine, 5% *v/v* sulfuric acid in ethanol, and/or 1% *w/v* potassium permanganate in aqueous solution containing 0.1% *w/v* sodium hydroxide and 7% *w/v* potassium carbonate, depending on the case. Flash column chromatography was performed on Merck silica gel (230–400 mesh, ASTM). Melting points were measured on a Büchi B-450 melting point apparatus and are uncorrected. Optical rotations were recorded on a Jasco P-1030 polarimeter at room temperature. $[\alpha]_D^{25}$ values are given in 10^{-1} deg cm^{-1} g^{-1}. Infrared spectra were recorded on a Bruker Alpha FTIR equipped with a Bruker universal ATR sampling accessory. ^1H, ^{13}C, and 2D NMR spectra were recorded on a Bruker Avance III HD 600 MHz spectrometer equipped with a QCI $^1H/^{13}C/^{15}N/^{31}P$ proton-optimized quadrupole inverse cryoprobe with ^1H and ^{13}C cryochannels, a Bruker Avance III HD 500 MHz spectrometer equipped with an inverse TBI $^1H/^{31}P$/BB probe, or a Bruker Nanobay Avance III HD 300 MHz spectrometer equipped with a QNP $^1H/^{13}C/^{19}F/^{31}P$ probe, depending on the

sample. Standard Bruker software was used for acquisition and processing routines. Chemical shifts (δ) are given in parts per million (ppm) and referenced to internal tetramethylsilane (TMS) signal (δ_H, δ_C 0.00). *J* values are given in hertz (Hz). MALDI-TOF mass spectra were recorded on a 4800 Plus AB SCIEX spectrometer with 2,5-dihydroxybenzoic acid (DHB) as the matrix. ESI-TOF mass spectra were measured on an Agilent LC/MSD-TOF spectrometer. Syringe filtering was conducted using nylon 0.45 μm Milipore Millex® syringe-driven filter units. Dialysis was performed using Thermo Scientific™ Slide-A-Lyzer™ G2 2000 MWCO Dialysis Cassette. A Hanna HI 98192 EC/TDS/NaCl/Resistivity meter was employed to monitor dialysate solutions conductivity during dialysis. Transmission electron microscope (TEM) images were acquired on a JEOL 1400 microscope working at 120 kV. Dynamic light scattering (DLS) measurements were performed on a Malvern Zetasizer Nano-ZS analyzer. Nitrogen sorption experiments were conducted on a Micromeritics ASAP 2020 equipment. Inductively coupled plasma mass spectrometry (ICP-MS) analysis was performed on an Agilent 8800 instrument equipped with a triple quadrupole. Isothermal titration calorimetry (ITC) experiments were conducted on an ultrasensitive Microcal VP-ITC calorimeter.

Acetic anhydride (Panreac, purum), per(6-azido-6-deoxy)-β-CD **1** (CycloLab L&D Ltd., Budapest, Hungary), copper(I) bromide (Sigma-Aldrich, St. Louis, MI, USA, ≥99.9%), copper(I) iodide (Aldrich, 98%), anhydrous copper(II) sulphate (Fluka, 98%), (+)-sodium L-ascorbate (NaAsc, Sigma, BioXtra, ≥99%), phosphorus pentoxide (Panreac, purum), 1-methoxypentatetraconta(ethyle- ne glycol) (Aldrich, M_n ~2000), 4-dimethylaminopyridine (DMAP, Fluka, ≥98%), methanesulfonyl chloride (Fluka, ≥99%), *tert*-butyldimethylsilyl chloride (Sigma-Aldrich, Steinheim, Germany, 97%), doxorubicin (DOX, Sigma-Aldrich, St. Louis, MI, USA, 98%), and β-CD phosphate sodium salt (CD-P, Cyclolab L&D Ltd., Budapest, Hugary, DS 2–6), were purchased from commercial sources and used without further purification unless otherwise indicated. β-CD (CycloLab L&D Ltd., Budapest, Hungary) was dried at 50 °C in vacuum in the presence of P_2O_5 until it reached a constant weight before using. Propargyl 2,3,4,6-tetra-*O*-acetyl-α-D-mannopyranoside **2** was prepared as described in literature [41,42] with small modifications. Specifically, purification of the compound after deacetylation was carried out by flash column chromatography using EtOAc-MeOH 6:1 as eluent. NMR data for this compound in D_2O completely agreed with that described by van der Peet et al. [43]. 1-Propargyloxy-3,6,9-trioxa-undecane-11-ol [44,45], 3,6,9,12-tetraoxapentadec-14-ynyl 2,3,4,6-tetra-*O*-acetyl-α-D-mannopyranoside **4** [46], heptakis(6-*O*-*tert*-butyldimethylsilyl-2,3-di-*O*-propargyl)cyclomaltoheptaose **12** [47], and heptakis(2,3-di-*O*-propargyl)cyclomaltoheptaose **13** [47] were prepared as described in literature. Pyridine (Panreac, purum), trimethylamine (Sigma-Aldrich, ≥99%), and organic solvents were dried according to literature procedures [48]. Dry DMF (AcroSeal, 99.8%, over molecular sieves) was purchased from Acros.

Iron (III) chloride hexahydrate (Alfa Aesar, 98%), 1,3,5-benzenetricarboxylic acid (BTC, Sigma-Aldrich, St. Louis, MI, USA, 95%), and absolute ethanol (Carlo Erba, 99%,) were used for the synthesis of nanoMOFs. CD-P was used for the coating of nanoMOFs along with the synthesized CD phosphate salt derivatives **8**–**10** and **16**. Dulbecco's PBS solution was used for nanoMOFs Zeta potential (ZP) measurements. Stability studies were performed in a complete cell culture medium (DMEM, in Dulbecco's Modified Eagle's Medium (Thermo Fischer, Waltham, MA, USA) complemented with 10% FBS, 1% penicillin/streptomycin (100 mg/mL), and 1% L-glutamine). Deionized MilliQ water was obtained from a Millipore apparatus with a 0.22 μm filter.

*2.2. Synthesis of 1-O-propargyl-13-O-acetyl-1,4,7,10,13-pentaoxatridecane (**3**)*

Acetic anhydride (3 mL, 0.032 mol) was added at 0 °C to a solution of 1-propargyloxy-3,6,9-trioxa-undecane-11-ol (1.228 g, 5.287 mmol) in dry pyridine (6 mL, 0.074 mol) and left at room temperature overnight. Solvent was rotary evaporated under high vacuum and the crude was purified by flash column chromatography using 2:3→1:2 Hexane-EtOAc as eluent to give compound **3** (1.370 g, 4.994 mmol, 94%) as a colorless oil. R_f = 0.6 (1:2 Hexane-EtOAc); IR ν/cm^{-1} 2872, 2116, 1733, 1238, 1095, 1049, 955, 919, 729; ^{1}H-NMR (500 MHz, $CDCl_3$), δ (ppm): 4.23–4.21 (m, 2H, H-12), 4.20 (d, 2H,

J = 2.4 Hz, $OCH_2C{\equiv}$), 3.71–3.68 (m, 6H, H-2,3,11), 3.67 (s, 4H, OCH_2CH_2O), 3.66 (s, 4H, OCH_2CH_2O), 2.43 (t, 1H, J = 2.4 Hz, ≡CH), 2.08 (s, 3H, CH_3); ^{13}C-RMN (125 MHz, $CDCl_3$), δ (ppm): 171.1 (CO), 79.7 (C≡), 74.6 (≡CH), 70.7–70.5 (C-3,5,6,8,9), 69.2–69.1 (C-2,11), 63.7 (C-12), 58.5 ($OCH_2C{\equiv}$), 21.0 (CH_3); ESI-TOF-MS m/z calcd. for $C_{13}H_{26}NO_6$ 292.1756, found 292.1755 $(M + NH_4)^+$; calcd. for $C_{13}H_{22}NaO_6$ 297.1309, found 297.1309 $(M + Na)^+$.

*2.3. Synthesis of Heptakis{6-deoxy-6-[4′-(2″,3″,4″,6″-tetra-*O*-acetyl-α-*D*-mannopyranosyloxymethyl)-1*H*-1,2,3-triazol-1′-yl]}cyclomaltoheptaose (**5**)*

A suspension of CuBr (426 mg, 2.97 mmol) in H_2O (45 mL) was added to a preheated (100 °C) solution of per(6-azido-6-deoxy)-β-CD **1** (200 mg, 0.142 mmol) and propargyl 2,3,4,6-tetra-*O*-acetyl-α-D-mannopyranose **2** (47 mg, 0.213 mmol) in DMF (15 mL). The mixture was stirred for 1 h at 100 °C. The solvent was evaporated under high vacuum and the residue was purified by a flash column chromatography using 10:1→5:1 CH_3CN-H_2O. Subsequently, the product was passed through a short pad of silica gel using 10:2:1 CH_3CN-H_2O-(30% *v*/*v* aq. NH_3) as eluent. The collected fractions were rapidly neutralized to pH ~7.0 by addition of 1 N HCl and extracted with CH_2Cl_2 (100 mL) to prevent deacetylation. The organic layer was washed with H_2O (2 × 100 mL), dried on Na_2SO_4, and evaporated to yield compound **5** (2.6 g, 0.655 mmol, 86%) as a pale yellow solid: R_f = 0.2 [25:1:5 CH_3CN-H_2O-(30% *v*/*v* aq. NH_3)]; mp 96 °C; $[\alpha]_D^{25}$ +70° (*c* 0.5, CH_2Cl_2); IR ν/cm^{-1} 3418, 2934, 1748, 1372, 1230, 1048; ^{1}H-NMR (500 MHz, DMSO-d_6, 80 °C), δ (ppm): 7.96 (s, 7H, H-5′), 5.66–5.65 (m, 14H, OH), 5.13–5.10 (m, 21H, H-1,3″,4″), 5.06 (dd, 7H, $^3J_{1″,2″}$ = 1.6 Hz, $^3J_{2″,3″}$ = 3.0 Hz, H-2″), 4.91 (d, 7H, $^3J_{1″,2″}$ = 1.6, H-1″), 4.65 (d, 7H, ^2J = 12.4 Hz, OCH^a-C_2HN_3), 4.57 (dd, 7H, $^2J_{6a,6b}$ = 14.1 Hz, $^3J_{5,6a}$ = 2.5 Hz, H-6^a), 4.48 (d, 7H, ^2J = 12.4 Hz, OCH^b-C_2HN_3), 4.46 (dd, 7H, $^2J_{6a,6b}$ = 14.1 Hz, $^3J_{5,6b}$ = 4.8 Hz, H-6^b), 4.16 (dd, $^2J_{6″a,6″b}$ = 12.2 Hz, $^3J_{5″,6″a}$ = 5.1 Hz, H-6″^{a}), 4.13 (m, 7H, H-5), 4.07 (dd, 7H, $^2J_{6″a,6″b}$ = 12.2 Hz, $^3J_{5″,6″b}$ = 2.8 Hz, H-6″^{b}), 3.99 (ddd, 7H, $^3J_{4″,5″}$ = 9.7 Hz, $^3J_{5″,6″a}$ = 5.1 Hz, $^3J_{5″,6″b}$ = 2.8 Hz, H-5″), 3.76 (td, 7H, ^3J = 9.5 Hz, ^3J = 2.3 Hz, H-3), 3.33–3.29 (m, 7H, H-2), 3.26 (t, 7H, J = 9.2 Hz, H-4), 2.07 (s, 21H, CH_3), 2.01 (s, 21H, CH_3), 1.99 (s, 21H, CH_3), 1.89 (s, 21H, CH_3); ^{13}C-NMR (125 MHz, DMSO-d_6, 80 °C), δ (ppm): 169.4, 168.9, 168.8, 168.7 (CO), 141.9 (C-4′), 125.7 (C-5′), 101.4 (C-1), 95.7 (C-1″), 82.2 (C-4), 72.0 (C-3), 71.6 (C-2), 69.1 (C-5), 68.5 (C-3″), 68.4 (C-2″), 67.8 (C-5″), 65.5 (C-4″), 61.6 (C-6″), 59.5 (OCH_2-C_2HN_3), 49.1 (C-6), 19.9, 19.8, 19.7, 19.6 (CH_3). MALDI-TOF-MS m/z calcd. for $C_{161}H_{217}N_{21}O_{98}Na^+$ 4035.3, found 4035.9 $(M+Na)^+$.

*2.4. Synthesis of Heptakis(6-deoxy-6-{4′-[14″-*O*-acetyl-(2″,5″,8″,11″,14″-pentaoxatetradecyl)]-1*H*-1,2,3-triazol-1′-yl})cyclomaltoheptose (**6**)*

A suspension of CuI (300 mg, 1.58 mmol) in H_2O (30 mL) was added to a preheated (100 °C) solution of per(6-azido-6-deoxy)-β-CD **1** (413 mg, 0.32 mmol) and 1-*O*-propargyl-13-*O*-acetyl-1,4,7,10,13-pentaoxatridecane **3** (1.73 g, 6.3 mmol) in DMF (30 mL). The mixture was stirred for 6 h at 100 °C. The reaction was followed by TLC using 5:1 1,4-dioxane-(30% *v*/*v* aq. NH_3) as eluent until only one spot at R_f = 0.4 was observed. The solvent was evaporated under high vacuum and the residue was purified by a flash column chromatography using 10:1:2 CH_3CN-H_2O-(30% *v*/*v* aq. NH_3) as eluent. The collected fractions were rapidly neutralized to pH ~7.0 by addition of 1 N HCl and extracted with CH_2Cl_2 (3 × 100 mL) to prevent deacetylation. The organic layer was washed with H_2O (1 × 50 mL), dried on $MgSO_4$, filtered, and rotary evaporated to yield compound **6** (418 mg, 0.129 mmol, 41%) as a sticky pale yellow solid: R_f = 0.4 [5:1 1,4-dioxane-(30% *v*/*v* aq. NH_3)]; $[\alpha]_D^{25}$ +8° (*c* 0.25, CH_2Cl_2); IR ν/cm^{-1} 3354, 2873, 1734, 1237, 1091, 1045; ^{1}H-NMR (500 MHz, DMSO-d_6, 80 °C), δ (ppm): 7.86 (s, 7H, H-5′), 5.64 (bs, 14H, OH-2,3), 5.08 (d, 7H, $^3J_{1,2}$ = 3.2 Hz, H-1), 4.45 (dd, 7H, $^2J_{6a,6b}$ = 14.5 Hz, $^3J_{5,6a}$ = 2.6 Hz, H-6^a), 4.40 (d, 7H, ^2J = 12.4 Hz, H-1″^{a}), 4.34 (d, 7H, ^2J = 12.4 Hz, H-1″^{b}), 4.32 (dd, 7H, $^2J_{6a,6b}$ = 14.5 Hz, $^3J_{5,6b}$ = 7.9 Hz, H-6^b), 4.11 (t, 14H, J = 5.0 Hz, H-13″), 4.10–4.07 (m, 7H, H-5), 3.75 (t, 7H, J = 9.2 Hz, H-3), 3.60 (t, 14H, J = 5.0 Hz, H-12″), 3.55–3.49 (m, 84H, H-2″,3″,6″,7″,9″,10″), 3.31 (dd, 7H, $^3J_{2,3}$ = 9.6 Hz, $^3J_{1,2}$ = 3.2 Hz, H-2), 3.28 (t, 7H, J = 9.4 Hz, H-4), 2.00 (s, 21H, CH_3); ^{13}C-NMR (125 MHz, DMSO-d_6, 80 °C), δ (ppm): 169.6 (CO), 143.4 (C-4′), 124.6 (C-5′), 101.3 (C-1), 82.4 (C-4), 72.0

(C-3), 71.6 (C-2), 69.4–69.2 (C-2″,3″,6″,7″,9″,10″), 68.7 (C-5), 67.9 (C-12″), 63.1 (C-1″), 62.6 (C-13″), 49.1 (C-6), 20.0 (CH_3); MALDI-TOF-MS *m*/*z* calcd. for $C_{133}H_{217}N_{21}O_{89}Na^+$ 3252.4, found 3252.7 $(M + Na)^+$.

*2.5. Synthesis of Heptakis(6-deoxy-6-{4′-[14″-O-(2‴,3‴,4‴,6‴-tetra-O-acetyl-α-D-mannopyranosyl)-2″,5″,8″,11″,14″-pentaoxatetradecyl]-1H-1,2,3-triazol-1′-yl})cyclomaltoheptose (**7**)*

A suspension of $CuSO_4$ (164 mg, 1.02 mmol) and sodium ascorbate (220 mg, 1.11 mmol) in H_2O (12 mL) was added to a preheated (65 °C) solution of per(6-azido-6-deoxy)-β-CD **1** (362 mg, 0.28 mmol) and compound **4** (1.4 g, 2.5 mmol) in DMF (25 mL). The mixture was stirred for 3 h at 100 °C. The reaction was followed by TLC using 5:1 1,4-dioxane-(30% *v*/*v* aq. NH_3) as eluent. The solvent was evaporated under high vacuum and the residue passed through a short pad of silica gel using 20:6:1 CH_3CN-H_2O-(30% *v*/*v* aq. NH_3) as eluent. The solution was freeze-dried and the resulting material was further purified by a flash column chromatography using 2:2:1:0→20:20:10:1 CH_2Cl_2-CH_3CN-EtOH-H_2O as eluent to yield compound **7** (860 mg, 0.164 mmol, 60%) as a sticky pale yellow solid after freeze-drying: R_f = 0.4 (5:1 1,4-dioxane-(30% *v*/*v* aq. NH_3)); $[\alpha]_D^{25}$ +27° (*c* 0.5, CH_2Cl_2); IR ν/cm^{-1} 2877, 1743, 1369, 1220, 1077, 1042, 732; ^{1}H-NMR (500 MHz, DMSO-d_6, 80 °C), δ (ppm): 7.86 (s, 7H, H-5′), 5.65–5.64 (m, 14H, OH-2,3), 5.17 (dd, 7H, $^3J_{3‴,4‴}$ = 10.1 Hz, $^3J_{2‴,3‴}$ = 3.3 Hz, H-3‴), 5.12 (dd, 7H, $^3J_{2‴,3‴}$ = 3.3 Hz, $^3J_{1‴,2‴}$ = 1.4 Hz, H-2‴), 5.11 (t, 7H, *J* = 9.8 Hz, H-4‴), 5.09 (d, 7H, $^3J_{1,2}$ = 3.2 Hz, H-1), 4.90 (d, 7H, $^3J_{1‴,2‴}$ = 1.4 Hz, H-1‴), 4.47 (dd, 7H, $^2J_{6a,6b}$ = 14.7 Hz, $^3J_{5,6a}$ = 2.7 Hz, H-6^a), 4.40 (d, 7H, $^2J_{1″a,1″b}$ = 12.4 Hz, H-1″^{a}), 4.35 (bd, 7H, *J* = 14.1 Hz, H-6^b), 4.34 (d, 7H, $^2J_{1″a,1″b}$ = 12.4 Hz, H-1″^{b}), 4.15 (dd, 7H, $^2J_{6‴a,6‴b}$ = 12.2 Hz, $^3J_{5‴,6‴a′}$ = 5.2 Hz, H-6‴^{a}), 4.11–4.09 (m, 7H, H-5), 4.08 (dd, 7H, $^2J_{6‴a,6‴b}$ = 12.2 Hz, $^3J_{5‴,6‴b}$ = 2.9 Hz, H-6‴^{b}), 4.01 (ddd, 7H, $^3J_{4‴,5‴}$ = 9.6 Hz, $^3J_{5‴,6‴a}$ = 5.2 Hz, $^3J_{5‴,6‴b}$ = 2.0 Hz, H-5‴), 3.77–3.75 (m, 7H, H-3), 3.74 (t, 7H, *J* = 4.5 Hz, H-13″^{a}), 3.66 (dd, 7H, ^2J = 9.6 Hz, ^3J = 5.1 Hz, H-13″^{b}), 3.62 (dd, 14H, *J* = 9.6 Hz, *J* = 5.0 Hz, H-12″), 3.57–3.48 (m, 84H, H-3″,4″,6″,7″,9″11″), 3.34–3.29 (m, 7H, H-2), 3.27 (t, 7H, *J* = 9.4 Hz, H-4), 2.10 (s, 21H, CH_3), 2.01 (s, 21H, CH_3), 2.00 (s, 21H, CH_3), 1.93 (s, 21H, CH_3); ^{13}C-NMR (125 MHz, DMSO-d_6, 80 °C), δ (ppm): 169.3 (CO), 168.9 (CO), 168.8 (CO), 167.8 (CO), 143.4 (C-4′), 124.7 (C-5′), 101.3 (C-1), 96.5 (C-1‴), 82.4 (C-4), 72.0 (C-3), 71.6 (C-2), 69.5–69.4 (OCH_2CH_2O), 69.3 (C-5), 68.9 (C-12″), 68.7 (OCH_2CH_2O), 68.6 (C-2‴), 68.4 (C-3‴), 67.7 (C-5‴), 66.4 (C-13″), 65.6 (C-4‴), 63.1 (C-1″), 61.8 (C-6‴), 49.1 (C-6), 19.9 (CH_3), 19.8 (CH_3), 19.7 (CH_3), 19.6 (CH_3); MALDI-TOF-MS *m*/*z* calcd. for $C_{217}H_{329}N_{21}O_{126}$ 5245.00, found 5245.7 $(M)^+$; calcd. for $C_{217}H_{329}N_{21}O_{126}Na^+$ 5268.0, found 5267.6 $(M + Na)^+$.

*2.6. Synthesis of Heptakis{6-deoxy-6-[4′-(α-D-mannopyranosyloxymethyl)-1H-1,2,3-triazol-1′-yl]}cyclomaltoheptaose Phosphate Sodium Salt (**8**)*

P_2O_5 (2.7 g, 19 mmol) was suspended in dry DMF (40 mL) and sonicated for 30 min, then compound **5** (1.25 g, 0.311 mmol) was added and the mixture was stirred at 40 °C until no starting material was detectable (after 4 h) by TLC [2:1:2 CH_3CN-H_2O-(30% *v*/*v* aq. NH_3)]. The mixture was then stirred for 12 h at room temperature at pH 11–13, which was maintained by addition of 1 M aqueous NaOH as needed. The solution was then neutralized with 5% aqueous HCl and the solvent was rotary evaporated under high vacuum. The residue was dissolved in the minimum amount of H_2O, syringe filtered (nylon 0.45 μm), and dialyzed (2000 MWCO) against distilled water by changing dialysate solution every 3 h until its conductivity was stable and below 1 μS/cm (5 days for final value of 0.96 μS/cm) to yield **8** (1.3 g) as a white solid after lyophilization: mp 250 °C (dec); IR ν/cm^{-1} 3420, 2933, 2790, 1645, 1255, 1126, 1052, 977, 889, 537; ^{1}H-NMR (600 MHz, D_2O), δ (ppm): 8.12 (bs, H-5′), 5.32–5.21, 4.8–4.11 (overlapped with HDO), 3.83–3.52; ^{13}C-NMR (150 MHz, D_2O), δ (ppm): 143.4 (C-4′), 126.9 (C-5′), 99.3 (C-1″), 72.9, 72.0, 70.4, 69.8, 66.6, 60.8 (C-6″), 59.5 (OCH_2-C_2HN_3), 50.5 (C-6); ^{13}P-RMN (242.9 MHz, D_2O), δ (ppm): 0.71 (orthophosphates), −8.38 (pyrophosphates), −21.51–(−23.65) (polyphosphates); HR-ICP-MS: P 16.3%.

*2.7. Synthesis of Heptakis{6-deoxy-6-[4′-(13″-hydroxy-2″,5″,8″,11″-tetraoxatridecyl)-1*H*-1,2,3-triazol-1′-yl]}cyclomaltoheptose Phosphate Sodium Salt (***9***)*

P_2O_5 (2.067 g, 14.560 mmol) was suspended in dry DMF (13 mL) and sonicated for 30 min, then compound **6** (847 mg, 0.260 mmol) was added and the mixture was stirred at 40 °C until no starting material was observed (after 4 h) by TLC [5:1 1,4-dioxane-(30% *v*/*v* aq. NH_3)]. The mixture was then stirred for 12 h at room temperature at pH 11–13, which was maintained by addition of 1 M aqueous NaOH as needed. The solution was then neutralized with 5% aqueous HCl and the solvent rotary evaporated under high vacuum. The residue was dissolved in the minimum amount of H_2O, syringe filtered (nylon 0.45 μm), and dialyzed (2000 MWCO) against distilled water by changing dialysate solution every 3 h until its conductivity was stable and below 1 μS/cm (5 days for final value of 0.90 μS/cm) to yield **9** (669 mg) as a white solid after lyophilization: mp 160 °C; IR ν/cm^{-1} 3432, 2922, 2877, 1640, 1267, 1090, 946, 522; ^{1}H-NMR (600 MHz, D_2O), δ (ppm): 7.94 (bs, H-5′), 5.11 (bs, H-1), 4.66–3.96 (m, H-1″,3,5,6^{a,b}), 3.55–3.46 (m, H-2,3″,4,4″,6″,7″.9″,10″,11″,12″); ^{13}C-NMR (150 MHz, D_2O), δ (ppm): 143.8 (C-4′), 126.8 (C-5′), 99.7 (C-1), 81.7, 79.1, 75.7–73.9, 71.7 (OCH_2CH_2O), 70.2, 69.5–69.0 (OCH_2CH_2O), 63.0 (C-1″), 60.3 (C-13″), 50.4 (C-6); ^{13}P-RMN (242.9 MHz, D_2O), δ (ppm): 0.20 (orthophosphates), −9.69 (pyrophosphates), −21.57–(−23.65) (polyphosphates); HR-ICP-MS: P 15.7%.

*2.8. Synthesis of Heptakis{6-desoxi-6-{4′-[14″-*O*-(α-*D*-mannopyranosyl)-2″,5″,8″,11″,14″-pentaoxatetradecyl]-1*H*-1,2,3-triazol-1′-yl}}ciclomaltoheptose Phosphate Sodium Salt (***10***)*

P_2O_5 (510 mg, 3.6 mmol) was suspended in dry DMF (13 mL) and sonicated for 30 min, then compound **7** (356 mg, 0.068 mmol) was added and the mixture was stirred at 40 °C until no starting material was observed (after 5 h) by TLC [5:1 1,4-dioxane-(30% *v*/*v* aq. NH_3)]. The mixture was then stirred for 12 h at room temperature at pH 11–13, which was maintained by addition of 1 M aqueous NaOH as needed. The solution was then neutralized with 5% aqueous HCl and the solvent rotary evaporated under high vacuum. The residue was dissolved in the minimum amount of H_2O, syringe filtered (nylon 0.45 μm), and dialyzed (2000 MWCO) against distilled water by changing dialysate solution every 3 h until its conductivity was stable and below 1 μS/cm (5 days for final value of 0.98 μS/cm) to yield **10** (806 mg) as a white solid after lyophilization: mp 110 °C; IR ν/cm^{-1} 3431, 2923, 1643, 1271, 1092, 1030, 975, 529; ^{1}H-NMR (600 MHz, D_2O), δ (ppm): 8.07 (bs, H-5′), 5.23–5.16, 4.55–4.10 (overlapped with HDO), 3.97, 3.88–3.82, 3.78–3.75, 3.72–3.65; ^{13}C-NMR (150 MHz, D_2O), δ (ppm): 143.8 (C-4′), 126.8 (C-5′), 100.0 (C-1,1′′′) 79.1, 75.2, 72.7, 71.7, 70.5, 70.0, 69.6, 69.5, 69.0, 67.4 66.7, 66.4 (C-13″), 63.0 (C-1″), 60.9 (C-6′′′), 50.3 (C-6); ^{13}P-RMN (242.9 MHz, D_2O), δ (ppm): 0.90 (orthophosphates), −7.09–(−8.06) (pyrophosphates), −21.01–(−23.66) (polyphosphates); HR-ICP-MS: P 19.9%.

*2.9. Synthesis of Heptakis(6-*O*-*tert*-butyldimethylsilyl)cyclomaltoheptaose (***11***)*

Compound **11** was prepared as described in literature [49] with a new purification protocol. Specifically, *tert*-butyldimethylsilyl chloride (5.577 g, 37.002 mmol) was added to a solution of β-CD (5 g, 4.405 mmol) in dry pyridine (80 mL) under nitrogen atmosphere and stirred at room temperature for 12 h. The reaction was followed by TLC (30:5:4 EtOAc–96% *v*/*v* EtOH–H_2O), which showed three spots at R_f = 0.7, 0.6, and 0.3 identified as oversilylated byproducts, derivative **11**, and undersilylated species, respectively. Portions of TBDMSCl (664 mg, 4.405 mmol) were added every 12 h until the most polar product was consumed. Water (500 mL) was added and the resulting solid was filtered, washed with water (250 mL), and azeotropically dried with toluene (3 × 150 mL). The residue was purified by a short (5 cm) flash chromatography using 40:40:20:4 CH_2Cl_2–MeCN–96% *v*/*v* EtOH–30% *v*/*v* aqueous NH_3 as eluent until the TLC spot at R_f = 0.73 completely eluted. The eluent was then changed to 40:40:20:4 CH_2Cl_2–MeCN–96% *v*/*v* EtOH–H_2O to yield **2** as a white powder which was dried at 50 °C under high vacuum until constant weight (7.302 g, 3.778 mmol, 86%). NMR data agreed with those previously reported [49]: ^{1}H NMR (500 MHz, $CDCl_3$), δ (ppm): 6.74 (bs, OH), 5.27 (bs, OH), 4.89 (d, 7H, $J_{1,2}$ = 3.5 Hz, H-1), 4.04 (t, 7H, J = 9.2 Hz, H-3), 3.90 (dd, $J_{6,6'}$ = 11.3 Hz, $J_{5,6}$ = 2.9 Hz, H-6), 3.71 (bd, 7H, J = 10.5 Hz, H-6′), 3.64 (dd, 7H, $J_{2,3}$ = 9.6 Hz, $J_{1,2}$ = 3.5 Hz, H-2), 3.62 (bs, 7H, H-5), 3.56

(t, 7H, *J* = 9.2 Hz, H-4), 0.87 (s, 63H, SiC(CH_3)$_3$), 0.04 (s, 21H, SiCH_3), 0.03 (s, 21H, SiCH_3); ^{13}C NMR (125 MHz, $CDCl_3$), δ (ppm): 102.1 (C-1), 81.9 (C-4), 73.7 (C-2), 73.5 (C-3), 72.7 (C-5), 61.8 (C-6), 26.0 (SiC(CH_3)$_3$), 18.4 (Si*C*(CH_3)$_3$), −4.9 (SiCH_3), −5.0 (SiCH_3).

*2.10. Synthesis of 1-azido-1-deoxy-ω-O-methoxypentatetraconta(ethylene glycol) (***14***)*

A solution of 1-methoxypentatetraconta(ethylene glycol) (35 g, 17.375 mmol), DMAP (428 mg, 3.5 mmol), and distilled Et_3N (5.6 mL, 40.250 mmol) in CH_2Cl_2 (40 mL) was cooled to 0 °C under inert atmosphere. MsCl (2.7 mL, 35 mmol) was added dropwise over 15 min and the mixture was stirred at 0 °C for 30 min and overnight at room temperature. The reaction mixture was then diluted with CH_2Cl_2 (50 mL) and washed with a 5% *v*/*v* aqueous HCl solution (3 × 50 mL) and brine (50 mL). The organic phase was dried over $MgSO_4$, filtered, and concentrated under reduced pressure to dryness. The solid was subsequently dissolved in dry DMF (40 mL) and NaN_3 (2.276 g, 35 mmol) was added. The mixture was stirred at 60 °C for 24 h before the solvent was rotary evaporated under high vacuum. The residue was suspended in THF (20 mL), sonicated (5 min), and the solid filtered off. The clear organic filtrate was rotary evaporated, and the resulting solid was suspended in Et_2O (50 mL), sonicated (5 min), and filtered. The solid was dissolved in H_2O (100 mL) and extracted with CH_2Cl_2 (3 × 100 mL). The organic phases were combined, dried ($MgSO_4$), rotary evaporated, and the residue dried under vacuum to give compound **14** (26.225 g, 12.858 mmol, 74%) as a slightly yellow powder: FT-IR (KBr) ν/cm^{-1}: 2868, 2105, 1093, 948, 842, 729; ^{1}H NMR (300 MHz, D_2O), δ (ppm): 3.96–3.93 (m, ^{13}C satellite peaks), 3.75–3.68 (m, 176H, OCH_2CH_2O), 3.65–3.61 (m, 2H, CH_2CH_2N_3), 3.53–3.49 (m, 2H, CH_2N_3), 3.49–3.46 (m, ^{13}C satellite peaks), 3.38 (s, CH_3O); ^{13}C NMR (75 MHz, D_2O), δ (ppm): 71.7 (CH_3OCH_2), 70.3 (OCH_2CH_2O), 70.2 (CH_3OCH_2CH_2O), 70.0 (OCH_2CH_2N_3), 58.8 (CH_3O), 50.9 (CH_2N_3).

*2.11. Synthesis of Heptakis{2,3-di-O-{1′-[methoxypentatetraconta(ethylene glycol)yl-1*H*-1,2,3-triazol-4′-yl]-methyl}}cyclomaltoheptaose (***15***)*

A solution of heptakis(2,3-*O*-propargyl)cyclomaltoheptaose **13** (70 mg, 0.042 mmol), 1-azido-1-deoxy-ω-*O*-methoxypentatetraconta(ethylene glycol) **14** (1.439 g, 0.706 mmol), and CuBr (16 mg, 0.118 mmol) in dry DMF (10 mL) under N_2 atmosphere was stirred at 100 °C for 24 h. After that period of time, starting compound **13** was not detectable by TLC (R_f = 0.47 in 30:5:4 EtOAc-EtOH-H_2O). The reaction mixture was cooled down and the solvent was rotary evaporated. The crude was purified by column chromatography (5:1 MeCN-30% *v*/*v* aqueous NH_3) to yield compound **15** (716 mg, 0.024 mmol, 57%) as a yellowish powder: mp 51 °C; IR (KBr) ν 3443, 2911, 2878, 1642, 1352, 1102, 952, 580 cm^{-1}; ^{1}H-RMN (600 MHz, D_2O), δ (ppm): 8.00 (s, 7H, H-5′), 7.98 (s, 7H, H-5′), 5.25 (bs, 7H, H-1), 4.98 (bs, 7H, OCH^a-C_2HN_3), 4.79–4.75 (m, OCH^b-C_2HN_3, overlapped with HDO), 4.55 (bs, 14H, CH_2N), 4.50 (bs, 14H, CH_2N), 4.05–3.53 (m, H-2,3,4,5,6^{a,b}, OCH_2CH_2O), 3.86–3.84 (m, ^{13}C satellite peaks), 3.62–3.60 (m, ^{13}C satellite peaks), 3.41 (s, 42H, CH_3O); ^{13}C-RMN (150 MHz, D_2O), δ (ppm): 144.9 (C-4′), 144.3 (C-4′), 125.2 (C-5′), 124.7 (C-5′), 97.6 (C-1), 80.6 (C-3), 78.1–77.8 (C-2,4), 71.0 (CH_2OCH_3), 69.6–68.7 (C-5, OCH_2CH_2O), 65.9 (OCH_2-C_2HN_3), 63.3 (OCH_2-C_2HN_3), 60.4 (C-6), 58.1 (CH_3O), 49.9 (CH_2N).

*2.12. Synthesis of Heptakis{2,3-di-O-{1′-[methoxypentatetraconta(ethylene glycol)yl-1*H*-1,2,3-triazol-4′-yl]-methyl}}cyclomaltoheptaose Phosphate Sodium Salt (***16***)*

P_2O_5 (30 mg, 0.208 mmol) was added to dry DMF (2 mL) and the mixture was sonicated in a tightly closed flask for 30 min. Compound **15** (300 mg, 0.010 mmol) was then added to the solution and the resulting mixture was stirred at 40 °C for 3 h. The mixture was cooled down and pH was adjusted to ~7.0 using 1N NaOH. The solvent was rotary evaporated and the residue was dissolved in the minimum amount of H_2O, syringe filtered (nylon 0.45 μm), and dialyzed (2000 MWCO) against distilled water by changing dialysate solution every 3 h until its conductivity was stable and below 1 μS/cm (5 days for final value of 0.90 μS/cm) to yield **16** (381 mg) as a white solid after lyophilization: mp 49 °C (dec); IR (KBr) ν 3444, 2914, 2879, 1640, 1294, 1255, 1104, 524 cm^{-1}; ^{1}H-RMN (600 MHz, D_2O), δ (ppm): 7.92 (bs, 14H, H-5′), 4.79 (bs, H-1, OCH_2-C_2HN_3, overlapped with HDO), 4.54 (bs, 14H,

CH_2N), 3.91–3.53 (m, H-2,3,4,5,6[a,b], OCH_2CH_2O), 3.86–3.84 (m, ^{13}C satellite peaks), 3.62–3.60 (m, ^{13}C satellite peaks), 3.41 (s, 42H, CH_3O); ^{13}P-RMN (242.9 MHz, D_2O), δ (ppm): 0.44 (orthophosphates), –9.33 (pyrophosphates), −21.47–(−23.88) (polyphosphates); HR-ICP-MS: P 8.0%.

2.13. Synthesis and Characterization of MIL-100(Fe) nanoMOFs

Iron trimesate nanoMOFs were synthesized using a microwave-assisted hydrothermal method described elsewhere [10,15]. Briefly, 30 mL of an aqueous mixture containing 6.0 mM iron chloride hexahydrate and 4.0 mM of BTC was heated at 130 °C under stirring for 6 min by microwave irradiation at 1600 W (Mars-5, CEM Corporation, Matthews, NC, USA). The synthesized nanoMOFs were recovered by centrifugation at 10,000 g for 15 min and purified by six times washing with absolute ethanol. Their morphology was observed with a transmission electron microscope. Mean hydrodynamic diameters and size distributions were determined by DLS. NanoMOFs' zeta potential (ZP) was measured at 25 °C by DLS in 10 mM PBS pH 7.4. For this, nanoMOFs were diluted to a final concentration of 100 μg/mL using Dulbecco's PBS solution. The nanoMOF Brunauer–Emmett–Teller (BET) surface area was measured by nitrogen sorption experiments at −196 °C after sample degassing at 100 °C for 15 h under high vacuum. X-ray powder diffraction (XRPD) patterns were recorded for crystallinity characterization. NanoMOFs were stored in ethanol at room temperature, and centrifuged and re-suspended in aqueous media whenever needed.

2.14. Surface Modification of MIL-100(Fe) nanoMOFs and Their Characterization

NanoMOFs were centrifuged at 10,000 *g* for 10 min to remove the storage solvent (ethanol) and then redispersed in water by vortex at final concentration of 2 mg/mL. For coating, equal volumes of nanoMOFs suspensions and phosphorylated CD derivatives (PCDs) CD-P, **8**–**10** or **16** solutions at 0.02, 0.2, 0.4, and 0.6 mg/mL (corresponding to nanoMOFs:PCDs 100:1, 10:1, 5:1, and 3:1 mass ratios, respectively) were incubated overnight at room temperature.

Nonattached coating PCDs molecules were removed by centrifugation (10000 g, 10 min). The pellets were dried and the amount of attached PCDs (CD-P, **8**–**10** or **16**) was quantified by ICP-MS. Briefly, uncoated and coated nanoMOFs were digested using aqua regia (15 min under ultrasonic bath), and phosphorous (P) quantification was performed by ICP-MS. Operation conditions were daily optimized using a tuning solution. P isotope was detected using "mass shift mode" ($^{47}PO^+$) after reaction with oxygen in the cell. Conversely, scandium (Sc) (added as internal standard on samples and calibration standards solutions at a concentration of 10 μg L^{-1}) was detected on "mass mode" ($^{45}Sc^+$). Oxygen was introduced into the collision/reaction cell at a flow rate of 0.35 mL min^{-1}. Dwell time for each of the targeted isotopes was 1 s. P was quantified using external calibration prepared using certified 1000 mg L^{-1} P standard solution (Merck, Darmstadt, Germany).

The amount of PCDs associated to nanoMOF was calculated on the basis of their P content by Equation (1):

$$PCDs\ adsorption\ (\%) = \frac{(P\ wt\%)_{sample}}{(P\ wt\%)_{PCDs}} \times 100 \quad (1)$$

where $(P\ wt\%)_{PCDs}$ is the phosphorous content in the PCDs coating agents (CD-P, **8**–**10** or **16**).

Uncoated and coated nanoMOFs were characterized to determine their size distribution, morphology, and surface charge. The crystallinity of PCDs-coated nanoMOF was characterized by X-ray powder diffraction (XRPD). The XRPD data were acquired using an in-house setup based on a copper rotating anode generator (RU-200BEH, Rigaku Ltd., Tokyo, Japan). The X-ray beam was filtered and focused by a confocal system consisting of two perpendicular graded multilayer mirrors (CMF-12-38Cu6 from Osmic Inc., Cleveland, OH, USA). The samples were contained in round glass capillaries (WJM-Glas Müller GmbH, Berlin, Germany), 1.5 mm in diameter, and mounted on a homemade motorized sample holder. The scattering signal was detected by a CCD detector cooled down to −30 °C (Photonic Science, Saint Leonards-on-sea, UK). The sample-to-detector distance was

296 mm, yielding an accessible scattering vector range of 0.035–0.5 $Å^{-1}$. The images were integrated, corrected, and calibrated using the Nika suite (version 1.74) running in Igor Pro 7.08.

The PCDs-coated nanoMOF colloidal stabilities were estimated in complete cell culture medium by measuring hydrodynamic diameters using DLS after 6 h incubation at 37 °C in cell culture media.

2.15. Quantification of nanoMOFs Uptake by Macrophage Cells

Macrophage cells (J774A.1) were seeded in 24-well plates at a density of 3.0×10^5 cells per well in cell culture medium and kept overnight at 37 °C in 5% CO_2. Cells were then incubated with 1 mL cell culture media containing uncoated or coated nanoMOFs (50 μg mL^{-1}) for 4 h. After incubation, the cells were washed with PBS three times to eliminate the nanoMOFs which did not interact with the cells. Cells were finally dried and digested using aqua regia (15 min under ultrasonic bath). Fe quantification was performed by ICP-MS. Operation conditions were daily optimized using a tuning solution. Fe and Co isotopes (added as internal standard on samples and calibration standards solution at a concentration of 10 μg L^{-1}) were detected using "on-mass mode" ($^{54}Fe^+$, $^{56}Fe^+$, $^{59}Co^+$). Helium was introduced into the collision/reaction cell at a flow rate of 3 mL min^{-1}. Dwell time for each of the targeted isotopes was 1 s. Fe was quantified using external calibration prepared using certified 1000 mg L^{-1} Fe standard solution (Merck, Darmstadt, Germany).

2.16. Surface Modification of Doxorubicin (DOX)-Loaded MIL-100(Fe) Nanomofs with **9**

An ethanolic suspension of MIL-100 (Fe) nanoMOFs was centrifuged (10 min, 10,000 *g*) and the sediment redispersed in MilliQ water. The nanoMOF aqueous suspension was further mixed with a DOX aqueous solution in 1:5 DOX:nanoMOFs weight ratio. The mixture was maintained under gentle stirring for 48 h at room temperature. The DOX-loaded nanoMOFs were recovered by centrifugation (10 min, 10,000 *g*) and the supernatants were used to quantify the drug payload according to Equation (2):

$$Payload\ (\%) = \frac{Encapsulated\ Drug(mg)}{nanoMOFs\ (mg)} \times 100 \quad (2)$$

The DOX-loaded nanoMOFs were further surface modified by incubation with an aqueous solution of **9** overnight. After surface functionalization, DOX-loaded nanoMOFs@**9** were recovered by centrifugation (10 min, 10000 g). The supernatant was also recovered to quantify the DOX amount.

2.17. Isothermal Titration Calorimetry (ITC) Measurements

Canavalia ensiformis (Jack bean) concanavalin A (ConA) lectin (Sigma, type VI, lyophilized powder) was used as received. All solutions were prepared in buffered MilliQ water (18.2 MΩcm), degassed for 10 min, and thermostated at 25 °C prior to each experiment. In the case of conjugates **8** and **10**, 20 mM phosphate buffer (pH 7.2) was used for both lectin and conjugates, which were considered as analyte and titrating agents, respectively. On the other hand, 10 mM TRIS buffer (pH 7.5) was employed for both lectin and nanoMOFs@**8** and nanoMOFs@**10**, which were defined as titrating agent and analytes, respectively. In all cases, lectin solution concentrations were determined by UV-Vis spectroscopy ($A^{1\%}_{280\ nm}$ = 13.7 for the tetrameric form). ITC experiments were conducted as previously described elsewhere [50]. After calibrating the calorimeter as recommended by the manufacturer, the reference and sample cells were filled with the corresponding pure buffer and the analyte solution, respectively, while a 250 μM syringe was filled with the solution of the respective titrating agent (Supplementary Materials, Table S2). The sample cell solution was continuously stirred at 416 rpm while the titrating agent solution was injected in 8 μL aliquots every 5 min. The titrating agents were also injected into the corresponding buffer in separate experiments in order to obtain the dilution background profiles, which turned out to be similar to the heat signals detected after saturation in the interaction experiments with the analytes. Obtained thermograms depicted the transfer of heat per second following each injection of the titrating agent into the analyte solution as a function of time. The integration of each peak gave

the amount of heat generated by each injection after subtracting the titrating agent dilution heat. The best fit of the experimental data to the model of n equal and independent sites provided the binding constant and the thermodynamic profile along with the corresponding standard deviations. For these calculations, we assumed that $\Delta H = \Delta H^0$, while the changes in the standard free energy (ΔG^0) and entropy (ΔS^0) were calculated as $\Delta G^0 = -RT\ln K$ and $T\Delta S^0 = \Delta H - \Delta G^0$, respectively.

3. Results and Discussion

3.1. Synthesis of Phosphate β-CD Derivatives (PCDs)

We carried out the synthesis of per-functionalized β-CD phosphate derivatives from per-6-azido-6-deoxy-β-CD **1** (Scheme 1) for their use as coating agents in the postsynthetic surface modification of the iron-based nanoMOFs MIL-100(Fe). Per-6-azido compound **1** was a convenient starting material for the attachment on its primary face of seven appendages by Cu(I)-catalyzed alkyne-azide cycloaddition reaction (CuAAC) [51–53]. As its azide counterpart, a terminal alkyne group was required on the motifs intended to be attached to the macrocycle. Thus, we performed the reaction of **1** with acetylated propargyl derivatives **2**–**4** containing mannose and/or TEG residues.

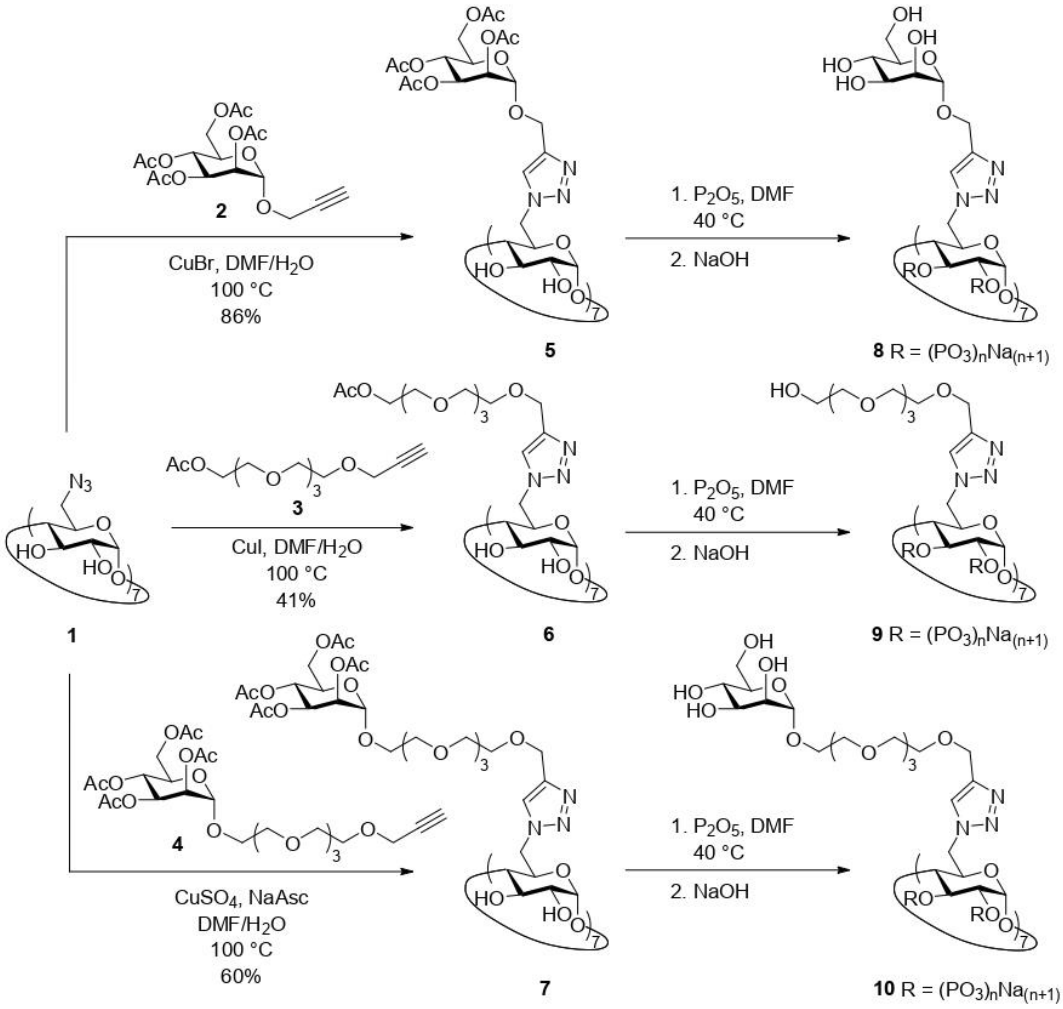

Scheme 1. Synthesis of per-functionalized β-cyclodextrin (β-CD) phosphate derivatives **8**–**10**.

We first tested the synthesis of compound **5** with seven acetylated mannopyranose residues by coupling propargyl 2,3,4,6-tetra-*O*-acetyl-α-D-mannopyranoside (**2**) to perazide **1** in the presence

of $CuI(C_2H_5O)_3P$ as catalyst in DMF at 100 °C. These conditions afforded a mixture, whose TLC showed different spots with very close R_f which turned out to be very difficult to separate by column chromatography using 25:1:5 CH_3CN-H_2O-(30% *v*/*v* aq. NH_3) as eluent. We observed that small variations in the eluent proportions sharply changed the column performance. However, a small amount of the pure product was obtained, and HPLC-MS and MALDI-TOF mass spectra allowed the detection of the target compound together with a number of under-substituted analogues, including one derivative bearing an amino group as a result of a partial reduction. In order to optimize the conversion to **5**, other copper catalysts (CuI, CuBr), solvents, and reaction temperatures were tested. By performing the reaction with CuBr in a 3:7 H_2O-DMF mixture, the desired compound was obtained as a white solid in 86% yield after a purification that included removal of copper traces. The molecular weight of **5** was confirmed by MALDI-TOF mass spectrometry, which showed the *m*/*z* pick corresponding to $[M+Na]^+$ ion. The formation of the triazole rings was confirmed by ^1H NMR spectroscopy as it showed a peak at δ 7.96 ppm corresponding to the triazole proton along with the absence of the triplet at δ 2.47 ppm of the alkyne proton of the starting mannoside. In addition, ^{13}C NMR spectrum also showed peaks at δ 141.9 and 125.7 ppm corresponding to the C-4′ and C-5′ of the triazole rings, respectively. Both ^1H and ^{13}C NMR spectra also revealed DMF residual peaks (Supplementary Materials, Figures S2 and S12). The efforts made to remove the solvent from the sample, including lyophilization, azeotropic distillation with toluene, and high vacuum at 50 °C, turned out to be unsuccessful. It is noteworthy that NMR spectra for **5** were recorded in DMSO-d_6 at 80 °C to overcome the conformational energy barriers of the molecule. NMR spectra at 25 °C showed several sets of signals indicating that the interconversion among different conformers of the structure were slow enough in the time scale of the experiments, probably due to the steric hindrance on the primary face of the macrocycle. In sharp contrast, increasing the temperature to 80 °C led to well-defined signals for each nuclei, confirming the C_7 symmetry of the molecule, and hence the presence of seven appendages on the macrocycle.

The synthesis of compound **6** bearing seven acetylated tetraethylene glycol branches also turned out to be troublesome. A set of catalysts and conditions were tested, and the obtained crude products were analyzed by TLC and HPLC-MS. Among the screened sets-up, CuI in 1:1 DMF-H_2O at 100 °C was found to be optimal for the cycloaddition reaction, affording **6** in 41% yield after purification. The low yield can be attributed to a partial deacetylation during the column elution, judging from TLC (5:1 1,4-dioxane-30% *v*/*v* aq. NH_3). MALDI-TOF confirmed the molecular weight of the target compound, which showed the *m*/*z* peak corresponding to $[M + Na]^+$ ion. The formation of the triazole rings (peak at δ 7.86 ppm in the ^1H-NMR spectrum) and the presence of acetyl moieties (peaks at δ 2.00 ppm in ^1H NMR spectrum, and at δ 169.6 (carboxyl) and 20.0 ppm (methyl) in ^{13}C NMR spectrum) were unambiguously confirmed by NMR spectroscopy. As in the case of derivative **5**, recording the NMR spectra in DMSO-d_6 at 80 °C was mandatory in order to obtain single, well-defined signals for nuclei of the glucose units of the macrocycle, thus confirming the C_7 symmetry of the molecule due to the per-modification at C-6 positions.

Next, CD derivative **7** (Scheme 1) decorated with seven acetylated mannose residues linked through a tetraethylene glycol (TEG) tether was prepared. In this case, among the tested reaction conditions the use of $CuSO_4$ and sodium ascorbate as catalyst promoters in 2:1 DMF-H_2O at 100 °C resulted to be optimal and gave **7** in 60% yield after purification. The structure of **7** was confirmed by MALDI-TOF mass spectrometry and NMR spectroscopy. ^1H NMR spectrum of **7** measured in DMSO-d_6 at 80 °C showed a singlet corresponding to the triazole hydrogen at δ 7.86 ppm, two doublets at δ 5.09 and 4.90 ppm corresponding to the anomeric protons of the glucose units of the macrocycle (H-1) and the mannose residues (H-1′′′), respectively, and four singlets at δ 2.10–1.93 ppm assignable to the 28 acetyl groups of the mannose units. The presence of the TEG tether was confirmed by the multiplet that appeared in the range of δ 3.57–3.48 ppm corresponding to the CH_2 groups of chain.

β-CD derivatives **5**–**7** presented fourteen free OH groups on the secondary face of the macrocycle still available for further modifications. In order to transform these compounds into potential coating agents for iron-based nanoMOFs MIL-100(Fe) [15,17], we decided to phosphorylate those OH to

yield phosphates **8**–**10** (Scheme 1). Phosphorylations of **5**–**7** were carried out by treatment with an excess of P_2O_5 in DMF at 40 °C. After the starting material was consumed, pH was increased to ~13 to remove the acetyl groups of the primary face appendages. The crude products were dialyzed towards distilled water. Based on the theoretical molecular weight of phosphates **8**–**10** by considering fourteen disodium phosphate groups on the secondary face (4572.71–5804.73 Da), membranes of 500–1000 Da MWCO were initially chosen. However, intense peaks of unknown impurities at around δ 8.40, 3.30, and 2.70 ppm were observed in the ^{1}H NMR spectra of the dialyzed products. Increasing membrane pore size to 2000 MWCO effectively removed the peaks at around δ 8.40 and 3.30 ppm, although it did not affect to the signal at ca. δ 2.70 ppm and significantly decreased the obtained amount of compounds **8**–**10**. Both ^{1}H and ^{13}C NMR spectra of **8**–**10** confirmed the absence of the peaks corresponding to acetyl groups presents in the starting materials **5**–**7** and showed broad signals for the nuclei of both the macrocycle and the appendages. It is important to highlight that random phosphorylation with P_2O_5 yields a mixture of ortho-, pyro-, and polyphosphates depending on the molar ratio between the hydroxyl groups and the added amount of P_2O_5, but also on the presence of traces of water during the reaction. Indeed, ^{31}P NMR spectra showed, in all cases, three sets of signals at around δ 0.5, −8.0, and −22.5 ppm corresponding to the ortho-, pyro-, and polyphosphate species, respectively [54], formed on the secondary face of the macrocycles. Furthermore, we determined the contents of P in derivatives **8**–**10** by HR-ICP-MS and used those data to calculate the number of phosphate groups (Supplementary Materials, Table S1). Assuming that all OH groups of the secondary face were phosphorylated, an average number of phosphate groups per OH of 2.55, 2.43, and 5.83 for compounds **8**, **9**, and **10**, respectively, was found, indicating that all ortho-, pyro-, and polyphosphate species were most probably present as ^{31}P NMR spectra previously suggested.

In a similar strategy, per(6-*O*-*tert*-butyldimethylsilyl)-β-CD **11** was used as starting material for the attachment of methoxy poly(ethylene glycol) branches on the secondary rim of the macrocycle and subsequent phosphorylation of the primary face (Scheme 2). Compound **11** was prepared by reacting β-CD with TBDMSCl in pyridine as previously reported [49], although a new rapid and reproducible purification method was developed. Thus, enough TBDMSCl was added in portions until TLC (30:5:4 EtOAc–96% *v*/*v* EtOH–H_2O) showed no undersilylated species (see Experimental part). Purification of **11** was easily performed by a short flash chromatography using first the quaternary mixture of solvents 40:40:20:4 CH_2Cl_2–MeCN–96% *v*/*v* EtOH–30% *v*/*v* aqueous NH_3 to rapidly elute the oversilylated byproducts, and then using 40:40:20:4 CH_2Cl_2–MeCN–96% *v*/*v* EtOH–H_2O to quickly wash out highly pure silyl **11** in 86% yield. Extensive propargylation and subsequent desilylation of cyclooligosaccharide **11** according to published procedures [47] led to derivative **13**, which in turn was reacted with 1-azido-1-deoxy-ω-*O*-methoxypentatetraconta(ethylene glycol) **14** (average MW ~2000) in the presence of CuBr as catalyst in DMF at 100 °C to give compound **15** in 57% yield after column chromatography. ^{1}H NMR spectrum of compound **15** showed two sharp peaks at δ 8.00 and 7.98 ppm for the protons of the triazole rings located at C-2 and C-3 positions of the glucose residues of the macrocycle, suggesting a C_7 symmetry and, hence, the cycloaddition of fourteen PEG chains on the secondary face of the β-CD. However, broad signals were found for the skeletal protons of the glucose moieties, which can be reasoned in terms of macrocycle rigidity due to the high steric hindrance of the molecule. The same effect was visible in the ^{13}C NMR spectrum, with well-defined signals for triazole rings but broad peaks for the glucose residues nuclei. Interestingly, the intense signals arising from methylene groups of the fourteen long PEG chains dominated the dynamic range in both ^{1}H and ^{13}C spectra. As a result, ^{13}C satellite peaks could be observed as multiplets at δ 3.86–3.84 and 3.62–3.60 ppm in ^{1}H NMR [55], as well as a set of sideband peaks symmetrically located at both sides of the PEG signal (δ 69.6 ppm) at chemical shifts that were whole multiples of ~315 Hz in ^{13}C NMR.

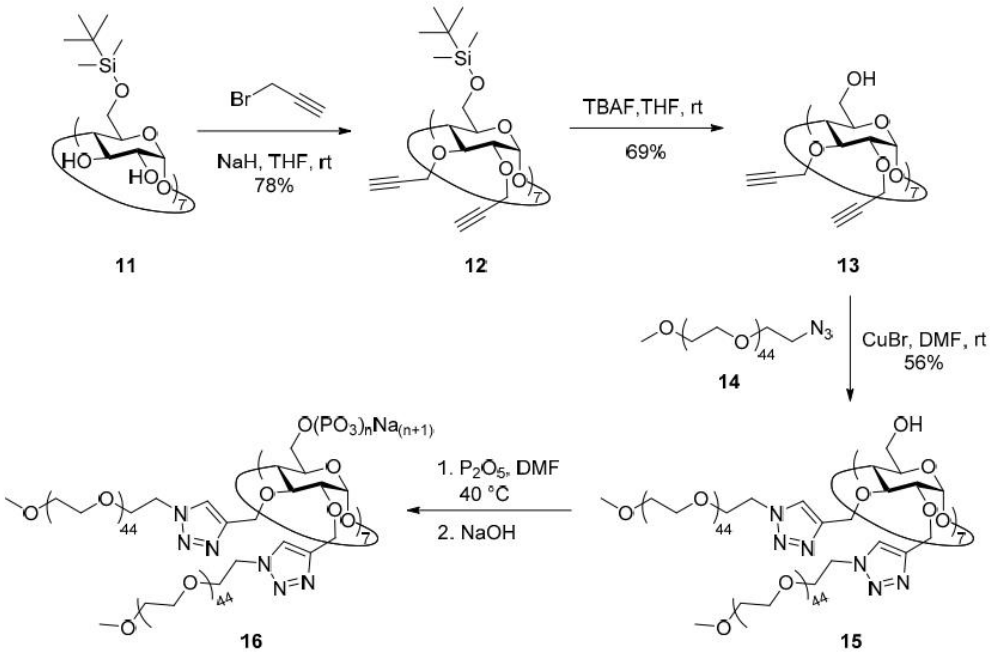

Scheme 2. Synthesis of per-functionalized β-CD phosphate derivative **16**.

Phosphorylation of the OH groups of the primary face of **15** was achieved by treatment with P_2O_5 in DMF at 40 °C as described above, although in this case pH was directly adjusted to ~7.0 after reaction as no acetyl groups were present on the starting material (Scheme 2). Dialysis towards distilled water through 2000 MWCO membrane finally achieved phosphate **16** after lyophilization. ^{1}H NMR spectrum showed less defined signals for both cyclooligosaccharide skeleton and triazole rings than that for the starting material **15**, evidencing an increase of the structure rigidity. Once again, the signal from PEG methylenes was very intense and accompanied by ^{13}C satellite peaks as multiplets at δ 3.86–3.84 and 3.62–3.60 ppm. Furthermore, the effect of the signal arising from those groups on the dynamic range of the ^{13}C NMR spectrum was so strong that it was not possible to see the rest of the molecule peaks even after long acquisition periods. ^{31}P NMR spectrum showed very intense signals at around δ −22.5 ppm along with much smaller peaks at δ 0.44 and −9.33 ppm peaks, suggesting that phosphorylation of primary face afforded mainly polyphosphate groups together with a few ortho- and pyrophosphate functionalities [54]. This result was also confirmed by HR-ICP-MS data for the phosphorus contents of derivative **16**, which allowed us to calculate an average number of 15.21 phosphate residues per primary OH group. This number is in sharp contrast with those obtained for derivatives **8**–**10** varying between 2.43 and 5.83 despite the fact that a similar molar ratio of P_2O_5 per free OH (between 2.3 and 4.4) was employed in the four cases.

3.2. MIL-100(Fe) nanoMOFs Synthesis and Surface Modification

MIL-100(Fe) nanoMOFs with a mean hydrodynamic diameter of 231 ± 14 nm and BET surface area of 1690 ± 80 m^2 g^{-1} were successfully synthesized by an organic solvent-free microwave-assisted hydrothermal method [15]. Resulting nanoMOFs had typical facetted structures (Figure 1a) and showed XRDP similar to those previously published (Supplementary Materials, Figure S24). Surface modification of MIL-100(Fe) nanoMOFs with PCDs was carried out through a "green" (meaning organic solvent-free) method consisting of impregnation of nanoMOFs in aqueous solutions of PCDs CD-P, **8**–**10** or **16** at different mass ratios nanoMOFs:PCDs, ranging from 100:1 to 3:1, to yield nanoMOFs@PCD core-shell. Both uncoated and coated MIL-100(Fe) nanoMOFs were characterized by a set of complementary techniques. Even at the 3:1 nanoMOFs:PCDs mass ratio the particles

maintained their facetted structures (Figure 1b–f). No morphological differences were found between coated and uncoated particles, independently of the coating material. Indeed, XRDP studies indicated that the crystalline structure of MIL-100(Fe) nanoMOFs was preserved after surface modification (Supplementary Materials, Figure S24) in spite of the relatively high amounts of PCDs associated to the nanoMOFs (see below). For instance, the strong reflections present in the uncoated sample were preserved in the treated ones, showing that the integrity of the lattice was preserved in the latter, which did however exhibit a supplementary flat background at wide angles and a stronger power-law contribution at small angles, consistent with the presence of an additional amorphous component. These observations are in agreement with previously reported data on different structures used as coating for the same nanoMOFs [15,17]. The hydrodynamic diameters of MIL-100(Fe) nanoMOFs in water were determined by DLS before and after surface modification. Measurements showed neither mean size nor polydispersity significant variations after the coating process, independently of the concentration and type of coating material. Mean diameters increased from 224 ± 21 nm for uncoated nanoMOFs to 229 ± 18, 248 ± 25, 239 ± 17, 237 ± 19, and 241 ± 23 for nanoMOFs coated with CD-P, **8**–**10** and **16**, respectively. These data indicated that the coating thickness was less than 15 nm in all cases, and that no aggregation occurred. Similar behavior was found in DMEM biological medium complemented with 10% FBS (Supplementary Materials, Figure S25). Again, no trace of aggregation was observed as the mean diameters remained constant after 6 h incubation at 37 °C. These results allow for biological studies on the interactions of coated nanoMOFs with macrophages.

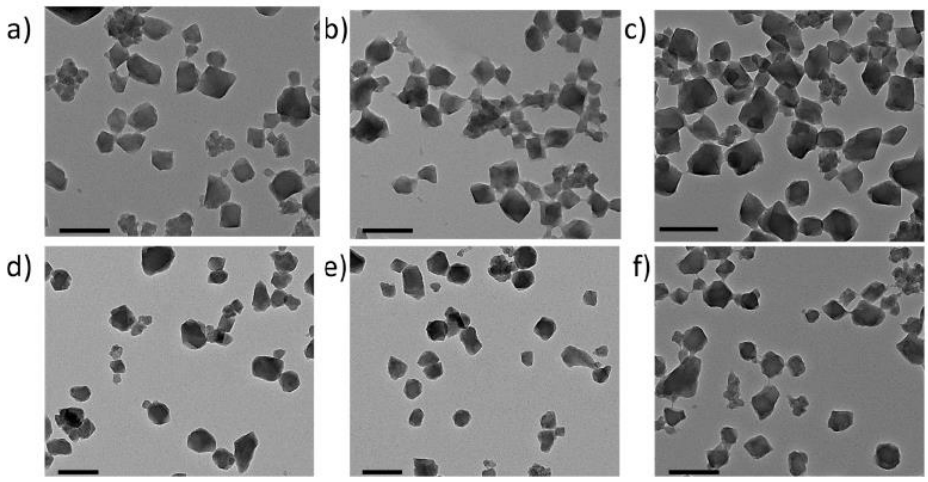

Figure 1. TEM images of nanosized metal-organic frameworks (nanoMOFs) before and after coating step: (**a**) Uncoated nanoMOFs; (**b**) nanoMOFs@CD-P; (**c**) nanoMOFs@**8**; (**d**) nanoMOFs@**9**; (**e**) nanoMOFs@**10**; (**f**) nanoMOFs@**16**. Scale bar: 200 nm.

The amount of PCDs associated with the nanoMOFs was determined by direct quantification of the P content in the coated samples by ICP-MS after sample digestion, taking advantage of the fact that P is the only element present in the PCDs derivatives but not in the nanoMOFs. As it can be seen in Figure 2, the amount of PCDs attached to nanoMOFs was directly proportional to the amount of the coating material employed for the nanoMOFs coating procedure. In parallel, the grafting efficiencies of the various PCDs derivatives decreased from ~70 to ~35% with increasing the amount of PCDs in the preparation procedure (Supplementary Materials, Figure S26). In the case of CD-P and **8**–**10**, the grafted amounts tended to reach a plateau when a 3:1 nanoMOFs:PCDs mass ratio was used. Thus, CD-P and derivative **8** decorated with seven mannose residues directly attached to its primary face reached a value of 10 ± 1 wt% of grafting, while PCD **10** coated the nanoMOFs in less extension (9 ± 1 wt%). In contrast, PCD **9** decorated with seven flexible and less bulky TEG chains was adsorbed onto the nanoMOF surface at 14 ± 1 wt%, suggesting that steric hindrance of the coating

structure might correlate with the nanoMOFs covering density. However, PCD **16** having fourteen long PEG chains on the secondary face showed the highest covering value of the series (16 ± 1 wt% at a 3:1 nanoMOF:**16** mass ratio). Nevertheless, the amounts of coating PCDs were in the same range of previously reported values for other PCDs derivatives on the same MIL-100(Fe) nanoMOFs (~17 wt%) [17].

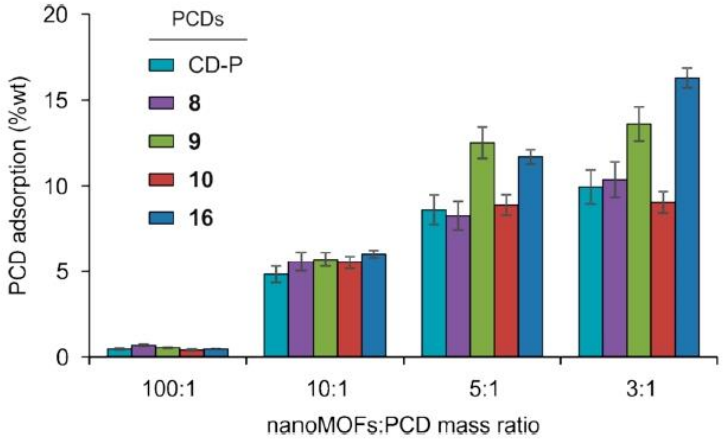

Figure 2. Phosphate β-CD derivatives (PCDs) grafting (wt%) versus nanoMOFs:PCDs mass ratio assayed.

Lack of colloidal stability is an important drawback hampering nanoparticle biomedical applications. Zeta potential analysis gives values of the nanoparticles global charge, which depends on pH, presence of ions, and nanoMOFs concentration. Measurements were performed at pH 7.4 and reflect the stability of the system. Results are depicted in Figure 3, which shows that the ZP values shifted from −26 ± 1 mV for the uncoated nanoMOFs to values between −21 ± 1 and −18 ± 1 mV for the nanoMOFs covered with PCDs CD-P and **8**–**10**. However, when PCD **16** was used, coated nanoMOFs reached ZP values close to 0 (−4 ± 1 mV). This behavior is a clear indication that the carboxylate surface groups on the nanoMOFs were shielded by the nonionic PEG chains. These observations are in agreement with previously reported ZP values close to zero in the case of other types of PEG-coated nanoparticles [37].

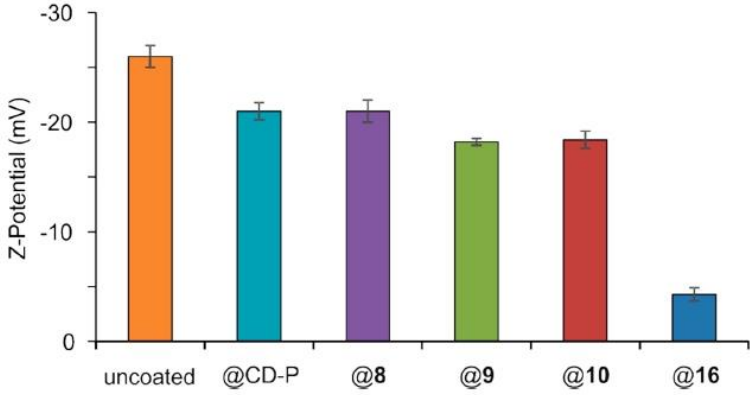

Figure 3. Zeta potential of nanoMOFs coated or not with PCDs in 10 mM PBS at pH 7.4.

3.3. ITC Experiments on ConA Biorecognition

Mannose-coated MIL-100(Fe) nanoMOFs are the result of the self-assembly of multiple heptavalent mannose clusters (**8** and **10**) on the surface of the nanoparticles. Displaying a multivalent presentation

of mannoside ligands would be equivalent to an artificial "glycocalix" [40]. To test the molecular recognition properties of such mannose-coated nanoMOFs, we studied the binding affinity of glycoclusters **8** and **10**, as well as mannose-coated nanoMOFs@**8** and nanoMOFs@**10**, towards the model mannose-specific lectin concanavalin A (ConA) by using isothermal titration calorimetry (ITC). This technique allows the quantification of the stoichiometry, affinity, and thermodynamic profile for the interaction between ligands and receptors by detecting the heat released or absorbed during the binding event. Indeed, ITC directly provides values for the enthalpy change of binding (ΔH), while the binding constant (K) and the stoichiometry (n), defined as the ratio between the concentration of the conjugates and the protein when the lectin binding sites are saturated, are estimated from the best fit to a model of n equal and independent sites by a nonlinear least square algorithm. It is important to highlight that the selected model lectin, ConA, and the actual human macrophage mannose receptor (hMMR) are different, both at structural and binding mechanism levels, and thus, any extrapolation from the former to the latter should be made with care. However, recently it has been reported that affinities of a series of mimics for both lectins in solution are qualitatively similar [56,57], which supports our choice.

Titration experiments for mannosylated PCDs **8** and **10** were performed in 20 mM phosphate buffer at pH 7.2 at 25 °C. Aliquots of each PCD were injected into a solution of ConA within the calorimeter cell and the amount of released heat following each injection was plotted against the molar ratio between the conjugate and the lectin (Figure 4 and Figure S27). In addition, control experiments were performed by injecting ligands into the cell containing buffer without lectin and showed insignificant heats of dilution. Thermodynamic profiles calculated by fitting the obtained data to the model can be found in Table 1 and Figure 5, and are in sharp agreement to those typically reported for protein-carbohydrate binding [50,58]. Indeed, ITC experiments showed clearly exothermic interactions with ConA for both conjugates **8** and **10**. Thus, their thermograms were characterized by negative peaks corresponding to a release of heat associated with the binding interaction, which diminished progressively due to the gradual saturation of the protein binding sites. Thermogram for PCD **10** reached a plateau at lesser concentration ratio than that for **8**, which can be reasoned taking into account that the binding constant for the former is 2.3-fold higher than that for the latter (Table 1). Both thermodynamic profiles were very similar and enthalpy-driven (Figure 5), comprising favorable (negative) enthalpic terms partially counterbalanced by smaller unfavorable (negative) entropic contributions.

Interestingly, binding enthalpy for conjugate **8** was slightly more favorable (~4%) than that for **10**, which may suggest a better docking of the mannose moieties of the former to the carbohydrate-binding sites of the protein. However, entropic unfavorable term was ~17% larger in the case of **8**, resulting in a compensation of ~50% of the enthalpy contribution for this conjugate while **10** showed an entropic counterbalance of only ~44%. This fact explains why the interaction was stronger in the case of conjugate **10** as their respective binding constants reveal, and it was clearly related to the presence of tetra(ethylene glycol) spacers between the mannose residues and the cyclooligosaccharide in its structure. These tethers most probably increased the distance and mobility of the monosaccharides around the primary face of the macrocycle, moderating the rigidity gain after protein binding and thus softening the concomitant entropic lost. Previous reports have shown the beneficial effects of introducing flexible and relatively long bridges between a β-CD core and sugar ligands on their ability to bind lectins in solution [59,60]. Regarding the stoichiometry of the interactions, the ratios between the concentration of the conjugates and the protein when the system reaches saturation (n) were calculated as 2.44 and 2.79 for compounds **8** and **10**, respectively (Table 1). ConA is well-known to present a tetrameric structure at pH values above 7.0, with a unique mannose-binding site per monomer [61]. Thus, n values below 4 suggest that not all binding sites of the protein were occupied when the system reached saturation, which might be reasoned in terms of crowded spatial arrangements taking into account the sharp differences in sizes between the lectin and the mannose-containing phosphates **8** and **10**.

Table 1. Thermodynamics and stability constants for the binding of conjugates **8**, **10**, nanoMOFs@**8**, and nanoMOFs@**10** to ConA according to an *n* equal and independent binding sites model.

Conjugate	N [a]	$K \times 10^{-5}$ (M^{-1})	ΔG^0 (kcal mol^{-1})	ΔH (kcal mol^{-1})	$T\Delta S^0$ (kcal mol^{-1})
8 [b]	2.44 ± 0.01	2.25 ± 0.08	−7.30 ± 0.02	−14.49 ± 0.06	−7.19
10 [b]	2.79 ± 0.01	5.12 ± 0.25	−7.79 ± 0.03	−13.96 ± 0.07	−6.17
nanoMOFs@**8** [c]	0.90 ± 0.01	14.20 ± 1.64	−8.39 ± 0.07	−334.20 ± 6.91	−325.81
nanoMOFs@**10** [c]	1.06 ± 0.01	24.50 ± 1.17	−8.72 ± 0.03	−314.10 ± 3.37	−305.38

[a] [conjugate]:[ConA] ratio when the lectin binding sites are fully saturated. Concentration of ConA was calculated as tetramer; [b] 20 mM phosphate buffer (pH 7.2) at 25 °C; [c] 10 mM TRIS buffer (pH 7.5) at 25 °C.

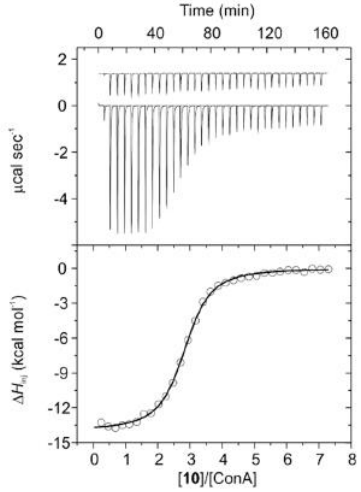

Figure 4. Titration of concanavalin A (ConA) with conjugate **10** in 20 mM phosphate buffer (pH 7.2) at 25 °C. The top panel shows the raw calorimetric data denoting the amount of generated (negative exothermic peaks) heat following each injection of the conjugate. The area under each peak represents the amount of heat released upon binding of the conjugate to the lectin. Note that as the titration progresses, the area under the peaks gradually becomes smaller because of the increasing saturation of the sugar binding sites of the protein. This area was integrated and plotted against the molar ratio of the conjugate to ConA (as tetramer). The smooth solid line represents the best fit of the experimental data to the model of *n* equal and independent binding sites.

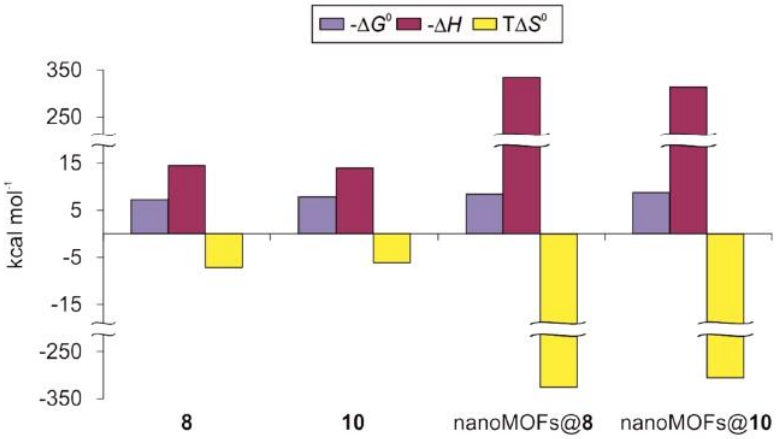

Figure 5. Thermodynamic profiles comprising free energy ($-\Delta G^0$), enthalpy ($-\Delta H$), and entropy changes ($T\Delta S^0$) for the interaction of conjugates **8**, **10**, nanoMOFs@**8**, and nanoMOFs@**10** with ConA in 20 mM phosphate buffer (pH 7.2) at 25 °C for **8** and **10**, and 10 mM TRIS buffer (pH 7.5) at 25 °C for nanoMOFs@**8** and nanoMOFs@**10**.

In contrast to **8** and **10**, ITC experiments with nanoMOFs@**8** and nanoMOFs@**10** were performed in 10 mM TRIS (pH 7.5) buffer due to the fact that phosphate buffer used above could compete for the iron sites within the nanoparticles surface, causing the coating depletion. Furthermore, inverse titration was required for nanoMOFs@**8** and nanoMOFs@**10** since colloidal stability for these nanoparticles had only been tested at concentrations below 1 mg/mL (~21 and ~15 μM of coating PCDs **8** and **10**, respectively, on the nanoMOFs surface) which turned out to be too low when direct titrations were attempted. Thus, in these cases aliquots of solutions of ConA lectin in concentration below its aggregation limit (80 μM as tetramer, in our hands) were injected within nanoparticle colloidal suspensions contained in the calorimeter cell. To the best of our knowledge, this was the first time that the interaction of nanoMOFs coated with biorecognizable moieties towards their biological receptor counterpart was evaluated by this technique. As previously discussed for free PCDs **8** and **10**, obtained thermograms for nanoMOFs@**8** and nanoMOFs@**10** were strongly exothermic, presenting negative peaks that become shorter after each injection (Supplementary Materials, Figure S27). Again, fitting obtained data to the model of *n* equal and independent binding sites gave us enthalpy-driven thermodynamic profiles for both coated systems (Table 1 and Figure 5). Noticeably, binding enthalpies turned out to be ~23-fold more favorable than those previously measured for the free coating agents **8** and **10**, reaching values more negative than −300 kcal mol^{-1}. Similarly, unfavorable entropic terms were of the same order of magnitude, compensating ~97% of the enthalpic contributions in both cases. Such behavior has also been reported in the case of gold nanoparticles coated with sugars when interacting with ConA [62], and it was most likely a consequence of the high density of ligands present on the nanoparticle surface resulting in a remarkable multivalent effect. In absolute terms, calculated ΔG^0 values were 12–15% more favorable for the nanoparticles than those for the free phosphates, and thus the binding constants for nanoMOFs@**8** and nanoMOFs@**10** were 6.33-fold and 4.8-fold larger, respectively. Once more, the binding affinity of nanoMOFs@**10** presenting TEG spacers was ~2-fold stronger than that for nanoMOFs@**8**, where the mannose residues were directly attached to the primary face of the macrocycle, most probably explained through the better fit of the ligand associated with the higher flexibility of the linker, reducing the steric hindrance. Again, *n* values for nanoMOFs@**8** and nanoMOFs@**10** were below 4 when interacting with the lectin (0.90 and 1.06, respectively), suggesting an extensive covering of the coated nanoparticles surface by protein tetramers at the system saturation point. This was possible due to the fact that the nanoparticles showed an average diameter of 231 nm, which was ~29-fold larger than the lectin, having a reported hydrodynamic diameter of ~8 nm [63].

Finally, it should be underlined that despite the sharp differences in the values of the thermodynamic parameters calculated for **8**, **10**, nanoMOFs@**8**, and nanoMOFs@**10**, all evaluated mannoside derivatives showed typical energetic profiles for protein-carbohydrate association events [50,58]. Indeed, the enthalpy–entropy compensation was strongly linear with a slope of ~1.00 and a correlation coefficient of 1 (Supplementary Materials, Figure S28).

3.4. Interactions of Surface-Modified nanoMOFs with a Macrophage Cell Line

Once demonstrated by ITC that mannose-coated nanoMOFs recognized a specific protein receptor with enhanced avidity, we evaluated the interactions of nanoMOFs coated with **8**–**10** and **16** with macrophages on the murine macrophage cell line J774A.1. To compare the efficacy of different coatings, an incubation time of 4 h was chosen. Indeed, for uncoated MIL-100(Fe) nanoMOFs, this time corresponded to an efficient uptake by J774A.1 macrophages [64] as is in the order of magnitude of blood circulation times of PEG-coated nanoparticles [20]. Quantitative measurement on the amounts of nanoMOFs uptaken in cells were obtained by ICP-MS, after contact of nanoparticles with cells followed by extensive washing to remove the nonassociated particles. As shown in Figure 6, around 75% of uncoated nanoMOFs were taken up in macrophages after 4 h incubation, corresponding to around 23 μg nanoMOFs/3 × 10^5 cells. This result demonstrates that macrophages avidly take up nanoMOFs, in agreement with reported data [64]. Remarkably, the presence of PCDs **8**–**10** or **16** on the nanoparticles surface significantly reduced the nanoMOFs internalization. The nanoMOFs amounts

uptaken by the cells decreased in the order CD-P > **8** > **16** > **10** > **9**, with uptake percentages of 41 ± 3, 33 ± 5, 32 ± 2, 22 ± 2, and 21 ± 3%, respectively (Figure 6). These results indicated that all of the PCDs coatings played a role on the nanoMOFs cell internalization, although the relationship between the uptaking reduction and the structure is not obvious.

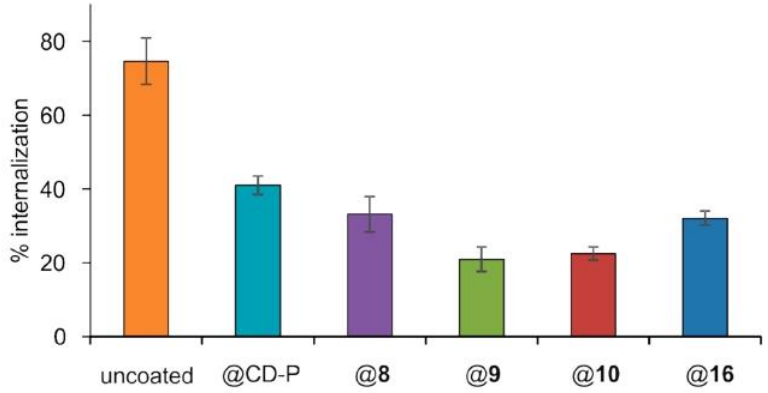

Figure 6. In vitro interaction of uncoated and coated nanoMOFs with PCDs CD-P, **8**–**10**, and **16** with a J774A.1 macrophage cell line. 50 μg/mL nanoMOFs were incubated with 3×10^5 J774A.1 cells for 4 h, and then washed to remove the nonfirmly bound nanoMOFs. After cell lysis, the amount of internalized nanoMOFs was determined by ICP-MS and was expressed as a % of the initial amount put in contact with the cells.

Interestingly, an almost two-fold reduction of internalization was observed for the nanoMOFs coated with CD-P without any further modification (from 75% for uncoated nanoMOFs to 41% for nanoMOFs coated with CD-P). This was a surprising result as to the best of our knowledge no study has reported yet that a CD coating could reduce macrophage uptake. When CD was further functionalized with PEG chains (**16**), which are well known to reduce macrophage uptake [65], a better "stealth" effect was obtained with around 32% cell association compared to 41% for nanoMOFs coated with CD-P. A similar effect was obtained in the case of PCD **8** (~33%), where mannose was attached to the macrocycle instead of PEG chains. The most efficient "stealth" behavior was observed for nanoMOFs@**9** and mannose-grafted nanoMOFs@**10**, both characterized by short TEG chain in the structure, showing less than one third uptake as compared to uncoated nanoMOFs (from 75% for uncoated nanoMOFs to 21% and 22% for nanoMOFs@**9** and nanoMOFs@**10**, respectively). This result suggests that the presence of short TEG chains optimizes the "stealth" effect with respect to longer PEG chains, which are not able to decrease very significantly the cellular uptake with respect to plain CD-P. Possibly, part of PEG chains might penetrate inside the nanoMOF pores, as previously reported [15]. Moreover, since the MW of PEG-CD **16** is much higher than that of **8**–**10**, and their coating efficiencies, which are based on P content in the coated samples, are similar, it was expected that the MOF surface would be coated with more molecules of **8**–**10** than molecules of **16**, and therefore the PEG density might not have been enough to promote a more efficient "stealth" effect.

In the cases of nanoMOFs@**8** and nanoMOFs@**10**, mannose grafting did not increase nanoMOFs uptake, as one would have expected. Macrophages internalize nanoparticles through different mechanisms depending on the physicochemical properties of the nanomaterials, including particle size, particle shape, surface charge, and surface modification with organic and/or biological molecules [66]. It is known that uncoated nanoMOFs uptake by J774A.1 macrophages is driven principally by phagocytosis [64], a mechanism which is strongly influenced by the specific composition of the protein corona [15,20,21]. "Stealth" effects of PEG coating on nanomaterials are not dependent on a reduction of protein corona adsorption but on a change of the type of proteins adsorbed on the surface from the blood plasma, more specifically to the binding of mainly clusterin protein [67]. Our results suggest that when mannose-coated nanoMOF@**8** and nanoMOF@**10** are placed in a complex biological environment,

the binding of clusterin to the surface of such nanoparticles not only contributes to an efficient "stealth" effect, but also may shield the accessibility of the mannose ligands to their macrophage surface specific receptors. Furthermore, mannose-vectorized nanomaterials towards macrophages are dominantly internalized by energy-dependent clathrin-mediated endocytosis [68–70]. Such mechanism is affected by the particle size and works well when particles are smaller than 200 nm [71]. Thus, nanoMOFs@**8** and nanoMOFs@**10** uptake may also be hindered by the relatively large size of the nanoparticles. These observations reflect the complexity of surface functionalization of highly porous MIL-100(Fe) nanoMOFs.

3.5. DOX-Loaded MIL-100(Fe) nanoMOFs Surface Modification

Finally, we investigated the coating of anticancer drug DOX-loaded nanoMOF with TEGylated PCD **9**, since nanoMOF@**9** displayed the most efficient "stealth" effect. DOX payload reached 17 ± 3 wt%, corresponding to a loading efficiency of 85 ± 2%. This good loading efficiency indicated the strong interaction between DOX and MIL-100(Fe) nanoMOFs, in agreement with the previous reports [72]. The drug-loaded nanoMOFs were further coated with **9**, by the same one-step procedure in water described above. The functionalized particles had similar diameters (235 ± 21 nm) to those of the unloaded ones (226 ± 24 nm). Interestingly, surface modification of nanoMOFs with **9** did not induce DOX release, showing less than 2 ± 0.4% DOX release after 12 h incubation with this PCD. The coating of DOX-loaded nanoMOFs with targeting ligands and DOX release studies in cancer cells will be the subject of further studies. These results showed that the coating strategy described herein can be applied to nanoMOFs previously loaded with a drug.

4. Conclusions

In conclusion, we have developed a convenient method for the coating of nanoMOFs MIL-100(Fe) with TEG, PEG, and mannose residues. The method consisted of the organic solvent-free self-assembly on the nanoMOFs surface of building-blocks based on β-CD having functional moieties (TEG, PEG, and mannose) on one face and multiple phosphate groups on the other side. The coating can also be applied to doxorubicin-loaded nanoMOFs MIL-100(Fe) without significantly affecting the payload of the nanoparticles. Mannose-coated nanoMOFs displayed a remarkable enhanced binding affinity towards a specific mannose receptor such as Concanavalin A due to the so-called multivalent effect. However, these remarkable mannose recognition properties were not translated into improved macrophage uptake. By contrast, such mannosylated systems showed reduced macrophage internalization as compared with uncoated nanoMOFs. Furthermore, our results showed that coating nanoMOFs with cyclodextrin phosphate led to a significant "stealth" effect, slightly improved by PEGylated or mannosylated cyclodextrin phosphate coating. More notable, the nanoMOFs surface modification with TEGylated and mannosyl-TEGylated PCDs, having a much shorter oligoethylene chain, displayed the most efficient "stealth" effect. These results highlight the complexity of the involved interactions, particularly in a biological environment. Further research will be performed to comprehensively understand the localization and functions of each cyclodextrin phosphate component as well as the structural requirements to ensure molecular recognition properties in a biological medium. Our results showed that PCDs offer a versatile platform to coat nanoMOFs in an organic solvent-free, one step manner, and to impart biorecognition properties to nanoMOFs.

Supplementary Materials: The following are available online at http://www.mdpi.com/2079-4991/9/8/1103/s1, Figure S1: ^{1}H NMR spectrum (500 MHz, $CDCl_3$, 25 °C) for compound **3**, Figure S2: ^{1}H NMR spectrum (500 MHz, DMSO-d_6, 80 °C) for compound **5**, Figure S3: ^{1}H NMR spectrum (500 MHz, DMSO-d_6, 80 °C) for compound **6**, Figure S4: ^{1}H NMR spectrum (500 MHz, DMSO-d_6, 80 °C) for compound **7**, Figure S5: ^{1}H NMR spectrum (600 MHz, D_2O, 25 °C) for compound **8**, Figure S6: ^{1}H NMR spectrum (600 MHz, D_2O, 25 °C) for compound **9**, Figure S7: ^{1}H NMR spectrum (600 MHz, D_2O, 25 °C) for compound **10**, Figure S8: ^{1}H NMR spectrum (300 MHz, D_2O, 25 °C) for compound **14**, Figure S9: ^{1}H NMR spectrum (600 MHz, D_2O, 25 °C) for compound **15**, Figure S10: ^{1}H NMR spectrum (600 MHz, D_2O, 25 °C) for compound **16**, Figure S11: ^{13}C NMR spectrum (125 MHz,

$CDCl_3$, 25 °C) for compound **3**, Figure S12: ^{13}C NMR spectrum (125 MHz, DMSO-d_6, 80 °C) for compound **5**, Figure S13: ^{13}C NMR spectrum (125 MHz, DMSO-d_6, 80 °C) for compound **6**, Figure S14: ^{13}C NMR spectrum (125 MHz, DMSO-d_6, 80 °C) for compound **7**, Figure S15: ^{13}C NMR spectrum (150 MHz, D_2O, 25 °C) for compound **8**, Figure S16: ^{13}C NMR spectrum (150 MHz, D_2O, 25 °C) for compound **9**, Figure S17: ^{13}C NMR spectrum (150 MHz, D_2O, 25 °C) for compound **10**, Figure S18: ^{13}C NMR spectrum (75 MHz, D_2O, 25 °C) for compound **14**, Figure S19: ^{13}C NMR spectrum (150 MHz, D_2O, 25 °C) for compound **15**, Figure S20: ^{31}P NMR spectrum (242.9 MHz, D_2O, 25°C) for compound **8**, Figure S21: ^{31}P NMR spectrum (242.9 MHz, D_2O, 25 °C) for compound **9**, Figure S22: ^{31}P NMR spectrum (242.9 MHz, D_2O, 25 °C) for compound **10**, Figure S23: ^{31}P NMR spectrum (242.9 MHz, D_2O, 25 °C) for compound **16**, Table S1: Determination of the number of phosphate groups for compounds **10**–**12** and **18**, Figure S24: XRPD patterns of uncoated nanoMOFs and nanoMOFs coated with CD-P, **8**–**10**, and **16**, Figure S25: DLS size measurements of uncoated nanoMOFs and nanoMOFs coated with CD-P, **8**-**10** and **16** after 6 h incubation in DMEM cell culture medium complemented with 10% FBS., Figure S26: PCDs derivatives grafting efficiency versus nanoMOFs:PCD mass ratio assayed, Table S2: ITC experiments for the interaction of **8**, **10**, nanoMOFs@**8**, and nanoMOFs@**10** with Concanavalin A, Figure S27: Titration of ConA with conjugates **8** and **10** in 20 mM phosphate buffer (pH 7.2) at 25 °C, and titration of conjugates nanoMOFs@**8** and nanoMOFs@**10** with ConA in 10 mM TRIS buffer (pH 7.5) at 25 °C, Figure S28: Enthalpy-entropy compensation for the interaction of **8**, **10**, nanoMOFs@**8**, and nanoMOFs@**10** with ConA lectin at 25 °C.

Author Contributions: Conceptualization, R.G. and A.V.-B.; methodology, R.G. and A.V.-B.; validation, J.M.C.-S., D.C., M.M., J.M.C.-F., and L.G.-F.; formal analysis, X.L. and J.M.C.-S.; investigation, G.C., X.L., J.M.C.-S., M.M.-M., J.Q., G.B., D.C., B.M.-A., J.M.C.-F., and L.G.-F.; data curation, J.M.C.-S.; writing—original draft preparation, G.C. and J.M.C.-S.; writing—review and editing, R.G. and A.V.-B.; supervision, R.G. and A.V.-B.; project administration, R.G. and A.V.-B.; funding acquisition, R.G. and A.V.-B.

Funding: Financial support for this work was provided by the European Union through FP7-PEOPLE-2013-ITN (http://itn-cyclonhit.eu) project (Grant Agreement no. 608407), the French National Research Agency (ANR-14-CE08-0017) and the Spanish Ministry of Economy and Competitiveness (Grants CTQ2017-90050-R and CTQ2016-79412-P). This work was also supported by a public grant overseen by the ANR as part of the "Investissements d'Avenir" program (Labex NanoSaclay, ANR-10-LABX-0035).

Acknowledgments: We are grateful to Ludivine Houel Renault for help with the cell culture facility in Centre Laser de l'Université Paris-Sud (CLUPS).

Conflicts of Interest: The authors declare no conflict of interest.

Abbreviations

β-CD	β-cyclodextrin
CD-P	β-cyclodextrin phosphate sodium salt
ConA	concanavalin A
DMAP	4-dimethylaminopyridine
DMEM	Dulbecco's modified Eagle's medium
DMF	dimethylformamide
DOX	doxorubicin
EtOAc	ethyl acetate
FBS	fetal bovine serum
HR-ICP-MS	high resolution inductively couples plasma mass spectrometry
ITC	isothermal titration calorimetry
MALDI-TOF-MS	matrix-assisted laser desorption/ionization time-of-flight mass spectrometry
MWCO	molecular weight cut-off
NaAsc	(+)-sodium L-ascorbate
nanoMOFs	nanosized metal-organic frameworks
PCDs	phosphorylated β-CD derivatives
PEG	polyethylene glycol
TEG	tetraethylene glycol
TEM	transmission electron microscopy
TLC	thin-layer chromatography
XRDP	X-ray diffraction patterns
ZP	zeta potential

References

1. Hoskins, B.F.; Robson, R. Infinite polymeric frameworks consisting of three dimensionally linked rod-like segments. *J. Am. Chem. Soc.* **1989**, *111*, 5962–5964. [CrossRef]
2. Rosi, N.L.; Eckert, J.; Eddaoudi, M.; Vodak, D.T.; Kim, J.; O'Keeffe, M.; Yaghi, O.M. Hydrogen storage in microporous metal-organic frameworks. *Science* **2003**, *300*, 1127–1129. [CrossRef] [PubMed]
3. Férey, G.; Serre, C.; Devic, T.; Maurin, G.; Jobic, H.; Llewellyn, P.L.; De Weireld, G.; Vimont, A.; Daturi, M.; Chang, J.-S. Why hybrid porous solids capture greenhouse gases? *Chem. Soc. Rev.* **2011**, *40*, 550–562. [CrossRef] [PubMed]
4. Dhakshinamoorthy, A.; Garcia, H. Catalysis by metal nanoparticles embedded on metal-organic frameworks. *Chem. Soc. Rev.* **2012**, *41*, 5262–5284. [CrossRef] [PubMed]
5. Zhou, H.-C.; Kitagawa, S. Metal-organic frameworks (MOFs). *Chem. Soc. Rev.* **2014**, *43*, 5415–5418. [CrossRef] [PubMed]
6. Wuttke, S.; Braig, S.; Preiß, T.; Zimpel, A.; Sicklinger, J.; Bellomo, C.; Rädler, J.O.; Vollmar, A.M.; Bein, T. MOF nanoparticles coated by lipid bilayers and their uptake by cancer cells. *Chem. Commun.* **2015**, *51*, 15752–15755. [CrossRef] [PubMed]
7. Parmar, B.; Patel, P.; Kureshy, R.I.; Khan, N.H.; Suresh, E. Sustainable heterogeneous catalysts for CO_2 utilization by using dual ligand Zn^{II}/Cd^{II} metal–organic frameworks. *Chem. Eur. J.* **2018**, *24*, 1–10. [CrossRef] [PubMed]
8. Llewellyn, P.L.; Bourrelly, S.; Serre, C.; Vimont, A.; Daturi, M.; Hamon, L.; De Weireld, G.; Chang, J.-S.; Hong, D.-Y.; Hwang, Y.K. High uptakes of CO_2 and CH_4 in mesoporous metal-organic frameworks MIL-100 and MIL-101. *Langmuir* **2008**, *24*, 7245–7250. [CrossRef] [PubMed]
9. Horcajada, P.; Chalati, T.; Serre, C.; Gillet, B.; Sebrie, C.; Baati, T.; Eubank, J.F.; Heurtaux, D.; Clayette, P.; Kreuz, C.; et al. Porous metal–organic-framework nanoscale carriers as a potential platform for drug delivery and imaging. *Nat. Mater.* **2010**, *9*, 172–178. [CrossRef]
10. Agostoni, V.; Chalati, T.; Horcajada, P.; Willaime, H.; Anand, R.; Semiramoth, N.; Baati, T.; Hall, S.; Maurin, G.; Chacun, H. Towards an improved anti-HIV activity of NRTI via metal-organic frameworks nanoparticles. *Adv. Healthc. Mater.* **2013**, *2*, 1630–1637. [CrossRef]
11. Simon-Yarza, T.; Giménez-Marqués, M.; Mrimi, R.; Mielcarek, A.; Gref, R.; Horcajada, P.; Serre, C.; Couvreur, P. A smart metal-organic framework nanomaterial for lung targeting. *Angew. Chem. Int. Ed.* **2017**, *56*, 15565–15569. [CrossRef] [PubMed]
12. Simon-Yarza, M.T.; Baati, T.; Paci, A.; Lesueur, L.L.; Seck, A.; Chiper, M.; Gref, R.; Serre, C.; Couvreur, P.; Horcajada, P. Antineoplastic busulfan encapsulated in metal organic framework nanocarrier: First in vivo results. *J. Mater. Chem. B* **2016**, *4*, 585–588. [CrossRef]
13. Li, H.; Lv, N.; Li, X.; Botao, L.; Feng, J.; Ren, X.; Guo, T.; Chen, D.; Stoddart, J.F.; Gref, R.; et al. Composite CD-MOF nanocrystals-containing microsphere for sustained drug delivery. *Nanoscale* **2017**, *9*, 7454–7463. [CrossRef] [PubMed]
14. Rojas, S.; Colinet, I.; Cunha, D.; Hidalgo, T.; Salles, F.; Serre, C.; Guillou, N.; Horcajada, P. Toward understanding drug incorporation and delivery from biocompatible metal-organic frameworks in view of cutaneous administration. *ACS Omega* **2018**, *3*, 2994–3003. [CrossRef] [PubMed]
15. Agostoni, V.; Horcajada, P.; Noiray, N.; Malanga, M.; Aykaç, A.; Jicsinszky, L.; Vargas-Berenguel, A.; Semiramoth, N.; Daoud-Mahammed, S.; Nicolas, V.; et al. A "green" strategy to construct non-covalent, stable and bioactive coatings on porous MOF nanoparticles. *Sci. Rep.* **2015**, *5*, 7925. [CrossRef] [PubMed]
16. Baati, T.; Njim, L.; Neffati, F.; Kerkeni, A.; Bouttemi, M.; Gref, R.; Fadhel Najjar, M.; Zakhama, A.; Couvreur, P.; Serre, C.; et al. In depth analysis of the in vivo toxicity of nanoparticles of porous iron(III) metal–organic frameworks. *Chem. Sci.* **2013**, *4*, 1597–1607. [CrossRef]
17. Aykaç, A.; Noiray, M.; Malanga, M.; Agostoni, V.; Casas-Solvas, J.M.; Fenyvesi, É.; Gref, R.; Vargas-Berenguel, A. A non-covalent "click chemistry" strategy to efficiently coat highly porous MOF nanoparticles with a stable polymeric shell. *Biochim. Biophys. Acta* **2017**, *1861*, 1606–1616. [CrossRef] [PubMed]
18. Pavlov, G.M.; Korneeva, E.V.; Smolina, N.A.; Schubert, U.S. Hydrodynamic properties of cyclodextrin molecules in dilute solutions. *Eur. Biophys. J.* **2010**, *39*, 371–379. [CrossRef] [PubMed]

19. Nguyen, V.H.; Lee, B.-J. Protein corona: A new approach for nanomedicine design. *Int. J. Nanomed.* **2017**, *12*, 3137–3151. [CrossRef]
20. Gref, R.; Minamitake, Y.; Peracchia, M.T.; Trubetskoy, V.; Torchilin, V.; Langer, R. Biodegradable long-circulating polymeric nanospheres. *Science* **1994**, *263*, 1600–1603. [CrossRef]
21. Gimenez-Marques, M.; Bellido, E.; Berthelot, T.; Simon-Yarza, T.; Hidalgo, T.; Simon-Vazquez, R.; Gonzalez-Fernandez, A.; Avila, J.; Asensio, M.C.; Gref, R.; et al. GraftFast surface engineering to improve MOF nanoparticles furtiveness. *Small* **2018**, *14*, 1801900–1801911. [CrossRef] [PubMed]
22. Casas-Solvas, J.M.; Vargas-Berenguel, A. Glycoclusters and their applications as anti-infective agents, vaccines, and targeted drug delivery systems. In *Carbohydrate Nanotechnology*; Stine, K.J., Ed.; John Wiley & Sons, Inc.: Hoboken, NJ, USA, 2016; Chapter 7, pp. 175–210. [CrossRef]
23. Kang, B.; Opatz, T.; Landfester, K.; Wurm, F.R. Carbohydrate nanocarriers in biomedical applications: Functionalization and construction. *Chem. Soc. Rev.* **2015**, *44*, 8301–8325. [CrossRef] [PubMed]
24. Liu, W.; Chaix, A.; Gary-Bobo, M.; Angeletti, B.; Masion, A.; Da Silva, A.; Daurat, M.; Lichon, L.; Garcia, M.; Morère, A.; et al. Stealth biocompatible Si-based nanoparticles for niomedical applications. *Nanomaterials* **2017**, *7*, 288. [CrossRef] [PubMed]
25. Kang, B.; Okwieka, P.; Schöttler, S.; Winzen, S.; Langhanki, J.; Mohr, K.; Opatz, T.; Mailänder, V.; Landfester, K.; Wurm, F.R. Carbohydrate-based nanocarriers exhibiting specific cell targeting with minimum influence from the protein corona. *Angew. Chem. Int. Ed.* **2015**, *54*, 7436–7440. [CrossRef] [PubMed]
26. Lis, H.; Sharon, N. Lectins: Carbohydrate-specific proteins that mediate cellular recognition. *Chem. Rev.* **1998**, *98*, 637–674. [CrossRef] [PubMed]
27. Lee, R.T.; Lee, Y.C. Affinity enhancement by multivalent lectin–carbohydrate interaction. *Glycoconj. J.* **2000**, *17*, 543–551. [CrossRef] [PubMed]
28. Hao, H.; Neranon, K.; Ramström, O.; Yan, M. Glyconanomaterials for biosensing applications. *Biosens. Bioelectron.* **2016**, *76*, 113–130. [CrossRef]
29. Reina, J.J.; Rojo, J. Carbohydrate multivalent systems: Synthesis and therapeutic opportunities. In *Carbohydrate Chemistry: State of the Art and Challenges for Drug Development*; Cipolla, L., Ed.; Imperial College Press: London, UK, 2015; pp. 419–439, Chapter 17. [CrossRef]
30. Swierzko, A.S.; Kilpatrick, D.C.; Cedzynski, M. Mannan-binding lectin in malignancy. *Mol. Immunol.* **2013**, *55*, 16–21. [CrossRef]
31. Wdowiak, K.; Francuz, T.; Gallego-Colon, E.; Ruiz-Agamez, N.; Kubeczko, M.; Grochoła, I.; Wojnar, J. Galectin targeted therapy in oncology: Current knowledge and perspectives. *Int. J. Mol. Sci.* **2018**, *19*, 210. [CrossRef]
32. Cutrone, G.; Casas-Solvas, J.M.; Vargas-Berenguel, A. Cyclodextrin-modified inorganic materials for the construction of nanocarriers. *Int. J. Pharm.* **2017**, *531*, 621–639. [CrossRef]
33. Zhang, X.; Huang, G.; Huang, H. The glyconanoparticle as carrier for drug delivery. *Drug Deliv.* **2018**, *25*, 1840–1845. [CrossRef] [PubMed]
34. Scharenberg, M.; Schwardt, O.; Rabbani, S.; Ernst, B. Target selectivity of FimH antagonists. *J. Med. Chem.* **2012**, *55*, 9810–9816. [CrossRef] [PubMed]
35. Azad, A.K.; Rajaram, M.V.S.; Schlesinger, L.S. Exploitation of the macrophage mannose receptor (CD206) in infectious disease diagnostics and therapeutics. *J. Cytol. Mol. Biol.* **2014**, *1*, 1000003. [CrossRef] [PubMed]
36. Ladaviere, C.; Gref, R. Toward an optimized treatment of intracellular bacterial infections: Input of nanoparticulate drug delivery systems. *Nanomedicine* **2015**, *10*, 3033–3055. [CrossRef] [PubMed]
37. Rouzes, C.; Gref, R.; Leonard, M.; De Sousa Delgado, A.; Dellacherie, E. Surface modification of poly(lactic acid) nanospheres using hydrophobically modified dextrans as stabilizers in an o/w emulsion/evaporation technique. *J. Biomed. Mater. Res.* **2000**, *50*, 557–565. [CrossRef]
38. Warther, D.; Jimenez, C.M.; Raehm, L.; Gérardin, C.; Durand, J.-O.; Morère, A.; El Cheikh, K.; Gallud, A.; Gary-Bobo, M.; Maynadier, M. Small sized mesoporous silica nanoparticles functionalized with mannose for retinoblastoma cell imaging. *RSC Adv.* **2014**, *4*, 37171–37179. [CrossRef]
39. Chaix, A.; El Cheikh, K.; Bouffard, E.; Maynadier, M.; Aggad, D.; Stojanovic, V.; Knezevic, N.; Garcia, M.; Maillard, P.; Morère, A.; et al. Mesoporous silicon nanoparticles for targeted two-photon theranostics of prostate cancer. *J. Mater. Chem. B* **2016**, *4*, 3639–3642. [CrossRef]
40. Müller, C.; Despras, G.; Lindhorst, T.K. Organizing multivalency in carbohydrate recognition. *Chem. Soc. Rev.* **2016**, *45*, 3275–3302. [CrossRef]

41. Poláková, M.; Beláňová, M.; Mikušová, K.; Lattová, E.; Perreault, H. Synthesis of 1,2,3-triazolo-linked octyl (1→6)-α-D-oligomannosides and their evaluation in mycobacterial mannosyltransferase assay. *Bioconj. Chem.* **2011**, *22*, 289–298. [CrossRef]
42. Zhao, J.; Liu, Y.; Park, H.-J.; Boggs, J.M.; Basu, A. Carbohydrate-coated fluorescent silica nanoparticles as probes for the galactose/3-sulfogalactose carbohydrate-carbohydrate interaction using model systems and cellular binding studies. *Bioconj. Chem.* **2012**, *23*, 1166–1173. [CrossRef]
43. van der Peet, P.; Gannon, C.T.; Walker, I.; Dinev, Z.; Angelin, M.; Tam, S.; Ralton, J.E.; McConville, M.J.; Williams, S.J. Use of click chemistry to define the substrate specificity of Leishmania β-1,2-mannosyltransferases. *ChemBioChem* **2006**, *7*, 1384–1391. [CrossRef] [PubMed]
44. Sung, S.R.; Han, S.C.; Jin, S.; Lee, J.W. Convergent synthesis and characterization of dumbbell type dendritic materials by click chemistry. *Bull. Korean Chem. Soc.* **2011**, *32*, 3933–3940. [CrossRef]
45. Park, K.D.; Morieux, P.; Salomé, C.; Cotten, S.W.; Reamtong, O.; Eyers, C.; Gaskell, S.J.; Stables, J.P.; Liu, R.; Kohn, H. Lacosamide isothiocyanate-based agents: Novel agents to target and identify lacosamide receptors. *J. Med. Chem.* **2009**, *52*, 6897–6911. [CrossRef] [PubMed]
46. Polito, L.; Monti, D.; Caneva, E.; Delnevo, E.; Russo, G.; Prosperi, D. One-step bioengineering of magnetic nanoparticles via a surface diazo transfer/azide-alkyne click reaction sequence. *Chem. Commun.* **2008**, 621–623. [CrossRef] [PubMed]
47. Ward, S.; Ling, C.-C. Efficient and versatile modification of the secondary face of cyclodextrins through copper-catalyzed Huisgen 1,3-dipolar cycloaddition. *Eur. J. Org. Chem.* **2011**, *2011*, 4853–4861. [CrossRef]
48. Perrin, D.D.; Armarego, W.F.L. *Purification of Laboratory Chemicals*, 3rd ed.; Pergamon: Oxford, UK, 1989.
49. Fügedi, P. Synthesis of heptakis (6-*O*-*tert*-butyldimethylsilyl) cyclomaltoheptaose and octakis (6-*O*-*tert*-butyldimethylsilyl) cyclomaltooctaose. *Carbohydr. Res.* **1989**, *192*, 366–369. [CrossRef]
50. Casas-Solvas, J.M.; Ortiz-Salmerón, E.; García-Fuentes, L.; Vargas-Berenguel, A. Ferrocene–mannose conjugates as electrochemical molecular sensors for concanavalin A lectin. *Org. Biomol. Chem.* **2008**, *6*, 4230–4235. [CrossRef] [PubMed]
51. Ortega-Muñoz, M.; Morales-Sanfrutos, J.; Perez-Balderas, F.; Hernandez-Mateo, F.; Giron-Gonzalez, M.D.; Sevillano-Tripero, N.; Salto-Gonzalez, R.; Santoyo-Gonzalez, F. Click multivalent neoglycoconjugates as synthetic activators in cell adhesion and stimulation of monocyte/machrophage cell lines. *Org. Biomol. Chem.* **2007**, *5*, 2291–2301. [CrossRef]
52. Martínez, Á.; Ortiz Mellet, C.; García Fernández, J.M. Cyclodextrin-based multivalent glycodisplays: Covalent and supramolecular conjugates to assess carbohydrate–protein interactions. *Chem. Soc. Rev.* **2013**, *42*, 4746–4773. [CrossRef]
53. Gallego-Yerga, L.; Benito, J.M.; Blanco-Fernández, L.; Martínez-Negro, M.; Vélaz, I.; Aicart, E.; Junquera, E.; Ortiz Mellet, C.; Tros de Ilarduya, C.; García Fernández, J.M. Plasmid-templated control of DNA–cyclodextrin nanoparticle morphology through molecular vector design for effective gene delivery. *Chem. Eur. J.* **2018**, *24*, 3825–3835. [CrossRef]
54. Twyman, R.M. NMR spectroscopy-applicable elements/phosphorous-31. In *Encyclopedia of Analytical Science*, 2nd ed.; Worsfold, P., Townshend, A., Poole, C., Eds.; Elsevier: Oxford, UK, 2005; Volume 6, pp. 278–286. [CrossRef]
55. Semple, J.E.; Sullivan, B.; Vojkovsky, T.; Sill, K.N. Synthesis and facile end-group quantification of functionalized PEG azides. *J. Polym. Sci. Part A Polym. Chem.* **2016**, *54*, 2888–2895. [CrossRef] [PubMed]
56. Díaz-Moscoso, A.; Guilloteau, N.; Bienvenu, C.; Méndez-Ardoy, A.; Jiménez Blanco, J.L.; Benito, J.M.; Le Gourriérec, L.; Di Giorgio, C.; Vierling, P.; Defaye, J.; et al. Mannosyl-coated nanocomplexes from amphiphilic cyclodextrins and pDNA for site-specific gene delivery. *Biomaterials* **2011**, *32*, 7263–7273. [CrossRef] [PubMed]
57. François-Heude, M.; Méndez-Ardoy, A.; Cendret, V.; Lafite, P.; Daniellou, R.; Ortiz Mellet, C.; García Fernández, J.M.; Moreau, V.; Djedaïni-Pilard, F. Synthesis of high-mannose oligosaccharide analogues through click chemistry: True functional mimics of their natural counterparts against lectins? *Chem. Eur. J.* **2015**, *21*, 1978–1991. [CrossRef] [PubMed]
58. Cutrone, G.; Benkovics, G.; Malanga, M.; Casas-Solvas, J.M.; Fenyvesi, É.; Sortino, S.; García-Fuentes, L.; Vargas-Berenguel, A. Mannoside and 1,2-mannobioside β-cyclodextrin-scaffolded NO-photodonors for targeting antibiotic resistant bacteria. *Carbohydr. Polym.* **2018**, *199*, 649–660. [CrossRef] [PubMed]

59. Baussanne, I.; Benito, J.M.; Ortiz Mellet, C.; García Fernández, J.M.; Defaye, J. Dependence of concanavalin A binding on anomeric configuration, linkage type, and ligand multiplicity for thiourea-bridged mannopyranosyl–β-cyclodextrin conjugates. *ChemBioChem* **2001**, *2*, 777–783. [CrossRef]
60. Smiljanic, N.; Moreau, V.; Yockot, D.; Benito, J.M.; García Fernández, J.M.; Djedaïni-Pilard, F. Supramolecular control of oligosaccharide–protein interactions: Switchable and tunable ligands for concanavalin A based on β-cyclodextrin. *Angew. Chem. Int. Ed.* **2006**, *45*, 5465–5468. [CrossRef] [PubMed]
61. Dam, T.K.; Brewer, C.F. Thermodynamic studies of lectin-carbohydrate interactions by isothermal titration calorimetry. *Chem. Rev.* **2002**, *102*, 387–430. [CrossRef]
62. Wang, X.; Matei, E.; Gronenborn, A.M.; Ramström, O.; Yan, M. Direct measurement of glyconanoparticles and lectin interactions by isothermal titration calorimetry. *Anal. Chem.* **2012**, *84*, 4248–4252. [CrossRef]
63. Mangold, S.L.; Cloninger, M.J. Binding of monomeric and dimeric Concanavalin A to mannose-functionalized dendrimers. *Org. Biomol. Chem.* **2006**, *4*, 2458–2465. [CrossRef]
64. Li, X.; Semiramoth, N.; Hall, S.; Tafani, V.; Josse, J.; Laurent, F.; Salzano, G.; Foulkes, D.; Brodin, P.; Majlessi, L.; et al. Compartmentalized encapsulation of two antibiotics in porous nanoparticles: An efficient strategy to treat intracellular infections. *Part. Part. Syst. Char.* **2019**, *36*, 1800360–1800369. [CrossRef]
65. Gref, R.; Lu, M.; Quellec, P.; Marchand, M.; Dellacheriec, E.; Harnisch, S.; Blunk, T.; Muller, R.H. 'Stealth' corona-core nanoparticles surface modified by polyethylene glycol (PEG): Influences of the corona (PEG chain length and surface density) and of the core composition on phagocytic uptake and plasma protein adsorption. *Coll. Surf. B Biointerfaces* **2000**, *18*, 301–313. [CrossRef]
66. Pei, Y.; Yeo, Y. Drug delivery to macrophages: Challeges and opportunities. *J. Control. Release* **2016**, *240*, 202–211. [CrossRef] [PubMed]
67. Schottler, S.; Becker, G.; Winzen, S.; Steinbach, T.; Mohr, K.; Landfester, K.; Mailander, V.; Wurm, F.R. Protein adsorption is required for stealth effect of poly(ethylene glycol)-and poly(phosphoester)-coated nanocarriers. *Nat. Nanotechnol.* **2016**, *11*, 372–377. [CrossRef] [PubMed]
68. Wu, L.; Zhang, Y.; Li, Z.; Yang, G.; Kochovski, Z.; Chen, G.; Jiang, M. "Sweet" architecture-dependent uptake of glycocalyx-mimicking nanoparticles based on biodegradable aliphatic polyesters by macrophages. *J. Am. Chem. Soc.* **2017**, *139*, 14684–14692. [CrossRef] [PubMed]
69. Vieira, A.C.C.; Chaves, L.L.; Pinheiro, M.; Costa Lima, S.A.; Ferreira, D.; Sarmento, B.; Reis, S. Mannosylated solid lipid nanoparticles for the selective delivery of rifampicin to macrophages. *Artif. Cells Nanomed. Biotechnol.* **2019**, *46* (Suppl. 1), 653–663. [CrossRef] [PubMed]
70. Shibaguchi, K.; Tamura, A.; Terauchi, M.; Matsumura, M.; Miura, H.; Yui, N. Mannosylated polyrotaxanes for increasing cellular uptake efficiency in macrophages through receptor-mediated endocytosis. *Molecules* **2019**, *24*, 439. [CrossRef] [PubMed]
71. Moros, M.; Hernáez, B.; Garet, E.; Dias, J.T.; Sáez, B.; Grazú, V.; González-Fernández, Á.; Alonso, C.; de la Fuente, J.M. Monosaccharides versus PEG-functionalized NPs: Influence in the celular uptake. *ACS Nano* **2012**, *6*, 1565–1577. [CrossRef]
72. Anand, R.; Borghi, F.; Manoli, F.; Manet, I.; Agostoni, V.; Reschiglian, P.; Gref, R.; Monti, S. Host–guest interactions in Fe(III)-trimesate MOF nanoparticles loaded with doxorubicin. *J. Phys. Chem. B* **2014**, *118*, 8532–8539. [CrossRef]

Design of Engineered Cyclodextrin Derivatives for Spontaneous Coating of Highly Porous Metal-Organic Framework Nanoparticles in Aqueous Media

Giovanna Cutrone [1], Xue Li [2], Juan M. Casas-Solvas [1], Mario Menendez-Miranda [2], Jingwen Qiu [2], Gabor Benkovics [3], Doru Constantin [4], Milo Malanga [3], Borja Moreira-Alvarez [5], José M. Costa-Fernández [5], Luis García-Fuentes [1], Ruxandra Gref [2,*] and Antonio Vargas-Berenguel [1,*]

[1] Department of Chemistry and Physics, University of Almería, Crta. de Sacramento s/n, E-04120, Almería, Spain

[2] Institut des Sciences Moléculaires d'Orsay, UMR CNRS 8214, Université Paris-Sud, Université Paris Saclay, 91400 Orsay, France

[3] CycloLab R&D Ltd, Illatos út 7, Budapest, H-1097, Hungary

[4] Laboratoire de Physique des Solides, UMR 8502, Université Paris-Sud, 91405 Orsay, France

[5] Department of Physical and Analytical Chemistry, University of Oviedo, Julián Clavería 8, 33006 Oviedo, Spain

* Corresponding author. E-mail address: ruxandra.gref@u-psud.fr (R. Gref); avargas@ual.es (A. Vargas-Berenguel)

Supplementary Materials

Table of Contents

I. ^{1}H-NMR spectra for compounds 3, 5-10 and 14-16

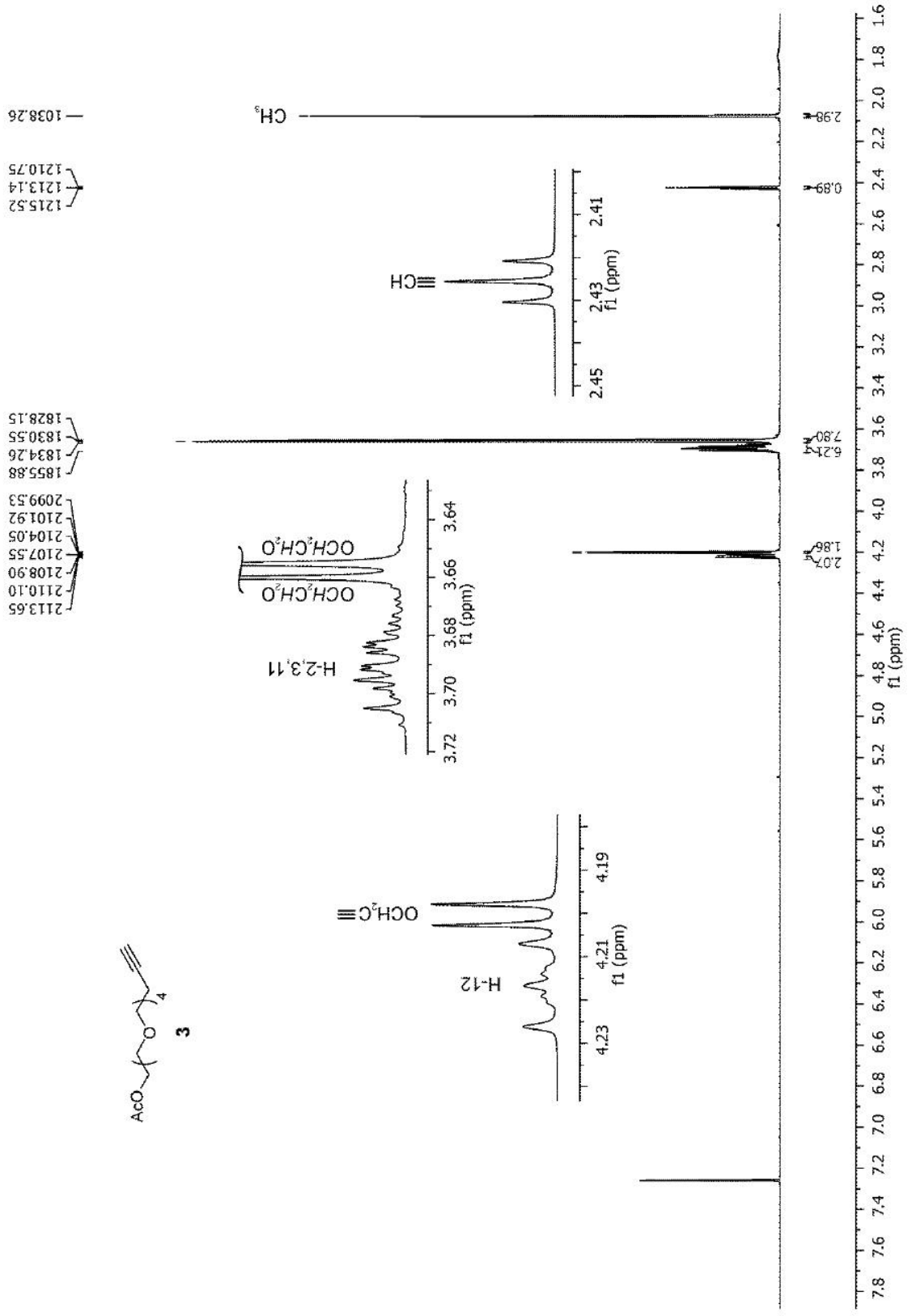

Figure S1. ^{1}H NMR spectrum (500 MHz, $CDCl_3$, 25 °C) for compound **3**

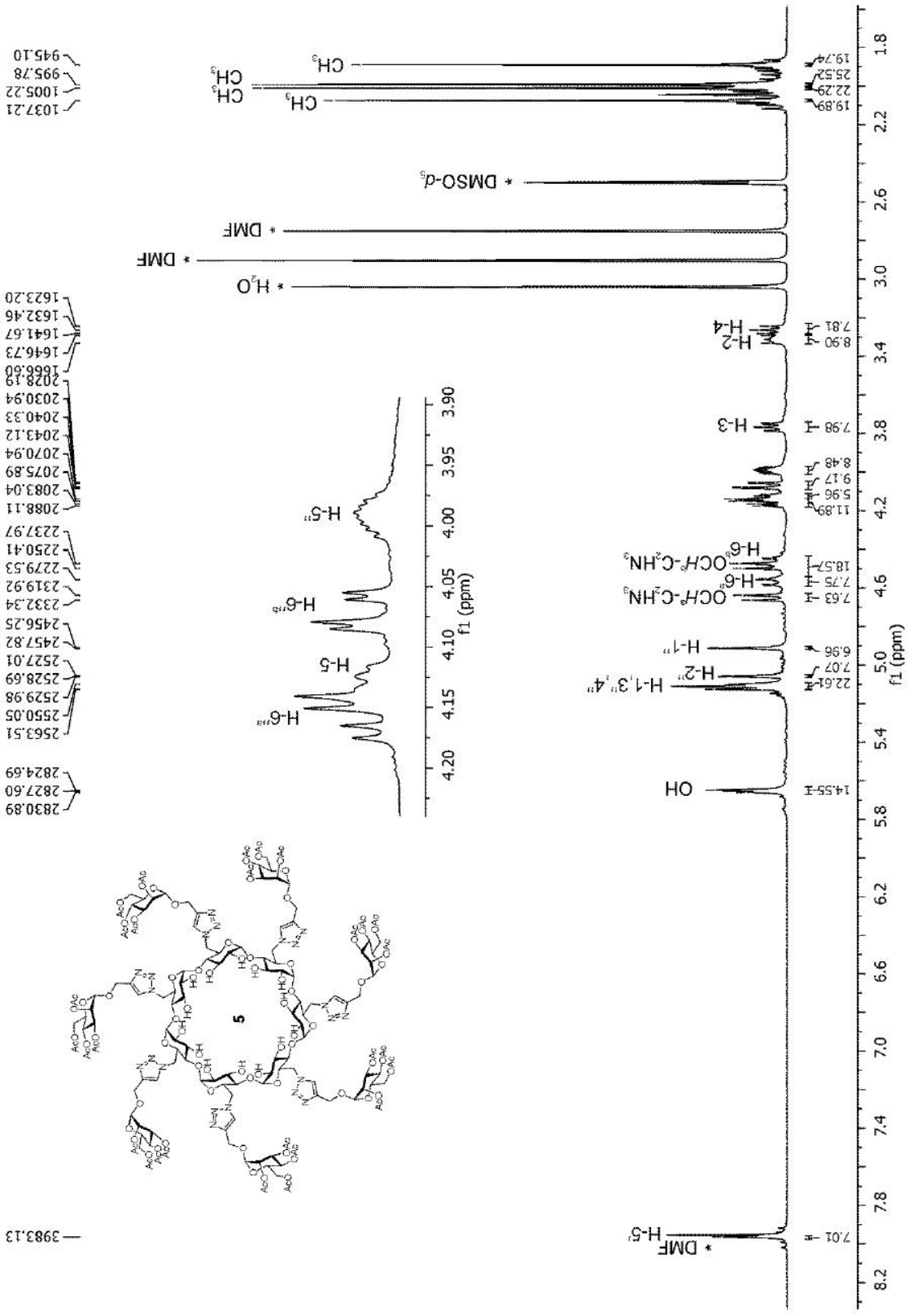

Figure S2. ^{1}H NMR spectrum (500 MHz, DMSO-d_6, 80 °C) for compound **5**

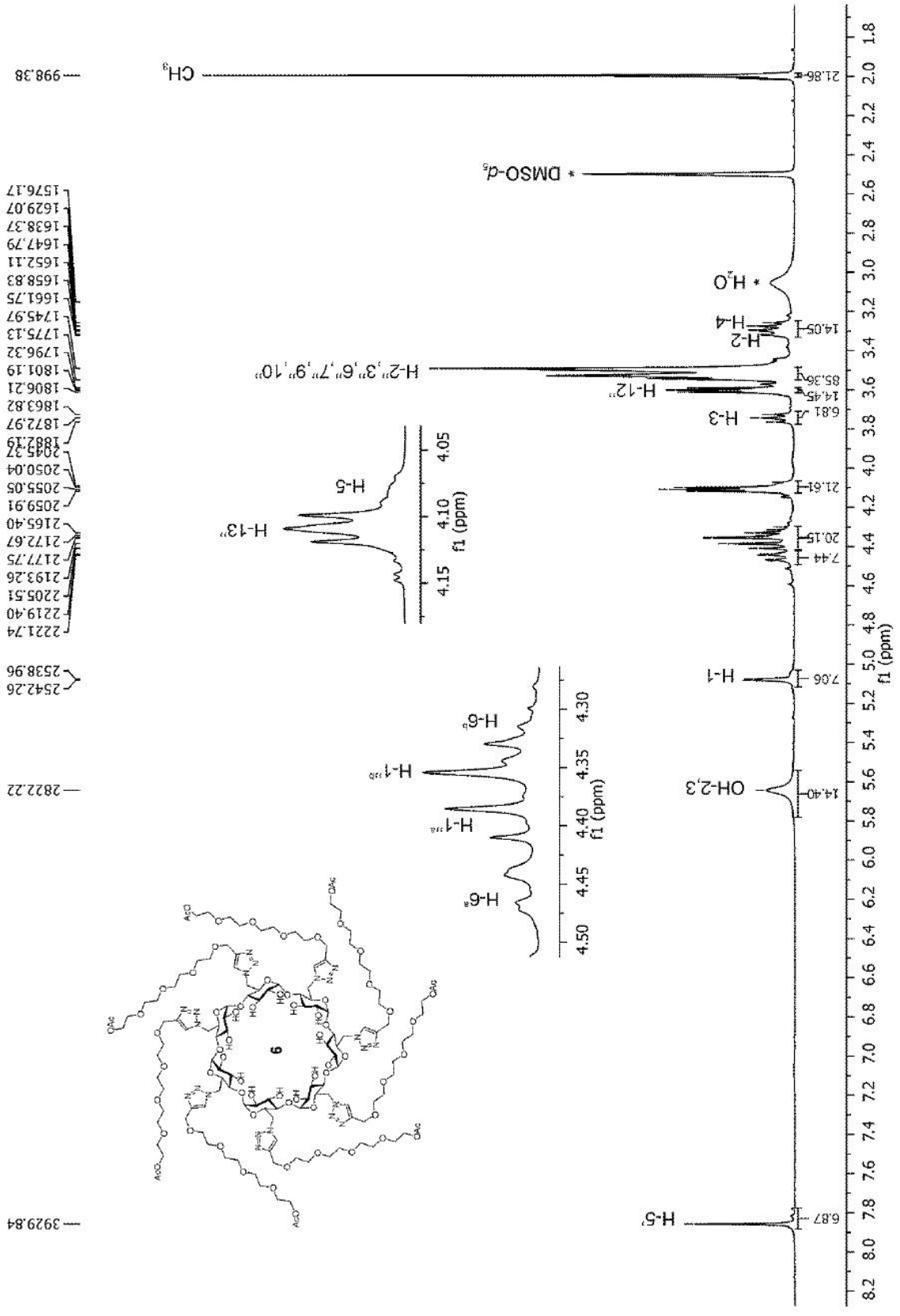

Figure S3. ^{1}H NMR spectrum (500 MHz, DMSO-d_6, 80 °C) for compound **6**

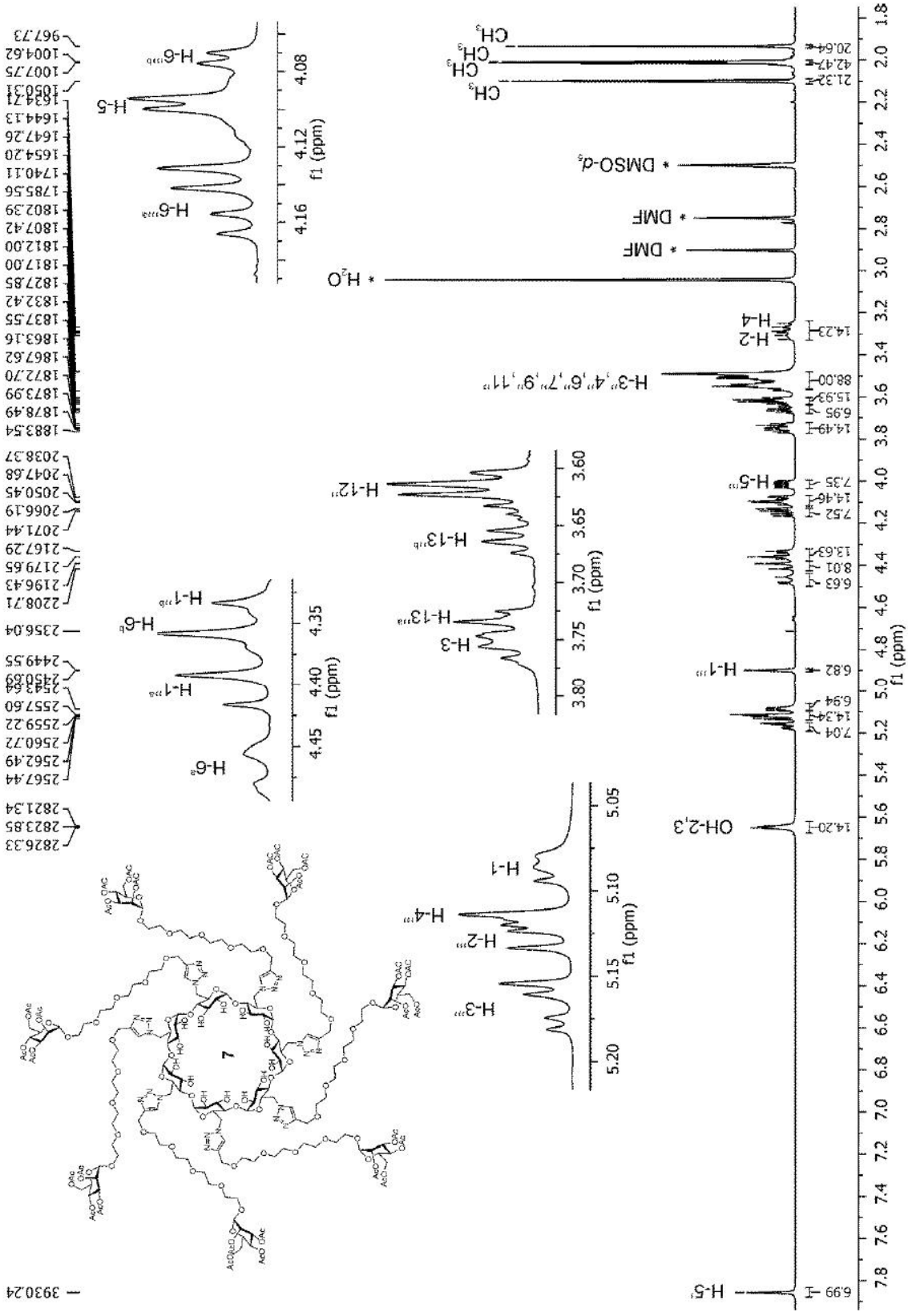

Figure S4. ^{1}H NMR spectrum (500 MHz, DMSO-d_6, 80 ºC) for compound **7**

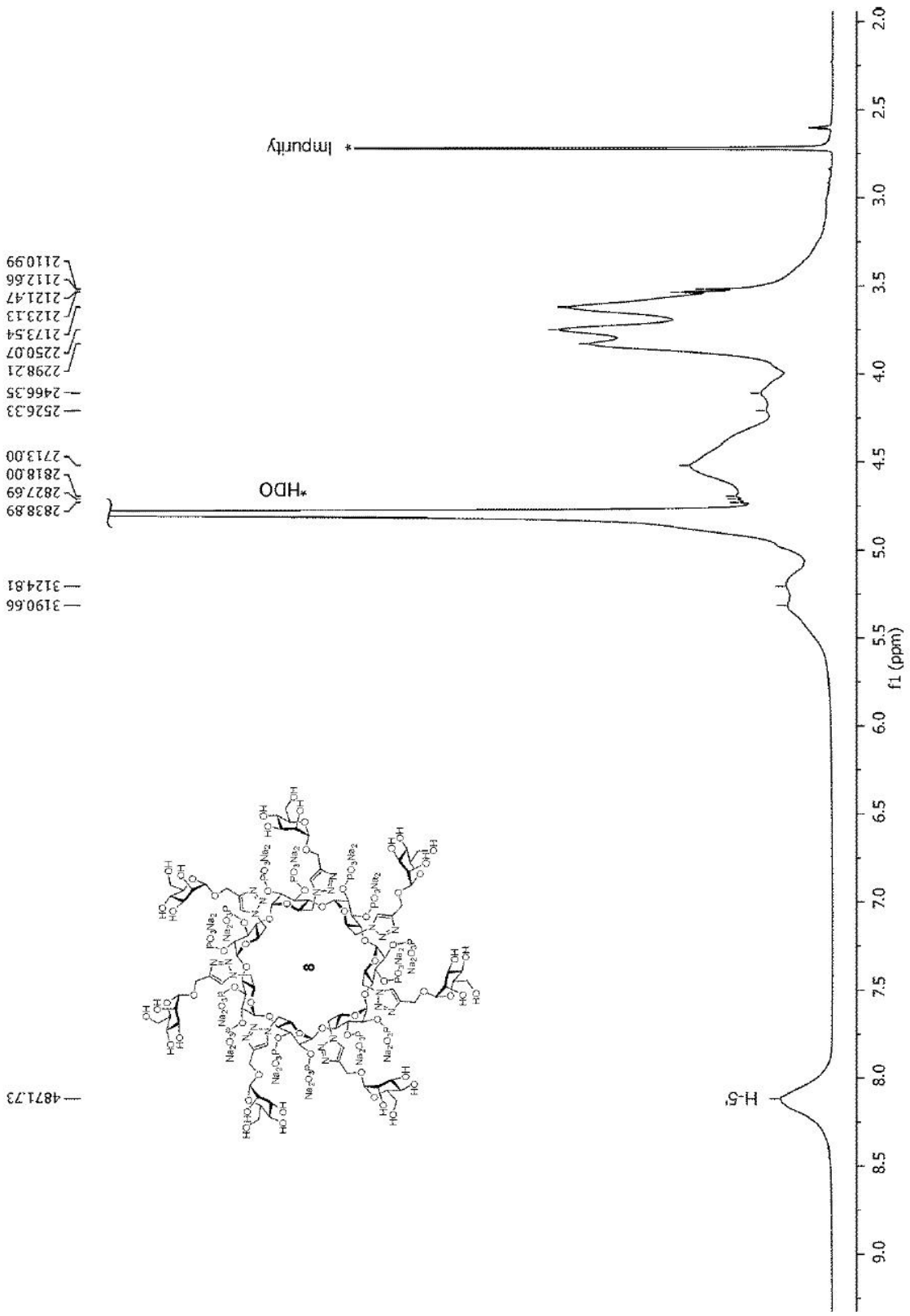

Figure S5. ^{1}H NMR spectrum (600 MHz, D_2O, 25 °C) for compound **8**

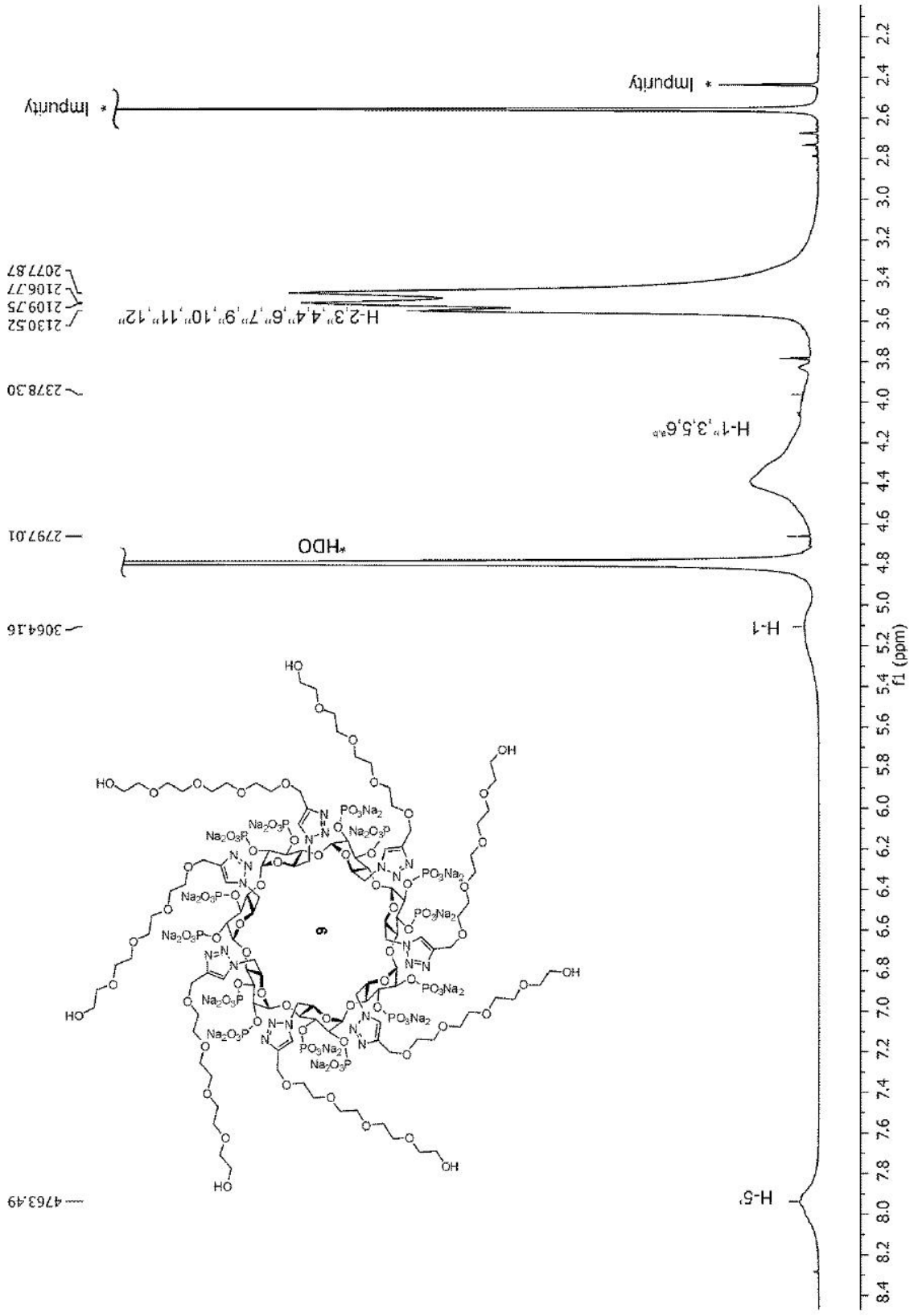

Figure S6. ^{1}H NMR spectrum (600 MHz, D_2O, 25 ºC) for compound **9**

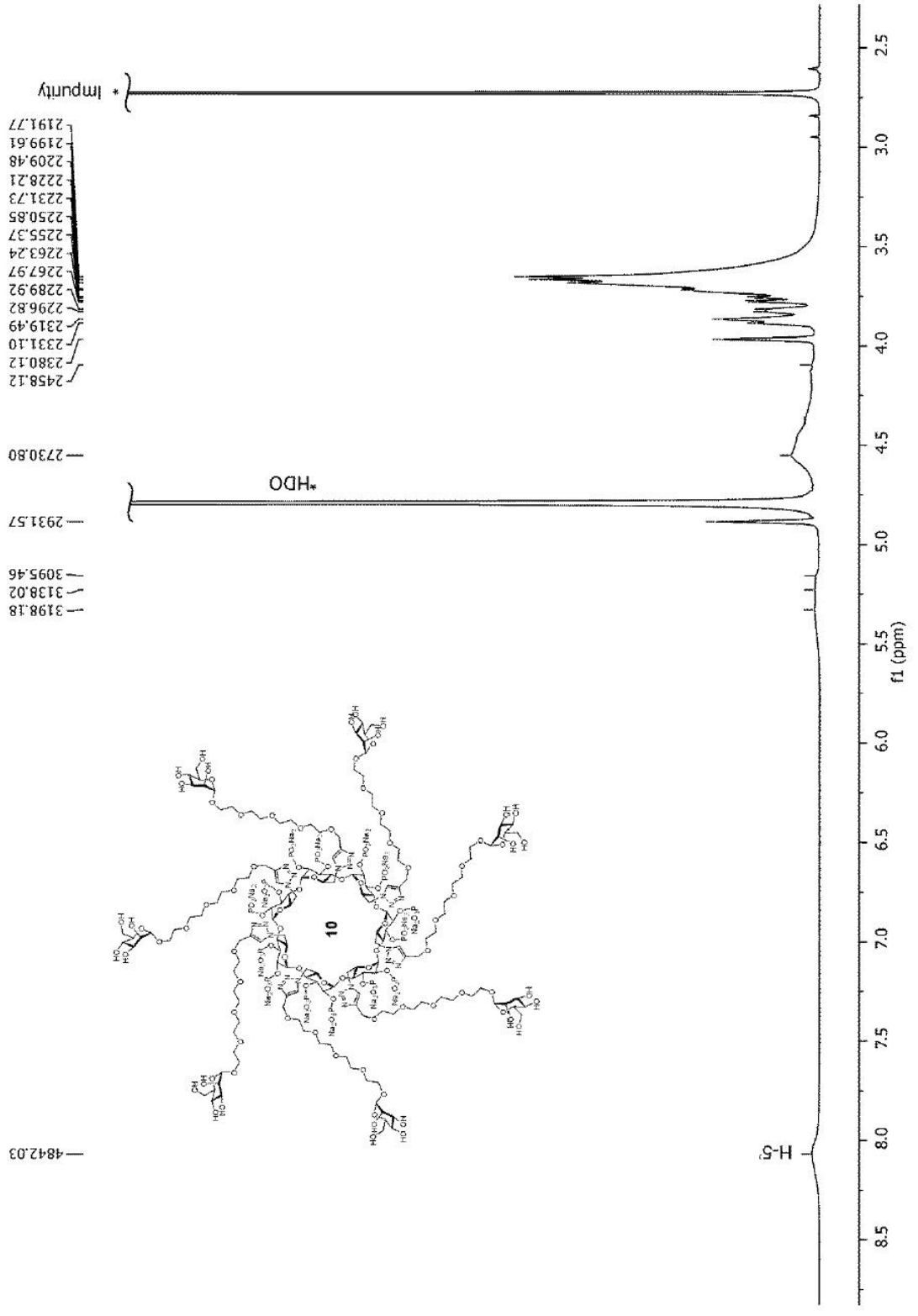

Figure S7. ^{1}H NMR spectrum (600 MHz, D_2O, 25 °C) for compound **10**

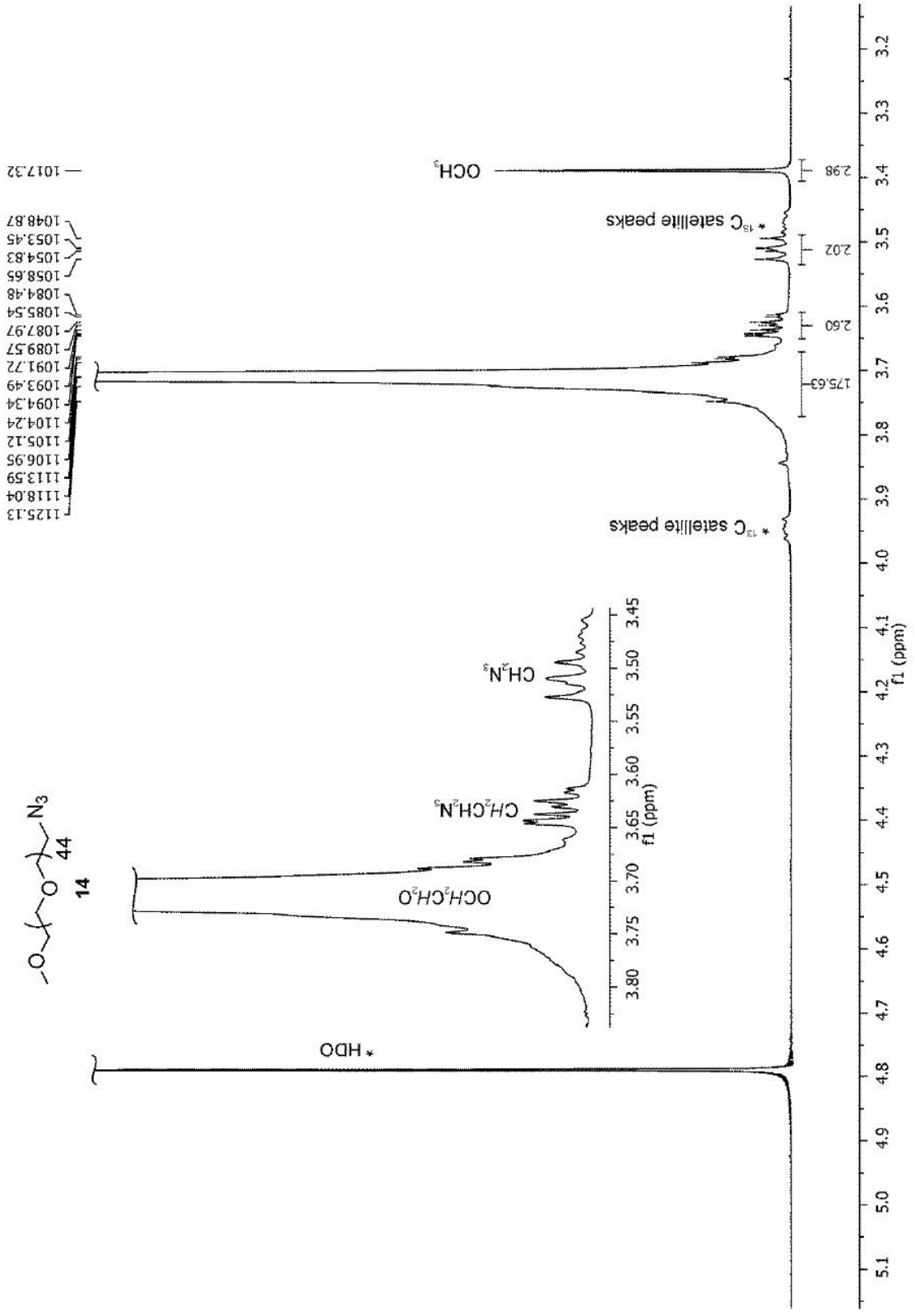

Figure S8. ^{1}H NMR spectrum (300 MHz, D_2O, 25 ºC) for compound **14**

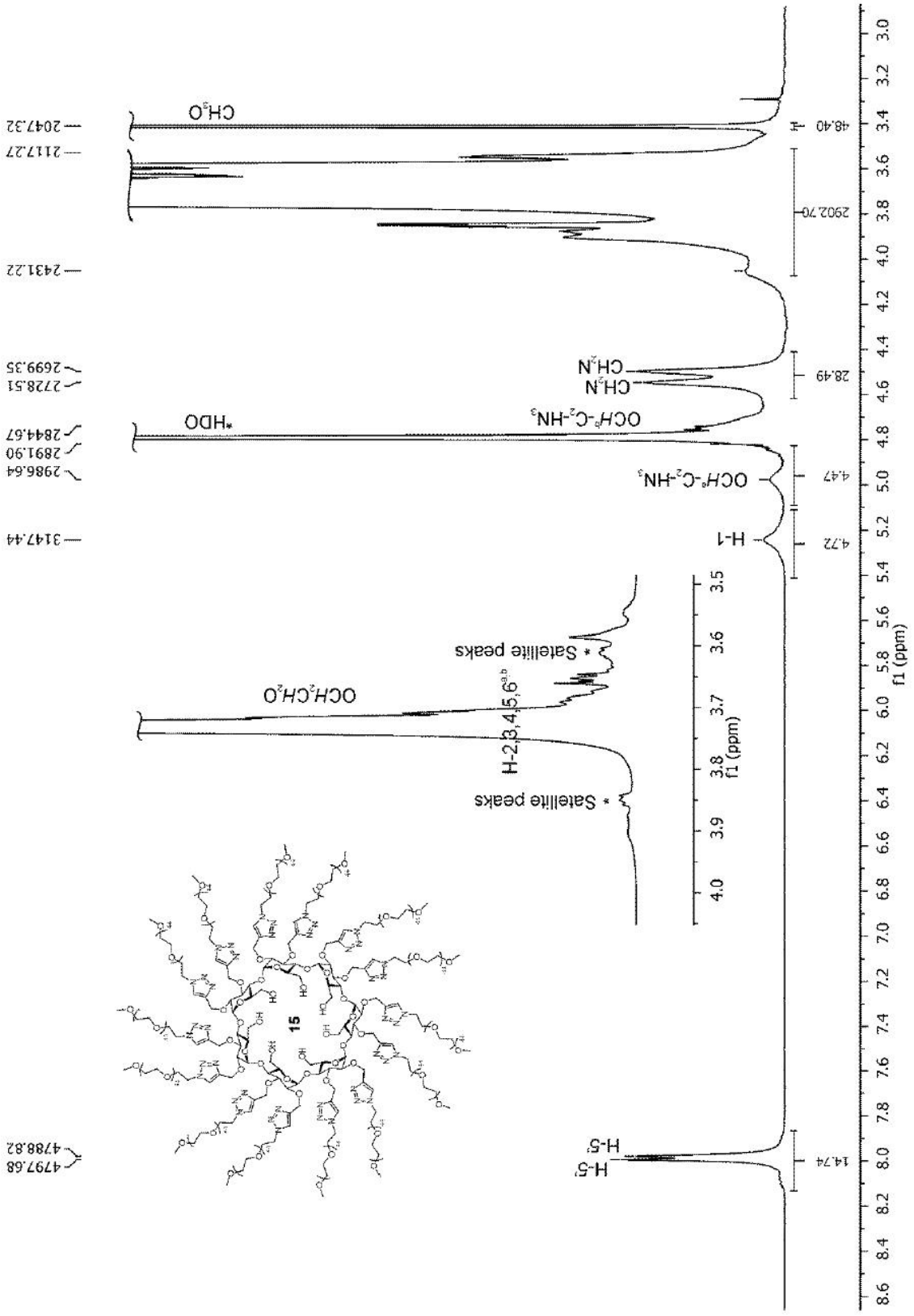

Figure S9. ^{1}H NMR spectrum (600 MHz, D_2O, 25 ºC) for compound **15**

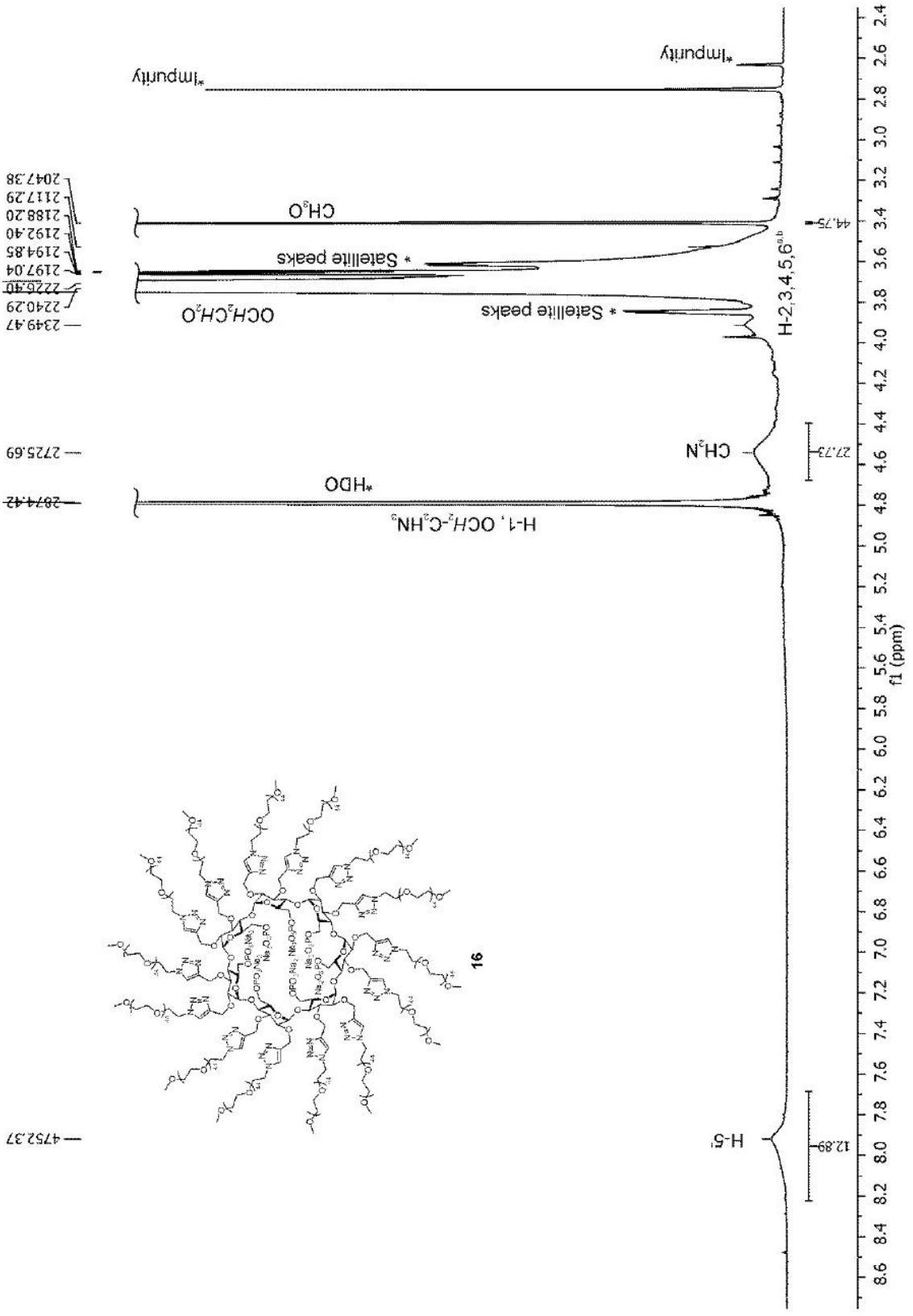

Figure S10. ^{1}H NMR spectrum (600 MHz, D_2O, 25 ºC) for compound **16**

II. ^{13}C-NMR spectra for compounds 3, 5-10 and 14-16

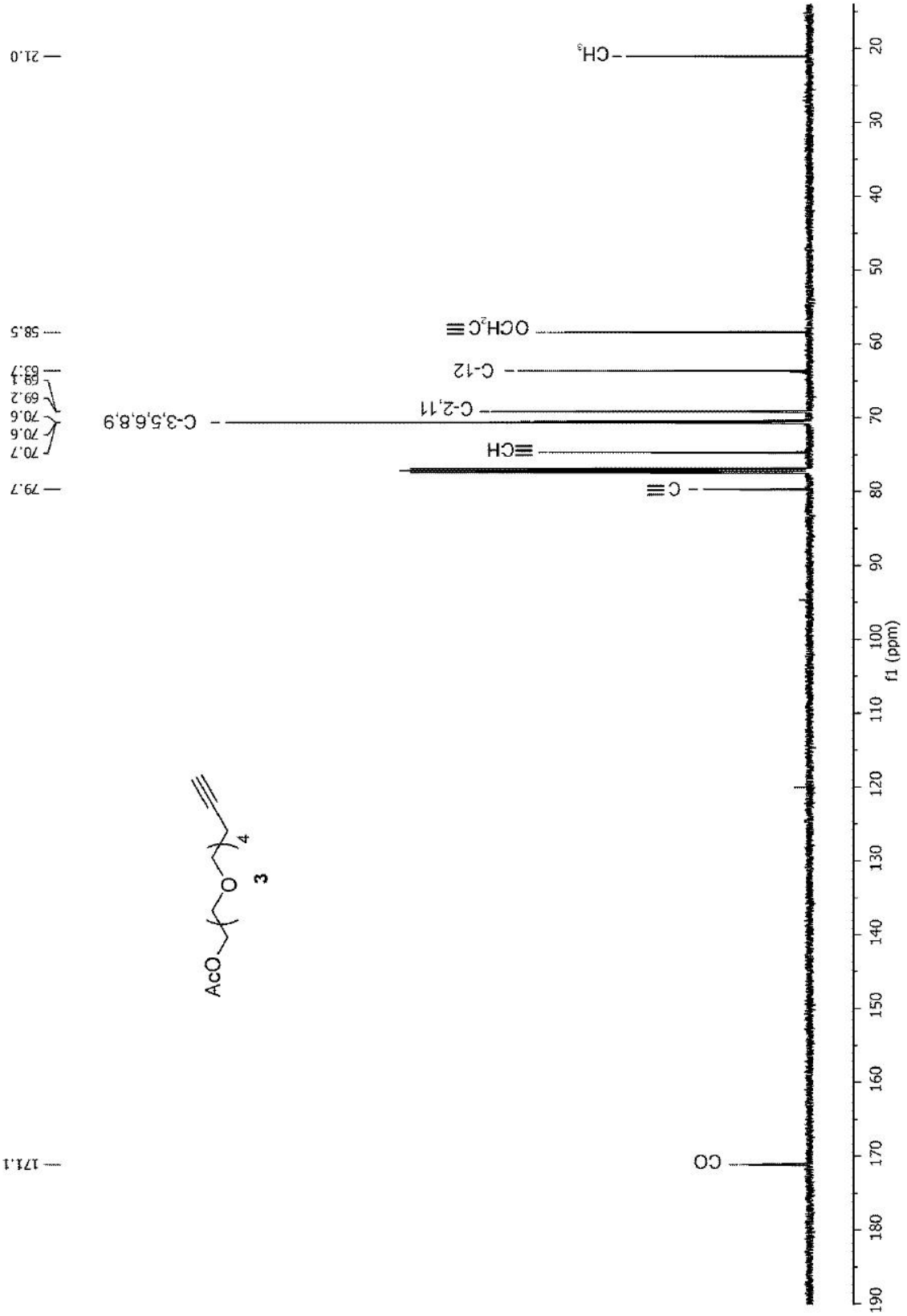

Figure S11. ^{13}C NMR spectrum (125 MHz, $CDCl_3$, 25 °C) for compound **3**

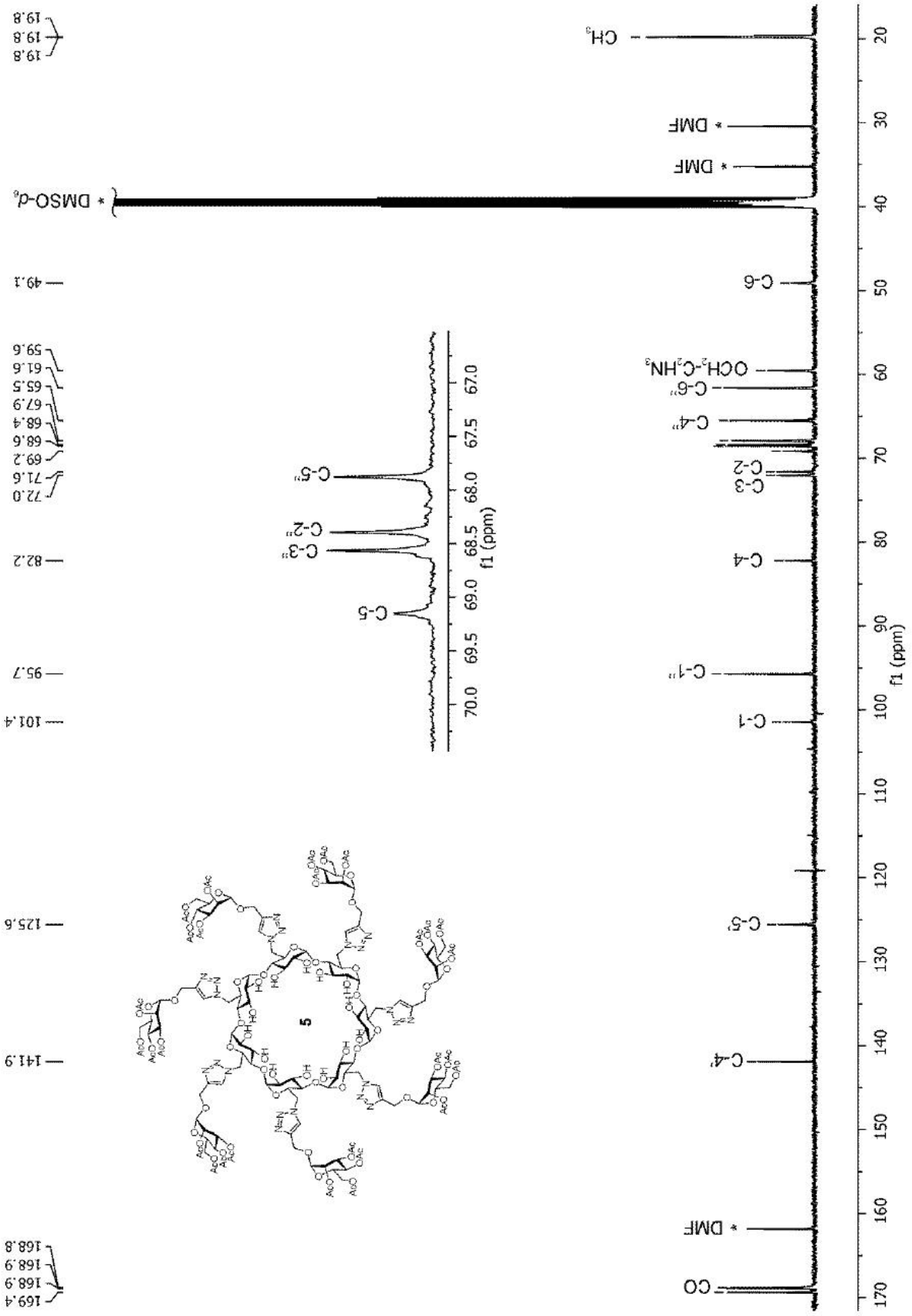

Figure S12. ^{13}C NMR spectrum (125 MHz, DMSO-d_6, 80 ºC) for compound **5**

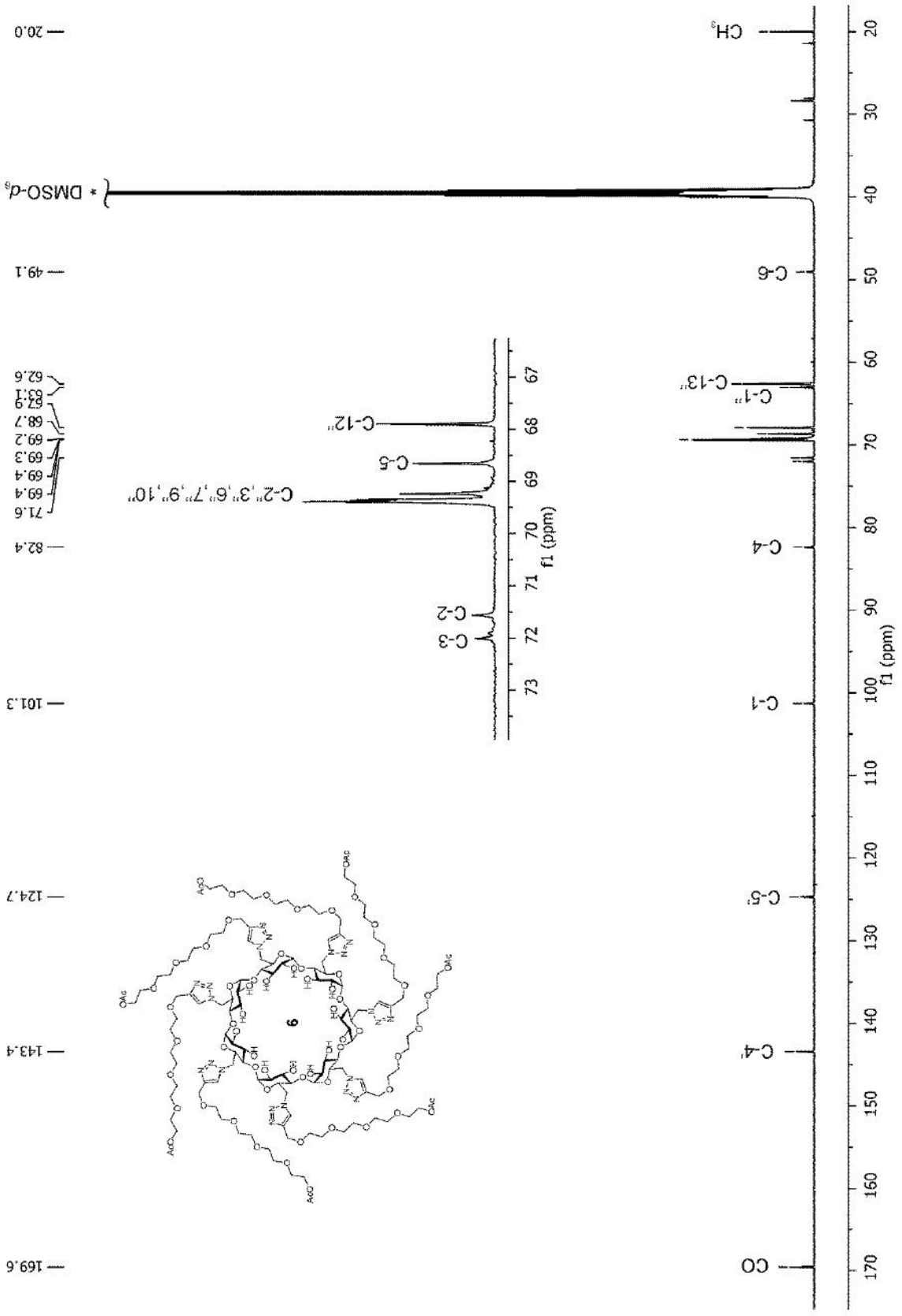

Figure S13. ^{13}C NMR spectrum (125 MHz, DMSO-d_6, 80 ºC) for compound **6**

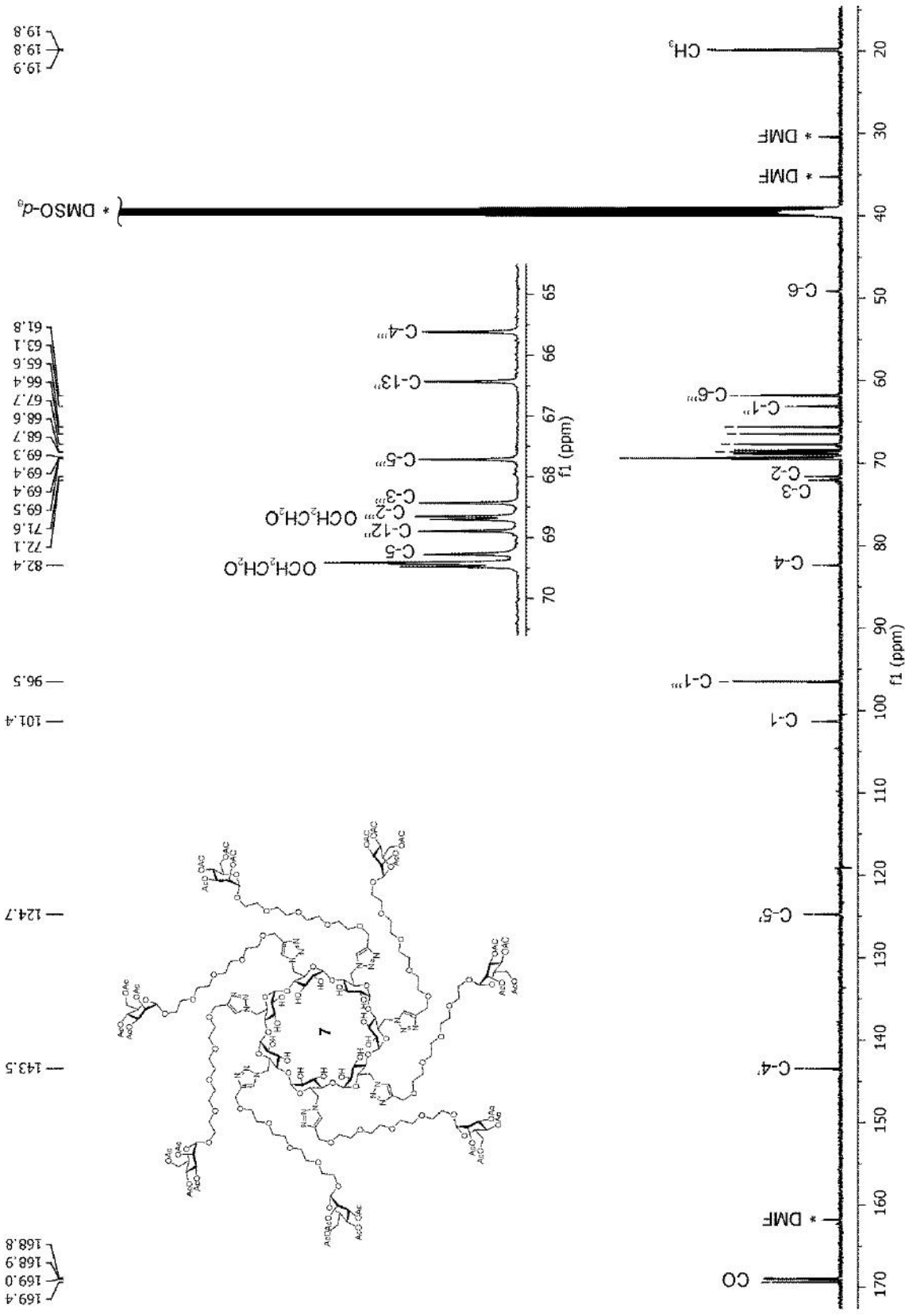

Figure S14. ^{13}C NMR spectrum (125 MHz, DMSO-d_6, 80 ºC) for compound **7**

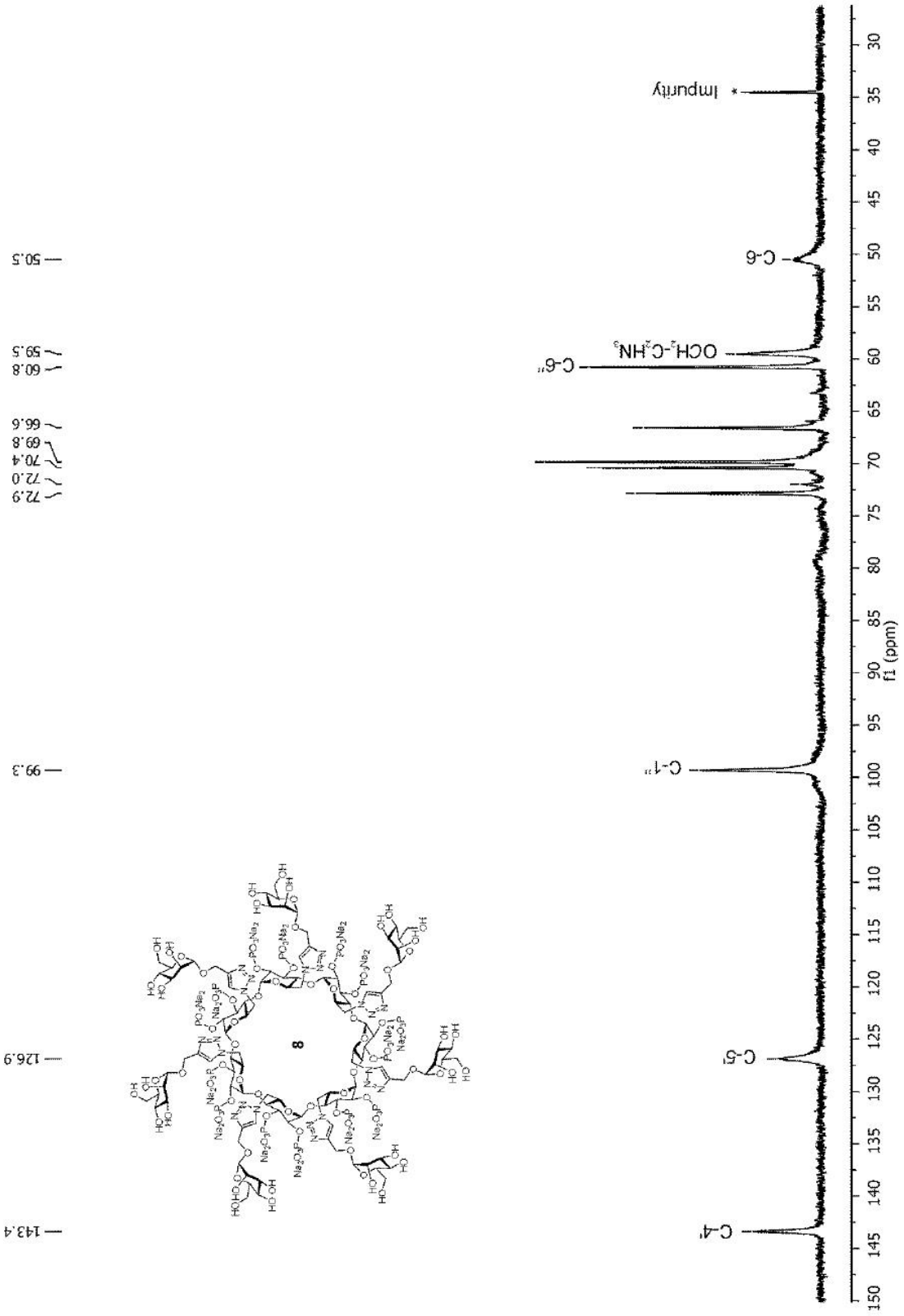

Figure S15. ^{13}C NMR spectrum (150 MHz, D_2O, 25 ºC) for compound **8**

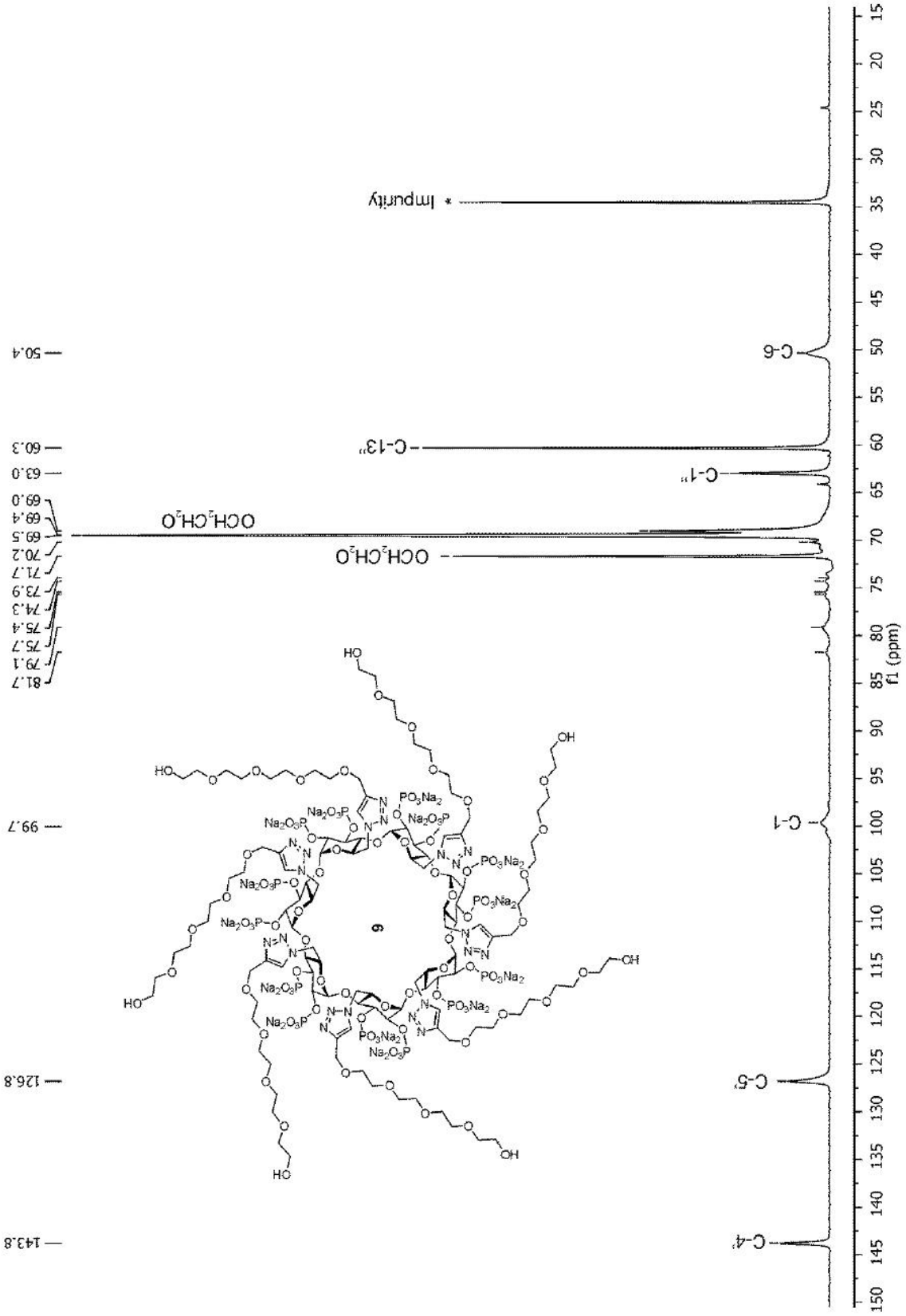

Figure S16. ^{13}C NMR spectrum (150 MHz, D_2O, 25 ºC) for compound **9**

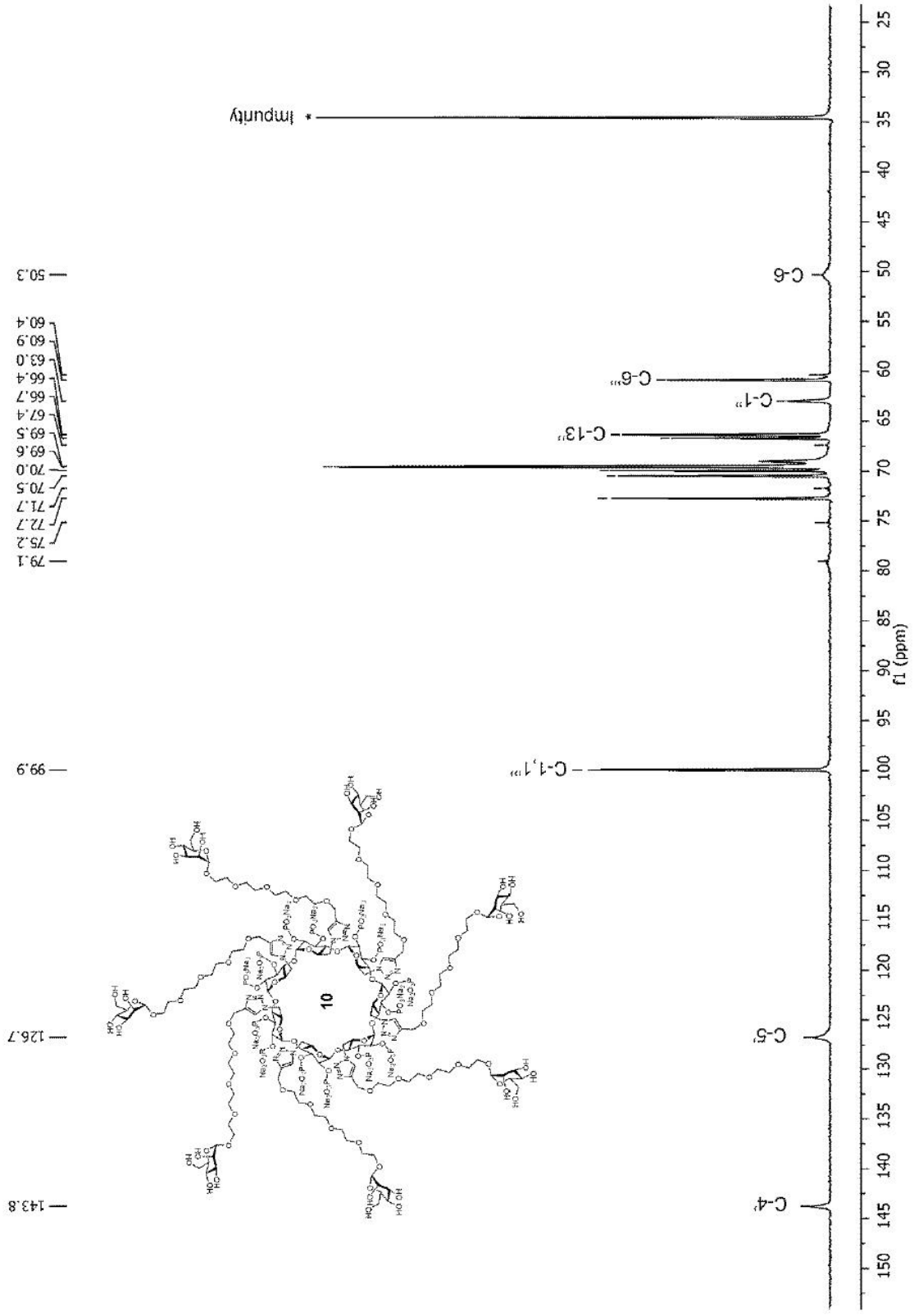

Figure S17. ^{13}C NMR spectrum (150 MHz, D_2O, 25 ºC) for compound **10**

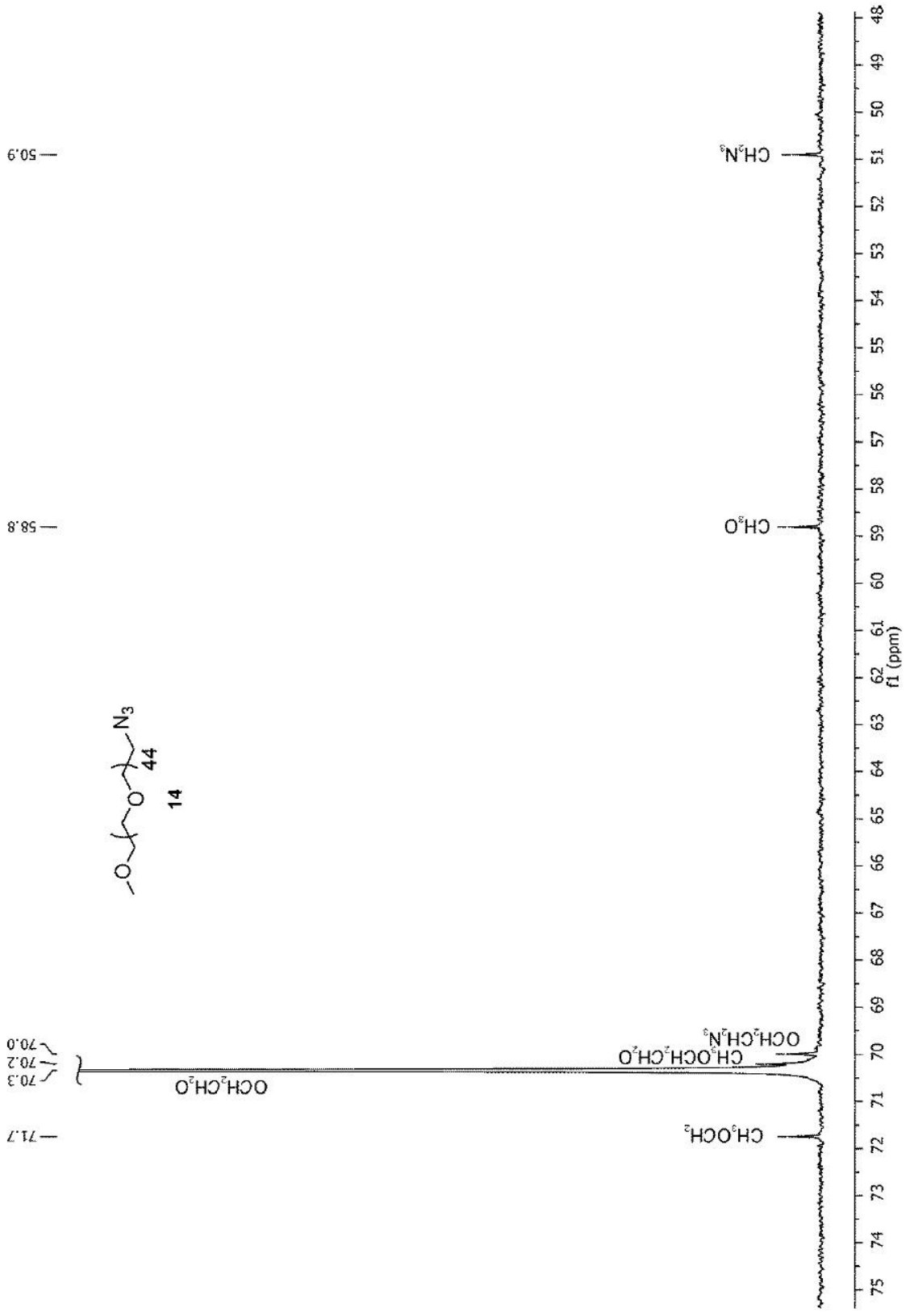

Figure S18. ^{13}C NMR spectrum (75 MHz, D_2O, 25 ºC) for compound **14**

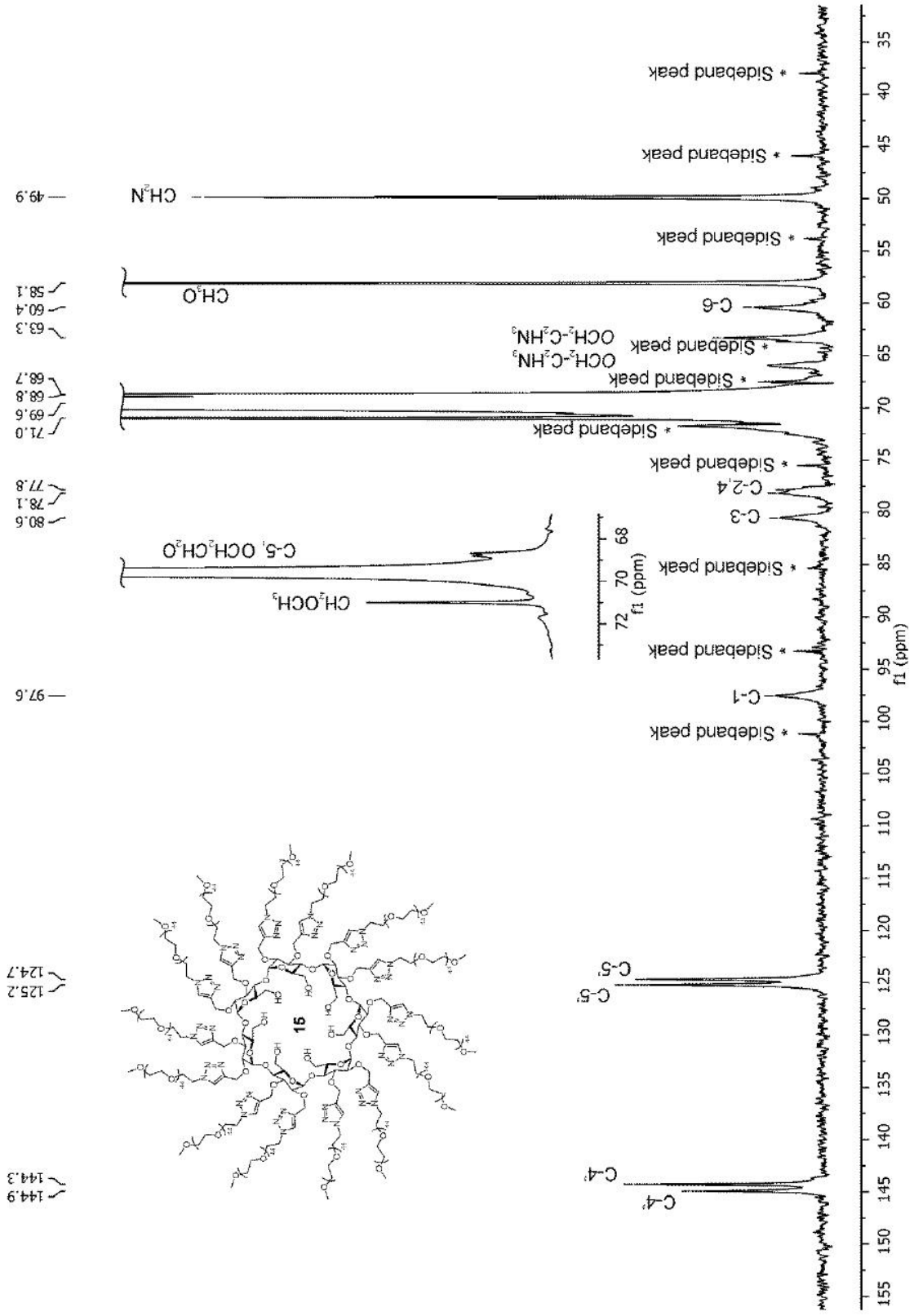

Figure S19. ^{13}C NMR spectrum (150 MHz, D_2O, 25 ºC) for compound **15**

III. ^{31}P-NMR spectra for compounds 8-10 and 16

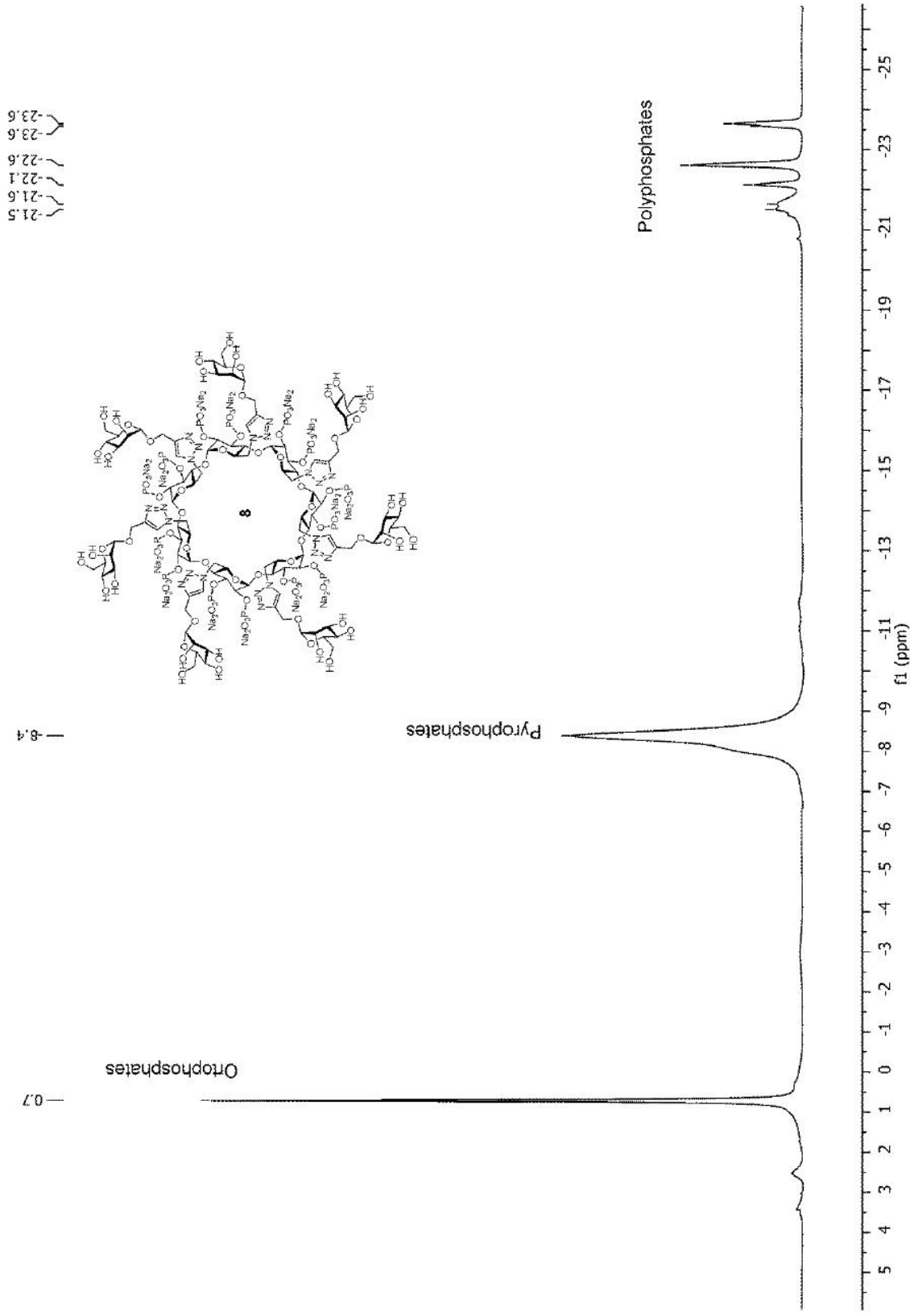

Figure S20. ^{31}P NMR spectrum (242.9 MHz, D_2O, 25 °C) for compound **8**

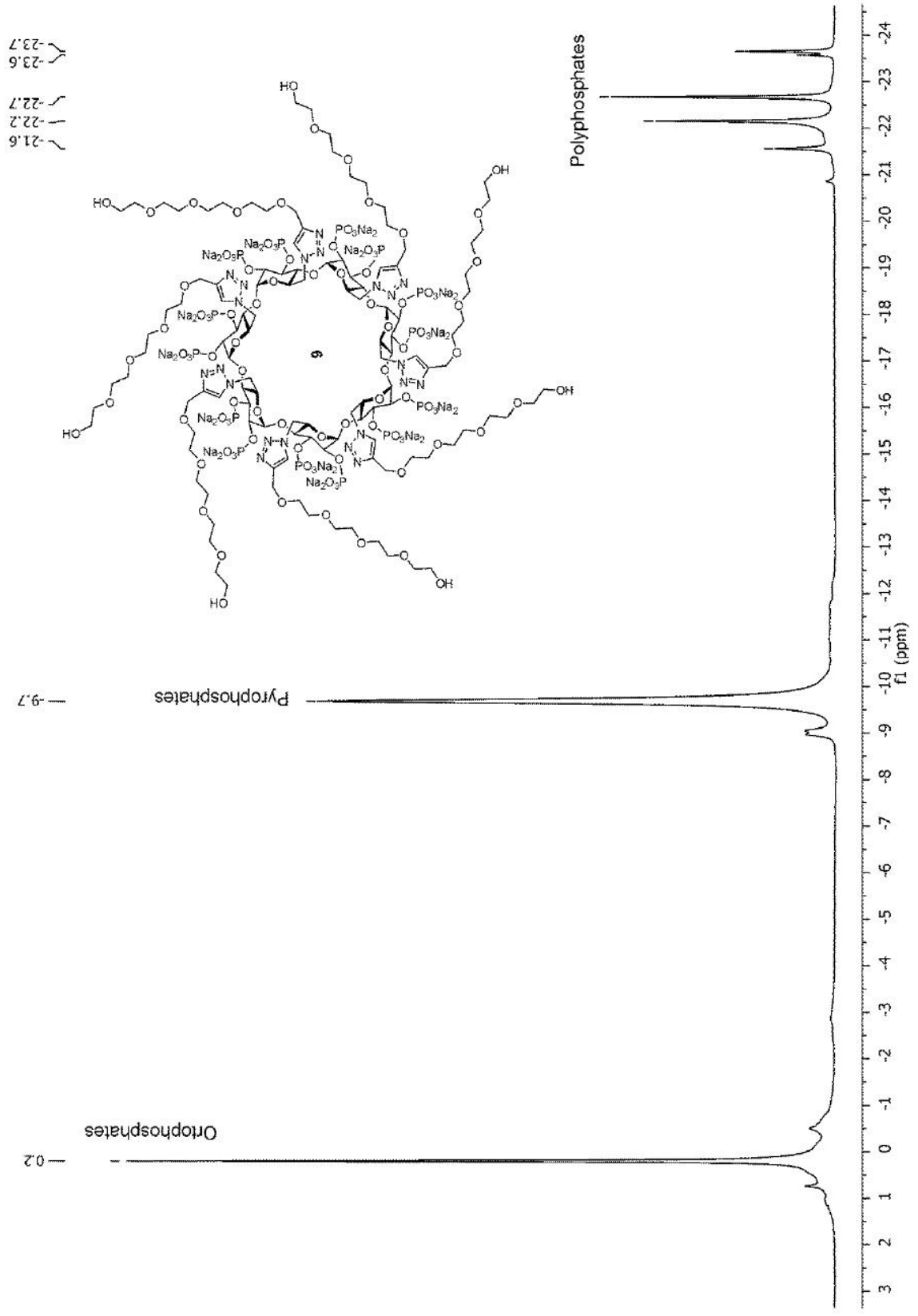

Figure S21. ^{31}P NMR spectrum (242.9 MHz, D_2O, 25 ºC) for compound **9**

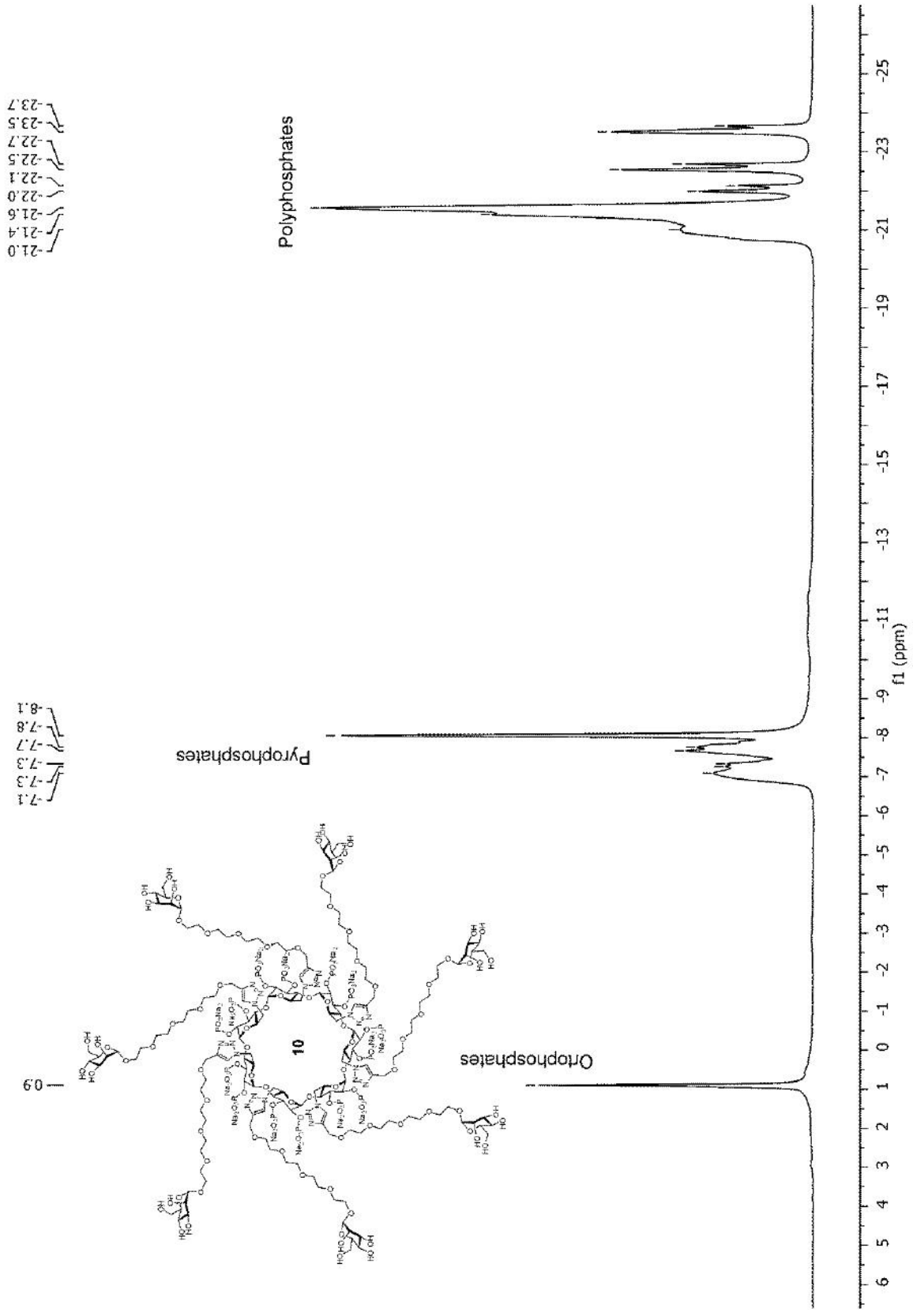

Figure S22. ^{31}P NMR spectrum (242.9 MHz, D_2O, 25 ºC) for compound **10**

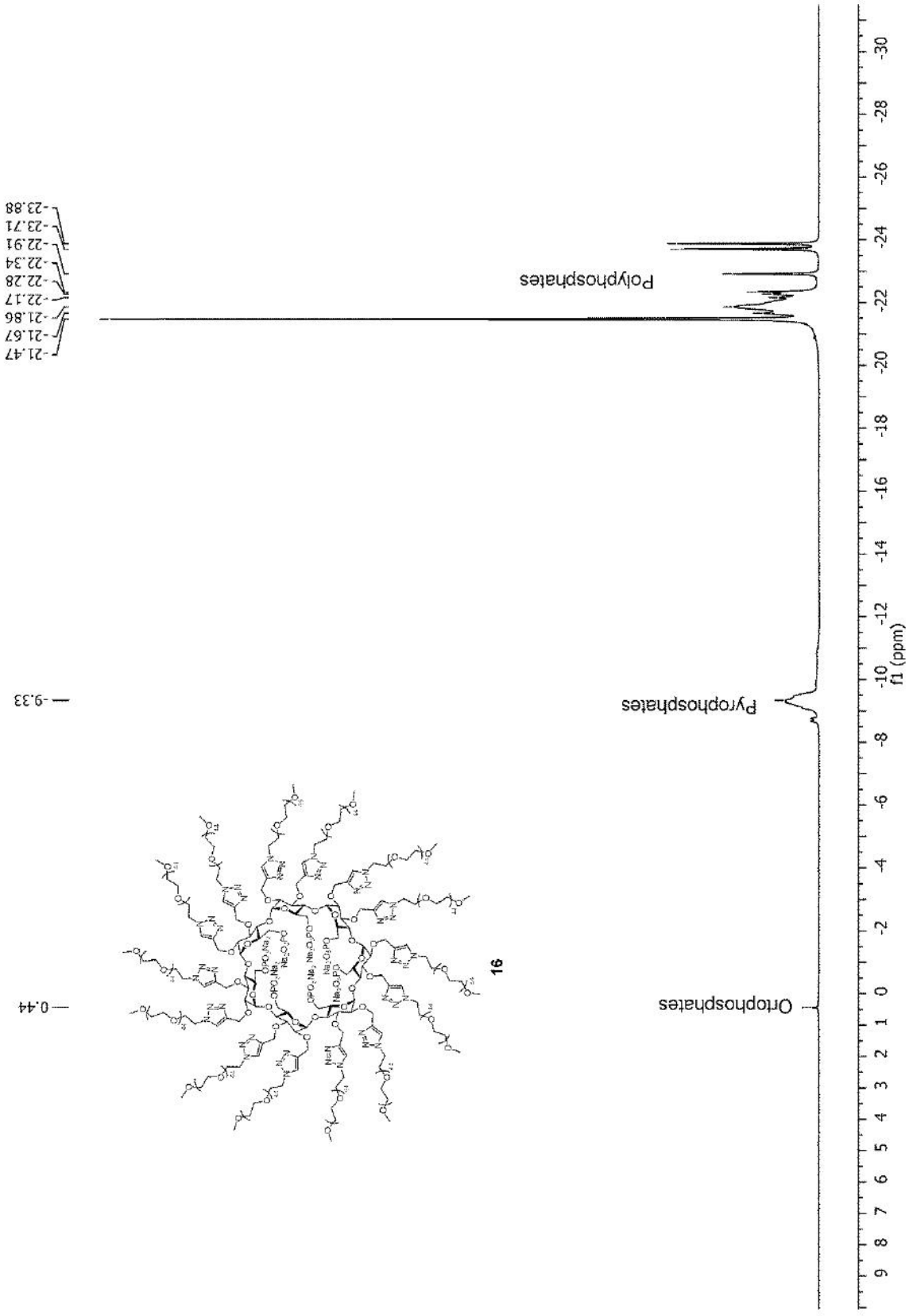

Figure S23. ^{31}P NMR spectrum (242.9 MHz, D_2O, 25 ºC) for compound **16**

IV. Determination of the number of phosphate groups for compounds 10-12 and 18

In order to estimate the number of phosphate groups presents on the structure of compounds **8-10** and **16**, we measured the %P w/w for each compound by HR-ICP-MS. Taking into account phosphorylation conditions that we have used during the synthesis, where an excess of P_2O_5 at 40 ºC was added, we assume that all free OH groups were phosphorylated in some extent to form orto-, pyro- and/or polyphosphate groups, according to the following reaction:

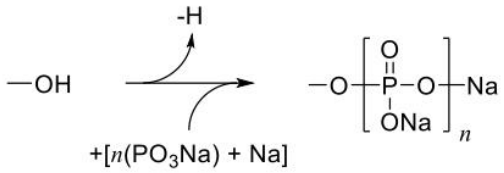

For a given molecule that contains phosphorus, we can define %P as:

$$\%\mathrm{P} = \frac{n\,x\,\mathrm{AW_P}}{\mathrm{MW}}\,x\,100 \qquad (1)$$

where n is the number of atoms of P, $\mathrm{AW_P}$ is the atomic weight of P, and MW is the molecular weight of the phosphorylated molecule.

If we assume that all free OH groups were phosphorylated, for cyclodextrin derivatives **8**-**10** having 14 free OH groups on secondary face, equation (1) can be convert into:

$$\%\mathrm{P}(\mathbf{8\text{-}10}) = \frac{n\,x\,\mathrm{AW_P}}{\mathrm{MW_{(8-10)}} - 14\mathrm{H} + n(\mathrm{PO_3Na}) + 14\mathrm{Na}}\,x\,100 \qquad (2)$$

where $\mathrm{MW_X}$ is the molecular weight of molecules **8**-**10**.

In the case of derivative **16** having only 7 free OH groups on the primary face, the equation (1) remains as:

$$\%\mathrm{P}(\mathbf{16}) = \frac{n\,x\,\mathrm{AW_P}}{\mathrm{MW_{16}} - 7\mathrm{H} + n(\mathrm{PO_3Na}) + 7\mathrm{Na}}\,x\,100 \qquad (3)$$

On the basis of equations (2) and (3), %P data obtained by HR-ICP-MS for compounds **8-10** and **16** allowed to estimate the following number of phosphate groups per molecule (n):

Table S1

Derivative	MW	%P (ICP)	Phosphate groups per molecule (n)	Average phosphate residues per free OH
8	2823.41	16.3	35.72	2.55
9	2921.91	15.7	34.03	2.43
10	4056.89	19.9	81.56	5.83
16	30212.48	8.0	106.49	15.21

V. MIL-100(Fe) nanoMOFs synthesis and surface modification

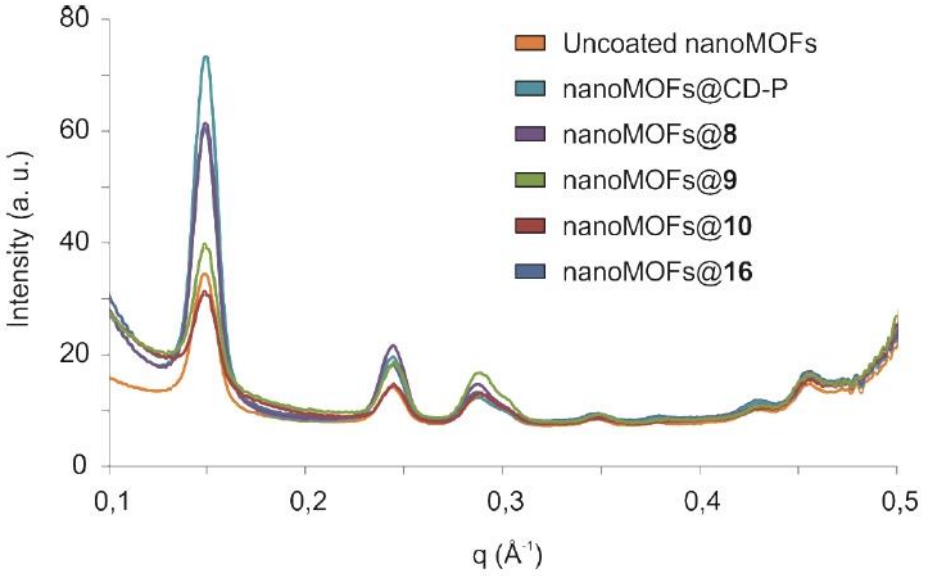

Figure S24. XRPD patterns of uncoated nanoMOFs and nanoMOFs coated with CD-P, **8-10** and **16**. To focus on the signal of the MOF lattice, only the range from 0.1 to 0.5 $Å^{-1}$ is displayed.

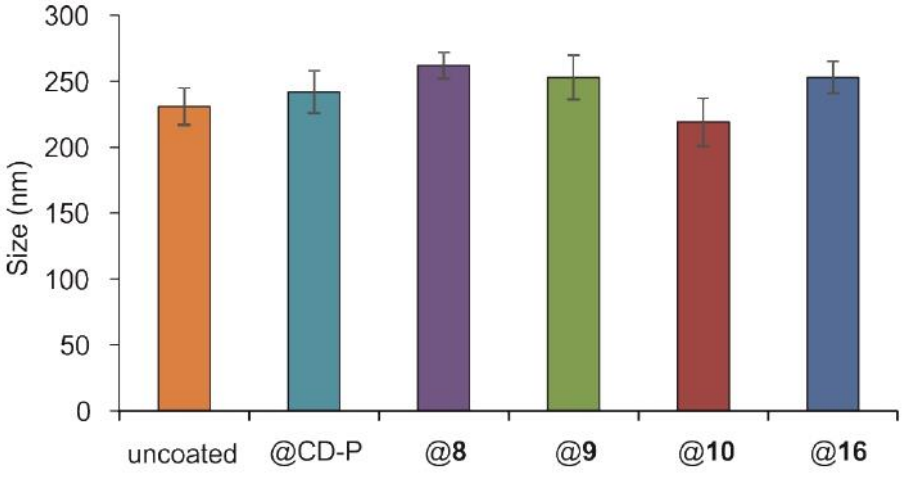

Figure S25. DLS size measurements of uncoated nanoMOFs and nanoMOFs coated with CD-P, **8-10** and **16** after 6 h incubation in DMEM cell culture medium complemented with 10% FBS.

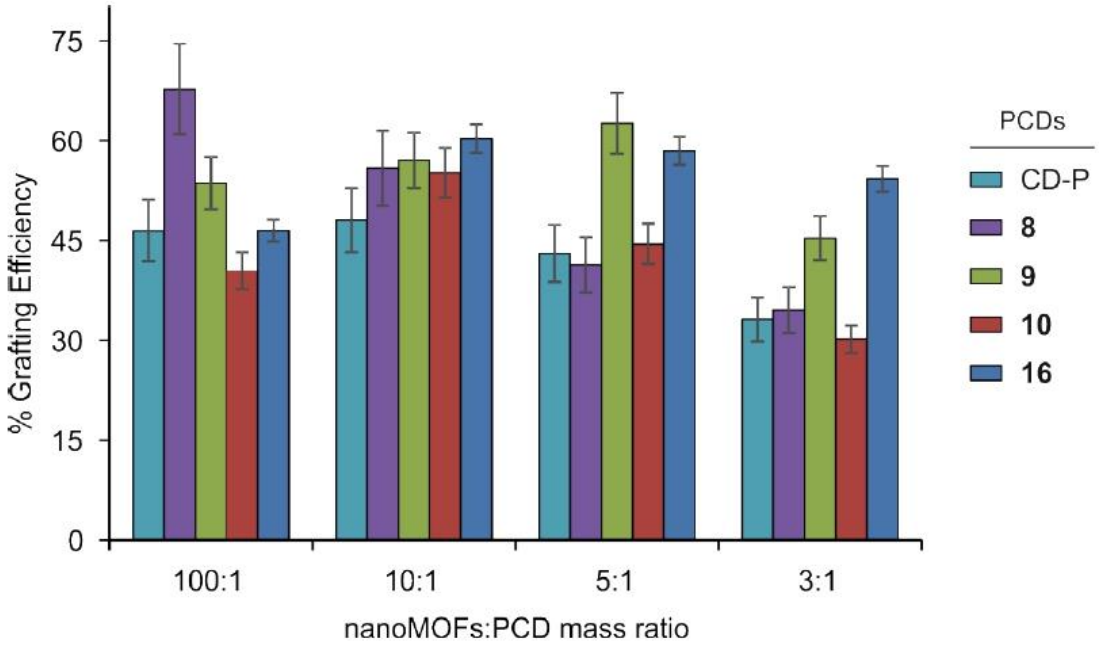

Figure S26. PCDs derivatives grafting efficiency versus nanoMOFs:PCD mass ratio assayed.

VI. ITC experiments for the interaction of 8, 10, nanoMOFs@8 and nanoMOFs@10 with Concanavalin A

Table S2

Conjugate	Buffer	[Conjugate]	[ConA][a] (μM)	Injection (μL)[b]
8	20 mM phosphate, pH 7.2	1.14 mM (syringe)	55.83 (cell)	8
10	20 mM phosphate, pH 7.2	1.29 mM (syringe)	33.61 (cell)	8
nanoMOFs@**8**	10 mM TRIS, pH 7.5	3.28 μM (cell)[c]	66.58 (syringe)	8
nanoMOFs@**10**	10 mM TRIS, pH 7.5	3.88 μM (cell)[c]	72.55 (syringe)	8

[a]Concentration of tetramer of ConA. [b]First injection was 2 μL in all cases. [c]Concentration of phosphates **8** and **10** anchored on the nanoMOFs surface considering an orthophosphate function per each OH group.

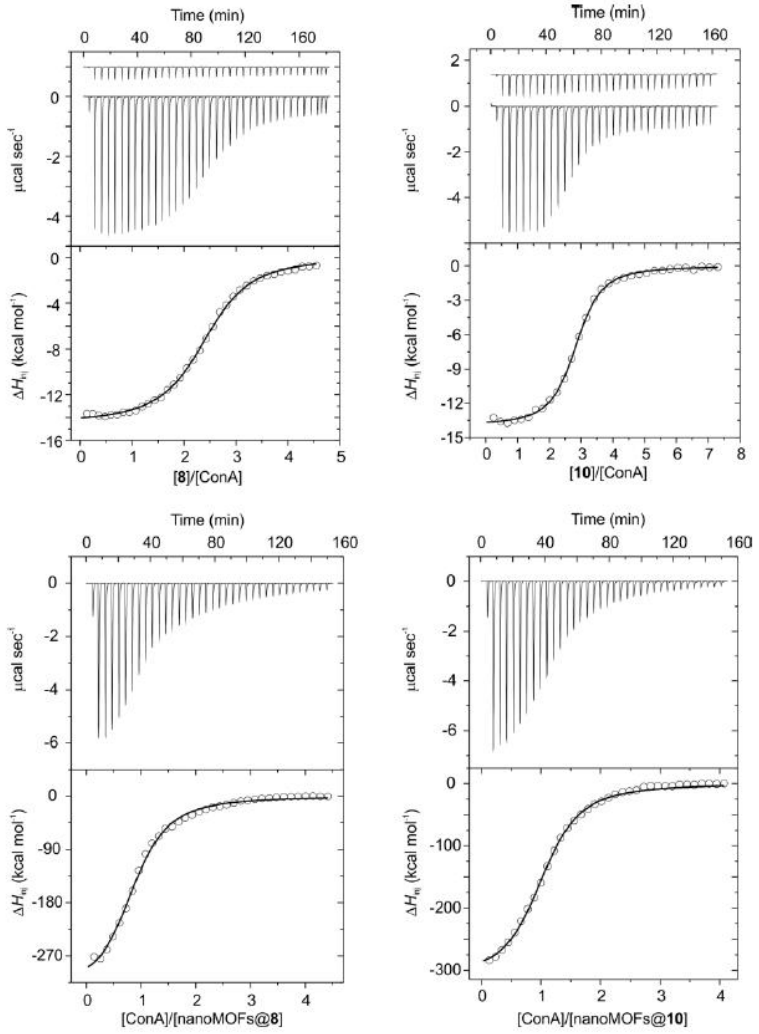

Figure S27. Titration of ConA with conjugates **8** (top, left) and **10** (top, right) in 20 mM phosphate buffer (pH 7.2) at 25 ºC, and titration of conjugates nanoMOFs@**8** (bottom, left) and nanoMOFs@**10** (bottom, right) with ConA in 10 mM TRIS buffer (pH 7.5) at 25 ºC. In all cases, the top panel shows the raw calorimetric data denoting the amount of exchanged heat following each injection of the titrating agent. The area under each peak represents the amount of heat released or absorbed upon binding of each conjugate to the lectin. Note that as the titrations progress the area under the peaks gradually becomes smaller because of the increasing saturation of the sugar binding sites of the protein. This area was integrated and plotted against the molar ratio of the titrating agent in syringe to the analyte in cell. The smooth solid lines represent the best fit of the experimental data to the model of *n* equal and independent binding sites.

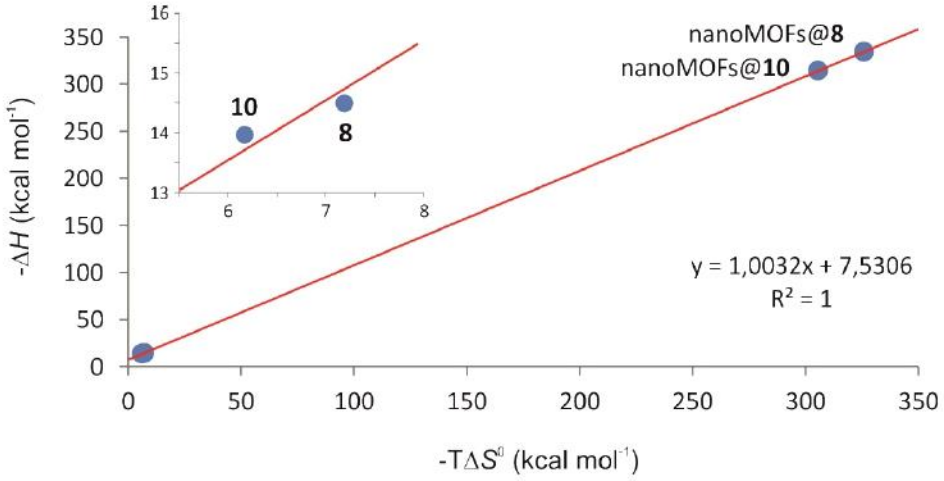

Figure S28. Enthalpy-entropy compensation for the interaction of **8**, **10**, nanoMOFs@**8** and nanoMOFs@**10** with ConA lectin at 25 °C.